

# A L I C E

## Technical Design Report

of the

## Transition Radiation Detector

This edition contains some updates and corrections in Chapters 6 and 12, relative to the first, limited, edition.

Cover: Collage of FaRo chip and AliRoot Event Display of TRD

Cover design by Hans-Jürgen Fuchs, [www.grafux.de](http://www.grafux.de)

Printed at CERN  
September 2001

ISBN 92-9083-184-7

# ALICE Collaboration

---

**Alessandria, Italy**, Facoltà di Scienze dell’Università:  
P. Cortese, G. Dellacasa, L. Ramello, E. Scalas and M. Sitta.

**Aligarh, India**, Physics Department, Aligarh Muslim University:  
N. Ahmad, S. Ahmad, T. Ahmad, W. Bari, M. Irfan., and M. Zafar.

**Athens, Greece**, Nuclear and Particle Physics Division, University of Athens:  
A.L.S. Angelis<sup>1)</sup>, P. Katsas, G. Mavromanolakis, A.D. Panagiotou and M. Spyropoulou-Stassinaki.

**Athens, Greece**, Institute of Nuclear Physics, NRC Demokritos:  
K. Kalfas.

**Bari, Italy**, Dipartimento di Fisica dell’Università and Sezione INFN:  
R. Caliandro, M. Caselle, D. Cozza, G. De Cataldo, D. Di Bari, D. Elia, R.A. Fini, B. Ghidini, V. Lenti,  
V. Manzari, E. Nappi, F. Navach and F. Posa.

**Bari, Italy**, Politecnico and Sezione INFN:  
M. Castellano, F. Corsi, D. De Venuto and C. Marzocca.

**Beijing, China**, China Institute of Atomic Energy:  
X. Li, S. Lu, Z. Lu, B. Sa, J. Yuan, J. Zhou, S. Zhou and X. Zhu.

**Bergen, Norway**, Faculty of Engineering, Bergen College:  
H. Helstrup and J.A. Lien.

**Bergen, Norway**, Department of Physics, University of Bergen:  
A. Klovnning, O.A. Mæland, O.H. Odland, D. Röhrich, R. Rongved, K. Ullaland and A.S. Vestbø.

**Bhubaneswar, India**, Institute of Physics:  
R.K. Choudhury, A.K. Dubey, D.P. Mahapatra, D.K. Mishra, B. Mohanty, S.C. Phatak and R. Sahoo.

**Birmingham, United Kingdom**, School of Physics and Space Research, University of Birmingham:  
I.J. Bloodworth, D. Evans, G.T. Jones, P. Jovanović, J.B. Kinson, P.I. Norman, O. Villalobos Baillie and  
M.F. Votruba.

**Bologna, Italy**, University/INFN:  
F. Anselmo, P. Antonioli, G. Bari, M. Basile, Y.-W. Baek, L. Bellagamba, D. Boscherini, A. Bruni,  
G. Bruni, G. Cara Romeo, E. Cerron-Zeballos, F. Cindolo, M. Corradi, S. De Pasquale, D. Falchieri,  
A. Gabrielli, E. Gandolfi, P. Giusti, D. Hatzifotiadou, G. Laurenti, M.L. Luvisetto, A. Margotti,  
M. Masetti, S. Morosov, R. Nania, F. Palmonari, A. Pesci, F. Pierella, A. Polini, G. Sartorelli, G. Scioli,  
G. Valenti, M.C.S. Williams<sup>1)</sup> and A. Zichichi.

**Bratislava, Slovakia**, Faculty of Mathematics and Physics, Comenius University:  
J. Braciník, V. Černý, J. Ftáčnik, V. Hlinka, R. Janík, R. Lietava, M. Pikna, J. Pišút, N. Pišútová,  
P. Rosinsky, B. Sitar, P. Strmeň, I. Szarka and M. Zagiba.

**Bucharest, Romania**, National Institute for Physics and Nuclear Engineering:  
C. Aiftimiei, A. Andronic, V. Cataneșcu, M. Ciobanu, M. Duma, C.I. Legrand, D. Moisa, M. Petrovici,  
A. Radu and G. Stoicea.

**Budapest, Hungary**, KFKI Research Institute for Particle and Nuclear Physics, Hungarian Academy of Sciences:

E. Denes, B. Eged, Z. Fodor, T. Kiss, G. Palla, C. Soos, J. Sulyan, J. Sziklai and J. Zimanyi.

**Cagliari, Italy**, Dipartimento di Fisica dell'Università and Sezione INFN:

C. Cicalóo, A. De Falco, M.P. Macciotta-Serpi, A. Masoni, D. Mura, G. Puddu, S. Serci, E. Siddi, L. Tocco and G. Usai.

**Calcutta, India**, Saha Institute of Nuclear Physics:

P. Bhattacharya, S. Bose, Sukalyan Chattopadhyay, L. Das, P. Datta, T. Ghosh, N. Majumdar, S. Mukhopadhyay, S. Pal, R. Saha, A. Sanyal, S. Sarkar, P. Sen, S.K. Sen, B.C. Sinha and T. Sinha.

**Calcutta, India**, Variable Energy Cyclotron Centre:

Subhasis Chattopadhyay, S. Das, M.R. Dutta Majumdar, M.S. Ganti, P. Ghosh, T.K. Nayak, S. Pal, R.N. Singaraju, Bikash Sinha, M.D. Trivedi and Y.P. Viyogi.

**Catania, Italy**, Dipartimento di Fisica dell'Università and Sezione INFN:

A. Badalà, R. Barbera, F. Librizzi, G. Lo Re, A. Palmeri, G.S. Pappalardo and F. Riggi.

**CERN, Switzerland**, European Organization for Nuclear Research:

G. Anelli, I. Augustin, A. Augustinus, J. Bächler, A. Braem, R. Brun, P. Buncic<sup>2)</sup>, R. Campagnolo, M. Campbell, F. Carena, W. Carena, F. Carminati, N. Carrer, P. Chochula<sup>3)</sup>, J. Christiansen, J. Chudoba, M. Davenport, J. de Groot, A. Di Mauro, R. Dinapoli, R. Divià, C. Eisenberg, C. Engster, R. Esteve Bosch, C. Fabjan, A. Fasso, F. Formenti, A. Gheata, P. Giubellino, I. Gonzalez Caballero, C. Gregory, M. Hoch, P. Hristov, I. Hrivnacova, P. Jarron, A. Jimenez de Parga, L. Jirden, C. Joram, A. Kluge, L. Leistam, C. Lourenço, J.-C. Marin, P. Martinengo, M. Masera, T. Meyer, P.R. Moreira, A. Moronval, A. Morsch, B. Mota, L. Musa, G. Paic, D. Perini, F. Piuz, S. Popescu, F. Rademakers, J.-P. Revol, P. Riedler, K. Šafařík, P. Saiz, J.-C. Santiard, K. Schossmaier, J. Schukraft, E. Schyns, W. Snoeys, C. Soos, G. Stefanini, D. Swoboda, P. Szymanski, H. Taureg, J. Van Hunen, P. Vande Vyvre, A. Vascotto, M.C.S. Williams, and K. Wyllie.

**Chandigarh, India**, Physics Department, Panjab University:

M.M. Aggarwal, A.K. Bhatia, V.S. Bhatia and G. Sood.

**Clermont-Ferrand, France**, Laboratoire de Physique Corpusculaire (LPC), IN2P3-CNRS and Université Blaise Pascal:

IN2P3: A. Baldit, V. Barret, N. Bastid, G. Blanchard, J. Castor, T. Chambon, P. Crochet, F. Daudon, A. Devaux, P. Dupieux, B. Espagnon, P. Force, B. Forestier, A. Genoux-Lubain, C. Insa, F. Jouve, L. Lamoine, J. Lecoq, F. Manso, L. Royer, P. Saturnini, G. Savinel and P. Rosnet.

**Coimbra, Portugal**, Departamento de Física, Faculdade de Ciências e Tecnologia:

R. Ferreira Marques, P. Fonte, J. Pinhao and A. Policarpo.

**Columbus, U.S.A.**, Department of Physics, Ohio State University:

H.M. Dyke, K. Flurchik, T.J. Humanic, D. Johnson, I.V. Kotov, M. Lisa, B.S. Nilsen, G. Paic<sup>1)</sup>, T.C. Randles and E. Sugarbaker.

**Copenhagen, Denmark**, Niels Bohr Institute:

I. Bearden, H. Bøggild, P. Christiansen, J.J. Gaardhøje, O. Hansen, A. Holm, B.S. Nielsen and D. Ouerdane.

**Cracow, Poland**, Henryk Niewodniczanski Institute of Nuclear Physics, High Energy Physics Department:

J. Bartke, E. Gładysz-Dziaduś, E. Górnicki, M. Kowalski, A. Rybicki and Z. Włodarczyk<sup>5)</sup>.

**Darmstadt, Germany**, Gesellschaft für Schwerionenforschung (GSI):

A. Andronic<sup>4)</sup>, E. Badura, C. Blume, P. Braun-Munzinger, O. Busch, A. Castillo-Ramirez, M. Ciobanu<sup>4)</sup>, M. Dahlinger, H.W. Daues, A. Devismes, C. Finck, P. Foka, U. Frankenfeld, C. Garabatos, I. Giese, H. Göringer, H.H. Gutbrod, G. Hering, M. Ivanov<sup>3)</sup>, J. Lühning, P. Malzacher, A. Marin, A. Mischke, D. Miśkowiec, W.F.J. Müller, H. Sako, A. Sandoval, H. Sann, H.R. Schmidt, K. Schwarz, S. Sedykh, H. Stelzer, R. Veenhof and D. Vranic.

**Darmstadt, Germany**, Institut für Kernphysik, Technische Universität:

U. Bonnes, A. Förster, H. Oeschler and F. Uhlig.

**Frankfurt, Germany**, Institut für Kernphysik, Johann Wolfgang Goethe-Universität:

C. Adler, W. Amend, J. Berger, J. Berschin, R. Bramm, D. Flierl, M. Gaździcki, J. Hehner, S. Lange, R. Renfordt, H. Rheinfels-Immans, R. Stock, H. Ströbele and C. Struck.

**Gatchina, Russia**, St. Petersburg Nuclear Physics Institute:

B. Komkov, N. Miftakhov, V. Nikouline, V. Polyakov, E. Roschin, V. Samsonov, V. Tarasenkov, O. Tarasenkova, G. Solodov, S. Volkov and Y.A. Berdnikov.

**Heidelberg, Germany**, Kirchhoff Institute for Physics:

R. Achenbach, V. Angelov, J. de Cuveland, M. Dorn, P. Hanke, L. Hess, F.O. Lesser, V. Lindenstruth, S. Martens, S. Philipp, F. Pister, C. Reichling, F. Rettig, T. Steinbeck, R. Schneider, U. Trunk and A. Wiebalck.

**Heidelberg, Germany**, Physikalisches Institut, Ruprecht-Karls Universität:

H. Appelhäuser, V. Catanescu<sup>4)</sup>, S. Damjanovic, L. Dietrich, P. Glässel, N. Herrmann, W. Ludolphs, T. Mahmoud, J. Milosevic, V. Petráček, I. Rusanov, R. Schicker, W. Schmitz, J. Slivova, H.K. Soltveit, H.J. Specht, J. Stachel, H. Tilsner, B. Vulpešcu, S. Wende, I. Weimann, J.P. Wessels, B. Windelband, C.C. Xu and S. Yurevich.

**Ioannina, Greece**, University of Ioannina, Department of Physics:

X. Aslanoglou and N.G. Nicolis.

**Jaipur, India**, Physics Department, University of Rajasthan:

R. Raniwala and S. Raniwala.

**Jammu, India**, Physics Department, Jammu University:

S.K. Badyal, A. Bhasin, A. Gupta, V.K. Gupta, S. Mahajan, L.K. Mangotra, B.V.K.S. Potukuchi, N.K. Rao and S.S. Sambyal.

**JINR, Russia**, Joint Institute for Nuclear Research:

P.G. Akichine, V.A. Arefiev, V.I. Astakhov, B.V. Batiounia, I.V. Boguslavsky, Z.V. Borissovskaia, G.S. Chabratova, V. Chepurnov, G. Cheremukhina, S. Chernenko, V.K. Dodokhov, L.G. Efimov, A.A. Efremov, O. Fateev, A.G. Fedounov, K. Fomenko, B.N. Guouskov, A. Ierusalimov, V.G. Kadychevsky, E.K. Koshurnikov, V.L. Lioubochits, V.I. Lobanov, A. Malakhov, E.A. Matiouchevski, K.V. Mikhailov, P.V. Nomokonov, I.A. Olex, Y.A. Panebrattsev, V. Pechenov, V.N. Penev, A. Petrov, I.V. Pouzynin, I. Roufanov, P. Sazhin, S. Shimanskiy, M.V. Shurygina, A.G. Shurygine, L. Smykov, M.K. Suleimanov, A.S. Vodopianov, V. Yurevich, Y. Zanevsky, S.A. Zaporozets and A. Zubarev.

V. Kuznetsov<sup>6)</sup> and V. Shestakov<sup>6)</sup>.

Ts. Baatar<sup>7)</sup>, B. Khurelbaatar<sup>7)</sup> and R. Togoo<sup>7)</sup>.

K.G. Akhobadze<sup>8)</sup>, A.K. Djavrishvili<sup>8)</sup>, T. Grigalashvili<sup>8)</sup>, E.S. Ioramashvili<sup>8)</sup>, A.V. Kharadze<sup>8)</sup>, L. Khizanishvili<sup>8)</sup>, T.V. Khuskivadze<sup>8)</sup>, L.V. Shalamberidze<sup>8)</sup> and N. Shubitidze<sup>8)</sup>.

N. Grigalashvili<sup>9)</sup>, M. Nioradze<sup>9)</sup>, M. Tabidze<sup>9)</sup> and Y. Tevzadze<sup>9)</sup>.

D. Felea<sup>10)</sup>, M. Gheata<sup>10)</sup>, M. Haiduc<sup>10)</sup>, D. Hasegan<sup>10)</sup>, R. Marginean<sup>10)</sup>, C. Ristea and S.I. Zgura<sup>10)</sup>.

**Jyväskylä, Finland**, Department of Physics, University of Jyväskylä and Helsinki Institute of Physics:  
M. Bondila<sup>10)</sup>, M. Komogorov, V. Lyapin, V. Ruuskanen and W. Trzaska.

**Kangnung, South Korea**, Kangnung National University:

H. Chae, C. Choi, Y. Jung, K.S. Kang, D.W. Kim, D. Kim, J. Kim, K. Lee and S. Lee.

**Kharkov, Ukraine**, National Scientific Centre ‘Kharkov Institute of Physics and Technology’:

G.L. Bochek, A.N. Dovbnja, V.I. Kulibaba, N.I. Maslov, S.V. Naumov, S.M. Potin, I.M. Prokhorets and A.F. Starodubtsev.

**Kharkov, Ukraine**, Scientific and Technological Research Institute of Instrument Engineering:

V.N. Borshchov, S.K. Kiprich, O.M. Listratenko, G. Protsay, A.N. Reznik, A.N. Ryabukhin and V.E. Starkov.

**Kiev, Ukraine**, Department of High Energy Density Physics, Bogolyubov Institute for Theoretical Physics, National Academy of Sciences of Ukraine:

E.S. Martynov, S.V. Molodtsov O.P. Pavlenko, G. Zinovjev and Y.M. Sinyukov.

**Košice, Slovakia**, Institute of Experimental Physics, Slovak Academy of Sciences and Faculty of Science P.J. Šafárik University:

J. Bán, M. Hnatič, A. Jusko, I. Králik, A. Kravčáková, F. Kriváň, M. Krivda, M. Lupták, G. Martinská, B. Pastircák, L. Šándor, J. Urbán, S. Vokál and J. Vrláková.

**Lausanne, Switzerland**, Integrated System Laboratory (ISL), Ecole Polytechnique Fédérale de Lausanne (EPFL):

A. Aizza, F.A. Cherigui, M. Mattavelli and D. Mlynek.

**Legnaro, Italy**, Laboratori Nazionali di Legnaro:

M. Cinausero, M. Lombardi, R.A. Ricci and L. Vannucci.

**Lisbon, Portugal**, Departamento de Física, Instituto Superior Técnico:

P. Branco, R. Carvalho, J. Seixas and R. Vilela Mendes.

**Lund, Sweden**, Division of Cosmic and Subatomic Physics, University of Lund:

L. Carlen, S.I.A. Garpman, H.-A. Gustafsson, P. Nilsson, J. Nystrand, A. Oskarsson, L. Osterman, I. Otterlund, R. du Rietz, D. Silvermyr, E.A. Stenlund and H. Tydesjo.

**Lyon, France**, Institut de Physique Nucléaire de Lyon (IPNL), IN2P3-CNRS and Université Claude Bernard Lyon-I:

M.Y. Chartoire, B. Cheynis, L. Ducroux, E. Gangler, M. Goyot, J.Y. Grossiord, R. Guernane, A. Guichard, G. Jacquet and S. Tissot.

**Mexico City, Mexico**, Centro de Investigación y de Estudios Avanzados (CINVESTAV) and Instituto de Ciencias Nucleares and Instituto de Fisica (UNAM):

R. Alfaro, A. Ayala, E. Belmont, J.G. Contreras, E. Cuautle, J.C. D'Olivo, G. Herrera Corral, A. Martinez, J. Martinez, A. Menchaca, L.M. Montaño and L. Nellen.

**Moscow, Russia**, Institute for Nuclear Research, Academy of Science:

K.A. Chileev, M.B. Goloubeva, F.F. Gouber, O. Karavichev, T.L. Karavitcheva, E. Karpechev, A.B. Kourepin, A.I. Maevskaia, V. Marin, I. Pshenichnov, V.I. Razine, A.I. Rechetine, V. Tiflov and N.S. Topilskaia.

**Moscow, Russia**, Institute for Theoretical and Experimental Physics:

A.N. Akindinov, V. Golovine, A.B. Kaidalov, M.M. Kats, I.T. Kiselev, S.M. Kiselev, E. Lioublev, M. Martemianov, A.N. Martemyanov, P.A. Polozov, V.S. Serov, A.V. Smirnitski, M.M. Tchoumakov, I.A. Veltlitski, K.G. Volochine, L.S. Vorobiev and B.V. Zagreev.

**Moscow, Russia**, Russian Research Center ‘Kurchatov Institute’:

V. Antonenko, S. Beliaev, I. Doubrovik, S. Fokine, M. Ippolitov, K. Karadjev, A.L. Lebedev, V. Lebedev, V.I. Manko, T. Moukhanova, A. Nianine, S. Nikolaev, S. Nikouline, O. Patarakine, D. Peressounko, I. Sibiriak, A. Vasiliev, A. Vinogradov and M. Volkov.

**Moscow, Russia**, Moscow Engineering Physics Institute:

V.A. Grigoriev, V.A. Kapline and V.A. Loguinov.

**Münster, Germany**, Institut für Kernphysik, Westfälische Wilhelms Universität:

D. Bucher, R. Glasow, N. Heine, S. Keßen, T. Lister, T. Peitzmann, K. Reygers, R. Santo, W. Verhoeven, O. Winkelmann and O. Zaudtke.

**Nantes, France**, Laboratoire de Physique Subatomique et des Technologies Associées (SUBATECH), Ecole des Mines de Nantes, IN2P3-CNRS and Université de Nantes:

L. Aphecetche, A. Boucham, S. Bouvier, H. Carduner, D. Charrier, J.P. Cussonneau, H. Delagrange, D. D'Enterria, M. Dialinas, M. Diaz, C. Drancourt, B. Erasmus, L. Lakehal-Ayat, P. Lautridou, F. Lefèvre, M. Le Guay, L. Luquin, L. Martin, G. Martinez-Garcia, P. Pichot, G. Puil, O. Ravel, C.S. Roy, D. Roy, Y. Schutz and A. Tournaire.

**NIKHEF, The Netherlands**, National Institute for Nuclear and High Energy Physics:

M. Botje<sup>11)</sup>, A. Buijs<sup>12)</sup>, J.J.F. Buskop<sup>11)</sup>, A.P. De Haas<sup>12)</sup>, R. Kamermans<sup>11,12)</sup>, P.G. Kuijer<sup>11,12)</sup>, G. Nooren<sup>11)</sup>, C.J. Oskamp<sup>12)</sup>, A. Van Den Brink<sup>12)</sup> and N. Van Eijndhoven<sup>12)</sup>.

**Novosibirsk, Russia**, Budker Institute for Nuclear Physics:

A.R. Frolov and I.N. Pestov.

**Oak Ridge, U.S.A.**, Instrumentation and Controls Division, Oak Ridge National Laboratory:

T. Awes, C.L. Britton, W.L. Bryan and A.L. Wintenberg.

**Orsay, France**, Institut de Physique Nucléaire (IPNO), IN2P3-CNRS and Université de Paris-Sud:

M.-P. Comets, P.F. Courtat, P. Edelbruck, B. Espagnon, D. Guez, Y. Le Bornec, M. Mac Cormick, J. Peyré, J. Pouthas, S. Rousseau and N. Willis.

**Oslo, Norway**, Department of Physics, University of Oslo:

A.K. Holme, G. Løvhøiden, B. Skaali, T.S. Tveter and D. Wormald.

**Padua, Italy,** Dipartimento di Fisica dell'Università and Sezione INFN:

F. Antinori<sup>1)</sup> N. Carrer, A. Dainese, D. Fabris, M. Morando, G. Nebbia, A. Pepato, E. Quercigh, F. Scarlassara, G. Segato, R. Turrisi and G. Viesti.

**Pohang, South Korea,** Pohang Accelerator Laboratory:

J. Choi, M.G. Kim, T.Y. Lee and E.S. Park.

**Prague, Czech Republic,** Institute of Physics, Academy of Science:

A. Beitlerova, J.A. Mareš, E. Mihoková, M. Nikl, K. Přška, K. Polák and P. Závada.

**Protvino, Russia,** Institute for High Energy Physics:

A.M. Blik, M. Bogolyubsky, G. Britvitch, G.V. Khaoustov, I.V. Kharlov, S. Konstantinov, M. Lobanov, N. Minaev, V. Petrov, B. Polichtchouk and S.A. Sadovski.

**Řež u Prahy, Czech Republic,** Academy of Sciences of Czech Republic, Nuclear Physics Institute:

D. Adamová, V. Hanzal, J. Hošek, I. Hřivnáčová<sup>1)</sup>, S. Kouchpil, V. Kouchpil, A. Kugler, M. Šumbera, P. Tlustý, V. Wagner and D. Zákoucký.

**Rome, Italy,** Dipartimento di Fisica, Università di Roma 'La Sapienza' and Sezione INFN:

S. Di Liberto, M.A. Mazzoni, F. Meddi<sup>1)</sup>, D. Prosperi and G. Rosa.

**Saclay, France,** Centre d'Etudes Nucléaires, DAPNIA:

A. Baldisseri, H. Borel, P. De Girolamo, J. Gosset, J.-C. Lugol, F. Orsini, S. Salasca and F.M. Staley.

**Salerno, Italy,** Dipartimento di Scienze Fisiche 'E.R.Caianiello' dell'Università and INFN:

L. Cifarelli, A. De Caro, A. Di Bartolomeo, M. Fusco Girard, G. Grella, M. Guida, J. Quartieri, G. Romano, S. Sellitto, D. Vicinanza and T. Virgili.

**Sarov, Russia,** Russian Federal Nuclear Center (VNIIEF):

V. Basmanov, D. Budnikov, V. Ianowski, R. Ilkaev, L. Ilkaeva, A. Ivanov, A. Khlebnikov, E. Kolokolnikov, S. Nazarenko, V. Punin, S. Poutevskoi, I. Selin, I. Vinogradov, S. Zhelezov and A. Zhitnik.

**Shanghai, China,** Shanghai Institute of Ceramics (SICCAS):

Q. Deng, P. Li, J. Liao and D. Yan.

**St. Petersburg, Russia,** Institute for Physics of St. Petersburg State University, Mendeleev Institute for Metrology and Meson Scientific Association:

L.Y. Abramova, V.S. Alexandrov, P. Bolokhov, A.A. Bolonine, M.A. Braun, V.M. Dobulevitch, G.A. Feofilov, S. Guerassimov, S.N. Igolkine, A.A. Kolojvari, V. Kondratiev, I.A. Novikov, S.V. Potapov, O.I. Stolyarov, A.M. Switchev, T.A. Toulina, F.A. Tsimbal, F.F. Valiev, V.V. Vetchernine and L.I. Vinogradov.

**Strasbourg, France,** Institut de Recherches Subatomiques (IReS), IN2P3-CNRS and Université Louis Pasteur:

L. Arnold, J. Baudot, D. Bonnet, J.P. Coffin, M. Germain, C. Gojak, M. Guedon, B. Hippolyte, C. Kuhn, J. Lutz, C. Suire and A. Tarchini.

**Trieste, Italy,** Dipartimento di Fisica dell'Università and Sezione INFN:

V. Bonvicini, L. Bosisio, M. Bregant, P. Camerini, S. Dittongo, E. Fragiacomo, N. Grion, R. Grossi, G.-V. Margagliotti, S. Piano, C. Piemonte, A. Rashevski, R. Rui, F. Soramel<sup>14)</sup> and A. Vacchi.

**Turin, Italy**, Dipartimenti di Fisica dell'Università and INFN:

G. Alberici, B. Alessandro, R. Arnaldi, S. Beolé, P. Cerello, E. Chiavassa, S. Coli, E. Crescio, F. Daudo, N. De Marco, A. Ferretti, L. Gaido, M. Gallio, G. Giraudo, P. Giubellino<sup>1)</sup>, M. Idzik, P.G. Innocenti, E. Lopez Torres, A. Marzari-Chiesa, M. Masera<sup>1)</sup>, G. Mazza, P. Mereu, M. Monteno, A. Musso, D. Nouais, C. Oppedisano, A. Piccotti, G. Piragino, F. Prino, L. Riccati, A. Rivetti, E. Scomparin, F. Sigaudo, F. Tosello, G. Travaglia, E. Vercellin, A. Werbrouck and R. Wheadon.

**Warsaw, Poland**, Soltan Institute for Nuclear Studies:

D. Czerwinski, A. Deloff, K. Karpio, S. Kozak, M. Kozlowski, H. Malinowski, K. Redlich, T. Siemianczuk, G. Stefanek, L. Tykarski and G. Wilk.

**Warsaw, Poland**, University of Technology, Institute of Physics:

J. Grabski, M. Janik, A. Kisiel, P. Leszczynski, T.J. Pawlak, W.S. Peryt, J. Pluta, M. Przewlocki, P. Skowronski and P. Szarwas

**Wuhan, China**, Institute of Particle Physics, Huazhong Normal University:

X. Cai, S.Q. Feng, Y. Hu, W. Li, F. Liu, F.M. Liu, H. Liu, L.S. Liu, Y. Liu, W.Y. Qian, X.R. Wang, S.Q. Wu, T. Wu, C.C. Xu, C.B. Yang, Z.B. Yin, D.C. Zhou and D.M. Zhou.

**Yerevan, Armenia**, Yerevan Physics Institute:

M. Atayan, V. Danielyan, A. Grigorian, S. Grigoryan, H. Gulkanyan, V. Kakoyan, Yu. Margaryan, L. Parlakyan, G. Sargsyan, R. Shahoyan and H. Vardanyan.

**Zagreb, Croatia**, Ruder Bošković Institute:

T. Anticic, K. Kadija and T. Susa.

**Zagreb, Croatia**, Prirodoslovno-Matematicki Fakultet:

R. Manger, M. Marusic, R. Piskac and K. Puljic.

<sup>1)</sup> Also at CERN, Geneva, Switzerland.

<sup>2)</sup> On leave from JINR, Dubna, Russia.

<sup>3)</sup> On leave from Comenius University, Bratislava, Slovakia.

<sup>4)</sup> On leave from National Institute for Physics and Nuclear Engineering, Bucharest, Romania.

<sup>5)</sup> Institute of Physics, Pedagogical University, Kielce, Poland.

<sup>6)</sup> Research Centre for Applied Nuclear Physics (RCANP), Dubna, Russia.

<sup>7)</sup> Institute of Physics and Technology, Mongolian Academy of Sciences, Ulaanbaatar, Mongolia.

<sup>8)</sup> Institute of Physics, Georgian Academy of Sciences, Tbilisi, Georgia.

<sup>9)</sup> High Energy Physics Institute, Tbilisi State University, Tbilisi, Georgia.

<sup>10)</sup> Institute of Space Sciences, Bucharest, Romania.

<sup>11)</sup> Foundation of Fundamental Research of Matter in The Netherlands.

<sup>12)</sup> Utrecht University, Utrecht, The Netherlands.

<sup>13)</sup> University of Wroclaw, Poland.

<sup>14)</sup> Dipartimento di Fisica di Udine.

## Acknowledgements

The collaboration wishes to thank all the technical and administrative staff involved during the preparation of this TDR.

We especially acknowledge the contributions made by the following persons:

Y. Andres, J.-P. Avondo-Bedone, J.-C. Berset, M. Billault, B. Blank, M. Bosteels (and his group),  
B. Boydell, O. Braun, M. Burns, B. Cantin, E. Carrone, F. Cossey Puget, F. Dalla Santa, C. David,  
C. Decosse, P. Duraffourg, R. Dye, F. Faccio, A. Ferrand, M. Feuerstack-Raible, W. Flegel,  
D. Fraissard, R. Gregory, S. Haider, F. Hahn, P. Hanke, C. Hervet, P. IJzermans, P. Jarron, A. Junique,  
M. Keller, W. Klempt, W. Kowalczyk, W. Kreiter, N. Kurz, X. Lagrue, P. Lenoir, Y. Lesenechal,  
M. Letheren, J. Mallock, S. Maridor, M. Mast, M. Morel, D. Picard, M.A. Pimenta Dos Santos,  
V. Radeka, J. Raynaud, B. Schmidt, P. Sonderegger, J. Stewart, W. Tejessy, R. Tielert, J. Van Beelen,  
H. Van De Graaf, and S. Witoszynski.

We also thank the staff from the Desktop Publishing Service, for their professional help with the editing.





# Summary

---

This Technical Design Report describes the ALICE Transition Radiation Detector (TRD). This detector provides electron identification as well as triggering capability for high transverse momentum processes. In the following we briefly summarize the main design considerations and the proposed technical solutions.

Hard processes, and in particular studies of charm and beauty production in both the open and hidden charm sector have become center stage for the ALICE physics program. The TRD, in conjunction with the ITS and TPC, provides the relevant capability for the measurement of high  $p_t$  electrons. In addition, the TRD can be used to trigger on high  $p_t$  ( $> 3 \text{ GeV}/c$ ) particles, thus providing not only enriched samples for  $\Upsilon$  production but also the capability to select jets. A survey of the physics capabilities and resulting design specifications is given in Chapter 1.

The design objectives and mechanical structure are presented in Chapter 2. An important issue in this context is the organization of the TRD chambers in supermodules and their support in the ALICE space frame.

The radiator structure and technical realization are discussed in Chapter 3. Based on the experience gained in a series of test beam measurements described in Chapter 14, a sandwich construction of foam and fibers was chosen. This not only yields the required amount of transition radiation but also provides the structural rigidity to support the front window of the readout chamber, at reasonable cost and small radiation length. The overall material budget is summarized in Chapter 10, and amounts to less than 14% of a radiation length for the active volume of the detector.

The 540 readout chambers contained in the full TRD are essentially radial drift chambers with conventional wire amplification and cathode pad readout. To ensure optimal absorption of transition radiation the chamber gas will be 85% Xe and 15% CO<sub>2</sub>. The demands in terms of resolution and operational conditions are not very high for each chamber: typically a few hundred microns of spatial resolution are sufficient. Detailed chamber design and optimization is given in Chapter 4.

In Chapters 5, 6, and 7 are described the front-end electronics, trigger electronics and performance, and the readout and data flow for the full detector. With  $1.16 \cdot 10^6$  channels a high degree of integration is required. To optimize the transition radiation performance and simultaneously to provide the necessary tracking capability the electronics chain is based on a charge sensitive pre-amplifier feeding signals into a sampling ADC integrated into a digital chip, where all the logic for the trigger resides. Design, prototyping, and expected performance of the front-end electronics are summarized in Chapter 5.

The trigger performance based on these electronics components is studied by detailed simulations and results are reported in Chapter 6. The simulations are based on measured test beam results and the detailed design of the trigger. The on-line tracking performance is near that of off-line tracking reported in Chapter 11 for low multiplicity events, but deteriorates somewhat for very high multiplicity. Nevertheless, even for the highest conceivable multiplicity density of  $dN_{\text{ch}}/dy = 8000$ , enhancement factors of about 20 are achieved for detection of  $\Upsilon$  states in minimum bias Pb–Pb collisions.

For the readout and data flow one needs to consider two main data streams to be handled in real time. One stream concerns the raw data readout, while another is connected to the shipping of the information on the tracklet candidates produced in the global tracking unit of the trigger. The details of the design are discussed in Chapter 7.

Because the TRD uses the rather expensive xenon as the main chamber gas component in its approximately 27 m<sup>3</sup> volume, special requirements had to be put on the design and performance of the gas system, presented in Chapter 8. The system described there is based on a closed loop design, making use of components standardized for all LHC detector gas systems. The main components and functionality have been tested in a prototype gas system built for the detector test runs described in Chapter 14.

The total power necessary to run the full TRD electronics is about 68 kW (52 kW for Pb–Pb colli-

sions). This places strict requirements on the services for the TRD detector, especially concerning the low voltage power distribution. The resulting detailed design is presented in Chapter 9.

Chapter 11 is devoted to a description of the detector performance, with main emphasis on the dependence of pion rejection and tracking on the expected high multiplicity environment in Pb–Pb collisions at LHC energy. For the relevant momenta of  $1 \text{ GeV}/c$  and larger, the tracking efficiency is above 80% and only weakly dependent on event multiplicity. As expected, the pion rejection deteriorates with event multiplicity. However, at 90% electron efficiency we expect a pion rejection factor of about 50, for the highest conceivable multiplicity density of  $dN_{\text{ch}}/dy = 8000$ .

In Chapter 12 are summarized the acceptances and resolutions expected for the TRD for different physics processes such as the measurement of open charm and beauty and of various quarkonia via their electron decay channels.

Detector control and safety are important issues for a detector as complex as the TRD and our proposed technical specifications and solutions are described in detail in Chapter 13.

All simulations described in this report are based on detailed test beam measurements performed with TRD prototype detectors. This has led to a wealth of results summarized in Chapter 14. The test beam results demonstrate both the required pion rejection and position resolution. Furthermore, the radiator and chamber design are based on the experience with the prototypes.

Careful attention to mass production is an obvious issue for a detector comprising 540 radiators and readout chambers with about  $770 \text{ m}^2$  total area. The main requirements are collected in Chapter 15.

In Chapter 16 are described the plans for implementation, installation, and access and maintenance for the TRD detector. The planned supermodule structure as well as the decision to concentrate all services on the side of the baby space frame (opposite to the muon arm) will facilitate installation and access significantly.

Organizational aspects, budgets and schedules are presented in Chapter 17. The TRD group now comprises 5 major institutions with significant experience and manpower. The overall budget of 14.8 MCHF is in line with previous estimates. We note, however, that the baseline budget for the TRD as outlined in the ALICE MoU contains only about half of the amount needed to build the full detector. Possible strategies are briefly discussed.

# Contents

---

<b>Summary</b>	<b>xi</b>
<b>1 Physics objectives and design considerations</b>	<b>1</b>
1.1 The ALICE experiment . . . . .	1
1.2 Physics requirements . . . . .	1
1.2.1 Heavy ion collisions . . . . .	1
1.2.2 Proton proton collisions . . . . .	3
1.3 TRD design considerations . . . . .	4
1.4 General description of the TRD . . . . .	5
<b>2 Design objectives and mechanical structure</b>	<b>7</b>
2.1 General considerations . . . . .	7
2.2 Mechanical structure . . . . .	7
2.2.1 Space frame . . . . .	7
2.2.2 TRD in the space frame . . . . .	9
2.2.3 TRD supermodule . . . . .	10
2.2.4 TRD readout chamber . . . . .	11
2.3 Support for services . . . . .	11
2.4 Tolerances and alignment . . . . .	12
2.4.1 Tolerances for the TRD readout chambers . . . . .	12
2.4.2 Alignment of readout chambers within a supermodule . . . . .	12
2.4.3 Alignment of supermodules within the space frame . . . . .	12
<b>3 Radiators</b>	<b>13</b>
3.1 General considerations and requirements . . . . .	13
3.2 Radiator design . . . . .	14
3.3 Radiator performance . . . . .	16
<b>4 Readout chambers</b>	<b>19</b>
4.1 Choice of gas . . . . .	19
4.1.1 Drift velocity and diffusion . . . . .	20
4.1.2 Lorentz angle . . . . .	20
4.1.3 Electron attachment . . . . .	21
4.2 Mechanical structure . . . . .	22
4.3 Wire planes . . . . .	24
4.4 Readout pads . . . . .	25
4.4.1 Pad response function . . . . .	27
4.4.2 Improvement of $z$ -resolution . . . . .	27
4.5 Track reconstruction . . . . .	29
4.6 Electrostatic calculations . . . . .	31
4.6.1 Gas gain . . . . .	31
4.6.2 Gain stability . . . . .	32
4.6.3 Pad coupling . . . . .	34
4.6.4 Ion feedback . . . . .	35
4.6.5 Isochrony . . . . .	35
4.6.6 Electrostatic matching . . . . .	36

<b>5 Front-End Electronics</b>	<b>39</b>
5.1 Electronics overview . . . . .	39
5.1.1 General requirements . . . . .	39
5.1.2 System overview . . . . .	41
5.2 Chip technology . . . . .	43
5.2.1 ADC Integration . . . . .	44
5.2.2 ADC technology choices . . . . .	44
5.3 Preamplifier / Shaper . . . . .	45
5.3.1 Requirements . . . . .	45
5.3.2 Implementation . . . . .	45
5.3.3 Prototypes . . . . .	47
5.4 ADC . . . . .	48
5.5 TRD trigger states . . . . .	49
5.6 Trigger timing . . . . .	50
5.6.1 Clock distribution and clock domains . . . . .	52
5.6.2 Distribution of fast signals . . . . .	52
5.7 Interface to the ALICE trigger system . . . . .	54
5.8 Multi-Chip Module (MCM) overview . . . . .	56
5.9 MCM prototypes and performance . . . . .	56
5.9.1 Prototype Motherboard . . . . .	56
5.9.2 Prototype MCM . . . . .	56
5.10 Design for test . . . . .	58
5.10.1 Preamplifier . . . . .	58
5.10.2 Local Tracking Unit (LTU) . . . . .	59
5.10.3 MCM testing and verification . . . . .	59
<b>6 Electron trigger with the TRD</b>	<b>61</b>
6.1 Physics motivation . . . . .	61
6.2 Concept . . . . .	62
6.3 Hardware implementation . . . . .	63
6.3.1 Trigger concept . . . . .	63
6.3.2 Local Tracking Unit (LTU) functionality . . . . .	65
6.3.3 Tracklet processor . . . . .	70
6.3.4 Readout Scheme . . . . .	83
6.3.5 Implementation of the Global Tracking Unit . . . . .	83
6.4 Simulation . . . . .	84
6.4.1 Local tracklet search . . . . .	85
6.4.2 Local tracking performance . . . . .	87
6.4.3 Tracklet Matching - Global Tracking Unit . . . . .	96
6.4.4 GTU tracking efficiency . . . . .	98
6.4.5 Electron identification . . . . .	101
6.4.6 Background . . . . .	103
6.5 Performance . . . . .	103
6.5.1 Generalities of Pb-Pb collisions . . . . .	103
6.5.2 $\Upsilon$ count rates . . . . .	105
6.5.3 Trigger rates . . . . .	107
<b>7 Readout and Data Flow</b>	<b>111</b>
7.1 Data types and format . . . . .	111
7.1.1 Tracklets . . . . .	111

7.1.2	Raw data . . . . .	112
7.2	Hardware implementation . . . . .	112
7.2.1	Readout scheme . . . . .	112
7.2.2	GTU link . . . . .	115
7.2.3	Detector link . . . . .	117
<b>8</b>	<b>The gas system</b>	<b>119</b>
8.1	Introduction . . . . .	119
8.2	Gas choice . . . . .	119
8.3	Layout . . . . .	120
8.3.1	Mixing unit . . . . .	120
8.3.2	Circulation and purification system . . . . .	121
8.3.3	Backup system . . . . .	123
8.3.4	Recovery station . . . . .	124
8.4	Gas distribution pipework . . . . .	125
8.5	Prototype . . . . .	126
<b>9</b>	<b>Services</b>	<b>129</b>
9.1	Low voltage power distribution . . . . .	129
9.1.1	Requirements . . . . .	129
9.1.2	Low voltage power supplies and cables . . . . .	130
9.1.3	Layout . . . . .	131
9.2	High voltage power distribution for drift field . . . . .	132
9.2.1	Requirements . . . . .	133
9.2.2	High voltage power supplies . . . . .	133
9.2.3	Layout . . . . .	133
9.3	High voltage power distribution for readout chambers . . . . .	133
9.3.1	Requirements . . . . .	133
9.3.2	High voltage power supplies . . . . .	133
9.3.3	Layout . . . . .	133
9.4	Cooling distribution . . . . .	134
9.4.1	Requirements . . . . .	134
9.4.2	Description of cooling system and layout . . . . .	134
9.5	Gas distribution . . . . .	137
9.5.1	Layout . . . . .	137
<b>10</b>	<b>Material budget</b>	<b>139</b>
<b>11</b>	<b>Detector performance</b>	<b>141</b>
11.1	Requirements . . . . .	141
11.2	Simulation of the detector response . . . . .	141
11.2.1	Energy loss . . . . .	141
11.2.2	Transition radiation . . . . .	144
11.2.3	Signal generation . . . . .	148
11.3	Point reconstruction . . . . .	152
11.3.1	Clustering method . . . . .	152
11.3.2	Occupancy . . . . .	152
11.3.3	Position resolution . . . . .	153
11.4	Tracking . . . . .	154
11.4.1	Algorithm . . . . .	154
11.4.2	Performance . . . . .	155

11.5 Pion rejection . . . . .	158
<b>12 Physics performance</b>	<b>163</b>
12.1 Introduction . . . . .	163
12.2 Primary collision . . . . .	163
12.3 Simulation environment . . . . .	165
12.3.1 Simulation of the detector layout . . . . .	166
12.3.2 Simulation of input particles . . . . .	166
12.3.3 Simulation studies . . . . .	167
12.4 $\Upsilon$ and J/ $\psi$ mesons . . . . .	167
12.4.1 Acceptance . . . . .	167
12.4.2 $\Upsilon$ invariant mass distribution . . . . .	170
12.5 B and D mesons . . . . .	172
12.6 TRD acceptance for different geometrical configurations . . . . .	177
12.7 Background . . . . .	180
12.8 Summary . . . . .	180
<b>13 Detector control</b>	<b>183</b>
13.1 Hardware . . . . .	184
13.2 Communication . . . . .	186
13.3 Software . . . . .	186
13.4 Safety and quality management . . . . .	187
13.4.1 Mechanical . . . . .	187
13.4.2 Gas . . . . .	187
13.5 Radiation protection . . . . .	187
13.6 Electrical system protection . . . . .	187
13.6.1 High voltage for readout chambers . . . . .	187
13.6.2 Low voltage . . . . .	187
<b>14 Tests with prototypes</b>	<b>191</b>
14.1 Prototype description . . . . .	191
14.2 Source tests with $^{55}\text{Fe}$ . . . . .	192
14.2.1 Signals and spectra . . . . .	192
14.2.2 Gas gain . . . . .	194
14.2.3 Pad response function . . . . .	194
14.3 Beam tests . . . . .	198
14.3.1 Setup . . . . .	198
14.3.2 General properties of the detector . . . . .	199
14.3.3 Pion and electron distributions . . . . .	204
14.3.4 Radiator comparison . . . . .	206
14.3.5 Pion rejection performance . . . . .	208
14.3.6 TR performance as a function of incident angle . . . . .	210
14.3.7 Position reconstruction performance . . . . .	212
14.4 Work in progress . . . . .	222
<b>15 Mass production</b>	<b>225</b>
15.1 General concepts . . . . .	225
15.2 Equipment of production sites . . . . .	225
15.3 Database . . . . .	225

<b>16 Implementation, infrastructure, and safety</b>	<b>227</b>
16.1 ALICE experimental area . . . . .	227
16.2 Implementation of the TRD detector . . . . .	228
16.2.1 General integration considerations . . . . .	228
16.2.2 The space frame . . . . .	228
16.2.3 Pre-assembly phase . . . . .	229
16.2.4 Installation in the underground cavern . . . . .	229
16.3 Access, maintenance and services . . . . .	230
16.3.1 Access for maintenance and repair . . . . .	230
16.3.2 Services . . . . .	230
16.4 Safety aspects . . . . .	232
<b>17 Responsibilities, cost, and schedule</b>	<b>233</b>
<b>References</b>	<b>237</b>
<b>Glossary</b>	<b>243</b>







# 1 Physics objectives and design considerations

---

## 1.1 The ALICE experiment

ALICE (A Large Ion Collider Experiment) [1] is an experiment at the Large Hadron Collider (LHC) optimized for the study of heavy ion collisions, at a centre-of-mass energy per nucleon pair of 5.5 TeV. The understanding is that in such high energy collisions of heavy nuclei a Quark-Gluon Plasma (QGP) will be formed. The chief difference as compared to RHIC e.g. is that gluon distribution functions at much lower values of  $x$  ( $x=x_t=2p_t/\sqrt{s} = 10^{-4} - 10^{-3}$ ) will be probed leading to a very high initial gluon density; values of up to 4000 gluons per unit rapidity near mid-rapidity have been quoted [2]. This is expected to lead to very fast equilibration [3] of at least the gluons on a time scale of 0.1 fm/c and hence to a very high initial energy density and temperature of the order of  $1000 \text{ GeV/fm}^3$  and 1 GeV, respectively. ALICE aims to study the properties of this hot QGP, its dynamical evolution, phenomena associated with the phase transition of rehadronization and finally the evolution of the hadronic final state until freeze-out. To achieve this goal ALICE, as the only dedicated heavy ion experiment at LHC, is designed to measure a large set of observables over as much of phase space as achievable and thereby covering hadronic and leptonic observables as well as photons.

The ALICE experimental set-up is shown in Colour Fig. 1. The experiment will have a central barrel, housed in the L3 magnet, covering in pseudorapidity the range  $-0.9 \leq \eta \leq 0.9$  with complete azimuthal coverage. This central barrel comprises an inner tracking system of Silicon detectors (ITS), a large time projection chamber (TPC), a transition radiation detector (TRD) – the subject of this technical design report –, and a time-of-flight array (TOF). In addition there will be close to mid-rapidity two single arm detectors, an array of ring-imaging Cherenkov counters (HMPID) to identify hadrons up to high momenta and an array of crystals (PHOS) for the detection of photons. This central barrel will be complemented [4] at pseudorapidities of  $2.5 \leq \eta \leq 4.0$  by a muon spectrometer with its own dipole magnet. At more forward and backward rapidities detectors will be located to measure the multiplicity of charged particles and the time of an interaction, both also for trigger purposes, as well as several more specialized detectors.

## 1.2 Physics requirements

The chief goal of the TRD is to provide electron identification in the central barrel at momenta in excess of  $1 \text{ GeV}/c$  where the pion rejection via energy loss measurement in the TPC is no longer sufficient. As a consequence, the addition of the TRD [5] significantly expands the physics objectives of the ALICE experiment [1, 4].

### 1.2.1 Heavy ion collisons

The TRD will provide, in conjunction with data from the TPC and ITS detectors, sufficient electron identification capability for the following measurements:

- **In the di-electron channel**, the production of light and heavy vector–meson resonances as well as the di-lepton continuum. This measurement, centered around mid-rapidity, is complementary to the measurement of quarkonia at more forward rapidities in the di-muon channel. Also, the vertex capabilities of the ITS will allow to distinguish and measure  $J/\psi$  mesons from B-decays. This will not only permit distinction between primary and secondary  $J/\psi$  mesons but also lead to a direct

measurement of the B-meson production cross section. Depending on the magnitude of thermal radiation of the QGP and the mixed phase, a measurement of the di-electron continuum between  $J/\psi$  and  $\Upsilon$  may be sensitive to this interesting probe. We aim for a pion rejection and luminosity sampled by the trigger to achieve sensitivity at the Drell-Yan level [5].

- **Via the single-electron channel** and requiring a **displaced vertex** using the ITS information, the semi-leptonic decays of hadrons with open charm and open beauty. This will be complementary to the very difficult measurement of hadrons with open charm via identification of the displaced secondary vertex in the hadronic decay channel. While interesting in its own right the measurement of open charm and beauty is essential as a reference against which to judge effects of the QGP concerning the yields of quarkonia.
- **Via coincidences of electrons** in the central barrel and **muons** in the forward muon arm, information on the correlated production of hadrons with open charm and open beauty at a rapidity interval bridging the coverage of the central barrel and the forward muon arm. This will provide information on charm and beauty production over the rapidity range  $y = 0\text{--}4$ .

The trigger capability of the detector (see Chapter 6 below) opens another interesting and unique possibility:

- **Jets with high  $E_t$**  can be selected at the trigger level by requiring several (3 or more) high  $p_t$  tracks in one TRD module, where the typical coverage is  $\Delta\eta \approx \Delta\phi \approx 0.35$ . With individual thresholds around 3–5 GeV/c this trigger reaches full efficiency at a jet  $E_t$  of 150 GeV just where rate considerations make a trigger useful.

The theoretical uncertainties in predicting the multiplicity of produced hadrons are large since even proton-proton collisions at this beam energy have not been studied and since the gluon distribution functions at the relevant values of  $x$  have not been measured in nuclei. Moreover, first results at RHIC as a function of centrality and in comparison to pp collisions have shown [6] a scaling with the number of nucleons participating in the collision containing a linear and a quadratic term. The overall centrality dependence is a complicated interplay between collective effects and saturation of the gluon density in the initial and final state, making quantitative predictions for this completely new energy regime difficult. The theoretical estimates [7] for the rapidity density of produced charged hadrons for central Pb–Pb collisions range<sup>1</sup> from 2000 to 8000. Using parton saturation and classical QCD [8] a scaling function for multiplicity as a function of beam energy was derived recently which was used for a successful prediction for the full RHIC energy (200 GeV) based on 130 GeV data. Extrapolating this scaling all the way up to LHC energies would yield a multiplicity density at the lower end of the predicted range (2000 or even somewhat below). Following the general ALICE strategy to be prepared to deal with even the highest conceivable multiplicities, the detector is designed for an upper limit in the charged particle rapidity density of 8000. In the parametrization used, actually the maximum rapidity density of primary charged particles averaged over the central two units of rapidity ( $-1 \leq y \leq +1$ ) is 8400 (called in the following ‘full multiplicity’). Decays of neutral hadrons, mostly  $K_S^0$ , within 5 cm of the primary vertex increase this number to 9300. Secondary particles generated in the detectors, frames, services, and other material lead to about double the primary charged multiplicity in the TRD.

Identification of electrons in this high occupancy environment is clearly very challenging. In Chapter 11, simulations will be shown of the performance of the TRD covering the whole range of expected multiplicity densities.

As a benefit of the high gluon densities at the small  $x$ -values relevant at LHC, the cross sections for charm and beauty production as well as the semi-hard jet cross sections are more than one order of magnitude enhanced as compared to RHIC.

---

<sup>1</sup>Early estimates based on Glauber models gave very high values of up to  $dN_{ch}/dy=8000$ ; newer calculations based on gluon distributions or Gribov-Regge theory reduce this estimate by nearly a factor 3

All rate estimates in this document are based on an anticipated maximum luminosity for Pb–Pb collisions of  $\mathcal{L} = 1.0 \cdot 10^{27} \text{ cm}^{-2} \text{s}^{-1}$  leading to a minimum bias interaction rate of 8 kHz and a rate of 0.8 kHz for central collisions with impact parameter less than 5 fm. With past and future protection during the TPC drift time, these rates are reduced by about a factor of 4. In fact, the number of clean events in the TPC is nearly the same at a luminosity of  $\mathcal{L} = 5 \cdot 10^{26} \text{ cm}^{-2} \text{s}^{-1}$ . The actual charged particle multiplicity will determine whether some overlap of intercalations in the TPC is acceptable.

In this luminosity range and assuming a data acquisition capability of 20 Hz for central collisions [9], statistics for J/ψ, open charm and open beauty is not an issue as outlined in [5]. The experiment is however statistics limited in the Υ measurement. At a luminosity of  $\mathcal{L} = 1.0 \cdot 10^{27} \text{ cm}^{-2} \text{s}^{-1}$  there will be about 13600 Υ with both decay electrons in the central barrel of the ALICE experiment in  $10^6$  s (a typical ALICE heavy ion year). This number refers to clean events in the TPC. Of these, 5400 will be for the 10% most central collisions. Assuming a DAQ performance of 20 Hz for central collisions and another 20 Hz for minimum bias events (without triggers this saturates the anticipated DAQ capability [9]) and 90% electron identification efficiency (the specification for the TRD), 110 and 440 Υ decays to electron pairs in the ALICE central barrel will be collected per ALICE heavy ion year for minimum bias and central collisions, respectively. These numbers do not yet include the tracking efficiency and are therefore upper limits. This demonstrates the need for a trigger. Without it there would be a marginal measurement of the Υ yield in central collisions and clearly not enough statistics to measure the centrality dependence, yields for the Υ substates (1S, 2S,...), or the spectral distributions. For a more detailed discussion and numbers including tracking efficiency for various scenarios, see Section 6.5.

- **Need for Trigger:** the Υ measurement and in particular its centrality dependence make it essential to sample the full minimum bias rate of Pb–Pb collisions of up to 4 kHz (past-protected events in TPC). The TRD is designed to provide this trigger capability. For the Υ measurement this would be a trigger on electron pairs with each electron typically having a transverse momentum above 3 GeV/c . This decision will be available on a time scale of 6 μs after the collision.

Without this trigger capability a measurement of the thermal continuum is not conceivable if it is near the Drell–Yan level. Having this trigger capability, it can also be applied to jet physics. This will be the subject of the Physics Performance Report of ALICE and here only the ideas are sketched. Requiring several (3–5) high  $p_t$  particles in a jet cone of a certain size a jet candidate can be identified. This would be effective for jet transverse energies larger than 150 GeV (see above). Then one could require two such candidates back to back, or one candidate opposite to PHOS could be combined with a high momentum photon, or two close high momentum electrons (photon jet) could be combined with an opposite jet candidate.

Another advantage this trigger provides is to identify the region of interest for the high momentum electron. This means, one could read out only the TPC sectors to which the electron candidates of the TRD point. The event size for central collisions could be reduced then to typically 3–4 out of  $2 \times 18$  sectors i.e. about to 1/10 of the full size, thus relaxing the 20 Hz limitation for the acquisition of central collision events. In addition, combination of the TRD trigger with the planned high level trigger (HLT) will lead to significant improvements in the trigger efficiency and selectivity.

### 1.2.2 Proton proton collisions

The TRD will also contribute significantly to the ALICE proton-proton physics program. Proton-proton (pp) collisions are an integral part of the ALICE running scenario, both to collect data needed as comparison for results from heavy ion collisions and to address topics of genuine interest in elementary hadron interactions. The detailed physics arguments for including ALICE in the LHC pp running scenario are summarized in [10].

ALICE, which is designed to cover the low to medium  $p_t$  range (between 100 MeV/c and 20 GeV/c ), is uniquely suited for these tasks. In addition to the physics topics which are discussed in the previous

subsection and which were the original motivation for the TRD, applicable both to heavy ion and pp running, we foresee the following items specific to pp running:

- **Charm and Beauty physics:** We expect to measure transverse momentum spectra of D and B mesons down to very low  $p_t$  (essentially below  $100 \text{ MeV}/c$ ). The knowledge of spectra at low values of  $p_t$  is of large interest for the extraction of the total c and b cross sections. Today's extraction of c and b total cross sections relies on large extrapolations towards low  $p_t$  because of relatively high  $p_t$  cut-off values in the acceptance. In addition, these cross sections are theoretically not well reproduced by present perturbative QCD calculations. Neither the Fermilab Tevatron experiments nor the dedicated pp LHC experiments will cover the low  $p_t$  regions for D and B mesons. Low  $p_t$   $\text{J}/\psi$  and  $\Upsilon$  measurements are also important since the present theoretical understanding of the production cross section is not entirely on safe ground. There are no low  $p_t$  measurements in  $p\bar{p}$  and pp collisions nor will there be any in the foreseeable future.
- **Topological trigger function for the HMPID:** The behaviour of the particle composition in pp collisions as a function of  $p_t$  and multiplicity is of large interest. The HMPID which is dedicated to extend the PID to momenta of  $3.5 \text{ GeV}/c$  for kaons and  $5 \text{ GeV}/c$  for protons covers only a small part of the central barrel acceptance. Therefore, it is important to be able to use the TRD to trigger on high momentum tracks pointing towards the HMPID. Otherwise the HMPID, due to the low track multiplicity, would be empty most of the time during pp running.
- **Measuring Jets in pp running:** The segmentation of the TRD modules allows to trigger on jets (monojets, dijets) as sketched above for heavy ion operation; in pp collisions the trigger on jets might be useful at much lower jet energies. In this context a topological trigger pointing toward PHOS could be useful. A trigger on the hard tracks of the charged particles pointing to PHOS could yield more detailed information about the total energy of the jet and the fragmentation functions, not achievable with charged particles only.

### 1.3 TRD design considerations

The physics requirements outlined in the previous section have driven the following design considerations:

- **The pion rejection capability** required is driven mostly by the  $\text{J}/\psi$  measurement and its  $p_t$  dependence. As outlined in the Addendum to the ALICE proposal [5] a factor 100 in pion rejection for electron transverse momenta above  $3 \text{ GeV}/c$  is the goal. While the requirement for the  $\Upsilon$  is less stringent, the light vector mesons  $\rho, \omega, \phi$  as well as the di-electron continuum between the  $\text{J}/\psi$  and the  $\Upsilon$  are only accessible with this performance.
- **The required momentum resolution** is primarily driven by the matching to the TPC. The momentum resolution requirements for the central barrel are fulfilled by combining TPC and ITS reaching e.g. a mass resolution of  $100 \text{ MeV}/c^2$  at the  $\Upsilon$  for  $B = 0.4 \text{ T}$  (see Chapter 12) and the function the TRD needs to fulfill is to add the electron identification. This goal can be reached by having a pointing capability from the TRD to the TPC with an accuracy of a fraction of a TPC pad. The TRD will provide a momentum resolution of 5% at  $5 \text{ GeV}$  (see Chapter 11) leading to a pointing accuracy of 30% of the padwidth allowing unambiguous matching with exception of very close hits. At the trigger level good momentum resolution leads to a sharper threshold and a smaller probability of fake tracks but no strict requirement can be derived from this.
- **The thickness of the TRD** in radiation lengths has to be kept to a minimum. Any unnecessary material provides additional background dominantly due to photon conversion and increases the

pixel occupancy. Also, electron energy loss due to bremsstrahlung removes electrons from the sample useful for reconstruction of resonances.

- **The granularity** of the TRD, i.e. of the cathode pads in the readout chambers, is driven in bend direction by the required momentum resolution (see before) and along beam direction by the required capability to identify (see above) and track electrons efficiently at the highest envisioned multiplicity. To not affect the reconstructed pair signal drastically we designed the detector to achieve 80% tracking efficiency (single track) for this case driving the design to pads of about  $6 \text{ cm}^2$ .
- **Occupancy:** This maximum assumed charged particle multiplicity density of 8000 leads in the TRD to a readout pixel occupancy in central collisions of about 34% (including secondary particles) for the pad size given above. The detector is designed to function at this occupancy.

## 1.4 General description of the TRD

The physics requirements and design considerations listed above have led to the present design of the TRD. Central aspects of the design are summarized in the text below and detailed in the following chapters. For a quick overview there is also a synopsis in Table 1.1. For the overall description of the TRD in the ALICE experiment we use cylindrical coordinates with the origin at the intersection of the beams and with the positive  $z$ -axis pointing towards the muon arm. The angle  $\varphi$  is then also the deflection angle in the magnetic field. Since the TRD chambers are flat and not on a cylindrical surface it is often more convenient, when discussing processes and resolutions inside a given chamber, to use cartesian coordinates. In this case we keep the same  $z$ -axis,  $y$  is the direction of the wires and of the deflection in the magnetic field,  $x$  is the direction of electron drift.

The coverage in pseudorapidity matches the coverage of the other central detectors ( $|\eta| \leq 0.9$ ). In radius the TRD fills the space between the TPC and the TOF detectors. As shown below, for quality of electron identification the TRD consists of 6 individual layers. Following the segmentation in azimuthal angle  $\varphi$  of the TPC there are 18 sectors. For practical considerations there is a 5-fold segmentation along the beam direction ( $z$ ). The 5 detector modules have similar but not identical length in  $z$  to match the areas in between modules with more material (in particular in the space frame) with boundaries of detectors at larger radii in a projective geometry. The dimensions of the active area of each detector module are given in Table 2.2. In total there are  $18 \times 5 \times 6 = 540$  detector modules.

Each module consists of a radiator of 4.8 cm thickness, a multiwire proportional readout chamber, and the front-end electronics for this chamber. The signal induced on the cathode pads is read out. Each chamber has 144 pads in direction of the amplification wires ( $r\varphi$ ) and between 12 and 16 pad rows in  $z$  direction. The pads have a typical area of  $6\text{--}7 \text{ cm}^2$  and cover a total active area of about  $736 \text{ m}^2$  with  $1.16 \cdot 10^6$  readout channels.

The gas mixture in the readout chambers is Xe/CO<sub>2</sub> in a ratio of 85/15. Each readout chamber consists of a drift region of 3.0 cm separated by cathode wires from an amplification region of 0.7 cm. The drift time for the drift region is  $2.0 \mu\text{s}$  requiring a drift velocity of  $1.5 \text{ cm}/\mu\text{s}$ . The nominal drift velocity will be reached with an electric field of 0.7 kV/cm. In this gas mixture a minimum ionizing particle liberates 275 electrons per cm. The gas gain will be of order  $5 \cdot 10^3$ . The induced signal at the cathode pad plane will be sampled in 15 time intervals spaced 2 mm or 133 ns over the drift region. Diffusion is negligible (see Table 1.1), and at the nominal magnetic field of 0.4 T the Lorentz angle is  $8^\circ$ .

At full multiplicity the pixel occupancy will be 34%. As shown in Chapter 11 a space point resolution in bend direction of  $400 \mu\text{m}$  can be achieved for low multiplicity at  $p_t = 1 \text{ GeV}/c$ . For full multiplicity this is degraded to  $600 \mu\text{m}$  with some unfolding. The momentum resolution of the TRD in stand-alone mode is determined by a constant term of 2.5% and a linear term of 0.5% per  $\text{GeV}/c$ . The linear term is degraded to 0.8% for full multiplicity.

**Table 1.1:** Synopsis of TRD parameters.

Pseudorapidity coverage	$-0.9 < \eta < 0.9$
Azimuthal coverage	$2\pi$
Radial position	$2.9 < r < 3.7$ m
Length	maximal 7.0 m
Segmentation in $\varphi$	18-fold
Segmentation in radius	6 layers
Segmentation in $z$	5-fold
Total number of modules	540
Largest module	$120 \times 159$ cm <sup>2</sup>
Detector active area	736 m <sup>2</sup>
Detector thickness radially	$X/X_0 = 14.3\%$
Radiator	fibres/foam sandwich, 4.8 cm per layer
Module segmentation in $\varphi$	144
Module segmentation in $z$	12–16
Typical pad geometry	$0.725 \times 8.75 = 6.34$ cm <sup>2</sup>
Time samples in $r$ (drift)	15
Number of readout channels	$1.16 \cdot 10^6$
Number of readout pixels	$1.74 \cdot 10^7$
Detector gas	Xe,CO <sub>2</sub> (15%)
Gas volume	27.2 m <sup>3</sup>
Depth of drift region	3 cm
Depth of amplification region	0.7 cm
Nominal magnetic field	0.4 T
Drift field	0.7 kV/cm
Drift velocity	1.5 cm/ $\mu$ s
Diffusion, longitudinal	$D_L = 250 \mu\text{m}/\sqrt{\text{cm}}$
Diffusion, transversal	$D_T = 180 \mu\text{m}/\sqrt{\text{cm}}$
Lorentz angle	8°
Occupancy (for full multiplicity)	34%
Typical space point resolution at 1 GeV/c	
in $r\varphi$	400(600) $\mu\text{m}$ for low (high) multiplicity
in $z$	2.3 cm (without tilt)
Momentum resolution	$\delta p/p = 2.5\% \oplus 0.5\%(0.8\%)p$ for low (high) multiplicity
Pion suppression at 90% electron efficiency and $p_t \geq 3$ GeV/c	better than 100

## 2 Design objectives and mechanical structure

---

### 2.1 General considerations

The TRD will identify electrons with high efficiency. At the same time it will provide a trigger signal for electrons with large transverse momentum  $p_t$  at Level 1. In order to fulfill both of these tasks a careful optimization of the thickness of the detector is required. A certain minimum thickness of the radiator is required for the efficient identification of electrons. While the total thickness in radiation length has to be kept as small as possible (for details refer to Chapter 10) to minimize small angle scattering, bremsstrahlung, and showering, it still needs to provide mechanical stiffness for the proper operation of the readout chamber. One of the major aims of the detector is the measurement of pairs of high  $p_t$  leptons. Therefore it is crucial to minimize dead areas between the individual detector units.

As outlined in Chapter 1 the detector will be comprised of 540 detector modules arranged in 18 supermodules. Each of the supermodules will contain six layers of detectors subdivided into 5 sections in  $z$ -direction. Each of the 18 supermodules will be a unit of installation and will be supplied as a whole with the services as described below.

The TRD is the detector with the largest number of readout channels in the ALICE setup. Given also the large number of individual detector units major design considerations need to focus on simplicity and cost effectiveness.

### 2.2 Mechanical structure

#### 2.2.1 Space frame

The space frame is the main support structure for almost all detectors of the central arm of ALICE. The current version of the space frame is depicted in Fig. 2.1. Its location and installation within ALICE is described in Chapter 16. The TRD will be mounted inside the space frame just outside the inner opening. The inner opening accommodates the TPC and the ITS. Still inside the space frame structure, immediately following the TRD, TOF modules will be inserted and special provisions are made to support the HMPID and PHOS.

For this version of the space frame a detailed list of all the weights that need to be supported has been compiled [1]. The total mass that needs to be supported by the space frame amounts to 75 t. In this total the TRD is included with about 21 t. The weight for the TRD was based on the following estimate: the weight per  $m^2$  of detector area is about 15 kg, where pad-/readout plane with its support, the radiator with its support, and electronics and services are contributing approximately 5 kg/ $m^2$  each. The services for low voltage, high voltage, and cooling running inside the supermodule are included in this number. The weight of the supermodule support frame, the heat shield, and the rails contribute another 10 kg/ $m^2$  (with a contingency of about 25% for the weight of the support). The revised weights of all detectors led to a redesign of the space frame using stainless steel profiles instead of aluminum with increased cross sections listed in Table 2.1 below [1].

Finite element calculations were performed using ANSYS<sup>®</sup> 5.6.2 [1]. Maximum relative displacements of the final positions of the detectors were calculated. Under the load of the detectors the space frame assumes a slightly elliptical shape. This leads to a maximum displacement of the TRD support points of 1.0 mm in horizontal and 2.0 mm in vertical direction.

One of the main conclusions drawn in [1] was that the supermodules need to be mounted with space for adjustment of the order of 3 mm. In that case none of the load due to deformation of the space frame

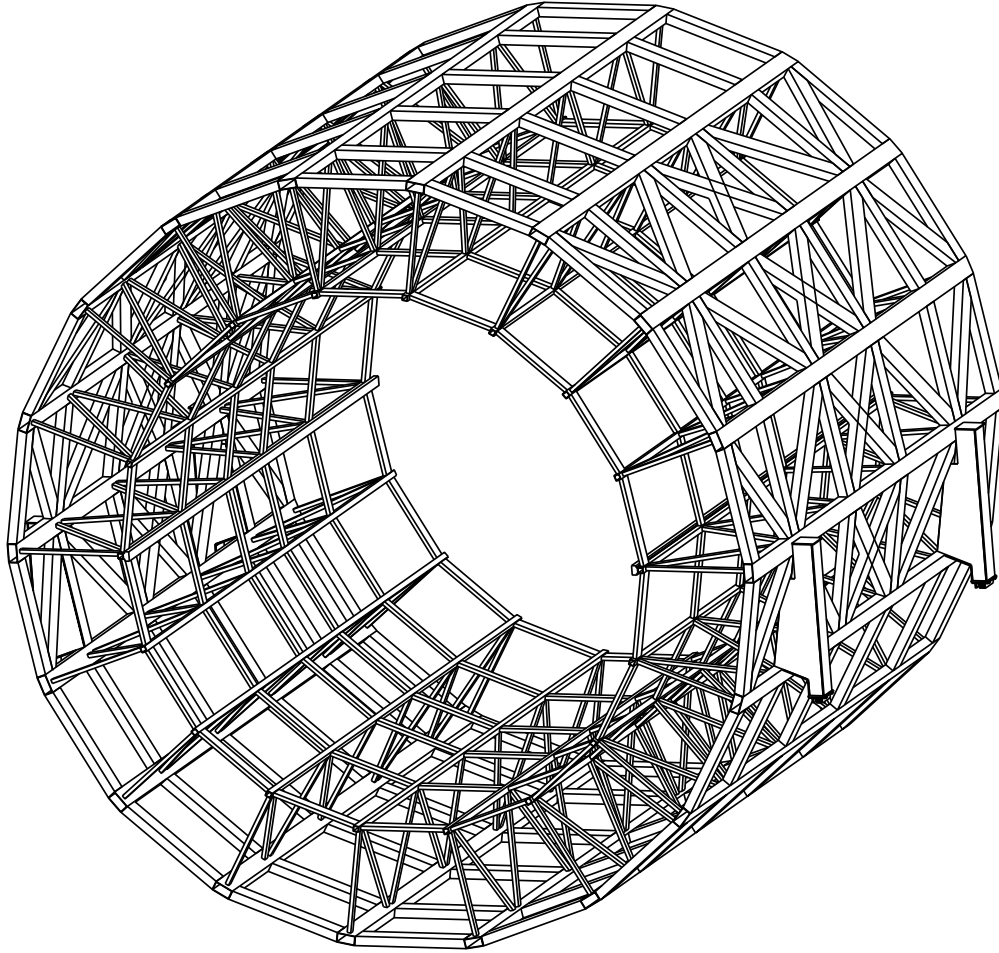


**Figure 2.1:** Axonometric view of the ALICE spaceframe.

**Table 2.1:** Dimensions of the space frame elements used in the simulations.

external frame beams	$100 \times 175 \times 3.5 \text{ mm}^3$
supporting rods	$200 \times 175 \times 4.0 \text{ mm}^3$
web rods	$60 \times 40 \times 4.0 \text{ mm}^3$
internal frame front/rear rings	$40 \times 135 \times 6.0 \text{ mm}^3$
inner rings	$40 \times 100 \times 6.0 \text{ mm}^3$
longitudinal beams	$60 \times 60 \times 3.0 \text{ mm}^3$
TPC beams with rails	$75 \times 100 \times 6.0 \text{ mm}^3$

would be transferred onto the supermodules themselves.

As the central detectors of ALICE evolve the design of the space frame may need to be reconsidered. The figures quoted here reflect the conditions implemented in the simulation framework AliRoot at the time when this document was prepared. As described in Chapter 16 the deformations have only recently been rechecked with the aforementioned total load on the space frame of 75 t.

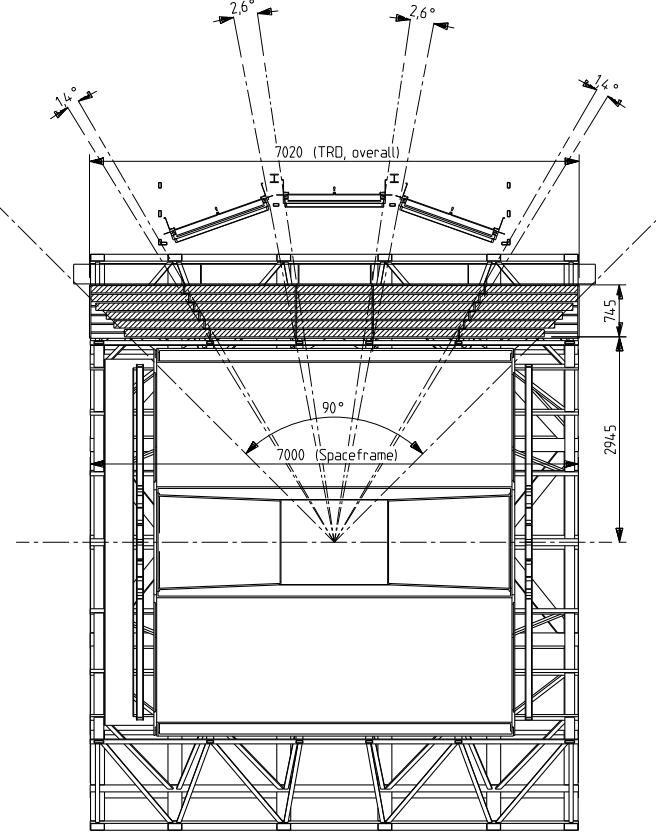


**Figure 2.2:** Cross-sectional view (cut through the  $xz$ -plane) of the space frame supporting the central detectors of ALICE. The angles on top of the figure indicate the shadows cast by the individual detector frames.

### 2.2.2 TRD in the space frame

In Fig. 2.2 a cut through the space frame with the TRD in  $xz$  plane is shown. Inside the supermodules the six layers of detectors are shown. In the layout chamber boundaries were aligned with the cross bars of

**Table 2.2:** Dimensions of the individual TRD modules.  $R_{Ra}$ : Radial distance from the interaction point at the front face of the radiator.  $L_2$ : overall length of the center module.  $L_{1,3}$ : overall length of the modules left and right of the center module.  $L_{0,4}$ : overall length of the outer modules.  $L_{tot}$ : overall length of layer.  $L_F$ : total length of frames in z-direction (length of the active area of each module is  $L_i - L_F/5$  ( $i = 0 \dots 4$ )).  $W_{tot}$ : overall width of a module in one layer.  $W_F$ : width of lateral profiles (width of active area of each module is  $W_{tot} - W_F$ ).  $A_{tot}$ : total area covered by detectors.  $A_{act}$ : total active area.

plane	$R_{Ra}$	$L_2$	$L_{1,3}$	$L_{0,4}$	$L_{tot}$	$L_F$	$W_{tot}$ [mm]	$W_F$ [mm]	$A_{tot}$ [ $m^2$ ]	$A_{act}$ [ $m^2$ ]
1	2945	1100	1235	1235	6040	150	956	20	5.77	5.51
2	3071	1100	1310	1310	6340	150	1001	20	6.35	6.07
3	3197	1100	1385	1345	6560	150	1045	20	6.85	6.57
4	3323	1100	1460	1420	6860	150	1089	20	7.47	7.17
5	3449	1100	1530	1420	7000	150	1134	20	7.93	7.63
6	3575	1100	1605	1345	7000	150	1178	20	8.23	7.93
total									766.8	735.8

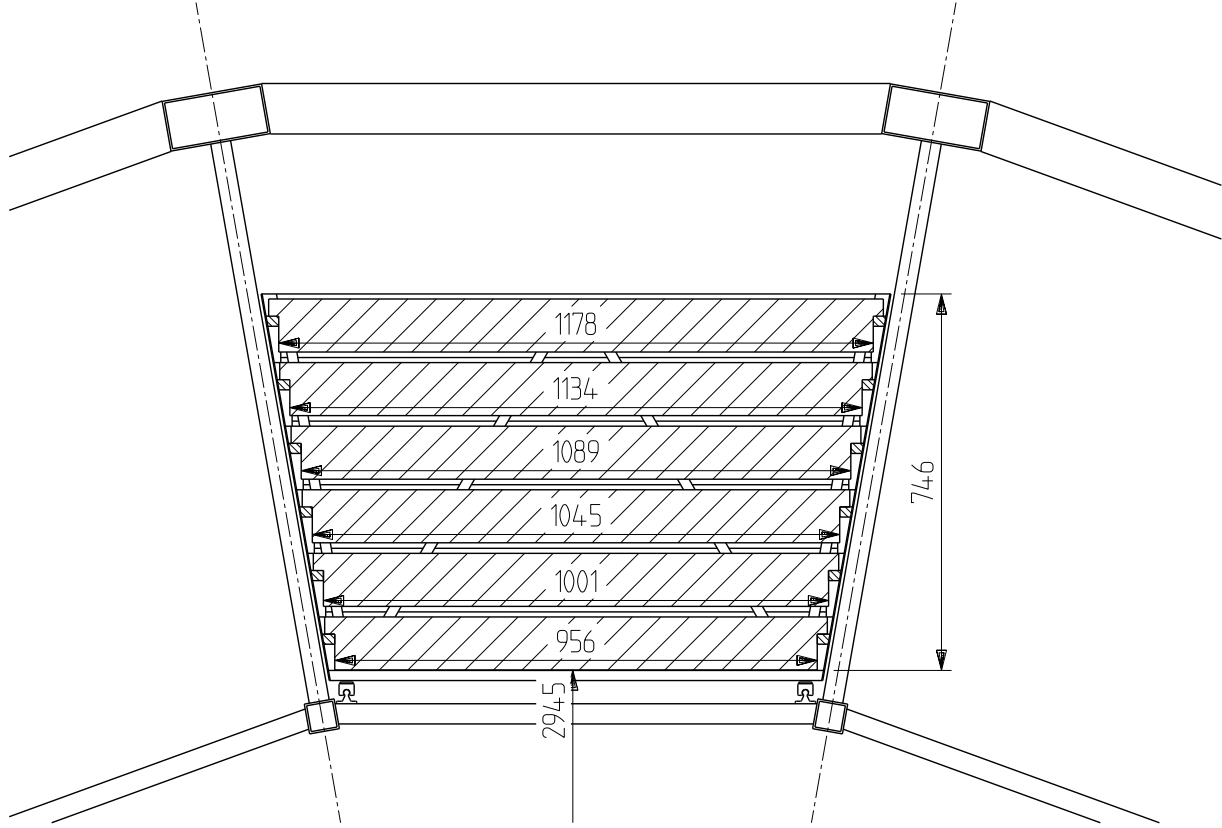


**Figure 2.3:** View of the TRD detectors cut in  $\phi$ -direction

the space frame and detector boundaries of subsequent detectors (eg. HMPID). This was done in order to minimize shadowing and dead areas.

A front view of one sector of detector is shown in Fig. 2.3 including the supermodule casing and the rails that facilitate the installation of the supermodule as one piece.

### 2.2.3 TRD supermodule

Fig. 2.4 shows a drawing of the supermodule container for one sector. Every supermodule contains 6 layers of 5 detectors each. The layers are aligned with respect to one side of the supermodule. On this side the travelers that go on the rails inside the space frame are fixed with high precision. The travelers on the other side allow for adjustment to compensate the above mentioned deformations of the space frame under full load.

Dimensions of the individual chambers inside the supermodule are listed in Table 2.2.

Each supermodule is a unit of installation. It will be a closed volume with only connections for services to the outside. The side panels will be thin panels of aluminum supporting the low voltage bus bars and cooling pipes. The front face toward the inside of the detector will be a thin heat shield ensuring constant operating conditions for the TPC field cage on the inside, where a temperature stability of  $\pm 0.1$  K has to be achieved. The outside face of the supermodule will be covered by a foil to minimize heat dissipation into the magnet volume.

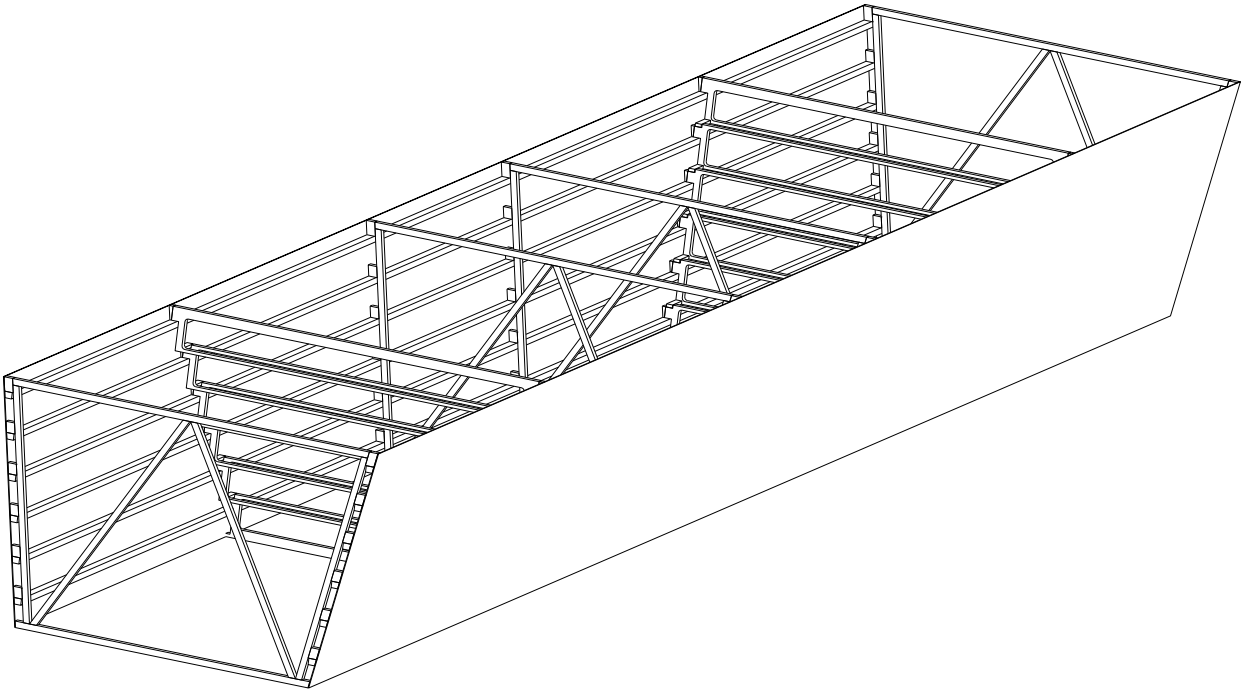


**Figure 2.4:** Axonometric view of the supermodule support structure with side panels.

#### 2.2.4 TRD readout chamber

The individual TRD readout chambers are described in detail in Chapter 4 along with a description of the boundary conditions that led to the design depicted in Fig. 4.6. A TRD readout chamber consists of 48 mm of a composite radiator made of Rohacell® and polyethylene fibers (for a description see Chapter 3) followed by the drift electrode, a drift region of 30 mm filled with Xe,CO<sub>2</sub> (15%) and 2 wire planes in the 7 mm amplification region. All components are mounted on the side frames of the readout chamber. The readout chamber is closed on top with a printed circuit board that contains the cathode pads. The backing of this printed circuit board is made of carbon fiber reinforced Rohacell®. On top of this the readout board for the electronics is mounted with all layers for power, ground, and the lines for the digital readout. The cooling is directly attached to the readout boards.

### 2.3 Support for services

All services (low voltage, high voltage, cooling, gas, readout and control lines) for the TRD will be supported by the so-called "baby" space frame. Currently it is foreseen that this structure is very similar to the space frame itself, but detached from it. In this way the additional load due to the services will not contribute to the deformation of the space frame where position accuracy is needed. The "baby" space frame will be equipped with guiding rails on the side of the magnet door for installation of the supermodules. A somewhat simpler structure will be installed on the side where the magnet stays closed. The largest single contributor in terms of weight of the services of the TRD will be the low voltage cables. If all necessary supply voltages are provided from the outside without DC-to-DC converters, the weight of the bare copper conductor that runs inside the magnet will be approximately 7.2 t. For further details refer to Chapter 9.

## 2.4 Tolerances and alignment

Several aspects need to be considered for the definition of tolerances of the various components of the TRD

- tolerances affecting the performance of individual TRD readout chambers,
- mechanical alignment tolerances of the readout chambers within a supermodule affecting track matching within one sector,
- mechanical alignment tolerances of the supermodules within the space frame affecting the global track matching with other detectors in the central part of ALICE.

### 2.4.1 Tolerances for the TRD readout chambers

To ensure good alignment of the modules inside the supermodule all reference points for support of the readout chambers are designed to have a precision of better than 0.1 mm. This is at the same time also the relative position error of each pad with respect to the outer alignment face of the detector. For the pad plane this implies that the position of the alignment marks relative to the pads needs to have an accuracy of better than 0.05 mm. Before final assembly of the readout chamber the positions of these alignment marks will be measured with respect to the alignment surface, which will be the side of the chamber, where the traveler of the supermodule is fixed.

For gain uniformity it is necessary to prevent the pad plane from bending due to its own weight and the dynamical overpressure from the gas flow. For the nominal distance of 3.5 mm between anode wire plane and pad plane the maximum allowed deviation is 150  $\mu\text{m}$ . Owing to the large number of wires crossing each pad, the wire placement in  $z$ -direction is not critical.

In order to ensure a uniform drift velocity across the whole readout chamber the flatness of the drift electrode needs to be better than 1 mm.

### 2.4.2 Alignment of readout chambers within a supermodule

One side of the supermodule, that where the traveler is fixed, will serve as reference surface for internal alignment of the readout chambers within the supermodule. During final assembly this side will be placed against an external reference surface from which measurements with respect to alignment marks on the top of the readout chambers will be made. The relative position of the reference marks themselves with respect to the individual pads will be precisely measured beforehand.

### 2.4.3 Alignment of supermodules within the space frame

Once the supermodules are installed in the space frame, they will be surveyed photogrammetrically from both sides of the space frame using external alignment marks on the supermodule. Its position will be measured precisely beforehand with respect to the reference surface and the fixed traveler.

# 3 Radiators

---

## 3.1 General considerations and requirements

Transition radiation (TR) is produced when a highly relativistic charged particle traverses the boundary between two media of different dielectric constants [1]. As the average energy of the emitted TR photon is approximately proportional to the Lorentz factor  $\gamma$  of the particle (for  $\gamma$  around a few thousand), this provides an excellent way for discriminating between electrons and pions for momenta of a few GeV/c and higher. However, the probability of photon emission from a single boundary is very small, so that a large number of boundaries have to be combined to obtain a reasonable efficiency. Commonly used are stacks of a few hundred polypropylene foils which have a regular periodic structure and which in earlier tests have been shown to be the most efficient radiators available [2, 3]. For a general review about transition radiation detectors see [4].

In the environment of the complete ALICE detector the radiator of the TRD, besides providing a high efficiency for transition radiation, has to fulfill geometrical and mechanical constraints. The detector consists of 6 identical layers each of which has full azimuthal coverage. Within these cylinders there has to be as little dead material as possible to avoid acceptance losses. Furthermore the total amount of material shadowing other detectors has to be minimized. Strong metal frames which would be required to mount hundreds of foils are therefore not adequate. Even then, for the size of the radiators foreseen, and taking into account the collider geometry, it would not be possible to maintain a uniform separation of the foils. Already these circumstances exclude the use of foil radiators. In addition, a foil based design would lead to an unacceptable complexity in the construction of the 540 radiators.

The radiator itself is intended to support the front window of the readout chambers which serves simultaneously as the drift electrode. The radiator has to guarantee that a maximum allowed deviation from a flat surface of the window is not exceeded. Slight but non negligible overpressure in the chambers due to gravity and flow of the Xe,CO<sub>2</sub> gas mixture leads to a bending of the window. This bending would lead to non uniform drift times in the chambers due to distortions in the drift field configuration and drift length. Also the radiator should add as much as possible to the total mechanical stability of the chambers.

Two other types of radiator materials have therefore been investigated:

- fibres layered in predominantly two-dimensional mats
- foams with more or less random internal structure.

The fibre mats can be regarded as approximations to foil stacks, as the fibre thickness provides a well defined spatial separation between two consecutive boundaries and a reasonably large fraction of the boundaries is approximately perpendicular to the measured particles, while foams with their irregular structure have both random orientation of the boundaries and variable size spatial gaps between them. It is therefore not surprising that the TR response of fibre radiators is comparable to foils and that foams are slightly less efficient. However, the mechanical properties of foams are far superior to those of fibre mats (see Chapter 14).

Since interactions like multiple scattering, conversion and bremsstrahlung in the used material affect the performance of the TRD itself and of the other ALICE subdetectors positioned behind it, the overall material budget is limited. This sets another restriction to the choice of materials.

The requirements on the TRD radiator can be summarized as follows:

- It has to generate transition radiation with sufficient efficiency while not exceeding the foreseen thickness of 4.8 cm .

- It should provide support to the entrance window and constrain its deflection caused by the gas pressure to below 1 mm .
- The 6 layers of radiator as the most important single contributor should bring the total amount of material of the TRD not significantly above 15% of a radiation length (see Chapter 10).

### 3.2 Radiator design

Various radiator materials and types (foils, foams and fibres) were tested during extensive test measurements at GSI darmstadt (see Chapter 14). From this experience, in conjunction with the requirements explained above, the following radiator design was chosen. We plan to use a sandwich construction of foam and fibres providing the optimal combination of TR efficiency and mechanical stability.

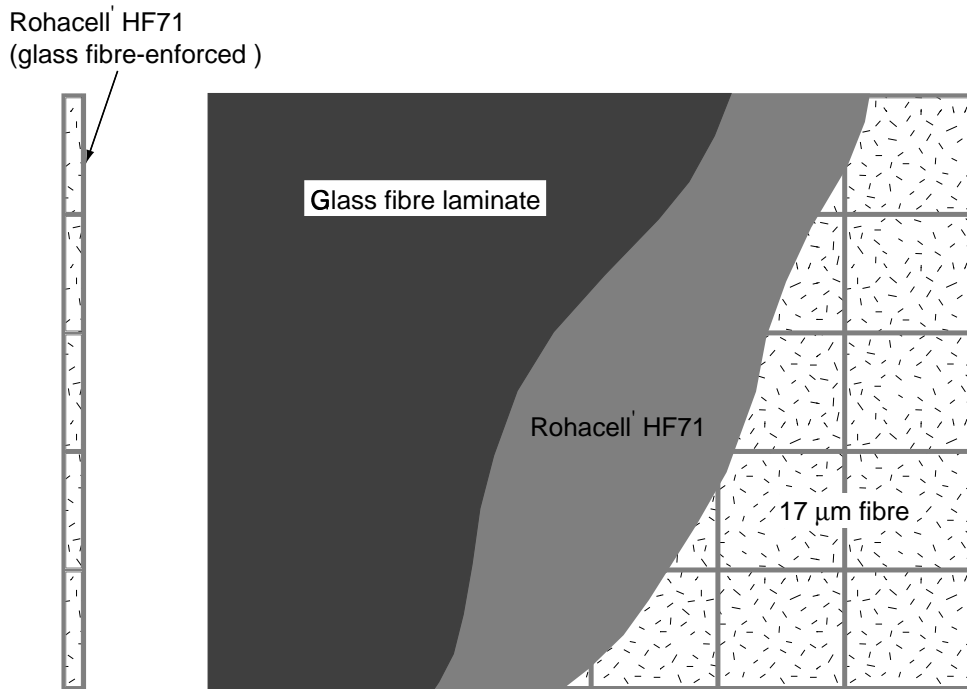


**Figure 3.1:** The principal design of the TRD sandwich radiator.

Fig. 3.1 shows the principal design of the radiator sandwich. The supporting structure is made out of Rohacell HF71 foam [5]. This material is a PMI (polymethacrylimide) foam with low density and high mechanical and chemical stability. In addition to the supporting function the foam has also a quite good transition radiation production rate (see Chapter 14). The upper and lower covers are made out of Rohacell plates with a thickness of 8 mm reinforced by glass fibre sheets. The glass fibre sheets laminated onto the surface have a thickness of 0.1 mm . The inner side of the radiator will be covered by a  $25 \mu\text{m}$  aluminized Mylar foil which forms the entrance window and the drift electrode of the readout chamber.

The upper and lower covers of the sandwich are connected by a grid-like structure also made out of 8 mm Rohacell. The cell sizes will be adjusted to the dimensions of each radiator. The inner volume of the sandwich cells is filled with polypropylene fibres [6] which serve as the main radiator material (later

on called *fibres17*). Tests have shown that the fibres are comparable in performance to foil radiators (see Chapter 14). Scanning electron microscope pictures of both materials are shown in Fig. 3.2. The properties of the used materials are given in Table 3.1.

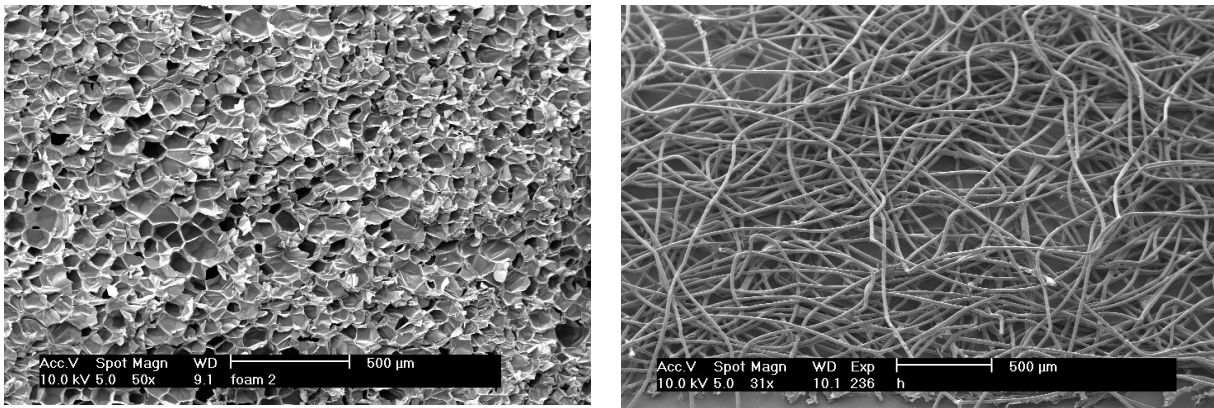


**Figure 3.2:** Scanning electron microscope images of the used radiator materials. Left panel: Rohacell HF71 foam; right panel: fibres mat.

**Table 3.1:** The properties of the compared radiators and their materials. The label *S-HF71* denotes the HF71/fibre sandwich construction.

radiator	material	density [g/cm <sup>3</sup> ]	elastic modulus [MPa]	radiation length $X_0$ [g/cm <sup>2</sup> ]	thickness absolute [cm ]	$X/X_0$ [*10 <sup>-3</sup> ]
<i>HF71</i>	Rohacell HF71	0.075	92	40.6	4.8	8.88
<i>fibres17</i>	Polypropylene	0.074	-	44.6	4.0	6.75
<i>S-HF71</i> sandwich	Rohacell HF71	0.075	92	40.6	$2 * 0.8$	2.96
	Polypropylene	0.074	-	44.6	3.0	5.30
	sum of materials	-	-	-	4.8	8.26
<i>S-HF71</i> with reinforcement	Glass fibre coating	1.7	$> 10^3$	33.0	$2 * 0.01$	1.03
	sum of materials	-	-	-	4.8	9.29

A prototype of a radiator sandwich which covers the largest readout chamber was constructed using Rohacell foam without reinforcement. Its mechanical properties have been measured. Assuming a maximum overpressure of 1 mbar the measured deviation from a flat surface was 3.25 mm. The measurements were done with a uniform areal overpressure simulated by adding water on top of the surface of the horizontally oriented radiator. In addition tests were made with a reinforced radiator model of the dimensions  $120 \times 20 \text{ cm}^2$ , which corresponds to the full size radiator only in the smaller dimension. The model was supported at the short edges and the deflection measured under load. These tests can be seen as conservative with respect to the full size radiator as the latter would have additional support at the other sides. A reinforcement with carbon fibre rods with a diameter of 2 mm on both sides reduced the deflection below 0.9 mm. In this test setup the reinforcement is approximately equivalent to a carbon fibre laminate of  $30 \mu\text{m}$  thickness on both sides of the radiator sandwich. A photograph of the reinforced radiator model during the tests is shown in Fig. 3.3.

Calculations show that a reinforcement with  $100 \mu\text{m}$  glass fibre on both sides of the sandwich also leads to a deformation of below 0.9 mm for an overpressure of 1 mbar, which meets the requirements.



**Figure 3.3:** The bending test of the reinforced radiator model. One can see the radiator model (white) and the carbon fibre rod (black) glued to it. The overpressure is simulated by weights (in this case screws) distributed over the whole length of the model. The deflection is measured by the dial gauge positioned at the center of the model.

### 3.3 Radiator performance

The transition radiation yield of the sandwich as discussed above and indicated in Fig. 3.1 was measured and compared with similar measurements of the individual materials used in this design. This was done during several test beamtimes at GSI. A mixed beam of electrons and pions was used. For a detailed description of the setup and the measurements refer to Chapter 14.

In the left plot of Fig. 3.4 one can see a typical spectrum of average pulse height vs. drift time for electrons of 1 GeV/c momentum. The signal was measured with an 8-bit flash-ADC system in 60 time bins of 50 ns each. The distribution shows a peak at early times, originating from the amplification region (see Chapter 14). Without transition radiation one would expect a plateau at later times, caused by the energy loss of particles in the drift region. The transition radiation signal sits on top of this plateau and causes a rise of the average signal. This rise is most prominent at later times (around 2.1  $\mu$ s in this configuration, corresponding to the entrance of the readout chamber) where it builds a second peak in the distribution.

To allow a qualitative comparison of the radiators, the ratio of electron and pion signals are plotted in the right part of Fig. 3.4 as a function of the depth of the chamber, expressed in drift zone number (0 is the amplification region and 4 corresponds to the entrance of the detector). Here the sandwich radiator *S-HF71* is compared with the pure materials *HF71* and *fibres17* for the momentum of 1 GeV/c. Without the contribution of TR one expects a flat distribution at about 1.45 (shaded area in the right panel of Fig. 3.4). At later times (large drift zone number) one can clearly see the effect of the TR, which causes a strong rise of the ratio (about 25 %). This rise is equally pronounced for all three radiators. In this measurement the absolute thickness of the radiator *fibres17* was smaller than that of the two others (40 mm instead of 48 mm). Therefore the electron to pion ratio of this radiator is slightly below the one of the sandwich radiator *S-HF71* at later drift times.

Whereas the ratio of the average signals for electrons and pions is useful for a comparison of different radiator types, for the final estimate of the performance of the detector it is more appropriate to look at

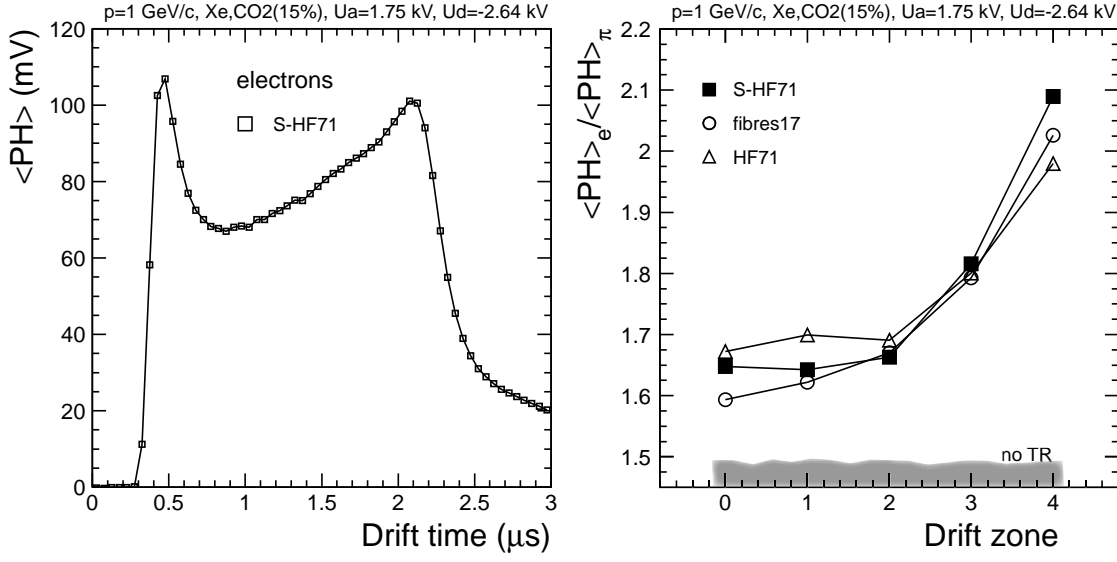


**Figure 3.4:** Left: Average pulse height vs. drift time for 1 GeV/c electrons measured with the sandwich radiator S-HF71. Right: Comparison of the different radiator materials (see table 3.1). Shown is the ratio of the mean signals for electrons and pions vs. the drift time for 5 drift zones for 1 GeV/c momentum. The fibre radiator had a smaller thickness of 40 mm compared to 48 mm in case of the other radiators.

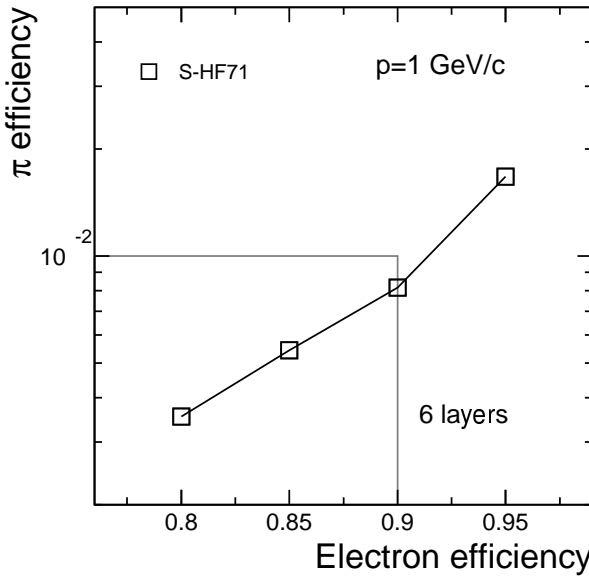


**Figure 3.5:** Pion efficiency as a function of the electron efficiency for the sandwich radiator S-HF71 extrapolated to 6 layers. The particle momentum was 1 GeV/c and the method of likelihood on integrated charge was used.

the pion rejection performance. In Fig. 3.5 the pion rejection efficiency is plotted as a function of electron efficiency extrapolated to a stack of 6 TRD modules. For this analysis a likelihood method was used, based on the energy deposited in the drift region ( $L-Q$ , see section 14.3.5). The proposed radiator meets the design criteria of a pion rejection of  $10^{-2}$  with an electron efficiency of 90% already at a particle momentum of 1 GeV/c.



## 4 Readout chambers

---

The ALICE TRD detector is subdivided into 540 individual detector modules, as described in Chapters 1 and 2. Their task is to identify electrons by their larger energy deposition due to transition radiation and their larger specific energy loss, combined with charged particle tracking capability [1]. Each of these detector modules is a full TR detector in itself, containing a radiator and a readout chamber. The readout chamber contains a conversion and drift gas volume and a conventional wire amplification region with cathode pad readout. While the TRD readout chambers are not very demanding in terms of resolution and operational conditions, the size and number is considerable. In addition, a low mass design of the readout chambers is mandatory to reduce the load of background to subsequent TRD modules and other ALICE detectors. Therefore, apart from the required performance in terms of electron ID and position resolution, emphasis was put on mechanical reliability at minimal radiation length, combined with technical simplicity.

In the following, we describe the concept for the readout chambers and demonstrate how the technical solution is adapted to the requirements.

### 4.1 Choice of gas

The baseline gas mixture for the ALICE TRD is 85% Xe and 15% CO<sub>2</sub>. The need of a high X-ray photoabsorption probability rules out any of the lower mass noble gases as major component, as demonstrated in Fig. 4.1. For a typical TR photon energy of 10 keV, the absorption length in Xenon is 1 cm.

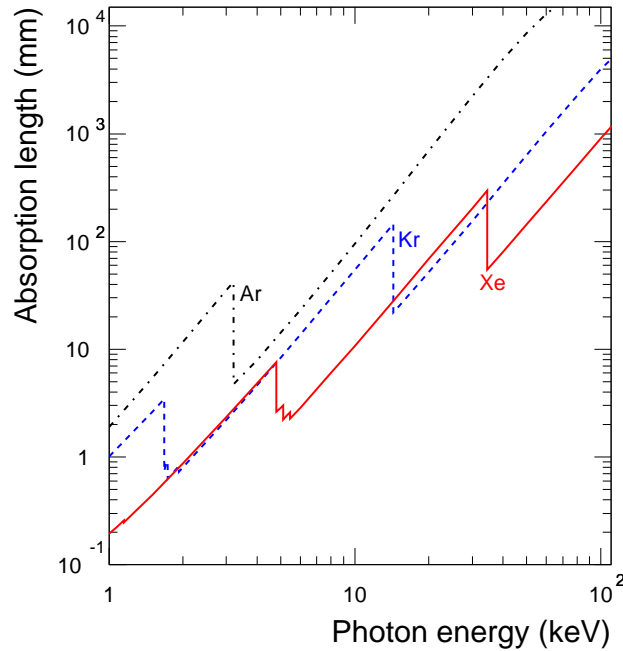


**Figure 4.1:** X-ray absorption length in different noble gases.

The use of CO<sub>2</sub> as quencher is attractive because it is nonflammable, in contrast to many organic gases. In addition, organic molecules contain hydrogen, which causes additional background from energetic knock-on protons. Since the field of the L3 magnet is perpendicular to the electric drift field of the readout chambers, also  $\vec{E} \times \vec{B}$ -effects have to be considered. With respect to this, the use of a ‘cool’ component, such as CO<sub>2</sub>, turns out to be advantageous.

### 4.1.1 Drift velocity and diffusion

We have chosen a drift velocity of  $1.5 \text{ cm}/\mu\text{s}$ , resulting in a total drift time of  $2 \mu\text{s}$  over the maximum drift distance of 3 cm. Figure 4.2 (left) shows GARFIELD/MAGBOLTZ [2,3] calculations of the drift velocity for different gas mixtures as function of the electric drift field. The drift field required in  $\text{Xe},\text{CO}_2$  (15%) is 700 V/cm, fixing the potential on the drift electrode to -2.1 kV. These calculations are consistent with our prototype measurements (see Chapter 14).

At this drift voltage, the longitudinal and transverse diffusion coefficients are  $D_L = 250 \mu\text{m}/\sqrt{\text{cm}}$  and  $D_T = 180 \mu\text{m}/\sqrt{\text{cm}}$  (Fig. 4.2, right panel). Due to the short drift distance of 3 cm, the maximum spread of an initially point-like charge cloud is 300-500  $\mu\text{m}$  only. Therefore, the impact of diffusion on pulse shape and position resolution is negligible. It should be noted that we found no significant dependence of the drift velocity and the diffusion coefficients on the magnetic field up to  $B=0.6 \text{ T}$ .

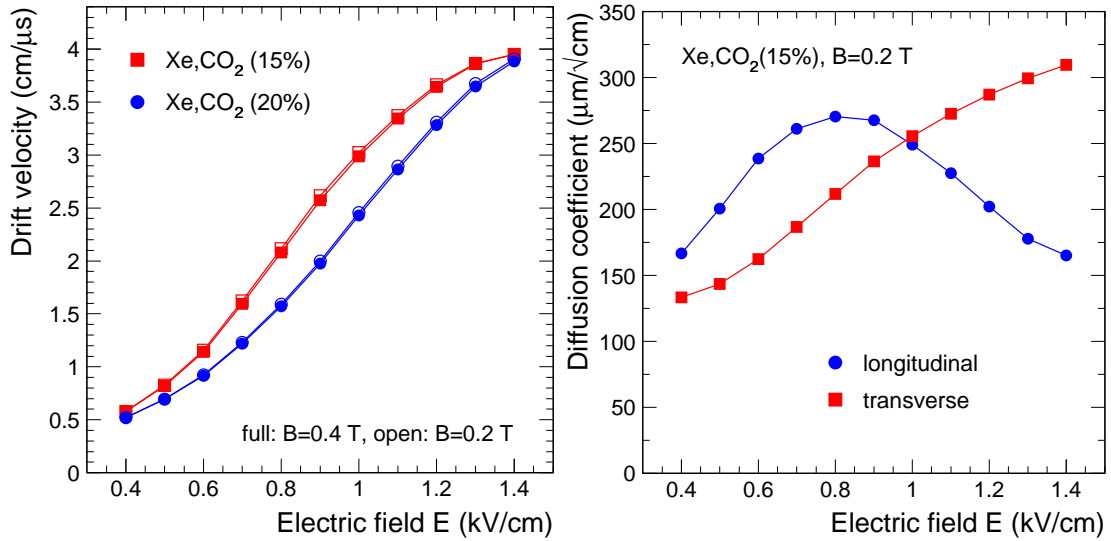


**Figure 4.2:** GARFIELD/MAGBOLTZ calculations of the drift velocity (left) and diffusion coefficients (right) as function of the electric drift field.

### 4.1.2 Lorentz angle

The ALICE TRD is operated inside the field of the L3 magnet ( $B_{\max}=0.5 \text{ T}$ ) which is perpendicular to the electric drift field. This forces the drifting electrons on a trajectory which is inclined with respect to the electric field (see Fig. 4.3).

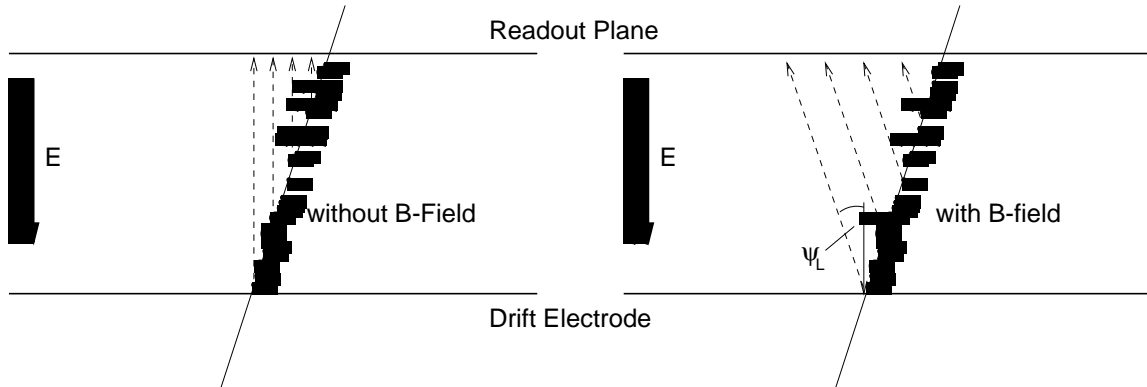


**Figure 4.3:** Drift path of electrons without (left) and with (right) magnetic field.

The so-called Lorentz angle  $\psi_L$  between  $\vec{v}_D$  and  $\vec{E}$  depends on the strength of  $\vec{E}$  and  $\vec{B}$  and the gas properties. It can be expressed by:

$$\tan \psi_L = \omega \tau. \quad (4.1)$$

The cyclotron frequency  $\omega$  depends on  $B$  while  $\tau$  is the mean time interval between two collisions of the electron in the gas, connected with the electron mobility  $\mu$ :

$$\omega = e/m \cdot B, \quad (4.2)$$

$$\mu = e/m \cdot \tau. \quad (4.3)$$

Given a precise knowledge of  $\vec{E}$  and  $\vec{B}$ , the displacement of the arriving electron with respect to its creation point is well determined and can be corrected for. However, the Lorentz angle leads on average to a deterioration of the position resolution because it enhances correlations between adjacent time bins, originating from Landau fluctuations and the finite width of the single electron response function in time direction (see Section 4.5). A minimization of the Lorentz angle is therefore desirable.

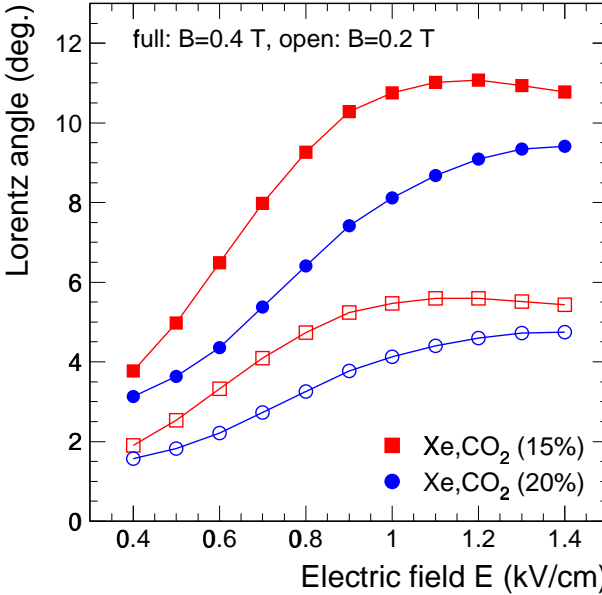


**Figure 4.4:** GARFIELD/MAGBOLTZ calculations of the Lorentz angle as function of the electric field for different Xe mixtures and magnetic field strengths.

The Lorentz angle as function of the drift field for different magnetic field strengths is shown in Fig. 4.4. At nominal operating conditions ( $E=700$  V/cm,  $B=0.4$  T), the Lorentz angle is  $8^\circ$  in  $\text{Xe},\text{CO}_2$  (15%). Clearly, the Lorentz angle could be decreased by reducing  $E$ . On the other hand, the resulting lower drift velocity would lead to a limitation of the trigger performance (see Chapter 6). Also the addition of more  $\text{CO}_2$  looks attractive. This would, however, tighten the requirements on the gas purity, as outlined below (see also Chapter 8).

### 4.1.3 Electron attachment

On their way to the amplification region, drifting electrons can be absorbed by electronegative impurities, mainly  $\text{O}_2$ . The signal loss due to this electron attachment for a given total pressure  $p$  and  $\text{O}_2$  partial pressure  $p(\text{O}_2)$  follows an exponential behaviour, depending on the drift time  $t_{\text{drift}}$ :

$$N(t_{\text{drift}}) = N(0) \cdot \exp(-p \cdot p(\text{O}_2) \cdot C_{\text{att}} \cdot t_{\text{drift}}). \quad (4.4)$$

The attachment coefficient  $C_{\text{att}}$  depends on the gas mixture. It turns out to be particularly large for gas mixtures containing CO<sub>2</sub> because of its large number of low-lying excitation levels. In Fig. 4.5 the attachment coefficient is shown as function of the electric drift field for different Ar mixtures and for Xe,CO<sub>2</sub> (15%). Similar results have been obtained for Ne mixtures containing CO<sub>2</sub> [4, 5]. A measurement of the signal attenuation at different oxygen contamination levels in Xe,CO<sub>2</sub> (15%) was performed with the TRD prototype (see Chapter 14). The resulting attachment coefficient  $C_{\text{att}}=400 \text{ atm}^{-2} \mu\text{s}^{-1}$  leads to a signal attenuation of less than 10% after the maximum drift time of 2  $\mu\text{s}$ , for an O<sub>2</sub> contamination of 100 ppm.

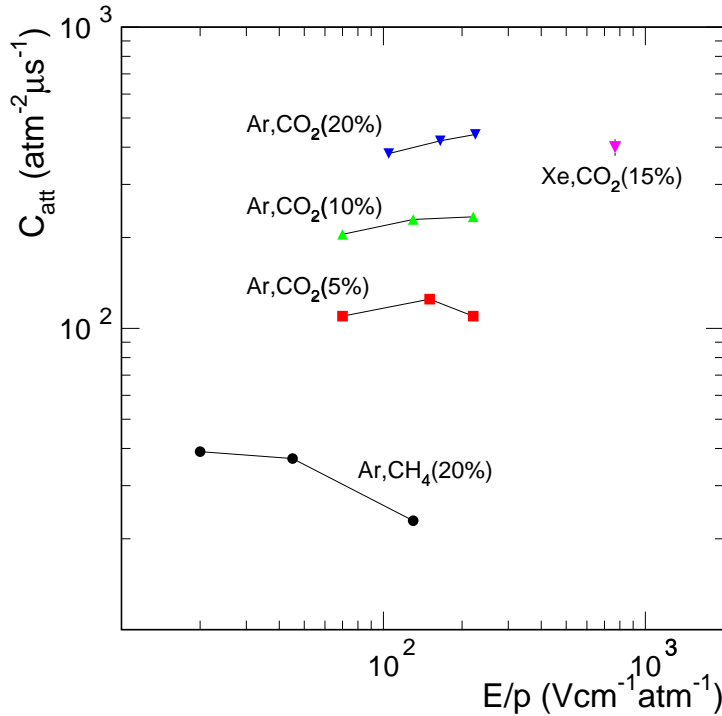


**Figure 4.5:** Electron attachment coefficient as function of the electric drift field and for different Ar mixtures [6] and for Xe,CO<sub>2</sub> (15%).

## 4.2 Mechanical structure

Figure 4.6 shows a cross section through a TRD detector module. The walls of the drift box are made of fibreglass-epoxy and reinforced by aluminium profiles. The drift voltage (-2.1 kV) is applied to an aluminium-coated 50  $\mu\text{m}$  mylar foil which is glued on the radiator unit (see Chapter 3). The radiator unit itself is glued into the drift box and adds mechanical stability to the detector module. It provides gas tightness of the drift volume and keeps the deformation of the drift electrode within the specification (<1 mm at an overpressure of 1 mbar).

The drift field is terminated by a plane of cathode wires which is attached to the upper rim of the drift box. It is followed by a plane of anode wires, providing the necessary gas amplification. In this scheme, the wire tension is transferred to the drift box, causing no mechanical stress on the readout plane.

To avoid drift field distortions at the edges of the readout chamber, potential strips are running along the inner wall of the drift box. The strip pattern is etched into a printed circuit board (Fig. 4.7). The potential of each of the strips has been chosen to minimize field distortions. The appropriate voltage to the potential strips is supplied by a voltage divider resistor chain (Fig. 4.7). The value of the last resistor in the chain has been tuned to optimize the electrostatic matching between drift region and amplification region (see Section 4.6).

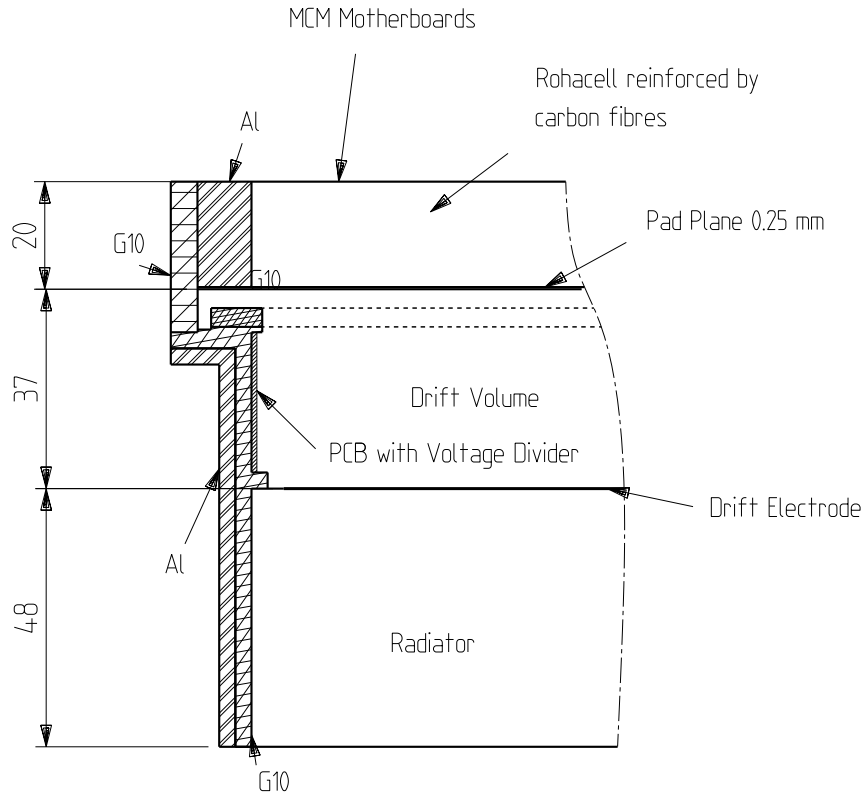


**Figure 4.6:** Cross section through a TRD detector module.

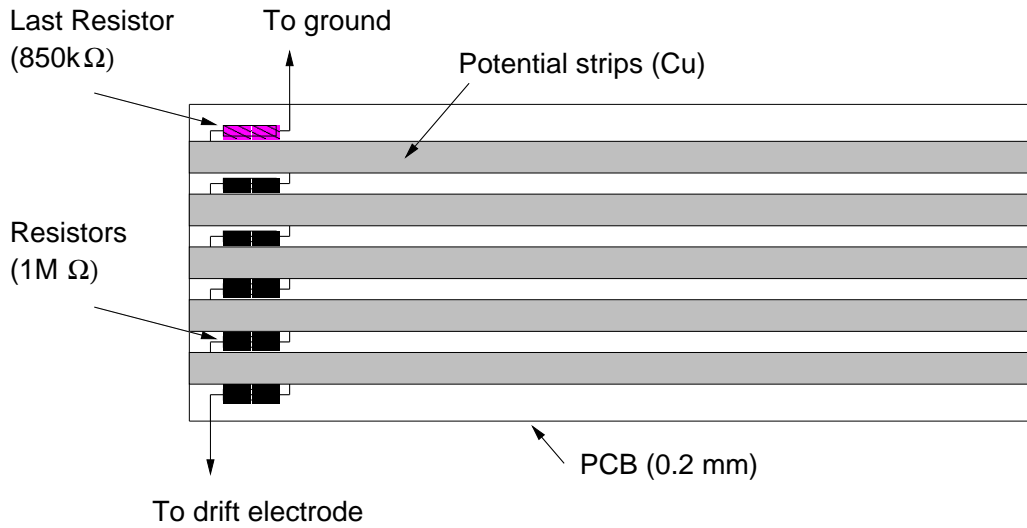


**Figure 4.7:** Potential strip PCB and voltage divider chain.

The current of the backdrifting positive ions ( $\approx 0.5 \mu\text{A}$  per readout chamber, see Section 4.6) could potentially cause a modification of the voltage settings on the potential strips and the drift electrode. The total resistance of  $5.85 \text{ M}\Omega$  from drift electrode to ground potential leads to a chain current of  $360 \mu\text{A}$  at a drift voltage of  $-2.1 \text{ kV}$ . This is sufficiently large to avoid significant ion-induced changes of the drift voltage settings. The power dissipation in the resistor chain is negligible ( $\approx 1 \text{ W}$ ).

The readout plane is a composite structure containing the pad plane, a layer of carbon fibre reinforced Rohacell® foam and the Multi Chip Module (MCM) motherboards which carry the front-end part of

the readout electronics (Fig. 4.8). The pad plane is made up of three individual printed circuit boards (2 layers, 0.25 mm), carrying the readout pad pattern at the inside of the detector. Charge signals induced on the pads are passed via plated-through connections to the back side of the pad plane. Flexible cables are soldered to the back side of the pad plane and transmit the analog signals to the MCMs which are mounted on the MCM motherboards (4 layers, 0.4 mm). These motherboards carry a ground plane, voltage and clock distributions and the digital signals.

The mechanical rigidity of the readout plane against gravitational forces and pressure gradients is provided by a 20 mm layer of Rohacell® foam. It is glued to the back side of the pad plane PCBs and guarantees the flatness of the pad surface. It also covers the plated-through holes and the joints between the individual pad plane PCBs to ensure gas tightness. For mechanical rigidity the back side of the Rohacell® foam is covered with a thin carbon fibre laminate, thus forming a sandwich-like structure. Optionally, also thin carbon fibre rods (2 mm diameter) can be used. Prototype measurements and calculations have indicated that the maximum deformation of the pad plane can be kept below  $150 \mu\text{m}$  at the maximum overpressure of 1 mbar if the Rohacell® foam is laminated with a  $200 \mu\text{m}$  carbon fibre layer.

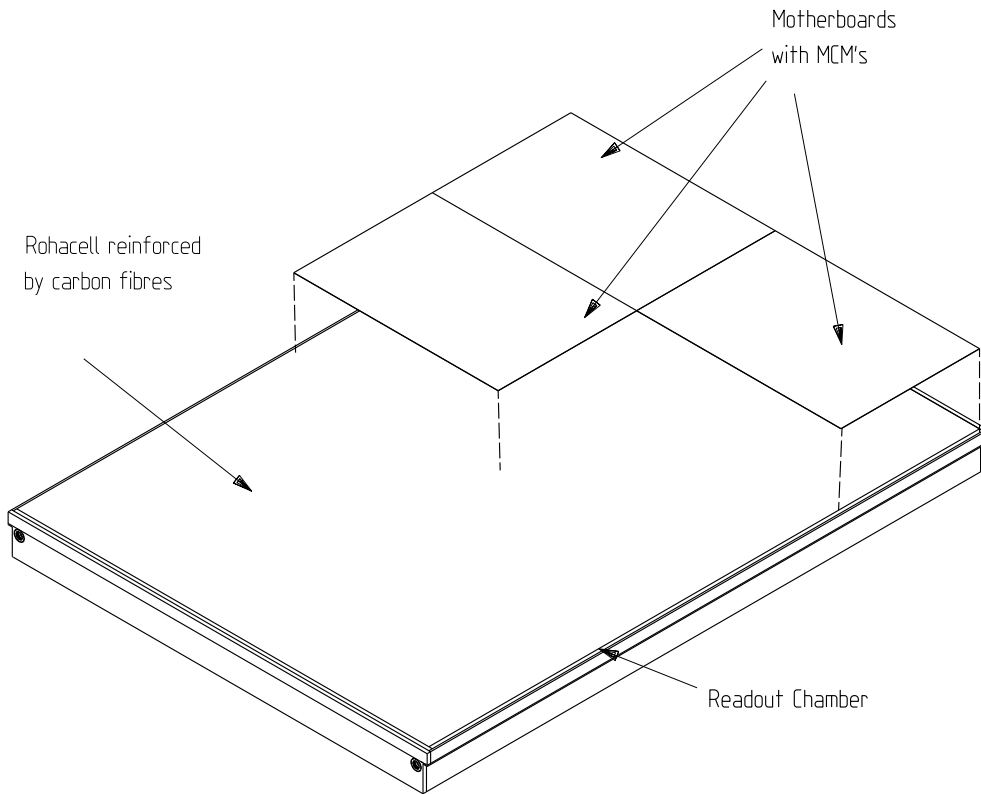


**Figure 4.8:** Top view of a TRD readout chamber.

### 4.3 Wire planes

The number of electrons liberated by the passage of a charged particle in the ALICE TRD (275 per cm for a minimum ionizing particle) is not sufficient to produce a measurable signal without further amplification. The readout chambers therefore employ a scheme of two planes of wires, both running in azimuthal direction. They provide gas amplification in the range of  $10^4$  by avalanche creation. At this gas gain we expect a chamber current of  $1 \mu\text{A}/\text{m}^2$ , resulting in a total charge accumulation of  $50 \mu\text{C}$  per year and per cm of wire. For these low doses, we do not expect particular problems with ageing [7], provided proper gas purity and choice of detector materials.

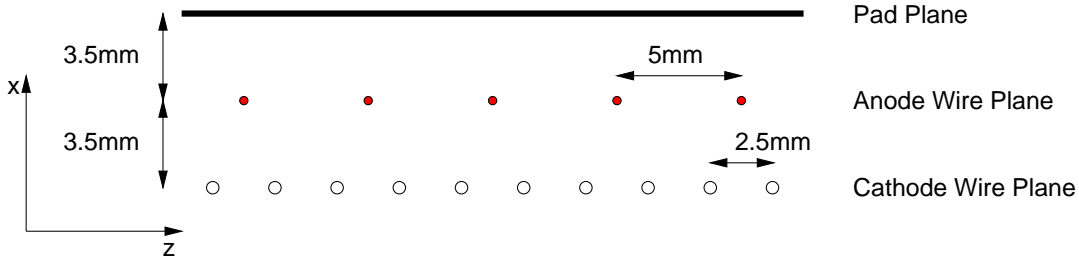


**Figure 4.9:** Wire geometry of the ALICE TRD readout chambers.

The drift and amplification region are separated by the cathode wire plane (Fig. 4.9). The cathode wires are kept at the same potential as the pad plane (ground). Electrons produced in the drift volume pass the cathode grid and start an avalanche close to the anode wires, which are biased by a positive potential (typically +1.4 kV, see Section 4.6).

The anode wire plane is centered between pad plane and cathode wire plane, with a gap of 3.5 mm between anode wires and pad plane. This gap has been optimized to provide appropriate charge sharing between adjacent pads (see Section 4.4). The pitch between anode wires is 5 mm.

The cathode wires are staggered with respect to the anode wires and have a pitch of 2.5 mm (see Fig. 4.9). The cathode wire plane decouples the drift field from the amplification region and thus allows independent adjustment of drift velocity and gas gain (see also Chapter 14). It is more than 99% transparent for electrons, but prevents about 72% of the positive ions produced in the avalanche from drifting back into the drift region (see Section 4.6).

Materials, dimensions, and tension of the wires used in the ALICE TRD are listed in Table 4.1.

**Table 4.1:** Materials, dimensions, and tension of the wires used in the ALICE TRD readout chambers.

	Anode wires	Cathode wires
Material	Au plated W	Cu/Be
Diameter	$20 \mu\text{m}$	$75 \mu\text{m}$
Tension	0.45 N	1.2 N
Length	100 – 120 cm	100 – 120 cm
Total number	140k	280k

## 4.4 Readout pads

The positive ions created in the avalanche process in the vicinity of the anode wire move towards the surrounding electrodes, inducing a positive signal on the pad plane. A precise determination of the location of the avalanche in azimuth can be obtained if the induced charge is shared among several adjacent readout pads. The measurement of the azimuthal position in each of the 15 time bins allows a determination of the track angle in the  $r\phi$ -plane in each TRD layer.

The actual sizes and numbers of pads in each of the readout chambers are listed in Table 4.2. We have chosen rectangular pads with average size  $7.25 \times 87.5 \text{ mm}^2$  (Fig. 4.10). This results in a pad area of about  $6.3 \text{ cm}^2$ . In each readout chamber the pads are grouped in rows of 144, running in azimuthal direction. The total number of pad rows in  $z$ -direction is 70–76, depending on the layer. The actual size of the pads is constant within a given readout chamber but varies slightly for different detector modules, because of the change of the overall detector module dimensions as function of radius and  $z$  (see Chapter 2). The total number of pads is 1 156 032.

**Table 4.2:** Dimensions that define the active area and pad sizes in different readout chambers. The numbering scheme for the detector modules is described in Chapter 2.

Layer	Module	Width (y)	Length (z)	Pad rows	Pad width $w$	Pad length $l$	Area
[0-5]	[0-4]	[cm]	[cm]	#	[cm]	[cm]	[cm $^2$ ]
0 (inner)	0	93.6	120.5	16	0.65	7.53	4.90
	1	93.6	120.5	16	0.65	7.53	4.90
	2	93.6	107.0	12	0.65	8.91	5.80
	3	93.6	120.5	16	0.65	7.53	4.90
	4	93.6	120.5	16	0.65	7.53	4.90
1	0	98.1	128.0	16	0.68	8.00	5.45
	1	98.1	128.0	16	0.68	8.00	5.45
	2	98.1	107.0	12	0.68	8.91	6.07
	3	98.1	128.0	16	0.68	8.00	5.45
	4	98.1	128.0	16	0.68	8.00	5.45
2	0	102.5	131.5	16	0.71	8.21	5.85
	1	102.5	135.5	16	0.71	8.46	6.03
	2	102.5	107.0	12	0.71	8.91	6.35
	3	102.5	135.5	16	0.71	8.46	6.03
	4	102.5	131.5	16	0.71	8.21	5.85
3	0	106.9	139.0	16	0.74	8.68	6.45
	1	106.9	143.0	16	0.74	8.93	6.63
	2	106.9	107.0	12	0.74	8.91	6.62
	3	106.9	143.0	16	0.74	8.93	6.63
	4	106.9	139.0	16	0.74	8.68	6.45
4	0	111.4	139.0	14	0.77	9.92	7.68
	1	111.4	150.0	16	0.77	9.37	7.25
	2	111.4	107.0	12	0.77	8.91	6.90
	3	111.4	150.0	16	0.77	9.37	7.25
	4	111.4	139.0	14	0.77	9.92	7.68
5 (outer)	0	115.8	131.5	13	0.80	10.11	8.13
	1	115.8	157.5	16	0.80	9.84	7.92
	2	115.8	107.0	12	0.80	8.91	7.17
	3	115.8	157.5	16	0.80	9.84	7.92
	4	115.8	131.5	13	0.80	10.11	8.13

Other pad sizes and shapes, such as *chevrons* [8] have also been considered during the R&D phase. An appropriate choice of the chevron geometry allows to adjust the shape of the pad response function over a wide range of pad widths and anode-pad distances (for an overview see Chapter 14). However, chevron pads require high precision during manufacturing of the pad plane and positioning of the anode wires. In addition, chevron pads compared to rectangular pads give rise to a higher pad-to-pad capacitance and thus larger signal cross-talk. Since we found a good solution to achieve the required charge sharing also with rectangular pads and a reasonable wire plane separation, chevron pads are not part of the baseline design presented here.

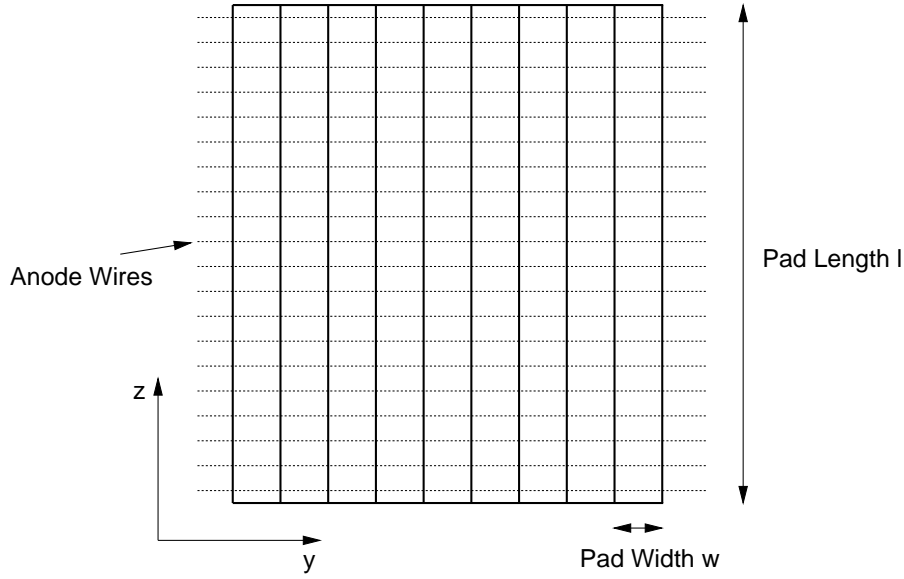


**Figure 4.10:** Pad geometry of the TRD readout chambers. Also shown are the anode wires.

#### 4.4.1 Pad response function

To achieve the best possible position resolution in azimuthal direction, the induced charge distribution needs to be shared by typically two or three adjacent pads. If more than three pads fire, the resolution suffers from a poorer signal-to-noise ratio, connected with an overall increase of the data volume and a limitation of the two-track separation. Therefore, a proper matching of the pad width  $w$  to the width of the induced charge distribution is required. The relative pulse height distribution on adjacent pads, induced by a point-like avalanche at the anode wire, is called the pad response function (PRF) [7]. It can be calculated by integration of the induced charge distribution over the pad area  $S$ :

$$\text{PRF}(x, y) = \int_S Q(x', y') dS. \quad (4.5)$$

The two-dimensional induced charge distribution  $Q(x', y')$  depends on the wire geometry and was calculated according to [9]. Figure 4.11 shows the calculated pad response functions for a distance of  $h = 3.5$  mm between the pad plane and the anode wire plane. For the range of pad widths in the ALICE TRD (see Table 4.2), the resulting PRFs are approximately Gaussian and a reasonable charge sharing can be achieved.

#### 4.4.2 Improvement of $z$ -resolution

In the present pad design, the coordinate  $\phi_i$  of a reconstructed point  $i$  is directly related to its center of gravity  $\langle y_{\text{pad}} \rangle$  in pad space, while the  $z$ -resolution is limited by the finite length  $l$  of the pads in a given pad row:

$$\phi_i = \phi(\langle y_{\text{pad}} \rangle), \quad (4.6)$$

$$z_{\text{row}} - \frac{l}{2} < z_i < z_{\text{row}} + \frac{l}{2}, \quad (4.7)$$

$z_{\text{row}}$  being the  $z$ -coordinate of the center of a pad row.

Optionally, we consider to tilt the pads slightly by an angle  $\alpha$  with respect to the  $z$ -axis. If this tilt is performed in opposite direction in consecutive layers of the TRD (Fig. 4.12), significant improvement of the  $z$ -resolution can be achieved.

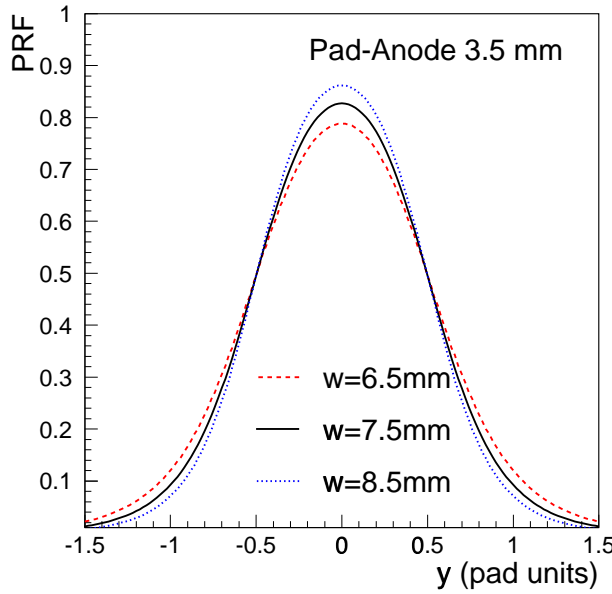


**Figure 4.11:** PRF for different pad widths.

In the case of tilted pads, the coordinates  $(\varphi_i, z_i)$  of a reconstructed point in a given layer are related to  $\langle y_{\text{pad}} \rangle$  and the tilt angle  $\alpha$ :

$$\varphi_i = \varphi(\langle y_{\text{pad}} \rangle) + (z_i - z_{\text{row}}) \sin \alpha. \quad (4.8)$$

This way, the measurements of  $\varphi_i$  and  $z_i$  in a single layer are no longer independent. However, if the next layer is tilted by  $-\alpha$  the point coordinates are given by:

$$\varphi_j = \varphi(\langle y_{\text{pad}} \rangle) - (z_j - z_{\text{row}}) \sin \alpha. \quad (4.9)$$

By matching track points from different layers and assuming an appropriate track model (helix), the best  $z$ -position can be determined by a minimization procedure.

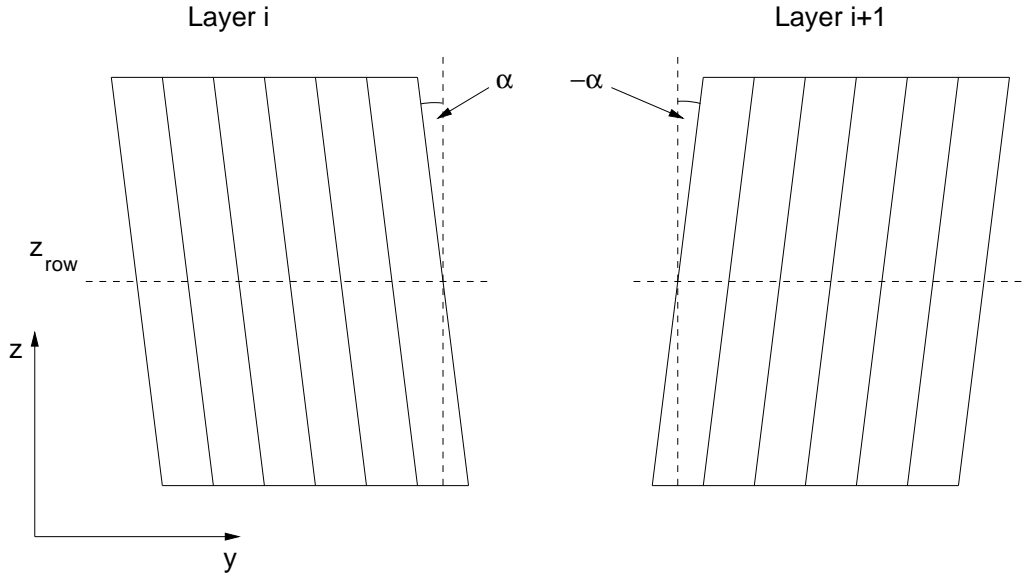


**Figure 4.12:** Geometry of tilted pads.

We have simulated the  $\varphi$ - and  $z$ -resolution as function of the pad tilt angle  $\alpha$ . For simplicity, we considered only two layers and straight tracks with  $\theta=90^\circ$ . In that case, the track model is very simple ( $\varphi=\text{const.}$ ,  $z=\text{const.}$ ). Figure 4.13 shows the resolution in  $\varphi$ - and  $z$ -direction as function of the pad tilt angle  $\alpha$ . The numbers correspond to the averaged  $\varphi$ - and  $z$ -positions of the track, using 10 points in each of the two layers. As expected, the resolutions scale with  $\alpha$ :

$$r\Delta\varphi \propto 1/\cos\alpha, \quad (4.10)$$

$$\Delta z \propto 1/\sin\alpha, \quad (4.11)$$

as indicated by the dashed lines in Fig. 4.13. Obviously, already at tilt angles around  $5^\circ$  the  $z$ -resolution can be substantially improved without a noticeable loss in  $\varphi$ -resolution. Note that for individual points the  $z$ -resolution is limited by the anode wire pitch (5 mm).

Since the impact of tilted pads on the trigger scheme and the offline reconstruction is not yet fully explored they are not part of the baseline design presented here.

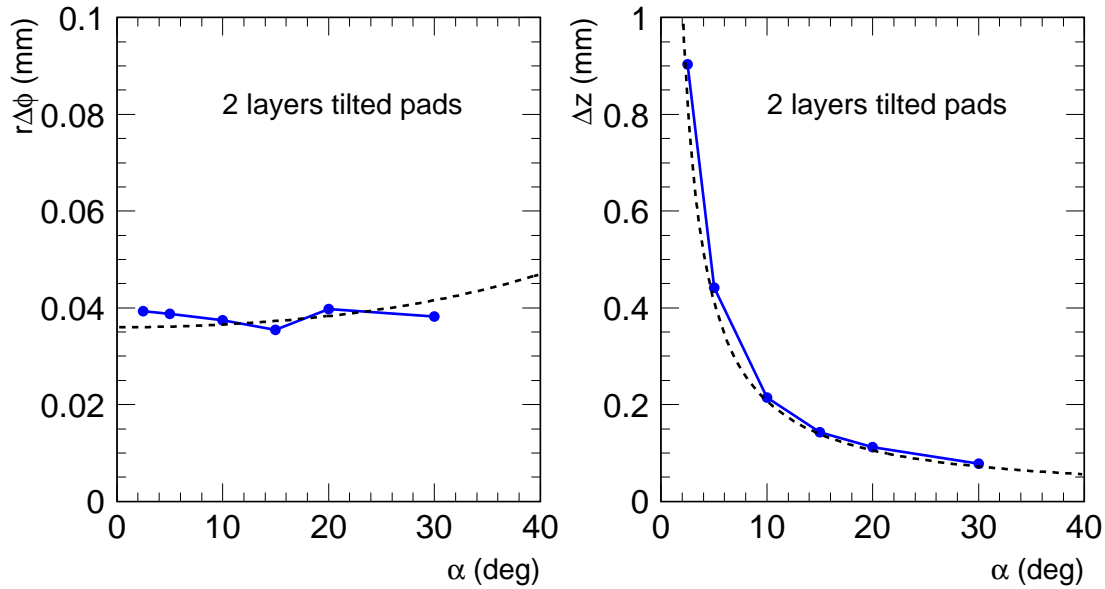


**Figure 4.13:** Resolution of track averaged  $\varphi$ - and  $z$ -positions as function of the pad tilt angle  $\alpha$  (see text). Two layers with tilt angle  $\pm\alpha$  are assumed.

## 4.5 Track reconstruction

Charged particles leave a trace of ionization in the drift volume. The momentum of a particle can be determined by the measurement of the deflection angle of the particle track in the  $r\varphi$ -plane. By sampling the time distribution of the arriving electrons in 15 time bins, a set of individual  $r,\varphi$  measurements for each track segment can be obtained. Given precise knowledge of the drift velocity, the  $r$ -coordinate of each point is given by the arrival time. The  $\varphi$ -coordinate can be derived from the distribution of the induced charge over two or three adjacent pads in each time bin.

The charge signal induced on the pad plane is that of the positive ions created in the avalanche process drifting away from the anode wire. Due to the very low mobility of Xe ions ( $0.57 \text{ cm}^2/\text{Vs}$ ) the induced signal on the pads of a point-like primary electron cluster has a considerable tail (see Fig. 4.14, upper panel). After pulse shaping (shaping time 125 ns FWHM) the signal has a width of approximately 200 ns. However, because of the ion tail the time response function (TRF) is non-Gaussian (see Fig. 4.14, lower panel).

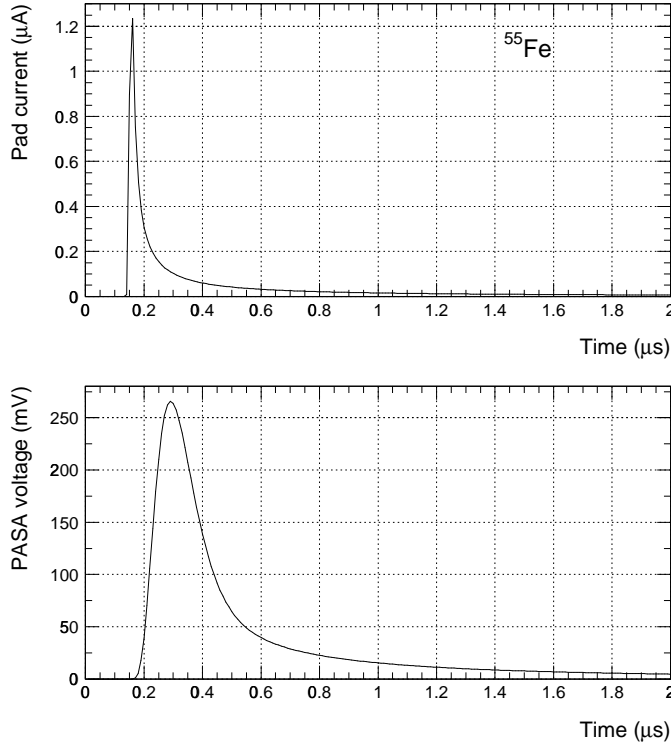


**Figure 4.14:** Simulated response to a  $^{55}\text{Fe}$  signal. Upper panel: the current induced on the readout pads. Lower panel: electronics response after pulse shaping (TRF).

Since the tail of the TRF is long compared to the distance of time bins (133 ns) it leads to a significant correlation among consecutive time bins. If a large charge deposition occurs due to Landau fluctuations or TR absorption on an inclined track, adjacent time bins are 'pulled' away from the trajectory (see Fig. 4.15 for simulated examples).

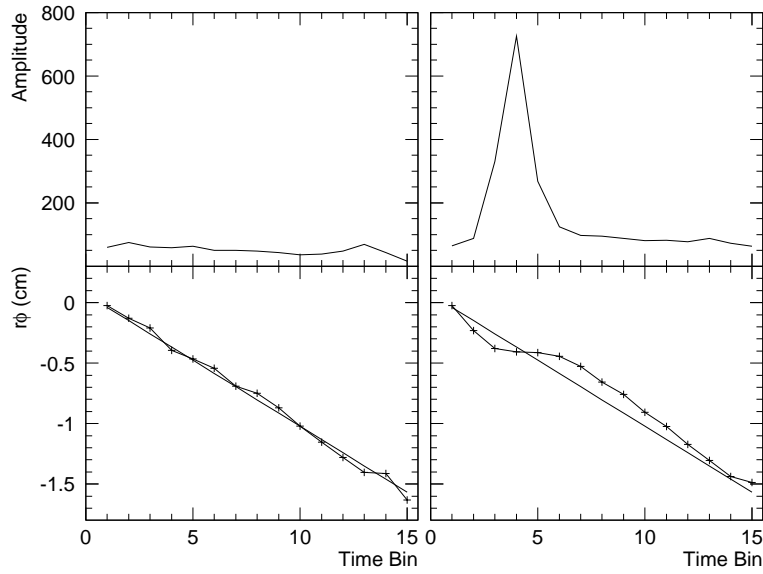


**Figure 4.15:** Two examples of simulated tracks. In the upper panels the pulse height integrated over neighboring pads is shown; in the lower panels the reconstructed space points (crosses) are compared to the real trajectory (straight line).

This results in a deterioration of the position resolution depending on the incident angle of the track, similar to the well-known  $\tan\alpha$ -effect in TPCs [7]. This is demonstrated in Fig. 4.16, where the angular resolution was simulated as function of the track angle of incidence relative to the pad plane normal. Note that in the presence of a magnetic field this distribution will be shifted by the Lorentz angle.

One way to reduce this effect is to stretch the time scale of the measurement. This can be achieved by a reduction of the drift velocity. However, a significant increase of the readout time would limit the online trigger capability.

The inclusion of an electronic tail cancellation is under way. Its effect has been demonstrated by applying an offline deconvolution of consecutive time bins to prototype data (see Chapter 14).

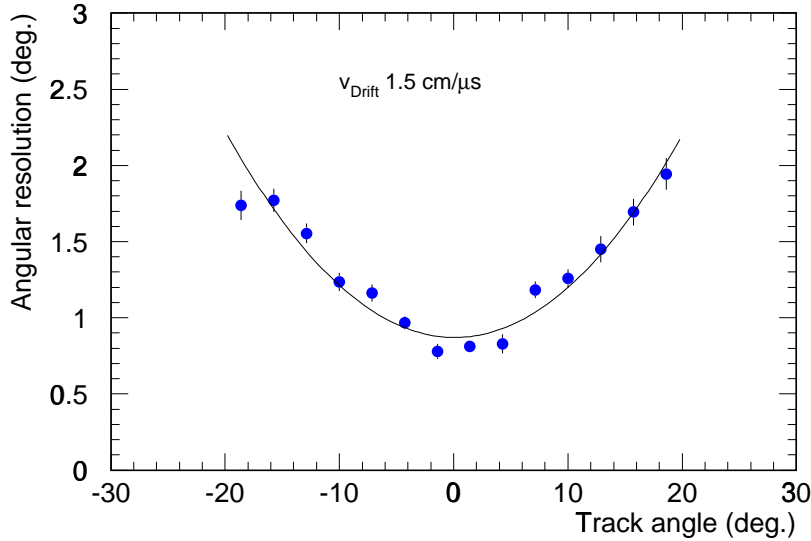


**Figure 4.16:** Angular resolution as function of the track angle relative to the pad plane normal ( $B=0$ ).

## 4.6 Electrostatic calculations

In this section we describe the electrostatic properties for the readout chamber design presented in the previous sections. We determine the operational points and show that the design we have chosen is suited to meet the requirements. All calculations presented here are performed in the framework of the GARFIELD [2] simulation package.

In the calculations, a Xe,CO<sub>2</sub> (15%) gas mixture at atmospheric pressure is assumed. Furthermore, the wire materials, diameters and tensions as listed in Table 4.1 are used.

### 4.6.1 Gas gain

To achieve a reasonable signal-to-noise ratio we are aiming for a gas amplification of  $5 \cdot 10^3$ - $10^4$ . The amplification achieved on the anode wire depends on the gas mixture, the pressure, the wire geometry, and the bias voltages. The gas mixture (Xe,CO<sub>2</sub> (15%)) and the operating pressure are mainly determined by other constraints (see Section 4.1 and Chapter 8).

The gas gain as function of the anode wire voltage is shown in Fig. 4.17. The result for our baseline design with an anode-cathode distance of  $h = 3.5$  mm and staggered wire planes is compared to a non-staggered wire geometry and to a smaller anode-cathode distance of  $h = 2.5$  mm. While there is no noticeable difference between staggered and non-staggered wire planes, the gas gain at a given voltage is larger by almost a factor 5 in the case of  $h = 2.5$  mm. However, the desired sharing of the induced charge

among several adjacent pads requires an anode-cathode separation of  $h = 3.5$  mm. For this geometry, we achieve a gas gain of 8000 at an anode voltage  $U_a = 1420$  V.

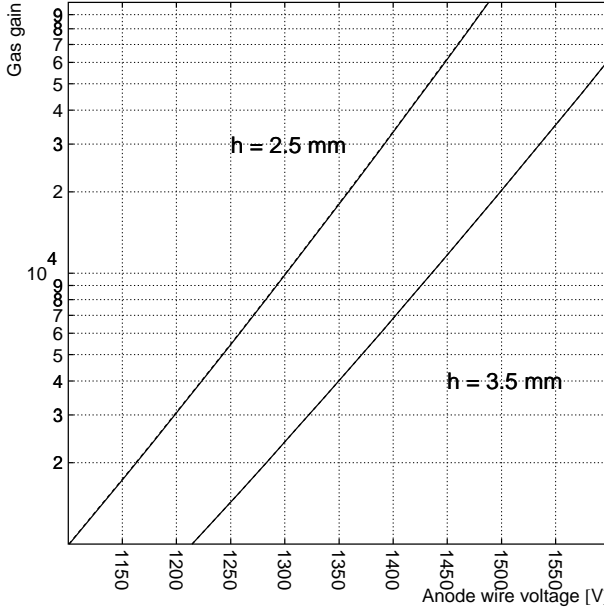


**Figure 4.17:** Gas gain as function of the anode voltage.

High momentum tracks originating from the main vertex traverse the TRD preferentially under small angles with respect to the wire normal. For a given track, this can lead to a relatively large charge deposition along a limited piece of anode wire. The ions created in the avalanche process build up a cloud of positive charge slowly moving away from the wire. This leads to a reduction of the electric field in the vicinity of the wire and therefore to a lower gas gain for subsequent electrons. As a consequence, the gas amplification decreases as function of the drift time for tracks which cross the TRD under small angles with respect to the wire normal. Following [7] we calculated the gain attenuation for minimum ionizing particles in Xe,CO<sub>2</sub> (15%). Figure 4.18 shows the pulse height as function of the drift time for different angles of incidence. The pulse height was normalized to that of 17° tracks where the effect is negligible. An attenuation of the gas gain is clearly visible, most pronounced for small track angles. The calculations for a gas gain of 10<sup>4</sup> are consistent with our prototype data (see also Chapter 14). This observation underlines that the TRD readout chambers should be operated at gas gains not exceeding 10<sup>4</sup>, in line with the planned values.

### 4.6.2 Gain stability

The positive voltage applied to the anode wires causes the anode wires to sag towards the pad plane. The sagitta of the sagging anode wire depends on the wire material, diameter, length and tension, the wire geometry, and the applied voltage  $U_a$ . For this computation, we use the maximum wire length in the TRD of 120 cm. We show the anode wire sag as function of  $U_a$  in Fig. 4.19 (left panel). Again, different wire geometries are compared. The sag is significantly smaller for  $h = 3.5$  mm compared to  $h = 2.5$  mm. At a typical operating voltage of  $U_a = 1400$  V ( $h = 3.5$  mm) the anode wire sag is 35 μm. Not shown is the contribution from gravity, which amounts to about ±20 μm, depending on the orientation of the readout chamber.

Also, the cathode wires are exposed to electrostatic forces. Their sag, however, is small due to the larger tension applied to them (Fig. 4.19 right panel). The impact of the cathode wire sag on the uniformity of the electric drift field is negligible.

The anode wire sag leads to a variation of the gas gain along the wire. The relative gain variation

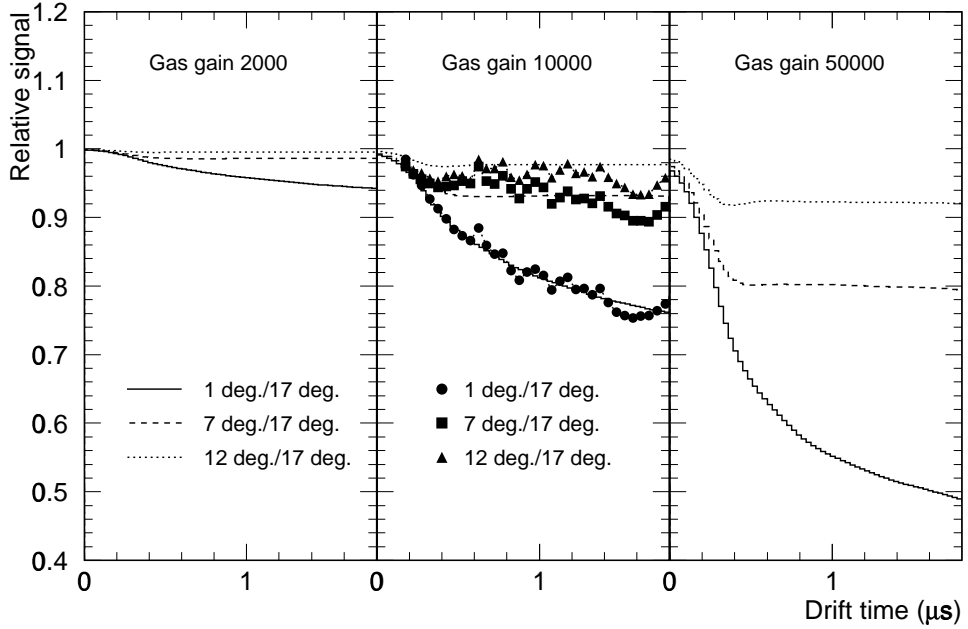


**Figure 4.18:** Calculated relative gas gain as function of the drift time for different gas gains and angles of incidence. The data points are from prototype measurements (see Chapter 14).

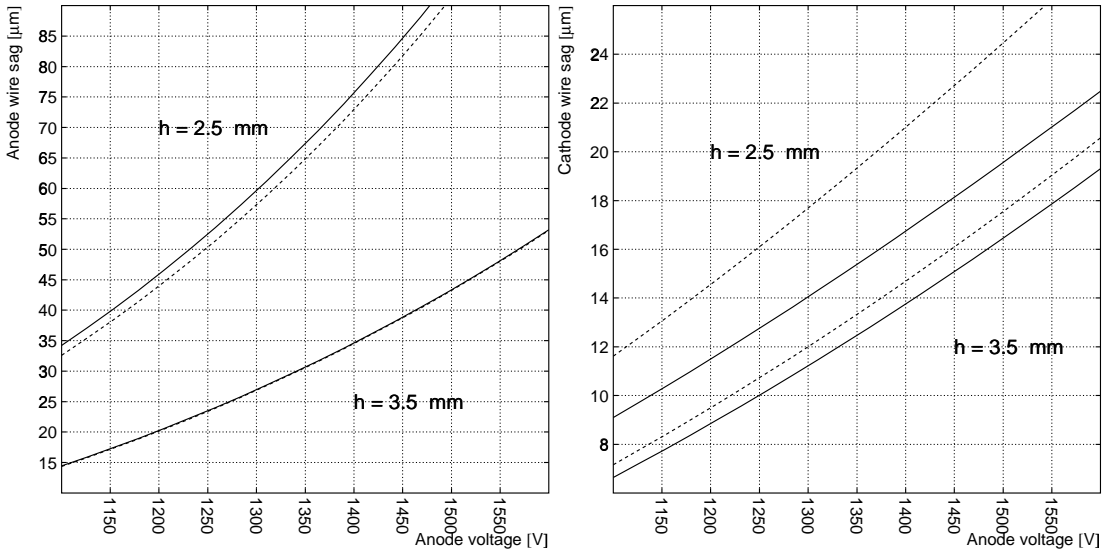


**Figure 4.19:** Anode wire sag (left) and cathode wire sag (right) as function of the anode voltage. The dashed line refers to the non-staggered geometry.

as function of the sag is computed for  $U_a = 1400$  V and shown in Fig. 4.20. At the maximum sag of  $35 \mu\text{m}$  we calculate a relative gain variation  $\Delta\text{Gain}/\text{Gain} \approx 1.7\%$ . Adding the contribution from gravity we conclude that the gain variations caused by wire sag are below 3% everywhere in the detector, assuming a perfectly flat pad plane.

The operation of the detector at a slight overpressure of 1 mbar leads to a deformation of the pad plane of about  $150 \mu\text{m}$ . From our calculations we expect this to cause a gain variation of 7%. This gain variation is partially compensated by the anode wire sag. The possibility of a minimization of the gain variations by placing the anode wire plane slightly asymmetric between cathode wire plane and pad plane is under investigation.

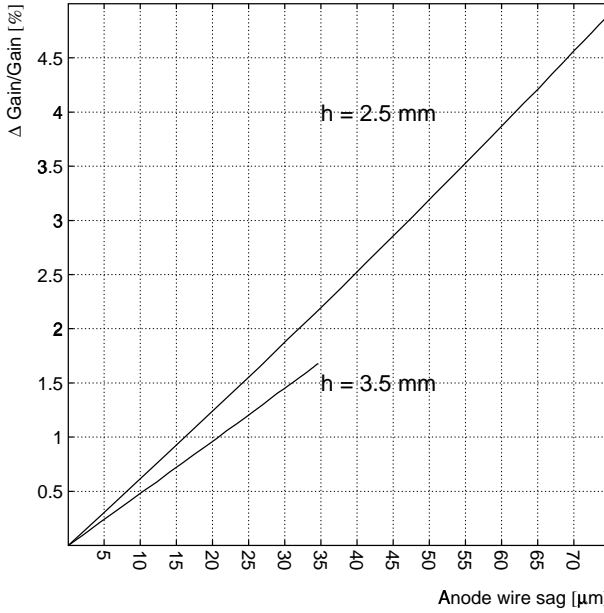


**Figure 4.20:** Relative gas gain variation as function of the anode wire sag.

#### 4.6.3 Pad coupling

The charge induced by the movement of the positive ions away from the anode wire is shared among all surrounding electrodes. Only a fraction of it couples to the readout pads and contributes to the measured signal. The fraction of the charge which couples to the pads is a function of the ion drift time and direction and therefore depends on the angular distribution of the avalanche. It should be noted that only for gas gains well above  $10^4$  the avalanche can be assumed to be isotropic around the wire [7].

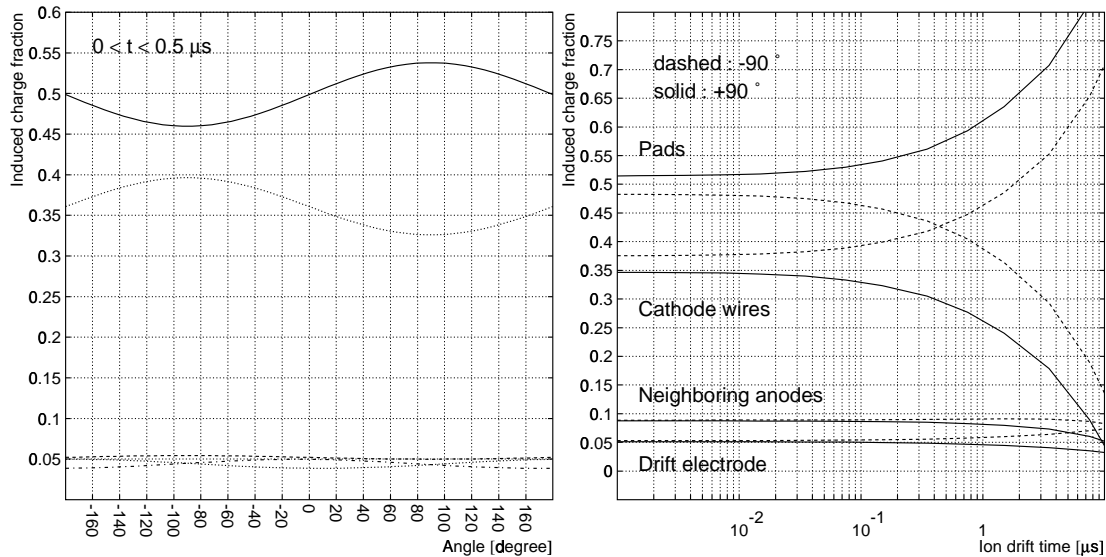


**Figure 4.21:** Left panel: fractions of charge induced on the various electrodes as a function of the angle under which the ions drift away from the wire. Solid: pads, dotted: cathode wires, dashed: drift electrode, dash-dotted and dotted: neighboring anode wires (left and right). Right panel: ion drift time dependence of the induced charge for  $90^\circ$  (ions drifting towards the pads) and  $-90^\circ$  (towards the cathode wires).

Figure 4.21 (left panel) shows the fraction of the induced charge flowing to the various electrodes during the first 500 ns as function of the angle under which the ions leave the anode wire. As expected,

the signal induced on the pads is maximal if the ion drifts into the direction of the pad plane ( $90^\circ$ ) and minimal if it drifts to the cathode wires ( $-90^\circ$ ). On average, we expect about 50% of the signal to be induced on the readout pads and 36% on the cathode wires. Note that a significant fraction of the signal is induced on the neighboring anode wires and the drift electrode.

The ion drift time dependence of the induced charge is shown in Fig. 4.21 (right panel) for ions drifting towards the pad plane ( $90^\circ$ ) and towards the cathode wires ( $-90^\circ$ ). The fraction of the induced charge on a given electrode is approximately constant over the first  $1 \mu\text{s}$  (note that the typical integration time of the readout electronics is  $<500 \text{ ns}$ , see Fig. 4.14). By that time, the ions have moved away from the anode wire by about  $200 \mu\text{m}$ .

#### 4.6.4 Ion feedback

Unlike many other drift detectors, the readout chambers in the ALICE TRD contain no gating grid. Therefore, all ionization produced in the drift region will inevitably lead to avalanche creation at the anode wires. This causes a continuous current of positive ions drifting back into the drift volume and ending at the drift electrode. However, not all ions find their way back into the drift volume. Figure 4.22 shows the drift lines and lines of equal drift time (isochrony lines) of positive ions produced at the anode wire. Only about 28% of them drift back into the drift volume, the remainder reaches the surrounding electrodes. This leads, under operating conditions, to an ion feedback current of about  $0.5 \mu\text{A}$  through the drift volume (see also Section 4.3). From that we expect a charge density in the drift volume of about  $1.6 \cdot 10^5 \text{ ions/cm}^3$ . The resulting distortions of the electric drift field can be calculated and were found to be well below  $10^{-3}$  with respect to the nominal field strength of  $700 \text{ V/cm}$ .

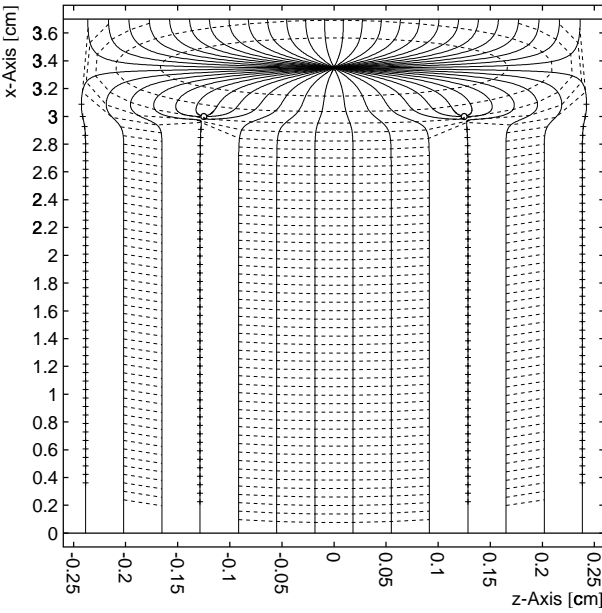


**Figure 4.22:** Drift lines (solid) and isochrony lines (dashed) of positive ions starting from the anode wire. The anode wire is at  $z=0 \text{ cm}$ , the cathode wires are at  $z = \pm 0.125 \text{ cm}$ .

#### 4.6.5 Isochrony

The finite pitch between the wires causes a systematic drift time variation for electrons starting at the same radius, but from different  $z$ -positions. In the presence of Landau fluctuations this can potentially lead to a deterioration of the drift time determination. The drift time variation for electrons starting at constant  $r$  close to the drift electrode is shown as function of their  $z$ -position relative to the anode wire

in Fig. 4.23. We have implemented the observed non-isochrony into a microscopic drift simulation and found no noticeable effect on the position resolution.

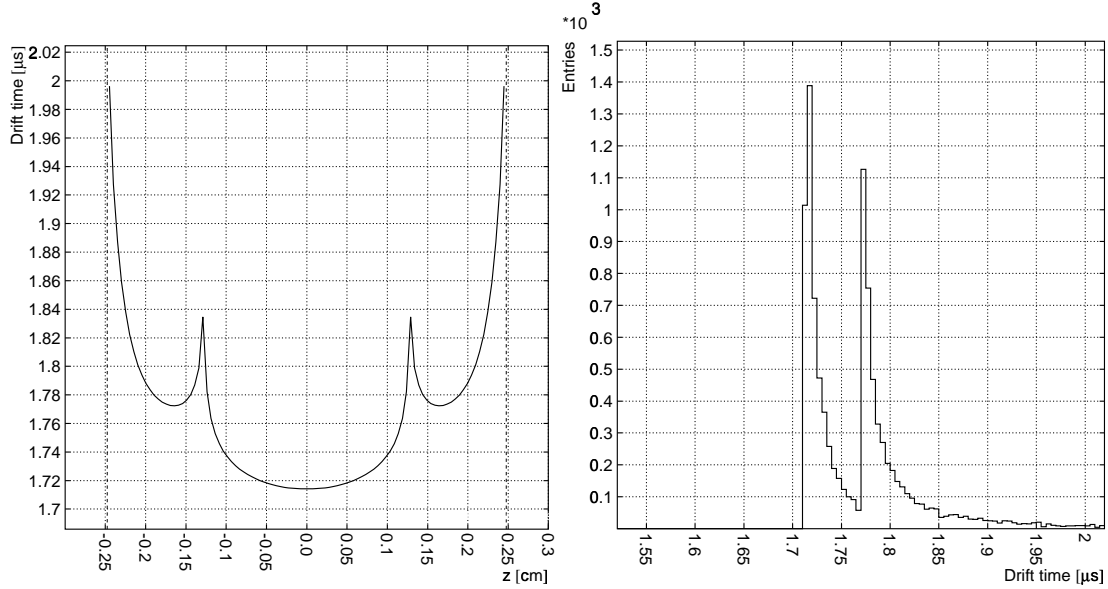


**Figure 4.23:** Left panel: drift time variation within a drift cell. The anode wire is at  $z=0$  cm, the cathode wires are at  $z = \pm 0.125$  cm. Right panel: projection on the time axis. The r.m.s. of the distribution is 71 ns.

#### 4.6.6 Electrostatic matching

Due to the finite pitch of the cathode wires (2.5 mm) not all field lines from the amplification region end on the cathode wires. As a result, the effective ground plane is not at the position of the cathode wires but shifted by about 0.7 mm towards the drift electrode (Fig. 4.24).

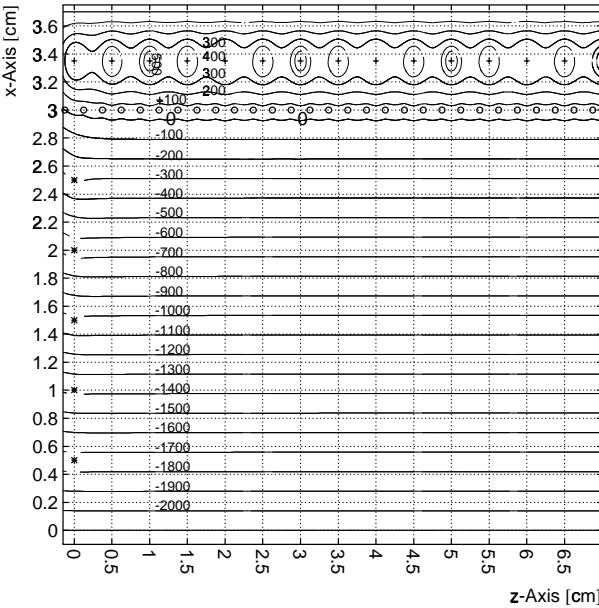


**Figure 4.24:** Equipotential lines in the readout chambers, using  $U_a = 1400$  V and  $U_{\text{drift}} = -2100$  V. The positions of the potential strips are indicated by the stars at  $z=0$ .

This can be compensated by proper choice of the last resistor in the voltage divider chain (see Section 4.2). Figure 4.25 shows the electric field 5 cm away from the voltage divider and as function of the distance from the drift electrode ( $U_a = 1400$  V and  $U_{\text{drift}} = -2100$  V). Fixing all other resistors in the chain to  $1 \text{ M}\Omega$ , we obtain the best result for  $R_{\text{last}}=850 \text{ k}\Omega$ .

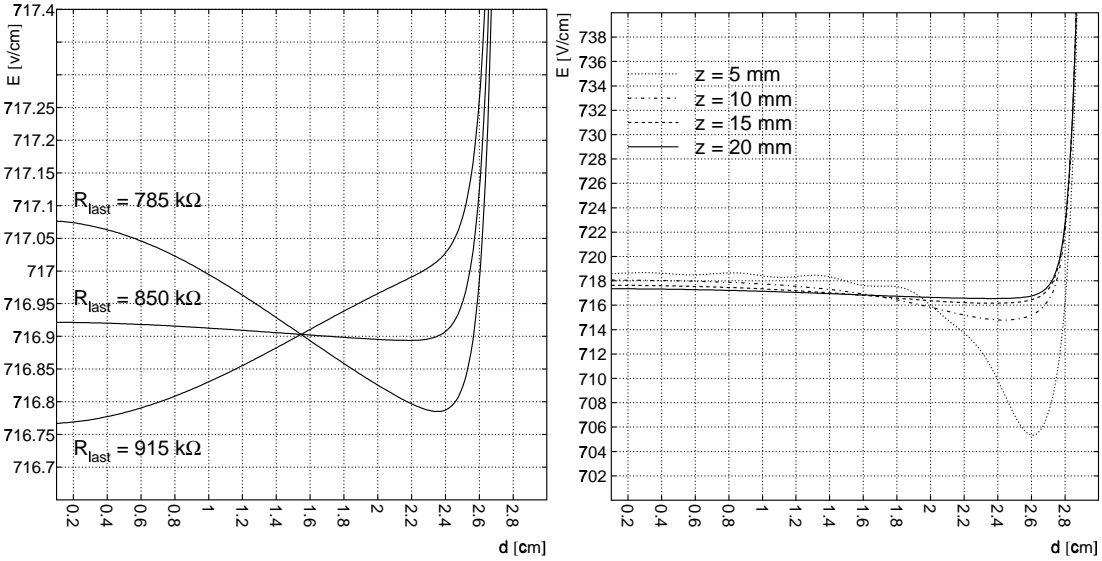


**Figure 4.25:** Left panel: electric drift field as function of the distance  $d$  to the drift electrode and for different values of  $R_{\text{last}}$ . The distance  $z$  to the potential strips is 5 cm, the voltage settings are  $U_a = 1400$  V and  $U_{\text{drift}} = -2100$  V. Right panel: same but for several distances  $z$  closer to the potential strips and fixing  $R_{\text{last}}=850 \text{ k}\Omega$ .

Moving closer to the edge of the drift volume, the granularity of the voltage divider becomes visible, as shown in the right panel of Fig. 4.25. However, only 10 mm away from the potential strips the field becomes smooth and varies by less than 0.5% with respect to its nominal value.



# 5 Front-End Electronics

---

This chapter describes the on-detector electronics as well as relevant work on prototyping that has already been performed. Concerning the TRD trigger, its functionality is outlined in Chapter 6 with emphasis on the implementation of the *tracklet* search and electron candidate identification. This Chapter details the implementation of the front-end electronics (FEE) with its real-time constraints, together with its integration into the ALICE trigger system.

## 5.1 Electronics overview

In this section the requirements for the FEE are reviewed and the general architecture and basic building blocks are introduced. Because we are interested in both the identification of the transition radiation (TR) signal and also in the TRD online tracking, momentum, and invariant mass reconstruction capability (see Chapter 6), the FEE is rather complex and more TPC-like involving a sampling ADC, tail cancellation, detection of overlapping hits etc. The trigger will generate a Level-1 accept (L1A) and therefore has to occur on a time scale of  $6 \mu\text{s}$ . This requirement drives the over all architecture, clock speeds and limits the extent of multiplexing possible.

### 5.1.1 General requirements

As detailed in Section 4.4 the FEE is used to read out and analyze for the Level-1 trigger the charge induced on 1.156.032 pads located in 540 individual readout chambers arranged in 6 layers in the TRD barrel. Most of the front-end electronics sits directly on the readout chambers. For the trigger, however, information from the 6 layers has to be combined at a convenient point close to all readout chambers. The readout chambers deliver on their pads a current signal with a very fast rise time and a long tail due to the slow motion of the Xe ions (see Fig. 4.14). The typical current for a minimum ionizing particle is of the order of  $0.2 \mu\text{A}$ . The pad on which the signal is induced can be viewed as a pure capacitance of 10-20 pF.

The main requirements for the front-end electronics are summarized in Table 5.1 and briefly discussed below.

- The space point resolution in the bending direction ( $y$ ) is derived by charge sharing between 3 adjacent pads. The pad response function is chosen such that for a hit centered on one pad each neighbour still sees 10 % of the signal (see Fig. 4.11 and 11.9). This means adequate space point resolution can be reached for a signal to noise ratio of at least 30:1. Also, it was shown that digitization errors contribute visibly to the space point resolution if the channel number of the peak pad is below 30.
- For a minimum ionizing particle typically a charge of  $3 \cdot 10^4$  electrons contributes to the signal on the maximum pad for each time bin. The requirement of signal to noise equal or larger than 30 defines the goal for an upper limit for the noise of 1000 electrons (r.m.s.).
- In order to not waste dynamic range, one aims to keep the noise amplitude within the ADCs LSB. For an ADC with 1 V dynamic range (see below), this fixes the conversion gain of the preamplifier-shaper (PASA) to 6.1 mV/fC.
- Our main interest is the detection of the TR signal superimposed on the normal ionization. As shown in Fig. 11.4 the TR photon energies reach with noticeable probability up to 20-30 keV. Simulations have shown that the electron-to-pion separation improves with dynamic range and for a minimum ionizing signal amplitude at ADC channel 30, a 10 bit ADC is desirable.

**Table 5.1:** Front-end electronics requirements.

Parameter	Value
Number of channels	$1.156 \cdot 10^6$
Signal-to-noise (MIP)	30:1
Dynamic range	1000:1
Noise (ENC)	$1000 e$
Conversion gain	6.1 mV/fC
Time bins in drift region	$\geq 15$
Separation of time bins	$\leq 133 \text{ ns} \cong 2 \text{ mm}$
Sampling frequency	(8-)10 MHz
Shaping time (FWHM)	$\cong 120 \text{ ns}$
Cross talk	$\leq 0.3 \%$
Bandwidth readout	15 TB/s
Bandwith detector to GTU	216 GB/s
Bandwith DDL	1.8 GB/s
Trigger latency at TRD	$6.0 \mu\text{s}$
Trigger dead time (L0/L1 reject)	$1.7 \dots 7.0 \mu\text{s}$
Trigger dead time (L1 accept)	$20 \dots 40.5 \mu\text{s}$
Power consumption	$\leq 50 \text{ mW/channel}$

- In Chapter 11 it is shown that in terms of tracking efficiency and momentum resolution it is sufficient to sample the drift region in 15 points (time bins).
- As shown in Section 4.5, for non-perpendicular angles of incidence the resolution is limited by the long ion tail of the Xe leading to a correlation of the individual time bins. This effect gets worse as the distance between time bins gets shorter or as the drift velocity is increased and the total drift time decreased. This constrains the drift time to be not smaller than  $2 \mu\text{s}$  and to an corresponding distance of two consecutive time bins of 133 ns for 15 time bins. That would correspond to a sampling frequency of 7.5 MHz. Since it is for other reasons convenient if the time intervals are multiples of the bunch separation a frequency of 8 MHz would be a good lower limit. Of course higher frequencies combined with a larger number of time samples would be possible and would slightly reduce the trigger latency due to the faster draining of the ADCs pipeline.
- In order to keep the correlation between the consecutive time bins of a track segment minimal to optimize resolution one would like a shaping time as short as possible. This is however connected with a loss in signal and also the existing long ion tail makes very short shaping times useless. A shaping time of 120 ns, comparable to the separation of the time bins, was found to be a good choice.
- The position and angular resolution can be improved by unfolding the time response function as demonstrated in Fig. 14.38 and 14.39 using a tail cancellation. Since this also noticeably improves the trigger performance (see Section 6.4.2.1) it is desirable that this deconvolution is done on the digital chip before the processing of the trigger information.
- The channel-to-channel cross talk is limited by the pad-to-pad capacitance which is between neighboring pads in one pad row 6.5 pF. This will lead to a cross talk of about 5 % for the present PASA design. The cross talk within the PASA chip itself and in the cable should be negligible as compared to this. It turns out that a value below 0.3 % was easily achievable in the existing PASA

prototype and this is the number quoted in Table 5.1.

### 5.1.2 System overview

The front-end electronics for the ALICE TRD consists of  $1.156 \cdot 10^6$  channels. The basic building blocks are shown for one channel in Fig. 5.1. They are: a charge sensitive PreAmplifier/ShAper (PASA), the analog chip, a 10 Bit 10 MHz low power ADC, and digital circuitry where data are processed and stored in event buffers for subsequent readout. The data processing is performed on one hand during the drift time at digitization rate by the *Tracklet Pre Processor* (TPP) in order to prepare the information necessary for the *Tracklet Processor* (TP). On the other hand at the end of the drift time the Tracklet Processor, a micro CPU implemented as Multiple Instruction Multiple Data (MIMD) processor, operating at 120 MHz, processes the data of all time bins in order to determine potential *tracklet*s. These *tracklet*s are shipped to a Global Tracking Unit (GTU), which combines and processes the trigger information from individual TRD readout chambers.

Upon receipt of a L1 accept, the MIMD processor also ships the zero suppressed raw data from the event buffers on the front-end chips to the GTU, where they are stored in a large memory until read-out (see Chap. 7).

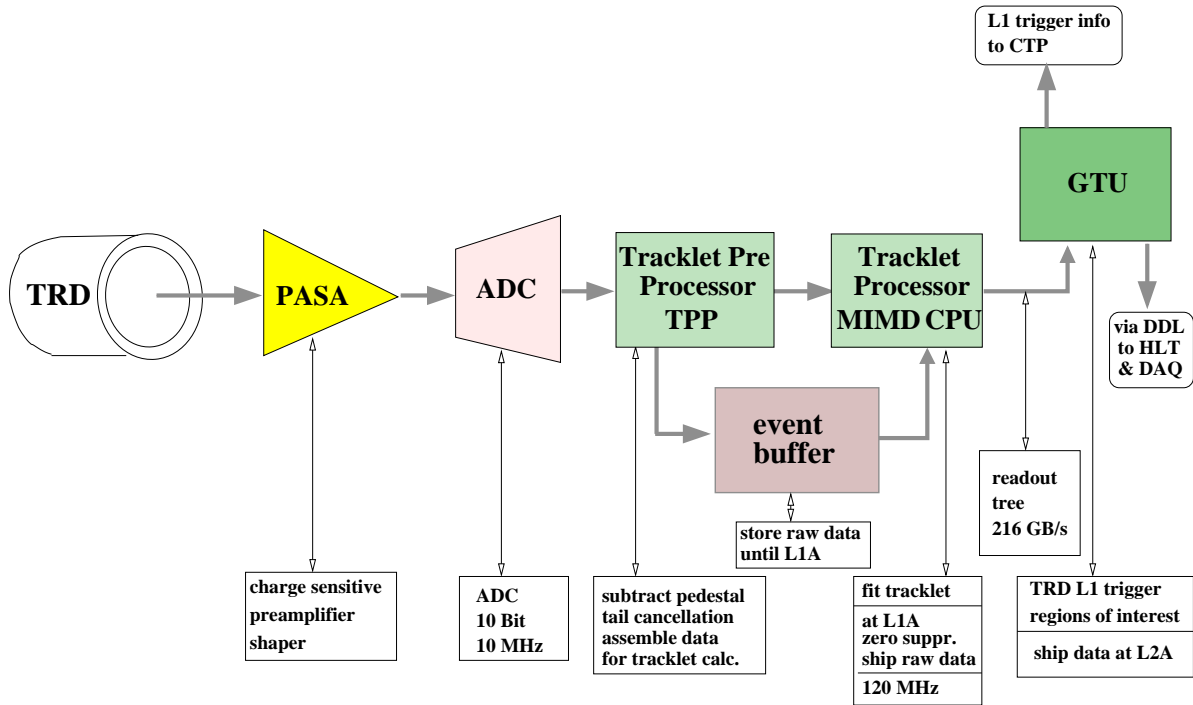


**Figure 5.1:** Basic logical components of the TRD front-end electronics. Everything but the GTU is located directly on the readout chamber. The ADC, digital circuitry, event buffer and MIMD CPU are combined into one digital chip. This chip determines the *tracklets* and is therefore also referred to as local tracking unit (LTU).

The requirement for minimal radiation length, power and cost drive the integration density as high as possible. In order to support mass production of the electronics, 18 channels are grouped together on one multi-chip module (MCM), housing both the preamplifier and the digital back-end (Section 5.8). The particular choice of 18 channels per MCM is a compromise of die size, MCM count and trace length of the analog pad signals. Figure 5.2 indicates the components on one MCM. Basically this module is targeted to contain just those two chips, and possibly the addition of minimal miscellaneous components, such as blocking capacitors. As sketched in Fig. 5.2, the 18 entities labelled 'PS' are on one chip, the PASA, everything enclosed by the thin grey rectangle is on a second digital chip. The logic integrated

on the digital chip includes the ADCs, the *tracklet* preprocessor, and the high-speed multi-threaded processor (MIMD CPU). Therefore this chip is called the local tracking unit (LTU). The pad plane itself carries the readout signals and they are routed to the PASA input via short cables. The MCMs, which are implemented as Ball Grid Arrays (BGA), are soldered directly onto the readout mother boards. The only additional circuitry required on the readout boards are the drivers for the clock fan-out and additional power filtering circuitry. All signals connecting the MCMs are routed on the readout mother board. There are 64224 MCMs mounted on the detector, making the MCM one of the most crucial electronics components, which have to be mass produced.

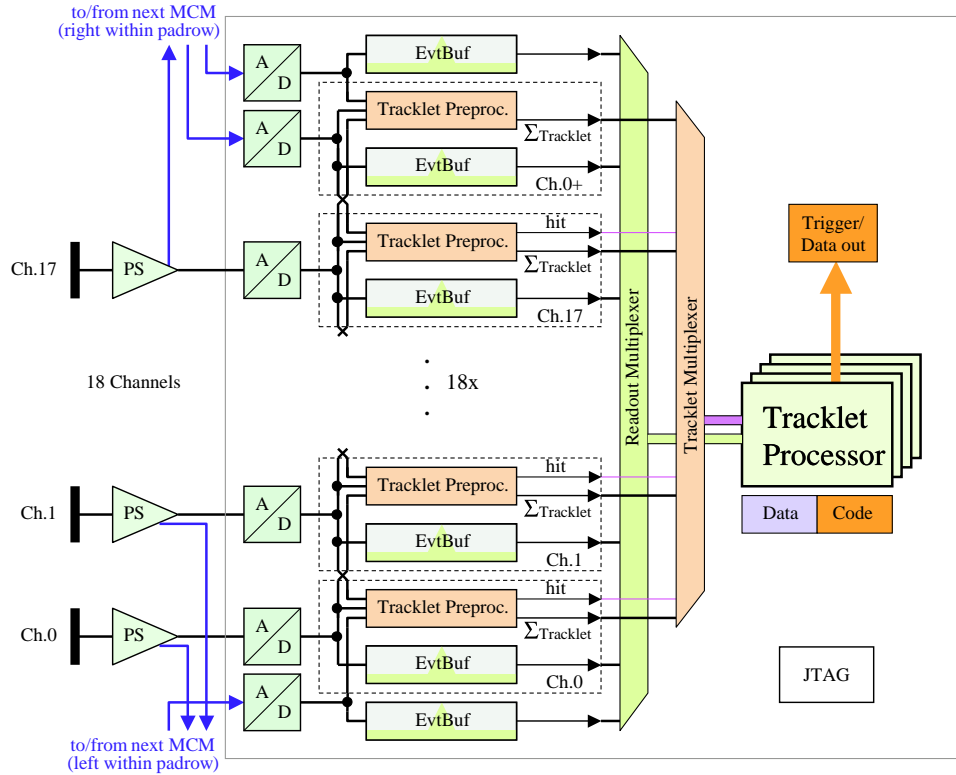


**Figure 5.2:** Overview of the electronics for 18 channels on one MCM.

Given the high (digital) clock rates and the low duty cycle of the trigger system of less than 3%, the digital part of the electronics is operated with gated clocks, allowing for the disabling of the clock to any part of the circuitry that is inactive. This method also permits the reduction of digital noise during digitization. All clocks are synchronous to the LHC clock.

In order to avoid granularity effects at the MCM border, some data need to be exchanged among the neighboring multi-chip modules. For a detailed description of the *tracklet* preprocessing architecture and the *tracklet* merging within the MCM and among neighboring MCMs, refer to Section 6.3. Since it is sufficient to merge *tracklets* only in ascending pad number direction, a total of three additional channels (two left and one right) is required to be processed, as indicated in the figure. Therefore, a total of 21 ADC channels is required for each 18-channel *tracklet* processor. Consequently, three out of 18 preamplifier outputs are required to drive two ADC inputs. In order to avoid any non-linearities, those channels implement two independent output stages, driving one ADC input each. The preamplifier outputs are analog differential signals.

All digitized ADC outputs, including the redundant channels, are stored in 32x10 Bit deep event buffers. During the digitization, the *tracklet* preprocessor identifies candidates and prepares them for later processing by the MIMD CPUs, the *tracklet* processor (Chapter 6.3). During that time, however, the digital back-end is operated at exactly the ADC clock rate.

At the end of the drift time, the fast digital clocks are enabled starting the MIMD processor. Any additional digital noise produced here is irrelevant as the relevant data already sit in the internal event buffers. During stand-by, all digital clocks are disabled. Figures 5.5 and 5.6 sketch which digital clocks are active at what point. The MIMD processor is capable of processing up to four *tracklet* candidates simultaneously. If a *tracklet* is identified and matches the required deflection cut requirements, its *tracklet* parameters are projected onto the global reference plane which is in the middle of the six planes and then forwarded to the readout tree.

The MCM output is a single 16 Bit differential data link, implementing Low Voltage Differential Signals (LVDS). There are additional 5 bits for correcting one bit errors and detecting two bit errors per data word. This format is used as standard link everywhere within the readout tree.

The readout tree terminates the differential output (LVDS) of all MCMs into four 16 Bit data links on either side of the detector per layer and sector, thus merging up to 304 MCMs into one high-speed data link to the global tracking unit. The readout is performed in a strictly ordered fashion to support consecutive readout and highly parallel global tracking. Any of the readout signals is kept inactive during acquisition or stand-by in order to minimize the electronic noise contribution. For a detailed description of the readout tree, refer to Chapter 7.

## 5.2 Chip technology

In general, there are five major components of the front-end electronics chain as summarized below:

- shaping preamplifier
- 10 Bit analog to digital converter
- digital filter for tail cancellation
- event buffer and *tracklet* preprocessor operating at ADC clock rates
- high-speed *tracklet* processor and filter
- high-speed readout tree

The shaping preamplifier is a full custom analog design tailored towards low noise and low power (in this order of priorities). The last three components are purely digital systems running at clock rates ranging from 10 MHz to 120 MHz. These clock rates can well be implemented using standard cell designs. The only requirement for full custom design are some special cells, such as the quad-port memories (refer to Chapter 6, Section 6.3.3.3). Although the first implementations of the digital circuits were designed for the AMS<sup>1</sup> 0.35  $\mu\text{m}$  process, they can be ported to basically any silicon process. All three components, the *tracklet* preprocessor, filter and readout, are purely digital. They can all be implemented on the same die without presenting any particular technological challenges. In order to separate the analog and digital circuitry, the preamplifier will be designed as a separate chip in AMS 0.35  $\mu\text{m}$  technology. One channel requires about 0.3 mm<sup>2</sup> in area, making this a fairly small chip.

The ADC, however, is a combination of analog and digital components and is acquired as an external cell. In principle, it could be implemented on both dies. The TPC design will integrate the ADC together with the ALTRO digital readout chip. A similar choice was made for the TRD. This choice represents a compromise with the advantages and disadvantages outlined below.

---

<sup>1</sup>Austria Micro Systems, [www.amsint.com](http://www.amsint.com)

### 5.2.1 ADC Integration

Here we discuss the arguments to integrate the ADC on either the PASA or the digital chip.

#### **Advantages of merging ADC with digital tracklet processors:**

- clear separation of the purely analog and mixed signal parts; no potential coupling of the ADCs digital state machines noise into the sensitive preamplifier front-end
- use of available space as the digital chip alone would be pad-limited
- separation of the preamplifier design cycles from the ADC selection process
- lowest digital/analog interconnection pin-count (one differential pair per channel instead of 10 signals per channel)

#### **Disadvantages of merging ADC with digital tracklet processors:**

- coupling of the digital design to the process chosen for the ADC, making retargeting of the digital *tracklet* processor difficult
- 21 ADCs required for 18 channels ( $\lesssim 2 \text{ mm}^2$  per ADC channel)
- some analog outputs have to drive two ADC inputs, and thus require two individual output stages with corresponding matching problems
- functional chip testing requires some additional logic on the analog front-end

Implementing a 21-channel ADC on a third chip on the MCM is not desirable as this chip would be either pad-limited or the readout would have to be multiplexed, resulting in higher (2x or 4x of digitization rate) clock rates on the ADC die. In any case, the additional number of wire bonds per MCM (336 if ADC readout is not multiplexed) would increase the cost. However, this issue will be revisited when the final size of the ADCs and digital circuitry, and thus the yield of the resulting chip, is determined.

### 5.2.2 ADC technology choices

The choice of ADC silicon technology is critical as it also drives the choice of the process to be used for the digital back-end. The majority of digital design is based on standard cells, providing for easy retargeting to another process, particularly if it implements a smaller feature size, and thus is inherently faster while using less power. However, there are a few special components required, such as LVDS I/O, PLLs for high-speed clock generation, temperature sensors, etc. These components are likely to be available for modern processes or will be easy to procure. However, there are also multiple instances of a quad-port memory that are required, which are implemented as full custom design and therefore have to be retargeted as well. Although the required clock rates are comparably slow, this retargeting is basically a redesign of the quad-port memory as the optimization parameters, area, speed and size, that drive a certain memory architecture depend on the available number of metal layers, via stacking, minimum spacing, size of contacts and vias, etc., typically change enough. For example, the AMS  $0.35 \mu\text{m}$  process supports three metal layers while all deep sub-micron processes support a minimum of five metal layers. On the other hand, it should be noted that a first prototype quad-port memory, which was taped out in June 2001 in the AMS  $0.35 \mu\text{m}$  process, already supports access times of about 3 ns, which are much faster than required (refer also to Chapter 6, Section 6.3.3.3).

The ADC chosen for the TPC (ST TSA1001) is adequate for the TRD as well (for ADC requirements, refer to Chapter 5). This ADC is a commercial product and available as intellectual property core. As the preamplifier output stage is designed to deliver both a 1 V differential voltage swing and the capability

to drive high capacitive loads, the particular choice of ADC is rather independent of the design of the preamplifier. The final choice of ADC depends on a variety of parameters, such as price of both chip real estate and licensing, power consumption, latency, the long-term availability of its silicon technology (which is relevant as the TRD production schedule is different from that of TPC, particularly when taking into account that one scenario is a staged production), and many other similar issues. Currently, several options are evaluated. However, in order to have a credible architecture, the ST TSA1001 ADC was chosen as baseline. This ADC is implemented in the ST HCMOS7 0.25  $\mu\text{m}$  process.

## 5.3 Preamplifier / Shaper

The preamplifier/shaper (PASA) is the first block of the front-end electronics, receiving the signals from the detector pads.

### 5.3.1 Requirements

The current signals of the detector pads are first amplified by a charge-sensitive preamplifier. It is followed by a pole-zero cancellation circuit and two second-order shaper-filters, assuring a shaped output pulse with about 120 ns FWHM. The last functional element of the preamplifier/shaper chain is an output amplifier, which delivers differential output signal according to the ADC requirements concerning driving capability and output levels.

The overall gain of the preamplifier/shaper is 6.1 mV/fC and the shaping type is CR – RC<sup>4</sup>. The differential outputs of the preamplifier/shaper drive a 10 Bit differential 1 V range ADC input.

The functional block diagram of the preamplifier/shaper is shown in Figure 5.3.

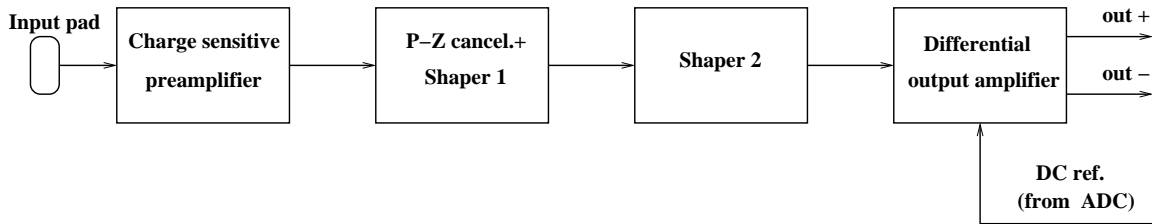


**Figure 5.3:** Block diagram of the preamplifier/shaper.

From the point of view of the implementation, 18 channels of preamplifier/shaper will be integrated on one chip with a core area of about 7.7 mm<sup>2</sup>.

The main requirements of PASA for the TRD front-end electronics and readout are given in Table 5.2.

### 5.3.2 Implementation

The final implementation takes into account the experience achieved from previously developed preamplifiers built with discrete components and from the first version of the preamplifier/shaper chip. Important input was also derived from a design review of the preamplifier/shaper circuit which took place at CERN on January 24-25, 2001.

The preamplifier is built around a NMOS input transistor folded cascode circuit. The NMOS input transistor allows achievement of a greater transconductance parameter than a PMOS input transistor and also enables a design with a single power supply. A greater transconductance leads to lower input impedance of the preamplifier and consequently to lower crosstalk. Also, it enables the main gain to be distributed towards the front of the preamplifier/shaper chain (preamplifier and pole-zero circuit). For the given short shaping time, the advantage of a PMOS input transistor concerning 1/f noise is not important.

**Table 5.2:** Preamplifier/shaper requirements.

Parameter	Value
Gain	6.1 mV/fC
Shaping time (FWHM)	$\sim 120$ ns
Shaping type	CR – RC <sup>4</sup>
Max. equivalent input noise (on the bench)	500 e
Max. equivalent input noise (in system)	1000 e
Input dynamic range	164 fC
Output pulse level	1 V differential
Max. internal chip crosstalk	0.3%
Max. power consumption/channel	10 mW

The preamplifier is followed by a pole-zero cancellation circuit and two second-order filters. The addition of two more poles, relative to the first version of the chip, translates into a more symmetrical response at the output of the preamplifier/shaper.

The output amplifier, as a differential-output type, drives a 10 Bit ADC. The differential output structure is less sensitive to perturbations.

The simulated main outputs of the preamplifier/shaper chain are shown in Figure 5.4.

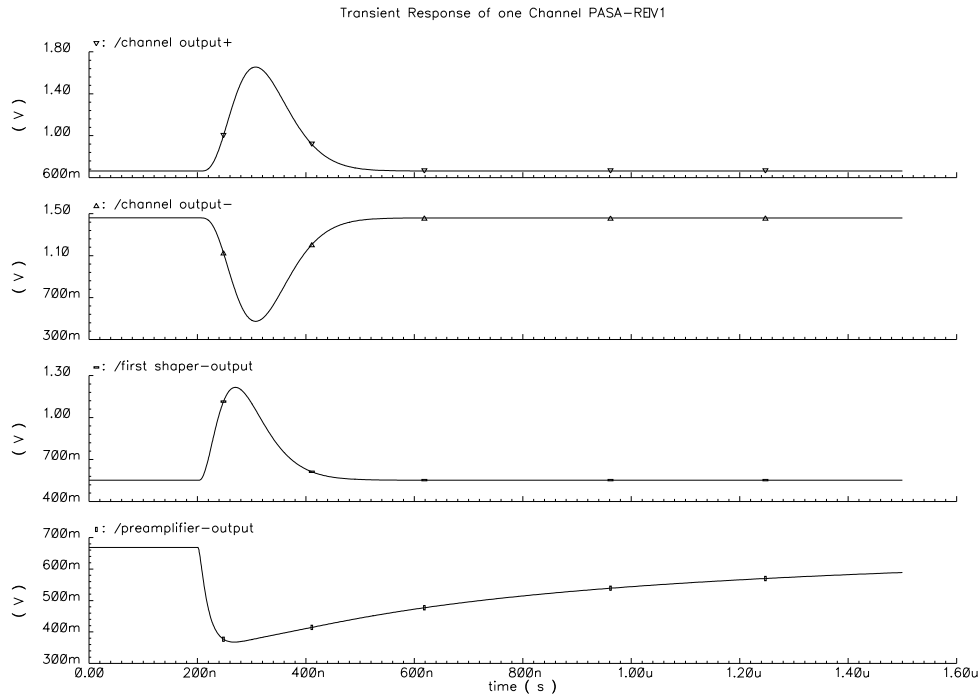


**Figure 5.4:** Simulated preamplifier-output, first shaper-output and channel output+/output- signal of the preamplifier/shaper. They correspond to the block diagram in Figure 5.3. As stimulus an equivalent input charge of 165 fC is used.

### Consideration concerning input protection

The classical protection circuit of the chip I/O pads avoids effects of electrical over-stress (EOS). There are three types of electrical over-stress [2]:

- electrostatic discharge (ESD)
- electromigration: slow wear-out mechanism caused by high current densities
- antenna effect: charge accumulation on gate electrodes during etching or ion implantation

From all of these, ESD protection must correspond to a human body model (HBM) and machine model (MM). For the TRD PASA, additional stress may come from abnormal detector signals (like sparks). For a normal protection to ESD, verified I/O standard pads from AMS were used. For negative input surges, two diodes are tied to ground. One diode tied to analog supply protects against positive input surges. To limit the peak transient currents and electromigration, a resistor of  $10.6\ \Omega$  is added in series with the pad input. The value of this resistor is limited by noise consideration. For example, for a  $25\ pF$  detector capacitance, a  $10.6\ \Omega$  resistor increases the overall noise by 8%. For the next version of the chip, an additional array of resistors to limit and dissipate the positive input surges will be added.

### Some considerations concerning latch-up protection:

Mixed PMOS-NMOS transistor structures are present in many parts of the PASA circuits. For example, in a simple CMOS inverter, parasitic structures of both transistors form an inactive PNPN sandwich, having inverse polarized junctions. Due to a parasitic current into the substrate or to a parasitic electrostatic coupling, the PNPN structure can accidentally become conductive from VDDA to GND, like a thyristor. The thyristor may be latched up and the whole chip may be destroyed due to high currents.

To avoid latch-up, two classical methods are used [4], [5]:

- Electrostatic protective structure for I/O pads, which allows low resistance paths for accidental currents like transient-type currents;
- Diffusion-type low resistance rings around MOS transistors.

For the TRD PASA, the latch-up is prevented by:

- The use of dedicated, verified I/O standard pads from AMS
- Guard rings for each MOS transistor
- A separate guard for each analog channel
- A complex guard of the type 'P diffusion -n well -P diffusion' is placed in between channels
- For each channel, the different functional blocks are separated by guard circuits

### 5.3.3 Prototypes

The first three models of preamplifier/shaper were built at GSI-Darmstadt with discrete components. Also, all were tested in beam with detector prototypes.

As the main component, the first one had the current feedback-type MAXIM<sup>2</sup> MAX4182 operational amplifier. It was used to design an eight channel preamplifier module. Having the capability to change the input impedance, it was also useful in determining the optimum input impedance for a good signal/noise ratio and crosstalk. The main specifications for  $1600\ \Omega$  input impedance are: gain  $0.7\ mV/fC$ , noise about  $11000\ e$ , and crosstalk between adjacent channels 10%.

The second preamplifier/shaper was also built around the MAX4182 operational amplifier, but in a current-type configuration. Having a low input impedance of about  $160\ \Omega$ , it exhibited low crosstalk for adjacent channels (only 2%). It had a gain of  $1.3\ mV/fC$ , and noise about  $7000\ e$ .

---

<sup>2</sup>Dallas Semiconductor MAXIM, [www.maxim-ic.com](http://www.maxim-ic.com)

The third preamplifier/shaper was a charge-sensitive type. With a gain of 2 mV/fC, CR – RC shaping and a noise of only 1500 e and a crosstalk of 8% between adjacent channels. It was used for most of the measurements with detector prototypes (see Chapter 14).

The first chip, with 21 channels, was submitted at the end of October 2000. The 21 analog channels are basically identical. The only difference is in the value of the input pad resistance. There are eight channels with  $0\ \Omega$ , eight channels with  $50\ \Omega$ , two channels with  $200\ \Omega$ , and two channels with  $500\ \Omega$ , to estimate the influence of the pad input resistance to the overall noise. One additional channel with  $50\ \Omega$  input impedance allows monitoring of the signals at each stage of the preamplifier/shaper.

Each of the 21 channels is implemented as a charge sensitive amplifier. The main specifications are: gain about 5.2 mV/fC; output pulse FWHM = 125 ns; shaper type CR –  $RC^2$ ; input dynamic range 0 to 330 fC for 2 V output signal; and noise about 1500 e. It was part of a multi-project run, together with the TPC preamplifier and a digital multi-port memory

The second prototype of the PASA chip has the characteristics presented in Table 5.2 and was submitted to AMS in June 2001. The photo of the layout of this second version (18 channels) is shown in Color Fig. 5. The evaluation of its performance is underway.

## 5.4 ADC

The requirements of the ADC for the TRD are summarized in Table 5.3. It should be noted that the whole system, including each MCM, will be actively cooled in order to guarantee enough temperature stability. Therefore, no particular requirements are presented with respect to temperature stability.

**Table 5.3:** ADC requirements

Parameter	Value
Resolution	10 Bit
Digitization rate	10 MHz
Max Power consumption	20 mW
Input	2 V differential (+/- 1 V)
Input bandwidth	5 MHz
Max. differential non-linearity	0.7 LSB for channels [0,511] 1.5 LSB for channels [512,1023]
Max. integral non-linearity	1.0 LSB for channels [0,511] 2.0 LSB for channels [512,1023]
Effective Number of Bits	> 9 Bit
Max. latency	5.5 clocks
Min. input impedance	100 k $\Omega$
Max. input capacity	7 pF
Max. area	2 mm <sup>2</sup>
Max. channel to channel variations on same die	0.5 %

The ADC cores will be operated with individual power and the digital chips floor plan arranged such that the ADCs are geometrically isolated from the digital back-end. One of the ADCs will be used for detector control and readout independently from the data readout channels.

## 5.5 TRD trigger states

The TRD trigger operates in different states corresponding to the different tasks it performs. An overview of these states, together with the associated external stimuli, is sketched in Figure 5.5. The TRD default state is in stand-by with all digital clocks switched off. A pretrigger starts the archival of the ADC's raw data and the *tracklet* preprocessor (TPP) and computes the appropriate sums (see Chapter 6). The ALICE Trigger system issues a Level-0 (L0) trigger at a fixed latency (about 900 ns) after the interaction. This L0 trigger is the first confirmation of the TRD pretrigger. Should the central trigger processor (CTP) have decided not to issue a trigger, the missing L0 trigger (which constitutes a L0 reject for the TRD as it starts early) will lead to the TRD being cleared, aborting the trigger sequence as indicated in Figure 5.5.

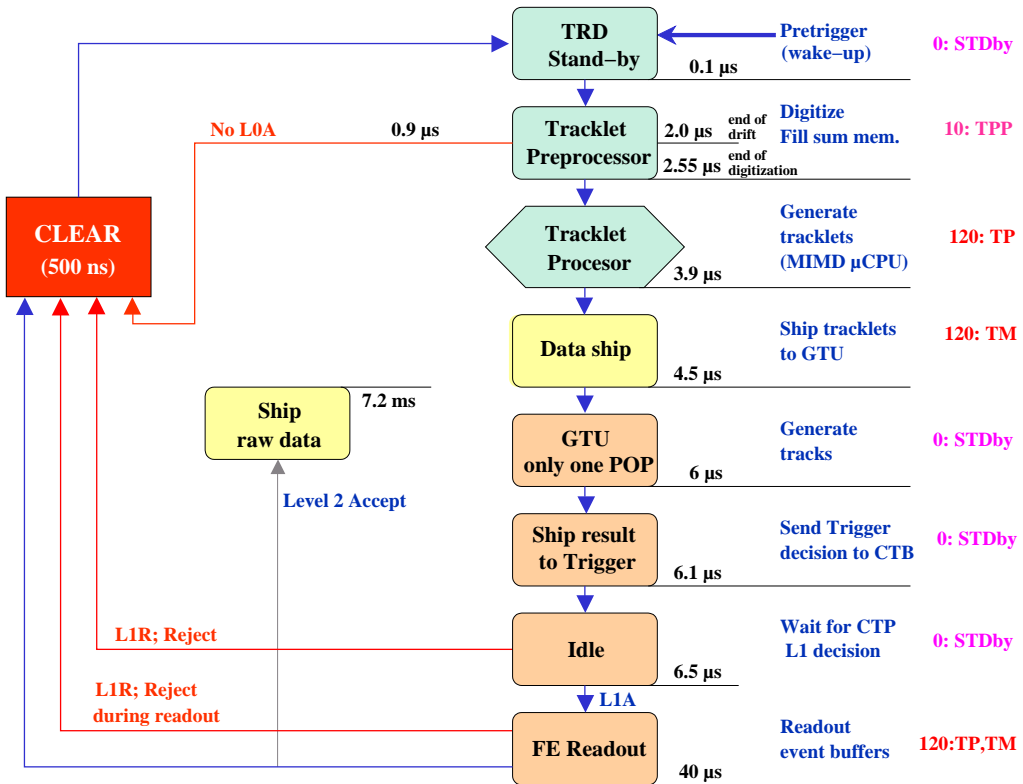


**Figure 5.5:** The various TRD trigger states from pretrigger to readout. Note that data shipping through the DDL is done concurrently and independent of the TRD front-end electronics. The various functions (TPP, TP, TM) are labeled together with their associated operating clock frequencies in MHz.

As it is described in Chapter 6, Section 6.3 at the end of the drift time and when the preprocessor has finished its task, the MIMD processor calculates the *tracklet* parameters and applies the configured selection cuts. After identification of the *tracklets* they are transposed into the TRD reference plane and formatted for shipping to the GTU, which is completed  $3.9 \mu s$  after the interaction. Data shipping concludes at the  $4.5 \mu s$  mark, assuming a maximum of 40 *tracklets* per chamber. Excess *tracklets* are ignored. The readout is performed in an ordered way, such that the global tracking unit can already start processing the first *tracklets* once they have arrived (see Chapter 7). The result of the GTU processing is a potential trigger and a 36 Bit vector, which defines the regions of interest for readout. This information is shipped to the CTP at the  $6 \mu s$  mark.

After delivering the trigger to the CTP, the TRD trigger awaits the response as Level-1 (L1) accept or reject. Note the ALICE CTP does not implement specific L1 accept and reject signals, but delivers a L1 trigger at a defined time slot after the interaction (about  $6.4 \mu s$  mark), like in the case of L0 triggers.

However, for improved legibility and less redundancy, a missing L1 trigger will hereinafter be referred to as L1 reject (L1R) and a L1 trigger at the appropriate time slot will be referred to as L1 accept (L1A). The TRD electronics operates in stand-by mode, with all fast clocks disabled to avoid excess noise, while waiting for the CTP L1 trigger decision. A L1 reject will abort the pending event, placing the system back into stand-by mode. However, a L1 accept will trigger the readout of the event buffers through the same data path that was used to ship the *tracklet* candidates to the GTU. The GTU implements appropriate readout buffers to absorb the 216 GB/sec data stream. Should the activation of the fast readout clocks generate any noise problems, for example within the TPC, the L1 accept signal can purposely be delayed transparently within the TRD to the trigger system.

The completion of the front-end readout leads to clearing the TRD electronics and putting them back into stand-by without further outside interaction. The given event resides now in an appropriate event buffer, which is implemented as part of the GTU. A Level-2 accept (L2A) will schedule the event for transmission off the detector. A L2 reject (L2R) will free the appropriate buffer space. The data transfer functionality is independent of the TRD state sequence (refer to Chapter 7).

It should be noted that the TRD trigger electronics is not pipelined. Once enabled, it cannot process any other event until it is cleared, which, in the case of a L1 accept, can be as late as  $40\ \mu\text{s}$  after the interaction. For details of the TRD readout, refer to Section 7.1.2. However, assuming a 200 Hz accept rate, which is the maximum TPC Pb-Pb gate opening rate, the corresponding dead time is 0.8 %. The handling of the corresponding TRD busy is discussed in Section 5.7. For a detailed discussion of the timing relationship between the various trigger states, refer to Section 5.6.

Some of the activities do not depend upon each other and are executed in parallel. For example, as soon as the first data words arrive at the global tracking unit (GTU), they are processed rather than waiting for the complete delivery of all *tracklets* from the front-end. Further, the data shipping to the high level trigger or event builder system is done in parallel upon a L2A while the TRD front-end may already be operating in stand-by, thus increasing its lifetime.

## 5.6 Trigger timing

For Pb-Pb running, the TPC trigger rate is limited to about 200 Hz. In order to inspect a larger number of events, the TRD has to derive its decision prior to the TPC gate opening. On the other hand, the TPC drift begins with the interaction. Therefore, any trigger latency effectively reduces the active volume of the TPC. Given a drift time of  $80\ \mu\text{s}$ , an overall TPC pretrigger latency of  $6.5\ \mu\text{s}$  corresponding to 8 % of the drift time is defined as an acceptable baseline.

Figure 5.6 outlines the resulting system timing. A very fast minimum bias TRD pretrigger, which is gated with the TRD BUSY, is used to wake up the TRD electronics. This pretrigger bypasses the ALICE CTP and is expected 100 ns after the interaction at the TRD point of presence (POP), from where it is fanned out to all the individual detector modules (see also Sections 5.6.1 and 5.6.2). Given the large surface area of the TRD detector, the definition of such a reference point (POP) is required in order to allow unambiguous definition of the required timing relationships. The pretrigger is also copied as L0 input into the CTP. The distribution of the TRD pretrigger to the various MCMs requires another 200 ns, corresponding to a total of 10% of the TRD drift time for pretrigger distribution as indicated in Figure 5.6. However, the first 250 ns are not crucial to be read out, as they contain the ionization of the primary track from the amplification region.

Low-power ADCs typically implement an internal pipeline. The particular device chosen as baseline implements a 5.5 clock pipeline, effectively storing 5.5 analog samples in a kind of analog memory, thus implementing an equivalent pretrigger history of 550 ns at a digitization rate of 10 MHz, which corresponds to 1/4 of the LHC clock. This is indicated as visible drift region in Figure 5.6. However, the same latency has to be added at the end of the drift time in order to drain the ADC's pipeline.

As outlined in Chapter 6, the computation of the sums required for the linear fit can already be performed during the drift time. For each time bin, every ADC channel is checked to match the criteria

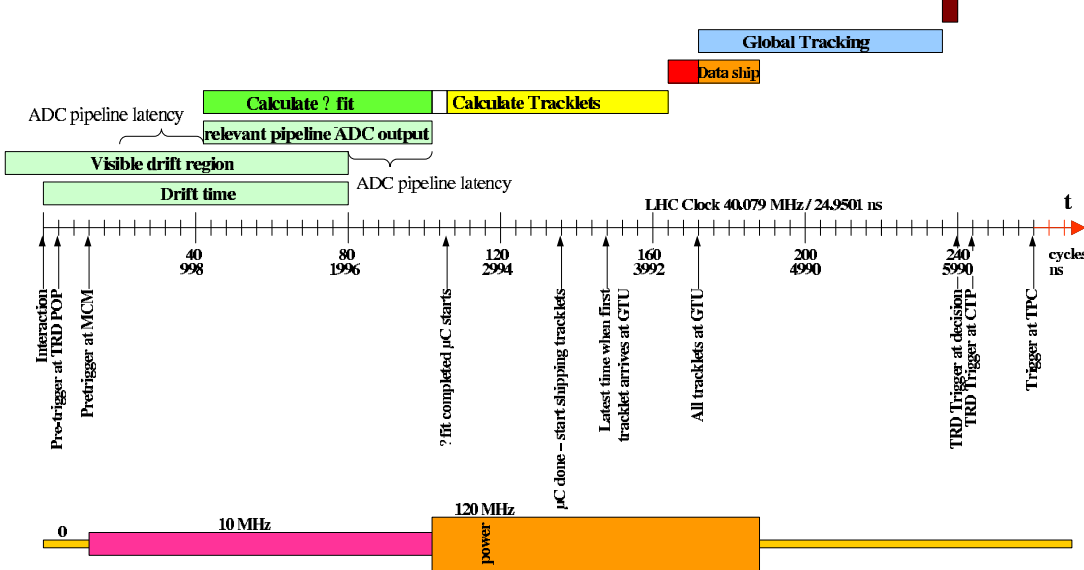


**Figure 5.6:** TRD Timing. The time axis is calibrated in units of LHC clocks, where each tick corresponds to four LHC clocks or about 100 ns.

for a cluster centroid. In such case, the appropriately derived entries for the sums are calculated and stored in the channels sum-memories using read-modify-write cycles. In order to influence the ADC performance as little as possible with the associated digital noise, the appropriate logic is run at the ADC digitization speed. One more ADC clock cycle is required at the end of the digitization period by the preprocessor in order to provide it's results. To shorten the latency, the digital clocks are switched to full speed operating mode, amounting to 120 MHz, at the end of the digitization. This reduces the preprocessor pipeline latency to 67 ns. Note that at this point, (about  $2.55 \mu s$  after the interaction) any digital noise produced will affect neither TRD nor TPC, as the TRD data is already stored in its event buffers and the TPC has not yet started digitizing.

The preprocessor pipeline is fully drained at the  $2.55 \mu s$  mark, at which the embedded MIMD microprocessor starts analyzing the various *tracklet* candidates. Up to four *tracklet* candidates are assigned automatically, one each to a processor thread, at the conclusion of the preprocessor task. Therefore, the *tracklet* processing time is independent of the number of *tracklets*. The available time for *tracklet* processing and selection is  $1.5 \mu s$ .

Each identified *tracklet* is forwarded to the global tracking unit using the high-speed TRD readout tree. Since the readout of each chamber is ordered, the global processing of the first regions of a chamber can happen while other parts are still being read out. However, there is a minimum readout latency, which corresponds to the worst case readout time of the first *tracklet* candidates. No pipelined processing can be done during this time, amounting to 200 ns as indicated in Figure 5.6. The remainder of the data shipping, which corresponds to a maximum of 40 *tracklets* per chamber, is overlapped with the global tracking of the GTU.

The first and last *tracklet* arrive at the GTU at latest  $4.3 \mu s$  and  $4.7 \mu s$  after the interaction, respectively, allowing  $1.3 \mu s$  for the global tracking functionality. It should be pointed out that this functionality will be implemented in FPGAs, running at a target clock rate of 40 MHz.

The TRD trigger decision has to be determined  $6 \mu s$  after the interaction, allowing a total of 500 ns for shipping it to the CTP and back to all involved detectors in case of a L1 accept.

### 5.6.1 Clock distribution and clock domains

In order to reduce clock noise, all TRD clocks are derived from and synchronized to the LHC clock. It is distributed using the RD48 Trigger, Timing and Control (TTC) system. Each detector implements one TTC receiver module as mezzanine card together with the appropriate slow controls functionality, which fans out the system clock to about 200 clock nodes per chamber using the IEEE 1596.5 LVDS standard [1]. The signal fan-out is implemented such that the individual skew between the various clock nodes is minimized. Clock rates higher than the LHC clock are generated on the detectors using PLLs.

The readout tree runs at 120 Mwords, using a 120 MHz clock. The digital processor also operates at 120 MHz, while the readout and *tracklet* preprocessor operates at 10 MHz or 1/4 of the LHC clock, using the same clock as the ADC.

In order to keep the digital electronics as quiet as possible and to save power, all digital clocks are gated and switched off when the TRD is idle. The only exception is the differential clock fan-out and the PLLs, which cannot be started quickly. The ADCs and digital filter for tail cancellation, however, are kept running during stand-by like the preamplifier circuits as they cannot be enabled quickly enough.

After a pretrigger, the 10 MHz clock to the *tracklet* preprocessor is enabled for the duration of the drift time. After 2.55  $\mu$ s, the fast 120 MHz clocks are enabled, starting the multiprocessor and the *tracklet* readout to the GTU. Upon completion of the *tracklet* readout, the various chips fall back into stand-by operation. They are re-enabled by either a L1 accept or a L1 reject, performing the necessary cleanup in order to get ready for the next pretrigger. The clock usage and corresponding power consumption is indicated in Figure 5.6. In this context it should be noted that the lifetime of the gated digital circuitry is as short as a few microseconds per activation. The required energy for this activity will be stored in filter capacitors, such that there will not be large currents switching on the power distribution lines if the TRD is activated.

### 5.6.2 Distribution of fast signals

Each TRD MCM requires the following fast logical input signals:

- Synchronized clock reference
- Pretrigger at TRD point of presence within 100 ns after the interaction
- L0 accept/reject at configured fixed LHC clock
- L1 accept/reject at configured fixed LHC clock (only after L0 accept)
- L2 accept/reject at undetermined time in chronological order for each L1 accept

All these signals are defined with respect to the LHC clock. In order to guarantee the correct phase, all LHC clock-related signals are routed together with the clocks for the given device.

The system default state is stand-by, operating at minimum power. The first TRD trigger is the pretrigger starting the system. The front-end chips will continue processing according to the time line as sketched in Figure 5.6 until a trigger decision is delivered to the CTP. During this process, the logic can be aborted any time, which is done by asserting the TRDTrigger signal for at least two consecutive clocks.

The pretrigger is the most time-critical signal. Table 5.4 shows a breakdown of all latencies involved in transmitting the pretrigger signal to all MCMs. Negative latencies are defined as signals arriving early. The most efficient way to avoid additional trigger cabling is utilizing the TTC system, which is going to be used for the distribution of the clock signals. The TTCCvi module will forward minimum bias pretriggers as TTC L0 accepts on its A channel only if the TRD electronics are operating in stand-by. It should be noted that the pipeline latency of the ADC chosen as baseline allows for much larger pretrigger latencies. However, the ADCs digitization latency is technology dependent and can be as little as one

clock. Therefore, in order to allow for other ADC technologies (refer to Section 5.4), this requirement is not relaxed. On the other hand, in the event the final ADC does not implement a pipeline and the pretrigger results in an unavoidable larger latency as specified here, an appropriate digital pipeline can be implemented, which would have the advantage of not adding latency at the end of the drift time as the pipeline ADC does. Such a digital pipeline, however, comes at the price of more digital circuitry continuously being operated.

**Table 5.4:** A breakdown of all latencies involved in distributing the TRD pretrigger signals. The same parameters are applicable to the other fast input signals.

What (source)	t/ns	[t <sub>min</sub> , t <sub>max</sub> ] / ns	clocks
Interaction to TRD point of presence input (ALICE requirement)	+100	[100, 150]	4...6
TTC system latency (RD12 measurement)	+68	[65, 100]	3...4
Signal propagation including fan-out (20 m, each TTC fan-out counts for 1 m)	+100	[50, 150]	4
Clock/Trigger signals fan-out on detector (2 stages estimated)	+15	[10, 25]	
Signal propagation on detector (3 meter estimated, periodic signals can be adjusted to compensate latency - trigger signals cannot; all signals are relative to reference clock)	+15	[10, 20]	
<b>Sum total</b>	<b>+298</b>	<b>[235, 445]</b>	<b>12</b>
Pipeline ADC @ 10 MHz (5.5 clocks)	-550	[0, 600]	25
Ignore beginning of drift time	-250	[200, 300]	8...12
<b>Total TRD Pretrigger latency</b> (negative means early)	<b>-502</b>		

The TRD Trigger system is not pipelined and is therefore BUSY starting with the pretrigger until the readout of the front-end buffers completes or the event is aborted. This allows for the use of the same trigger input (hereinafter referred to as TRDTrigger) for different functions depending on the state of the TRD trigger. Different inputs at one state can be encoded in pulse length as multiple back-to-back triggers are not possible. The signal TRDTrigger is fanned out to all front-end systems as TTC L0A trigger on the TTC A channel. For example a pulse of the TRDTrigger during the TRD idle state is considered a pretrigger, a TRDTrigger pulse at the 900 ns mark (L0A time slot) is a L0 trigger. Longer TRDTrigger bursts can be used to encode other functionality, such as clears.

The fixed latency of the ALICE Trigger system's L0 trigger allows implementation of a L0 reject as a missing L0 trigger. This condition is detected at the TTCvi root module. In the case of a missing L0 trigger, two consecutive L0A triggers are transmitted through the TTC system to all chambers. The logic required to generate the this pulse length clear code of the TTC L0A signal is required only once for the entire detector.

After delivering the TRD trigger decision, the system enters a wait state (idle state) while awaiting receipt of the CTP's L1 decision as another TRDTrigger pulse, which is now interpreted as a L1 accept. This L1 accept allows to start the readout of the TRD front-end buffers at any time after the TRD entered this idle state. Thus this readout can purposely be delayed past the TPC drift time in case of TPC coincident triggers in order to keep the TRD electronics chain quiet during the TPC drift, should this become a noise problem. However, such functionality would be implemented at the TTCvi root module like the L0 clear functionality, which is entirely transparent to the CTP. Note that the CTP's decision can be completely independent of the TRD's trigger suggestion, resulting in TRD L1 accepts after a TRD reject and vice versa. However, no L1 accept is expected by the TRD without having received an appropriate pretrigger.

The L1 accept results in the readout of the front-end system, and thus allows release of the TRD BUSY as soon as this function completes. The system returns to the stand-by state while awaiting the next pretrigger.

The data readout through the detector links is triggered upon a L2A. The L2A and reject signals are not required at the detector front-end and are shipped to the appropriate functional units of the global tracking unit. The Level-2 (L2) decisions are in isochronous order, thus simple accept/reject signal pairs are adequate. A L2R simply frees the appropriate event buffer space within the global tracking unit.

The architecture outlined above allows the implementation of the local tracking units (LTU) as simple state machines that operate after a pretrigger up until they receive a clear. Only two fast signals (TRDTrigger and clock) are required to be distributed to all MCMs. The LTUs implement the additional feature handling the assertion of the TRDTrigger signal for two or more contiguous LHC clocks as clear. No specific clear signal is required. This scenario operates the TTC in a simplified mode, using the L0A channel for all synchronous triggers. However, given the short latency budget for the pretrigger, the TTCvi root module would have to be located close to the TTC point of presence. Should this turn out to be a problem, then the pretrigger has to be distributed individually. The rest of the signal coding would remain unchanged. The implementation of this coding can be done in a simple programmable logic device (PLD) as part of the TRD trigger logic.

## 5.7 Interface to the ALICE trigger system

The TRD requires a fast pretrigger as a wake-up signal. The sole purpose of this signal is to allow the operation of the digital components within the system in low-power mode while the system is in stand-by. The timing requirements for this signal are discussed in Section 5.6. The pretrigger has to be issued before the ALICE CTP has issued a L0 trigger. It is implemented as a minimum-bias trigger. Further, in order to have clean events within the TRD, particularly for Pb-Pb running, the TRD requires the pretrigger to be pre-history and pile-up protected. Future protection is implemented by rejecting appropriate pile-up events at L1 time. All TRD related triggers have to be counted before and after dead time by the CTP in order to allow proper calibration.

Given those requirements, the integration of the TRD is more complex than a canonical, stateless, dead-time free trigger detector or a generic detector, which is triggered by L0A or L1A, such as the TPC. Figure 5.7 sketches the architecture. The critical path timing of the pretrigger is designated by the thick line (the signal). The pretrigger is issued by a fast minimum-bias trigger detector, which is routed directly to the TRD using the shortest possible path in order to minimize its latency. A second independent copy of the signal, which is less time critical, is routed to the CTP. In order to avoid unnecessarily waking-up the TRD electronics, the pretrigger is to be issued only in case of a clean history. This functionality has to be implemented by the TRD system as it is in the critical path of the pretrigger and the time to route signals to and from the CTP would far exceed the maximum allowable latency. The clean TRD minimum bias signal can be recreated by the CTP. In general, past protection is easily implemented by using a retriggerable one-shot, which is triggered with the minimum-bias trigger and which has a decay time corresponding to the TRD drift time. The resulting pretrigger signal is relevant only in case of the TRD being idle, which is sketched in 5.7, by gating the clean minimum bias signal with the TRD BUSY status. The TRD BUSY itself is started by each valid pretrigger and cleared either by rejecting the event or after the L1A related readout has completed. The valid TRD pretrigger wakes up the TRD digital electronics and starts the TRD state machine as sketched in Figure 5.5. This signal is forwarded to the CTP, where it is treated as regular L0 trigger input. All trigger classes, including the TRD, require this signal to be present.

A TRD pretrigger may or may not result in an appropriate TRD L0 trigger. Not receiving a L0 trigger at the specified time slot will be handled as an abort. Should the TRD receive a L0 trigger at any other time, an error is flagged and the trigger is ignored. Such a scenario would most likely be caused by L0 trigger classes involving the TRD, but without requiring the TRD pretrigger as input.

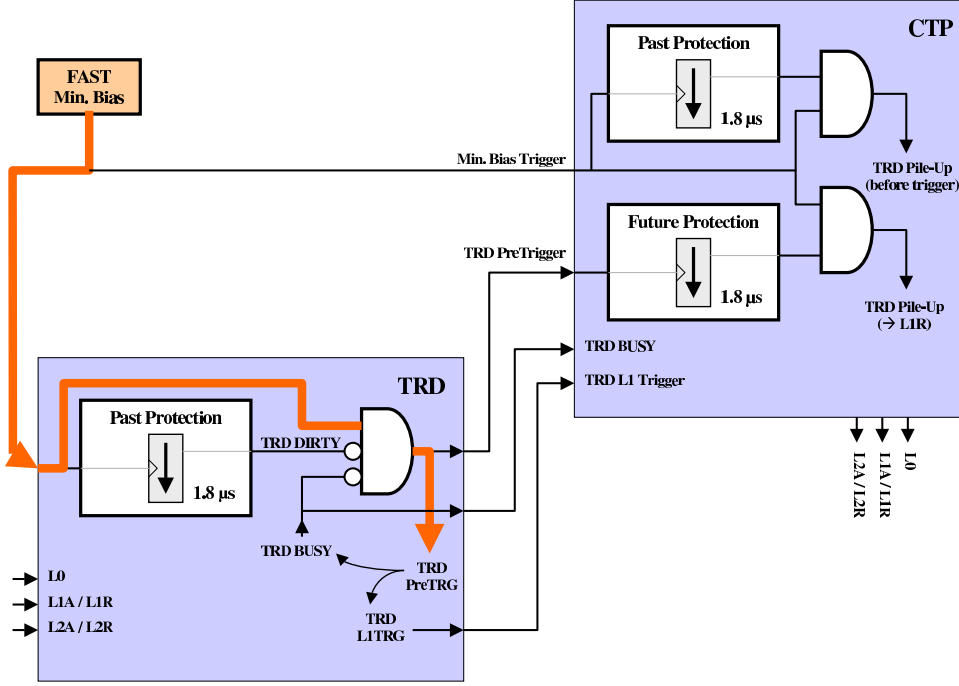


**Figure 5.7:** TRD Pretrigger architecture. Note: the TRD past/future protection is implemented as programmable counters, and such can be configured within a range of 1...100  $\mu\text{s}$ . The past protection located on the TRD detector is logically part of the CTP and configured by the CTP in order to guarantee coherent configuration. In case of coincident running with another detector requiring a larger past protection, such as the TPC, the TRD past protection will be adjusted accordingly.

After receipt of the L0, the TRD trigger will proceed to determine its trigger decision, which it forwards to the CTP at the 6  $\mu\text{s}$  mark, and which may result in either a L1 accept or reject, depending on the trigger class or classes.

The TRD can be aborted at both L0 and L1 time. It should be explicitly noted that the TRD will abort only upon an appropriate CTP decision and never by itself. Any pile-up related aborts have to be issued by the CTP.

Past and future protection is standard circuitry, which is implemented by the CTP. Another detector requiring such logic is the TPC. The only variation is the different time constant of 2  $\mu\text{s}$  instead of 80  $\mu\text{s}$  in case of the TPC. The fact that the past protection circuitry is mirrored by the TRD should be considered as an implementation detail solely driven by the pretrigger being in the critical path. The appropriate logic within the TRD front-end will be connected to the Trigger DCS in order to ensure coherent configuration. However, only a very small number of parameters is concerned here, which do not change often. Architecturally, the past and future protection logic has to be part of the CTP in order to allow for proper cross-section calibration. All future protection is implemented by the CTP and results in rejecting pile-up events at L1 time. However, in order to reduce the overall TRD dead time and power consumption, TRD pile-up should also be used as qualifying input to the appropriate L0 trigger. This results in all pile-up events happening during the first half of the drift time being rejected before the high-power digital circuitry is even enabled.

The TRD BUSY signal is not required for normal trigger operation as it is already included in the TRD pretrigger. This is also driven by the long roundtrip delays to and from the CTP. However, in order to allow for proper counting of before/after dead time, this signal is sent to the CTP.

It should be noted that the TRD BUSY must not be qualified for trigger selection as this would always prevent TRD L0 triggers due to the nature of the TRD starting early with the pretrigger and, thus, also asserting its BUSY early.

In summary, the TRD will deliver to the trigger system its dead-time state (BUSY) plus the TRD trigger bits, consisting of one bit for each trigger type plus the region of interest bit mask selecting sector and hemisphere (2x36 Bit). All other trigger signals received from the CTP (L0A, L1A, L1R, L2A, L2R) are received centrally at the TRD point of presence and distributed appropriately within the TRD.

## 5.8 Multi-Chip Module (MCM) overview

The number of channels per MCM is driven by various parameters, resulting in the choice of 18 channels per MCM. On one hand, the *tracklet* preprocessor architecture requires only processing of neighboring pads of one pad row. The preamplifier inputs are the direct pad signals. In order to minimize the pad capacity, signal crosstalk and pad-to-pad variations, the maximum length of any given pad trace is limited to about 100 mm. Further, the number of channels per MCM or local tracking unit (LTU) and preamplifier chip (PASA), respectively, drives up the chip size, and thus drives down the yield. However, this additional cost is offset by the production cost of the MCM itself, which does not scale much with the number of channels, as one channel adds only one analog input and a few bonding wires because most of the additional circuitry is consolidated into the LTU on the MCM. The resulting optimum is 18 channels per MCM and 8 MCMs per pad row.

A number of scenarios was iterated with respect to the architecture of the MCM. The original approach of rather large readout boards required the MCMs to be mounted using mezzanine connectors. Therefore, the only components on the motherboards would have been such connectors, simplifying the production. However, even in that scenario, the cost for just the connectors was rather high.

The baseline scenario (refer to Chapter 4) implements small enough readout boards, so that they could be mass-produced using standard production facilities. This architectural choice enabled the implementation of the MCM as Ball Grid Array (BGA), which can be produced and soldered without requiring expensive mezzanine connectors. The disadvantage is the increased complexity for replacement of a given MCM. However, taking into account the effort required to remove a chamber for repair, the additional BGA soldering to replace an MCM becomes a minor issue. On the other hand, the number of I/O pins per module is now a small contribution to the overall cost. The choice to use soldered BGAs as opposed to MCM mezzanine cards mounted via connectors resembles a trade-off between overall cost, material budget and maintainability.

## 5.9 MCM prototypes and performance

### 5.9.1 Prototype Motherboard

The first digital chip that was designed is a prototype of the *tracklet* preprocessor (TPP) in the AMS 0.35  $\mu\text{m}$  process, which also implements appropriate readout circuitry. One of the goals for this chip was to better understand the noise introduced by the close proximity of fast digital clocks and sensitive analog preamplifiers. In order to test the *tracklet* preprocessor prototype, together with the well-understood existing discrete preamplifier, an appropriate motherboard was designed, hosting both the *tracklet* preprocessor and the digital readout chip. Figure 5.8 shows the device. It hosts eight ADCs, the digital chip in the ceramic package, and some additional glue logic for generation of miscellaneous signals, such as clocks.

### 5.9.2 Prototype MCM

The block structure of the MCM reflects the already discussed connection diagram of the *tracklet* preprocessor prototype 1 with eight channels: Preamplifier Chip with 8 analog inputs/outputs, 10 ADCs (including two neighbouring channels, 8 Bit NSC<sup>3</sup> ADC08351), the *tracklet* preprocessor itself, and the

---

<sup>3</sup>National Semiconductor, [www.national.com](http://www.national.com)

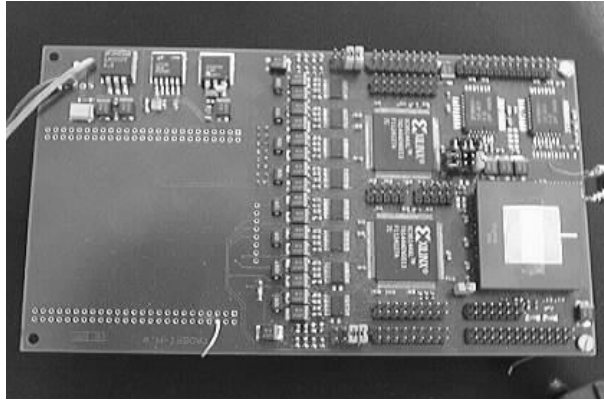


**Figure 5.8:** Prototype Motherboard.

connectors. There are two possibilities to deliver the data of neighbouring analog channels of MCMs: analog or digital. In the fist case, there are two extra ADCs on the MCM that digitize the analog signal, coming from the neighboring MCMs. In the second case, the digital outputs of the boundary ADCs from adjacent MCMs are fed in parallel to the MCM. The *tracklet* preprocessor prototype 1 has  $5 \times 8$  Bit inputs for ADC data; each of the two ADCs are combined together with a common readout bus and multiplexed in time. This is possible, as the ADC sampling rate is 10 or 20 MHz, while the *tracklet* preprocessor works at the  $4 \times$  speed (40 or 80 MHz). The two ADCs, belonging to the same readout bus, have 18 common pins and only the OE (output enable) and Vin (analog input) lie on different networks. We decided to solder the second ADC directly onto the first one, while the two pins mentioned above are connected to the board via small vertically-mounted SMT  $0\ \Omega$  resistors. This topology saves a lot of space and vias on board. Some technical details: the MCM is a twin-layer board, and with minimal distances/route widths 6 mil/6 mil ( $152\ \mu\text{m}$ ), the size of the board is  $51 \times 40\ \text{mm}^2$ . There are two FPC connectors (30 pins) for inter-MCM communication, one FPC connector (18 pins) for the command bus and one FPC connector (18 pins) for the analog inputs. All FPC connectors are commercial 0.5 mm pitch connectors (eg. HARWIN<sup>4</sup>).

The first MCM was mounted on a small universal board. Color Fig. 7 shows a photo with both the preamplifier and digital back-end chip integrated. The ADCs are implemented as discrete chips with two stacked on top of each other in order to save space. This carrier board contains the voltage regulators (two 3.3 V, one 1.65 V), a quartz oscillator, and normal connectors for easier tests. The digital control/readout was made by an universal PCI I/O board (already used for tests of the *tracklet* preprocessor). Due to difficulties at bonding of the digital chip, some inputs from one pair of ADCs were accidentally shorted to ground and therefore the corresponding two ADCs were not soldered on the MCM. The primary aim of the MCM was not to test the *tracklet* preprocessor as a digital chip, but to test the MCM technology and to estimate the performance when we put in close proximity a high-speed digital chip (TPP), several pipelined ADCs, and a very sensitive analog chip (PASA).

Figure 5.9 shows the digital output of one ADC with reduced reference voltage. The input of the corresponding preamplifier channel was open. If there is a signal applied to an adjacent channel of the preamplifier (so that we have maximal amplitude at the preamplifier output), there appears a disturbance for 1-2 time bins, with amplitude 1-2 LSB of the ADC. If we short the input of the preamplifier to ground and apply the same signal to the adjacent preamplifier input, we do not see any change at the output of the ADC. In this case, however, the first stage of the preamplifier with grounded input is out of DC stability, while the second stage of the preamplifier is still DC stable and delivers normal voltage to the output. In Fig. 5.10 the shaped pulses measured from six ADCs are shown. There is a slight shape variation in one of the channel.

---

<sup>4</sup>HARWIN Components, [www.harwin.com](http://www.harwin.com)

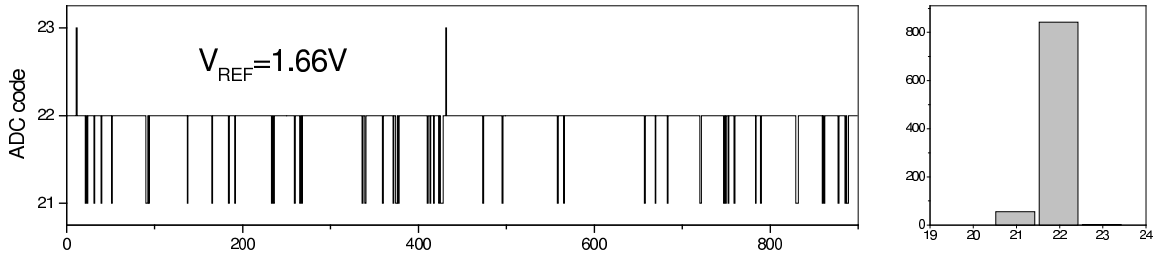


**Figure 5.9:** ADC response on MCM with digital clock enabled. For this test, the ADC reference voltage was reduced in order to increase its gain. Only the least significant bit changes.

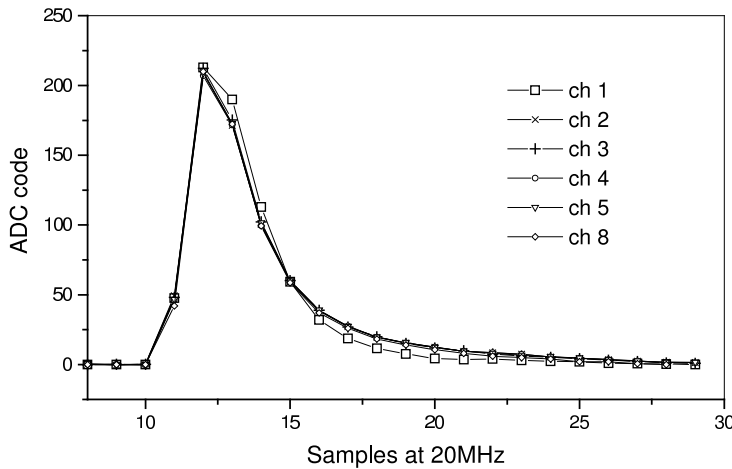


**Figure 5.10:** Superposition of all analog channels digitized with the ADCs on the MCM and readout by the tracklet preprocessor. The ADCs are implemented as discrete chips.

## 5.10 Design for test

For a high yield in the production of multi-chip modules, it is essential to verify the chips before bonding. There are two chips on the MCM, which will have to be tested independently prior to assembly. However, this testing requires only simple functionality testing as it already will identify most of the broken chips.

### 5.10.1 Preamplifier

A cheap and fast solution for analog functional testing is the use of a factory standard automatic digital tester. A 4 Bit DAC will be implemented on the preamplifier die together with the appropriate means to inject different charges, defined by the DAC, into the preamplifier front-end. The highest DAC setting would correspond to a PASA output pulse which has an amplitude close to the ADC full scale. This pulse can be easily measured by the digital tester if its readout thresholds are adjusted appropriately. Care must be taken in order to prevent this circuitry from increasing the preamplifier's channel-to-channel crosstalk and input capacitance. A simple internal state machine is programmed through an external single-ended two-wire serial interface, such as Philips<sup>5</sup> I<sup>2</sup>C. This state machine implements one enable bit per channel, thus allowing any combination of channels to be activated. The DAC is programmed through the same interface. The clock required for this test controller is held low during normal operation, thus keeping the logic in stand-by and not generating any digital noise. This circuitry allows simple functional verification of the preamplifier chip while being operated on a digital tester and using its digital inputs with an adjustable threshold.

<sup>5</sup>Philips Semiconductors, [www.semiconductors.philips.com](http://www.semiconductors.philips.com)

### 5.10.2 Local Tracking Unit (LTU)

All major building blocks of the LTU will be encapsulated by JTAG boundary scan logic (IEEE 1149.1), allowing for the isolation and diagnostics of errors. However, since the LTU implements a multi-processor, in-situ self-testing is implemented, which includes the testing of all internal memories and registers. The event buffers can be uploaded with simulated events. The *tracklet* preprocessor can be configured to process this data, instead of reading the ADC outputs and filling the event buffers. The test routines can be uploaded quickly via the readout tree when configured in upload mode. Given the available four processor kernels, four test instructions can be executed per clock cycle, for example, simultaneously testing four regions of the data memory, thus allowing shortening of the test time. This mode results in the test vectors basically uploading the test program and data, providing the clock, and expecting the test results.

### 5.10.3 MCM testing and verification

After assembly, the MCMs require testing and burn in. The test infrastructure required shall be as simple as possible in order to allow a large number of modules to be tested. Allowing six months for the testing of all MCMs for the entire detector requires, for example, the completion of one MCM per minute, assuming an eight-hour work day. These tests are expected to be performed periodically in-situ when the detector is idle. The MCM shall be able to complete such testing with a minimum of external additional logic. The list below specifies the MCMs self-test functionality.

- verification of checksum on internal code and data RAM
- memory read/write testing on all internal memories (code, data, event buffer, look-up tables, configuration registers)
- processor configuration, synchronization
- test of core register file
- test of *tracklet* preprocessor by uploading simulated events first into event buffers, then configuring the *tracklet* preprocessor to accept input from the event buffers rather than from the ADCs, and finally by performing a regular trigger and verifying the results in the sum memories
- measurement of supply voltage while switching on fast clocks
- measurement of *tracklet* processor chip core temperature during burn-in and in-situ
- injection of test charge (6 Bit granularity) into any individual or group of preamplifier channels, allowing the measurement of crosstalk and linearity of each individual channel.
- measurement of analog supply voltage during acquisition

Each MCM will carry an unique ID. Test and repair cycles will be archived in a database and stored for the lifetime of the experiment, based on this ID. The MCM test software running on the *tracklet* processor will utilize its readout bus in order to forward status and progress messages to the test environment. This scenario allows a large number of MCMs to be tested simultaneously.



# 6 Electron trigger with the TRD

---

## 6.1 Physics motivation

The study of rare probes with cross sections in the order of  $\approx 100 \mu\text{b}$  (corresponding to probabilities per collision of  $\approx 10^{-5}$ ) to diagnose the properties of the QGP requires dedicated triggers to enhance the events containing the signals. Especially electromagnetic probes that are not affected by hadronic reinteractions and therefore provide the most direct view of the reaction scenario need a substantial effort due to their small cross section. Equally rare are the electromagnetic decays of hadron resonances, of which the heavy vector mesons  $\text{J}/\psi$  and  $\Upsilon$  are of special importance due to the expected signatures of their yield for specific plasma conditions [1–3].

The ALICE data acquisition has to serve all the different parallel trigger requests for the various physics observables; for the sake of the present discussion it is assumed that the bandwidth available for high  $p_t$  electron physics is limited to an equivalent of 20 Hz of central events. Under those conditions about  $2 \cdot 10^7$  events per year of ALICE operation will be recorded for the TRD trigger.

To test various models and resolve ambiguities it is of utmost importance to measure differential distributions, i.e. the transverse momentum ( $p_t$ ) and the centrality dependence of the signals. A trigger is especially needed for i) large transverse momenta of the resonances that are typically suppressed due to the exponential fall-off of the spectra and ii) for large impact parameter events for which the probability to produce the interesting probes is substantially reduced.

In order to make a variety of physics signatures accessible to ALICE with sufficient statistics, the TRD trigger is designed to i) find and select tracks with transverse momenta of **more than 3 GeV/c**, ii) separate **electrons** from pions and iii) allow to compute correlation quantities like the invariant mass of track pairs or the multiplicity in spatial regions.

The physics observables that benefit from the TRD trigger are:

- $\text{J}/\psi$  production at large transverse momentum
- $\Upsilon$  production
- The Thermal Dilepton Continuum in the invariant mass range from 4 to 9  $\text{GeV}/c^2$
- Jet production with Jet Energies of more than 100 GeV

The di-electron capability of the TRD will be used to measure observables at midrapidity and thus delivers (complementary to the di-muon arm) valuable information for the diagnostics of the plasma under the most clean conditions, i.e. at the highest energy density combined with the lowest net baryon density. An unique advantage is the possibility to correlate rare probes with the other information obtained with the central ALICE detector in the same rapidity interval on an event-by-event basis.

To make efficient use of the solid angle available for the TRD, the trigger system has to cover the whole range in rapidity and transverse momentum with a high and uniform efficiency. The system is designed for a minimum bias measurement since important information is contained in the production rates the rare probes for different impact parameter [2, 4].

There is a large uncertainty about the multiplicity to be expected for Pb-Pb collisions at LHC energies (see discussion in Chapter 12). The system works well even for the maximum possible central multiplicities of  $dN/dy = 8000$ , but substantial improvements are achieved for minimum bias conditions or if the central multiplicity is significantly below 8000.

## 6.2 Concept

The TRD trigger (and the whole detection scheme) is implemented to select on high  $p_t$  electron pairs exploiting the transition radiation signature on a  $5 \mu\text{s}$  time scale. Therefore the trigger scheme is organized in the following way (see Fig. 6.1):

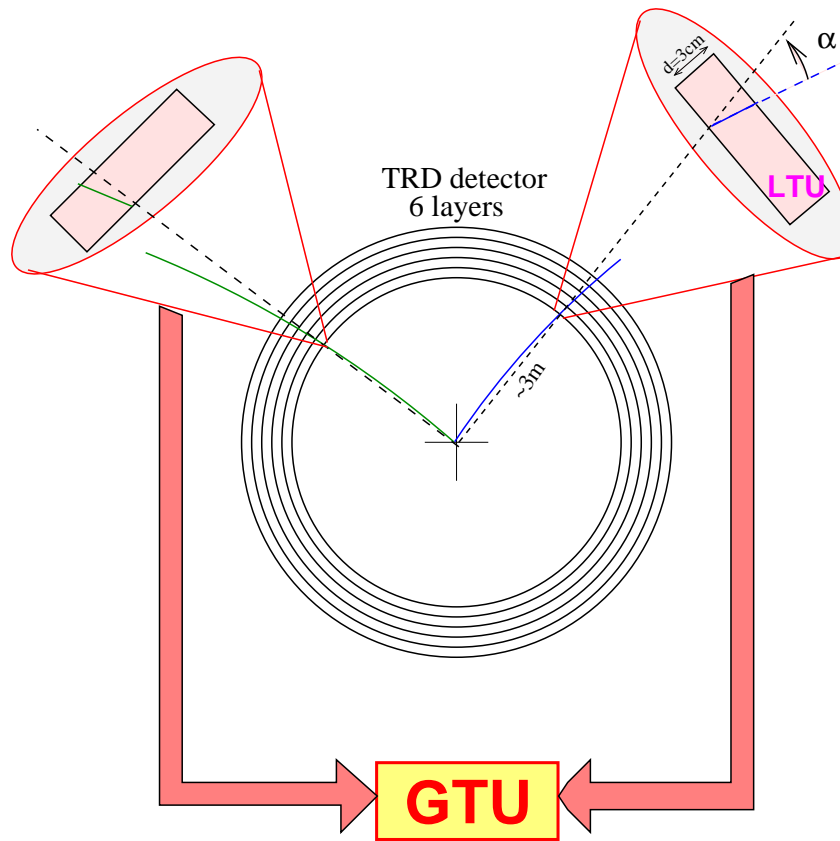


**Figure 6.1:** Trigger scheme.

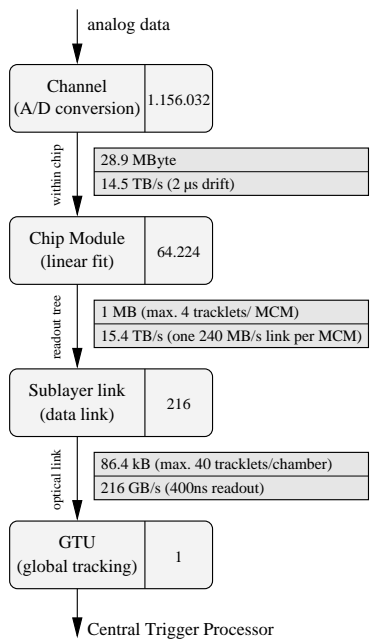
1. Local track segment (*tracklet*) search independently in all chambers of the detector in parallel processors called Local Tracking Units (LTU).
2. Selection of stiff *tracklets* by means of maximal deflection compared to that expected for straight ( $p_t = \infty$ ) trajectories.
3. Computation of particle identification (PID) information based on the total energy loss and the depth profile of the deposited energy.
4. Shipping of data from all stiff tracklet candidates ( $p_t \geq 2 \text{ GeV}/c$ ) to a global tracking unit (GTU).
5. Selection of high transverse momentum candidates by requiring a sufficient number of merged tracklets (3 out of 6) with a global deflection corresponding to  $p_t \geq 2.7 \text{ GeV}/c$ .
6. Computation of the global particle identification information from combination of the local PID measures.
7. Global counting of positive and negative track candidates (possibly also within a given area).
8. Computation of two-particle correlation quantities like the invariant mass.

### 9. Transmission of the result to the ALICE trigger (Central Trigger Processor).

The identification of interesting physics signals by the TRD requires to inspect all Pb-Pb interactions for the occurrence of rare probes, i.e. the trigger has to run at minimum bias event rates. Since the gating grid of the ALICE TPC cannot be opened at this rate the trigger decision based on the TRD detector alone has to become available on a time scale that is short as compared to the total drift time of the TPC ( $T_{TPC} = 88 \mu s$ ). A decision time of about  $6 \mu s$  is considered acceptable since the delay in opening the gating grid involves at most a shortening of some tracks in the TPC at large forward/backward polar angles. Alternate scenarios like opening the gating grid with the minimum bias trigger rate and closing it with the non occurrence of the TRD trigger are also under discussion. In any case the whole trigger sequence needs to be completed within a maximum decision time of about  $6 \mu s$ .

With the envisioned maximum multiplicities of up to 20000 primary charged particles in the acceptance of the TRD detector the implementation of the trigger scheme dictates a massively parallel computing model. The most demanding part is the online tracking of the full event with high enough quality to select events that occur with probabilities of the order of  $10^{-5}$ . The whole architecture described in the following is optimized to achieve this goal.

## 6.3 Hardware implementation



Within the detector enormous amounts of data are produced on the lowest level, which have to be processed in a very short time. To reduce the incoming data volume as early as possible successive selection steps are implemented. Figure 6.2 shows the different processing steps with the associated amount of data.

**Figure 6.2:** Trigger System Overview

### 6.3.1 Trigger concept

The basic idea of the trigger system is to find high-momentum electrons and separate them from pions by a reconstructed track line and a transition radiation (TR) signature. The electron-pion separation is performed via the TR photons, which are primarily detected at the end of the drift-time (see Figs. 11.10 and 14.20). The track reconstruction algorithm takes the known track model for high- $p_t$  particles into account. Such particle tracks are essentially perpendicular to the readout chambers pad plane, neglecting the Lorentz angle and the fact that the chambers are flat. For a detailed geometric layout of the chambers, refer to Chapters 2 and 4. Only a small number of channels is required to read out a complete track, allowing for the implementation of a *tracklet* reconstruction engine in a highly parallel fashion. In the

following we will refer to a *tracklet* as the segment of a track in one readout chamber. Tracks with a large inclination angle, and thus a low transverse momentum, are not included in the tracking model and are therefore ignored. All space points above one given pad are considered to belong to the same *tracklet* and are included in a straight-line fit. This method performs worse as the occupancy increases and eventually fails in case of a multi-track pileup above a given pad. This has been taken into account in the microscopic simulations of the trigger (see Section 6.4). Tracks with a large deflection angle crossing a stiff track will distort the position resolution in the region of overlap. However, the corresponding pileup clusters can be detected at the hit level and will be excluded from the fit.

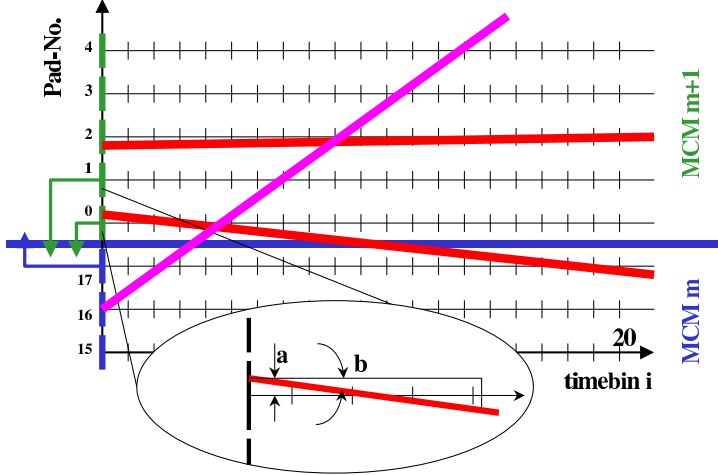


**Figure 6.3:** The *tracklet* fitting principle. The pad row runs in  $y$  direction. The drift direction is radial.

An overview of the tracking principle is sketched in Fig. 6.3. The ordinate identifies the pad row of the detector, along which the track is bent in the magnetic field. The abscissa shows the drift direction, discretized in a number of time bins (configurable up to 32). The trigger system calculates for each time bin and channel the position of a cluster based on charge sharing.

Due to the pad response function, on average, 2.4 pads are hit by a high momentum track. Pads with a local maximum in charge deposit are selected and the precise  $y$  position of the corresponding hit is determined from the pulse height of this pad and its two neighbors for every time bin. The position is determined based on lookup tables and indexed by the pad amplitude ratios center/right and center/left. For a well defined charge sharing one of this ratios suffices for position reconstruction. Given the involvement of three pads and therefore a second redundant position measurement per time bin, pileup hits can be detected and rejected on a time bin basis. Refer to Section 6.4 for a detailed discussion of the online chamber position resolution.

The trigger is designed to perform a straight-line fit based on the calculated space points in  $y$  as a function of drift-time. As described in more detail in the next section, during the drift-time, for each channel the input parameters for a straight-line fit are calculated and updated in sum memories. After the drift-time, the trigger processor calculates the final *tracklet* parameters such as the slope, intercept, variance, etc.. Only *tracklets* are considered, which involve a maximum of four pads, corresponding to a maximum  $y$ -deflection of one pad. After this operation each individual *tracklet* candidate is subject to an angle and (possibly) particle identification (PID) cut, selecting high- $p_t$  *tracklets*. The PID is based on energy deposit (see Sections 6.4.5 and 11.5). Low momentum particles have a large deflection in the bending plane. They will be rejected either by slope or they will not meet the criterion on minimum number of space points required for a valid *tracklet*. The *tracklets* identified as high  $p_t$  (electron) candidates are shipped through a read out tree to the global track matching unit, which combines the *tracklets* of the six TRD layers into one track with improved momentum resolution and PID.

The whole of TRD electronics is arranged in groups of 18 channels (adjacent pads in the same pad row), mounted on multi-chip-modules (MCM). The charge-sharing and finite deflection of high- $p_t$

*tracklets* require the neighboring MCMs to share the data of their borderline channels. For example, for the position determination via charge-sharing of channel 17 (counting from 0) of MCM  $m$ , channel 0 of MCM  $m + 1$  is required and vice versa. In order to not have tracking inefficiencies at MCM borders, *tracklets* with the maximum foreseen inclination have to be considered, as sketched in Fig. 6.3. One possible implementation could be the exchange of the content of the *tracklet* SUM memories, which is calculated during the drift-time, at the end of the drift-time for the calculation of the complete *tracklet* parameters. However, this would result in an increased processing latency due to the required data exchange, which cannot be pipelined. On the other hand, the inclusion of a second channel (for example channel 1 of MCM  $m + 1$ ) would allow the complete reconstruction of a boundary-crossing *tracklet* on MCM  $m$ . Note that no further efficiency will be gained by the shipping of channel 16 of MCM  $m$  to MCM  $m + 1$  as the given *tracklet* will already be reconstructed by MCM  $m$ . Therefore, the total number of inputs on each 18-channel MCM is 21, where two channels are shipped to and one is received from MCM  $m - 1$  and one channel is shipped to and two are received from MCM  $m + 1$ .

Simulations have shown that communication between two chips in  $z$  direction is not necessary (see Section 6.4). *Tracklets* split in that direction can be recombined at the level of the global tracking unit.

### 6.3.2 Local Tracking Unit (LTU) functionality

An overall picture of the electronics is given in Fig. 5.2. The LTU functionality includes everything after the ADC. It comprises a so called *tracklet* preprocessor (TPP), which includes storage of the raw ADC data in the event buffer, a SIMD microprocessor, which subsequently computes and selects the *tracklet* and the read out part.

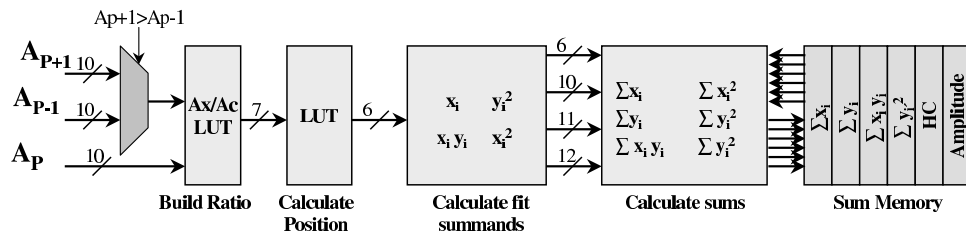


**Figure 6.4:** Functionality one dedicated channel of the preprocessor.

The TPP performs data acquisition from the 21 ADCs and, in parallel, executes the required *tracklet* preprocessing in order to speed up the determination of the track parameters after the drift-time ends. Its functionality is shown in Fig. 6.4. The tracking model assumes a straight-line fit according to :

$$y_i = a + bx_i, \quad (6.1)$$

where  $i$  is the time bin number. The resulting slope and intercept for  $N$  space points  $(x_i, y_i)$  are defined as :

$$b = \frac{N \sum x_i y_i - \sum x_i \sum y_i}{N \sum x_i^2 - (\sum x_i)^2} \quad , \quad a = \frac{\sum x_i^2 \sum y_i - \sum x_i \sum x_i y_i}{N \sum x_i^2 - (\sum x_i)^2}. \quad (6.2)$$

The space points are given by the drift distance  $x_i$  and the measured position  $y_i$  along the wire. Although the y-position resolution depends on the total charge of the cluster, the fit is not performed with weights as those would have required more hardware. All  $N$  clusters are just required to have a minimum total charge (the sum of three neighboring pads), which can be configured.

All digitized ADC values are stored in the event buffer. The various sums shown in equation 6.2 can be accumulated during the drift-time in a multi-ported register file (FIT), implementing read-modify-write cycles. At the end of the drift-time, all required input parameters for the fit are stored in the

appropriate registers of the fit register file. At that point, the fast clocks are enabled, starting the multiple-instruction–multiple–data (MIMD) processors and computing the *tracklet* parameters according to equation 6.2. This final computation requires only multiplication, addition and one division. The start and end time of the fit algorithm can be configured within an interval of up to 32 time bins.

A space point is always assigned to the pad carrying the maximum signal. However, valid *tracklets* can span two pads, which results in those *tracklets* being split over these two pads as their cluster maximum moves from one pad to the next (Fig. 6.3).

In order to avoid tracking inefficiencies, those *tracklet* segments have to be merged. The merging makes use of the constant width  $\Delta y$  of the individual pads which allows for the derivation of the combined sums from the two adjacent channels ( $p, p+1$ ). Parameters for the full *tracklet* with respect to channel  $p$  are computed by merging its data with the data from channel  $p+1$ :

$$\sum x_i = \sum_p x_i + \sum_{p+1} x_i \quad , \quad \sum x_i^2 = \sum_p x_i^2 + \sum_{p+1} x_i^2 \quad (6.3)$$

,

$$\sum y_i = \sum_p y_i + \sum_{p+1} y_i + N_{p+1} \Delta y \quad , \quad \sum x_i y_i = \sum_p x_i y_i + \sum_{p+1} x_i y_i + \Delta y \sum_{p+1} x_i, \quad (6.4)$$

$$\sum y_i^2 = \sum_p y_i^2 + \sum_{p+1} y_i^2 + 2\Delta y \sum_{p+1} y_i^2 + N_{p+1} \Delta y^2. \quad (6.5)$$

The sum of  $y_i^2$  is required for the computation of a fit quality parameter.

This functionality is implemented by the MIMD processor. In order for a *tracklet* segment to be considered, it has a programmable minimum length of typically four measured space points. The equations are symmetric whether a left or right neighbor is merged. Therefore, it is sufficient to always have one predetermined side here, which will be the ascending pad number.

### 6.3.2.1 Tracklet Preprocessor

The TPP calculates parameters from stiff tracks of 18 data channels for a linear fit during the drift-time of  $2 \mu s$ . All TPP configuration parameters can be set externally. The whole architecture (as shown in Fig. 6.5) can be split into three sections.

- The first part is the front-end interfacing to the ADCs, which are also implemented on the chip. This stage integrates the event buffers to store the raw data for later read out upon a L2 accept and a logic block to select space points in real-time for all channels simultaneously. Also, two lookup tables (LUT) per channel are implemented. The first LUT builds the ratios between the center and neighbor pads, and the second calculates the position on the current pad.
- The second part of the TPP calculates the parameters needed for the fit.
- The third part is the read-modify-write block (FIT), which allows for updating of the various sums in one clock cycle and provides support for the interface to the MIMD processor described in Section 6.3.2.

Now follows a more detailed description of the functionality and architecture of all three parts.

For each clock cycle, the sum of three adjacent channels is built for each channel. An incoming data value is accepted as an interesting data point if two conditions are met:

- (i) The amplitude of the left,  $A_l$ , and right,  $A_r$ , channels are smaller than the middle channel  $A_c$  ( $A_l < A_c$  and  $A_r \leq A_c$ ).
- (ii) The sum of these three amplitudes is greater than a configurable threshold  $th$ , i.e.  $A_l + A_c + A_r > th$ , which can be set to full scale in order to mask any given channel.

This first block operates at the sampling frequency of the ADCs of about 10 MHz. Note that in order to keep all internal clock frequencies as low as possible (ADC clock), more logic than absolutely necessary is used here. The arithmetics is fast enough, easily supporting a  $4\times$  or higher multiplexing, which is not implemented in order to avoid higher clock frequencies and related digital noise.

If a three-channel amplitude group meets the specified conditions, a four-parameter block ( $A_x$ ,  $A_s$ ,  $ID$ ,  $hit$ ) is queued for further calculations. It contains the amplitude  $A_x$  of the larger of the left or right neighbors of the current channel, the sum amplitude  $A_s$  of these three channels, the channel number  $ID$ , and a flag  $hit$  that indicates that the data from this channel form a valid candidate to compute further fit parameters. If no channel complies with the  $hit$  conditions, nothing is calculated or stored in the register file (FIT). For each valid time bin, the acquisition kernel computes the following set of parameters :  $x_i$ ,  $y_i$ ,  $x_i \cdot y_i$ ,  $x_i^2$ ,  $y_i^2$ ,  $hc$ ,  $trd$ . The parameter  $x_i$  represents the position in drift direction and is encoded as a sampling time bin number. The parameter  $y_i$  is the location of the charge cloud in the given time bin in  $y$  direction, which is determined using two lookup tables, encoding the pad response function and providing two independent measures of the position. The comparison of the two ratios with the tabulated expectation based on the pad response function allows at this stage also to reject merged hits. The parameter  $hc$  is a flag that for a valid group is one and the update of which in FIT encodes in the end the number  $N$  of space points for a *tracklet* (see equation 6.2). The parameter  $trd$  reflects the amplitude of the group.

In the third part, the calculated parameters are used to update a read-modify-write memory (FIT). In each cycle, a full parameter line is read out and the sums of the calculated parameters are written back to the memory. For each data channel, a memory line for all parameters is implemented. The fit register is also the interface to the MIMD processor, which works on these calculated data after the drift-time. While the TPP works in acquisition mode, the MIMD processor is in sleep mode with its clocks disabled. At the end of the drift-time, if parameters were calculated, the TPP wakes up the MIMD.

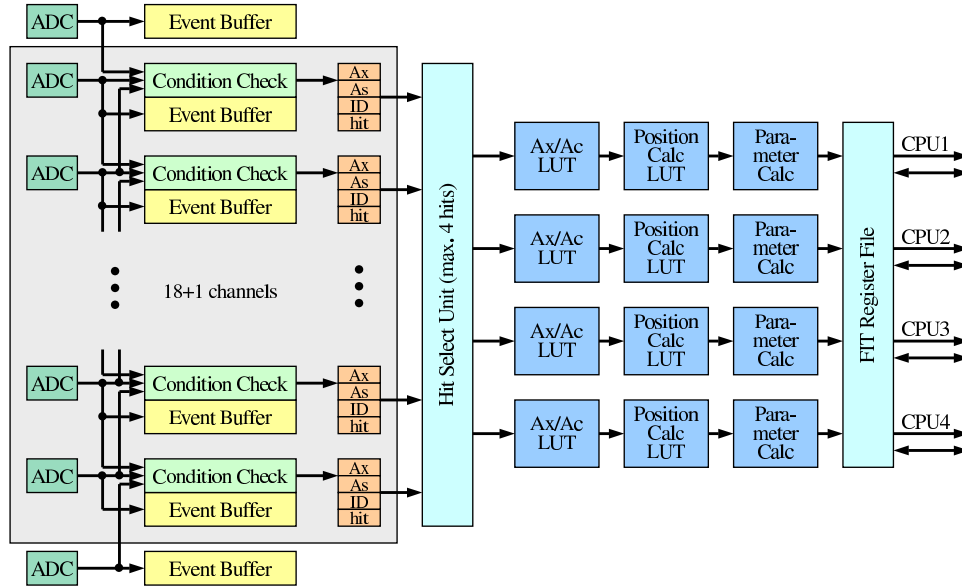


**Figure 6.5:** Schematic block diagram of the TPP chip.

The TPP block diagram is shown in Fig. 6.5. Altogether, the TPP comprises the following building blocks : 19 data channels with event buffers capable to store the ADC values; a cluster finder to select

interesting data and sum three channels ('Condition Check'); a unit that selects up to four clusters (largest amplitudes) for further processing ('Hit Select Unit'); a position calculation block to calculate the fit input parameters; and a read-modify-write memory block to store the calculated data in the register file ('FIT') which is also the interface to the MIMD processor. Note that the 19 channel TPP includes 2+1 additional channels of its neighboring MCMs and thus from different preamplifier chips (refer to section 6.3.1), which are already digitized and stored at these neighboring MCMs. In order to verify the gain matching between the different chips these shared channels are archived also within the TPP. In addition to the basic functional blocks, each channel has a configurable block to subtract a pedestal and apply a threshold. Each block contains two fast multipliers, as provided by the library of the silicon synthesizer, and one special divider that is implemented as a lookup table. The special divider actually approximates the division by transforming the data to a logarithmic scale. This is realized by generating logic from lookup tables and adjusting the precision of the calculation to the quality of the measurement process. The next chapter describes the building blocks in more detail.

## Front End

The front-end works with a frequency of about 10 MHz, and provides the interface to the integrated ADCs. Each chip receives data from 21 ADCs, and each data channel receives data from three ADCs : from the current ADC, and from its left and right neighbor. First, a multiplexer selects the larger value out of the right and left channel; this choice is made by a comparator block (see Fig. 6.4). Then the ratio to the center channel is built and the position  $y_i$  is calculated. Both, the normalization and the position reconstruction can be performed by programmable look-up tables.

## Configuration

The TPP allows for individual configuration of pedestal, thresholds and drift length. The pedestal value can be configured for each channel in the TPP. The pedestal is 10 Bit wide, thus allowing for the elimination of defect channels. The second is the 12 Bit wide threshold that is used to check the  $i$ th condition in the TPP. It also serves for the zero suppression that eliminates noise. The drift length, a 6 Bit number, is necessary to configure the address counter of the event buffer. The event buffer starts to fetch data when the pretrigger is detected in the chip and stops when the address counter reaches the drift length. This is common for all 19 channels in a chip.

The TPP configuration is done by the MIMD processor in a programmed I/O fashion, when in the configuration state. A device is added to the I/O memory space supporting the TPP configuration functionality. In order to keep on-chip routing simple and to avoid complex configuration buses the TPP configuration is shifted in or out sequentially, allowing to implement the configuration registers as shift registers. There is, however, a shadow register allowing to (re)define the actual configuration in one clock by copying to/from the shadow register. In order to set the configuration shift registers efficiently, one of the MIMD CPUs writes to the TPP configuration logic. As a consequence an internal state machine shifts the received 32 Bit wide configuration word sequentially into a shadow shift register of the real configuration register. The MIMD processor continues until all bits have been shifted in. The number of bits in the shadow configuration register are always multiple of 32 bits. The shadow register is then copied into the actual configuration registers by asserting an appropriate strobe signal, which is triggered by writing to another defined region within the TPP configuration block. Configuration reads are implemented equivalently, with the exception that the shadow configuration register is copied first from the actual configuration registers and then read out by the MIMD processor, reading 32 bits per transaction.

The configuration parameters are taken from the MIMD processors global data RAM. They can be uploaded during the LTU configuration using the serial configuration link. This link is terminated in a configuration unit, having access to both the I/O bus and the global data RAM, using the address and data bus of CPU 1 as sketched in Fig. 6.6 (see also section 6.3.3.6). However, the serial configuration

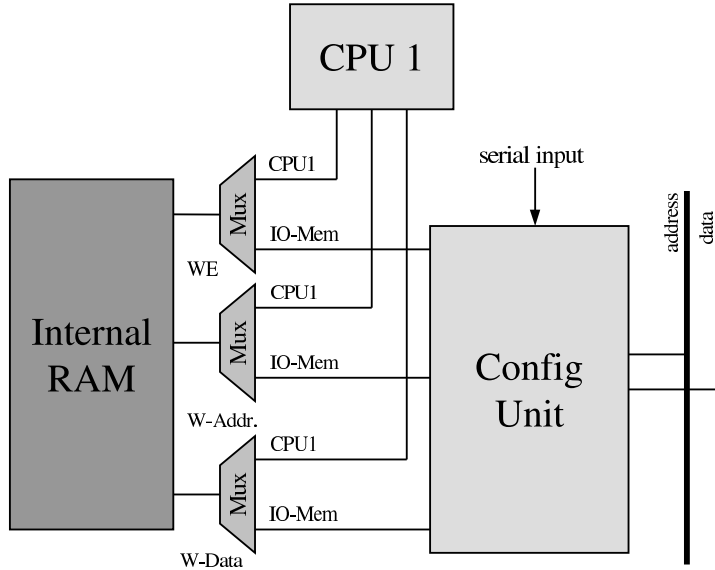


**Figure 6.6:** Configuration of internal RAMs.

unit can also write directly to the memory mapped TPP configuration registers mocking the programming functionality of the MIMD processor, supporting external configuration of the TPP without the assistance of the MIMD processor.

### Different operating modes

The TPP has three operating modes. By default, if not idle, it is in acquisition mode to receive data from the ADCs and calculate all fit parameters. In the second mode, the event buffer is accessible by the MIMD processor. Since there is no explicit store instruction for the event buffer, the ports are accessed via the global I/O memory region and will be controlled by a dedicated register in the global I/O memory. This mode will be used for self test functionality of the LTU. In the third mode, the TPP reads its input from the event buffer rather than from the ADCs. In this mode an event can be replayed or a known simulated event can be downloaded and run through the system in order to verify system integrity. If chip real estate permits, it is planned to implement the event buffers deep enough in order to allow having always a backup or stored event on-line, which allows to inject a simulated event with zero dead time.

### TPP prototype chip FaRo 1

The first prototype (FaRo 1) has been produced using the AMS<sup>1</sup> 0.35  $\mu\text{m}$  CMOS process. This prototype has eight data channels. The front-end is designed to work externally at 20 MHz and internally at 80 MHz. The resulting chip integrates about 50k gates and has a core size of 14.4 mm<sup>2</sup>. A test board generating the required external clocks has been produced. As a pattern generator, an appropriate FPGA was used, which implements a PCI core, thereby allowing access via PCI. The test vectors are generated by software and downloaded through the PCI bus into the internal memory of the FPGA. On a trigger signal, the FaRo chip is subjected to the previously downloaded test data and subsequently performs the processing that takes place during the data acquisition time. Following this, the FPGA generates read out signals and collects the results from the prototype. Then all data are shipped through the PCI bus into a Linux PC's memory and are compared with the expected data. The FaRo 1 chip was validated by testing it with more than three million test vectors. The set of test vectors was designed to cover critical areas of

---

<sup>1</sup>Austria Micro Systems, [www.amsint.com](http://www.amsint.com)

the design. In addition, randomly generated test vectors have been used. During the tests, no errors were detected. The FaRo 1 test-board with the Orca FPGA board is shown in Fig. 6.7.

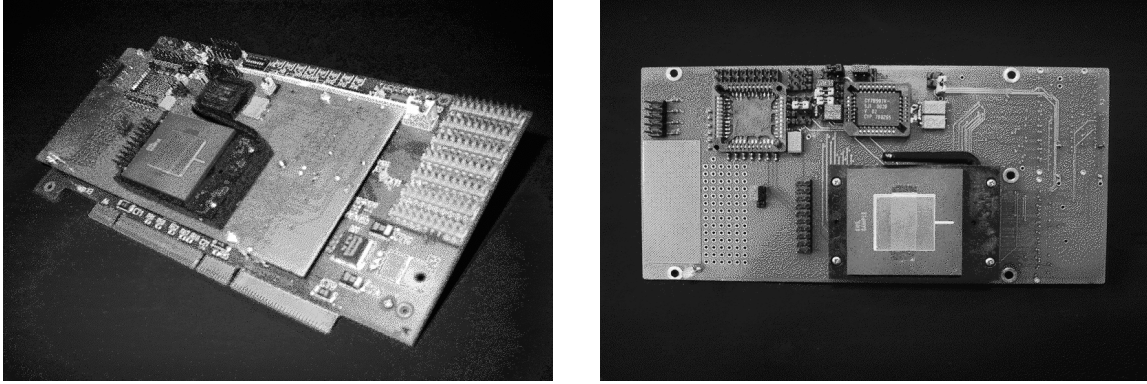


**Figure 6.7:** FaRo test board.

Calculation of the power consumption of the FaRo 1 TPP is done with a separate power supply for FaRo in the test setup. A fatigue test shows that the power consumption is only dependent on the clock frequency. One channel in the whole architecture has a power consumption of about 100 mW. The test chip works internally with a fourfold clock frequency compared to the front-end. The test results are shown in Fig. 6.8.

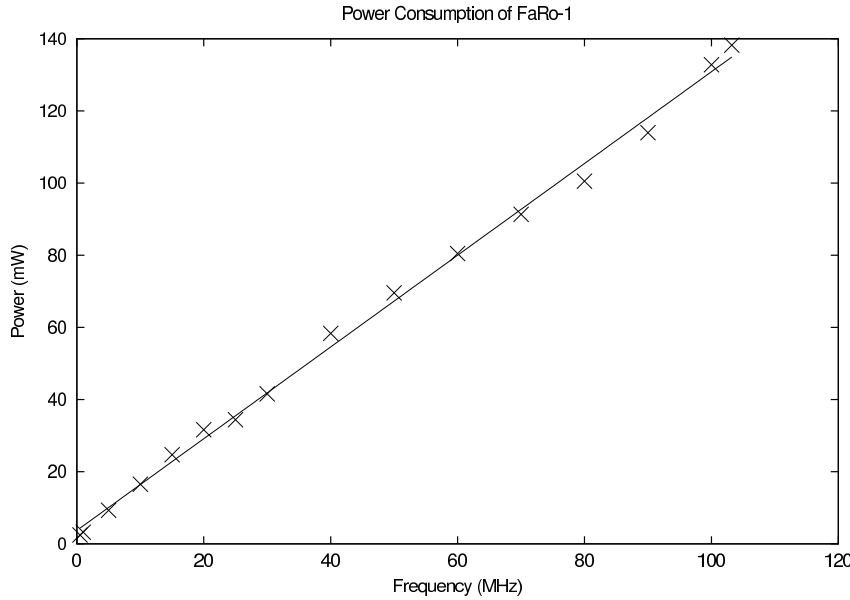


**Figure 6.8:** Power consumption of the FaRo 1 chip.

### 6.3.3 Tracklet processor

This chapter focuses on the architecture and functionality of the MIMD trigger processor which is integrated into the read out system and will be implemented on the MCM that is described in Section 5.8.

#### 6.3.3.1 Architecture and functionality

The architecture allows the concurrent execution of multiple threads on a shared memory and provides an efficient means for inter-thread communication and synchronization. Four Harvard-style CPUs are

closely coupled by sharing the same data and instruction memory. In addition, a subset of their registers is globally accessible.

The task of the system is to execute flexible trigger code in less than  $1 \mu\text{s}$ . As described, the TTP digitizes and captures the amplitudes of 18 channels and executes a hard-coded algorithm, which provides a first selection of up to four track candidates and calculates parameters for the linear fit.

This processing stage is performed by a four-node MIMD processor. Each node implements a private register file and a global register file to share parameters and provide a means for synchronization. To simplify the decode/fetch phase, all arithmetic instructions work register-to-register. The size of an instruction is limited to a single 24 Bit word. The Harvard-style architecture foresees only two pipeline stages: one fetch/decode stage and one execute/write back stage. The data and program stores are implemented as shared internal quad-ported RAMs. The data RAM is accessible via load and store operations. Data from the acquisition stage of the TPP are retrieved by a dedicated load instruction. The instruction set is RISC-like. In addition to the common arithmetic and logical operations, instructions have been added to handle synchronization between the CPUs. An overview of the architecture is sketched in Fig. 6.9.

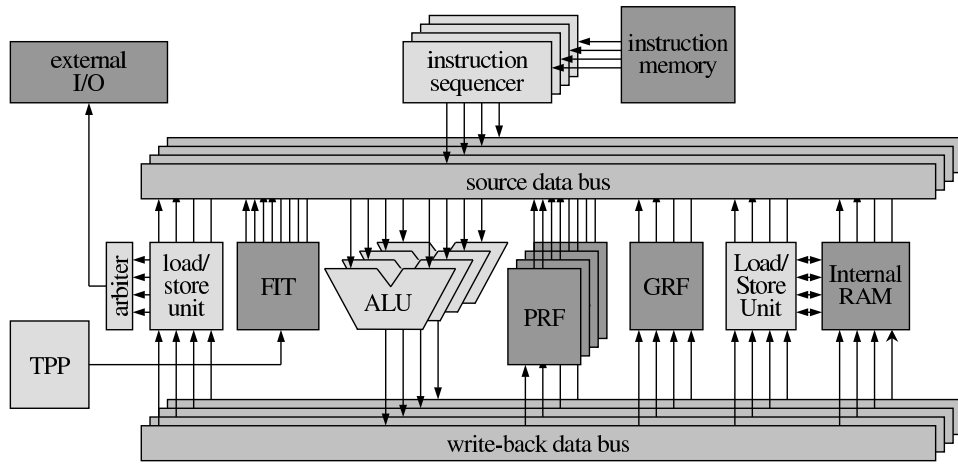


**Figure 6.9:** Schematic block diagram of the MIMD processor.

Most instructions can be executed in two clock cycles. The four independent CPUs work on the data from the TPP to execute four independent trigger algorithms simultaneously. Due to the read-modify-write capability of the global registers, data conflicts in the pipeline are avoided. This allows for the production of highly efficient code for the expected computations. First versions of the code indicate that, in many cases, the results from one instruction are used during the next cycle. In deeply pipelined RISC architectures, the results must be forwarded using dedicated data paths. As an alternative, no-operation instructions (NOP) can be inserted into the instruction stream. This architecture avoids both, the hardware and software the complications resulting from data dependencies.

The interface to external components is realized via the private register file. The CPU also supports synchronization between the nodes by a synchronization register file. Writing to those registers creates signals which, together with some additional instructions, provide a versatile means of synchronization.

Each node has a 32 Bit wide data path. Thus, for those arithmetic elements employing more than 32 Bit wide operands/results, multiple registers have to be used. As can be seen in Section 6.3.3.2, only three operands can be addressed by one instruction. Thus, for the upper part of the results, a dedicated register is used. Each implemented data memory is 32 Bit wide. The processor has four independent instruction sequencers. The instruction memory is a full custom 24 Bit wide quad-ported memory that is implemented as internal RAM with 2048 entries. The first test program requires about 200 entries (excluding the zero suppressing readout program) and we estimate that 2048 is enough for

all enhancements. Each node has a separate decode block to decode the current instruction. The decoded instructions are stored in a pipeline register. In every cycle, the nodes can fetch data from one of the following sources : the private register file (pRF); the global register file (GRF); the fit register file (FIT) containing the results of the TPP; the internal RAM; the global I/O memory; and the event buffer from the TPP. To allow simultaneous access, the interface to the TPP is implemented as a multi-ported register file (FIT) with a fixed assignment of a given *tracklet* candidate to a CPU, which is determined by the TPP at the end of the drift time. Results can be written back either to the PRF or the GRF. It is expected that a node works mainly on its PRF. To exchange data between nodes, the GRF or the RAM can be used. To access the RAM, load/store instructions are used. The GRF has to provide four write and four read ports to allow concurrent access by all the nodes. It has proven to be convenient to keep certain constants in read-only registers. In this architecture, we have foreseen some constant values. These constants are implemented by using two of the bits that encode the source register block. This mechanism can be used to introduce up to 16 constants.

### 6.3.3.2 Instruction set and format

The RISC instruction set implements fixed-length 24 Bit wide instructions. Four major addressing modes are supported : immediate, register direct, register indirect, and memory direct. Figure 6.10 sketches the seven different supported instruction formats.

a)	23      17 16      11 10      5 4      0
b)	23      17      14      11 10      5 4      0
c)	23      17 16                5 4      0
d)	23      17 16      11 10           0
e)	23      17      13           5 3      0
f)	23      17 16      11           3      0
g)	23      17      15           0
	Opcode      Source 1      Source 2      Destination
	Opcode           Immediate      Source 2      Destination
	Opcode           Immediate           Destination
	Opcode      Source 1           Immediate
	Opcode           Immediate           Branch
	Opcode      Source 1           Branch
	Opcode           Immediate

**Figure 6.10:** Instruction formats.

The instruction code is represented by a 7 Bit wide field to allow sufficient room for additional instructions. Currently, 70 instructions are implemented. The supported instructions sketched in Fig. 6.10 are in the given order :

- Arithmetic, logical, rotate, move, compare, interrupt instructions, instructions for synchronization, and register indirect load/store instructions
- Shift instructions
- Immediate Move and Load
- Immediate Compare and Store
- Immediate Branch instructions
- Register indirect jumps

- Special instructions for synchronization and interrupts

Most of the instructions, known from general purpose processors are supported. However, there is one extra group of instructions for synchronization between the CPUs.

The instruction set has no explicit instruction for subroutine calls. However, any register can be used as stack pointer and the program counter can be linked, thus allowing the implementation of subroutine calls. The whole instruction set is shown in Table 6.1.

### 6.3.3.3 Quad Ported Memory

A static RAM cell was designed to be used in the TRD trigger system. In the MIMD processor, it will serve as instruction memory and internal RAM to provide access for the four CPUs in each clock cycle. The shared instruction memory allows considerable savings in die area. Since the static RAM is as fast as registers are, the system design is simplified.

To minimize chip area and power consumption, both of which are critical for this trigger processor, a full custom macro cell has been developed in the AMS 0.35  $\mu\text{m}$  CMOS process with three metal layers and a VDD voltage of 3.3 V. It is a scalable memory block with a maximum block size of 64 lines and a maximum line width of approximately 60 Bit. Special emphasis has been put on access time and chip space utilization. Both implemented memories are organized in blocks of 64 lines. The instruction memory includes eight multiplexed blocks with 24 Bit per line. The data memory consists of four blocks with 16 Bit per line. All data ports are bi-directional.

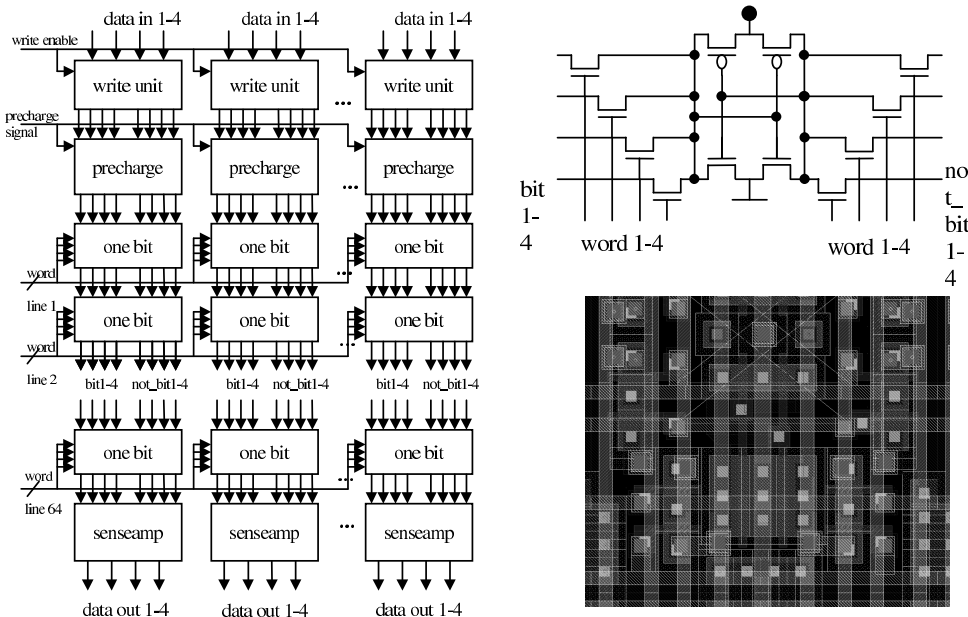


**Figure 6.11:** Block diagram of a memory block, as well as a schematic and layout view of a one-bit cell.

The structure of one memory block is shown at the left side in Fig. 6.11. Each block includes an independent set of address decoders (not shown), a write unit, a precharge unit, and a sense amplifier for each port, which allows them to operate asynchronously. In addition, a block contains an array of 64 lines of SRAM bit cells.

A single bit cell, shown in Fig. 6.11 (right panels), consists of two cross-coupled inverters. Each inverter is made up of one PMOS and one NMOS transistor. The PMOS transistor is connected to VDD and pulls the output potential to VDD if the input is on ground level. The NMOS transistor is connected to ground and pulls the output to ground if the input is VDD. The output of the first inverter is the input of the second and vice versa. This system has two states. If the input of inverter one is at VDD, it pulls the

**Table 6.1:** Instruction set of the MIMD processor.

No.	Opcode	Source 1	Source 2	Destination	Description
0	NOP	-	-	-	No Operation
1	ADD	PRF, FitReg	GRF, PRF, FitReg	GRF, PRF	C = a + b
2	ADC	PRF, FitReg	GRF, PRF, FitReg	GRF, PRF	C = a + b + carry
3	SUB	PRF, FitReg	GRF, PRF, FitReg	GRF, PRF	C = a - b
4	SBC	PRF, FitReg	GRF, PRF, FitReg	GRF, PRF	C = a - b - carry
5	MUL	PRF, FitReg	GRF, PRF, FitReg	GRF, PRF	C = a * b
6	MUS	PRF, FitReg	GRF, PRF, FitReg	GRF, PRF	C = a * b
7	DIV	PRF, FitReg	GRF, PRF, FitReg	-	C = a / b
8	DIE	-	-	-	C = a / b
9	AND	PRF, FitReg	GRF, PRF, FitReg	GRF, PRF	C = a & b
10	ATT	PRF, FitReg	GRF, PRF, FitReg	GRF, PRF	a & b
11	ORR	PRF, FitReg	GRF, PRF, FitReg	GRF, PRF	C = a   b
12	COM	-	PRF, FitReg	GRF, PRF	C = ! a
13	NEG	-	PRF, FitReg	GRF, PRF	C = (1: a) + 1
14	EOR	PRF, FitReg	GRF, PRF, FitReg	GRF, PRF	C = a ^ b
15	SHA	implicit	GRF, PRF, FitReg	GRF, PRF	C = a shar X
16	SHT	implicit	GRF, PRF, FitReg	GRF, PRF	C = a << X
17	ROR	-	GRF, PRF, FitReg	GRF, PRF	C = ROR(a, carry)
18	MOV	-	GRF, PRF, FitReg	GRF, PRF	C = a
19	MVI	-	implicit	GRF, PRF	C = implicit
20	CMP	PRF, FitReg	GRF, PRF, FitReg	-	a - b
21	CPI	PRF, FitReg	implicit	-	a - b
22	CPC	PRF	GRF, PRF, FitReg	-	a - b - c
23	BSS	-	implicit	-	branch if s
24	JSS	PRF	-	-	branch if s
25	BSC	-	implicit	-	branch if not s
26	JSC	PRF	-	-	branch if not s
27	BZS	-	implicit	-	branch if zero
28	JZS	PRF	-	-	branch if zero
29	BZC	-	implicit	-	branch if not zero
30	JZC	PRF	-	-	branch if not zero
31	BVS	-	implicit	-	branch if overflow (V)
32	JVS	PRF	-	-	branch if overflow (V)
33	BVC	-	implicit	-	branch if not overflow (V)
34	JVC	PRF	-	-	branch if not overflow (V)
35	BNS	-	implicit	-	branch if n
36	JNS	PRF	-	-	branch if n
37	BNC	-	implicit	-	branch if not n
38	JNC	PRF	-	-	branch if not n
39	BCS	-	implicit	-	branch if c
40	JCS	PRF	-	-	branch if c
41	BCC	-	implicit	-	branch if not c
42	JCC	PRF	-	-	branch if not c
43	BBS	-	implicit	-	branch if b
44	JBS	PRF	-	-	branch if b
45	BBC	-	implicit	-	branch if not b
46	JBC	PRF	-	-	branch if not b
47	BRA	-	implicit	-	unconditional branch
48	JMP	PRF	-	-	unconditional branch
49	SYN	-	-	-	wait on ALU
50	SYT	-	-	PRF, GRF	test wait
51	SEM	-	implicit	-	Set Syn mask
52	LRA	-	PRF	PRF, GRF	Load from RAM
53	LRI	-	implicit	PRF, GRF	Load from RAM
54	SRA	PRF	PRF	-	Store to RAM
55	SRI	PRF	-	implicit	Store to RAM
56	LBU	-	PRF	PRF, GRF	Load Evt.-Buff
57	LBI	-	implicit	PRF, GRF	Load Evt.-Buff
58	LPA	-	PRF	PRF, GRF	Load from private I/O Mem
59	LPI	-	implicit	PRF, GRF	Load from private I/O Mem
60	SPA	PRF	PRF	-	Store to private I/O Mem
61	SPI	PRF	-	implicit	Store to private I/O Mem
62	LGA	-	PRF	PRF, GRF	Load from global I/O Mem
63	LGI	-	implicit	PRF, GRF	Load from global I/O Mem
64	SGA	PRF	PRF	-	Store to global I/O Mem
65	SGI	PRF	-	implicit	Store to global I/O Mem
66	CLI	-	-	-	Clear Interrupt
67	STI	-	-	-	Set Interrupt
68	INT	-	implicit	-	Software interrupt
69	IRT	-	-	-	Back form interrupt

input of inverter two down, which subsequently pulls the input of inverter one up, and by this stabilizes the system. This state can represent the digital value one. By reversing the inverters' input potential, the second state is achieved, representing the digital zero.

A single port of the bit cell consists of two minimum size NMOS transistors connecting the input of inverter one to the bit line and the input of the second inverter to the not\_bit line. The gates of these pass

transistors are connected to the word line, which is driven by the address decoder as mentioned later.

This setup is used for each of the four ports. The resulting load has to be taken into account in the design of the inverters. In the worst case scenario, a single bit cell is addressed by all four ports. Then the capacity of four bit/not\_bit lines has to be driven. This mainly results from the parasitic capacity of the pass transistors of all bit cells in a column. This requires a layout of the NMOS transistors of the two inverters with the threefold area of a minimum-sized transistor. The PMOS transistors can be kept at minimum size. As a result, the cell can discharge a bit/not\_bit line quickly, but charging is significantly slower, of the order of a factor 10. In total, a single bit cell includes two PMOS transistors, two threefold NMOS and eight NMOS pass transistors. The cells are arranged in a rectangular grid. The power, ground and bit/not\_bit lines run vertically through the cells, and the traces for the word lines are arranged horizontally.

The area of a single bit cell is determined mainly by the eight pass transistors and the routing of the four word lines and the eight bit/not\_bit lines. The resulting cell is  $12.9 \mu\text{m}$  wide and  $9.6 \mu\text{m}$  high. The needed area is approximately 1.6 times that of a single ported SRAM cell with two pass transistors and minimum size inverters.

The number of memory lines per block is limited by the maximum capacity a cell can drive in the permitted time frame. As a compromise between large blocks and small inverters, we chose a block length of 64. A bigger inverter can drive more memory lines. To realize a 128 word block, at least fourfold-sized NMOS transistors are required. These transistors increase the effective size of a cell in such a way that the block would require more space than two 64-line blocks. The reason for this is mainly due to the fact that the threefold sized NMOS transistors can be placed in an otherwise free rectangle formed by four pass transistors. These estimates take into account the peripheral logic.

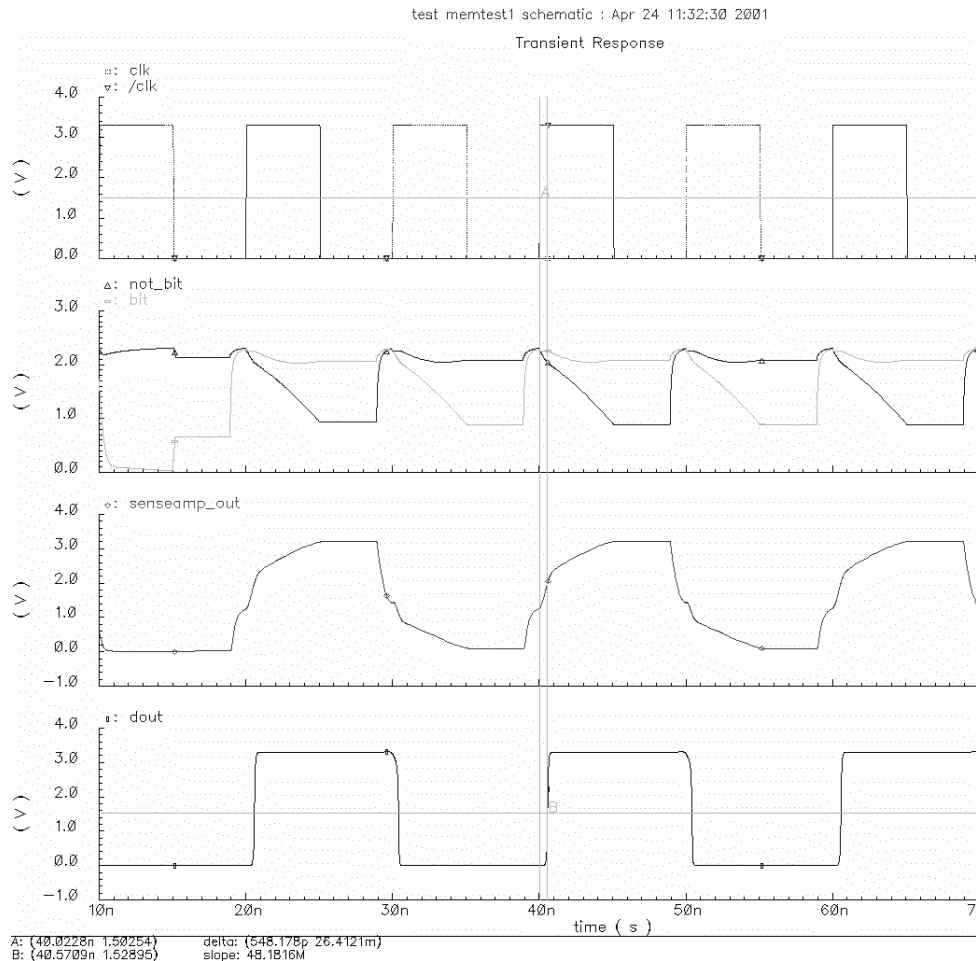
To read out a memory line through one of the four ports, all bit/not\_bit lines of this port are first precharged. Simultaneously, the address decoder decodes the address. Then the address decoder drives the addressed word line. This triggers all bit cells from this word line to drive the precharged bit/not\_bit lines. The sense amplifiers detect the voltage differences between these lines and write out the stored bits. To write data, the address decoder has to decode the address and drive the addressed word line. Instead of precharging, the write unit must drive bit and not\_bit lines to opposite levels. Depending on the desired data value, the bit line is driven at VDD and the not\_bit line is driven at ground level or vice versa.

Figure 6.12 shows the results from the simulation. In the simulation, a logical zero and a logical one is read alternating from two bit cells. The first graph (top) shows the global clock signal that triggers the pass transistors. The bit/not\_bit lines are precharged between two reading cycles, shown in the second graph. To emulate the effect of the rest of the memory block, they are connected to the capacity representing the block. After all pass transistors have been enabled to simulate reading on all four ports, the bit cell needs 4 ns to discharge either the bit or the not\_bit line. However, the sense amplifier needs only 1.7 ns to drive its output to 90% of VDD in case of a digital one, shown in the third graph. A standard buffer (BU2) connected to the sense amplifier's output provides the digital value 0.5 ns after the pass transistors have been enabled, shown in the last graph. The address decoder needs 1.6 ns from applying the address to enabling the word line. This time is used for precharging the bit/not\_bit lines. A complete read cycle needs 2.1 ns from applying the address to the output of the digital data.

The whole memory block has also been simulated and the times mentioned above have been verified. The chips have been received from the manufacturer but testing has not completed in time for this report.

#### 6.3.3.4 Arithmetic Logical Unit

The ALU applies arithmetic and logic operations on two integer operands. It implements binary logic (and, or, xor) and the full set of basic arithmetic operations, i.e., addition, subtraction, multiplication and division as it's used for the equations 6.1 to 6.5. In addition, bit shifts of variable distance can be applied



**Figure 6.12:** Simulation results of reading from one memory cell of the Quad Ported Memory. The address is produced with the clock signal clk. The second row shows the effected bit line and inverted bit line. The signals senseamp\_out and dout show the output of the memory cell before and after the output buffer. The vertical lines at 40 ns show an access time of the core cell of less than 1 ns (plus address decode).

to one of the operands.

To allow efficient control of the program flow, the ALU generates five status flags : carry, zero, two's-complement overflow, negative, and signed. An auxiliary input port is available to allow integer division with double-width dividends. Similarly, an auxiliary output port allows double-width multiplication results. All operations can work on negative integers in two's complement representation. Operation is controlled by a 4 Bit opcode, which is specifically optimized to minimize the need for internal control logic. To improve design flexibility and reusability, the input and output data width is fully parameterizable.

The primary implementation objective was to allow for high clock rates, while still performing most arithmetic operations in a single clock cycle using a non-pipelined architecture. Further requirements were low power consumption and the possibility to optimize the implementation for different clock rates. These implementation goals suggest a modular design, thus decoupling parts for different complexity and speed and allowing to switch the implementation of a component according to specific requirements.

The ALU main module implements only the basic operations like addition/subtraction and Boolean logic. These operations are non-pipelined. Multiplication and division, being more complex operations, are performed by separate modules for which several different implementations are available. These implementations include both pipelined and non-pipelined designs. The available implementations for

the divider include a CSA-based radix-4 divider [6], which has been constructed for high clock rates. For the present version of the ALU, a data word width of 32 Bit is required. To minimize data dependency problems with most of the operations, a fully combinatorial multiplier has been selected.

### 6.3.3.5 Synchronization

The MIMD implements four CPUs operating independently of each other. However, a means for synchronization, wake-up from stand-by and the like, is required. Figure 6.13 shows a schematic view of the GRF and the associated flag bits in each of the CPUs, forming a private 16 Bit synchronization register. While each CPU has read/write access to all 16 GRF registers, the GRF is grouped into four sets of four registers, where each given set is assigned to a particular CPU for use as a mailbox-type register in order to implement the desired synchronization primitives. When writing to one of the GRF registers within a set that is associated to a CPU, a corresponding bit is cleared in the synchronization register of all the other CPUs. This global setting of flags, triggered by register access, is the foundation on which the synchronization is based.

Three instructions are used for synchronization : SYN, SEM and SYT. SEM sets the local synchronization register to the mask provided by the argument mask16. Then the program counter of this CPU is suspended by the SYN instruction until the mask is completely cleared by write access of the corresponding CPUs to their associated registers in the GRF. The SYT instruction copies the content of the local synchronization register to the private register specified by the pRF argument. This mechanism allows for the implementation of flexible synchronization patterns in software.

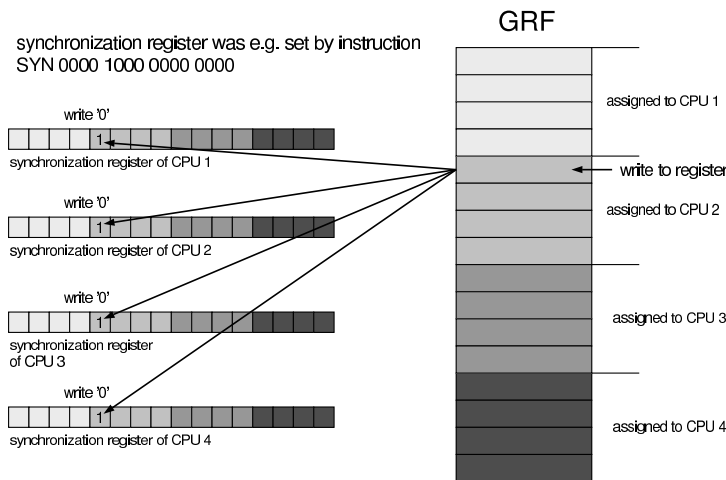


**Figure 6.13:** Synchronization mechanism.

### 6.3.3.6 Configuration

The trigger processor is configurable in the instruction memory, internal memory and some constants that are used in the trigger program. The memory that contains the used constants is 16 words deep. The currently used constants are listed in Table 6.2.

The memory of the interrupt handler from each CPU is accessible via the global I/O space. Each interrupt handler has 16 entries in the I/O space. In total 64 words are required from the memory space for the interrupt handler and can be configured by any bus master.

The internal RAM and the instruction memory are not located in the global I/O space, and thus a priori not directly accessible. Hence, it is necessary to implement a mechanism that allows to configure the internal memories. The instruction memory is programmable by a dedicated port from CPU 1. First,

**Table 6.2:** Entries in the constant memory.

No.	Constant
0	0
1	1
2	2
3	3
4	4
5	CPU ID (0-3)
6	chip ID
7	max. time bins
8	effective distance to the projection plane
9	unused
10	width of pad (in bins)
11	square of No. 10
12	0x8000
13	unused
14	-2
15	-1

the configuration unit (bus master) writes a specific word in the global I/O address space. Then the data and address port are decoupled from CPU 1 and switched to a hard-wired path to the global I/O address space. The memory is now accessible by reading/writing appropriate regions in the global I/O address space. This is done by presetting a start address register first and then reading or writing subsequent data words in an auto increment fashion. Finally, the data path is switched back to CPU 1, which is done by another write cycle with a dedicated word in the I/O address space (refer to Fig. 6.6). The internal RAM is configured in a similar manner.

The size of the I/O memory space is limited by the addressing scheme of the processor. Hence, the memory has a limit of 2 k words. By using an indirect addressing mode, there is no space limit. Each entry is 32 Bit wide. All connected clients at the global I/O bus have a synchronous behavior. They can only work on private data and receive data from the CPUs. It is not allowed for the clients to work on internal data of the processor.

### 6.3.3.7 Interface to Tracklet Preprocessor

The interface between the tracklet preprocessor (TPP) and the MIMD processor is the FIT register file. It is an eight-ported register file that is write-only by the TPP and is read-only for the MIMD processor. Each CPU has two read ports, however, each CPU has access to every line in the register. During the drift time, the TPP fills the register with the fit parameters in read-modify-write cycles. The FIT register has 19 lines with six words, and the line number corresponds to the channel number of the chip. After the drift time, up to four *tracklets* are selected. Also, the parameters from the next channels are addressable. This allows for merging of parameters from two channels without the need to increment the address register. The selection criterion is the number of accumulated hits during the drift time. A channel is selected as a stiff track candidate if it has a minimum of eight hits during the drift time. The data from two channels are merged if both channels have a minimum of four hits each during the drift time. There are three additional data channels on each LTU (refer to Fig. 5.2). In order to prevent shadow tracks, the last channel (labeled 0+) is only used to merge two channels on the given LTU between channel 17 and 0+. If the hit count in channel 0+ is larger than seven, the hits are omitted in this chip and the tracklet is calculated in the next chip.

### 6.3.3.8 Input/Output interface

The interface to the read out module (see Chapter 7) is located in the private I/O address space of each CPU. Each CPU can write directly to this region without arbitration logic, using a dedicated store in-

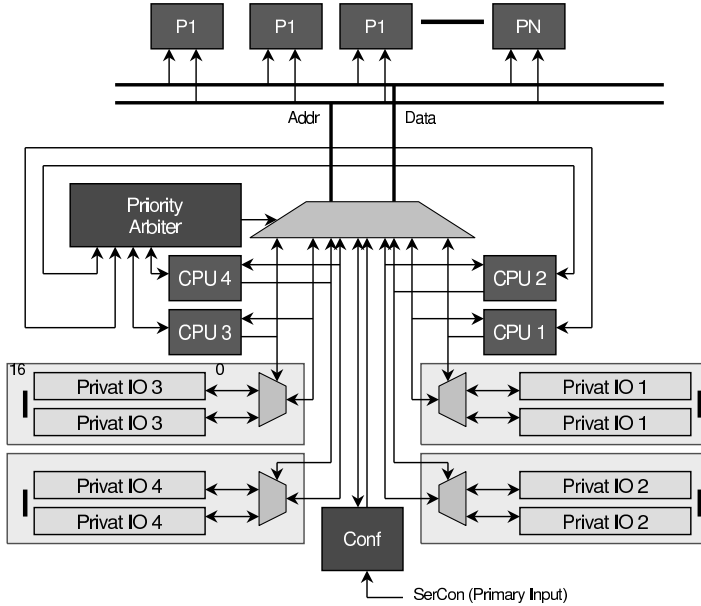


**Figure 6.14:** Interface to I/O address space.

struction. The interface to all other integrated peripheries is located in the global I/O address space. Only one CPU can access this I/O bus at the same time. The access is managed by a priority arbiter. The serial configuration node is a bus master and has access to the memory bus like a CPU. This enables writing data into the global I/O address space by the configuration node. It has a serial primary input port to receive data from external devices. An overview is shown in Fig. 6.14.

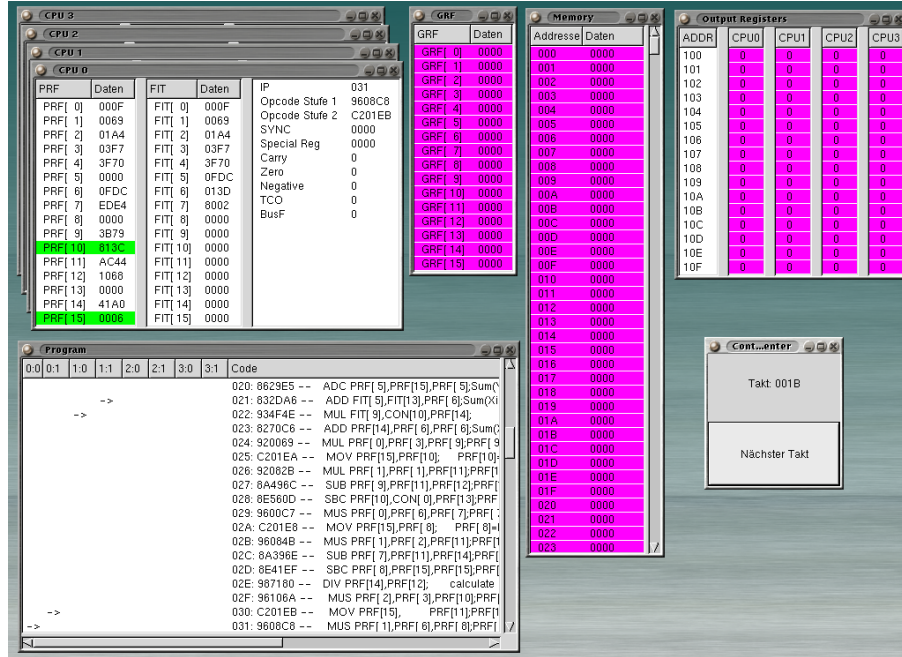


**Figure 6.15:** Screen-shot of the MIMD processors simulator running the trigger routine.

### 6.3.3.9 Interrupt

The trigger processor has eight interrupts with two priority levels. The instruction set includes four instructions to handle these interrupts : CLI, STI, INT, and IRT. CLI disables interrupts with low priority, STI allows low-level interrupts, INT is the interrupt instruction, and IRT is the return instruction from a interrupt routine. The interrupt vector table is accessible in the global I/O memory. Each CPU has sixteen entries, eight words for jump addresses and one word that provides the current level of the eight possible interrupts. The rest is yet unused. Two flag flip-flops (FF) are implemented. The first FF suspends low-level interrupts if a CLI instruction is executed or a low-level interrupt is running. The second FF suspends all interrupts if a high-level interrupt is running. Each interrupt suspends the execution of an interrupt with the same or lower priority. Basically, each interrupt checks the current priority level and the suspend flags, then stores the next program counter and jumps to the selected interrupt address. A low-level interrupt will not be executed until the decode stage contains no CLI or branch instruction. After execution of the interrupt code (low priority), the processor restores the program counter and continues the program.

### 6.3.3.10 Trigger and read out program

The given latency requirement allows for about 150 instructions to perform the trigger algorithm, which is an assembler routine. The data read out is not constrained much by latency, and it does not require very complex software either. Therefore, no high-level language support, such as C or C++, is expected. In order to facilitate the software development, particularly with respect to the multi-threading capability of the processor, an emulator was developed, which allows simulation of the whole processor including all its states and internal registers. Figure 6.15 shows a screen shot of the processor while executing instructions of the trigger program with raw data taken from the slow simulator described in Section 6.4.

The emulator is also being used to validate the maximum trigger processing latency. The trigger program shown in Tables 6.3 and 6.4 calculates the slope, intercept and the variance of a stiff track. Also, the intercept is projected onto the middle plain of the detector. The calculated data are stored in the private I/O memory of each CPU, which provides the interface to the track merger module, feeding the readout tree to the global tracking unit (GTU). In the worst case scenario, the algorithm will take 101 clock cycles, which correspond with a latency of  $0.84 \mu\text{s}$  with a cycle time of 8.3 ns.

Unlike the trigger program, the read out program has far less stringent latency requirements, which are basically defined by the maximum available time to drain the zero suppressed raw data through the read out tree. There are many read out scenarios conceivable, which can be selected on a per-event basis. They can be dynamically changed since this is a real read out program. The baseline read out foresees zero suppression.

The power routing on the pad plane is going to be in parallel to a pad row as this is the shortest distance across the pad plane. Therefore, the eight MCMs per pad row are supported by one power strip. It has to be taken into account that the power of the MIMD processors cannot be supported by the power supplies for all CPUs simultaneously. In the case of a trigger program, those processors are powered by appropriate buffer capacitors next to the digital chip. Therefore, the read out sequence is scheduled such that, at any given point in time, only one CPU per pad row is active so as not to overload the power supply rails. However, given 12 - 16 pad rows, there is still enough parallelism in the read out to guarantee saturation of the read out link.

The read out is performed in programmed I/O fashion, reading all raw data from the event buffers and storing a pre-formatted zero suppressed event fragment in the internal global data RAM, from where the data are then fetched for shipment to the read out tree.

**Table 6.3:** Trigger assembler routine of the MIMD processor.

#	Label	Instruction	Operands	Description
1	Start:	ATT	FIT[ 7],CON[12]	Test FIT[ 7] where to start
2	_Start:	BZS	_Start	MSB is set if Faro is ready with his data
3		ATT	FIT[ 7],CON[12]	MSB is set if Faro is ready with his data
4		ATT	FIT[ 7],CON[ 2]	Bit 1 is Set if CPU has to calculate data
5		BZS	End	
				Copy or merge Data from FIT-Registers to PRF – given are: FIT[0..7]: N, $\sum x_i$ , $\sum y_i$ , $\sum x_i^2$ , $\sum y_i^2$ , $\sum x_i y_i$ , b, Flags FIT[8] - FIT[15] the same for the next pad TO: PRF[0..6]: N, $\sum x_i$ , $\sum y_i$ , $\sum x_i^2$ , $\sum y_i^2$ LSW, $\sum x_i y_i$ MSW, $\sum x_i y_i$
6		ATT	FIT[ 7],CON[ 1]	Test whether to merge or not
7		BZC	merge	Merge if Bit 0 is set in FIT[ 7]
				Copy data
8	nmerge:	MOV	FIT[ 0],PRF[ 0]	
9		MOV	FIT[ 1],PRF[ 1]	
10		MOV	FIT[ 2],PRF[ 2]	
11		MOV	FIT[ 3],PRF[ 3]	
12		MOV	FIT[ 4],PRF[ 4]	
13		MOV	CON[ 0],PRF[ 5]	
14		BRA	Linefit	
15		MOV	FIT[ 5],PRF[ 6]	
				Merge the data
16	merge:	ADD	FIT[ 0],FIT[ 8],PRF[ 0]	$N = N_{(1)} + N_{(2)}$
17		ADD	FIT[ 1],FIT[ 9],PRF[ 1]	$\sum x_i = \sum x_{i(1)} + \sum x_{i(2)}$
18		ADD	FIT[ 2],FIT[ 10],PRF[ 2]	
19		MUL	FIT[ 8],CON[10],PRF[ 3]	$N_{(2)} * 127$
20		ADD	PRF[ 2],PRF[ 3],PRF[ 2]	$\sum y_i = \sum y_{i(1)} + \sum y_{i(2)} + N_{(2)} * 127$
21		ADD	FIT[ 3],FIT[11],PRF[ 3]	$\sum x_i^2 = \sum x_{i(1)}^2 + \sum x_{i(2)}^2$
22		MUL	FIT[ 8],CON[11],PRF[14]	
23		ADD	PRF[14],FIT[ 4],PRF[ 4]	
24		ADC	PRF[15],CON[ 0],PRF[ 5]	$\sum y_i^2 = \sum y_{i(1)}^2 + N_{(2)} * 127^2$
25		ADD	PRF[ 4],FIT[12],PRF[ 4]	$\sum x_i^2 = \sum x_{i(1)}^2 + \sum x_{i(2)}^2 + N_{(2)} * 127^2$
26		ADC	PRF[ 5],CON[ 0],PRF[ 5]	
27		MUS	FIT[10],CON[10],PRF[14]	
28		SHT	1,PRF[15],PRF[15]	
29		ATT	PRF[14],CON[12]	
30		BZS	not1	
31		SHT	1,PRF[14],PRF[14]	
32		ORR	PRF[15],CON[ 1],PRF[15]	
33	not1:	ADD	PRF[ 4],PRF[14],PRF[ 4]	
34		ADC	PRF[ 5],PRF[15],PRF[ 5]	$\sum y_i^2 = \sum y_{i(1)}^2 + \sum y_{i(2)}^2 + N_{(2)} * 127^2 + 2 * 127 * \sum y_{i(2)}$
35		ADD	FIT[ 5],FIT[13],PRF[ 6]	$\sum x_i y_i = \sum x_{i(1)} y_{i(1)} + \sum x_{i(2)} y_{i(2)}$
36		MUL	FIT[ 9],CON[10],PRF[14]	
37		ADD	PRF[14],PRF[ 6],PRF[ 6]	$\sum x_i y_i = \sum x_{i(1)} y_{i(1)} + \sum x_{i(2)} y_{i(2)} + 127 * \sum x_{i(2)}$
				Linear Fit: PRF[0..6]: N, $\sum x_i$ , $\sum y_i$ , $\sum x_i^2$ , $\sum y_i^2$ LSW, $\sum y_i$ MSW, $\sum x_i y_i$
38	Linefit	MUL	PRF[ 0],PRF[ 3],PRF[ 9]	$PRF[9] = N * \sum x_i^2 low$
39		MOV	PRF[15],PRF[10]	$PRF[10] = N * \sum x_i^2 high$
40		MUL	PRF[ 1],PRF[ 1],PRF[11]	$PRF[11] = (\sum x_i)^2$
41		SUB	PRF[ 9],PRF[11],PRF[12]	$PRF[12] = N * \sum x_i^2 - (\sum x_i)^2 (denominator) low$
42		SBC	PRF[10],CON[ 0],PRF[13]	$PRF[13] = N * \sum x_i^2 - (\sum x_i)^2 (denominator) high$
43		MUS	PRF[0],PRF[ 6],PRF[ 7]	$PRF[7] = N * \sum x_i y_i low$
44		MOV	PRF[15],PRF[ 8]	$PRF[8] = N * \sum x_i y_i high$
45		MUS	PRF[ 1],PRF[ 2],PRF[11]	$PRF[11] = \sum x_i * \sum y_i$
46		SUB	PRF[ 7],PRF[11],PRF[14]	$PRF[14] = N * \sum x_i y_i - \sum x_i * \sum y_i (nominator) low$
47		SBC	PRF[ 8],PRF[15],PRF[15]	$PRF[15] = N * \sum x_i y_i - \sum x_i * \sum y_i (nominator) high$
48		DIV	PRF[14],PRF[12]	Calculate m (32 BIT : 32 BIT)
49		MUS	PRF[ 2],PRF[ 3],PRF[10]	$PRF[10] = \sum y_i * \sum x_i^2 low$
50		MOV	PRF[15],PRF[11]	$PRF[11] = \sum y_i * \sum x_i^2 high$
51		MUS	PRF[ 1],PRF[ 6],PRF[ 8]	$PRF[8] = \sum x_i * \sum x_i y_i low$
52		MOV	PRF[15],PRF[ 9]	$PRF[9] = \sum x_i * \sum x_i y_i high$
53		NOP		
54		NOP		
55		NOP		
56		DIE	PRF[ 7]=m	

**Table 6.4:** Trigger assembler routine of the MIMD processor (part 2).

#	Label	Instruction	Operands	Description
				Caution DIE writes PRF[15]
57	SUB	PRF[10],PRF[8],PRF[14]		$PRF[14] = \sum y_i * \sum x_i^2 - \sum x_i * \sum x_i y_i$ (nominatorb) low
58	SBC	PRF[11],PRF[9],PRF[15]		$PRF[15] = \sum y_i * \sum x_i^2 - \sum x_i * \sum x_i y_i$ (nominatorb) high
59	DIV	PRF[14],PRF[12]		Calculate b
60	SHT	I,PRF[7],PRF[14]		$PRF[14] = 2 * m$
61	MUS	PRF[14],PRF[6],PRF[10]		$PRF[10] = 2 * m * \sum x_i y_i$ low
62	SUB	PRF[4],PRF[10],PRF[10]		$PRF[10] = \sum x_i^2 - 2 * m * \sum x_i y_i$ low
63	SBC	PRF[5],PRF[15],PRF[11]		$PRF[11] = \sum x_i^2 - 2 * m * \sum x_i y_i$ high
64	MUS	PRF[7],PRF[7],PRF[9]		$PRF[9] = m^2$
65	MUL	PRF[9],PRF[3],PRF[9]		$PRF[9] = m^2 * \sum x_i^2$
66	MOV	PRF[15],PRF[12]		Save highword
67	DIE	PRF[8]		$PRF[8] = b$
68	ADD	PRF[10],PRF[9],PRF[10]		$PRF[10] = \sum y_i^2 - 2 * m * \sum x_i y_i + m^2 * \sum x_i^2$ low
69	ADC	PRF[11],PRF[12],PRF[11]		$PRF[11] = \sum y_i^2 - 2 * m * \sum x_i y_i + m^2 * \sum x_i^2$ high
70	MUS	PRF[14],PRF[1],PRF[12]		$PRF[12] = 2 * m * \sum x_i$
71	MUS	PRF[12],PRF[8],PRF[12]		$PRF[12] = 2 * m * b * \sum x_i$
72	ADD	PRF[10],PRF[12],PRF[10]		$PRF[10] = \sum y_i^2 - 2 * m * \sum x_i y_i + m^2 * \sum x_i^2 + 2 * m * b * \sum x_i$ low
73	ADC	PRF[11],PRF[15],PRF[11]		$PRF[11] = \sum y_i^2 - 2 * m * \sum x_i y_i + m^2 * \sum x_i^2 + 2 * m * b * \sum x_i$ high
74	SHT	I,PRF[8],PRF[12]		$PRF[12] = 2 * b$
75	MUS	PRF[12],PRF[2],PRF[12]		$PRF[12] = 2 * b * \sum y_i$
76	SUB	PRF[10],PRF[12],PRF[10]		$PRF[10] = \sum y_i^2 - 2 * m * \sum x_i y_i + m^2 * \sum x_i^2 + 2 * m * b * \sum x_i - 2 * b * \sum y_i$ low
77	SBC	PRF[11],PRF[15],PRF[11]		$PRF[11] = \text{Sum}(Y_{11}) - 2 * m * \sum x_i y_i + m^2 * \sum x_i^2 + 2 * m * b * \sum x_i - 2 * b * \sum y_i$ high
78	MUS	PRF[0],PRF[8],PRF[12]		$PRF[12] = N + b$
79	MUS	PRF[12],PRF[8],PRF[12]		$PRF[12] = N + b^2$
80	ADD	PRF[10],PRF[12],PRF[14]		$PRF[14] = \sum y_i^2 - 2 * m * \sum x_i y_i + m^2 * \sum x_i^2 - 2 * b * \sum y_i + 2 * m * b * \sum x_i + N * b^2$ low
81	ADC	PRF[11],PRF[15],PRF[15]		$PRF[15] = \sum y_i^2 - 2 * m * \sum x_i y_i + m^2 * \sum x_i^2 - 2 * b * \sum y_i + 2 * m * b * \sum x_i + N * b^2$ high
82	MOV	CON[0],PRF[13]		DIV uses PRF[13] !!
83	ATT	PRF[7],CON[12]		$m <= 0 ?$
84	DIV	PRF[14],PRF[0]		Calculate variance (scale on N), DIV only changes Zero-Flag!!
85	BZS	mbz		
86	NOP			
87	NEG	PRF[7],PRF[10]		$PRF[10] = \text{abs}(m)$
88	CPI	PRF[10], 18		Max. relevant m = 17 (only 11 Bit cmp, no signextend)
89	BNC	End,		jJump to end if $m_i = 18$
90	BRA	mgn,		
91	mbz:	NOP		
92	CPI	PRF[7], 18		Maximum m (only 11 Bit, no signextend!)
93	BNC	End		Jump to end if $m_i = 18$
94	nop			
95	nop			
96	mgn,:_	DIE	PRF[14]	$PRF[14] = \text{Variance low}$ $PRF[15] = \text{Variance high}$
97	ATT	PRF[8],CON[12]		$b <= 0 ?$
98	BZS	bbz		
99	MOV	PRF[8],PRF[9]		
100	NEG	PRF[8],PRF[9]		
101	bbz:	CPI	PRF[9],191	$\text{abs}(b) <= 191 ?$
102	BNC	End		Jump to end if not
103	CPI	PRF[14],256		Test variance (11 Bit test!!)
104	BNC	End		
105	ADD	PRF[8],FIT[6],PRF[8]		Calculate "CHIP global" b
106	MUL	PRF[7],CON[8],PRF[13]		
107	ADD	PRF[13],PRF[8],PRF[8]		Projection on reference-plane - here we have PRF[0...8]: $N, \sum x_i, \sum y_i, \sum x_i^2, \sum y_i^2 LSW, \sum y_i^2 MSW, \sum x_i y_i, m, b$ $PRF[14]$ : Variance (only 16 Bit!) To Be Done: Data valid; Inform rest of the system
108	SPI	PRF[7],0x101		$\text{PIO}[0] = m$
109	SPI	PRF[8],0x102		$\text{PIO}[1] = b$
110	SPI	PRF[14],0x103		$\text{PIO}[2] = \text{Variance}$ (only low word is interesting)
111	MOV	CON[1],PRF[15]		
112	SPI	PRF[15],0x100		Inform Data valid!
113	stop:	bra	stop	
114	nop			TODO: Zero suppression
115	End,:_	BRA	End	
116	End:	NOP		Should be NOP!!
117	MOV	CON[0],PRF[15]		
118	SPI	PRF[15],0x100		Inform Data invalid! TODO: SPI end-programm, no data
119	BRA	Start		And return to the beginning
120	idle:	BRA	idle	
121		NOP		

### 6.3.4 Readout Scheme

The structure and the layout of the read out system of the 72000 MCMs is described in Chapter 7. From the trigger point of view it has to accomplish the transfer of the locally determined *tracklet* parameter to the central Global Tracking Unit (GTU) as fast as possible (see Fig. 6.1). The list of transferred bits per *tracklet* is given in Table 7.1.

### 6.3.5 Implementation of the Global Tracking Unit

All *tracklets* determined by the local tracking units are shipped to a global tracking unit for final trigger decision. This is implemented as a readout tree. The trigger data of a stack of six chambers are collected in the GTU. The GTU implements a Track-Matching-Unit (TMU) per phi sector. There will be no high  $p_t$  tracks traversing between sectors. Each TMU tries to find stiff tracks as shown in Fig. 6.31. This can be done logically by appropriate histogramming the projected tracklets. The GTU will be implemented in large scale FPGAs to guarantee a flexible and massive parallel implementation.

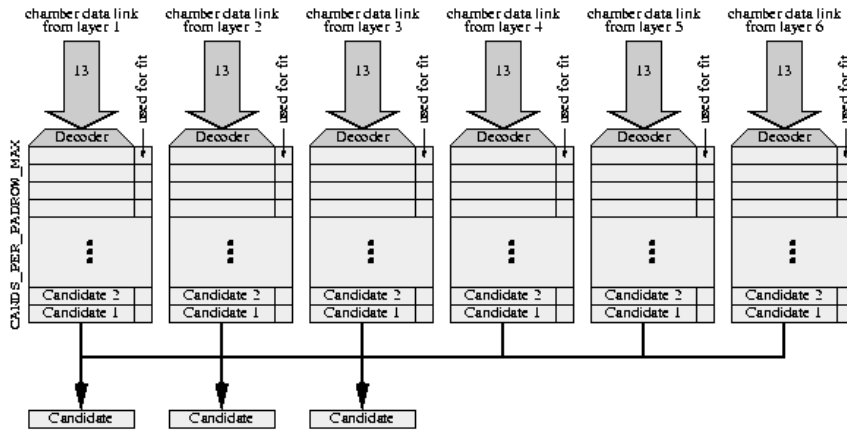


**Figure 6.16:** Implementation of the track matching units (TMU).

The structure shown in figure 6.16 takes into account that the data of the respective chambers arrive in a defined sequence and candidates of a track are in the same column. Therefore the processing can start as soon as the first *tracklets* arrive. All candidates of a column are stored in and accessed from a table. The number of candidates per column is fixed. The entries for chamber 1-4 are compared with all entries of all other tables. If an accumulation is found, these entries are marked, so that they cannot be used several times. It is sufficient to apply this method to only four of the six tables since a track must consist of at least three candidates. Therefore the resulting GTU architecture is a massively parallel, systolic FPGA processor performing as many as possible of such tracklet comparisons in parallel.

## 6.4 Simulation

The trigger concept relies heavily on the fact that a local *tracklet* search can be performed efficiently (step 1 of the trigger sequence shown in Section 6.2). The basic idea is to feed the data from consecutive time bins into pipeline ADCs and perform an online analysis of the digitized data in order to determine the inclination of the track segments with respect to the direction towards the nominal interaction vertex. All possible complications and distortions (as discussed in Chapters 5 and 11) like the  $E \times B$  effect in the electron drift, the pad response function of the readout chambers, the time response function of the signal generation mechanism and of the electronics, and the differential nonlinearities of the digitization process must be taken into account quantitatively. The first step is performed in the Local Tracking Units (LTU). Due to the massively parallel processing the number of units is very large ( $\approx 70000$ ) and therefore consuming most of the resources in material thickness, power and money. The number of independent channels must be optimized to obtain an acceptable signal to background ratio at affordable cost.

The modeling of the trigger response was done making use of the AliRoot environment. It allows for full event simulation employing different event generators and was used to study the occupancy, efficiency, and background performance of the envisioned trigger scheme. For a detailed description of the TRD simulation environment see Chapter 11.

**Table 6.5:** Parameter of the trigger simulation.

event generator	HIJING-param + signal electrons
multiplicity	varying: $400 < dN/dy < 8700$
digitization accuracy	10 Bit
number of time samples	15 - 30
signal pulse height for minimum ionizing tracks	channel 40 (for cluster)
Signal to Noise ratio	30
Time response function	ON (as in Fig. 11.8) / OFF
Pad response function	as in Fig. 11.9
magnetic field	0.4 T

The input parameters used for the trigger simulations are listed in Table 6.5. The main objective is to find out about the most crucial parameter for detecting and selecting high momentum electrons. The effect of three quantities was investigated systematically: the event multiplicity, the digitization clock rate (number of digits) and the pulse shaping. For the latter the standard scenario described in Chapter 5 and 11 was compared to an analysis incorporating a digital filter for tail cancellation (see section 6.4.2.1) and to an academic case, where the time response function was modeled by a  $\delta$ -function (TRF OFF).

To generate enough statistics for high  $p_t$  electron tracks, 200  $e^+$  and 200  $e^-$  tracks were added to a parametrisation of pions and kaons called HIJING-param (see Section 12.3) with the option *genbox* of AliRoot. The momentum distribution of the electrons was chosen to be flat in the range 3-5 GeV/c .

An example of the input transverse momentum distribution for an event multiplicity corresponding to  $< dN/dy > = 8500$  is shown in Fig. 6.17. Due to the added signal electrons, the effective multiplicity density for the trigger simulation is  $< dN/dy > = 8700$ . It should be noted again, that there is a large uncertainty about the spectral shape of the hadrons, in particular the power-law hard scattering component (see Chapter 12). The HIJING parametrisation used represents the worst case scenario. To map out the multiplicity dependence of the tracking performance the total number of primary particles emitted into the polar angle range of  $35^\circ < \theta < 145^\circ$  was varied with the spectral shape in transverse direction kept as shown in Fig. 6.17.

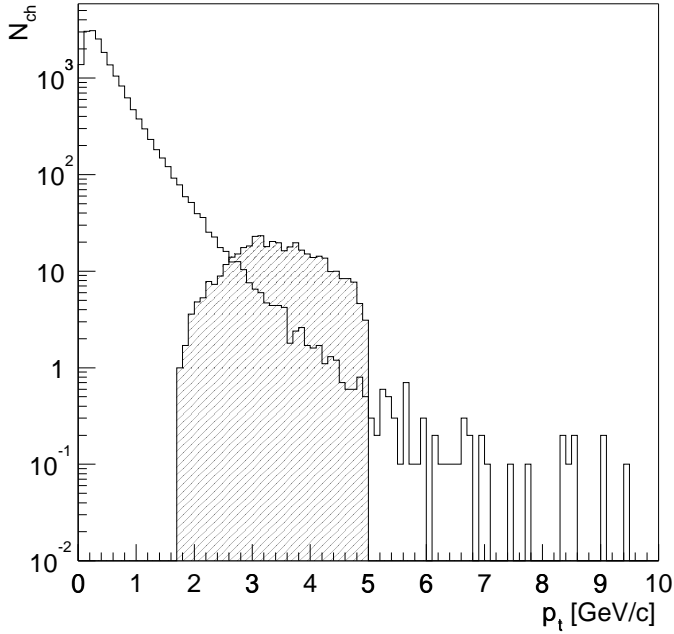


**Figure 6.17:** Transverse momentum distribution used as input to the trigger simulations. The hatched distribution corresponds to electrons that were added to the HIJING-param particle mix.

#### 6.4.1 Local tracklet search

The task to be performed is visualized in Figs. 6.18 and 6.19. In Fig. 6.18 the basic quantities of the local *tracklet* search are defined. In Fig. 6.19 the digitized pulse height is shown within one pad row of one of the readout chambers of the TRD (at a polar angle of  $\theta = 85^\circ$ ). For each time bin the pulse height is obtained after the drift of the primary electrons under the influence of the electric and magnetic field, taking into account diffusion and including transition radiation contributions. As indicated in Fig. 6.18 the position of the clusters is systematically shifted as function of the drift time due to the presence of the magnetic field. The task of the trigger system is to recognize with high efficiency stiff tracks ( $p_t \geq 3 \text{ GeV}/c$ ) despite the shift due to the Lorentz angle  $\Psi_L$ . The characteristics of the interesting tracks is their small deviation from the infinite momentum limit, i.e. they have only a small angular deflection with respect to the reference line that can be constructed by connecting the point of impact with the nominal interaction vertex. As indicated in Fig. 6.18 the stiff tracks of interest occupy with the centroids of their clusters at most two neighboring pads. Charge sharing due to the pad response function distributes the signal consequently to at most 4 neighboring pads. Therefore the trigger is based on the analysis of 3 neighboring pads. For each time bin a position in pad direction (corresponding to the  $y$ -direction in the following) is determined according to the inverse pad response function that can be parameterized in a look-up table. The resulting  $y$ -positions as function of the time coordinate  $t_{drift}$  or drift distance  $s_{drift}$  are fitted by a straight line

$$y = a_0 + a_1 \cdot v_{drift} \cdot t_{drift} = a_0 + a_1 \cdot s_{drift}.$$

The fit parameters can be corrected for the effect of the Lorentz angle by the following expressions

$$a_0^{corr} = a_0 + \tan \Psi_L \cdot s_{max},$$

$$a_1^{corr} = a_1 + \tan \Psi_L.$$

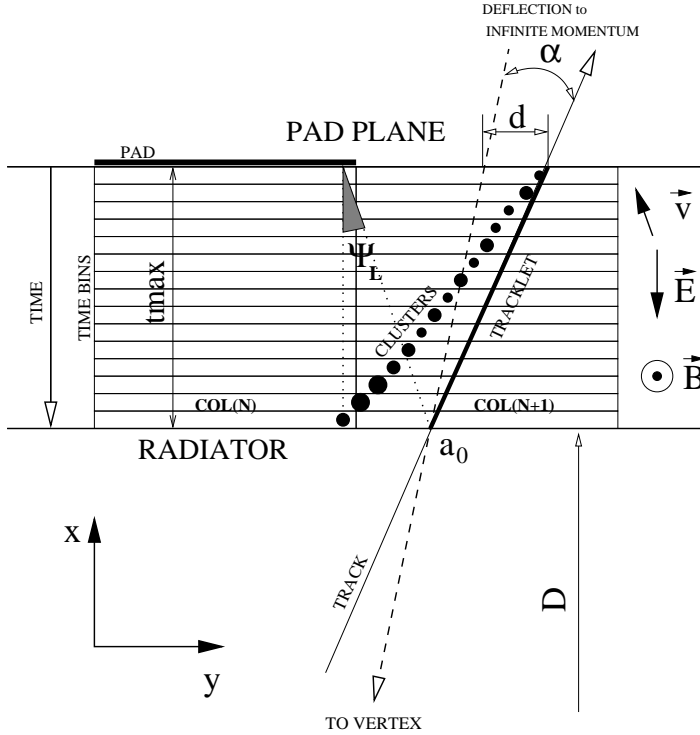


**Figure 6.18:** Local tracklet quantities

The linear deflection  $d$  (shown in Fig. 6.18) over the depth  $s_{max}$  of the drift region of a single chamber is given by

$$d = (a_1^{corr} - \frac{a_0}{D}) \cdot s_{max},$$

with  $s_{max} = 3$  cm.  $D$  is the radial distance of the front surface of the readout chamber to the interaction vertex.

The angular deflection  $\alpha$  is given by the expression

$$\alpha = \arctan \frac{a_1^{corr} - \frac{a_0^{corr}}{D}}{1 + \frac{a_1^{corr} \cdot a_0^{corr}}{D}} \approx \arctan(a_1^{corr} - \frac{a_0^{corr}}{D}).$$

Since for the tracks of interest the slope parameters are small, the second term in the denominator can be neglected (for  $p_t = 3$  GeV/c :  $|\frac{a_1^{corr} \cdot a_0^{corr}}{D}| < 0.015$  ).

For particles originating from the interaction vertex the deflection is related to the momentum by

$$p_t^{rec} = 0.3 \cdot B \cdot 0.01 \cdot \frac{\sqrt{(a_0^{corr})^2 + D^2}}{2 \cdot d / s_{max}} = 0.3 \cdot B \cdot 0.01 \cdot \frac{\sqrt{(a_0^{corr})^2 + D^2}}{2 \cdot \sin \alpha},$$

where all the spatial quantities are given in cm, the magnetic field  $B$  is expressed in Tesla and the reconstructed momentum is in GeV/c .

For a magnetic field of  $B = 0.4$  T the deflection of a charged particle with a transverse momentum of 3 GeV/c over the drift range of one TRD chamber amounts to  $\alpha = 3.3^\circ$  or  $d = 1.7$  mm. The linear deflection is well below the pad width of 8 mm. The trigger concept will stay valid as long as the centroids of from stiff tracks stay within a region of 3 neighboring pads, i.e.  $d_{max} = 1.6$  cm or  $\alpha_{max} = 28^\circ$ . The total inclination angle of the measured track has contributions from the transverse momentum ( $\alpha_{max}^{p_t} = 3.3^\circ$  ),

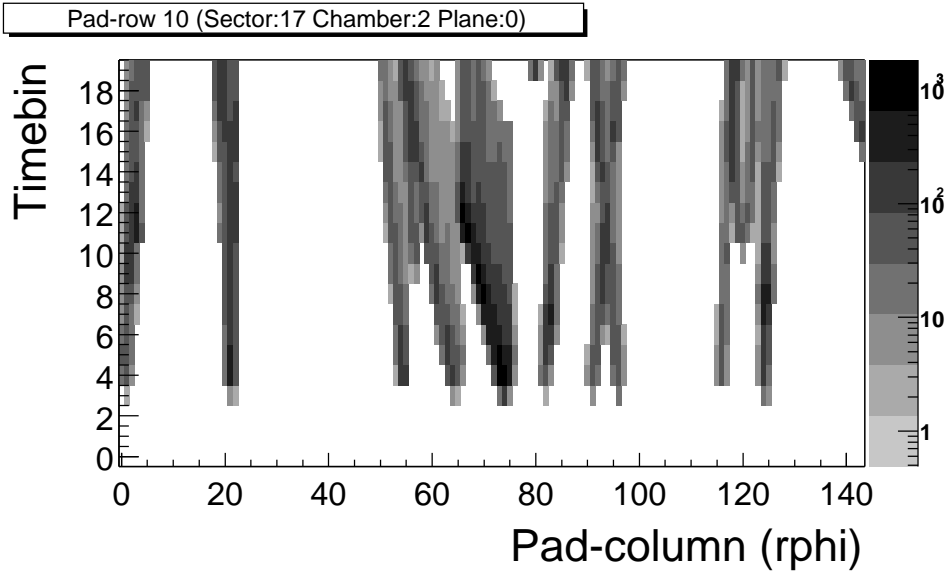


**Figure 6.19:** Local tracklet event display. The contour histogram shows a typical input distribution for the local tracking, i.e. the ADC contents for one pad row versus time for a full multiplicity event. 5 time bins are added before the 15 time bins sampling the drift range of the readout chamber.

the angle of incidence due to the flat surface of the chambers ( $\alpha_{max}^{geo} = 10^\circ$ ) and from the Lorentz angle  $\Psi_L$ . The maximum allowed Lorentz angle is therefore limited to  $\Psi_L = \alpha_{max} - \alpha_{max}^{p_t} - \alpha_{max}^{geo} = 14.7^\circ$ . The Lorentz angle of the default gas mixture Xe,CO<sub>2</sub> (15%),  $\Psi_L=8^\circ$ , is well within the operational limits of the TRD trigger.

#### 6.4.2 Local tracking performance

In order to achieve a sufficient resolution, the pulse height of minimum ionizing tracks has to reach a certain minimum as compared to noise and digitization errors (see Section 5.1). Due to the non-Gaussian features of the pad response function (Fig. 11.9) the most general method to calculate the position from pulse heights is realized by a look-up table (LUT). With the signal and signal to background ratio listed in Table 6.5 position resolutions of better than  $\sigma_y = 400\mu\text{m}$  are obtained for stiff tracks (Figs. 11.12 and 11.13) and if the incidence angle is small the values are of order  $200\mu\text{m}$  (Fig. 11.14). Therefore the achievable position resolution should allow to select *tracklets* with deflections of low as  $d=1\text{mm}$  ( $\alpha = 2^\circ$ ).

Before discussing the performance of the local tracking concept in terms of efficiency and output rate, two important configurable steps will be described in the following sections: the application of a digital filter (Section 6.4.2.1) to the preamplifier/shaper (PASA) signal and the cluster quality selection (Section 6.4.2.3).

##### 6.4.2.1 Digital cancellation of the tail in PASA signal

The ion tail of the signal as shown in Fig. 11.8 can be parameterized by the functional form  $1/(1+t/t_0)$ . Such a tail can be reduced by passing the pulse through a filter (pole/zero network). The procedure is described in [7] and consists of approximating the above expression by a sum of three exponentials and adjusting the constants of the filter (resistors and capacitances in analog circuitry) such that one of them is canceled out. It has been shown [8] that a tail cancellation of equal quality can be performed on the digital signal. In order to benefit from the improvements, a scenario is considered where the functionality of the tail cancellation is included in the LTU. If it were not for the trigger performance this tail cancellation could also be performed offline.

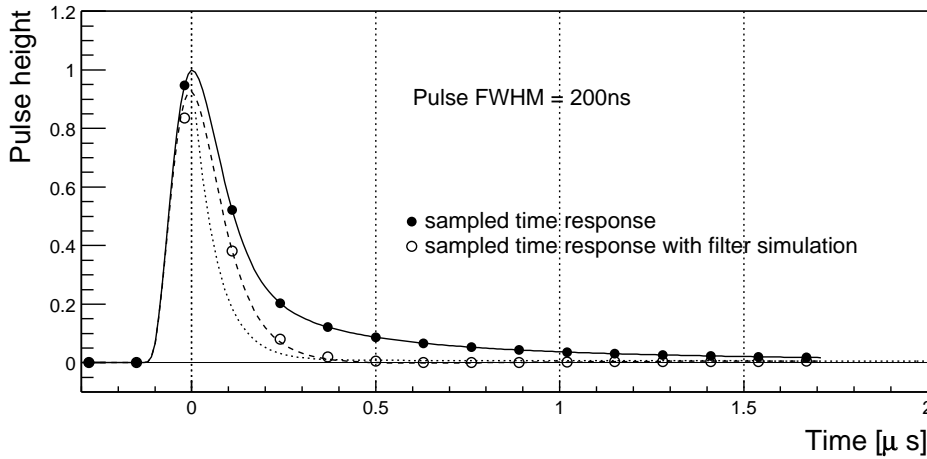


**Figure 6.20:** PASA signal and tail cancellation corresponding to a one pole/zero network. The solid line (filled circles) represents the input distribution (see Fig. 11.8), the dashed line (open circles) shows the response of a one pole/zero filter, the dotted curve depicts a perfect filter behavior.

In the online tracking the tail cancellation is used as an option to analyze the performance of such additional signal processing. It is implemented as a feature of the LTU algorithm in the AliRoot environment. The 15 time samples within one pad column are “filtered” using the transfer function of the pole/zero network with values calculated from [7] and adjusted to get best results. This simulates a digital implementation, superior in performance to an RC filter.

In the simulation of the Time Response Function, the PASA signal is numerically given in steps of 10 ns (the solid line in Fig. 6.20). The sampling done in 15 time bins, corresponding to 133 ns spacing, is shown in Fig. 6.20 by the closed symbols. The effect of the tail cancellation with a single pole/zero network is shown by the dashed line and the open symbols. The dotted line shows the expected tail cancellation according to the theory in [7]. With the parameters chosen and implemented in the following, the time response is almost Gaussian and extends to a maximum of 350 ns.

#### 6.4.2.2 Occupancy

The most demanding requirement for the TRD trigger is defined by the multiplicity of the Pb-Pb collisions. The trigger concept should stay valid up to occupancies of 35% as shown in Fig. 6.21 that are expected for a rapidity density of  $dN/dy = 8700$ . The occupancy is evaluated with the current pad geometry described in Section 4.4 for events (generated with the event generator *HJING-param* as described above) of different multiplicities. The occupancy for the standard scenario (i.e. 15 time bins, time response function ON, RMS width of the electronic noise equals 1 ADC channel, as described in more detail in Section 11) is given in Fig. 11.11. There as well as in Fig. 6.21 a pixel is called occupied once the pulse height exceeds the ADC channel 2. In order to save computational time the primary distributions were generated in a restricted range of polar angles ( $35^\circ < \theta < 145^\circ$ ) leading to a reduction of the occupancy by about 14% with respect to the full calculation (solid circle as compared to the solid square at  $dN/dy = 8700$ ). In Fig. 6.21 the average occupancy is shown as function of the event multiplicity for various additional scenarios: the influence of part of the structural material was studied by replacing the tracking medium of the space frame with air (“NO frame”, open symbols). The effect of the time response function was analyzed by turning it off (“TRF off (15tb)”, filled triangle up), i.e. by replacing it with a  $\delta$ -function. The sampling frequency was additionally increased (“TRF off (30tb)”, filled triangle down) from 15 to 30 time bins. As can be seen from Fig. 6.21 a major source of the occupancy at fixed multiplicity is the time response of the chamber/electronics that amounts to about 25% of the observed

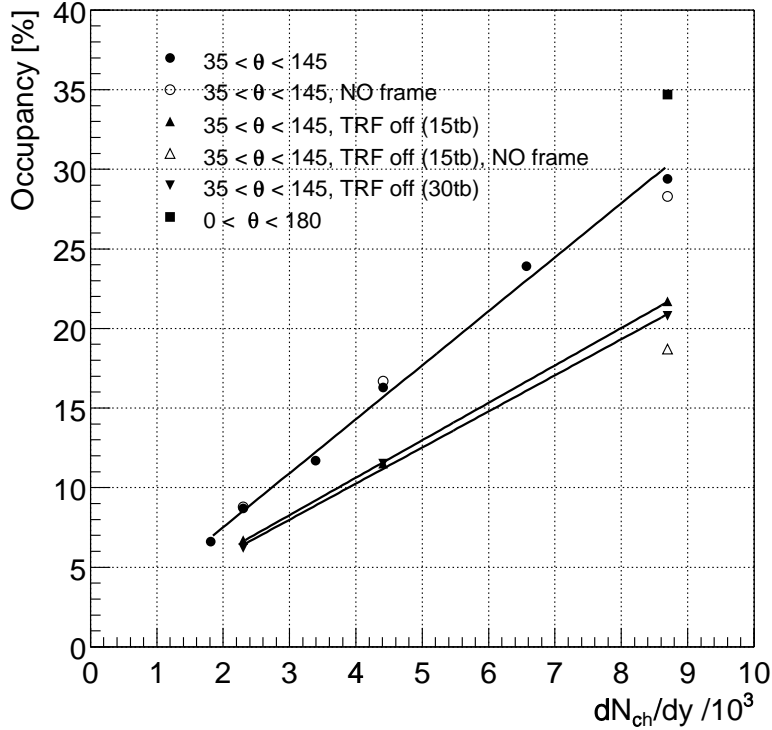


**Figure 6.21:** Occupancy of the TRD detector as function of multiplicity.

occupancy due to the long tails (see also Fig. 6.19). The space frame material as well as the sampling frequency have no strong influence on the occupancy.

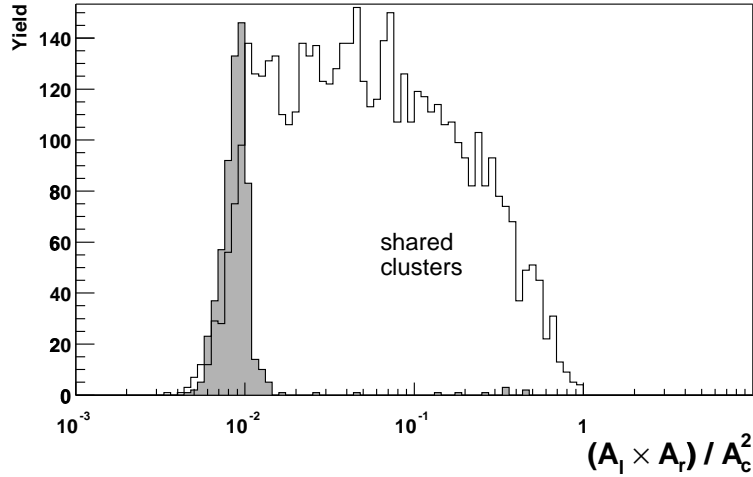


**Figure 6.22:** Distribution of the measure of cluster quality built from amplitude ratios ( $A_l \times A_r / A_c^2$ , as explained in the text) for stiff *tracklets* ( $p_t > 1 \text{ GeV}/c$ ) in full multiplicity events ( $\langle dN/dy \rangle = 8700$ ). The grey shaded distribution is obtained for clean clusters, the solid line histogram represents clusters with contributions from more than one track (shared clusters).

#### 6.4.2.3 Cluster quality selection

In order to achieve the best resolution (as shown below in Fig. 6.25) one has to avoid as much as possible distortion of the information by overlapping tracks (pile-up). It is therefore mandatory to inspect all contributing clusters for pile-up. This can be done by comparing the amplitude ratios of adjacent pads with the expectations for a single hit from the pad response function. The distribution of a simple measure of cluster quality, the product of the amplitudes of the side pads ( $A_L, A_r$ ) normalized to the square of the amplitude of the central pad  $A_c$ , is shown in Fig. 6.22 for two cluster classes. The samples are defined with the information available within the simulation program, namely with the knowledge which tracks contributed to which cluster. The first sample (grey shaded histogram) corresponds to clean clusters, i.e. those that are generated from a single particle. The second class called shared clusters (solid line) originates from overlapping tracks. The clear difference visible in Fig. 6.22 means that a cut can be applied in the ONLINE processing, requesting an upper limit in the cluster quality. This requirement removes to a large extent clusters that otherwise would spoil the parameters of the straight line fit.

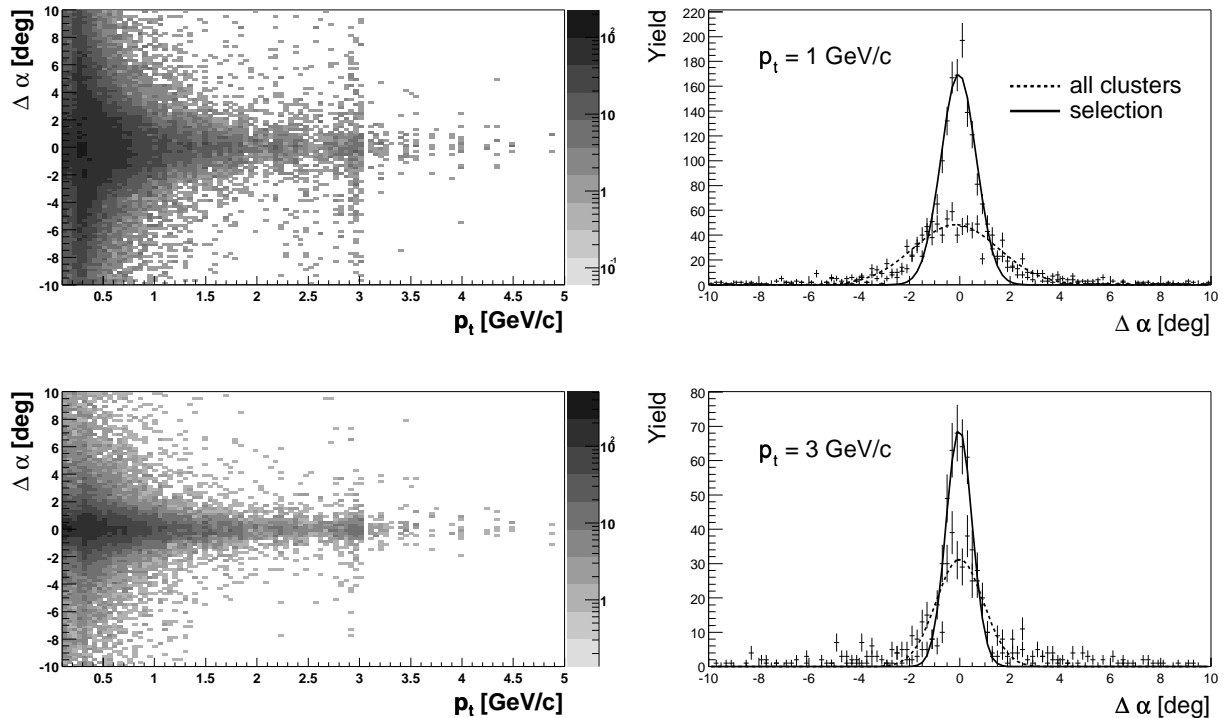


**Figure 6.23:** Local deflection angle resolution for *tracklets* with (left top) and without (left bottom) cluster quality check as function of the transverse momentum. On the right hand side, projections of the 2-dimensional distributions are show for a transverse momentum of  $p_t = 1 \text{ GeV}/c$  (right top) and  $p_t = 3 \text{ GeV}/c$  (right bottom). Solid (dotted) histograms represent the results with (without) cluster quality selection.

The effect of applying a selection cut for good quality clusters ( $A_L \cdot A_r / A_c^2 < 0.0136$ ) is visualized in Fig. 6.23 where the *tracklet* quality as defined by the deviation of the deflection angle  $\Delta\alpha = \alpha_{\text{tracklet}} - \alpha_{\text{track}}$  is shown with and without the cluster quality selection step for multiplicities corresponding to  $\langle dN/dy \rangle = 8700$ . The difference of the expected track deflection to the reconstructed one is plotted versus the transverse momentum of the particle. The figure is done for those *tracklets* that have contributions from only one single particle (called clean *tracklets* in the following). The tails in the distribution are substantially reduced for all transverse momenta. The cluster cleaning improves the local *tracklet* momentum resolution by about a factor of 2 for transverse momenta in the range 1 - 3  $\text{GeV}/c$ , i.e. the RMS width of the  $\Delta\alpha$ -distribution changes from  $1.7^\circ$  ( $0.9^\circ$ ) to  $0.7^\circ$  ( $0.5^\circ$ ) for 1  $\text{GeV}/c$  (3  $\text{GeV}/c$ ),

respectively. It should be noted that the cluster quality selection is not limited to the simple measure displayed in Fig. 6.22 but can be parameterized in a general way also for non-Gaussian pad response functions in a look-up table. As described in Section 6.3.2 this selection step can be implemented in the *tracklet* reconstruction hardware.

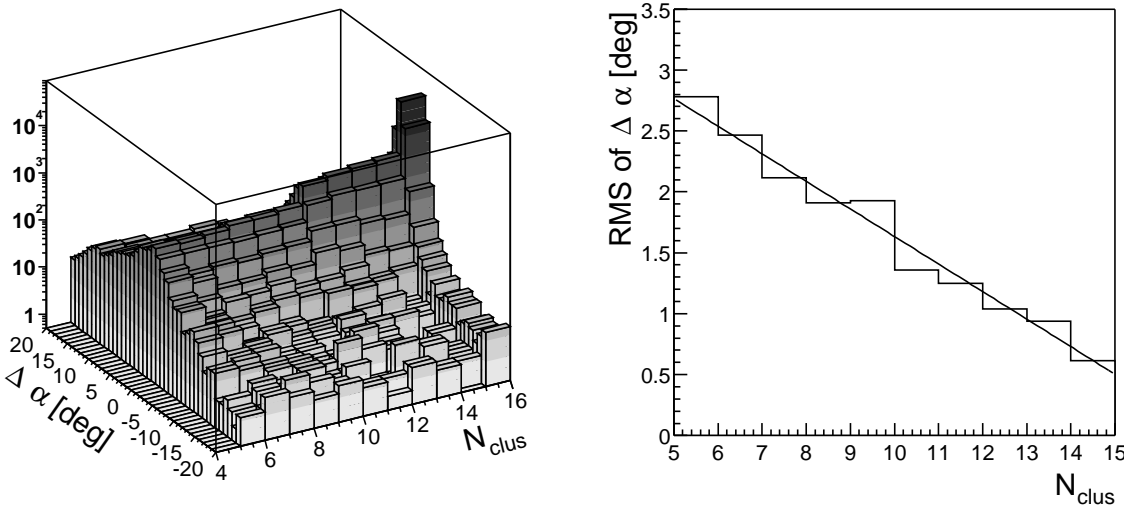


**Figure 6.24:** Local deflection angle resolution for high  $p_t$  clean *tracklets* as function of the number of clusters (left). The right panel shows the RMS width of the difference of the measured deflection angle to the expected angle as function of number of clean clusters contributing to the *tracklet*.

Changes of the *tracklet* resolution with event multiplicity can be expected in terms of a reduced number of clusters that are contributing to a *tracklet*. For a larger multiplicity environment fewer clean clusters passing the cluster quality selection will be found. The effect is shown in Fig. 6.24 where the resolution of the deflection angle with respect to that expected is shown for clean *tracklets* as function of the number of contributing clusters. On the right hand side the corresponding RMS width is given as function of the number of clusters. It is obvious that the width of the deflection is increasing with decreasing cluster number. In order to maintain a sufficient accuracy the number of clusters should not decrease too much. Reasons for losses of clusters within the online algorithm are

- tracks crossing pad rows,
- tracks crossing more than 3 pads in y-direction,
- pile-up.

When a track crosses pad rows (in  $z$ -direction) the *tracklet* is split into 2 halves. The number of clusters is reduced until 2 *tracklets* are generated in the symmetric case with one half of the original cluster number. As can be seen from Fig. 6.24 the resolution of these *tracklets* is worse by about a factor of 2 - 3 compared to the best cases. This has to be taken into account when trying to match the local *tracklets* in the global tracking step. The quality of the individual *tracklets* is still good enough that no attempt was made to merge them in the LTU. Therefore no communication of processors working on different pad rows is foreseen (see Chapter 5).

#### 6.4.2.4 Local momentum resolution

The position resolution and the distortions due to the TRF and the pile-up define how well a *tracklet* can be measured within a single layer of the TRD detector. Fig. 6.25 presents the deflection angle  $\alpha$

as obtained from a linear regression analysis of the clusters within 3 neighboring pads as described in Section 6.3.2. This selection of clean *tracklets* allows to plot the reconstructed deflection angle  $\alpha$  versus the momentum of the particle that generated the tracklet. Note that the momentum is taken from the production vertex of each particle.

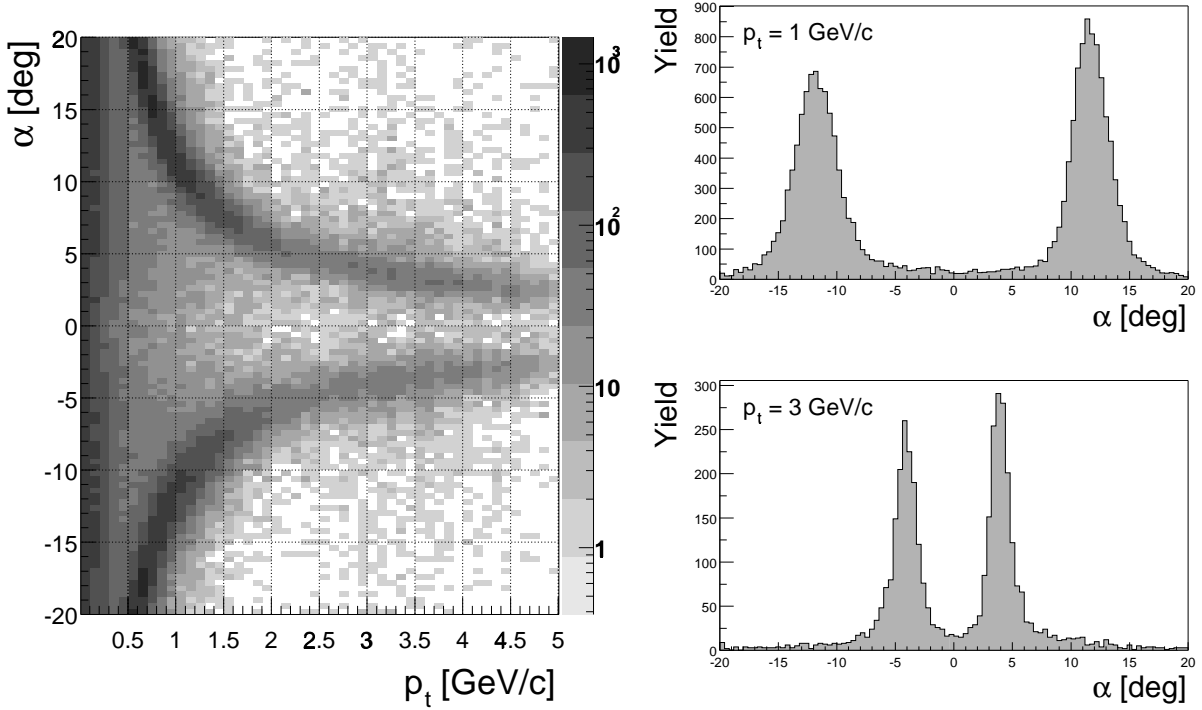


**Figure 6.25:** Tracklet deflection angle for clean tracklets as function of the transverse momentum (left). On the right hand side two projections are shown for transverse momenta of  $p_t = 1$  (top) and 3 (bottom) GeV/c .

Fig. 6.25 makes use of the tail cancellation method described in Section 6.4.2.1 and the cluster quality selection described in Section 6.4.2.3. Under those conditions the position resolution for clean *tracklets* is clearly sufficient to select tracks of about 3 GeV/c with good efficiency and high discrimination power against low momentum *tracklets* , e.g. by requesting a deflection angle of  $\alpha < 6^\circ$ .

It is, however, apparent from Fig. 6.25 that, besides background due to energy loss and elastic scattering that widen the branches around the expected deflection angles, there is a strong component originating from low momentum particles. Low momentum particles originating from conversions and interactions are producing *tracklets* with an almost uniform deflection angle distribution.

With the cluster quality selection defined above the local transverse momentum resolution of the online method is shown in Fig. 6.26. Large differences are observed between the different scenarios. The resolution obtained with the standard scenario is worse by about a factor of 2 - 3 with respect to the academic case, where the TRF is modeled by a  $\delta$ -function. Applying a digital filter recovers the resolution at low momenta and substantially improves the situation for high transverse momenta. For transverse momenta of  $p_t = 3$  GeV/c a resolution of  $\sigma(p_t)/p_t = 20\%$  is obtained.

#### 6.4.2.5 Local Tracking Efficiency

The efficiency of the trigger system can be decomposed into two steps, the track finding efficiency and the track selection efficiency. Track finding is achieved by asking for a certain number of clusters contributing within three neighboring pads. Track selection requires a certain number and quality of contributing clusters resulting in a sufficient quality of the fit parameter.

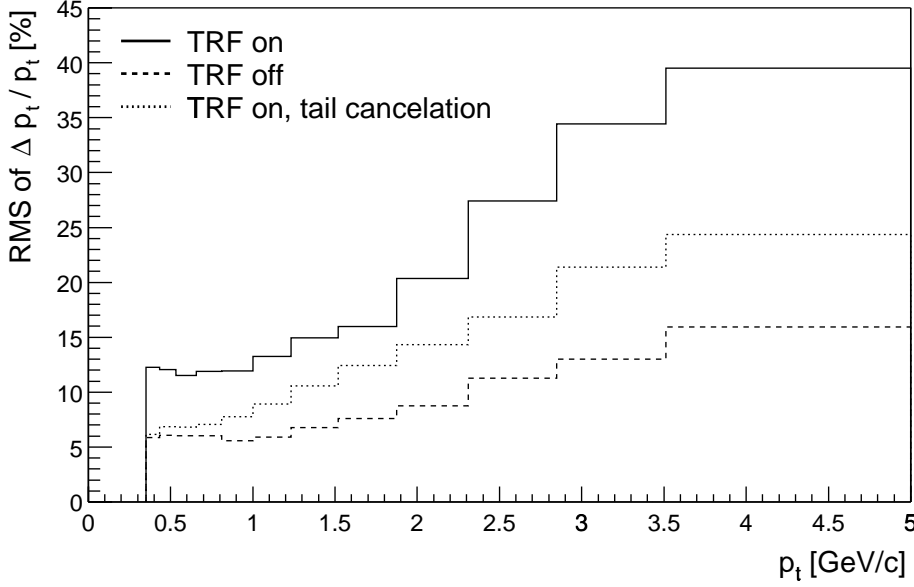


**Figure 6.26:** Local momentum resolution for clean *tracklets* as a function of the primary transverse momentum for an event multiplicity of  $\langle dN/dy \rangle = 8700$ . The different line styles correspond to different scenarios: TRF on (solid), TRF off (dashed) and employing a digital tail cancellation (dotted).

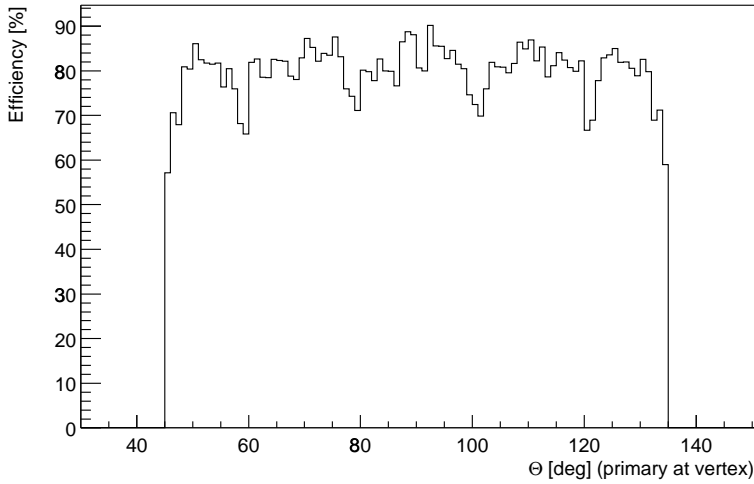


**Figure 6.27:** Tracklet efficiency for stiff tracks ( $p_t > 1\text{GeV}/c$ ) as a function of the polar angle. The minimum number of clusters required for a *tracklet* is 5.

### Polar angle dependence of local track finding efficiency

As indicated above, due to the chamber and pad geometry and the range in track topologies the tracks will not always stay within one pad row. Especially at forward/backward angles, a substantial number will be split into two pieces. It was analyzed to which extent the efficiency of the *tracklet* finding algorithm suffers due to this. The average number of clusters per *tracklet* as function of the polar angle is found to be constant, and the variation of the *tracklet* length with polar angle is rather weak. The dependence of the track finding efficiency (displayed in Fig. 6.27) is even weaker since *tracklets* are accepted if the contributing number of cluster is above a certain minimum value ( $N_{cluster}^{min} = 5$  in the

specific case). The polar angle coverage of the online tracking scheme is rather uniform except for the dips visible in Fig. 6.27 at polar angles of  $60^\circ$ ,  $80^\circ$ ,  $100^\circ$  and  $120^\circ$ , corresponding to the chamber boundaries.

### Local selection efficiency

The influence of selecting *tracklets* with deflections corresponding to different momenta is presented in Fig. 6.28. The efficiency is defined as number of *tracklets* originating from particles from the primary vertex that were found with a deflection angle smaller than the cut value, normalized to the total number of primary particles with according momenta emitted into the solid angle of the TRD. The efficiency is evaluated as function of the transverse momentum taken from the primary vertex (referred to as primary transverse momentum in the following).

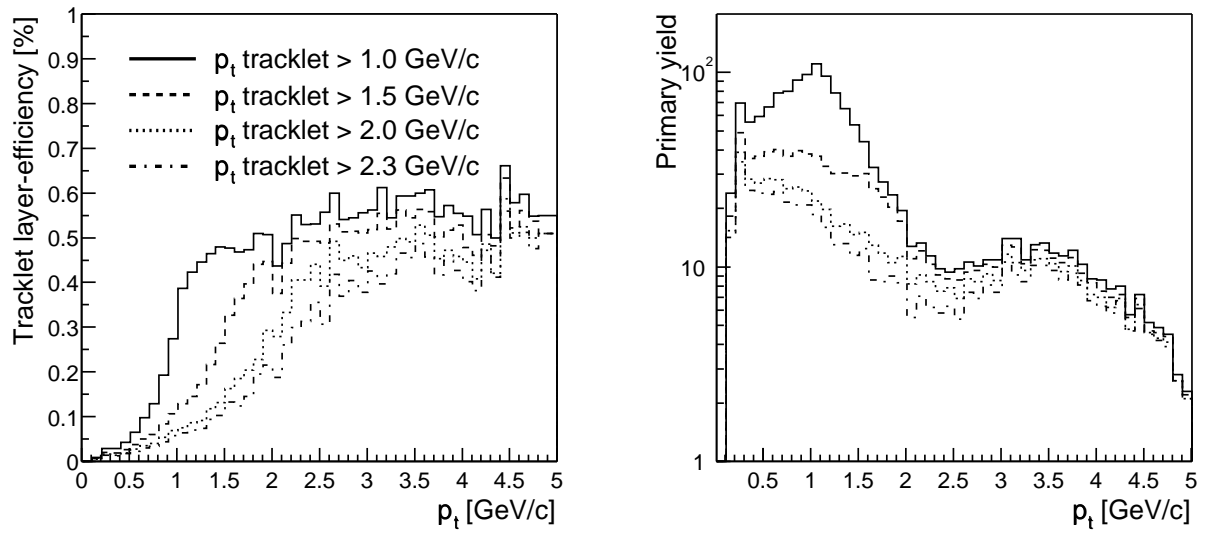


**Figure 6.28:** Online *tracklet* selection efficiency as function of transverse momentum. The histograms show the efficiency (left panel) and the total accepted number of primary *tracklets* (right panel) under various deflection cuts corresponding to transverse momenta of 1, 1.5, 2 and 2.3 GeV/c for full multiplicity events at a magnetic field of  $B = 0.4$  T.

The efficiency curves show a typical threshold behavior. By decreasing the cut value (i.e. increasing the lower momentum limit) the threshold is smeared out and the plateau efficiency at large momenta decreases slightly. The effect of the selection on the measured spectra is shown in the right panel of Fig. 6.28. A substantial decrease in total number of *tracklets* is achieved by employing a larger transverse momentum threshold. Note that the peak in the spectra at  $p_t \approx 3.5$  GeV/c stems from the additional electrons of the input distribution. The threshold needs to be optimized since there is a balance between the total number dominated by low transverse momentum *tracklets* that should be minimized and the local tracking efficiency at large transverse momentum that should be maximized. The total number of found *tracklets* should be minimized since accepting more low momentum *tracklets* will increase the occupancy at the global matching stage and present higher demands to the readout bandwidth of the trigger system.

### Quality dependence of local tracking efficiency

Another effect of the cluster quality and the resulting *tracklet* quality is shown in Fig. 6.29 where the influence of the TRF is demonstrated. With the better cluster quality available by the undistorted signal

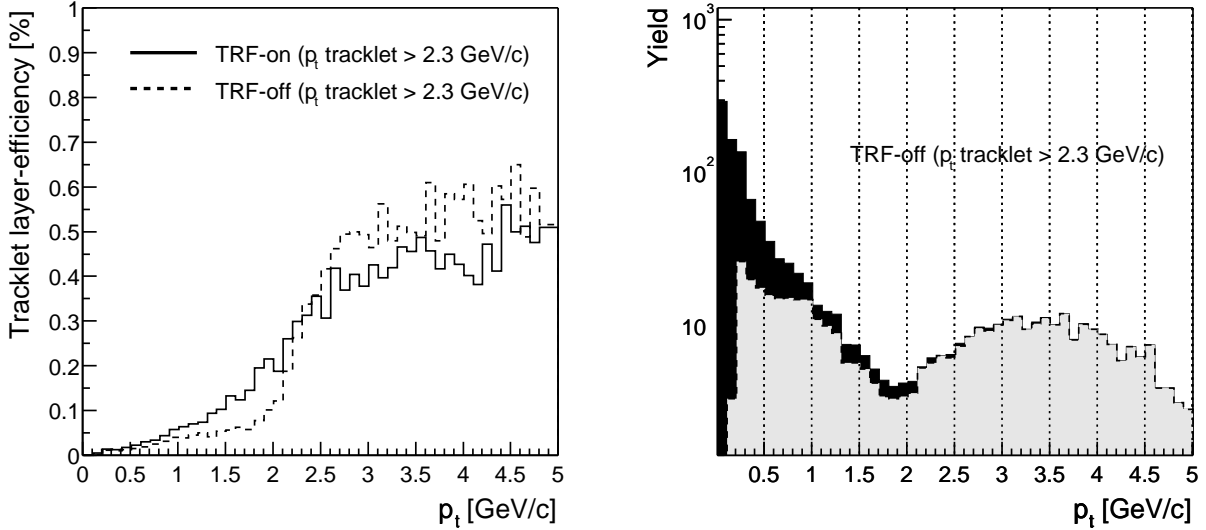


**Figure 6.29:** Same as Fig. 6.28 with a selection cut of  $2.3 \text{ GeV}/c$  with and without the time response function (left). The right panel shows the spectral shape of the selected tracklets: the black histogram corresponds to the total numbers, of which the grey portion represents the contribution of tracklets originating from tracks from the primary vertex.

shape, the threshold is much sharper and the yield of low momentum particles below the threshold of  $p_t = 2 \text{ GeV}/c$  is reduced by about a factor of 1.6. In both scenarios a plateau in the efficiency is reached at the target momentum of  $p_t = 3 \text{ GeV}/c$ . The plateau values of the efficiency differ by about 5%. On the right panel of Fig. 6.29 the spectral shape of the selected tracklets is shown for the 'TRF off' case. It is evident that even under the favorable conditions of good resolution, the total number of found tracklets is dominated by tracklets originating from low momentum particles. Although the overall number of found tracks does not differ significantly from the case with the time response function turned on, the better definition of the high momentum threshold for true tracks from the primary vertex is again an argument in favor of applying deconvolution schemes to the pulse shapes trying to remove the influence of the tail.

#### 6.4.2.6 Multiplicities from local tracking units

The load of the TRD chambers in terms of found *tracklets* is studied in Fig. 6.30. This is relevant in order to determine the necessary bandwidth within the trigger system from the local processors to the global tracking/matching unit. The largest local threshold momentum, for which the plateau efficiency is reached at  $p_t = 3 \text{ GeV}/c$ , was determined to be  $p_t^{threshold} = 2.3 \text{ GeV}/c$  as demonstrated in Figs. 6.28 and 6.29. The number of *tracklets* found per readout chamber with a cut corresponding to  $p_t = 2.3 \text{ GeV}/c$  is shown in the left panel for different event multiplicities. The distributions are Gaussian shaped and can be quantified by a mean and a width. In order to define the requirement of the transmission bandwidth, the mean and the maximum number of *tracklets* per chamber are plotted on the right panel of the figure as function of the event multiplicity.

Since the shipping of the data from all the different TRD chambers to the GTU is done in parallel, the chamber with the largest number of *tracklets* determines the dead time. Therefore a minimal requirement for the design of the readout scheme can be derived: the trigger hardware has to have a bandwidth for about 40 *tracklet* per chamber (maximum value for a full multiplicity event with a selection threshold of  $2 \text{ GeV}/c$ ).

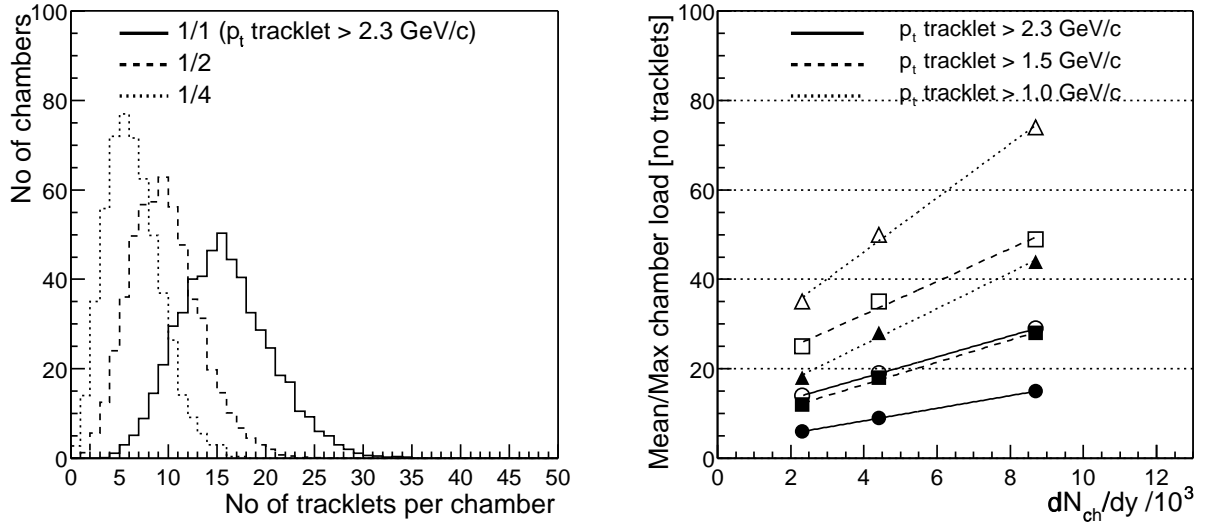


**Figure 6.30:** Chamber load. The distribution of the number of found *tracklets* per readout chamber for various event multiplicities is shown in the left panel. The multiplicity dependence of the mean (solid symbols) and the maximum (mean+3 $\sigma$  level, open symbols) *tracklet* number is given in the right diagram for various selection thresholds.

#### 6.4.3 Tracklet Matching - Global Tracking Unit

All track candidates of the individual layers consisting of position, angle, amplitude, quality etc., are projected to a (virtual) middle plane by computing the proper azimuthal angle of intercept, the longitudinal  $z$ -position and the deflection angle  $\alpha$ . This transformation can be done already within the LTU, practically without any additional time. The principal concept of the global tracking units is sketched in Fig. 6.31.

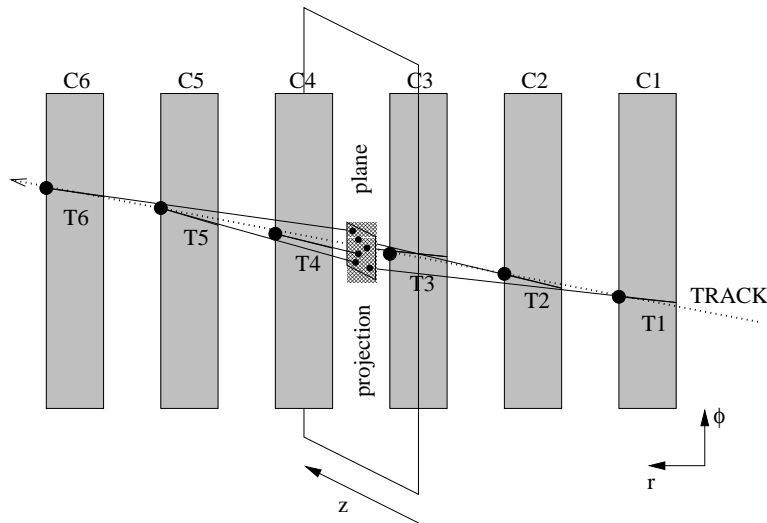


**Figure 6.31:** Global tracking concept

The basic task is to count the number of *tracklets* within certain regions. This can be achieved most conveniently by a global histogram, where the three matching quantities (azimuthal angle  $\phi$ ,  $z$ -coordinate and deflection angle  $\alpha$ ) are recorded. The granularity of the global matching histogram needs to be adjusted to the extrapolation uncertainty caused by the resolution of the *tracklet* parameters obtained and the occupancy of the global histogram. For a good performance a high  $p_t$ -cut from the single layers helps to reduce the occupancy. As shown in Fig. 6.30 under the condition of a relatively high local momentum cut of 2 GeV/c on average 20 *tracklets* are shipped to the GTU, i.e. the histogram has 8100 entries per central event.

To achieve a sufficient global tracking efficiency and a sufficient electron-pion separation 3 out of possibly 6 *tracklets* are required for the definition of a good primary track. With a single layer tracking efficiency in the order of  $\epsilon(p_t > 3 \text{ GeV}/c) \approx 0.5$ , the expected global tracking efficiency can be evaluated to

$$p_{\text{global}} = \sum_{i=3}^6 \frac{6!}{i!(6-i)!} p_{\text{local}}^i (1 - p_{\text{local}})^{(6-i)} = 0.66$$

provided that all the inspection widths of the global histogram extend to  $3\sigma$  in the  $\phi$ ,  $z$  and  $\alpha$  direction. To achieve a global tracking efficiency of 90% local tracking efficiencies in the order of 67% would have to be realized.

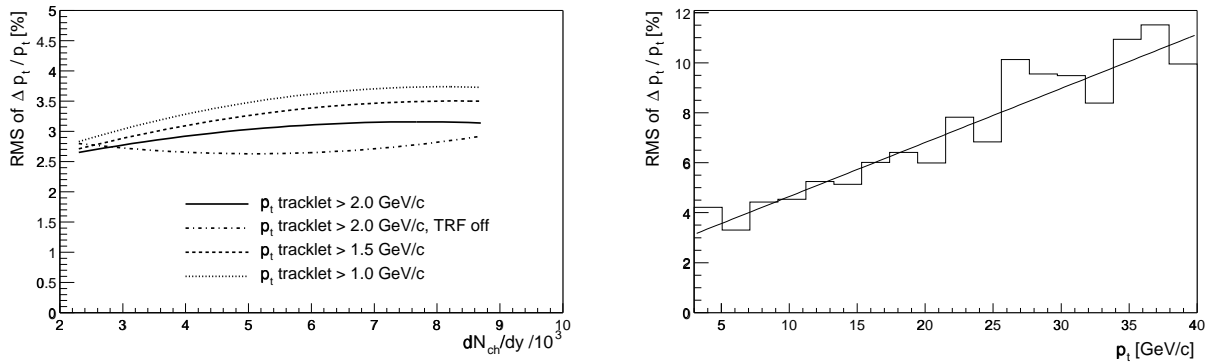


**Figure 6.32:** Momentum resolution of online globally reconstructed tracks. The left panel displays the global relative momentum resolution  $\sigma(p_t)/p_t$  for tracks with primary transverse momenta of  $p_t = 3 \text{ GeV}/c$  as function of multiplicity for various local transverse momentum selection thresholds. On the right panel the transverse momentum dependence of the global momentum resolution is shown for full multiplicity conditions of  $\langle dN/dy \rangle = 8700$ .

The important role of the GTU is i) to define a sharp transverse momentum threshold close to  $3 \text{ GeV}/c$ , ii) to select stiff tracks of electrons (positrons) and iii) to calculate invariant masses or find jets. The global transverse momentum is calculated with the same formalism like the local transverse momentum by evaluating the global deflection angle with respect to the nominal primary vertex direction. The global momentum resolution as function of  $p_t$  is shown in Fig. 6.32. With a common set of parameters like in Table 6.6 the momentum resolution for tracks originating from the primary vertex is found to be rather independent of the event multiplicity (occupancy) and the local momentum selection threshold. Typical values are  $\sigma(p_t)/p_t = 3 - 4 \%$  for transverse momenta of  $p_t = 3 - 4 \text{ GeV}/c$ . Due to the longer lever arm for determining the transverse momentum, this resolution does not depend significantly on the local resolution (as shown by the "TRF-off" calculation in Fig. 6.32). With matching widths as chosen in Table 6.6 the distortions due to chance coincidences in the GTU matching histogram are rather weak even under the worst case condition of the full multiplicity of  $\langle dN/dy \rangle = 8700$ . In summary, keeping a distance of  $3\sigma$  to the target transverse momentum a threshold of  $p_t > 2.7 \text{ GeV}/c$  can be implemented in order to select primary tracks with a transverse momentum of  $p_t > 3 \text{ GeV}/c$ . Note that electrons experience significant momentum losses due to bremsstrahlung, i.e. the expected efficiency

losses are larger than for Gaussian distributions (see Fig. 6.33).

The momentum resolution shown in Fig. 6.32 stays below 5% for transverse momenta up to  $10 \text{ GeV}/c$ . This resolution is obtained for all charged particles. Therefore one has a large flexibility of defining triggers requiring a number of stiff tracks in a given solid angle (jet triggers), e.g. it is certainly possible to select three stiff tracks within the solid angle of one readout chamber requiring for each of the tracks a transverse momentum of  $p_t > 5 \text{ GeV}/c$ .

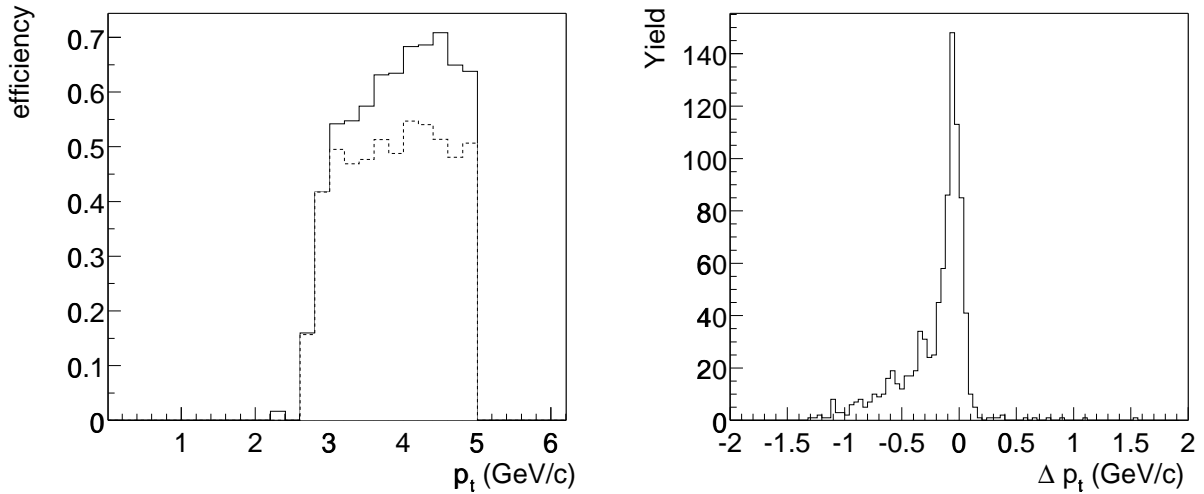


**Figure 6.33:** GTU tracking efficiency for electrons in a low multiplicity (400) environment (left). The solid histogram represents the track finding efficiency, the dashed histogram displays the efficiency to reconstruct the primary electron with a transverse momentum that deviates less than 10% from the primary transverse momentum. The right panel shows the momentum loss distribution of electrons when entering the first plane of the TRD.

#### 6.4.4 GTU tracking efficiency

The efficiency of the GTU was studied in comparison to the offline performance and under various scenarios. The detection efficiency as function of momentum for clean electron tracks (at event multiplicity 400) is shown in Fig. 6.33. A particle is called detected, once its reconstructed momentum has passed a certain threshold ( $p_t^{rec} > 2.7 \text{ GeV}/c$ ). In the figure the number of those particles is plotted versus their primary momentum normalized to all the primary particles that are emitted into the solid angle of the TRD detector ( $45^\circ < \theta_{lab} < 135^\circ$ ). The global track finding efficiency (solid histogram in Fig. 6.33) is rising as function of the primary transverse momentum due to the long radiation tail of the incident electron momentum distribution. This is evident when inspecting the momentum loss distribution  $\Delta p_t = p_t^{incident} - p_t^{primary}$  that is plotted on the right hand side of Fig. 6.33 for electrons that are emitted with a transverse momentum of  $3 \text{ GeV}/c$  from the primary vertex. Cutting this distribution at  $\Delta p_t = -0.3 \text{ GeV}/c$  corresponding to a global trigger selection threshold of  $p_t^{min} = 2.7 \text{ GeV}/c$  reduces the number of found tracks by 28%. At the threshold the momenta of the found tracks are essentially all within a 10% window around the original momentum from the primary vertex, as shown by the dashed histogram in Fig. 6.33. This fraction of about 50% of all the emitted electron that are found within a 10% window stays constant with increasing transverse momentum while the track finding efficiency rises due to the constant selection threshold. The correct momentum of those additional tracks that have experienced a substantial energy loss before reaching the TRD can only be determined by tracking through the full ALICE detector and identifying the initial curvature of the track with the ITS and TPC.

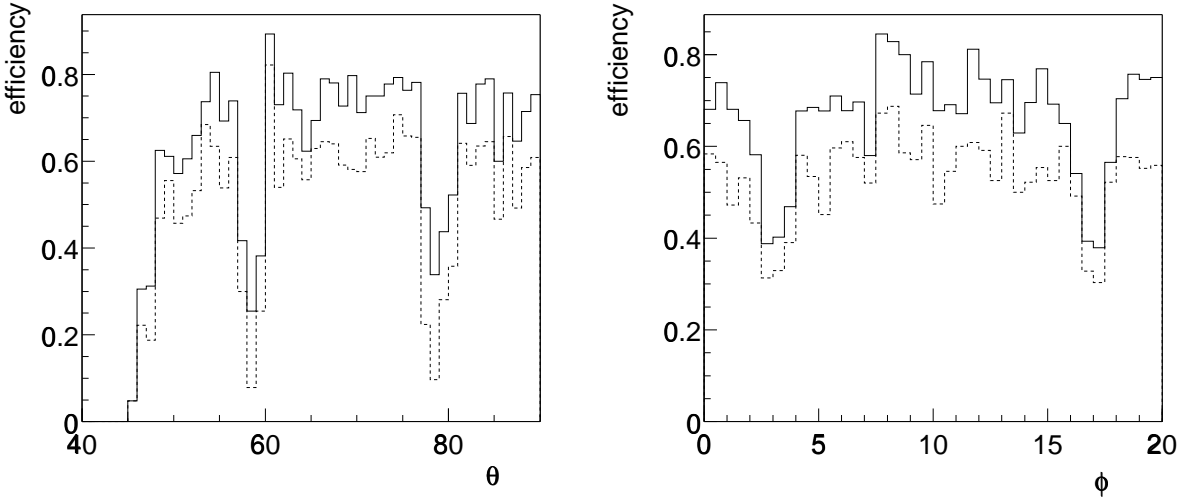


**Figure 6.34:** GTU tracking efficiency for electrons at low multiplicity versus polar angle (left) and versus projected azimuthal angle (right). The line types of the histograms are the same as in Fig. 6.33 (left panel).

The uniformity of the efficiency over the solid angle is shown in Fig. 6.34, demonstrating the validity of the underlying tracking concept. The values are obtained by averaging over the signal part of the transverse momentum spectra (Fig. 6.17) with the efficiencies shown in Fig. 6.33. The dips visible in the efficiency are caused by the structural material and the gaps in the acceptance. For the azimuthal distribution the whole angular acceptance was projected onto the opening angle of a single chamber ( $\Delta\phi = 20^\circ$ ). Since primary emission angles of the tracks are displayed in the histogram, the inefficiency caused by the frames and gaps are shifted by the deflection angle of those tracks, e.g.  $\alpha \approx \pm 3^\circ$  for the electron/positron momenta under study here.

The summary of the results obtained with the GTU tracking algorithm are shown in Fig. 6.35 as function of the normalized event multiplicity. The normalization is such that unity corresponds to  $dN/dy = 8700$ . The left panel shows the track finding efficiency for primary electrons with transverse momenta of more than  $3 \text{ GeV}/c$  including the requirement  $p_t^{rec} > 3 \text{ GeV}/c$ . The number is calculated by integrating over the signal electron spectrum as shown in Fig. 6.17. Figure 6.35 (middle) shows the total number of reconstructed tracks originating from any charged particle and Fig. 6.35 (right) shows the number of found electron background tracks, i.e. tracks that originate from secondary electrons that will not be distinguishable from primary electrons due to the TR signature.

A systematic study was performed aiming at the reduction of secondary electron tracks to the level of 1-2 for full multiplicity events for trigger rate reasons (see section 6.5). This can be achieved by cutting on the quantities listed in Table 6.6. In order to suppress secondary electron tracks that are mostly due to conversions of  $\gamma$ -rays in the inner parts of the ALICE detector as much as possible in addition to *tracklet* quality cuts the curvature of the track was determined without reference to the primary vertex. This can be done for track candidates with 3 or more contributing *tracklets* in different planes. The derived quantity, the unconstrained transverse momentum (called  $p_t^{free}$ ), has worse momentum resolution but was found to efficiently suppress background from secondary electrons. The effect is visible in Fig. 6.35 (right) when comparing the solid squares and triangles corresponding to Cut A and Cut B as given in Table 6.6.

In order to map out the dependencies of the efficiency and the background, several scenarios are investigated in Fig. 6.35:

1. Offline tracking performance with default digitization scenario (solid circles),

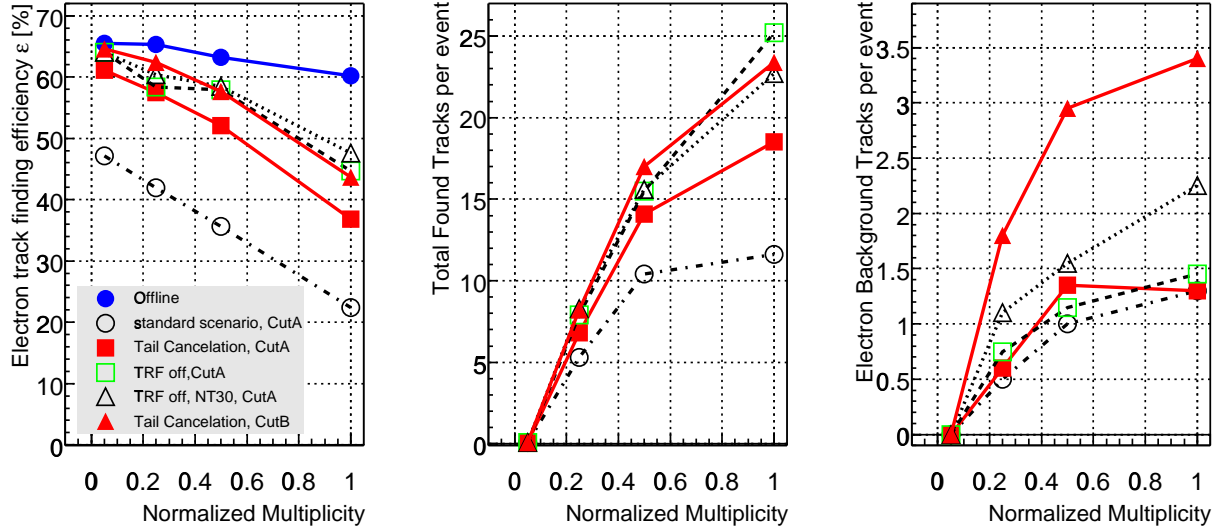


**Figure 6.35:** GTU tracking performance as function of normalized event multiplicity. The normalization is such that unity corresponds to  $dN/dy = 8700$ . The left panel shows the track finding efficiency for primary electrons with transverse momenta of more than  $3 \text{ GeV}/c$ . Figure 6.35 (middle) shows the total number of reconstructed tracks originating from any charged particle and Fig. 6.35 (right) shows the number of found electron background tracks.

**Table 6.6:** Global tracking parameters.

quantity	Cut A	Cut B
matching width in azimuthal angle	$0.11^\circ$	$0.13^\circ$
matching width in $z$ -direction	8 cm	8 cm
matching window for deflection angle	$2.4^\circ$	$2.4^\circ$
local momentum threshold	$2.3 \text{ GeV}/c$	$2.3 \text{ GeV}/c$
minimum number of clusters per <i>tracklet</i>	6	5
upper $\chi^2$ -limit for accepted <i>tracklets</i>	4.0	4.0
minimal number of <i>tracklets</i>	3	3
minimal number of planes crossed by track	4	4
threshold for $p_t^{rec} - p_t^{free}$	$1.7 \text{ GeV}/c$	$2.5 \text{ GeV}/c$
global momentum threshold	$2.7 \text{ GeV}/c$	$2.7 \text{ GeV}/c$

2. Standard scenario: Online tracking scheme based on 15 time bins with the nominal TRF (see Fig. 11.8) (open circles),
3. Same as 2 but including tail cancellation (see Section 6.4.2.1) (solid squares),
4. Same as 2 but with a  $\delta$ -function as TRF (open squares),
5. Same as 4 but with 30 time bins (open triangles).

The filled triangles in Fig. 6.35 correspond to scenario 3 with different parameters (Cut B from Table 6.6). Several observations are made from Fig. 6.35:

- The track finding efficiency is at best about 65% for low multiplicities as determined with the

full offline tracking algorithm (solid circles). This value is caused by the radiation losses of the electrons in the material inside of the TRD and the application of a fixed momentum threshold.

- The standard online tracking scenario (open circles) reaches for low multiplicities a peak efficiency of about 50% only. The reduction with respect to the offline case is due to i) implementing the background suppression cuts (Cut A of Table 6.6) and ii) distortions of the *tracklet* parameter due to the TRF. The TRF is responsible for an efficiency loss of about 12% of the total number of electrons as visible in Fig. 6.35 when replacing it by a  $\delta$ -function (open squares). The various selection cuts cost in total about 4% of the electrons (for low multiplicities).
- 80%-90% of the losses caused by the TRF can be recovered by implementing the digital tail cancellation described in Section 6.4.2.1 (filled squares) employing a single pole/zero network. Since this feature turns out to be useful for the online tracking efficiency, it is planned to implement the digital filter into the digital chip. This scenario is considered the effective default for the online tracking.
- The track finding efficiency decreases linearly with increasing multiplicity. The decrease of the efficiency is proportional to the occupancy (see Fig. 6.21). Such a scaling is to be expected due to the method to remove overlapping clusters while in the offline case deconvolution algorithms can be applied.
- For full multiplicity conditions increasing the number of independent time samples in the TRF off case (open triangles) improves the efficiency by about 10%. To which extent this observation holds with a tail cancellation algorithm and realistic pulse shapes needs to be studied further. This scenario would suggest to optimize the total drift time under the constraint of a TRF determined by the drifting ions.
- The improvement in the electron efficiency is reflected in the average number of tracks that are found under the global momentum cut (middle panel).
- The number of background electron tracks (right panel) depends on the set of cut values. The most crucial cut for removing secondary electrons is constructed from the unconstrained transverse momentum fit. The effect is seen by comparing Cut A (solid squares) to Cut B (solid triangles). At normalized multiplicities of 0.25 and 0.5 relaxing the selection condition increases the electron finding efficiency by about 6 - 8%. This is, however, accompanied by an increase in the background yield by about a factor of 2 - 3.

With the complex features observed for the online tracking algorithm and the large uncertainties of the input distributions it is difficult to make quantitative statements that are generally valid. It should be stressed, however, that the event multiplicities and the spectral shapes of the hadrons used in the simulation represent the worst case scenario. Even under those conditions the electron trigger scheme described above allows to reconstruct a sufficient number of resonances as will be shown in Section 6.5.

#### 6.4.5 Electron identification

In addition to the track finding problem described in the previous section, the found tracks need to be identified as electrons for the  $e^+e^-$  trigger. For a jet trigger application this step is omitted. The left panel of Fig. 6.36 presents the pulse heights distribution in a single chamber obtained for pions and electrons with transverse momenta of  $3 < p_t < 5 \text{ GeV}/c$  when integrating over the full drift time of the readout chamber in low multiplicity events. A threshold can be set so that by keeping 90% of the electrons we reject the pions with a factor of 25.

A more sophisticated analysis can be done following the procedure described in Section 11.5. The likelihood shown in the right panel of Fig. 6.36 is calculated from the normalized distributions of the

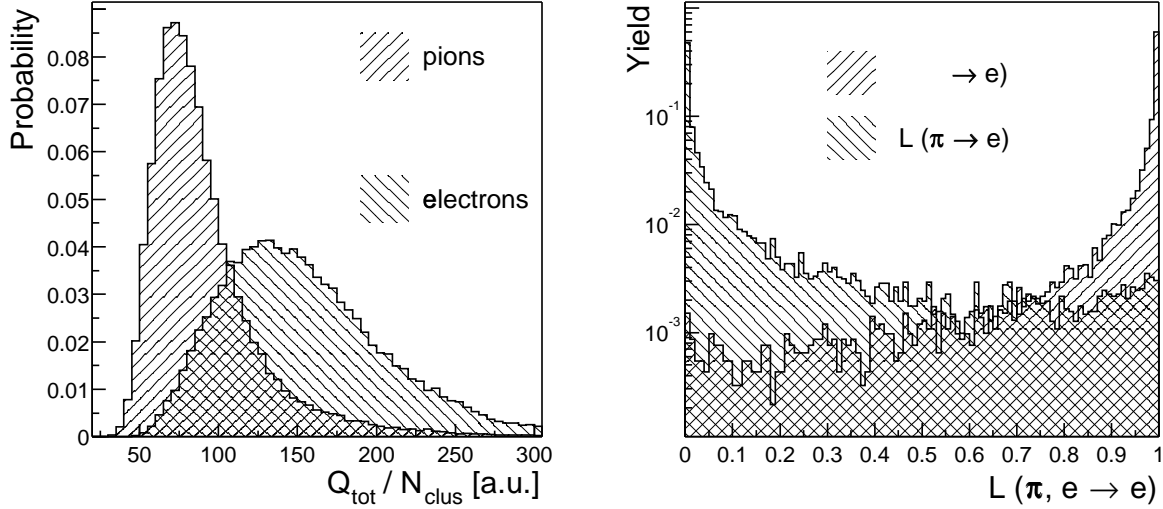


**Figure 6.36:** Pulse height distributions for electrons and pions with transverse momenta  $p_t > 3 \text{ GeV}/c$  integrating all time bins in one chamber (left) and derived likelihood distributions to infer an electron from the electron ( $L(e \rightarrow e)$ ) and pion ( $L(\pi \rightarrow e)$ ) pulse height distributions (right).

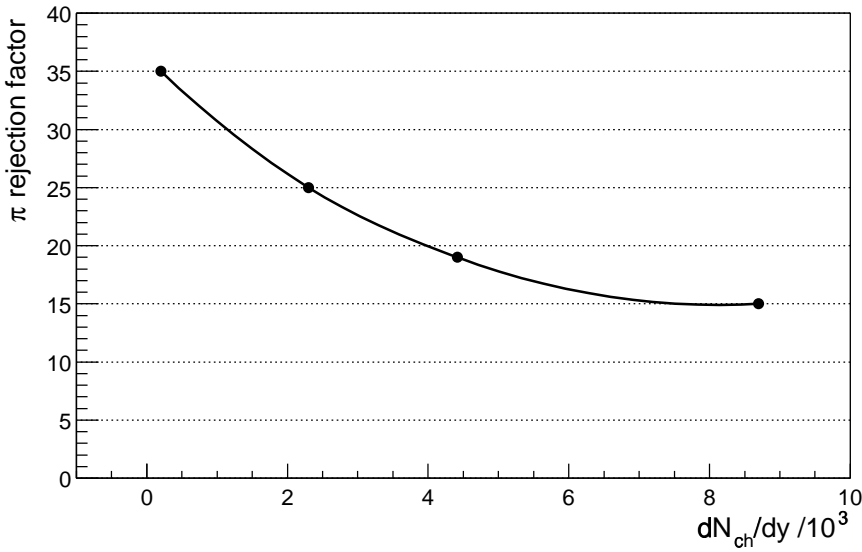


**Figure 6.37:** Pion rejection factor for 90% electron efficiency, determined from the average charge in half chamber, as function of the multiplicity.

energy deposited in one TRD module by electrons and pions, which can be implemented as two look-up-tables. For a given globally reconstructed track the information consists of  $n$  values of normalized energy deposit  $\Delta E_i$  for a track reconstructed from  $n$  tracklets. From the LUTs the probabilities  $p_i^e$  and  $p_i^\pi$  are obtained, thus the total probabilities can be calculated as  $P_e = \prod p_i^e$  and  $P_\pi = \prod p_i^\pi$  over the  $n$  layers. The likelihood for the particle to be an electron is given by the ratio  $P_e/(P_e + P_\pi)$ . To this value a cut is applied, chosen in such a way that 90% of the electrons are retained. The result of the online PID procedure is plotted in Fig. 6.37 as function of the centrality of the collision. The drop in the rejection power is caused by the decreasing number of tracklets that form the globally accepted track.

### 6.4.6 Background

Background sources for high  $p_t$  electrons:

- background electrons: conversions,  $\delta$  - electrons,
- fake tracks,
- misidentified charged pions.

While the fake tracks and secondary electrons are a problem for all triggers, the background due to charged pions affect only the di-electron trigger. As visible by the solid squares of Fig. 6.35 (middle), 18 tracks are found on average per central collision, of which 1.4 are clean electron tracks (right panel of Fig. 6.35). Applying the online particle identification capability described in Section 6.4.5 reduces the totally found tracks to about one electron track candidate per central collision. The background due to misidentified pions and fakes and the one from secondary electrons are, for restrictive parameters like 'Cut A', of the same order of magnitude.

The background multiplicity is of crucial importance for the fake trigger rate that is discussed in Section 6.5.3. It should be noted that the background multiplicity can be reduced further in a post-processing of the event in the HLT compute farm:

- The pion suppression of misidentified pion tracks can be improved to the offline performance (see Section 11.5).
- The secondary electron tracks passing through the selection cuts have a wide true momentum distribution. 60% of them have transverse momenta below  $3 \text{ GeV}/c$ . Tracking of the TRD electron candidates through the TPC would determine the curvature of the track with a better accuracy and can be used to remove this component. The large momentum background tracks result from photon conversions in the inner part of the ALICE detector. They can be recognized at least partially by full tracking through the TPC and ITS as well.

The corresponding trigger rates for  $e^+e^-$  coincidences and the important role of the HLT is discussed in Section 6.5.3.

## 6.5 Performance

The various physics observables are discussed in [3]. A typical example of an interesting hard probe physics observable is the family of  $\Upsilon$  resonances [9]. The performance of the trigger scheme described above is presented in this section for the  $\Upsilon$  system.

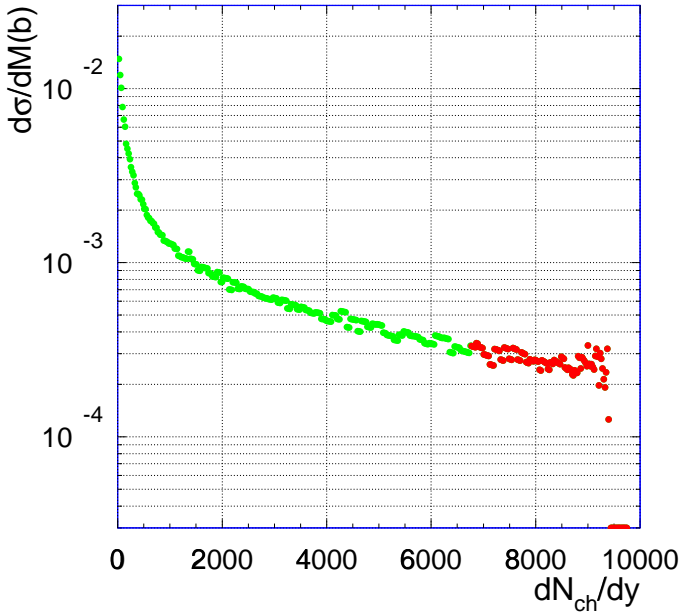
### 6.5.1 Generalities of Pb-Pb collisions

With an extrapolated inelastic nucleon-nucleon cross section of  $\sigma_{NN} = 60 \text{ mb}$  a total reaction cross section of  $\sigma_{PbPb} = 7.5 \text{ b}$  is anticipated. At a luminosity of  $\mathcal{L} = 1 \cdot 10^{27} \text{ cm}^{-2}\text{s}^{-1}$  this cross section gives rise to minimum bias interaction rate of  $R_{int}^{MB} = 7.5 \text{ kHz}$ . In order to make use of the high quality tracking available within the ALICE TPC, only the fraction of events without pile-up within the TPC drift time of  $T_{drift}^{TPC} = 88\mu\text{s}$  is considered at this stage for further analysis. Therefore at the trigger level the rate is reduced to a past protected interaction rate of  $R_{past}^{MB} = 3.9 \text{ kHz}$ , while for high level trigger processing, a rate of  $R_{past\&future}^{MB} = 2.0 \text{ kHz}$  is anticipated. The numbers are summarized in Table 6.7 for luminosities from  $0.5 - 1.0 \cdot 10^{27} \text{ cm}^{-2}\text{s}^{-1}$ .

**Table 6.7:** Event and trigger rates for Pb+Pb at 5.5 A TeV.

$\mathcal{L}(\text{cm}^{-2}\text{s}^{-1})$	$R_{int}^{MB}$ (kHz)	$R_{past}^{MB}$ (kHz)	$R_{past\&future}^{MB}$ (kHz)
$1 \cdot 10^{27}$	7.5	3.9	2.00
$7.5 \cdot 10^{26}$	5.7	3.5	2.10
$5 \cdot 10^{26}$	3.8	2.7	1.95

With the past-future protection, the optimum conditions are reached at a luminosity of  $\mathcal{L} = 7.5 \cdot 10^{26} \text{ cm}^{-2} \text{ s}^{-1}$ . For the following estimates an integrated luminosity of  $\mathcal{L}_{int}^{PbPb} = 0.5/\text{nb}$  per year is assumed, based on a time averaged luminosity of  $\mathcal{L} = 5 \cdot 10^{26} \text{ cm}^{-2} \text{ s}^{-1}$  and an effective data taking time of  $10^6$  s within one month of heavy ion running per year [10]. As can bee seen from Table 6.7, due to the past/future protection imposed by the TPC drift time, the number of acceptable events does not change when the luminosity is increased by a factor of 2.

**Figure 6.38:** Differential cross section versus multiplicity for Pb+Pb at 5.5 A TeV.

The distribution of multiplicities can be obtained by assuming that the multiplicity scales with the number of participants that are calculated by the nuclear overlap integral as function of the impact parameter. Fig. 6.38 shows the scenario with a mean value of the rapidity density  $\langle dN/dy \rangle = 8000$  for the most central 10% of all the reactions. The event class of the most central 10% of the cross section is called in the following *CEN*. It starts at a multiplicity of  $dN/dy_{low} = 6770$  and is marked in Fig. 6.38 by the dark circles.

Hard probes are produced according to the number of primary NN - collisions that can be obtained from the same formalism. Background is created according to the occupancy of the TRD chambers that scales linearly with the multiplicity (see Fig. 6.21).

### 6.5.2 $\Upsilon$ count rates

The integrated production cross section of the  $\Upsilon$  resonances at  $\sqrt{s} = 5.5$  TeV is obtained by extrapolating existing data in the framework of the color evaporation model [11–13]. For Pb-Pb collisions a total production cross section for the combined  $\Upsilon$  states ( $\Upsilon$ ,  $\Upsilon'$  and  $\Upsilon''$ ) decaying into two electrons ( $B=2.52\%$ ) of  $B\sigma_{PbPb}^{\Upsilon} = 570 \mu b$  is predicted [12]. The relative fractions are  $\Upsilon : \Upsilon' : \Upsilon'' = 1 : 0.3 : 0.1$ . The cross section estimate is based on an extrapolated pp cross section of  $d\sigma_{pp}/dy|_{y=0} = 3 \text{ nb}$ . The corresponding rapidity distribution is approximately flat over  $\pm 4$  units of rapidity resulting in an integrated cross section of  $\sigma_{pp} = 22.5 \text{ nb}$ . Scaling from pp to AA collisions is done by the scaling law observed in the Fermilab fixed target data

$$\sigma_{AA} = A^{2\alpha} \sigma_{NN},$$

with  $\alpha = 0.95$  [14].

With these assumptions a minimum bias rapidity density for  $\Upsilon \rightarrow e^+e^-$  of  $dN/dy|_{y=0} = 1 \cdot 10^{-5}$  is predicted for minimum bias Pb-Pb collisions. An integral number of  $N_{int}^{\Upsilon} = 2.85 \cdot 10^5$  is produced within one year of ALICE running. Note that this number is obtained from scaling pp results with the number of primary collisions, i.e. no suppression or enhancement from the QGP is considered at this level. The current estimate is lower by a factor of 1.6 as compared to the numbers used in the Technical Proposal [3] due to the use of the empirical mass scaling. With all the extrapolations and uncertainties the following numbers can only be considered a case study that describe the capability of the TRD trigger system.

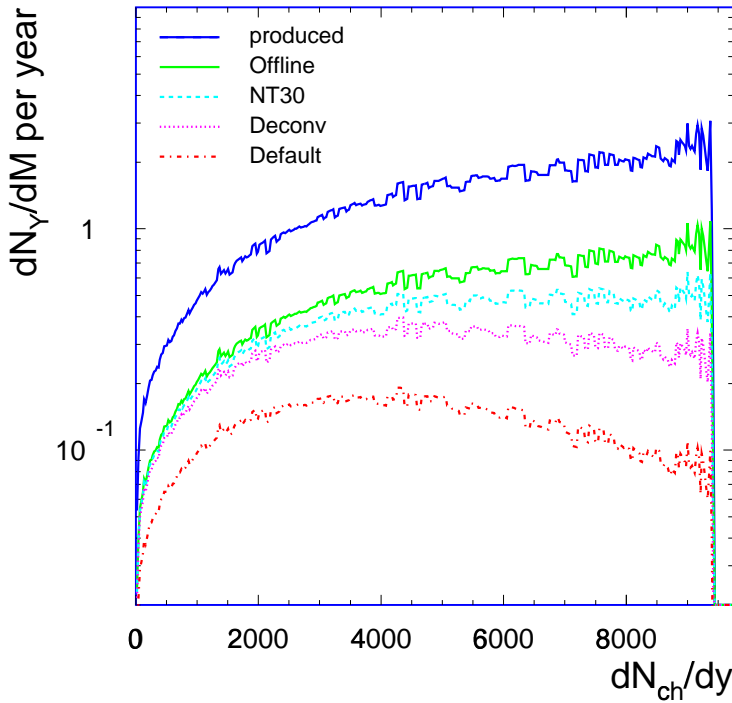


**Figure 6.39:** Differential  $\Upsilon$ - yields for various scenarios as function of multiplicity for Pb+Pb at 5.5 A TeV. The scenarios Offline (solid), NT30 (dashed), Deconv (dotted) and Default (dashed-dotted) correspond to the scenarios 1,5,3, and 2 of Section 6.4.4.

As shown in the Technical Proposal [3] the geometrical acceptance  $\epsilon_{geo}$  for detecting an electron and a positron with  $p_t^e > 3 \text{ GeV}/c$  each with the full size TRD ( $|\eta| < 0.9$ ) from  $\Upsilon$  decay is  $\epsilon_{geo} = \frac{N_{accepted}}{dN/dy \cdot \Delta y} = 0.65/\Delta y$  where  $\Delta y$  is the width in rapidity of the uniform input distribution (see also Chapter 12). For the reconstruction of resonances two electrons need to be found and identified in coincidence. The reconstruction efficiency for  $\Upsilon$  therefore reads

$$\epsilon_{det} = (\epsilon_{act} \cdot \epsilon_{tracking} \cdot \epsilon_{PID})^2,$$

with  $\epsilon_{act}$  - the effective active fraction of the solid angle,  $\epsilon_{tracking}$  - the efficiency to find a track that hits the active area and  $\epsilon_{PID}$  the survival probability of electrons passing the PID cut (see section 6.4.5). The product  $\epsilon_{act} \cdot \epsilon_{tracking}$  is shown in Fig. 6.35 for single tracks,  $\epsilon_{PID}$  is targeted to be 90%, at which a pion efficiency of  $\epsilon_{PID}^\pi = 0.02$  (for  $dN/dy = 8000$ ) can be reached in the offline analysis from the TRD data alone (see Section 11.5).

**Table 6.8:** Integral number of  $\Upsilon$  under various conditions for an integrated luminosity of  $\mathcal{L}_{int}^{PbPb} = 0.5/\text{nb}$ . Cut A of Table 6.6 was employed (\* using Cut B).

	$N_{T8000}^Y$	$N_{T2000}^Y$	$N_{MB8000}^Y$	$N_{T8000}^Y(\text{Muon})$
Maximum charged particle multiplicity $dN/dy$	8000	2000	8000	8000
produced number of $\Upsilon$ , $N_{int}^Y$	285000			
decaying into acceptance	24750		15019	
decaying into acceptance without TPC pile-up	12672		-	
reconstructible with OFFLINE efficiency	4041	4437	4041	9349
reconstructed with standard options	1056	2016	154	8414
reconstructed with TRF off, 30 time bins	3053	4052	-	-
reconstructed with deconvolution of TRF	2269	(4180)* 3628	-	-

The single track efficiencies for the different scenarios as shown in Fig. 6.35 and described in Section 6.4.4 have been parameterized by straight lines. The resulting differential distribution of reconstructed  $\Upsilon$  resonances as function of centrality for a multiplicity density of 8000 for central collisions is shown in Fig. 6.39. Note that the number of produced  $\Upsilon$  grows like  $N_{part}^{4/3} \propto (dN/dy)^{4/3}$ . The lower histograms in Fig. 6.39 reflect the reconstruction efficiency and its drop with increasing multiplicity. The solid grey histogram is obtained by employing offline efficiencies at the trigger level (including the cut on single particle transverse momentum of  $p_t > 3 \text{ GeV}/c$ ) and follows the production probabilities. For the more realistic online trigger scenarios a reduction, especially for central collisions, is observed. The corresponding integral numbers over the full centrality range are given in Table 6.8 in the column labeled  $N_{T8000}^Y$ . Under those conditions about 2300 reconstructible  $\Upsilon$  can be expected per year of ALICE running (employing the deconvolution scheme of the TRF). This number has to be compared to an untriggered scenario where the whole analysis is performed offline. When still aiming at the full centrality coverage as motivated by the physics case, the total available bandwidth to the dielectron physics (assumed to be 20 Hz of central events) would be filled with minimum bias events (74 Hz due to the smaller event size). The number of reconstructible  $\Upsilon$  for this scenario has to be down-scaled by the ratio of DAQ rate to minimum bias interaction rate. The values are shown in Table 6.8 in the column labeled  $N_{MB8000}^Y$ . About 150  $\Upsilon$  could be reconstructed per year of ALICE running. One could trade performance in centrality coverage for more statistics in central collisions under the constraint of the same DAQ bandwidth. An extreme option would be to give up the centrality coverage completely and focus on central events only. In the 10% most central events about 1600  $\Upsilon$  can be found with offline efficiencies under the conditions used for Table 6.8. According to Table 6.7 the central events occur with a frequency of 195 Hz. Given the bandwidth of the DAQ system of 20 Hz, 164  $\Upsilon$  can be reconstructed in such an event sample. These numbers clearly demonstrate that the TRD dielectron trigger is essential for this physics topic.

The numbers of reconstructed  $\Upsilon$  can be substantially improved by exploiting the capabilities of the HLT system [15]. This system is designed to allow for an input bandwidth of 200 Hz. Assuming that half of that bandwidth is allocated for central event processing (for the other half see Section 6.5.3) 100 Hz of central events can be inspected. With offline detection performance 820  $\Upsilon$  can be gathered within one ALICE year. This number has to be compared to the number of  $\Upsilon$  that is already in the triggered sample,

e.g. 680 for the scenario with tail cancellation. The running mode with a full scale HLT TRD analysis delivers very similar total  $\Upsilon$  numbers as is given by the central subset that is included in the minimum bias TRD triggered event sample. While the numbers are comparable for central events, it is, however, not possible to cover the centrality dependence of  $\Upsilon$  production with the HLT scheme due to the rate limitations of opening the TPC gating grid.

The inspection of central collisions by the HLT analysis can be used in addition to increase the number of reconstructed  $\Upsilon$ : combining both modes of data taking a final number of 1160  $\Upsilon$  in central collisions can be achieved in one ALICE year.

As discussed in Chapter 12, the extrapolation of latest RHIC results predict a rapidity density of  $dN/dy \approx 1600$ . While the beam energy increase is too large to allow a reliable extrapolation, we will still consider 2 scenarios for the discussion of the trigger performance, as the implications for the performance of the TRD trigger system are significant. The numbers corresponding to a multiplicity in central events of  $dN/dy_{cen} = 2000$  are listed in the column labeled  $N_{T2000}^{\Upsilon}$  in Table 6.8. The number of reconstructed  $\Upsilon$  is almost doubled for the scenario that employs the tail cancellation technique. Additionally about 15% can be gained by opening the selection cuts (Cut B from Table 6.6) leading to a total of 4200 triggered  $\Upsilon$ .

Note that complementary efforts to detect  $\Upsilon$  states in Pb-Pb collisions yield similar numbers. When using the same production cross section and scaling to the same integral luminosity of  $\mathcal{L}_{int}^{PbPb} = 0.5/\text{nb}$  per year, the CMS experiment would reconstruct an integral number of 6400  $\Upsilon$  per year [12]. The performance of the ALICE muon arm is given in Table 6.8 and is expected to be still better.

The numbers presented in Table 6.8 correspond to the full size TRD detector without any holes. Should the active area have to be reduced to 50% of the nominal solid angle, a reduction of the measured signal to about a quarter of the numbers in Table 6.8 would be the consequence (see also Chapter 12). The physics program of exploring QGP properties with  $\Upsilon$  states would be severely limited if the TRD could not have complete coverage.

### 6.5.3 Trigger rates

The true  $\Upsilon$  trigger rate is very small ( $10^{-2}$  Hz). The rate of the TRD dielectron trigger is dominated by background and has contributions from 3 sources:

1. misidentified pion tracks
2. fake tracks from combination of clusters from different primary tracks
3. true electron tracks due to conversion of photons before the TRD

The single track background multiplicities are shown in the center and right panel of Fig. 6.35. The center panel represents the sum of all the background contributions. In the right panel the background from true electrons (component 3 from above) is separately plotted, since for this component no reduction can be achieved from the PID. For the components 1 and 2 the pion suppression factor  $\xi$  shown in Fig. 6.37 was used. The total background multiplicity  $M_{bck}$  can then be constructed from the total found tracks  $M_{found}$  and the found electron tracks  $M_{found-e}$  by  $M_{bck} = (M_{found} - M_{found-e})/\xi + M_{found-e}$ . For the scenario employing the tail cancellation (see Fig. 6.35) this background multiplicity  $m(M)$  was parameterized as function of centrality  $M$  by a square root behavior. The background consists of tracks of positive and negative charges with equal probability. Due to the statistical nature of the background tracks the distribution is assumed to be Poissonian and the differential background pair trigger rate  $R_{pair}$  is given by

$$\frac{dR_{pair}}{dM} = \frac{dR_{mb}}{dM} \cdot (1 - e^{-m(M)/2})^2,$$

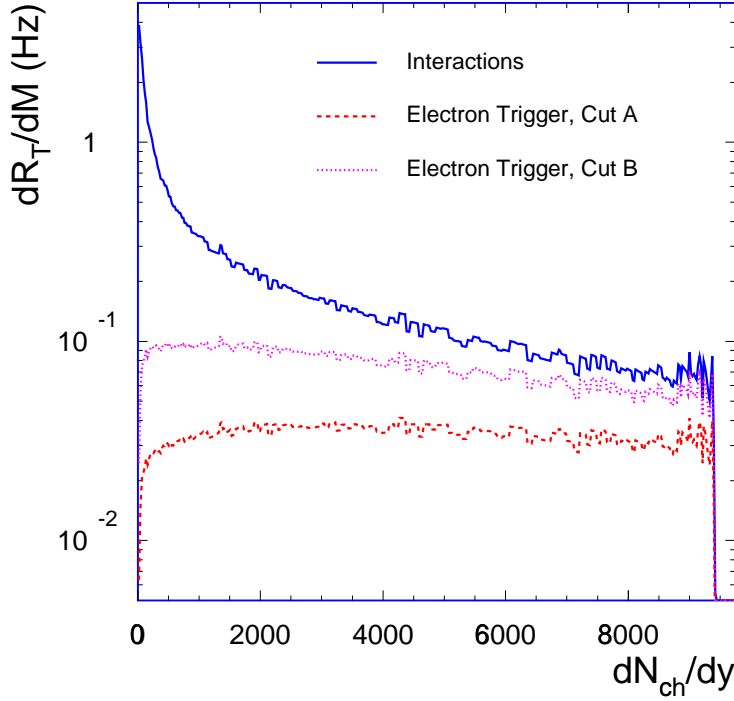


**Figure 6.40:** Differential background trigger rate  $R_T$  as function of centrality for Pb+Pb at 5.5A TeV with a multiplicity for central events of  $dN/dy = 8000$ . Different Cuts listed in Table 6.6 were used to select stiff electron candidates.

where  $R_{mb}$  is the minimum bias interaction rate. The differential trigger rate as function of centrality given in terms of  $dN_{ch}/dy$  is shown in Fig. 6.40 for the two sets of parameters listed in Table 6.6. The integral numbers are shown in Table 6.9 in the rows labeled ' $e^+e^-$ '.

**Table 6.9:** Trigger rates for Pb+Pb at 5.5 A TeV.

$dN/dy_{central}$		2000	8000
Cut A	$e^+e^-$	128 Hz	351 Hz
	Quarkonia	43 Hz	117 Hz
Cut B	$e^+e^-$	340 Hz	732 Hz
	Quarkonia	113 Hz	244 Hz

A further reduction of the trigger rate is achieved by calculating the invariant mass of the electron pair in the GTU. As was found in the Technical Proposal (Fig. 38) [3] the background spectrum is essentially flat over the invariant mass range from 1 to 10 GeV/c<sup>2</sup>. With the transverse momentum resolution as given in Fig. 6.32 an invariant mass resolution of 8% at the  $\Upsilon$  mass is achieved by the TRD trigger. Selecting only 2 intervals of invariant mass around the J/ $\psi$  ( $2.8 < m_{e^+e^-} < 4.0 \text{ GeV}/c^2$ ) and the  $\Upsilon$  family ( $m_{e^+e^-} > 8 \text{ GeV}/c^2$ ) reduces the total trigger rate by about a factor of 3, while the physics signal is reduced only by about 10% as can be seen from Fig. 12.7. The corresponding integrated rates are given in Table 6.9 in the rows labeled 'Quarkonia'.

The parameter values for 'Cut A' ('Cut B') were tuned at the expense of some efficiency loss to have an acceptable trigger rate even for the multiplicity scenarios  $dN/dy_{cen} = 8000$  ( $dN/dy_{cen} = 2000$ ) for central collisions. So, in each case the dielectron trigger rate would be about 110 Hz. Such a trigger rate into the High Level Trigger (HLT) seems to be appropriate. The current HLT design foresees a maximum

input bandwidth of about 200 Hz [15]. The 'Quarkonia' dielectron trigger would occupy one half of the total available bandwidth. Further optimization of the online background strategies is currently under investigation. The numbers given here should be taken as orientations of what can be achieved already with very simple algorithms.

An overall suppression of the event rate by more than a factor 10 is expected from an offline like analysis in the HLT compute farm. The task of the HLT is to further sort out the correct events by:

1. Applying the full pion suppression power with a maximum likelihood analysis of the pulse height distributions (see Section 11.5). Since the online pion rejection was assumed to be only 1:20 independent of centrality at least a reduction by a factor of 2 can be expected from this step.
2. Tracking of all candidates through the TPC and ITS to remove fakes and conversions. Approximately 60% of the electron background tracks originate from particles with transverse momenta below  $3 \text{ GeV}/c$ . The curvature and the closest distance to the vertex are much better determined by the global tracking. The latter quantity can also be used to reduce the other 40% of the background, i.e. stiff tracks not originating from the primary vertex. In total, a minimal reduction by a factor of 2 is anticipated. A detailed analysis of the global tracking performance of the central ALICE arm is in progress.

Such a reduction of the single candidate multiplicities by a factor of 4 results in a reduction of fake pairs by a factor of 16 resulting in an output trigger rate of the HLT system is in the order of 7 Hz for the 'Quarkonia' trigger scenarios ' $dN/dy_{cen} = 8000$ , Cut A' and ' $dN/dy_{cen} = 2000$ , Cut B'. For the lower multiplicity scenario the ' $e^+e^-$ ' trigger without invariant mass cut represents an alternative option compatible with the allocated DAQ bandwidth.

Bandwidth requirements to the data acquisition system can be further reduced by considering partial readout of regions of interest. The stiff tracks will cross only 3-4 out of  $2 \times 18$  TPC sectors. Therefore a reduction by about 10 is possible. Such a readout scenario will not allow for a detailed cross correlation of the dielectron signal with global TPC quantities. This could be an option for an intermediate time period when possibly the HLT is still under study and development.

Summarizing, the selection criteria of the combined TRD / HLT dielectron trigger can be adjusted such that the output rate to DAQ is in the order of 10 Hz when triggering on the quarkonia states and about a factor 2 higher without the invariant mass selection. The bandwidth can stay well below the anticipated limit of the equivalent of 20 Hz of central events of  $dN/dy_{cen} = 8000$ .



# 7 Readout and Data Flow

---

This chapter discusses all aspects of the TRD data flow. Generally, there are two main data streams in three areas to be handled in real time. Both data streams require the simultaneous readout of all 64224 MCMs.

The first data stream is the shipping of the *tracklet* candidates produced on the individual MCMs to the global tracking unit (GTU). This *tracklet* shipping has to be performed during the critical trigger decision time and is limited to 400 ns (refer to Fig. 5.6, note the 200 ns setup time for the first *tracklet* to percolate through the readout tree). During that time, a total of up to  $40 \times 32$  Bit *tracklets* per chamber have to be shipped to their appropriate  $\phi$  sector of the GTU, resulting in an aggregate data stream of 216 GByte/s.

The second data stream is the raw data readout, which is performed upon a Level-2 accept (L2A). At that time, the event buffers on the MCMs are being read out. This readout is performed during the TRD dead time as the TRD front-end is not pipelined. For a detailed discussion of the TRD states and timing, refer to Chapter 5.

The data path begins at the MCMs, and ends, in case of a L2A, with the data shipment via the ALICE optical detector links (DDL). Therefore, there are three general regions of data shipping involved : the data flow on the chambers; the cabling between the chambers and the GTU; and, the data shipping off the GTU itself. All three regions are detailed below in the appropriate sections.

## 7.1 Data types and format

A major cost factor is the required connectivity between the MCMs as this drives the number of pins and connections required. Further, a large number of I/O signals increases the complexity of the readout plane. On the other hand, the tight latency requirement drives up the data transfer rates and bus widths. Therefore, the readout trees are designed to meet the requirements of the *tracklet* shipping. The raw data readout upon L2A uses the defined *tracklet* readout tree, which at that time is idle.

### 7.1.1 Tracklets

*Tracklet* candidates, which pass the defined  $p_t$  and PID cuts within one plane (MCM), have to be shipped to the global tracking unit for track matching. In order to assist the track matching, each *tracklet* candidate is projected onto the GTU reference plane prior to the shipping.

**Table 7.1:** Data fields of *tracklet* and TRD tracks

Type	<i>tracklet</i> Bits	TRD Track Bits	Description
y-position	13	18	$8 \times 18 \times 7.2$ mm with a resolution of $400 \mu\text{m}$
y-deflection	5	7	$\pm 8$ mm to pass cut incl. one sign bit
z-position	4	10	max. 16 pad rows per chamber
charge	6	8	normalized charge above MIP
TR	2	4	TR quality flags
variance	1	4	fit quality flags
spare	1	4	fit quality flags
$\Sigma$	32	64	w/o Hamming Code

The *tracklet* parameters include y-position, y-deflection, the z-position or pad row number in the reference plane, the normalized charge relative to MIP, the fit variance, and some TR quality flags. The

number of bits required for each of these parameters is determined by the resolution and dynamic range. Table 7.1 shows the appropriate encoding. Correspondingly, each *tracklet* requires 32 Bit for encoding.

### 7.1.2 Raw data

All digitized ADC values are stored in event buffers, which are being read out upon a L2A. This readout is performed by the CPUs of the *tracklet* processors and, therefore, is completely programmable. Any preprocessing or reprocessing of the data is conceivable using the 256896 processors available. However, in order to understand the data flow, the largest typical data format is the zero suppressed raw data. Zero suppression is implemented in the standard form, running on the freely programmable *tracklet* processors. The zero suppression algorithm implements a configurable threshold, plus some pre and post history, while always reading out the appropriate neighboring channels in order to guarantee the complete readout of a cluster and while maintaining relatively high thresholds. The resulting data is run-length encoded in order to suppress the baseline zeroes. The raw data values are presented in Table 7.2. Here 'black event' represents all available pixels, including the readout of redundant borderline ADC channels.

**Table 7.2:** Average raw data parameters for Pb–Pb collisions.

Type	Value	Notes
Number of ADC channels	1348704	each MCM supports 18 PADs, plus three ADCs at borders
ADC resolution	10 Bit	
Number of time bins (event buffer can handle 32 )	20	active drift time with start and end time configured
Size of 'black event'	39.4 MByte	assuming the readout of redundant borderline ADC channels
Overall occupancy	14%	overall pixel occupancy
Raw event size	7.1 MByte	zero suppressed raw event including 20% coding overhead

There are various options to compress the raw event further in a binary lossless fashion. This can be implemented both at the front-end and the back-end. Given that the TRD raw event is the second largest in ALICE, some effort will be invested within the framework of the high-level trigger project to reduce this sub-event to its minimum size. However, given the experience of the TPC data compression R&D [1] [2], it is expected that only a factor of 50% might be feasible. Huffman encoding can easily be implemented in the front-end. Other compression techniques might be implemented in the back-end.

## 7.2 Hardware implementation

As described in the introduction, the total transfer time for the trigger is limited to 600 ns. This is the sum of two contributions, i.e., the latency and the duration of the data transfer phase. To allow the operation of the GTU parallel to the data transfer, the readout sequence has to be chosen carefully as described later in this document. To maximize the overlap between processing and data transport, the latency has to be kept to a minimum.

### 7.2.1 Readout scheme

The organization of the readout follows the structure given by the hardware layout. A readout tree covers a plane of a supermodule consisting of five chambers with up to 16 pad rows. From simulations, it is known that a chamber will provide a maximum of 40 *tracklets* (Chapter 6) with a size of two 16 Bit words. Since the readout for the data acquisition poses a much lower constraint on the system than the trigger, the design is driven by the requirements of the latter.

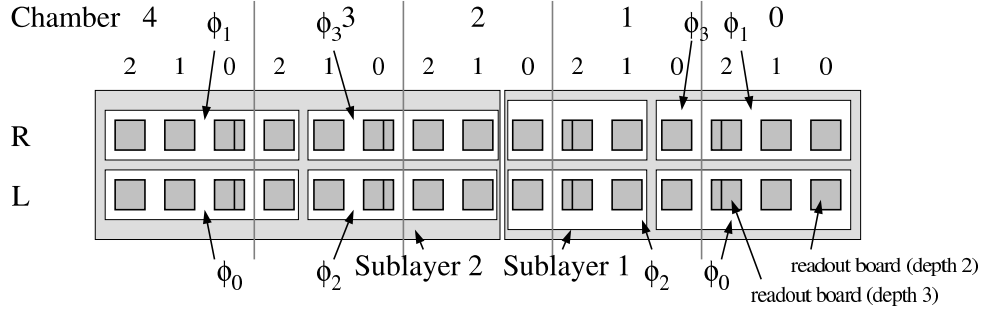


**Figure 7.1:** Layout of readout boards. The phases  $\phi_0.. \phi_3$  correspond to the time multiplexed inputs of the root of the tree feeding the optical detector links (refer to Fig. 7.2). Each chamber implements two rows of readout boards labelled as right and left. The readout boards within a chamber are numbered in ascending order in z direction. The same numbering scheme is applied to the chambers themselves. Each layer of a super module is being readout at both sides, therefore implementing two readout trees. The corresponding two logical areas are called sublayer 1 and 2.

To minimize the number of components in the trigger system, most of the readout tree is integrated into the digital part of the MCM, the LTU. To keep the system simple, the same frequency of 120 MHz is used for the *tracklet* processor and the transfer between MCMs. To achieve a small latency, the readout tree has to be as short as possible. However, the width is limited by the number of pins available. To achieve the necessary robustness, LVDS [4] and a 1 Bit error correction and 2 Bit error detection using Hamming coding [5] is foreseen. As a consequence, 46 pins for a 16 Bit data port are needed corresponding to the 16 Bit data, the 5 Bit for the Hamming code, 1 Bit for parity and 1 Bit for the strobe. A tree width of four requires five ports resulting in 230 I/O pins, which, together with pins for control signals and power, are a possible compromise. In the current design, five clock cycles are needed to ship data through a node of the tree. This is a result of the four cycles needed to register and synchronize the input and the one cycle to register the output. With the given clock rate, this corresponds to roughly 42 ns. For a tree with depth  $d$ , the latency is  $(d \times 5 + 2)$  cycles.

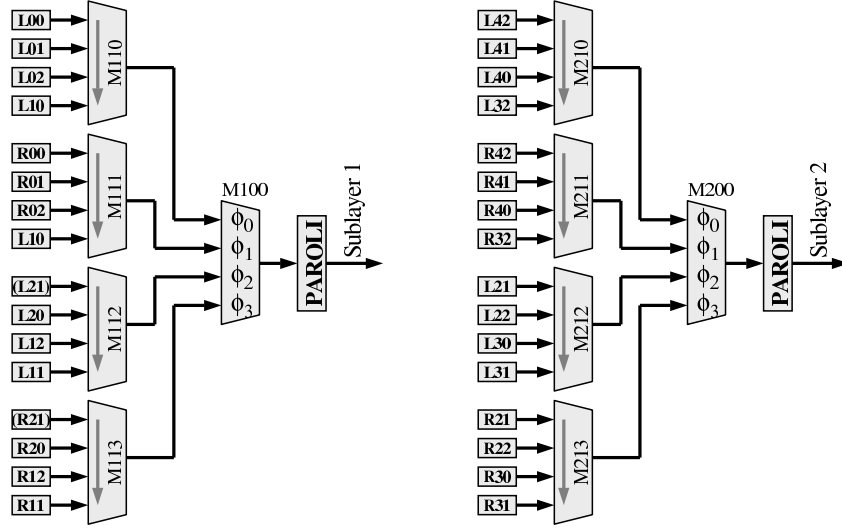


**Figure 7.2:** Tree structure for a layer. The readout boards are labeled in the following way : ABC. A distinguishes between the left and right row in Fig. 7.1. B is the chamber number and C indicates the pad row group inside a chamber. The gray arrows inside the mergers define the readout sequence.

The latency of the readout tree defines the worst case time between the shipment of the first *tracklet* and its receipt by the GTU. During this time no overlapped processing is possible and therefore it should

be kept as short as possible. On the other hand the depth of the readout tree is determined by the fixed number of data sources and the number of links one merger chip can process. The larger the link count of a merger chip is, the larger is its pin count and the more complex is the resulting routing on the readout board. Therefore the number of links and the readout trees latency are competing parameters to be optimized. A large number of scenarios were studied, where the given granularity effects were specifically taken into account. The result is a merger with four inputs and one output.

With the given five ports on a merger chip, a layer is partitioned as shown in Fig. 7.1 and 7.2. The chambers are read out by MCMs grouped together logically on two types of readout boards. These boards can house a maximum of 21 and 25-MCMs, as sketched in Fig. 7.3. One represents two levels and the larger one represents three levels of the tree. The larger sized boards are needed to cover the chambers with 16 pad rows. By ordering the readout sequence, the extra level of the second one can be hidden. As shown in Fig. 7.2, the output of four boards is merged together by the units named Mxxx. These mergers are the same MCMs as used for readout and *tracklet* processing. However the existing LTU functionality is disabled if the MCM is operated in merger mode. On the next tree level the outputs of the previous level are also grouped together by an MCM. The modules M100 and M200 send the data time multiplexed to a gigabit parallel optical link (PAROLI). The PAROLI device is described in greater detail in Section 7.2.2.1.

### 7.2.1.1 The readout logic on the MCM

The readout system is based on two different hardware components. The MCM, configured as readout tree module (Mxxx), and the parallel optical link (PAROLI). Note that LTU and readout tree functionality can be combined on one MCM by enabling both parts of the digital chip. Referring to the left scenario in Fig. 7.3, implementing 21 MCMs, the first four columns (MCM 4...1, 9...6, etc.) implement regular LTU functionality as discussed in chapter 6.3. The outputs of these LTUs are routed horizontally and are terminated at the rightmost column (MCM 0, 5, 10, 15). These MCMs operate both LTU and track merger functionality. Therefore they effectively merge the inputs of five LTUs into their output link. Finally the output links of the four MCM rows are combined by one MCM (sketched as trapezoid), which only operates track merger functionality, keeping its built-in LTU disabled. Therefore this MCM does not add internal data to the data stream like the ones discussed above. The output of the readout boards sketched in Fig. 7.3 form the inputs labelled Lxx, Rxx to the actual readout tree as sketched in Fig. 7.2. The numbering scheme is defined in Fig. 7.1. The subsequent layer of the readout tree implements MCMs in the same configuration. The last stage of the readout tree interfaces to the parallel optical output link (PAROLI) and is discussed in chapter 7.2.2.

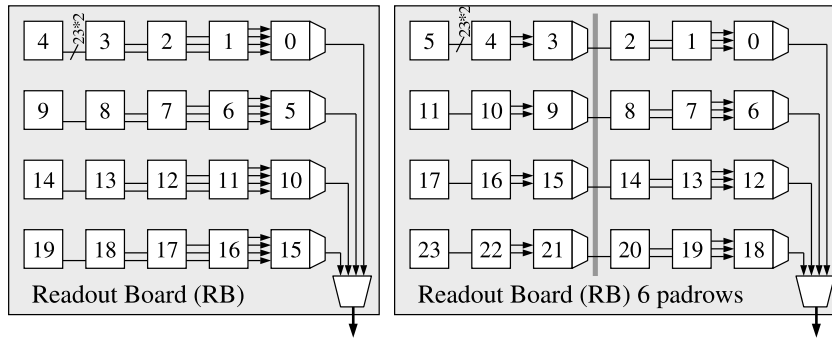


**Figure 7.3:** Structure within the readout boards. The left board represents a two-level tree, which is used for reading out five pad rows. The readout board on the right can handle six pad rows and adds an additional level to the tree.

Fig. 7.4 gives an overview of the data path inside the readout tree module. The ports and tree control are connected to the MIMD *tracklet* processor (TP) as a periphery mapped into the local and global

address space of the processors. Each CPU has a dedicated output interface, which it can serve independently and asynchronously. However it can also access any other port via the global I/O address space. To allow for maximum flexibility, each port is completely independent and the mapping of the ports is determined by configuration registers in the global I/O address space. In addition, the ports are designed for bi-directional use. These architectural measures simplify the layout and routing of the readout boards and their interconnects. Each physical port can be configured to be either input or output. Referring to Fig. 7.3, many MCMs do not fully utilize their available links, which can be used to implement alternate routes in order to implement some degree of fault tolerance.

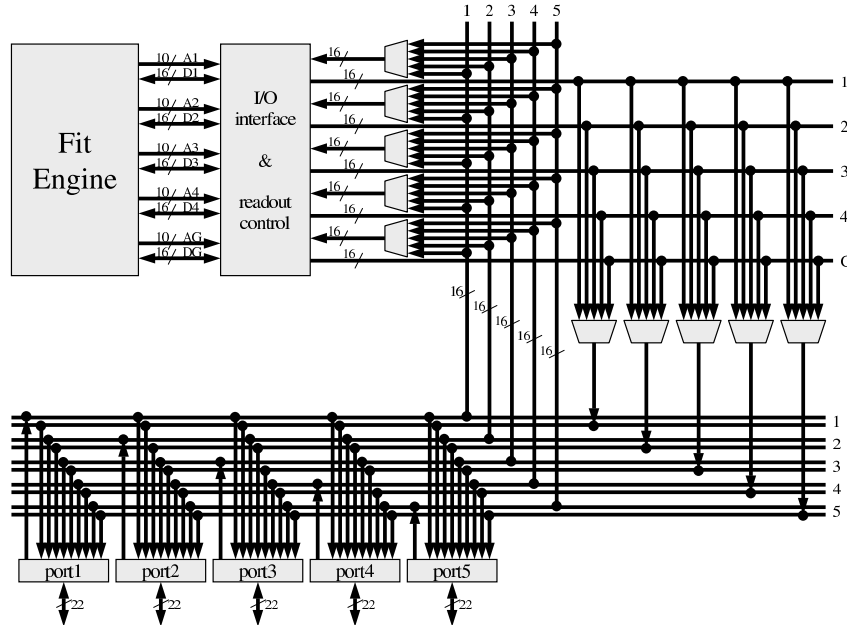


**Figure 7.4:** Data path of a readout module with the five bi-directional independent ports.

A more detailed view of the ports is given in Fig. 7.5. The bi-directional I/O ports synchronize the data of a previous MCM to its internal clock. This increases the latency, but makes a detector wide synchronous data transfer possible. The Hamming en-/decoder, increases the reliability of the system by implementing one-Bit error correction and two-Bit error detection. The Hamming status is evaluated and linked to the outgoing data stream. The physical signals adhere to the LVDS standard. Using differential signals improves the robustness of the system in a noisy environment.

### 7.2.2 GTU link

The link to the global tracking unit (see Chapter 5) is used for both *tracklets* and raw data. A layer, consisting of five chambers, is subdivided into two sublayers as shown in Fig. 7.1. To minimize the length for transmission each sublayer is read out to its closest side of the detector. The data are collected at the root of a readout tree and forwarded to a parallel optical link (PAROLI). This results 216 links off the detector.

#### 7.2.2.1 Parallel optical link PAROLI

The Infineon<sup>1</sup> PAROLI links are parallel optical links for high speed data transmission. A complete system consists of a transmitter, a receiver and a fiber optic cable. A PAROLI link has the following main features:

<sup>1</sup>Infineon Technologies AG, [www.infineon.com](http://www.infineon.com)

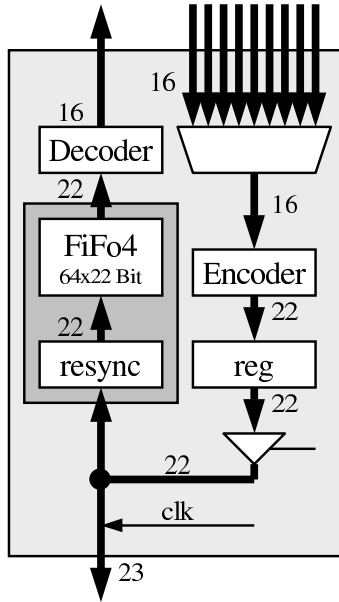


**Figure 7.5:** Bidirectional I/O port, including the Hamming en-/decoder, synchronization unit and input FiFo. The LVDS transceivers are not shown.

- 3.3 V power supply
- Low Voltage Differential Signal (LVDS) interface
- 22 data + 1 clock channel
- 12 optical data channels
- transmission rate of up to 500 MBit/s per channel
- transmission distance up to 75 m at max. data rate

The transmitter (V23814-K1306-M230) features multiplexing and encoding of 22 electrical data input channels to 11 optical data output channels via time multiplexing. It is closely coupled to the readout module, which builds up the root of a sublayer tree and quadruples the data bandwidth.

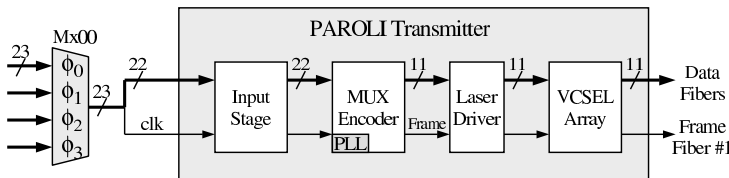


**Figure 7.6:** Interconnection of readout tree and PAROLI link.

The PAROLI link is operated at 4x the MCM readout link. Therefore the readout modules interfacing to the PAROLI will time multiplex their four inputs. Therefore the data of the four inputs correspond to four phases  $\phi_0 \dots \phi_3$  on the PAROLI link. The incoming data arrive at modules M100 and M200 and are being transmitted at the rising edge of the 120 MHz clock. These modules are running with an internal frequency of 480 MHz and forward the data of the four inputs with a 240 MHz dual-edge clock, corresponding to 480 MWord/s, to the PAROLI link. The receiver (V23815-K1306-M230), as front-end of the global tracking unit, generates a synchronous data output with 480 MWord/s, which will be demultiplexed to  $4 \times 120$  MWord/s using another instance of the readout tree MCM, operating in reverse mode.

### 7.2.3 Detector link

Readout of the compressed raw data, which are produced by and read from the local tracking units upon the Level-1 accept (L1A) condition, is triggered by a L2A. At that time the data reside at the TMUs within the GTU. A Level-2 reject (L2R) simply clears the appropriate buffers, which is implemented by advancing the appropriate readout pointers as both Level-1 (L1) and Level-2 (L2) triggers are executed in chronological order within their class and with respect to their associated interaction.

The readout off the detector from the GTU is performed in parallel to any other possible on-going TRD trigger activity, and thus does not contribute to the TRD dead-time except for the derandomizing readout buffer in the GTU threatening to overflow, which can be avoided by making this buffer reasonably large. For example, one 128 MByte DRAM SIMM per detector link will provide space for more than 300 compressed Pb–Pb raw events.

The individual TRD  $\phi$  sectors can be operated independently even at the level of the global track matching (TMU). The only exception is the collection of the summary data for the L1 trigger decision. Therefore, there will be an event buffer as well as a detector link off the detector for each sector. The corresponding aggregate data bandwidth of 1.8 GByte/s allows for a maximum readout rate of 250 Hz, assuming the stated average event sizes. Should this prove inadequate, the number of links per sector can easily be increased by a factor of two, similar to the sublayer readout of the super modules (refer to Fig. 7.1).

One important processing scenario with respect to data analysis within the high-level trigger is the region of interest processing. Those regions are already distributed with a per sector granularity at L1 time. However, the high- $p_t$  track candidates to be validated in the TPC are better defined in the GTU than in their appropriate sector number. Therefore, an appropriate summary event is planned to be compiled containing the track vectors of all identified high- $p_t$  candidates. The data format is comparable to the one used for the *tracklet* candidates, however, implemented as 64 Bit word as sketched in Table 7.1. Only high- $p_t$  tracks with configurable cuts would be shipped. However, even assuming the maximum shipment of all charged particle tracks, together with a TRD efficiency of 100%, it would result in 16k tracks being transmitted with an event size of 128 kB or a maximum L2 accept rate of 780 Hz.

The data required to be uploaded to the TRD are configuration and calibration parameters, such as the defined thresholds and TMU lookup tables. These data objects, however, are to be provided and maintained by the Detector Control System (DCS). It is an essential system requirement that the DCS be independent of any other system such as DAQ or trigger.

A second logical data stream is the uploading of test data for system integrity checking. An independent data path to the front-end will be implemented in order to enable uploading of test data, and to implement an alternate transparent monitoring data path allowing to monitor system integrity even during normal operation. This data path is an ideal method for redundant but slow readout of any TRD sector, allowing simple off line detector testing without the requirement of an operational DAQ or trigger system.

The TRD data link off the detector uses the ALICE DDL, which consists of three major components : the link feed (SIU), which resides within the GTU; the actual optical link itself; and, the optical receiver card (DIU). The interface to the SIU essentially implements a synchronous 32 Bit data bus running at 40 MHz [3].

In order to keep the TRD on-detector electronics as simple as possible, a data driven push architecture is planned. Upon a L2 accept, all available data is formatted and transmitted through the detector links at design speed. The back-end has to be designed to cope with this data stream of up to 100 MByte/s. Such requirement does not present any particular challenge and is also being used for the TPC readout. Given the availability of very large low-cost elasticity buffers at the back end, the latency requirement for the necessary throttling is relaxed. A canonical 1 GByte event buffer there corresponds to 2500 events or more than a minute of running time when running at full speed. Therefore, the necessary throttling can easily be implemented as a single dead-time signal off the detector, generated at one central place by

implementing an appropriate high water mark. No back pressure towards the detectors is being required or implemented as this would only move the throttling and creation of the dead-time signal onto multiple instances of the front-end, requiring their merging into one common TRD dead-time signal. However, the functionality of the DDL allows to implement a back pressure functionality, allowing to throttle the detector front-end. The potential use and implications of this feature will be revisited at a later stage. In any case, the minimal requirement for the DDL is sustained 100 MB/s half duplex throughput.

# 8 The gas system

---

## 8.1 Introduction

The Transition Radiation Detector has an overall volume of  $27.2 \text{ m}^3$  which surrounds the TPC and spans radii between 2.94 and 3.68 m. The detector follows the ALICE segmentation in  $\varphi$  of  $20^\circ$  and a 5-fold segmentation in the  $z$  direction. Each of these 18 supermodules consist of 6 layers (radiator, chamber and electronics) in radial direction, and 5 modules in  $z$  direction. A schematic cross section in the  $r\varphi$  plane of the TRD module arrangement is shown in Fig. 8.1. The total number of gas enclosures in the system is 540. The dimensions of the chambers vary according to their positions in  $r$  and  $z$ , and are typically of order 1 m in  $r\varphi$ , 1 m in  $z$ . The depth in  $r$  is always 3.7 cm. This results in a rather disadvantageous, from the gas tightness point of view, volume-to-surface ratio of 0.017 m. For this reason, special provisions are taken in order to minimise gas leakage (see Chapter 4).

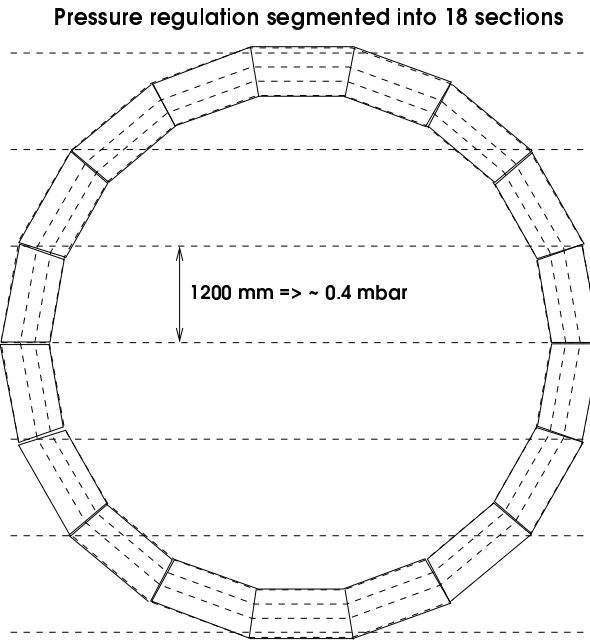


**Figure 8.1:** Schematic view of the TRD in the  $r\varphi$  plane, showing the 18-fold segmentation of individually pressure-regulated sections.

In addition, a low-mass construction of the detectors is needed for minimising electron multiple scattering and TR photon absorption in the materials. The light construction mechanically limits the absolute overpressure of the chambers to 2-3 mbar. In order to avoid electrostatic distortions due to deformation of the enclosing drift and pad electrodes, the overpressure at which the chambers are operated is limited at 1 mbar.

## 8.2 Gas choice

The traditional choice of xenon as the noble gas of the running mixture is determined by its large absorption, and subsequent ionisation, cross section for transition radiation X-rays produced in a suitable radiator material. This effect constitutes the principle of electron identification of such a detector. Because

xenon is a high-cost gas (11.66 CHF/l), the recirculation in a closed loop, the purification, and the recovery of the purged gas is mandatory.

In addition, xenon is a rather heavy gas (density 5.58 g/l). This means that the pressure gradient over a volume which extends over a height of 7.36 m is 2.5 mbar. For reasons of geometrical parallelism of the thin entrance foil and pad plane structure, and of uniformity of operation of the whole system in terms of E/p (see section 4.2), the maximum overpressure in each individual chamber should not be higher than 1 mbar. Thus, a suitable segmentation of the pressure regulation along slices in height of the detector is imposed by the choice of the noble gas.

The typical quencher used in other TRD systems is methane, since its well known transport and quenching properties makes it a rather convenient choice. However, safety, neutron interactions, and lifetime considerations make CH<sub>4</sub> a gas to be avoided. Therefore, the choice of the quencher is CO<sub>2</sub>, because it is non-flammable, it contains no hydrogen, it is a low-cost gas, and it performs adequately. The concentration of quencher is 15% (see section 4.1).

Because the maximum drift distance in a TRD module is only 3 cm, problems associated with electron attachment due to oxygen contamination in the presence of CO<sub>2</sub> are expected to be negligible. Concentrations of O<sub>2</sub> as high as 100 ppm are therefore affordable, since such a contamination would only affect the signal by < 10%. Other contaminants from air such as N<sub>2</sub> will be removed from the mixture in the recovery process (see section 8.3.4).

## 8.3 Layout

As explained in the previous section, the use of a high-cost gas component makes a closed loop circulation system mandatory. The proposed system will consist of functional modules that are designed as standardised units for all LHC gas systems. Table 8.1 indicates the location of these modules. The mixing, purifying, and gas recovery are located on the shielding plug in the pit PX24. The component sizes and ranges will be adapted to meet the specific requirements of the TRD gas system. An overview of the distribution system can be seen in Fig. 8.2. The basic function of the gas system is to mix the components in the appropriate proportions and circulate the gas through the TRD chambers at a pressure of  $\leq 1$  mbar above atmospheric pressure. Some of the basic parameters of the TRD gas system are given in Table 8.2.

**Table 8.1:** Functional modules of the TRD gas system and their location.

Functional module	Location
Primary gas supplies	SGX Building
Mixer	SGX Building
Circulation loop	
Distribution rack	PX24 Pit
Pump	UX24 Pit
Pressure regulation	UX25 Cavern
Recovery	SGX Building

### 8.3.1 Mixing unit

An LHC gas mixing unit, schematically shown in Fig. 8.3, will be used to mix the components in the appropriate proportions. The flows of component gases are metered by mass-flow controllers, which have an absolute stability of 0.3% over one year, and a medium term stability of 0.1% under steady state conditions. Flows are monitored by a process flow control computer, which continually calculates

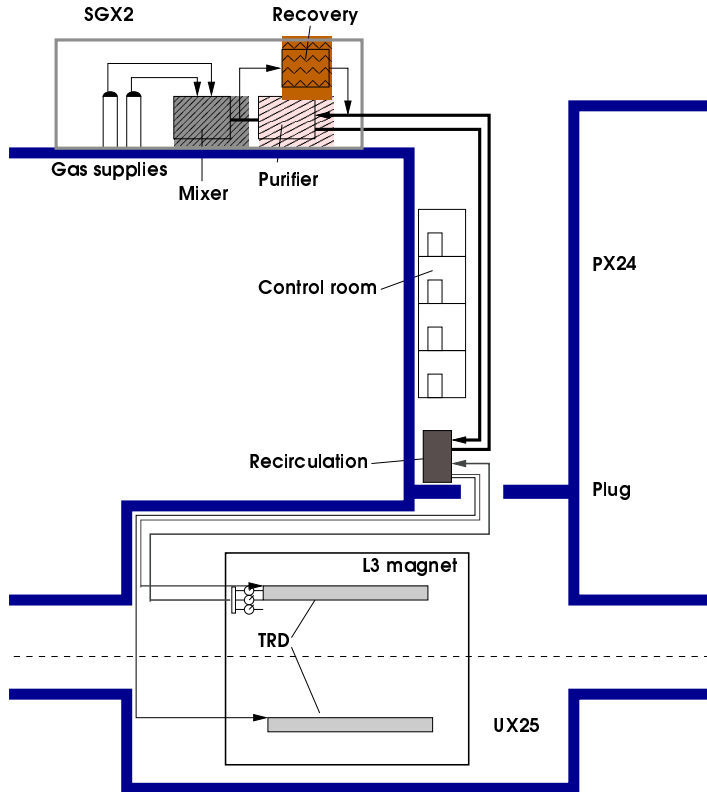


**Figure 8.2:** Schematic layout of the TRD gas system, showing the location of the different modules.

**Table 8.2:** Basic parameters of the TRD gas system.

Max. No. of modules	540
Maximum volume	27.2 m <sup>3</sup>
Gas mixture	Xe,CO <sub>2</sub>
Working overpressure	1 mbar
Filling rate	5 m <sup>3</sup> /h
Circulation flow rate	5 m <sup>3</sup> /h
Operation period per year	8 months

the mixture percentages supplied to the system. The anticipated fresh gas flow at operating conditions, which depends strongly on the leak rate, is expected to be not higher than 0.5 l/h.

Filling of the detector will be done in a closed loop circulation mode, where the purging N<sub>2</sub> gas is gradually replaced by the operation mixture. The separation and recovery of the Xe,CO<sub>2</sub> mixture will be done in the recovery plant. The start up period is estimated to take 11 days for a purification-injection rate of 20% of the total volume, i. e. 5 m<sup>3</sup>/h. Under normal operating conditions the mixing unit will top up the gas which is removed from the system for purification purposes or by losses due to leaks within the circuit.

### 8.3.2 Circulation and purification system

The gas mixture is circulated in a closed loop as has been shown in Fig. 8.2. Return gas from the detector must be compressed well above atmospheric pressure to pump it back to the surface gas building where it will be recycled through the purifier. The pump itself will be located on the shielding plug in PX24.

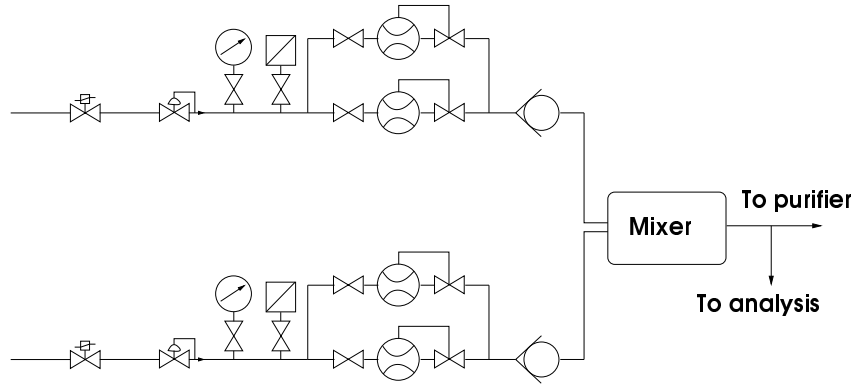


**Figure 8.3:** Gas mixing unit, located in the surface gas building. The substantially different gas flows in the filling and running modes are controlled by two different mass flowmeters per gas line.

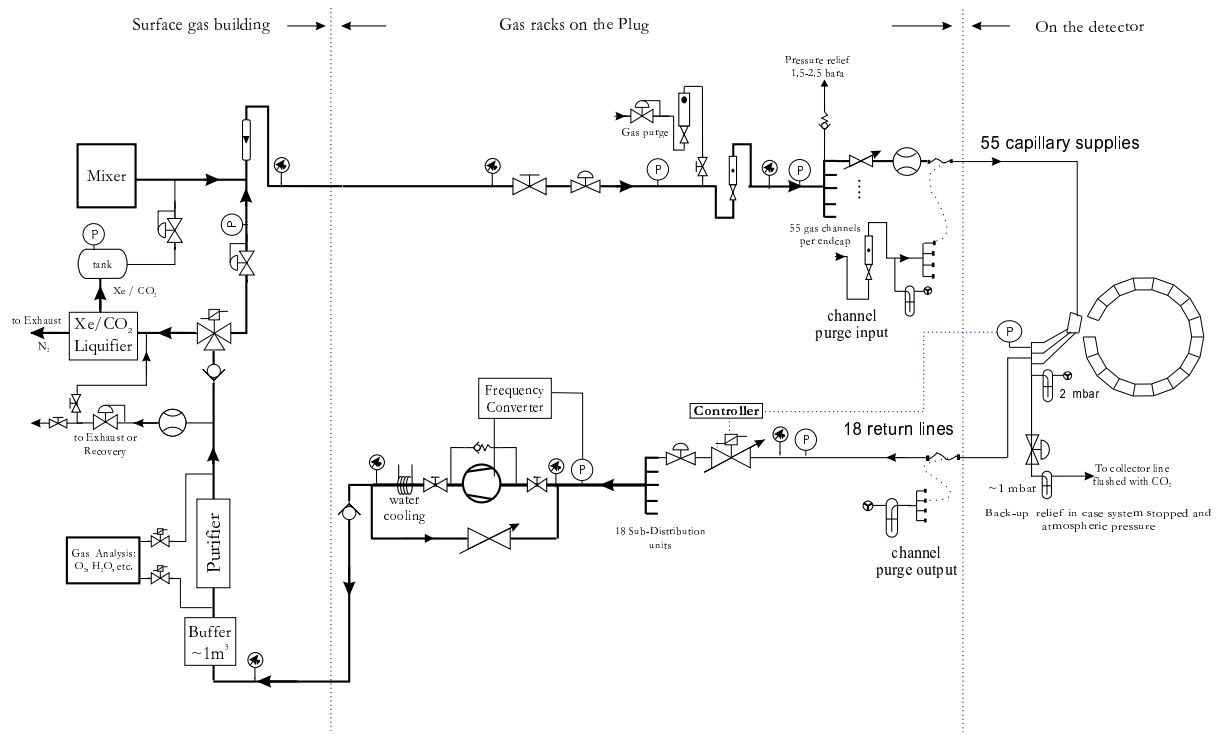


**Figure 8.4:** General layout of the circulation gas loop.

As already pointed out, the hydrostatic pressure over the total height of the detector is 2.5 mbar. Since the detector working pressure is limited, for mechanical reasons, to 1 mbar, a subdivision of the full detector into height sections is necessary. Furthermore, the flow and pressure regulation must be done in each section independently. In particular, the sensor for the pressure regulation must be as close as possible to the detector inlet or outlet, in order to minimise hydrostatic and hydrodynamical pressure differences between the chamber and the sensor. On the other hand, due to space limitations inside and around the L3 magnet, it is desirable to place as much hardware as possible in other areas.

Taking into account these considerations, the following gas distribution into the detectors is proposed and shown in Figs. 8.4 and 8.5: gas in the recirculation unit at the plug (see Fig. 8.2) is distributed through a 54-line manifold where the lines going to the detector are thin enough (4 mm inner diameter) in order

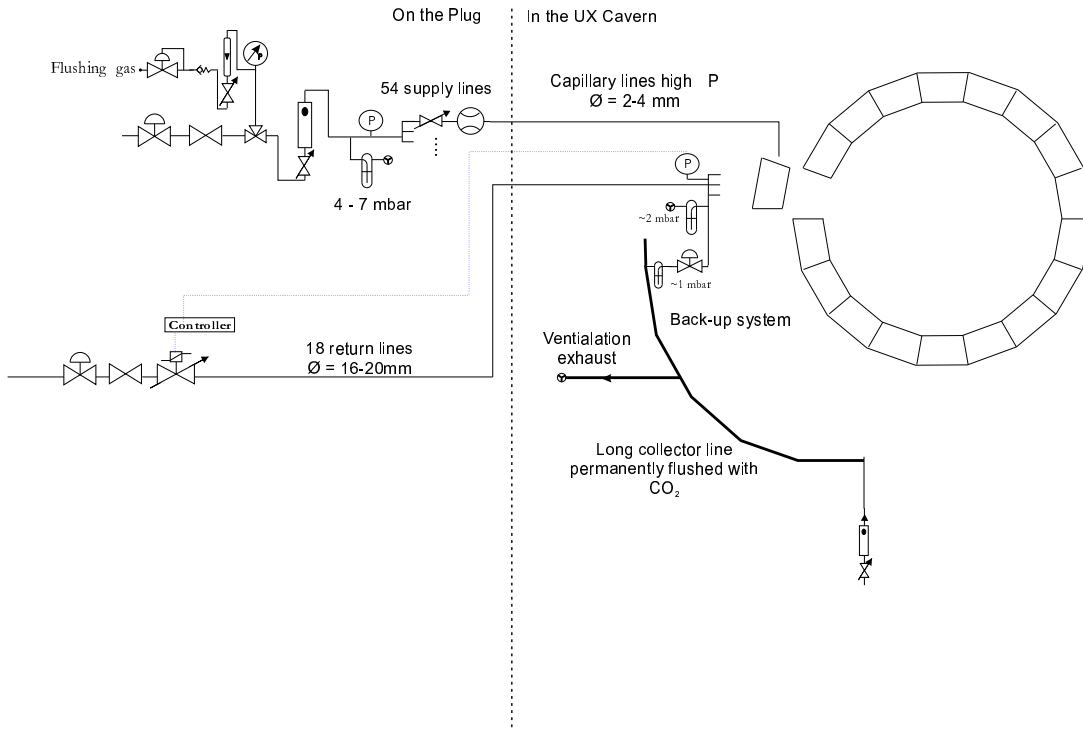


**Figure 8.5:** The distribution of the gas mixture into the 18 sectors of the detector by thin lines, with the flow and pressure regulation, and the back-up system

to achieve a uniform, substantial pressure drop of almost 100 mbar. If all the lines have the same length, the pressure drop in each line will be much larger than the hydrostatic differences between sectors. In this manner, the individual flow regulation can be skipped. Each line serves one set of 10 chambers (two layers back and forth in  $z$  direction) and the pressure regulation sensor is placed at the outlet, thus being the only component inside the L3 magnet. All the other components will be located at the plug.

The feedthrough from chamber to chamber will be a short (3 cm) pipe with an inner diameter of 18 mm, which results in a negligible (0.04 mbar) total impedance to the gas along the 10 served chambers. The pressure regulation will be performed at the outlet of each sub-circuit (three per sector) by placing the pressure sensor near the last chamber. Still inside the L3 magnet a 3-fold manifold will merge the lines from each sector into one 16 mm line. Therefore, a total of 18 outlet lines will run up to an accessible area at the plug, where the rest of the instruments for flow and pressure regulation will be installed. All of these circuits will route into the L3 magnet space from the RB26 side (the side of the muon arm).

The loop pressure regulation is performed by acting on the suction speed of the compressor. A pressure sensor located at the detector outlet drives the reaction mechanism. In addition, gas losses are compensated for by acting on the mixing unit flowmeters according to a pressure sensor located at the high pressure buffer after the compressor. In this manner, the regeneration rate can be chosen anywhere within the range of the mixing flowmeters, and the unrecoverable gas is limited to the leaks.

The purification system will remove, as usual, oxygen and water contamination in the gas. This will be done with cartridges filled with activated copper. A configuration in parallel allows one to run gas through one purification cylinder while the other one is being regenerated. Regeneration is done by heating the cartridges to 200° C under an Ar,H<sub>2</sub>(7%) (Noxal) mixture.

### 8.3.3 Backup system

In case of a malfunctioning of the pressure regulation, for example due to a power failure, the two-way safety bubblers, located near the detectors, shall ensure that the maximum over- and underpressures that

the detectors can stand does not exceed 2-3 mbar. However, this mechanism should be regarded as the ultimate safety for the system. In case of an increase of the atmospheric pressure during such periods, the safety bubblers would allow air to be sucked into the detectors thus deteriorating the purity of the operating gas. The purifiers and the recovery station might therefore get rapidly saturated.

In order to prevent air to enter the gas loop, a backup system for cases of failure has been foreseen. It consists of a permanent flow of CO<sub>2</sub> that circulates to an exhaust which passes by one of the sides of a bubbler. In this manner, positive fluctuations of the ambient pressure results in an enrichment of CO<sub>2</sub> in the mixture, which can be gradually compensated for by the fresh gas injection mechanism as the experiment is restarted. Negative fluctuations of the ambient pressure will lead, in any case, to the loss of some precious xenon. The flow of backup CO<sub>2</sub>, and the expected rate of xenon loss, is estimated from experience to be driven by short maximum pressure fluctuations of 5 mbar/h.

### 8.3.4 Recovery station

Nitrogen, which enters the recirculation loop through leaks, cannot be removed by the purification system. Thus, a separation station is needed in order to extract the N<sub>2</sub> from the system and recover the xenon for recycling. The precise gas purge rate into the recovery unit, estimated to be 0.1% of the detector volume per hour (2.4 l/h), will be determined by the actual leak rate of the system.

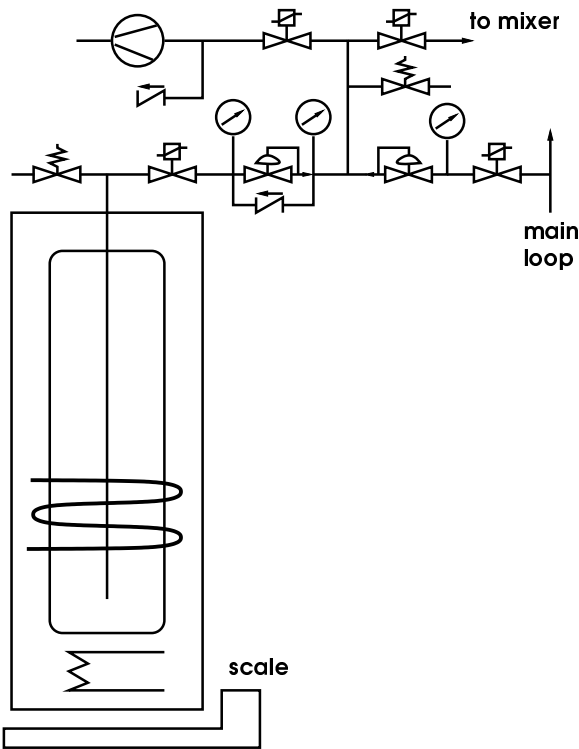


**Figure 8.6:** Schematic layout of the cryogenic plant used to separate the nitrogen from the components of the gas mixture.

The proposed cryogenic recovery unit is shown in Fig. 8.6. Similar concepts have already been used by the NOMAD [1] and ALEPH [2] experiments. The operating principle is based on the selective distillation of the gas by cooling it down to nearly the temperature of liquid nitrogen (LN<sub>2</sub>). Because the freezing point of both the xenon and the CO<sub>2</sub> are above that of the nitrogen, as shown in Table 8.3, by cooling down with LN<sub>2</sub> a storage vessel, one can freeze both the xenon and the CO<sub>2</sub> as the gas enters the

vessel, while still keeping the nitrogen in the gas phase. A scale that weighs the vessel is used to control the amount of gas that enters the vessel. Once the desired amount - such that at room temperature the pressure would not exceed 200 bars - has been frozen, the gas left in the vessel is pumped and vented out until the pressure drops to essentially zero. Then, the vessel is brought back to room temperature. The time-pressure diagram corresponding to this operation is shown in Fig. 8.7. One can see the shoulders at which condensation and evaporation of the gas components take place as the temperature cycles down and up. The non-volatile component, namely the nitrogen, is pumped out at 60 min. This method, which accounts for no loss of xenon, results in a nitrogen-free mixture, although at some loss of CO<sub>2</sub>. When the mixture is injected back into the loop, appropriate monitoring of and compensation for the loss of CO<sub>2</sub> will take place by injecting fresh quencher according to the reading of a dedicated CO<sub>2</sub> analyser.

This procedure will be carried out in parallel by doubling up the recovery vessel, such that while one vessel is being filled, the second one is used to feed gas into the loop. The frequency at which the recovery cycle has to be carried out depends strongly on the actual leak rate of the detector.

The recovery vessels will be filled up to the equivalent of 100 bars in a 9 m<sup>3</sup> bottle. For this purpose, the vessels will be cooled down with LN<sub>2</sub> as the gas enters it, such that a normal compressor can be used. This operation may require that the temperature cycle is repeated twice, since the freezing of the mixture in a turbulent regime may lead to trapping of some nitrogen into the condensed gas.

We consider the possibility to reuse an existing recovery plant which has been used in the ALEPH experiment for the same purpose and with the same gas mixture. We now have this plant in hand. Although conceived to work in a double temperature cycle for distilling the pure Xe, it has actually been used in exactly the same manner [3] as we propose in this document and have tested in a small set-up.

**Table 8.3:** Freezing and boiling points, in ° C, of some gases relevant to the present gas system.

Gas	Freezing point	Boiling point
N <sub>2</sub>	-209.86	-195.8
Xe	-111.9	-108.1
CO <sub>2</sub>	-78.4 (subl.)	

## 8.4 Gas distribution pipework

All pipes and fittings in the TRD gas system will be made of stainless steel. The pipes will be butt-welded together to reduce the possibility of contamination and leaks to a minimum. Existing gas pipes at point 2 will be reused as far as possible. Table 8.4 shows an overall view of the main piping parameters. A total of 54 pipes run from the plug into the detectors, all on the RB26 side, left and right of the TRD.

**Table 8.4:** Main piping parameters.

	Number of pipes	Pipe inner diameter [mm]	Pipe length [m]	Nominal flow [m <sup>3</sup> /h]	Reynolds number	Pressure drop [mbar]
SGX building to plug	1	73	90	5	5052	.12
Plug to RB26 side	54	4	100	0.1	1893	97
RB26 side to plug	18	16	100	0.28	1325	1.1
Plug SGX building	1	73	90	5	5052	.12

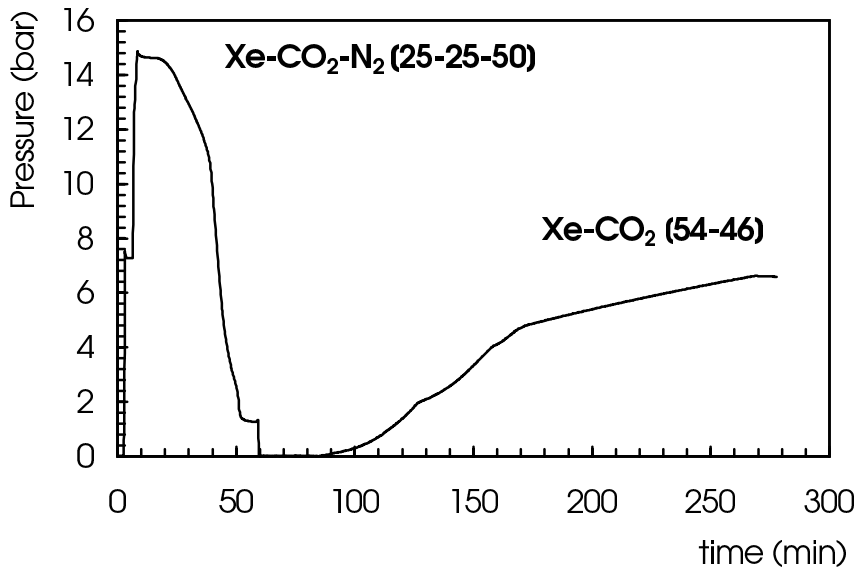


**Figure 8.7:** The evolution in time of the pressure of a Xe-CO<sub>2</sub>-N<sub>2</sub> gas mixture as it is cooled with LN<sub>2</sub>. At 40 min solidification of CO<sub>2</sub> takes place, followed by the xenon at 50 min. At 60 min the gas (nitrogen) left in the sample bottle is pumped out and the LN<sub>2</sub> flow stopped until the mixture returns to the gas phase. The gas was analysed with a mass spectrometer gas chromatograph system before and after the cryogenic treatment.

## 8.5 Prototype

A prototype gas system has been designed in collaboration with the CERN ST/CV group and built by Tecnodeelta (Italy). The schematic layout in its present configuration is shown in Fig. 8.8. This gas system is being used in the current test beam experiments. Because the prototype chambers used so far have only a few liters gas volume, the gas is made to flow through the detector prior to entering the loop, where a higher circulation flow is best adapted to the strong pump of the system. The gas is then stored in a recovery bottle where the cryogenic cycle, described in section 8.3.4, takes place. The detectors under test can be included in the recirculation loop whenever their size and number increases. First operation of this gas system, at the test beam in spring 2001, has shown adequate performance both in terms of gas tightness and overpressure regulation of the gas in the test detector at the 0.1 mbar level.

It is intended to reuse both the principle of operation and most of the parts of this gas system for the final one. The manual valves will be replaced by remote-controlled ones (or completed with remote-controlled turning devices) and the manifolds and subsequent flow and pressure regulation hardware will be added, which will account for most of the cost. In addition, two more extra compressors, one of them being spare, will be added in order to be able to pump the gas from the plug to the surface and fill the recovery bottles at the required flow.

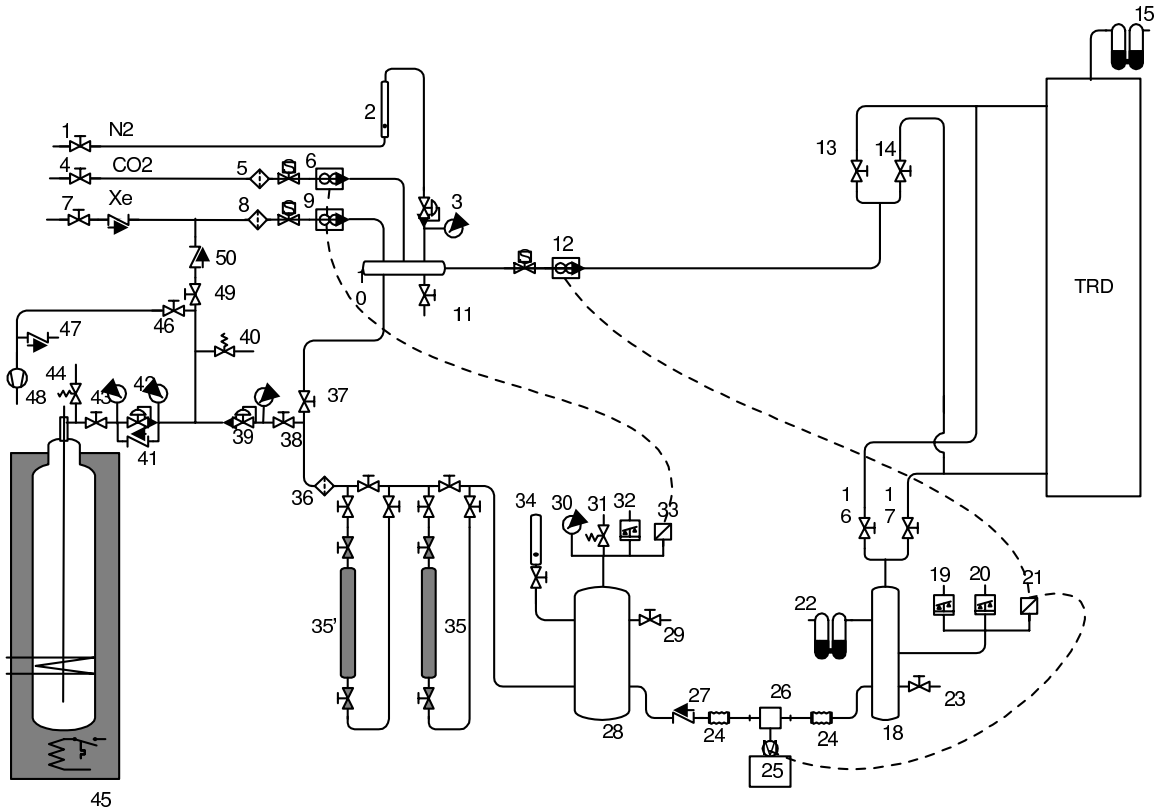


**Figure 8.8:** Layout of the gas system prototype used for the current TRD tests. For small detector volumes, the chamber is placed outside, upstream of the loop and the recirculation is regulated only by automatic tuning of the compressor speed. A fraction of the gas, equal to the fresh gas injected into the system, is pumped into the recovery bottle. The configuration shown in the figure corresponds to the case of larger detector volumes. The flow is regulated by acting both on the compressor speed (25) and on the loop main flowmeter (12) so as to keep the detector overpressure to the value set at the outlet pressure sensor (21). Leaks, if existing, are sensed at the high pressure vessel at the compressor output by the corresponding sensor (33), which opens the fresh gas injection flowmeters (6 and 9) whenever necessary. In order to keep the electrical complexity of the system low, all valves are manual.



# 9 Services

---

## 9.1 Low voltage power distribution

The TRD electronics is located on the readout plane of each chamber. Low voltage has to be distributed to these areas of the detector to power the multichip modules (MCM), see Chapter 5. Two possible solutions are being considered for supplying power to the detector front-end electronics, inside the L3 magnet:

- power supplies located outside the magnet, in the experimental hall, delivering the required voltage and current directly to the load. In this case the power cable conductor cross-section must be large enough to limit the voltage drop, and cable bulk as well as copper conductor weight are major concerns;
- DC-to-DC converters placed inside the magnet and close to the load. In this case the cross-section of the input power cables can be significantly reduced. However the converters must be able to operate in the magnetic field up to 0.5 T, either by shielding or by using a special design. The possible effects of radiated or conducted noise from the switching supplies need to be understood. Moreover, the reliability constraints are increased since access for maintenance is very limited.

In both cases low-drop voltage regulators are installed on the electronics boards. The first solution has been worked out in detail and is presented here. The second one is being investigated.

### 9.1.1 Requirements

The low voltage system must deliver a large current (about  $\sim 18\text{kA}$  in total for Pb-Pb collisions) at 3.3 V and 2.5 V. For noise isolation, the power will be distributed separately for the preamplifier/shaper (analog-1), ADC/filter (analog-2) and digital parts (digital-1). Low-drop linear regulators installed just before the electronics are used to regulate the bias voltage. The power supply requirements, expected currents and resulting power are summarized in Table 9.1. The numbers are calculated using  $0.35\ \mu\text{m}$  technology for the preamplifier/shaper and  $0.25\ \mu\text{m}$  technology for the ADC and digital components, see Chapter 5.

**Table 9.1:** Power supply requirements of the electronics. V: required voltage.  $P_{ch}$ : Power consumption per channel.  $P^{total}$  and  $I^{total}$ : Total power and total current required by the electronics.  $P_{reg}^{total}$ : Total power dissipated in the low-drop linear regulators. The numbers are based on  $1.16 \times 10^6$  channels and the expected trigger rates for Pb-Pb and p-p collisions.

	V(V)	$P_{ch}(\text{mW})$	$P^{total}(\text{kW})$	$I^{total}(\text{A})$	$P_{reg}^{total}(\text{kW})$
analog-1(PASA)	3.3 V	10	11.6	3503	1.4
analog-2(ADC,filter)	2.5 V	27.4	31.7	12690	5.2
digital-1 <sup>Pb-Pb</sup>	2.5 V	1.1	1.2	1515	0.6
digital-1 <sup>p-p</sup>	2.5 V	11.9	13.7	10139	4.2

For the digital part the power consumption and required currents depend on the trigger rate, the numbers for both Pb-Pb collisions (10 kHz and 1 kHz L1A, see Section 1.2) and p-p collisions (150 kHz and 5 kHz L1A) are quoted but the p-p values are taken for the design. The power in the analog parts

is constant. For example, doubling the trigger rate increases the total power consumption only by 3% but the required current in the digital-1 supply by 68%. The maximum power consumption is 49.3 mW/channel for p-p collisions. Taking into account the total amount of channels of  $1.16 \times 10^6$  and the power dissipated in the regulators, the total power dissipated by the electronics is 67.8 kW (51.7 kW for Pb-Pb collisions).

### 9.1.2 Low voltage power supplies and cables

The low voltage system will be subdivided into independent low voltage channels. The actual number of LV channels is a compromise between cost and performance. Each of them will power a complete layer, that corresponds to 5 chambers. This means a total of  $3 \times 108$  cables (analog-1, analog-2 and digital-1) and their respective return lines. The power supplies will be located outside the L3 magnet (UX25 cavern) on both sides of the detector (RB24 and RB26) in an area not accessible during LHC operation. In this scenario a cable length of about 31 m is needed, 15 m from the power supplies to the magnet and 16 m from the magnet up to the distributing ring and all the layer length. The cables will pass through the L3 magnet doors, at about half the height of the detector.

**Table 9.2:** Characteristics of each cable (c) for a low voltage system based on 108 channels and trigger rate as corresponding to p-p collisions.  $I_c$ : Current carried in each cable. S and  $L_c$ : Cross section and length of each cable.  $W_c$ : Cable weight,  $R_c$ : Cable resistance.  $P_c^{total}$ : Total power dissipated on the cables.

	V(V)	$I_c$ (A)	$S \times L_c$ (mm <sup>2</sup> × m)	$W_c$ (kg)	$R_c$ (mΩ)	$P_c^{total}$ (kW)
analog-1	4.3 V	33	(58 × 15 + 31 × 16)	12.3	17.7	4.2
analog-2	3.5 V	121	(211 × 15 + 113 × 16)	44.6	4.9	15.4
digital-1 <sup>Pb-Pb</sup>	3.5 V	14	(25 × 15 + 14 × 16)	5.3	41	1.8
digital-1 <sup>p-p</sup>	3.5 V	96	(169 × 15 + 90 × 16)	35.6	6.1	12.2

The cable characteristics, summarized in Table 9.2, are selected as a compromise between voltage drop, power dissipation and cross section. The p-p scenario has been used for the design. Cables are designed with two widths, one part of 15 m length from the power supplies up to the L3 magnet. This selection is done to minimize the power dissipation in a region where there is no space limitation. The other part, of 16 m length, from the magnet doors to the detectors where the width is reduced to the half to fit into the available space (see Fig. 9.1). With this design the voltage drop in the cables is 0.59 V and the total surface occupied for the bare cables is 505 cm<sup>2</sup>. The total weight of such Cu cables is about 19 t. In addition to the 505 cm<sup>2</sup> some space has to be considered for isolation and cooling of the cables, since the total power dissipated on the cables is 21.4 kW for Pb-Pb collisions and 31.8 kW for p-p collisions (see Table 9.2). If we account for a voltage drop of 0.59 V along the cable and of 0.4 V for the local regulation, the power supplies should provide 4.3 V and 3.5 V, respectively.

A schematic layout of the low voltage system is shown in Fig. 9.1. The power supplies are floating. The return lines are connected to the front-end detector ground. The low voltage system as previously described presents some disadvantages with regard to cable cost and heat losses in the cables, and also to the space occupied by the cables passing through the L3 magnet doors. Therefore, an alternative scheme based on delivering the power at a higher voltage (48 V) and converting it to the required one very close to the detector is also under consideration. Inside the L3 magnet in the distributing ring two types of Vicor DC-to-DC converters (V48B3V3C150A and V48A3V3C264A, for example) could be used for voltage conversion. It still needs to be proven that these devices can work inside the L3 magnet. Some calculations [1] show that a magnetic shield of 2-3 cm will be needed to have acceptable attenuation of magnetic field densities of 0.4 T. As the amount of converters is not negligible, the distortions created inside the L3 magnet need to be studied. On the other hand, other companies like CAEN are also developing DC-to-DC converters which could in principle work in magnetic fields. Recently, a prototype

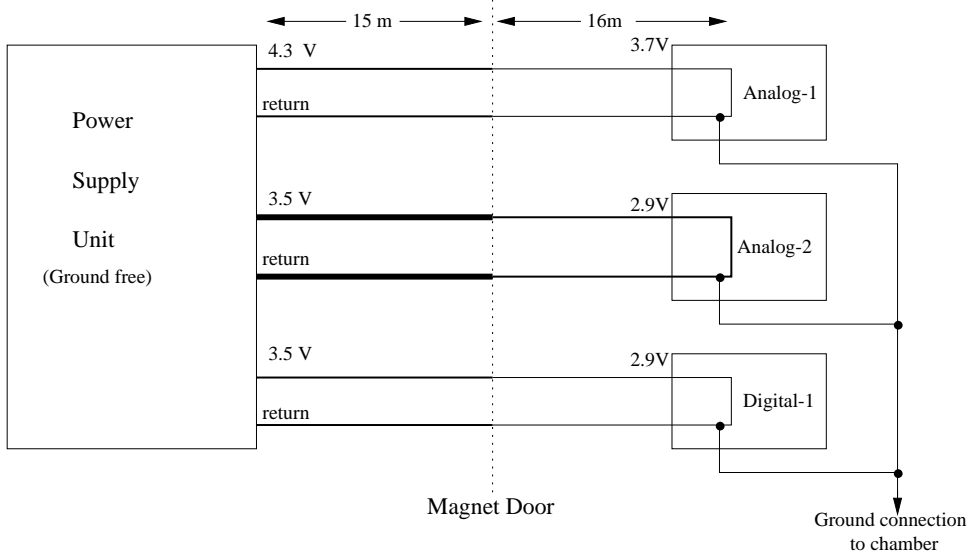


**Figure 9.1:** Connection of low voltage power supplies to electronics

has been tested at CERN showing a good behaviour up to 0.18 T. Higher values of magnetic field were not available during the test. A second test in a magnetic field up to 1 T has also been done. The device showed a behaviour according to specifications up to 0.5 T. After proper operation at 1 T some components failed. As the principle of operation of the prototype is proven to work, the company plans to work on improving its reliability.

### 9.1.3 Layout

#### 9.1.3.1 From power supplies to each chamber

The low voltage power cables will come from the power supplies to both sides of the detector through the L3 magnet doors. The cable configuration through the magnet doors can be seen in Fig. 16.2. The cables will have a connector at the distributing ring to be able to disconnect from the supermodule for maintenance. A flexible cable might be foreseen there.

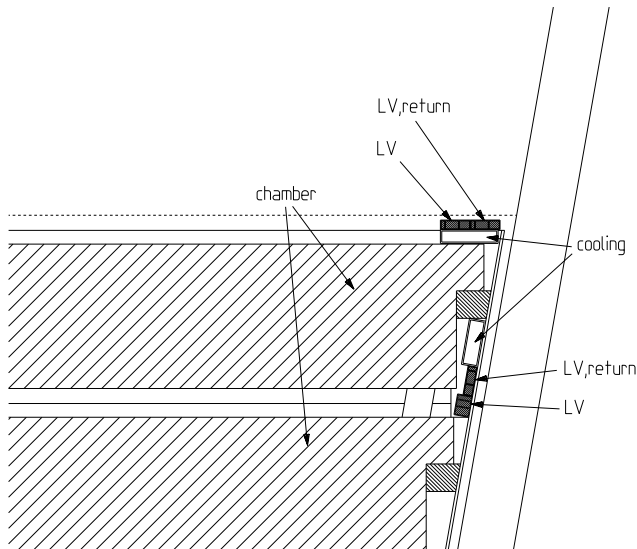


**Figure 9.2:** Routing of the low voltage power cables along a layer.

In order to avoid current loops in the detector the power cables and their respective return lines will be routed in the same side of the layer. In addition, the chamber readout PCB is split into two  $\varphi$  sections, the power to each layer will come from both  $\varphi$  sides. To keep the number of LV channels constant at 108, each cable will be split into two at the level of the distributing ring. The space between the chamber holder and the supermodule case will be used to route the cables along  $z$  in each layer, see Fig. 9.2. The cables will supply the voltage to the chamber underneath. This part of the cable also needs cooling.

### 9.1.3.2 Inside the chamber

Depending on the chamber position and the layer the MCMs in a chamber are organized in rows of 4+4 MCM each making a total of up to 76 rows per layer. Each cable will have up to 76 connections consisting of a low-drop voltage regulator and 4 MCMs connected in series. The 4 MCMs will also be connected in series for the return line cable. The power distribution scheme inside a chamber is depicted in Fig. 9.3.

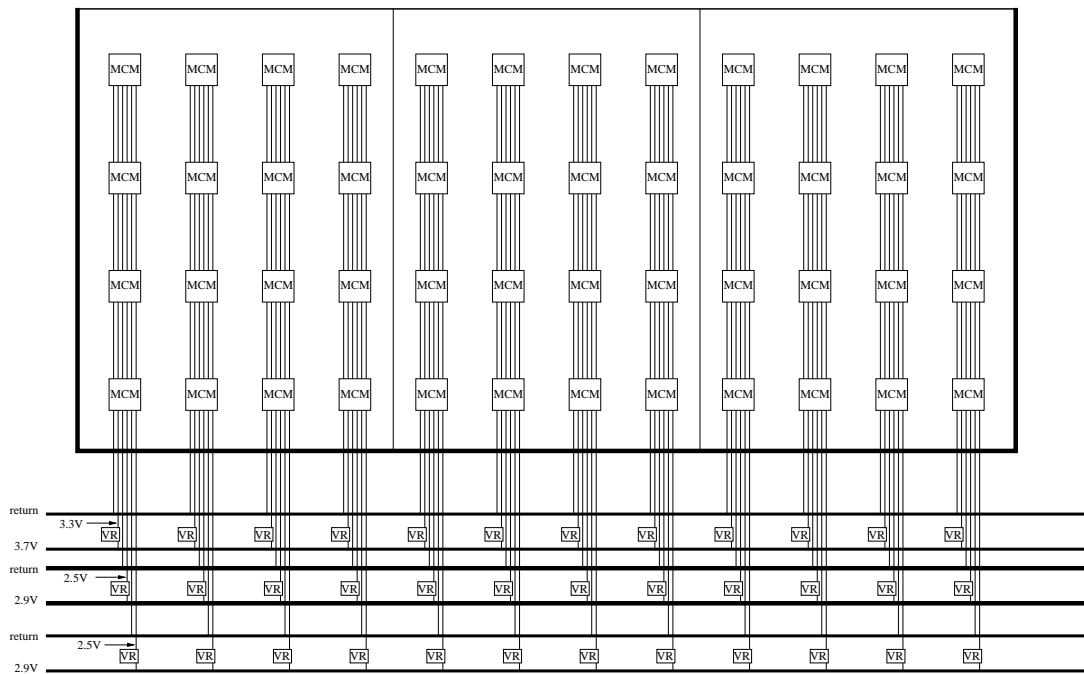


**Figure 9.3:** Routing of the low voltage power cables in the readout plane (only half chamber is depicted) to power each of the MCM rows. The cables along a layer are also shown.

Each of the MCM rows in the chamber will receive the necessary power from the low voltage power cables running along  $z$  on both sides of the layer. Cables up to 0.61 m length for the largest chamber will be necessary. Assuming that 20% of the chamber plane is covered by Cu, the width of the power lines could extend up to 0.8 mm, 4.0 mm and 2.7 mm for analog-1, analog-2 and digital, respectively, with a standard thickness of 34  $\mu\text{m}$ . The return lines are designed with the same parameters. With these characteristics a voltage drop of 113 mV, 82 mV and 97 mV can be expected in the worst case. The power dissipated in these traces will be 27.7 W per layer for Pb-Pb collisions (45.9 W per layer for p-p collisions), i.e. adding 4.7% to the total heat dissipated in a layer.

## 9.2 High voltage power distribution for drift field

The high voltage distribution for the drift field will be done according to chambers. The total number of HV channels is 540. Each channel should be independent in terms of voltage setting, current limit, ramp

up and down, switching on and off and monitoring of current and voltage.

### 9.2.1 Requirements

In order to create the necessary drift field a high voltage of -2.1 kV is needed (See Chapter 4). The ripple has to be kept smaller than 50 mV peak to peak and the stability should be better than 0.1% over 24 hours.

### 9.2.2 High voltage power supplies

The power supplies should be able to deliver up to -3.5 kV with a current of up to  $500 \mu\text{A}/\text{channel}$ . These values contain already a safety margin compared to nominal running conditions. The high voltage power supplies will be positioned on both sides of the detector (RB24 and RB26) outside the L3 magnet in the UX25 cavern. A total length of about 60 m is anticipated between the high voltage power supplies and the detectors. A  $42 \Omega$  cable type HTC-50-1-1 (standard CERN) can be used (in accordance with IS23 regulations) from the power supplies to the detector. This HV cable is 3.30 mm in diameter, leading to a total cross section of  $540 \times 0.086 \text{ cm}^2 = 46.2 \text{ cm}^2$  for all 540 cables.

### 9.2.3 Layout

The cables will be grouped together, passed through the L3 magnet doors, and brought up to the distribution ring. A connector is foreseen there in order to be detachable from the detector for maintenance. The cables will then be separated in order to power the individual field cages, see Fig. 4.7. Consecutive  $\phi$ -sectors will be powered from opposite sides of the magnet.

## 9.3 High voltage power distribution for readout chambers

The anode wire plane of each chamber will be supplied with HV independently. The total number of individual HV channels is 540. Such granularity is important in case of failure, because it reduces the affected area to one chamber.

### 9.3.1 Requirements

The anode wires need a voltage of around 1.7 kV in order to reach the required gas gain. (See Chapter 4). The ripple should be smaller than 50 mV peak to peak and the stability better than 0.1% over 24 hours.

### 9.3.2 High voltage power supplies

The power supplies should be able to deliver up to 2.5 kV with a maximum current of about  $40 \mu\text{A}/\text{channel}$ . These numbers contain already a safety margin compared to nominal running conditions. The high voltage power supplies will be positioned on both sides (RB24 and RB26) of the detector outside the L3 magnet (UX25 cavern). A total length of about 60 m is anticipated between the high voltage power supplies and the detectors. A  $42 \Omega$  cable type HTC-50-1-1 (standard CERN) can be used (in accordance with IS23 regulations) from the power supplies to the detector. The diameter of this cable type is 3.30 mm, leading to an area of  $540 \times 0.086 \text{ cm}^2 = 46.2 \text{ cm}^2$ .

### 9.3.3 Layout

The cables will be grouped together, passed through the L3 magnet doors, and brought up to the distribution ring. In order to be detachable from the detector a connector is foreseen there. The cables will then

be separated in order to power the anode wire plane of each individual chamber. Consecutive  $\varphi$ -sectors will be powered from opposite sides of the magnet.

## 9.4 Cooling distribution

### 9.4.1 Requirements

The TRD cooling system needs to remove a large amount of heat (up to 76 kW for Pb-Pb collisions and up to 105 kW for p-p collisions). A large part of it, 64.1 kW and 86.7 kW respectively, are generated inside the supermodules by the front-end electronics and low voltage distribution inside the supermodules. This heat is dissipated over a large area  $\sim 800 \text{ m}^2$ . The 6 layers are separated by only about  $\sim 4 \text{ mm}$ . These factors determine the choice of the cooling agent to be demineralized water. Forced air cooling technique has also been considered for its obvious advantage of introducing no additional material within the TRD acceptance. Calculations have shown that effective cooling cannot be achieved with such an approach without applying prohibitively high air pressure on the cathode planes of the detectors. Moreover, the configuration of the TRD and other ALICE subsystems make it difficult to introduce an air supply duct of large cross-section required for the air flow. Water cooling will be free of these limitations and will provide effective cooling with relatively little material. The second generation Leakless Liquid Cooling System (LCS2) has been selected. This type of system has been successfully used by other experiments at CERN (CERES/NA45, NA49) and at BNL (STAR) and has been proposed for other LHC experiments as well (ALICE TPC, ATLAS calorimeter and CMS pixel detector) [2, 3].

### 9.4.2 Description of cooling system and layout

The scheme of the cooling system developed in collaboration with the CERN/ST/CV group is depicted in Fig. 9.4. The main parameters of the cooling system are described in Table 9.3.

**Table 9.3:** Main piping parameters of the cooling system based on the heat dissipation for Pb-Pb collisions. The pipe profile inside a supermodule along  $z$  is chosen to be rectangular to fit in the available space. The equivalent diameter assuming a cylindrical pipe is quoted.

	Number of pipes	Material	Inner diameter (mm)	Length (m)	Nominal flow	Pressure drop (mbar)
RB26 to L3 magnet	1	polyethylene	60	30	19.3 $\text{m}^3/\text{h}$	
return	1	polyethylene	60	30	19.3 $\text{m}^3/\text{h}$	
magnet to supermodules	18	polyethylene	20	15	1.1 $\text{m}^3/\text{h}$	
return	18	polyethylene	20	15	1.1 $\text{m}^3/\text{h}$	
supermodules to layers (along $z$ )	108	inox	20	7	178.3 l/h	29
return	108	inox	20	7	178.3 l/h	29
layer to MCM	2736	Al	2	5.6	6.9 l/h	267

The cooling system will be positioned on one side of the detector (RB26) outside the L3 magnet (UX25 cavern). Each of the 18 sectors will be supplied and controlled independently. This scheme presents the advantage of easier regulation and control. Moreover, the pressure regulators used to maintain the pressure below the atmospheric can be positioned outside the magnet avoiding the use of special equipment. Flow regulators instead of pressure regulators might be considered. Each of the 18 circuits will supply cooling water to the 6 layers in a supermodule. The cooling liquid is kept in the storage tank

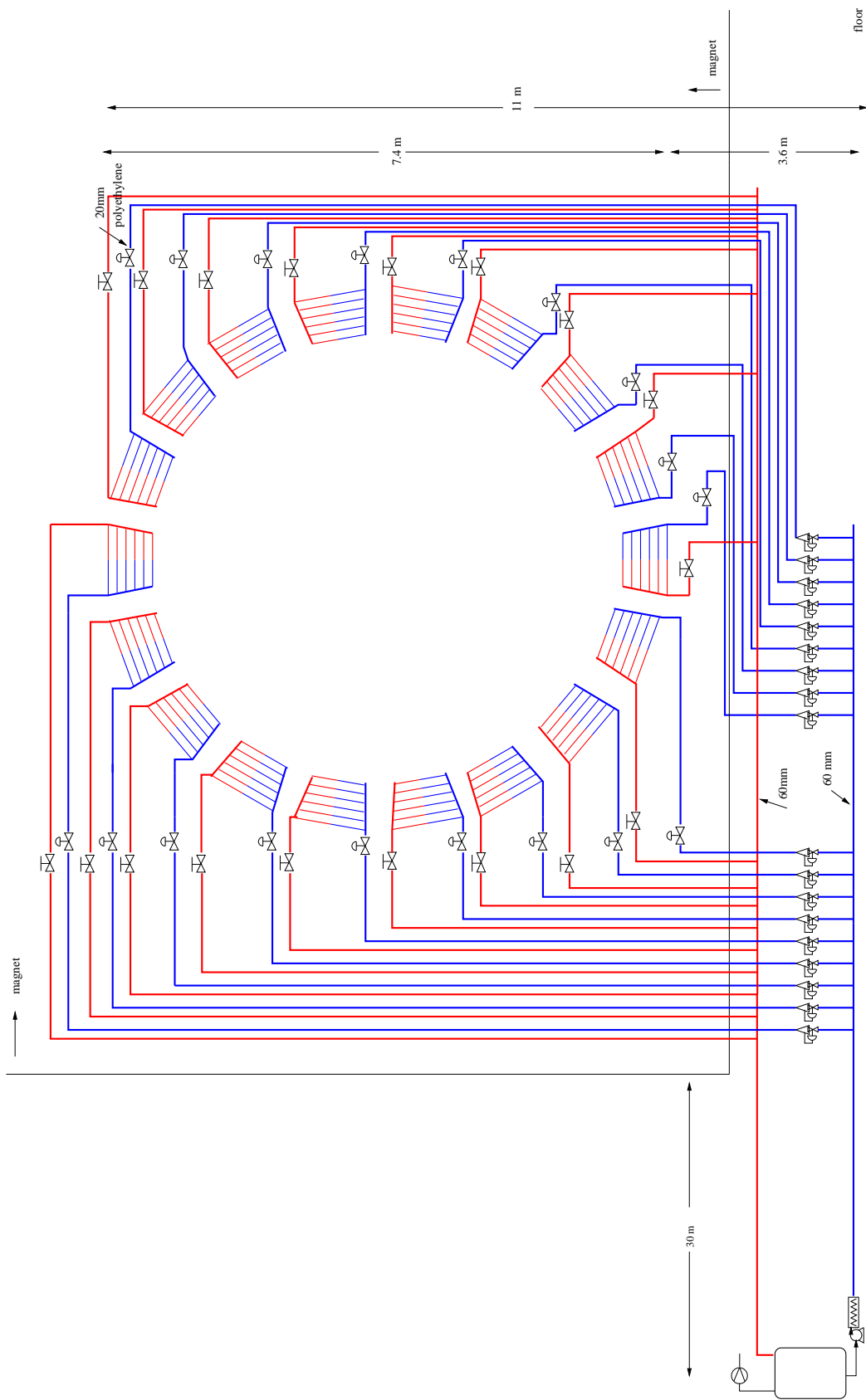


**Figure 9.4:** Water cooling system scheme based on sector distribution.

positioned at the lowest point of the system at a distance of about 30 m from the L3 magnet. The liquid is moved by a circulator pump into the heat exchanger cooled by chilled water from the CERN network. Two main pipes 60 mm diameter made of polyethylene, with cold and warm water respectively, bring the water from the tank to the base of the magnet and vice versa. From the base of the magnet 18 pipes of 20 mm diameter each pass through the magnet doors and bring the water to the sectors. On the return side the 18 pipes pass through the magnet doors and are collected together outside the magnet. In the present scheme, it is foreseen to provide the cold water in the lowest point of each sector and to collect the warm water on the highest point in order to have more homogeneous water flow in all pipes. Each circuit has a valve at the input and at the output at the level of the distributing ring to be detachable in case of maintenance. One of them is pneumatically controlled to be able to stop the water flow in case of problems during running time. At the input of the pressure regulators the pressure is above atmospheric pressure. The regulators adjust the pressure in the individual lines to a value that is below atmospheric pressure. They also guarantee that in all subsections of the cooling circuit a value below atmospheric pressure is maintained. Any leak in these lines and connections will not lead to a leak of cooling liquid. A vacuum pump in the return line sustains a pressure below atmospheric pressure and discharges any excess air collected.

#### 9.4.2.1 Water distribution to the layer

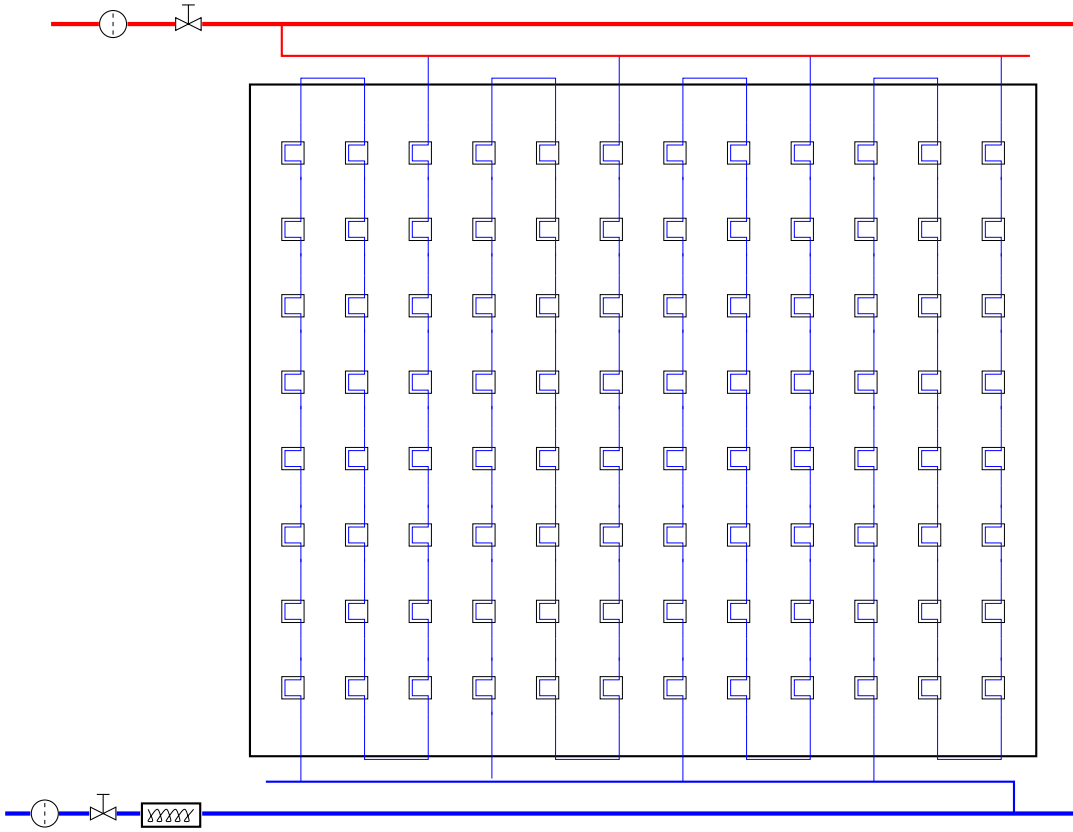


**Figure 9.5:** Main distribution of cooling water in a layer. For simplicity only one chamber with 12 rows is shown.

The layer subcircuit consist of 2 main rectangular pipes (20 mm equivalent diameter) along  $z$  made of stainless steel, see Fig. 9.2 and Fig. 9.5. Their function is to supply water to the individual pipes running in  $\varphi$  across the chamber where the heat sources are and to serve as a collector for the warm water. The flow in these pipes is turbulent. The pressure drop for a turbulent flow of 179.3 l/h (see below) in a straight pipe of 7 m is of about 29 mbar. The space between chambers and the supermodule casing will

be used to route the cooling pipes, see Fig. 9.2. Each layer has a heater to regulate the water temperature and a filter to avoid impurities coming into the system. Each layer also has a manual valve to be able to close individual layers independently during tests. As the pressure drop along  $z$  is negligible with respect to the one across  $\phi$  the water input and output can be on the same side.

#### 9.4.2.2 Water distribution inside the layer

The readout boards will be designed such that the components radiating most of the heat (MCMs) will be aligned. Each MCM will be covered by a thin plate of Al for good thermal contact. An Al tube of 2 mm diameter will run across  $\phi$ , to take away the heat produced in a row of MCMs (see Fig. 9.5). The path of the water pipe on the Al plate corresponds to approximately three times its width in order to increase the heat transfer to the water. The water flow in these pipes will be 6.9 l/h, and the flow is laminar. Three rows will be connected together to have a large pressure drop in  $\phi$  and to reduce the number of connectors. As the number of rows in a chamber is not a multiple of 3, rows of different chambers will be connected together. The temperature difference between input and output of the small pipes is 3 degrees for the flow of 6.9 l/h. However, as the warm and cold lines are inserted together the overall temperature gradient will be minimized. The total flow for a layer is 179.3 l/h corresponding to 19.3 m<sup>3</sup>/h for the complete detector.

## 9.5 Gas distribution

The gas system has been described in Chapter 8. Therefore, only the relevant parameters from the services point of view will be mentioned here.

### 9.5.1 Layout

As already mentioned in Chapter 8, the hydrostatic pressure over the total height of the detector is 2.5 mbar. Since the detector working pressure is limited, for mechanical reasons, to 1 mbar, a subdivision of the full detector is necessary. Furthermore, the flow and pressure regulation must be done in each section independently. On the other hand, due to space limitations inside and around the L3 magnet, it is desirable to place as much hardware as possible in other areas. Taking into account these considerations gas is distributed through a 54-line manifold. Each line serves one set of 10 chambers -two layers back and forth in  $z$ -, and the pressure regulation sensor is placed at the outlet, thus being the only component inside the L3 magnet. All the other components will be located at the plug. Table 9.4 shows an overall view of the main piping parameters.

**Table 9.4:** Main piping parameters of the gas system.

	Number of pipes	Pipe diameter [mm]	Length [m]	Nominal flow [m <sup>3</sup> /h]
SGX building to plug	1	73	90	5
Plug to RB26 side	54	4	100	0.1
RB26 side to plug	18	16	100	0.28
Plug SGX building	1	73	90	5

The feedthrough from chamber to chamber will be a short (3 cm) pipe with an inner diameter of 18 mm. The pressure regulation will be performed at the outlet of each sub-circuit (three per sector) by placing the pressure sensor close to the last chamber. Still inside the L3 magnet a 3-fold manifold will merge the lines from each sector into one 16 mm line. Therefore, a total of 18 outlet lines will run up to

an accessible area at the plug, where the rest of the instruments for flow and pressure regulation will be installed. All of these circuits will route into the L3 magnet space from the RB26 side (the side of the muon arm).

# 10 Material budget

---

As already emphasized many times the performance of the TRD will crucially depend on its overall radiation thickness. In Table 10.1 we summarize the radiation thickness of all components in the active area of the detector. In the simulations (see Chapters 6, 11, and 12) also detector material outside the active area has been considered to properly account for the induced background due to structural elements and other detectors of the central barrel.

**Table 10.1:** Material budget of the TRD. Only components contributing within the detector's active area are listed.

Element	Material	X/X <sub>0</sub> [%] at $\eta = 0$
radiator	G10/Rohacell/fiber	0.93
radiator gas	air	0.02
drift electrode	metallized Mylar	0.02
drift chamber gas	Xe/CO <sub>2</sub>	0.24
pad plane	G10/Cu	0.13
foam backing	Rohacell	0.18
stiffening fibers	carbon fiber	0.09
readout motherboards	G10/Cu	0.44
multichip module	G10/Si/epoxy	0.14
cooling	H <sub>2</sub> O/Al	0.20
1 TRD module		2.39
full TRD		14.34

The total radiation thickness of the radiator includes all components listed for the S-HF71 sandwich radiator with reinforcement as listed in Table 3.1 of Chapter 3. In the material budget of the radiator gas the air gap between consecutive layers of the TRD was also included. If the surfaces of the laminated radiator foam are very smooth, it may be possible to reduce the thickness of the drift electrode somewhat (it has been included assuming a thickness of 50  $\mu\text{m}$ ).

For the drift chamber gas, Xe/CO<sub>2</sub> (85/15) with a total thickness of 37 mm has been considered. The padplane is included with a thickness of 250  $\mu\text{m}$  and a copper coating of 5  $\mu\text{m}$ . The pad planes are supported by a Rohacell® HF31 foam backing. The backing itself is reinforced by glueing carbon fiber rods with a diameter of 1.8 mm into grooves with a regular spacing of 1.5 cm. Averaging the material of the carbon fibers over the detector surface, this is equivalent to a homogeneous layer of 200  $\mu\text{m}$  thickness. The readout motherboards will be 4-layer printed circuit boards of 400  $\mu\text{m}$  thickness. Two layers will be used for power and ground. Both of these layers will have an areal coverage of copper of 20% each. The other two layers will be signal layers with a coverage of copper of 30% each. It is foreseen to use a standard multilayer printed circuit board here, so the copper thickness is 34  $\mu\text{m}$ . Passive components such as small chip capacitors for decoupling and storage, voltage regulators, the PAROLI link, and the TTCrx chip have not been considered. However, they should only contribute a very moderate and localized increase in the overall radiation length.

The multichip modules will be implemented as ball grid arrays (BGA). The size of them will be below 10 cm<sup>2</sup>. They cover only about 10% of the active area. The radiation length quoted is averaged over the detector area. In the estimate of the radiation length of such a modules the chip carrier(G10), the silicon wafers, their glob top, and the solder balls were included. The multichip modules will be actively cooled as outlined in Chapter 9. The individual cooling pads will be thin aluminum panels

(1mm) in thermal contact with an aluminum pipe of 2 mm diameter filled with water. The areal coverage corresponds to about 12% of the active area.

# 11 Detector performance

---

## 11.1 Requirements

The main purpose of the TRD is to provide electron identification and tracking in the momentum range above  $1 \text{ GeV}/c$ . Therefore it has to be assured that a sufficient pion suppression can be achieved, even in the high multiplicity environment expected in the ALICE experiment. Additionally, a high tracking efficiency and good momentum resolution for particles in the momentum range of interest is required. In Chapter 1 the physics objectives and the correspondingly following detector requirements are already described. Table 11.1 summarizes again the basic requirements on the detector performance that have to be achieved.

**Table 11.1:** Detector requirements.

momentum resolution	5% (for $p = 5 \text{ GeV}/c$ )
tracking efficiency	90% (for $p > 1 \text{ GeV}/c$ )
$\pi$ -rejection factor	100 (for 90% e-efficiency and $p_t \geq 3 \text{ GeV}/c$ )

## 11.2 Simulation of the detector response

In order to study the performance of the TRD detector in a high multiplicity environment, a detailed simulation of the detector response is necessary. The output of this simulation should be as close as possible to the raw data that will be produced in a real experimental run. This allows to apply the same reconstruction software to simulated data that later on will be used for the analysis of the real data.

In the following the procedure to simulate the detector response is described. It can be divided into two basic steps: The first is the generation of electron clusters in the drift volume by the energy loss of charged particles and the absorption of TR-photons. The second step involves the transformation of the deposited charge into raw-data like ADC-signals, which then can serve as input to the reconstruction. Boths steps are implemented in AliRoot [1], the ALICE software package, which provides an object oriented framework for the simulation and the reconstruction. Therefore most of the software is written in C++ and based on the ROOT package [2], although for the tracking of Monte Carlo generated particles routines from GEANT 3.21 [3] are used.

Throughout this chapter the cartesian coordinates ( $x, y, z$ ) are in the coordinate frame of a single readout chamber. The  $z$ -direction is parallel to the beam axis,  $y$  is the direction parallel to the anode wires and follows the  $r\phi$ -direction of the detector, and  $x$  is the drift direction. The Color Fig. 3 shows the geometry of the TRD as it is implemented in the AliRoot package.

### 11.2.1 Energy loss

The simulation of the energy loss in the TRD gas follows in principle the same recipe already employed for the ALICE TPC [5]. In a first step the electromagnetic interaction of a charged particle releases primary electrons from the atoms of the TRD gas. The probability for primary ionization as a function of the distance  $s$  travelled follows an exponential probability distribution [6, 7]:

$$P(s) = \frac{1}{D} \exp\left(\frac{-s}{D}\right). \quad (11.1)$$

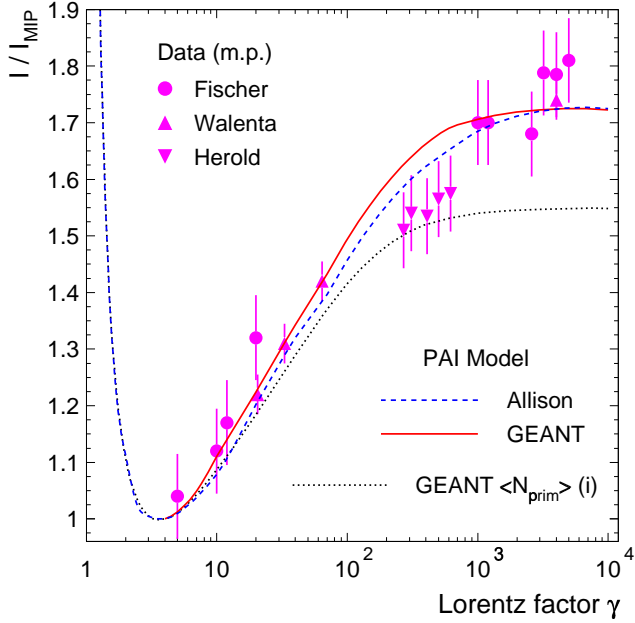


**Figure 11.1:** The relativistic rise for Xe gas, given most probable (m.p.) values, normalized to MIP case ( $\gamma = 4$ ). The symbols represent the available measurements and the lines show model predictions.

Here  $D$  denotes the mean distance between the primary ionizations and is defined as:

$$D = \frac{1}{\langle N_{\text{prim}} \rangle f(\beta\gamma)}. \quad (11.2)$$

The quantity  $\langle N_{\text{prim}} \rangle$  is the average number of primary electrons per cm created by a minimum ionizing particle (MIP) and  $f(\beta\gamma) = I/I_{\text{MIP}}$  is the Bethe-Bloch curve. There are large differences in the literature concerning the value of  $\langle N_{\text{prim}} \rangle$  and the height of the Fermi plateau of the Bethe-Bloch curve for Xe, as is illustrated by Table 11.2:

**Table 11.2:** Different parameters concerning the primary ionization of MIPs.

	GEANT [3]	Sauli [8]	Ermilova [4]
$\langle N_{\text{prim}} \rangle$ (1/cm)	20.5	44.0	48.0
Fermi plateau (mean)	1.56	-	1.36

In Fig. 11.1 we show the magnitude of the relativistic rise for Xe in terms of the most probable (m.p.) values. All values are normalized to the MIP case ( $\gamma = 4$ ). The average values of the number of primary collisions per cm,  $\langle N_{\text{prim}} \rangle(i)$ , as calculated using GEANT is the input to the simulations. The resulting most probable values of the energy deposit are plotted as solid line. The results of the simulation are compared to the existing measured data [9–11], to which they agree well. Also included is a Photon Absorption and Ionization (PAI) model calculation (dashed line, labelled Allison) [12], giving very similar results (naturally, as GEANT is using PAI for the calculation of  $\langle N_{\text{prim}} \rangle$ ). A similar agreement to the experimental data was obtained by a PAI implementation in GEANT4 [13].

If a charged particle is found to be passing through the Xe filled drift volume of a readout chamber, its average step size is set according to eq. 11.2. After each step, calculated using Eq. 11.1, a primary

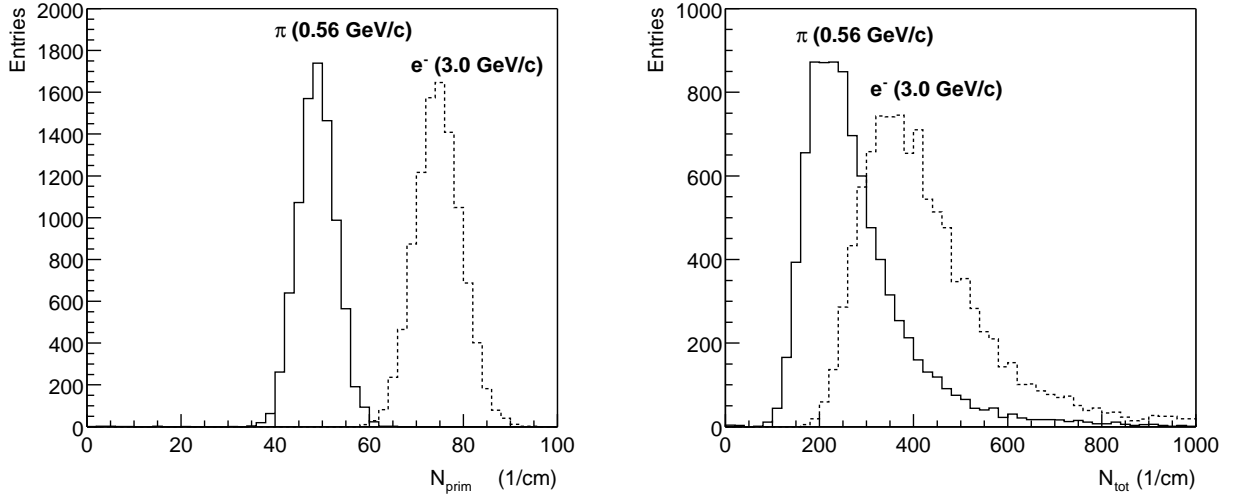


**Figure 11.2:** The distribution of the number of primary electrons  $N_{\text{prim}}$  (left panel) and of the total number of electrons  $N_{\text{tot}}$  (right panel).

ionization process is assumed and correspondingly an electron cluster is created. The left panel of Fig. 11.2 contains the distribution of the number of primary electrons (i.e. number of electron clusters)  $N_{\text{prim}}$  for a MIP (0.56 GeV/c pions, solid line) and for 3.0 GeV/c electrons (dashed line). According to the Ermilova value of  $\langle N_{\text{prim}} \rangle$  chosen in this simulation, the MIP distribution centers around 48.0/cm.

In order to determine the number of electrons in each cluster, the energy spectrum of the primary electrons has to be known. Due to the lack of measurements for Xe, one has to rely on models here. Based on the PAI model, the authors of [4] derive a spectrum, which results in reasonable values for the average ionization energy loss and which is therefore implemented in our simulation. Figure 11.3 displays this distribution (labelled Ermilova) and also includes a comparison to a distribution taken from GEANT [3] (using the X-ray cross sections from Sandia) and a  $1/E$  distribution, which is frequently used for these purposes [8]. The curves in Fig. 11.3 are the integrated distributions

$$\left( \frac{dN}{dx} \right)_{>E} = \int_E^\infty \frac{d^2N}{dx dE'} dE' \quad (11.3)$$

and therefore represent the number of inelastic collisions per cm with an energy transfer above  $E$ . The distributions start at the first ionization potential, which is  $I_{\text{pot}} = 12.1$  eV for Xe, and extends into the region where GEANT starts generating tracks from  $\delta$ -rays ( $> 10$  keV). We have chosen the Ermilova model and the GEANT Fermi plateau in our simulations, since this generates a higher ionization and therefore represents a worst case estimate in view of the particle identification capabilities. Note also that the simulation of the energy loss is done for pure Xe gas. For the actually used gas mixture (Xe,CO<sub>2</sub> (15%)) the ionization is additionally lower than what is implemented in the simulation.

Following the above described procedure, after each inelastic collision an electron cluster is produced. The number of electrons contained in this cluster  $N_{\text{tot}}$  is determined by the energy of the primary electron  $E$ , which is chosen according to the Ermilova distribution, and the effective energy  $W$  that is required to produce a free electron ( $W \simeq 22$  eV for Xe).

$$N_{\text{tot}} = \frac{E - I_{\text{pot}}}{W} + 1 \quad (11.4)$$

The right panel of Fig. 11.2 shows the distribution of the total number of electrons  $N_{\text{tot}}$  per cm in Xe for a MIP (0.56 GeV/c pions, solid line) and for 3.0 GeV/c electrons (dashed line). The mean value for a MIP is 280  $e^-/\text{cm}$  and 425  $e^-/\text{cm}$  for 3.0 GeV/c electrons.

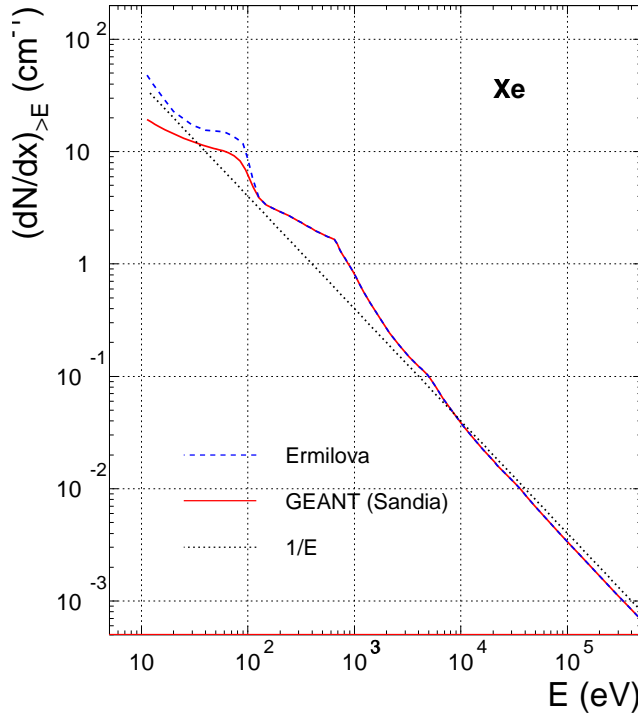


**Figure 11.3:** The number of inelastic collisions per unit length releasing a primary electron with energy  $E$  as a function of the energy for Xe gas.

The Color Fig. 4 shows an event display with the simulated hits in the TPC and TRD generated in the above described way for particles of different species. One can clearly recognize the tracklets in the 6 TRD layers.

### 11.2.2 Transition radiation

For the study of the electron identification capabilities the production of transition radiation (TR) has to be part of the simulation. Since this is not included in GEANT 3.21 it had to be added to AliRoot. A straightforward calculation of a TR spectrum is only possible for a regular structure of interfaces like it is realized in a foilstack radiator. The following section therefore describes how this is done in this case and what is used within the simulation code.

#### Theory of TR

A practical theory of the TR production is presented in ref. [14–16]. Here only the most important results are summarized.

The energy density spectrum radiated at polar angle  $\theta$  by a charged particle with the Lorentz factor  $\gamma$  traversing an interface between two dielectric media (with the dielectric constants  $\epsilon_1$  and  $\epsilon_2$ ) has the following expression:

$$\frac{d^2W}{d\omega d\Omega} = \frac{\alpha}{\pi^2} \left( \frac{\theta}{\gamma^2 + \theta^2 + \xi_1^2} - \frac{\theta}{\gamma^2 + \theta^2 + \xi_2^2} \right)^2. \quad (11.5)$$

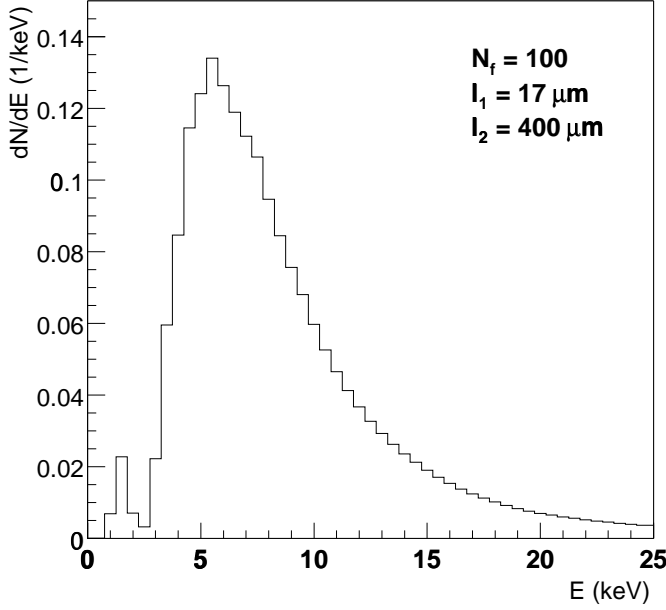


**Figure 11.4:** The energy spectrum of the TR photons calculated using eq.11.14 together with the parameters given in Table 11.3.

This is deduced for  $\gamma \gg 1$ ,  $\xi_1^2, \xi_2^2 \ll 1$ ,  $\theta \ll 1$ . Here  $\xi_i^2 = \omega_{P,i}^2/\omega^2 = 1 - \epsilon_i(\omega)$ , where  $\omega_{P,i}$  is the plasma frequency for the two media and  $\alpha$  is the fine structure constant ( $\alpha = 1/137$ ). The plasma frequency is a material property and has the following expression:

$$\omega_P = \sqrt{\frac{4\pi\alpha n_e}{m_e}} = 28.8 \sqrt{\rho \frac{Z}{A}} \text{ eV}, \quad (11.6)$$

where  $n_e$  and  $m_e$  are the electron density in the material and the electron mass. Typical values for plasma frequency are  $\omega_{P,\text{CH}_2} = 20 \text{ eV}$ ,  $\omega_{P,\text{Air}} = 0.7 \text{ eV}$ .

As the emission angle of the TR is small ( $\theta \simeq 1/\gamma$ ) one usually integrates over the solid angle and gets the (differential) energy spectrum:

$$\left( \frac{dW}{d\omega} \right)_{\text{interface}} = \frac{\alpha}{\pi} \left[ \frac{\xi_1^2 + \xi_2^2 + 2\gamma^{-2}}{\xi_1^2 - \xi_2^2} \ln \left( \frac{\gamma^{-2} + \xi_1^2}{\gamma^{-2} + \xi_2^2} \right) - 2 \right]. \quad (11.7)$$

For one foil one has to sum up the contributions of the two interfaces, resulting in the expression:

$$\left( \frac{d^2W}{d\omega d\Omega} \right)_{\text{foil}} = \left( \frac{d^2W}{d\omega d\Omega} \right)_{\text{interface}} \times 4 \sin^2(\phi_1/2), \quad (11.8)$$

where  $4 \sin^2(\phi_1/2)$  is the interference factor.

For a stack of  $N_f$  foils of thickness  $l_1$ , separated by a medium (usually a gas) of thickness  $l_2$ , one has:

$$\left( \frac{d^2W}{d\omega d\Omega} \right)_{\text{stack}} = \left( \frac{d^2W}{d\omega d\Omega} \right)_{\text{foil}} \times \exp \left( \frac{1 - N_f}{2} \sigma \right) \frac{\sin^2(N_f \phi_{12}/2) + \sinh^2(N_f \sigma/4)}{\sin^2(\phi_{12}/2) + \sinh^2(\sigma/4)}, \quad (11.9)$$

where  $\phi_{12} = \phi_1 + \phi_2$  is the phase retardation,  $\phi_i \simeq (\gamma^{-2} + \theta^2 + \xi_i^2)\omega l_i/2$  and  $\sigma = \sigma_1 + \sigma_2$  is the total absorption cross section for the radiator (foil + gas).

The TR produced by a multifoil radiator can be characterized by the following qualitative features:

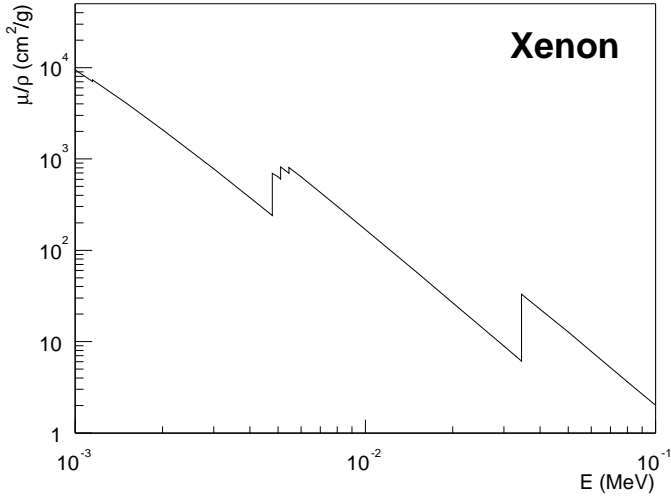


**Figure 11.5:** The mass attenuation coefficient  $\mu/\rho$  in Xe gas [19].

- One can define the so-called “formation zone”:  $Z_i = (\gamma^{-2} + \theta^2 + \xi_i^2)^{-1/2}/\omega$ , which is interpreted as the distance after which the separation between particle and emitted photon is of the order of the photon wavelength [14]. The yield is suppressed if  $l_i \ll Z_i$  and this is called “formation zone effect”.

In the opposite case  $l_i \gg Z_i$  interference can be neglected and one has:

$$\left( \frac{d^2W}{d\omega d\Omega} \right)_{\text{foil}} = 2 \times \left( \frac{d^2W}{d\omega d\Omega} \right)_{\text{interface}} ; \quad \left( \frac{d^2W}{d\omega d\Omega} \right)_{\text{stack}} = N_f \times \left( \frac{d^2W}{d\omega d\Omega} \right)_{\text{foil}} . \quad (11.10)$$

- The TR spectrum has the most relevant maximum at  $\omega_{\max} = l_1 \omega_{P,1}^2 / 2\pi$  and this allows the “tuning” of the performance of a TRD by varying the material and thickness of the radiator foils.
- For  $l_2/l_1 \gg 1$  the TR spectrum is mainly determined by the single foil interference.
- The multiple foil interference governs the saturation at high  $\gamma$ , above the value:

$$\gamma_s = \frac{1}{4\pi} \left[ (l_1 + l_2) \omega_{P,1} + \frac{1}{\omega_{P,1}} (l_1 \omega_{P,1}^2 + l_2 \omega_{P,2}^2) \right] . \quad (11.11)$$

A convenient way to study the TR features is to use scaled variables [15]:

$$\Gamma = \gamma/\gamma_1, \quad v = \omega/\omega_1, \quad (11.12)$$

where  $\gamma_1 = l_1 \omega_{P,1}/2$ ,  $\omega_1 = \gamma_1 \omega_{P,1}$ . In terms of the above variables, the TR production of a foil can then be written as:

$$\left( \frac{dW}{d\omega} \right)_{\text{foil}} = \frac{2\alpha}{\pi} G(v, \Gamma) . \quad (11.13)$$

A simple expression that describes the TR production and is used in our simulation is the following [17]:

$$\frac{dW}{d\omega} = \frac{4\alpha}{\sigma(\kappa+1)} (1 - \exp(-N_f \sigma)) \times \sum_{n=1}^{\infty} \theta_n \left( \frac{1}{\rho_1 + \theta_n} - \frac{1}{\rho_2 + \theta_n} \right)^2 [1 - \cos(\rho_1 + \theta_n)] , \quad (11.14)$$

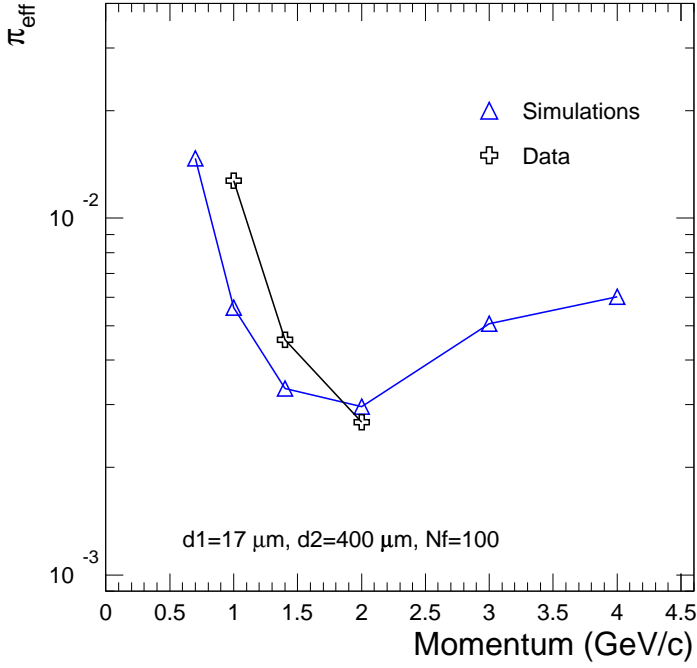


**Figure 11.6:** The simulated momentum dependence of the pion efficiency for isolated tracks together with results from the test beam measurements.

where:

$$\rho_i = \omega l_1 / 2c(\gamma^{-2} + \xi_1^2), \quad \kappa = l_2 / l_1, \quad \theta_n = \frac{2\pi n - (\rho_1 + \kappa\rho_2)}{1 + \kappa} > 0. \quad (11.15)$$

### Implementation in simulation

For each electron entering the drift volume of a readout chamber, TR photons are created with a distribution described by Eq. 11.14 (see Fig. 11.4). The position of the absorption of the TR photons is determined by the mass attenuation coefficient  $\mu/\rho$  (shown for pure Xe gas in Fig. 11.5, in the simulation  $\mu/\rho$  for the Xe,CO<sub>2</sub> (15%) gas mixture is used) and the direction of the incoming particle, defined by its momentum components. If the absorption is inside the gas volume a hit is created at this point whose charge content is given by

$$N_{\text{tot}}^{TR} = \frac{E_{\text{TR}} - I_{\text{pot}}}{W} + 1, \quad (11.16)$$

where  $E_{\text{TR}}$  is the energy of a given TR photon.

**Table 11.3:** Parameters in the TR photon simulation.

Number of foils $N_f$	100
Thickness of the foils $l_1$	17 \mu m
Thickness of the gaps $l_2$	400 \mu m
Density of the foils $\rho_1$	0.92 g/cm <sup>3</sup>
Density of the gas $\rho_2$	$1.977 \cdot 10^{-3}$ g/cm <sup>3</sup>

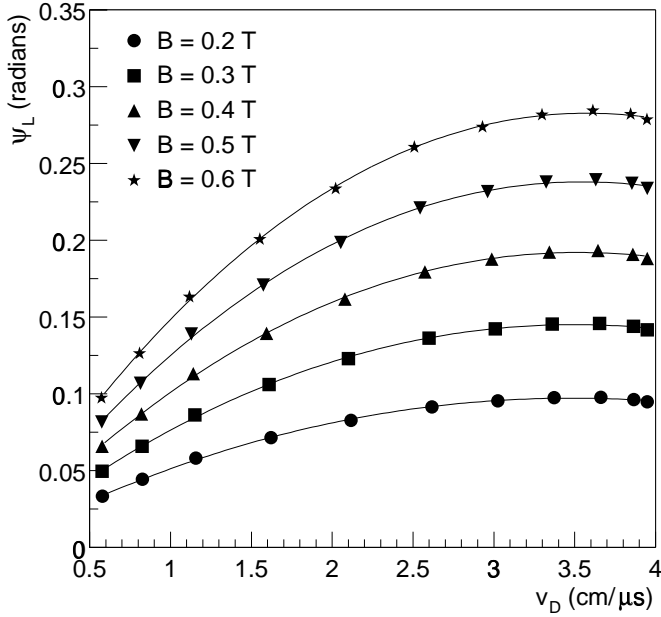


**Figure 11.7:** The Lorentz angle  $\psi_L$  as a function of the drift velocity  $v_D$  for different magnetic field strengths. The points represent results of a GARFIELD simulation for a Xe,CO<sub>2</sub> (15%) gas mixture. The lines are polynomial fits to the points and are used as parametrization inside AliRoot.

The parameters of the TR photon spectrum for a foil radiator (see Eq. 11.14) have been tuned to approximately reproduce the test beam data at  $p = 2 \text{ GeV}/c$  (see Chap. 14), measured with the final much more complicated radiator configuration. Figure 11.6 shows the simulated pion efficiency using the likelihood method on the total charge deposit for different momenta in the ideal case of isolated tracks for the parameters given in Table 11.3. The simulation results are compared with data obtained in prototype tests. Despite reproducing the gross trend of the data, we found it difficult to reproduce the measurements with an unique set of parameters. The parameters were tuned to the data at a momentum of  $2 \text{ GeV}/c$ , and for the same parameters pion efficiency is sizeably better for the simulations than the data at lower momenta. Also, our simulations show a deterioration of the pion efficiency for higher momenta which is not seen in the data taken from the literature [18].

### 11.2.3 Signal generation

In the second step the electron clusters (hits in AliRoot) have to be transformed into ADC-like signals (digits). Therefore the charge that the electrons in a given time bin induce on a given pad has to be computed. Apart from summing up the charge deposited by different tracks in one detector pixel (pad and time bin) and transforming it into an ADC channel number, this procedure requires to also take into account all known detector properties.

#### Diffusion

While drifting through the gas volume the electron cloud, produced at position  $(x_0, y_0, z_0)$ , is smeared out in space due to diffusion. Its spatial distribution can be described in the following way:

$$P(x, y, z) = \frac{1}{\sqrt{2\pi}\delta_L} \exp\left[-\frac{(x-x_0)^2}{2\delta_L^2}\right] \frac{1}{\sqrt{2\pi}\delta_T} \exp\left[-\frac{(y-y_0)^2}{2\delta_T^2}\right] \frac{1}{\sqrt{2\pi}\delta_T} \exp\left[-\frac{(z-z_0)^2}{2\delta_T^2}\right], \quad (11.17)$$

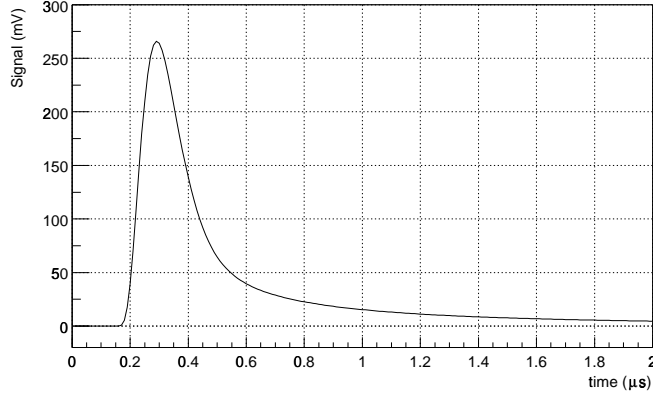


**Figure 11.8:** The response of the preamplifier shaper (120 ns FWHM, 6.1 mV/fC) to a pad signal simulated with GARFIELD for a 6 keV point charge deposit (corresponding to 9-10 times the signal of a MIP).

with

$$\begin{aligned}\delta_T &= D_T \sqrt{L_{\text{drift}}} \\ \delta_L &= D_L \sqrt{L_{\text{drift}}}.\end{aligned}$$

Here  $D_T$  and  $D_L$  denote the diffusion constants in the transverse and longitudinal direction and  $L_{\text{drift}}$  is the drift length. In order to simulate this effect each electron therefore is assigned a new position according to Eq. 11.17.

### E × B effect

For the TRD readout chambers the drift direction is always perpendicular to the magnetic field vector. This means that the drifting electrons will experience a Lorentz force resulting in a displacement of the position in the direction along the wires. For an electron produced at position  $(x_0, y_0, z_0)$ , where  $y$  and  $z$  directions are perpendicular to the drift direction along  $x$  and the  $y$ -axis is parallel to the wires, the new  $y$ -position can be calculated by the expression:

$$y = y_0 + \omega \tau (x - x_0), \quad \omega \tau = \tan \psi_L, \quad (11.18)$$

where  $\psi_L$  is the Lorentz angle. This parameter depends strongly on the strength of the magnetic and electric fields in the readout chamber. Figure 11.7 shows the variation of  $\psi_L$  with the drift velocity  $v_D$  for different magnetic fields, as calculated by a GARFIELD [20] simulation. These dependencies were parametrized and used inside AliRoot to automatically set the Lorentz angle according to the chosen drift velocity for a given B-field. For the standard combination of  $B = 0.4$  T and  $v_D = 1.5$  cm/ $\mu$ s this results in a value of  $\psi_L = 7.7^\circ$  and a maximal displacement of  $y_{\text{max}} - y_0 = 0.4$  cm for the full drift length.

### Gas gain fluctuations

Each electron arriving at the anode wire creates an avalanche of charge  $q$ . The magnitude of the average amplified charge  $\bar{q}$  is determined by the applied high voltage. Following [6, 7] the fluctuations of the gas gain are modelled using an exponential distribution:

$$P(q) = \frac{1}{\bar{q}} \exp\left(-\frac{q}{\bar{q}}\right). \quad (11.19)$$

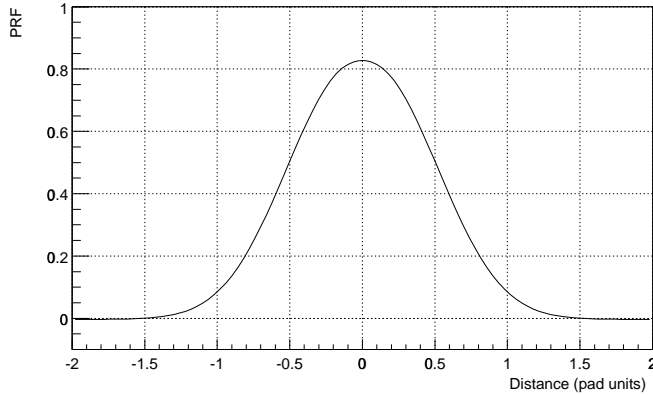


**Figure 11.9:** The pad response function.

### Time response

The signals recorded on the pads are determined by the following effects:

- The slow drift of the Xe ions which introduces a long tail in the time distribution.
- The non-isochrony of the electron drift, depending on the position of the electron relative to the anode wire position.
- The response of the preamplifier shaper to the incoming detector signal.

To determine the total time response of the detector and preamplifier to a single electron a simulation has been performed that takes all three effects into account. Figure 11.8 shows the result of a simulation of the preamplifier shaper response to a signal (corresponding roughly to a 6 keV point charge deposit) that has been generated with GARFIELD. This curve, normalized at the maximum to 1, is then used in the digitization part of AliRoot to sample the time distribution of each electron signal according to the given ADC frequency. It is further assumed that due to the shaping the ratio of the integrated charge to the input signal is equal to 0.4.

### Pad response

The charge that is induced on the pad plane by the electrons collected at the anode wire is spread over several pads. Using the Mathieson formalism [21], the pad response function (PRF) that describes how the charge is distributed over adjacent pads can be calculated. Figure 11.9 shows the PRF for chevron type pads with a width of  $w = 10\text{ mm}$ , a step of  $s = 5\text{ mm}$ , and a distance to the wire plane of  $h = 2.5\text{ mm}$ , which is used in the current simulations. Note that this PRF is very similar to the one of rectangular pads (see chapters 4 and 14), which are used in the actual pad geometry. A pad coupling factor equal to 0.5 (see section 4.6.3) is applied, which takes into account that only a fraction of the charge collected at the wire is seen by the readout pads.

### Electronic noise and conversion gain

To provide a realistic description of the output signal, also the electronic noise has to be included. In the present simulation it is assumed that the noise distribution can be described by a Gaussian with a sigma of  $\sigma_{\text{noise}} = 1000\text{ e}^-$ . Following from this the conversion gain of the amplifier is chosen such that  $\sigma_{\text{noise}}$  corresponds to ADC channel 1.

## Digitization parameters

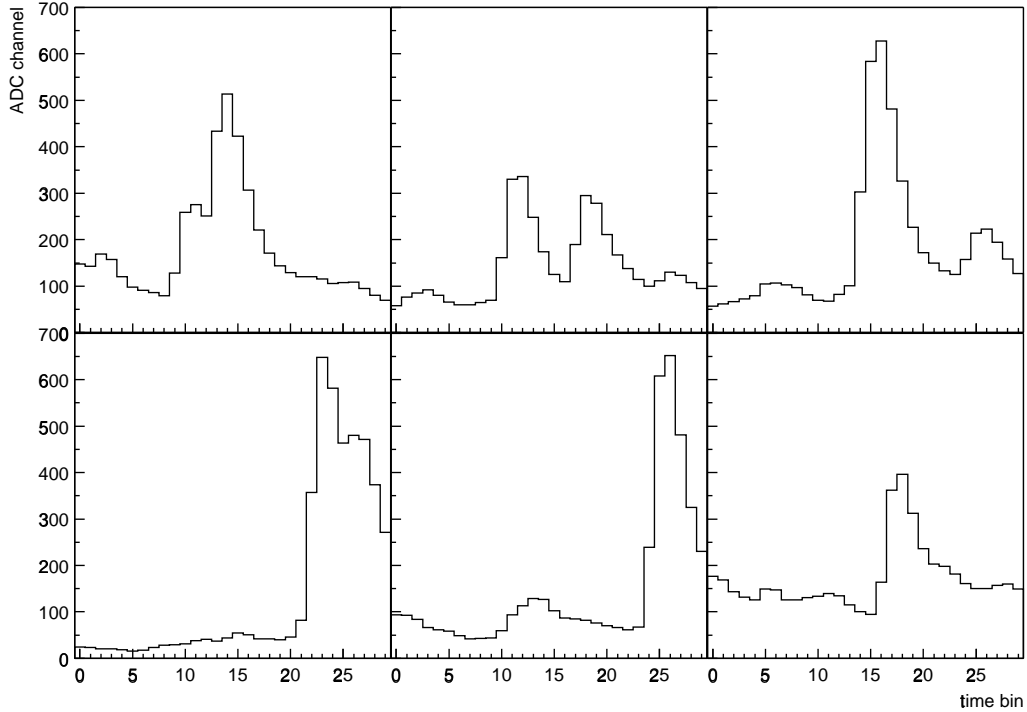


**Figure 11.10:** A typical sample of signals as a function of the drift time produced by  $p = 3.0 \text{ GeV}/c$  electrons in one readout chamber.

**Table 11.4:** The digitization parameters.

B-field	0.4 T
Drift velocity $v_D$	1.5 cm / $\mu\text{s}$
Transverse diffusion coefficient	$180 \mu\text{m} / \sqrt{\text{cm}}$
Longitudinal diffusion coefficient	$250 \mu\text{m} / \sqrt{\text{cm}}$
Lorentz angle $\psi_L$	$7.7^\circ$
Gas gain $\bar{q}$	$2.8 \cdot 10^3$
Electronics gain	6.1 mV/fC
Electronics noise $\sigma_{\text{noise}}$	$1000 \text{ e}^-$
Pad coupling factor	0.5
Time coupling factor	0.4
ADC range	1 V
ADC resolution	10 bit

Table 11.4 summarizes the parameters that are used in the simulation of the TRD response. The diffusion coefficients and the Lorentz angle are determined by the actual values of drift velocity and B-field. The average gas gain is chosen such ( $2.8 \cdot 10^3$ ) that the energy loss signal of a minimum ionizing particle is around ADC channel 40. Figure 11.10 shows some typical electron signals that result from the above described digitization procedure.

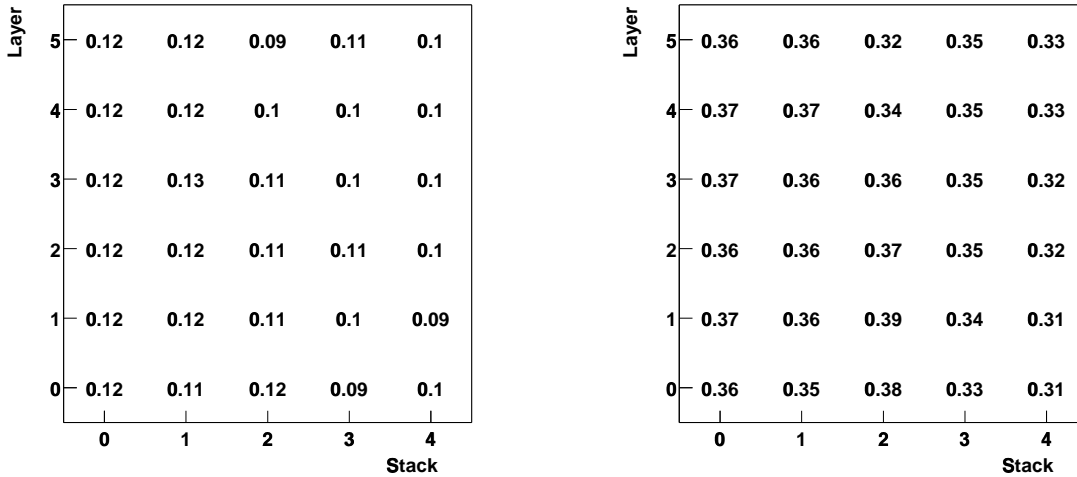


**Figure 11.11:** The occupancy in different stacks of the TRD for  $dN_{\text{ch}}/dy = 2000$  (left) and  $dN_{\text{ch}}/dy = 8000$  (right).

## 11.3 Point reconstruction

### 11.3.1 Clustering method

The currently employed clustering mechanism searches for adjacent pads in  $y$ -direction with a signal above threshold that could form a pad cluster. Since there is only little charge sharing in  $z$ -direction no clustering is performed here. The same is true for the drift direction, since a track, due to the high ionization in Xe, creates a signal in basically every time bin. Therefore the position of a cluster in  $z$ - and drift direction is determined by the pad and time bin position. The position in  $y$ -direction, where a good resolution is mandatory for the momentum measurement, can be extracted with much higher precision, due to the charge sharing. Here one can either calculate the center of gravity of the charge distribution inside a cluster, or use a lookup table to determine the position of the cluster. The latter method, where the position is taken from a table that contains the deviation from the pad center as a function of the ratio of the two largest signals provides generally a better resolution.

Ideally, all clusters contain only signals from two or three pads (2.4 on average for an isolated hit). In the high multiplicity environment of the ALICE experiment, however, there is a large probability that clusters overlap. Currently, only clusters containing signals from five pads are unfolded, using the pad response function as an estimator for the cluster shape. By applying a more sophisticated mechanism one also can disentangle clusters composed of 4 and more pads, thereby reaching a further improvement in resolution at high multiplicity.

### 11.3.2 Occupancy

The occupancy, defined as the percentage of detector pixels (pad and time bin) with a signal above a threshold (2 ADC-channels), influences crucially the detector performance. Figure 11.11 displays the occupancy numbers in the case of full ( $dN_{\text{ch}}/dy = 8000$ ) and quarter ( $dN_{\text{ch}}/dy = 2000$ ) multiplicity. The numbers are given for the five stacks in  $z$ -direction and for the six detector layers. The occupancy is highest for the stack closest to mid-rapidity in the innermost layer. For the middle stack it decreases slightly when going to the outermost layers, while for the more forward stacks no  $r$ -dependence is visible. In the stack on the side with the absorber for the muon arm (stack 4) a lower occupancy can be observed than in the stack on the other side (stack 0).

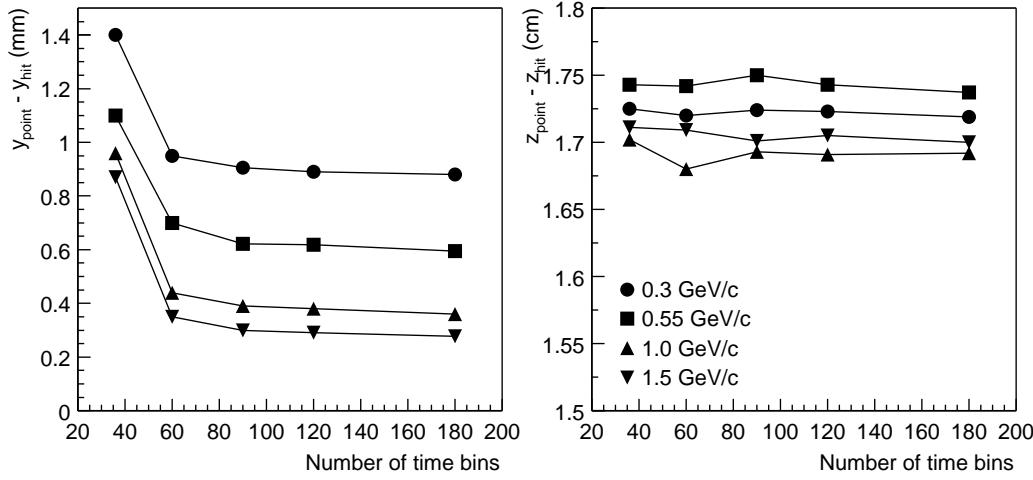


**Figure 11.12:** The point resolution as a function of the number of time bins for different transverse momenta of the particles (low multiplicity,  $dN_{\text{ch}}/dy = 150$ ). The data points are from fits of a Gaussian to the distribution of the difference between simulated and reconstructed position. Only non-overlapping clusters were used.

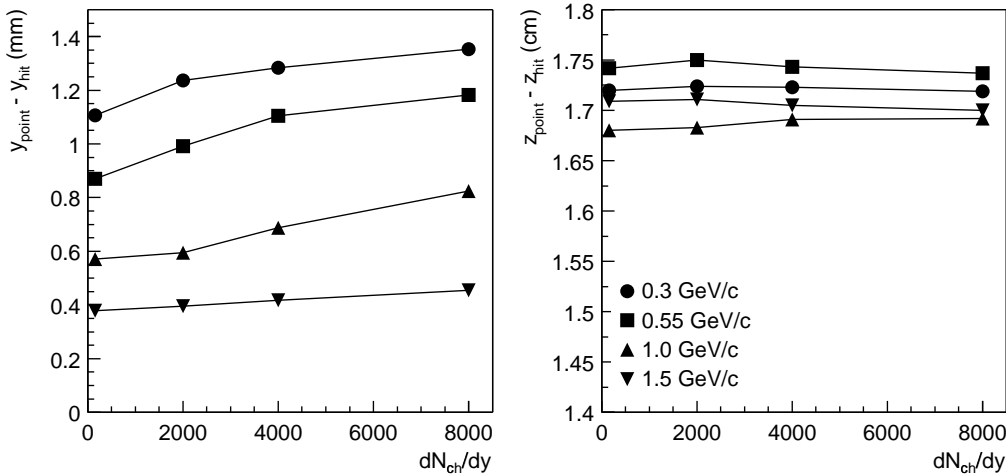


**Figure 11.13:** The point resolution as a function of the event multiplicity for different transverse momenta of the particles. The data points are from fits using a Gaussian to the distribution of the difference between simulated and reconstructed position. In this analysis also overlapping clusters were included.

### 11.3.3 Position resolution

#### Dependence on the number of time bins

One important question is whether there is an optimal choice in the number of time bins. To reduce the data volume, a small number of time bins is preferable. However, any deteriorations in the resolution and efficiencies due to a restricted number of time bins should be minimal. Varying the number of time bins here means to vary the sampling frequency and to keep the drift length constant. Figure 11.12 shows the dependence of the point resolution as a function of the number of time bins in all 6 layers for different transverse momenta. In the left column the difference between the  $y$ -position of the reconstructed point and the corresponding simulated hit is plotted, while the right column shows the same for the  $z$ -position. While the  $z$ -resolution does not depend on the number of time bins, the  $y$ -resolution is getting worse for less than 60-80 time bins. Based on this result we choose 90 time bins (15 per layer) as default value.

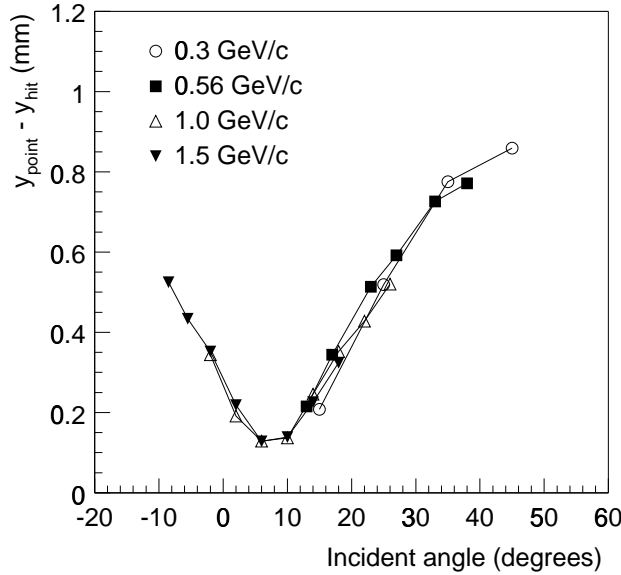


**Figure 11.14:** The point resolution for positive tracks in  $y$ -direction as a function of the incident angle for different track total momenta using only non-overlapping clusters (Gaussian fit, low multiplicity,  $dN_{ch}/dy = 150$ ).

The strong momentum dependence is an angular effect as discussed below (see also Fig. 11.14).

### Dependence on event multiplicity

Figure 11.13 summarizes how the point resolution depends on the event multiplicity. While a worsening of the resolution in  $y$ -direction on the order of 10-20% observed, in  $z$ -direction the resolution is essentially independent of the multiplicity. This is quite understandable since the  $z$ -resolution is essentially determined by the pad length. In  $y$ -direction, however, the position is measured via charge sharing between adjacent pads, which is subject to deterioration with increasing occupancy due to overlapping clusters.

### Dependence on the track angle

The momentum dependence in the point resolution is mainly caused by the different average incident angles for different momenta. This can be seen from Fig. 11.14, showing that the position resolution in  $y$  as a function of the incident angle, measured with respect to the normal of the readout chambers, closely follows a unique curve for all tracks, regardless of their momentum. Due to their higher curvature low momentum tracks have a larger incident angle and therefore spread charge over a larger region, resulting in a deteriorated position resolution (see also Fig. 4.16). The optimal resolution is achieved for tracks with an incident angle close to the Lorentz angle  $\psi_L = 7.7^\circ$ , when all the charge produced by the particle is focused on the same point on the anode wire.

## 11.4 Tracking

### 11.4.1 Algorithm

Offline tracking in the TRD is based on the Kalman-filtering approach, which we have chosen taking into account the similarities of the tracking environment in the ALICE TPC and in the TRD and based on the successful implementation of the Kalman-filter for tracking in the TPC and ITS. As mentioned in the TPC TDR [5], one of the advantages of the Kalman-filter concept is that it provides a straightforward

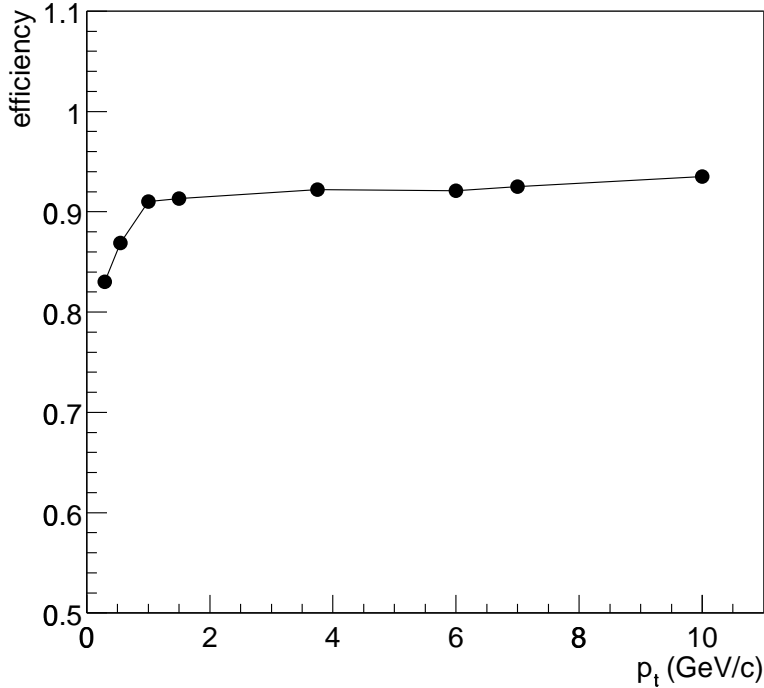


**Figure 11.15:** The tracking efficiency as a function of the transverse momentum for pion tracks in low multiplicity events ( $dN_{ch}/dy = 150$ ).

way to propagate track segments between subdetectors, in our case between the adjacent TRD layers as well as between the TRD and TPC.

The implementation of the TRD tracking shares many features developed for the ALICE TPC tracking described in detail in the TPC TDR. The tracking starts with finding track seeds in the outermost detector layers. The track candidate is followed inside the drift volume of the readout chambers in steps which correspond to the effective radial distance between two consecutive time bins. At each extrapolation the track helix parameters and covariance matrix are re-evaluated using information about the expected multiple scattering and energy loss. The uncertainties in track parameters define windows along the  $y$  and  $z$  direction, within which it is checked whether there is a close cluster which can be associated with the track candidate. Since the measurement in  $z$  direction is relatively coarse, we first require that the residual in  $z$  direction does not exceed half the size of one pad row in  $z$  direction. The width of a window in  $y$  direction is defined by the uncertainty in the track position and the expected error of the cluster measurement. If two or more clusters are found in a  $y$  window, the one closest to the track position is assigned to the track candidate. If no clusters are found in a  $y$  window, we repeat the  $y$  selection for clusters with residuals in  $z$  direction increased to 1.5 times the pad size in  $z$  direction. If a close cluster is found, the track parameters and covariance matrix are updated. In the case that no cluster satisfies the above criteria the procedure of track extrapolation and cluster search is allowed to continue for several iterations (due to the dead regions between the sensitive volumes of the readout chambers the allowed gap in the track candidate can be as large as 1.5 times the radial depth of the readout chamber).

### 11.4.2 Performance

To study the performance of the tracking algorithm, events of different multiplicities up to  $dN_{ch}/dy = 8000$  have been simulated with AliRoot using the parametrized HIJING event generator. These events,

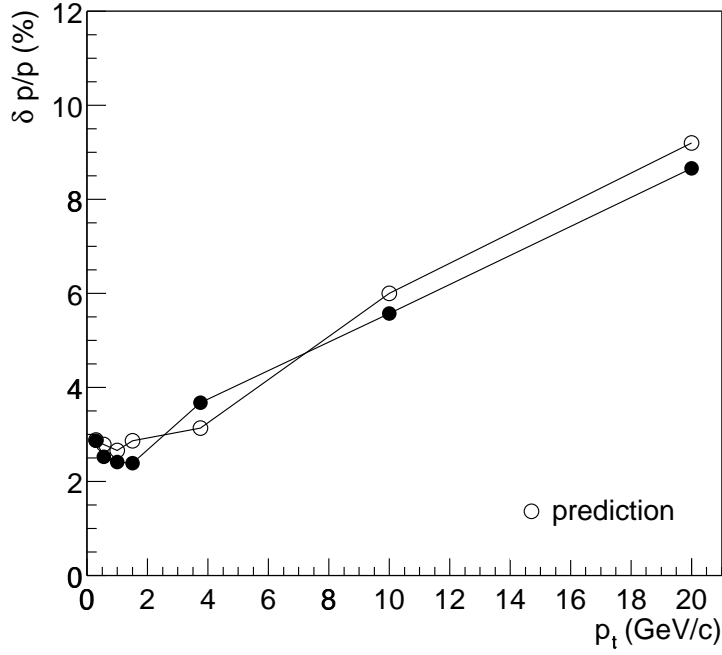


**Figure 11.16:** The momentum resolution as a function of the transverse momentum for pion tracks in events with low multiplicity ( $dN_{ch}/dy = 150$ ) using a number of time bins of 180. The prediction (open circles) is for the case of 68 independent measurements.

composed of primary pions, kaons, and protons, have been processed through the full reconstruction chain, using the above described procedures.

### Efficiency

Figure 11.15 shows the TRD tracking efficiency as a function of the track momentum. This efficiency is defined as the ratio of the number of reconstructed tracks and the number of “trackable” tracks. To fulfill this requirement, a track has to have points in the three outermost layers of the TRD. This definition results in a fraction of  $\sim 80\%$  of all charged primary tracks with  $45^\circ < \theta < 135^\circ$  and  $p_t > 0.2\text{ GeV}/c$  that are considered as trackable. The analysis shown in Fig. 11.15 was done on events with low multiplicity. For transverse momenta greater than  $1\text{ GeV}/c$  the efficiency is above 90%, while it drops sharply when going to lower momenta.

### Momentum resolution

The achieved momentum resolution is shown in Fig. 11.16. The extracted points are compared with a prediction for the resolution. This prediction is based on the following formula [22]:

$$(\delta k)^2 = (\delta k_{\text{res}})^2 + (\delta k_{\text{ms}})^2. \quad (11.20)$$

Here  $\delta k$  denotes the error in the track curvature, composed of the contribution from finite measurement resolution  $\delta k_{\text{res}}$  and from multiple scattering  $\delta k_{\text{ms}}$ . Under the assumption that the total error in the very low momentum regime is dominated by multiple scattering, the latter contribution can be estimated to

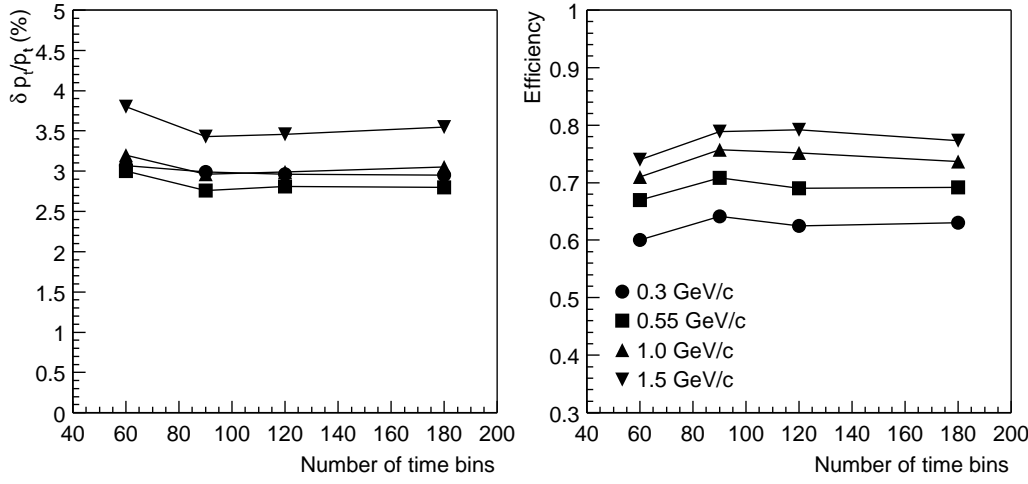


**Figure 11.17:** The tracking performance for pion tracks as a function of the number of time bins for different transverse momenta in a high multiplicity environment ( $dN_{ch}/dy = 8000$ ). The left panel shows the resolution in transverse momentum and the right panel the efficiency.

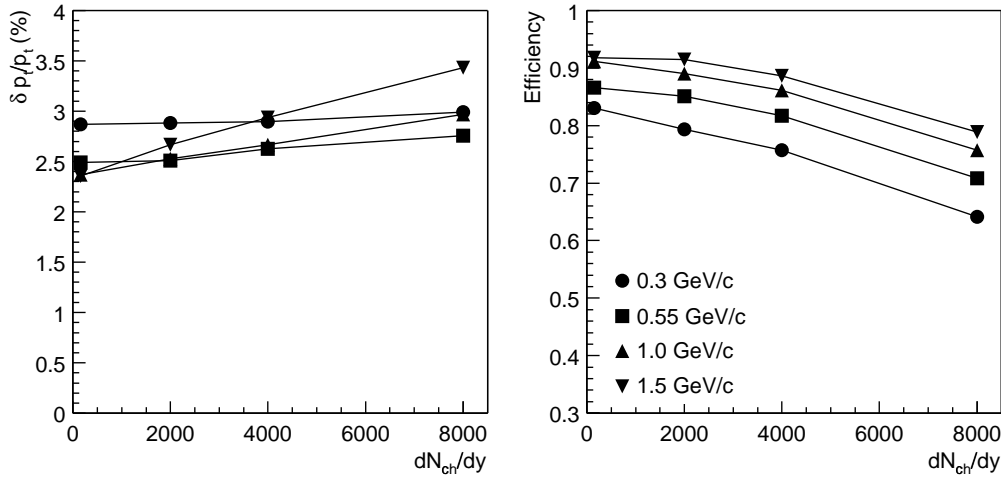


**Figure 11.18:** The tracking performance for pion tracks as a function of the event multiplicity for different transverse momenta (90 time bins). The left panel shows the resolution in transverse momentum and the right panel the efficiency.

be  $\delta k_{ms} \approx 0.003/p$ . The first contribution can be described by:

$$\delta k_{res} = \frac{\epsilon}{L'^2} \sqrt{\frac{360}{N+4}}. \quad (11.21)$$

Here  $N$  is the number of independently measured points along the track,  $L'$  the length of the track projected onto the bending plane, and  $\epsilon$  the measurement error for each point, perpendicular to the trajectory. Since  $L'$  and  $\epsilon$  are known for a given momentum,  $N$  can be derived from the momentum dependence of the resolution (the ion tail and the shaping lead to correlations). It is found that a good agreement with the simulations can be achieved by assuming  $N = 68$ . Since the number of time bins directly determines the maximum number of independently measured points, we conclude, based on this finding and on Fig. 11.12, that a number of time bins of 90 is sufficient to achieve the desired performance of the detector.

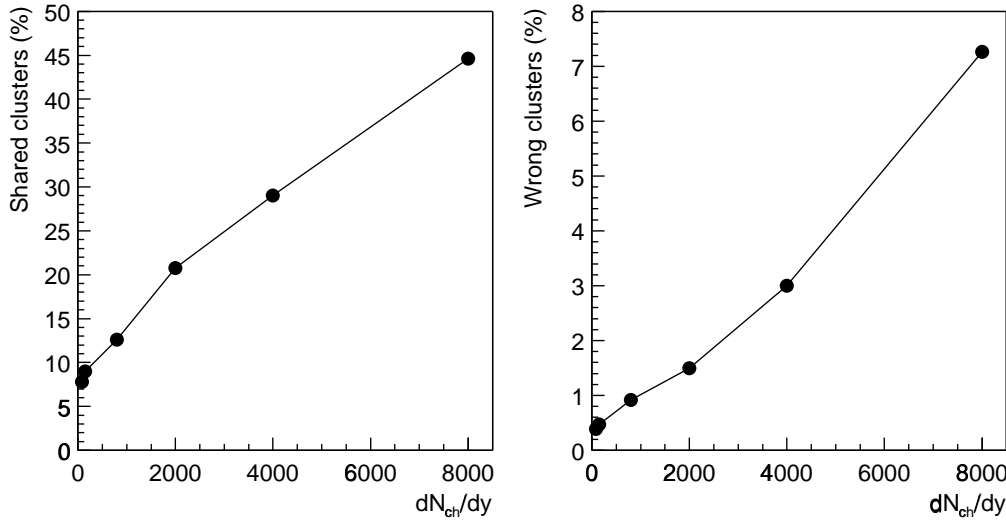


**Figure 11.19:** The percentage of overlapping clusters (left) and wrongly assigned clusters (right) as a function of the event multiplicity.

### Dependence on the number of time bins

The choice of the number of time bins has no significant effect on the offline tracking performance, if the number of time bins is above 80. This is evident from Fig. 11.17, showing the resolution in transverse momentum in the left panel and the tracking efficiency in the right panel as a function of the chosen number of time bins. The same behaviour was already visible in the point resolution of isolated clusters (see Fig. 11.12), which is already constant for more than 60 time bins.

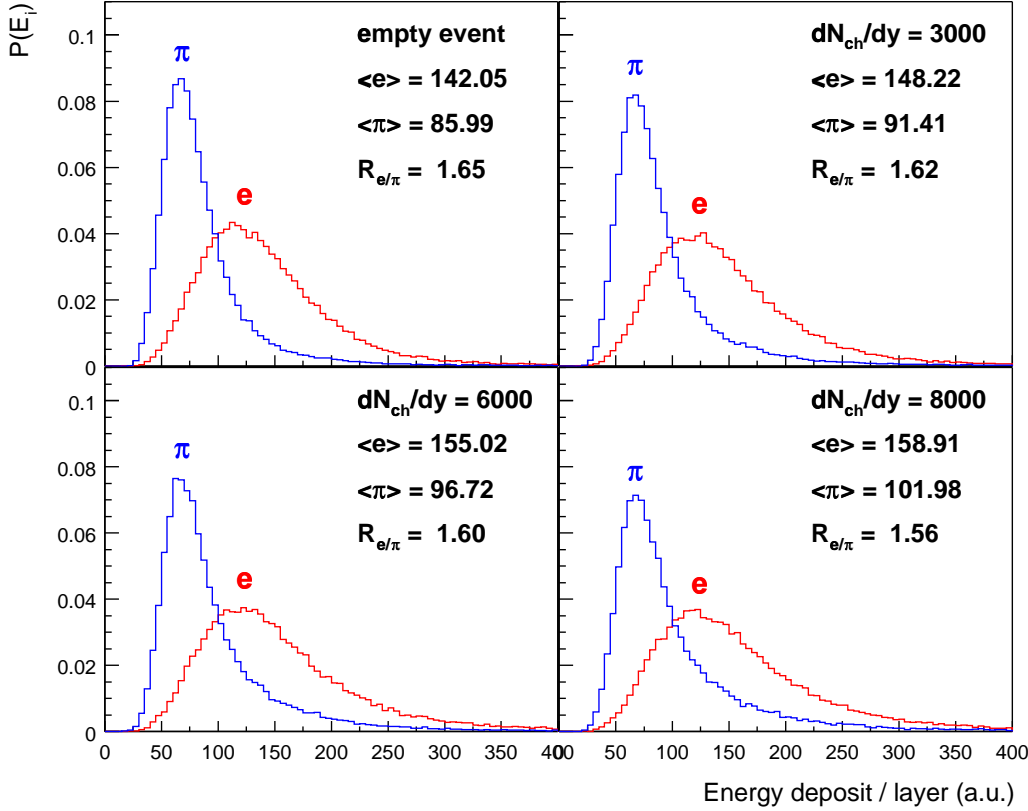
### Dependence on event multiplicity

Figure 11.18 summarizes how the tracking performance depends on the event multiplicity. The resolution in transverse momentum deteriorates only slightly, but remains well below 4% at  $p_t = 1.5 \text{ GeV}/c$ , when going from low multiplicity to the maximum multiplicity of  $dN_{ch}/dy = 8000$ . The tracking efficiency drops with increasing event multiplicity by  $\sim 15\%$  for  $p_t = 1.5 \text{ GeV}/c$  and almost  $\sim 25\%$  for very low transverse momenta. The reason for this can be seen in Fig. 11.19 that displays in the left panel how the percentage of clusters that have contributions from more than one track increases with the event multiplicity. Similarly, the fraction of points that are assigned to the wrong track increases (right panel). However, a preliminary analysis has shown that by employing a mechanism to unfold overlapping clusters an improvement in the tracking efficiency by  $\sim 10\%$  is easily achieved so that efficiencies of about 85% and higher for tracks with  $p_t > 1.0 \text{ GeV}/c$  are possible.

## 11.5 Pion rejection

While test beam results with isolated tracks in the TRD prototypes have shown that a pion rejection factor in the range of 300 to 500 can be achieved (see Chapter 14), the performance of the detector as a function of event multiplicity has to be evaluated using Monte Carlo methods. Therefore the pion rejection factor was studied as a function of the event multiplicity with AliRoot simulations.

In this simulation the parametrized HIJING event generator was used to create a realistic event background, with a full event corresponding to  $dN_{ch}/dy = 8000$ . Into this background 500 electrons or pions, of a fixed momentum were embedded. These simulated events were then reconstructed with the full reconstruction chain described above. Finally, distributions of the energy deposit were accumulated from



**Figure 11.20:** The distribution of the deposited energy for electrons and pion of a momentum of  $p = 3 \text{ GeV}/c$  after they are reconstructed in events with different multiplicities. The data are corrected for the number of points contributing and for the track inclination.

the clusters assigned to the reconstructed electron (pion) tracks. A track is defined to belong to an electron (pion) if the majority of its points were generated by the input Monte Carlo electron (pion). Using these distributions the pion rejection factor for a specific electron efficiency can be determined by employing the likelihood method (L-Q). A full description of the commonly used methods of extracting the pion rejection factor is given in Chapter 14. This procedure allows to study the degradation of the pion rejection due to the following effects:

- In a high occupancy environment clusters might pick up charge from another particle and therefore the charge measurement gets distorted (see Fig 11.19, left panel). Even when restricting the analysis to small (2 and 3 pad) clusters this effect is visible.
- The tracking algorithm assigns wrong clusters to a given track (see Fig 11.19, right panel), also resulting in an incorrect measurement of the energy deposition.
- Clusters are not found, because their position is distorted, which deteriorates the resolution of the charge measurement.

Figure 11.20 shows the distributions of the reconstructed deposited energy  $E_i$  per detector layer  $i$  for different event multiplicities. The energy deposit is only calculated using clusters composed of 2 or 3 pads. An additional requirement is that a track has at least 10 points (out of maximal 15) in a given chamber, which removes  $\sim 7\%$  of the single measurements for isolated tracks and  $\sim 33\%$  in the full

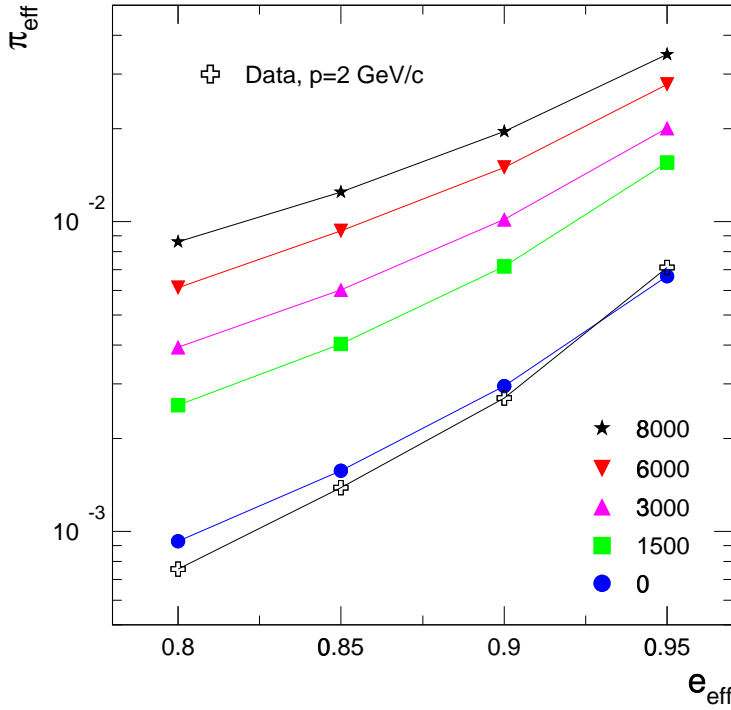


**Figure 11.21:** The pion efficiency as a function of the electron efficiency for different event multiplicities and tracks of  $p = 2 \text{ GeV}/c$  total momentum.

multiplicity case:

$$E_i = 1/N_{\text{points}} \sum_{\text{point}}^{N_{\text{points}}} Q_{\text{point}}^C \quad \text{with} \quad N_{\text{points}} > 10. \quad (11.22)$$

Here  $Q_{\text{point}}^C$  is the corrected charge of a single point. Since a track with non-perpendicular incidence relative to the readout chamber surface deposits more charge in a given time bin than a track that has no inclination, a correction factor, depending on the geometry of the track, has been applied. It can be clearly seen from Fig. 11.20 that the mean energy deposit increases with increasing event multiplicity. This effect is more pronounced for the pions, which, since they have no contribution from TR photon absorption, deposit less energy than the electrons and are therefore stronger affected by threshold effects. The ratio  $R_{e/\pi} = \langle E_{i,e} \rangle / \langle E_{i,\pi} \rangle$ , giving an indication for the rejection power, therefore decreases with increasing event multiplicity.

The effect of this multiplicity dependence of the energy distributions on the pion rejection factor  $\pi_{\text{eff}}$  can be seen in Fig. 11.21. The values for  $\pi_{\text{eff}}$  have been extracted for different electron efficiencies  $e_{\text{eff}}$  using the distributions shown in Fig. 11.20 as probability distributions. Following the discussion in section 11.2.2 it is evident that the simulation does not reproduce all the available data with a single set of parameters (see Fig. 11.6). Therefore, a calculation of the absolute pion efficiency in the high multiplicity environment from the simulation alone would not be reliable. However, the relative deterioration of the pion efficiency with increasing multiplicity should be described very well. By adjusting the simulation to the test beam data, measured at  $p = 2 \text{ GeV}/c$ , therefore a good estimate of the achievable pion efficiency at full multiplicity can be derived. Going from well isolated tracks to a full multiplicity event, a worsening of the pion rejection by a factor of 6-7 is observed. For an electron efficiency of 90% the pion efficiency  $\pi_{\text{eff}}$  is still about 2% when using the likelihood method on the deposited charge. Therefore even this “worst case” scenario still leads to pion rejection factors close to the desired factor

100 as discussed in chapter 1. As will be shown in chapter 14 a further improvement of 30-40% can be achieved by employing a combined charge/position likelihood analysis.



# 12 Physics performance

---

## 12.1 Introduction

The Transition Radiation Detector (TRD) was added in the central barrel of the ALICE experiment [1] to identify electrons and positrons in the central rapidity region primarily in central Pb–Pb collisions at the full LHC energy of 5.5 TeV /nucleon pair [2]. The physics motivation is the measurement of heavy-vector resonances,  $J/\psi$  and  $\Upsilon$  families in the dielectron channel and of open charm and open beauty, i.e. the D and B mesons, via their semi-leptonic decays. Furthermore, coincidences of electrons in the central barrel with muons in the forward muon arm are expected to provide information on the production of D and B mesons at the rapidity interval  $1 < y < 3$ , intermediate between that of the central barrel and the dimuon arm. With the TRD providing a L1 trigger on high  $p_t$  charged particles the measurement of high  $E_t$  jets might be possible in the central barrel. The contribution of such measurements to the understanding of the phase transition and the properties of the deconfined phase is detailed in the TRD TP [2], in Ref. [3] and references therein.

This chapter focuses on central Pb–Pb collisions that present the major challenge for a dedicated heavy-ion experiment. Emphasis is placed on acceptances of the TRD for measurement of quarkonia and open charm and open beauty. We also provide information on resolution and background sources.

## 12.2 Primary collision

There are large uncertainties in the theoretical predictions of the particle multiplicities and their spectral distributions produced in central Pb–Pb collisions at LHC energies. Hence the uncertainties of the input distributions used in the simulations presented here dominate by far the statistical and systematical errors of the presented results.

The strategy in ALICE has been to perform all the TDR studies for the detector optimization assuming the highest anticipated charged particle rapidity density  $dN_{\text{ch}}/dy = 8000$  at mid-rapidity, for central Pb–Pb collisions, in accordance with the one used for the ALICE TP [1]. The predictions at the time, summarized in Ref. [4] vary in the range of 1600 to 8000.

The rapidity density of  $dN_{\text{ch}}/dy = 8000$  results in  $\approx 20000$  charged particles entering the TRD. However, there is increasing evidence that such extreme multiplicity densities might not be reached. Recent data from the Relativistic Heavy Ion Collider (RHIC) on central Au–Au collisions including this summer’s measurements at  $\sqrt{s} = 200$  GeV provide today first constraints on the theoretical models. Within a high density QCD model Kharzeev and Levin [5] have recently derived an analytical scaling function for the multiplicity density as a function of  $\sqrt{s}$ . We have used their model to fit the results of the charged particle density for Au–Au at  $\sqrt{s} = 56$ ,  $\sqrt{s} = 130$  and  $\sqrt{s} = 200$  GeV measured by the PHOBOS Collaboration [6]. The extrapolation to LHC energy, a factor of  $\sim 27$  higher, gives an estimate of  $dN_{\text{ch}}/dy = 1700$ . The errors in the measurement are still large and give a maximum of  $dN_{\text{ch}}/dy = 2600$  and a minimum of  $dN_{\text{ch}}/dy = 1100$ . Further evidence supporting the expectation of lower multiplicities is provided by the calculation of Eskola et. al. [7] of the  $\sqrt{s}$  dependence of the charged particle density in terms of a perturbative QCD model including parton saturation. Their results are shown in Fig 12.1 and predict a  $dN_{\text{ch}}/d\eta = 2300$  at LHC energies.

Considering the uncertainty in extrapolation from RHIC to LHC energy as well as the systematic uncertainty in the models for particle production the prudent strategy adopted by ALICE for all other detectors, was also followed in the present TDR.

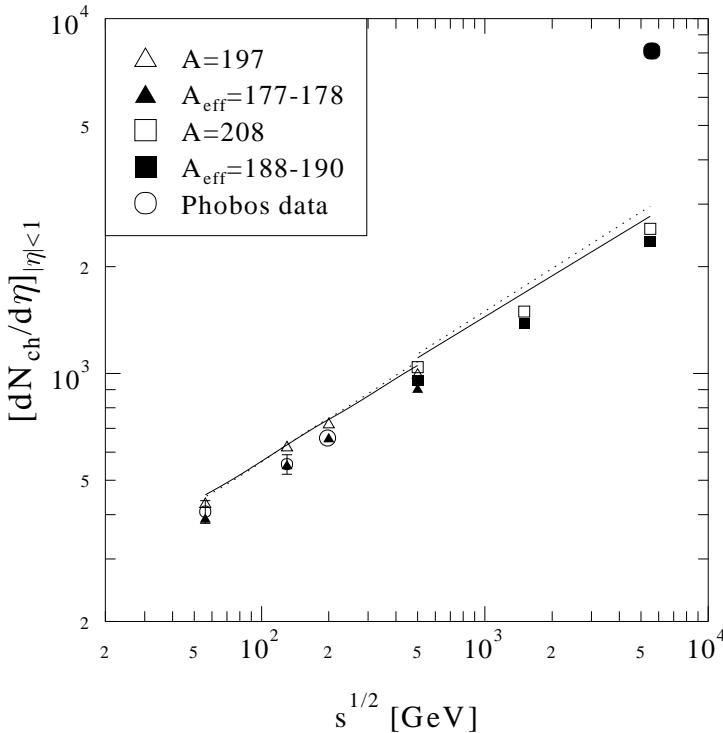


**Figure 12.1:** Midrapidity charged particle densities calculated in a perturbative QCD model by Eskola et. al. as function of  $\sqrt{s}$ . The full dot corresponds to the worst case scenario used in the present simulations.

The shape of the transverse momentum spectra of produced particles is also not known for LHC energy. For the simulation of pions to evaluate the performance of the TRD the shape of the  $p_t$  spectra was parametrized by a power law fitted to the CDF data [8] in agreement with the shape predicted by the HIJING [9] model. For kaons a  $p_t$  scaling from the pion distribution has been used. However, the pion spectra measured in central Au–Au collisions by the PHENIX collaboration [10] are considerably steeper than those of pp and the HIJING model, see Fig. 12.2. Spectra in Pb–Pb collisions at LHC energies that are softer than currently assumed, would result in a much smaller pion yield at high  $p_t$ .

Thus, the recent RHIC data indicate that both the charged particle density at mid-rapidity and the shape of the pion  $p_t$  spectra assumed in the present simulation and upon which depends the background in the TRD detector, represent the worst case scenario and might already provide a large safety factor.

The yields of  $J/\psi$  and  $\Upsilon$ , also unknown in such collisions, were estimated extrapolating from existing pp data in the framework of the colour evaporation model and scaling up to central Pb–Pb collisions, as described in the CMS note [11], see also Section 6.5. According to this extrapolation 0.5  $J/\psi$  and 0.012  $\Upsilon$  per event are expected.

The yields of D and B mesons in central Pb–Pb collisions are expected to be large. To estimate them [12] a reasonable baseline for the production of  $c\bar{c}$  and  $b\bar{b}$  in pp collisions at  $\sqrt{s} = 5.5$  TeV had to be obtained first. For this, PYTHIA [13] was used to calculate in leading order  $\sigma(c\bar{c})$  and  $\sigma(b\bar{b})$  using the MRST [14], CTEQ5M1 [15] and GRV(98)HO [16] set of parton density functions including the ESK98 [17] parametrisation of nuclear shadowing effects. A  $K$  factor of 2 was used to estimate the next to leading order corrections. The yields were then scaled up from pp to central Pb–Pb using the average number of collisions from a Glauber calculation. The average of these calculations give  $dN(c\bar{c})/dy = 115$  and  $dN(b\bar{b})/dy = 4.6$ . PYTHIA was then used to calculate the hadronization, resulting in a total multiplicity per event of 230 D mesons: 140  $D^0$  and  $\bar{D}^0$ , 45  $D^\pm$ , 27  $\bar{D}_s^0$  and 9 B mesons: 3.7  $B_d^0$  and  $\bar{B}_d^0$ , 3.6  $B^\pm$  and 1.1  $B_s^0$ .

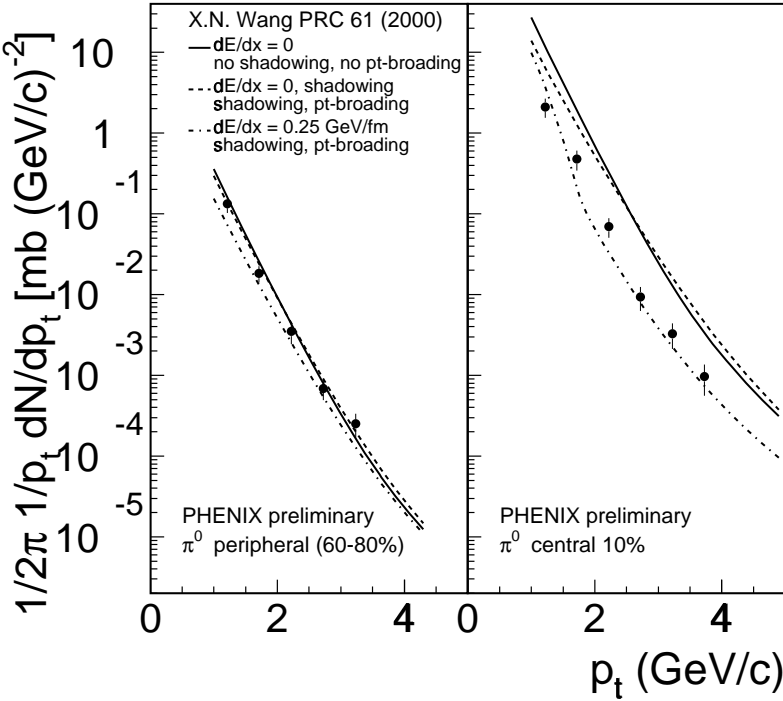


**Figure 12.2:** Transverse momentum spectra measured by PHENIX for Au–Au collisions at  $\sqrt{s} = 130$  GeV compared to the HIJING predictions.

In Ref. [2], the signal/background ratio  $R_s$  for the detection of  $J/\psi$  and  $\Upsilon$  mesons was evaluated for  $dN_{ch}/dy = 8000$  and using cross sections and transverse momentum distributions as discussed above. It lead to  $R_s > 1$  for  $\Upsilon$  and  $R_s > 0.1$  for  $J/\psi$ . Since global tracking through the whole ALICE apparatus is not yet available, we will not provide new estimates of  $R_s$  here. We note, however, that with charged particle multiplicities and  $p_t$  spectral shapes as extrapolated from recent RHIC data the  $R_s$  values might increase substantially, perhaps by an order of magnitude.

## 12.3 Simulation environment

AliRoot [18], the object-oriented framework developed in ALICE, version V3.05, was used for the generation, detector response simulation and analysis of the simulated data as described in Chapter 11. The framework provides a seamless interface to GEANT3 [19], GEANT4 [20] and soon to FLUKA [21] for particle transport. It provides the flexibility to use GEANT3 or GEANT4 with the same definition of detector geometry. FLUKA is used standalone for radiation background studies, with a less detailed description of the geometry of the layout which is described using the ALIFE module [22]. Recently FLUKA was extended with the implementation of thermal neutron capture in Xenon for the TRD background calculations [23].

In AliRoot there are different modules for the generation of the input particles as well as for the simulation of the detector response for each detector. The geometry of the detectors is described in detail while for the detector response a ‘detailed’ and a ‘fast’ mode have been implemented. The reconstruction strategies and algorithms for the different detectors as well as for the global tracking in the central barrel are currently being actively developed aiming at a ‘physics run’ for the ALICE Physics Performance Report.

### 12.3.1 Simulation of the detector layout

The detection of di-leptonic decays of heavy quarkonia and semi-leptonic decays of B and D mesons require the measurement of high  $p_t$  electrons; therefore this study was performed assuming a 0.4 T magnetic field, which the L3 magnet can provide according to current evaluations and tests [24]. The production vertex of the primary particles was fixed at the center of the experiment. The full configuration of the TRD detector was used as is implemented in AliRoot and described in Chapter 11. A picture of the TRD layout is shown in Colour Fig. 3. The TRD detector is embedded in the space frame as shown in Fig. 2.1. The space frame geometry is always included in the simulation when the TRD is activated.

In the ‘detailed’ TRD simulation mode, charged particles losing energy in the chamber gas produce primary and secondary electrons from ionization as described in Chapter 11. Each electron produces a ‘hit’ from which the digitized signal for every pad is derived. That way detailed studies of the chamber performance can be carried out. However, for some purposes this is a too detailed and slow procedure. Therefore, a ‘fast’ simulation mode for the detector response was also implemented; charged particles that cross the active area of one of the multiwire proportional chambers produce one hit only which is placed in the center of the active part of the chamber. Hence particles traversing all 6 planes of the TRD through their active area produce a total of 6 hits.

### 12.3.2 Simulation of input particles

Different type of event generators, provided in AliRoot, were used to generate the different type of input particles depending on the performed study:

- the ‘signal’-generating particles were produced according to a parametrization of their  $y$  and  $p_t$  distributions
- the bulk of produced particles in a Pb–Pb collision, pions and kaons, were generated using the so called ‘parametrized HIJING’ event generator, using their parametrized  $y$  and  $p_t$  distributions as well as their relative yields, normalized to a total number of charged particles of 8000 in the region  $-0.5 < \eta < 0.5$ .

The ‘signal’-generating particles  $\Upsilon$ ,  $J/\psi$ , as well as B and D mesons, were produced with flat rapidity and  $p_t$  distributions and then were weighted with a realistic  $p_t$  distribution [2]:

$$\frac{dn}{dp_t} = \frac{p_t}{[1 + (\frac{p_t}{p_t^0})^2]^n} \quad (12.1)$$

with the parameters  $p_t^0$  and  $n$  as given in Table 12.1 for the different particles.

**Table 12.1:** Parameters of the functional form used to describe the  $p_t$  distribution of different particles.

particle	$p_t^0$	$n$
$\Upsilon$	4.7	3.5
$J/\psi$	3.5	2.3
B	4.0	3.6
D	4.08	9.4

$\Upsilon$  mesons were generated in the rapidity interval  $-1.2 < y < 1.2$  and  $p_t < 10 \text{ GeV}/c$ ,  $J/\psi$  in  $-1.5 < y < 1.5$  and  $p_t < 10 \text{ GeV}/c$ , B and D mesons in the interval  $-5 < y < 5$  and  $p_t < 10 \text{ GeV}/c$ . PYTHIA was

used to force the decay of the primary particles:  $\Upsilon$  and  $J/\psi$  exclusively into di-electrons, B and D mesons exclusively into the semi-leptonic channels. The rapidity interval was chosen such that primary particles outside this interval do not emit their decay products into the TRD acceptance. Those distributions were used to evaluate the TRD acceptance and the effect of the L1 trigger.

The ‘parametrized HIJING’ event generator was used to generate pions and kaons of central Pb–Pb collision for background estimates.

### 12.3.3 Simulation studies

For the evaluation of the acceptances only the TRD detector and the space frame were included in the simulation of the ALICE set-up. For the transport of all generated particles through the TRD layout only decays, energy loss and multiple scattering were enabled from all physics processes implemented in GEANT3. In this way all primary electrons could be accounted for until they exited the TRD and there was no other source of background electrons. The ‘fast’ detector response simulation option was used. The acceptance for any of the parent particles was defined by the requirement that its daughter particles have to traverse at least 5 planes of the TRD through their active area, i.e. to produce at least 5 hits in total. Optimization of the reconstruction algorithms using the data produced by the ‘detailed’ simulation has shown that this would insure a good track reconstruction and particle identification probability. The L1 TRD trigger, as described in Chapter 6, is designed to select charged particles with  $p_t > 3 \text{ GeV}/c$  traversing the TRD detector. A  $\Upsilon$  or  $J/\psi$  trigger requires a pair of opposite charged electrons with  $p_t$  above this threshold.

For the reconstruction of the invariant mass and the estimate of the background due to primary and secondary particles, as well as  $\gamma$  conversions, all detectors in the central barrel were included in the simulation and all physics processes in GEANT3 were activated.

## 12.4 $\Upsilon$ and $J/\psi$ mesons

### 12.4.1 Acceptance

To evaluate the  $\Upsilon$  and  $J/\psi$  acceptance 900 000 primary particles of each kind were generated with flat rapidity and  $p_t$  distributions in the interval  $-1.2 < y < 1.2$  ( $-1.5 < y < 1.5$  for  $J/\psi$ ) and  $p_t < 10 \text{ GeV}/c$ , all decaying into  $e^+e^-$  pairs. The acceptance and the effect of the L1 trigger was then evaluated using the  $p_t$ -weighted distributions of the parent particles. The  $p_t$ -weights were generated using eq. 12.1 and the corresponding parameters given in Table 12.1.

Figures 12.3 and 12.4 show, on the top row, the rapidity and  $p_t$  distributions of the parent particles and, on the lower row, those of their decay electrons. The full curve in each figure corresponds to the input distribution. The dashed curves show the distributions of particles in the TRD acceptance with the condition that both decay particles cross at least 5 chambers. The main condition for a L1 trigger is a  $p_t$  cut of, e.g.,  $3 \text{ GeV}/c$  for each particle (see Chapter 6). The dotted histogram shows the effect of the L1 trigger: the distributions are plotted with an additional requirement of  $p_t > 3 \text{ GeV}/c$  for both decay particles. The rapidity distribution of the accepted  $\Upsilon$  covers the range  $|y| < 1.0$  and is Gaussian-like with a  $\sigma = 0.39$ ; that for  $J/\psi$  has the same coverage and is somewhat flatter with a  $\sigma = 0.41$ .

The  $\Upsilon$  and  $J/\psi$  acceptances under the trigger requirement are shown differentially in the  $y$ - $p_t$  plane in Fig. 12.5 for  $\Upsilon$  and in Fig. 12.6 for  $J/\psi$ . In the lego plot of the  $\Upsilon$  acceptance a small dip is clearly seen developing at  $p_t \sim 6 \text{ GeV}/c$ . This is due to the fact that low  $p_t$   $\Upsilon$  mesons decay by emitting  $e^+e^-$  pairs where both leptons have a  $p_t$  above  $3 \text{ GeV}/c$  and hence pass the trigger condition. The decay of intermediate  $p_t$   $\Upsilon$  mesons, of  $p_t \sim 6 \text{ GeV}/c$ , can be asymmetric in the laboratory frame with one of the decay particles having  $p_t$  less than  $3 \text{ GeV}/c$ ; therefore those  $\Upsilon$  are lost due to the L1 trigger condition. The differential  $\Upsilon$  acceptance at mid-rapidity and  $p_t < 1 \text{ GeV}/c$  is 54%, while at  $p_t = 6 \text{ GeV}/c$ , is 47%.

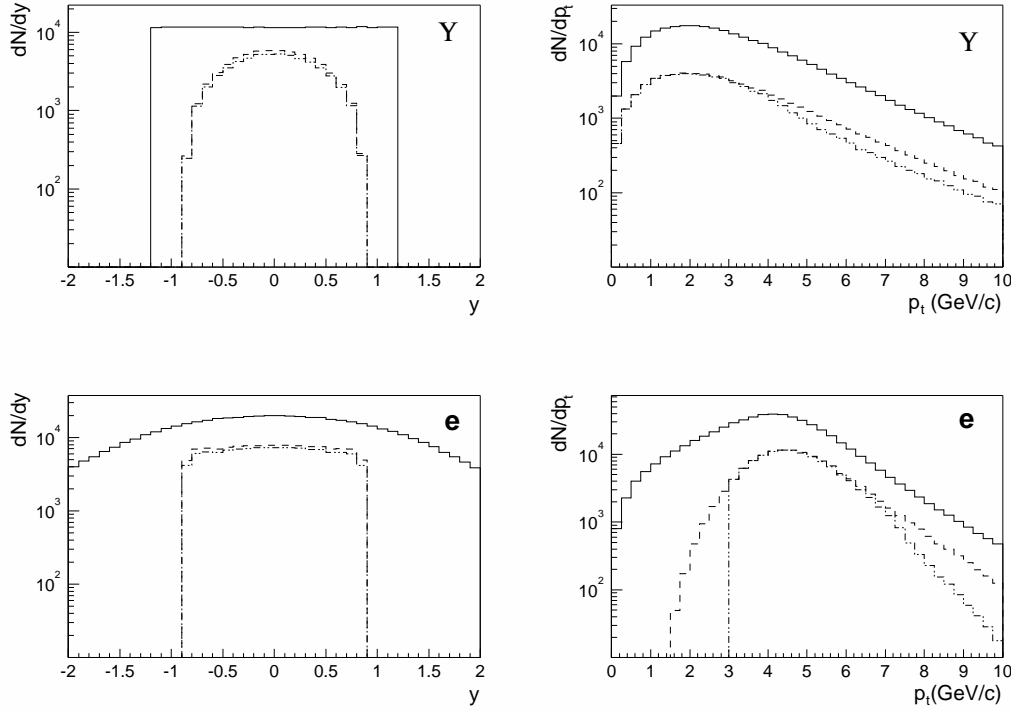


**Figure 12.3:** Rapidity and  $p_t$  distributions of  $\gamma$  and its decay  $e^+e^-$ . The solid lines show the input distributions, dashed are those accepted in the TRD and the dotted histograms show the fraction accepted in the TRD with the L1 trigger requirement of  $p_t > 3$  GeV/c on the decay particles.

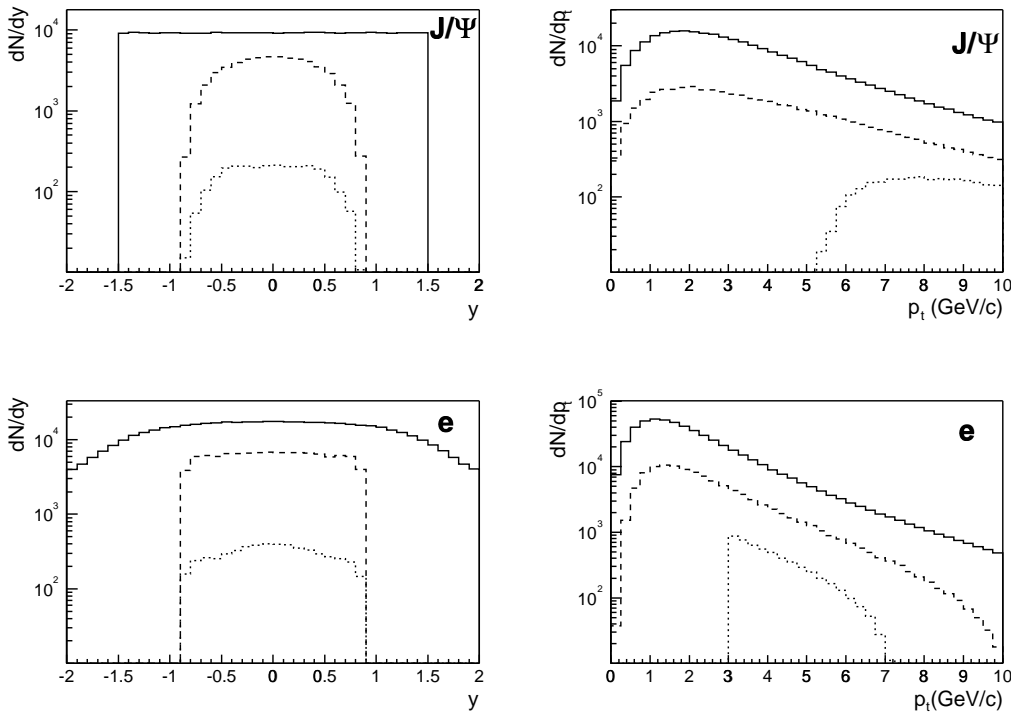


**Figure 12.4:** Rapidity and  $p_t$  distributions of  $J/\psi$  and its decay  $e^+e^-$ . The solid lines show the input distributions, dashed are those accepted in the TRD and the dotted histograms show the fraction accepted in the TRD with the L1 trigger requirement of  $p_t > 3$  GeV/c on the decay particles.

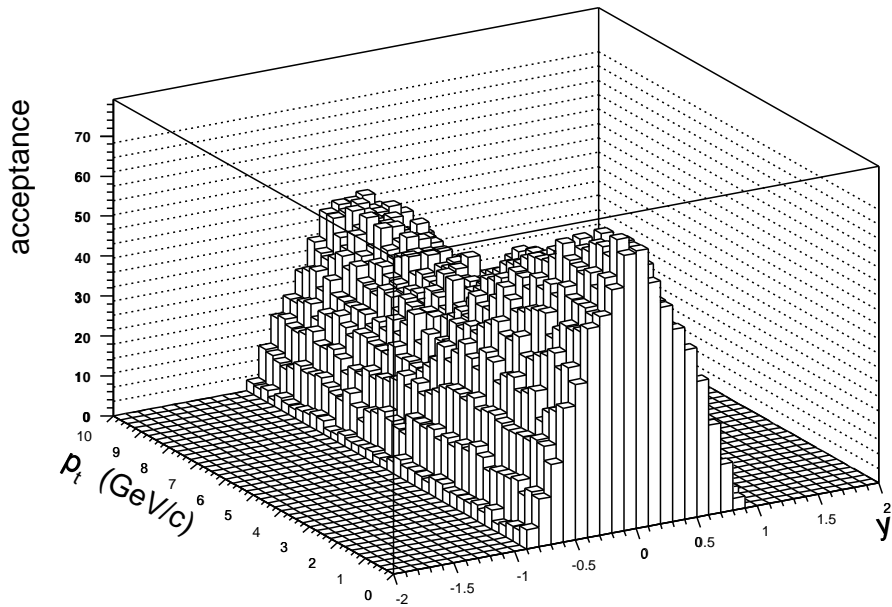


**Figure 12.5:** Differential  $y$ - $p_t$  acceptance in % for the detection of  $\Upsilon$  in the TRD under the L1 trigger condition.

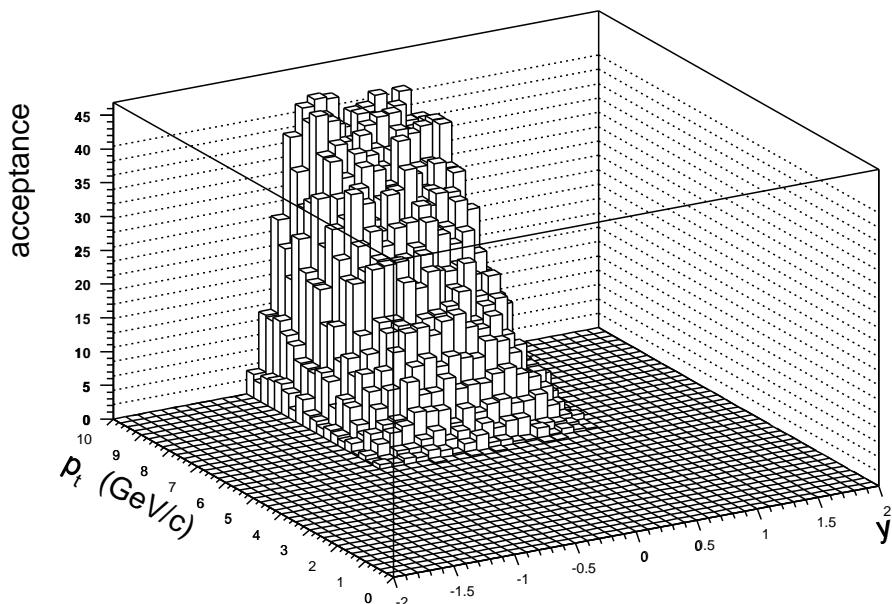


**Figure 12.6:** Differential  $y$ - $p_t$  acceptance in % for the detection of  $J/\psi$  in the TRD under the L1 trigger condition.

The trigger cut on the  $p_t$  of  $e^+e^-$  has a much stronger effect on the  $J/\psi$  distribution since the mass difference of the  $J/\psi$  is much smaller than that of the  $\Upsilon$ ; hence the decays of low  $p_t$   $J/\psi$  produce  $e^+e^-$  pairs that do not make it through the  $p_t$  threshold of  $3 \text{ GeV}/c$  of the trigger. It is only at rather large  $p_t$  that the  $J/\psi$  decay kinematics allow both of the  $e^+e^-$  to have  $p_t > 3 \text{ GeV}/c$ . This results in no  $J/\psi$  acceptance below a  $p_t$  of  $\sim 5.2 \text{ GeV}/c$  under the L1 trigger condition. The differential acceptance at mid-rapidity reaches 37% for a  $p_t$  of  $10 \text{ GeV}/c$ .

The geometrical acceptances for  $\Upsilon$  and  $J/\psi$  integrated over the rapidity range  $-1.0 < y < 1.0$ , the region where there is some acceptance, are summarized in Table 12.2. They are tabulated without and with the L1 trigger condition on their decay particles and for different  $p_t$  range of the parent particle.

**Table 12.2:** Geometrical acceptance for the detection of  $\Upsilon$  and  $J/\psi$  in the TRD. They are given for different  $y$  and  $p_t$  ranges of the parent particles, with and without the L1 trigger  $p_t$  cut on the  $e^+e^-$  pair.

parent particle	$p_t$ of $e^+e^-$	$y$ and $p_t$ of parent	TRD accept. (%)
$\Upsilon$	no cut	$ y  < 1.0$ , all $p_t$	26.6
$\Upsilon$	no cut	$ y  < 0.5$ , $p_t < 3 \text{ GeV}/c$	42.4
$\Upsilon$	$p_t > 3 \text{ GeV}/c$	$ y  < 1.0$ , all $p_t$	24.0
$\Upsilon$	$p_t > 3 \text{ GeV}/c$	$ y  < 0.5$ , $p_t < 3 \text{ GeV}/c$	41.7
$J/\psi$	no cut	$ y  < 1.0$ , all $p_t$	29.5
$J/\psi$	no cut	$ y  < 0.5$ , $p_t > 6 \text{ GeV}/c$	62.8
$J/\psi$	$p_t > 3 \text{ GeV}/c$	$ y  < 1.0$ , all $p_t$	1.4
$J/\psi$	$p_t > 3 \text{ GeV}/c$	$ y  < 0.5$ , $p_t > 6 \text{ GeV}/c$	16.3

### 12.4.2 $\Upsilon$ invariant mass distribution

The best momentum resolution for electrons identified in the TRD will be obtained by combining the information of the TRD, TPC and ITS in a global track fit. Such a procedure using Kalman-filter tracking techniques was implemented in the AliRoot framework and is currently being optimized.

To evaluate the mass resolution with tracking in the TRD only, events containing only  $\Upsilon$  in the rapidity interval  $-0.5 < y < 0.5$  and with a realistic  $p_t$  distribution given by eq. 12.1 were generated. All the detectors of the central barrel and all physics processes were enabled for the particle transport. The ‘detailed’ TRD detector response simulation mode was used. The point reconstruction and tracking were performed as described in Section 11.3 and 11.4. From the momentum resolutions obtained with the full off-line tracking the mass resolutions were determined using the same algorithm as was used in the simulations for the TRD trigger (see Chapter 6).

Applying the TRD L1 trigger condition that both  $e^+e^-$  have a  $p_t > 3 \text{ GeV}/c$  results in an  $e^+e^-$  invariant mass distribution shown in Fig. 12.7. The invariant mass distribution is asymmetric with a tail to lower masses due to radiative losses of the electrons in the material before the TRD. The mass resolution for tracking in the TRD only, ignoring the low mass tail resulting from bremsstrahlung losses, has a  $\sigma = 245 \text{ MeV}/c^2$ .

The global track fit gives an improved estimator for the original momentum of the  $e^+e^-$  pair and, at the same time, will provide a much better momentum resolution. A study was performed using the track reconstruction in the TPC and ITS, but yet without the TRD, to evaluate the mass resolution at the mass of the  $\Upsilon$  as function of the event multiplicity for two magnetic field values. The results, shown in Fig. 12.8, give a mass resolution of about 1% for the full multiplicity and  $B = 0.4 \text{ T}$ .

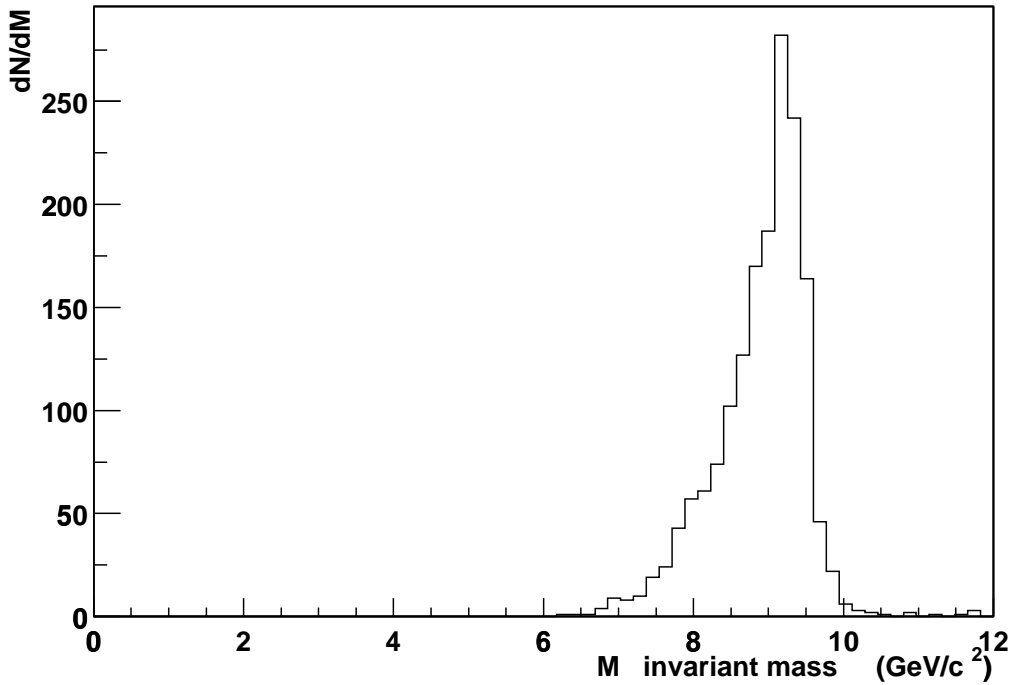


**Figure 12.7:** Di-electron invariant mass distribution for  $e^+e^-$  pairs from  $\Upsilon$  decays as reconstructed in the TRD, including the TRD L1 trigger condition.

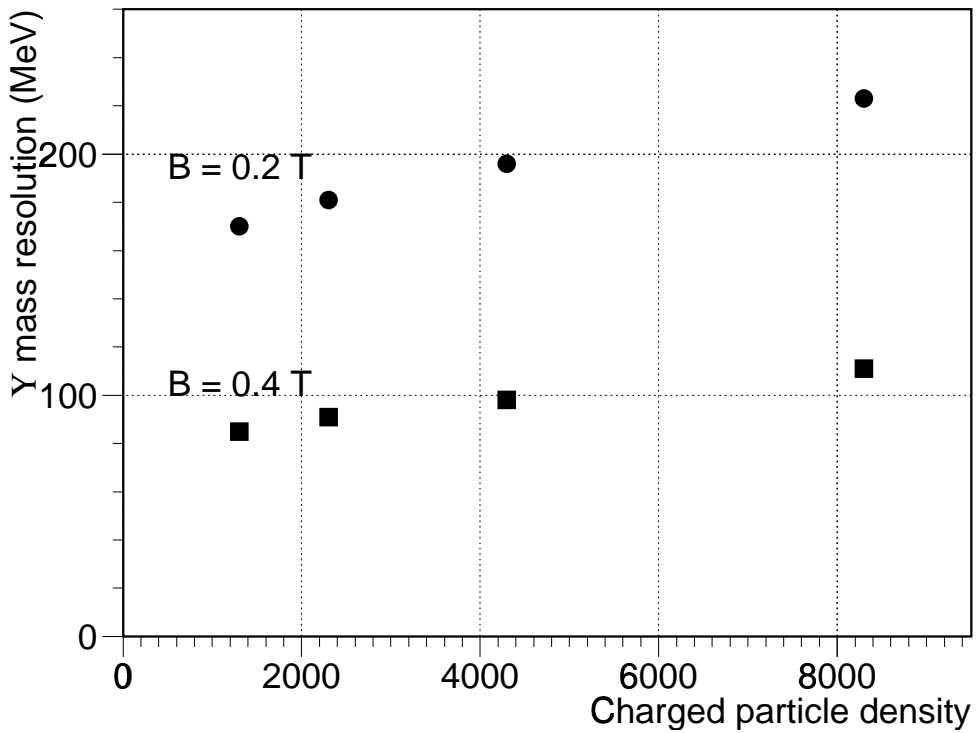


**Figure 12.8:** Invariant mass resolution for  $\Upsilon$  decaying into  $e^+e^-$  as function of the event multiplicity when both tracks are reconstructed in the TPC and ITS.

## 12.5 B and D mesons

For the calculation of the acceptance for B and D mesons 4 million primary particles, of each kind, were generated with flat distributions in the interval  $-5 < y < 5$  and  $p_t < 10 \text{ GeV}/c$ . All particles were forced to decay semi-leptonically. The  $p_t$ -weighted distributions were then obtained as described in Section 12.3.

The rapidity and  $p_t$  distributions of the parent particles and of their decay electrons are shown in Fig. 12.9 and Fig. 12.10 for B and D mesons, respectively. The upper row shows the parent particle distributions, the lower one the distributions of their decay electron. The rapidity interval of the primary particles was restricted to  $-4 < y < 4$  in these projections. The solid lines correspond to the input distributions. The dashed lines show the same distributions in the TRD acceptance. The rapidity distributions of accepted B and D mesons are Gaussian-like with a  $\sigma = 0.93$  for B and  $\sigma = 0.89$  for D mesons. The accepted electrons from B decays have  $a < p_t > = 2.54 \text{ GeV}/c$ , those from D decays yield  $a < p_t > = 1.32 \text{ GeV}/c$ . The B and D differential acceptance as function of rapidity and  $p_t$  are shown in Fig. 12.11 and Fig. 12.12 respectively. At mid-rapidity the acceptance varies between 50% and 90%.

The finite lifetime of B and D mesons,  $c\tau = 496 \mu\text{m}$  and  $c\tau = 315 \mu\text{m}$ , respectively, was used to develop a strategy to separate electrons coming from B and D decays from those originating from other (promptly decaying) particles ( $\pi^0, \rho, \omega, \phi, J/\psi$ ) as described in the TRD TP [2]. It is based on the selection of non-primary high  $p_t$  electrons by optimizing selection criteria based on their transverse distance of closest approach to the primary vertex,  $d_0$ , and on their  $p_t$ . Complete simulation of the impact parameter resolution will be obtained only after optimization of the global tracking, matching the TRD tracks to those in the TPC and ITS. For the present geometrical studies  $d_0$  is calculated from the nominal momentum of the decay lepton and the positions of the primary and secondary vertices without taking into account any detector resolutions. The effect of the detector resolution was investigated in the TRD TP [2].

Figures 12.13 and 12.14 show the rapidity and transverse momentum distributions of accepted B mesons under different selection criteria. The solid line shows the distributions of accepted B's with no further cuts on the  $d_0$  and  $p_t$  of the decay electron, the other lines the same distributions for  $d_0 > 200 \mu\text{m}$  and  $p_t > 0.5 \text{ GeV}/c$  (dashed line),  $p_t > 1 \text{ GeV}/c$  (dotted line) and  $p_t > 3 \text{ GeV}/c$  (dash-dotted line). The integrated acceptances are summarized in Table 12.3. Those cuts need to be optimized on the basis of the global tracking results. However, in Refs. [26, 27] it was shown that while a  $d_0 > 100 \mu\text{m}$  might be optimistic, a  $200 \mu\text{m}$  cut should be safe. It was also shown in the TRD TP [2] that  $p_t$  cuts significantly reduce the background due to the primary particle multiplicity.

Similarly, Fig. 12.15 and Fig. 12.16 show the same distributions for D mesons, and the integrated acceptances are summarized in Table 12.3. The  $d_0$  and  $p_t$  cuts make a stronger effect on the D acceptance.

**Table 12.3:** Integrated acceptance for B and D mesons in the rapidity range  $|y| < 4.0$  without and with the  $d_0 > 200 \mu\text{m}$  and  $p_t$  cuts on the decay electron accepted in the TRD.

parent particle	$d_0$ cut	accept $p_t > 0$	accept $p_t > 0.5$	accept $p_t > 1$	accept $p_t > 3$
B	no cut	17.3 %	12.3 %	8.1 %	1.5 %
B	$d_0 > 200 \mu\text{m}$	7.4 %	3.7 %	1.9 %	0.17 %
D	no cut	15.0 %	5.9 %	2.1 %	0.055 %
D	$d_0 > 200 \mu\text{m}$	5.5 %	4.4 %	0.05 %	-

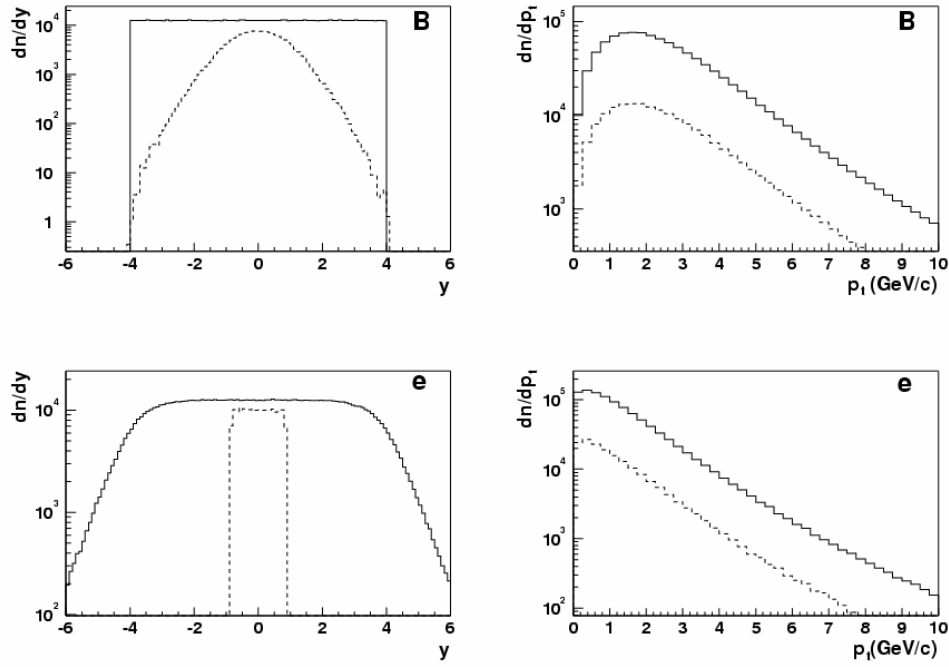


**Figure 12.9:** Rapidity and  $p_t$  distributions of  $B$  mesons top row, and its decay electron bottom row; full line, input distributions and dashed line accepted in TRD.

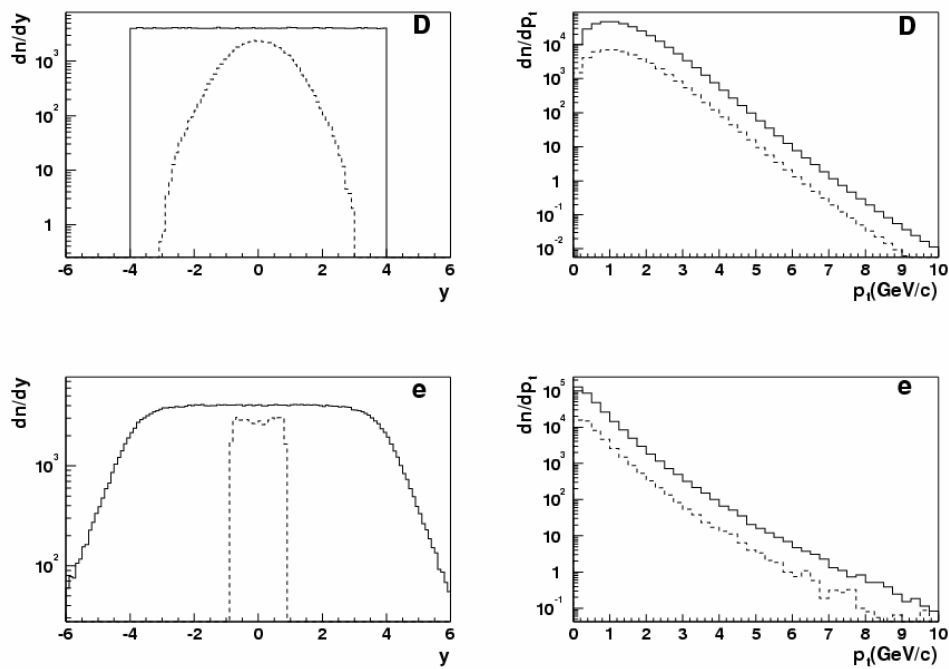


**Figure 12.10:** Rapidity and  $p_t$  distributions of  $D$  mesons (top row), and corresponding decay electrons (bottom row); full lines depict input distributions, dashed lines are for particles accepted in TRD.

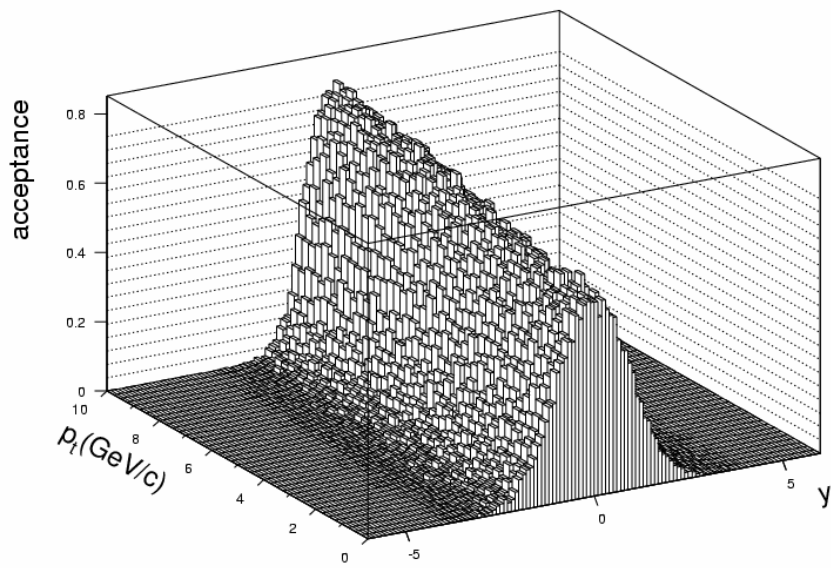


**Figure 12.11:** Acceptance for B mesons in the  $y$ - $p_t$  plane.

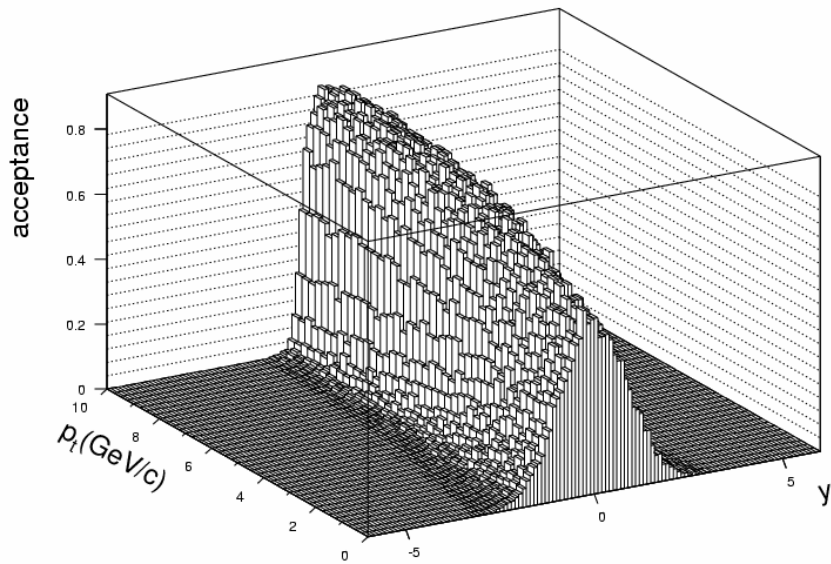


**Figure 12.12:** Acceptance for D mesons in the  $y$ - $p_t$  plane.

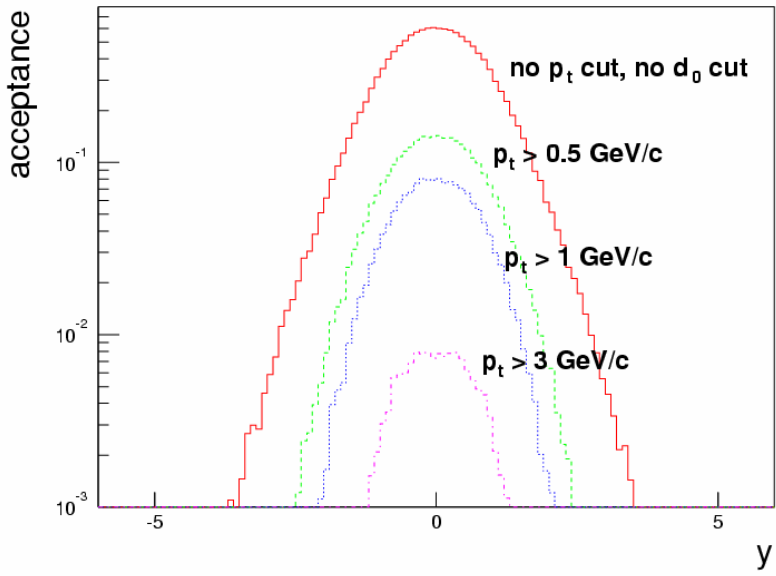


**Figure 12.13:** Rapidity acceptance for B mesons without cuts and for various cuts on the  $p_t$  of the decay electron. All  $p_t$  cuts contain also a cut on the  $d_0$  variable discussed in the text.

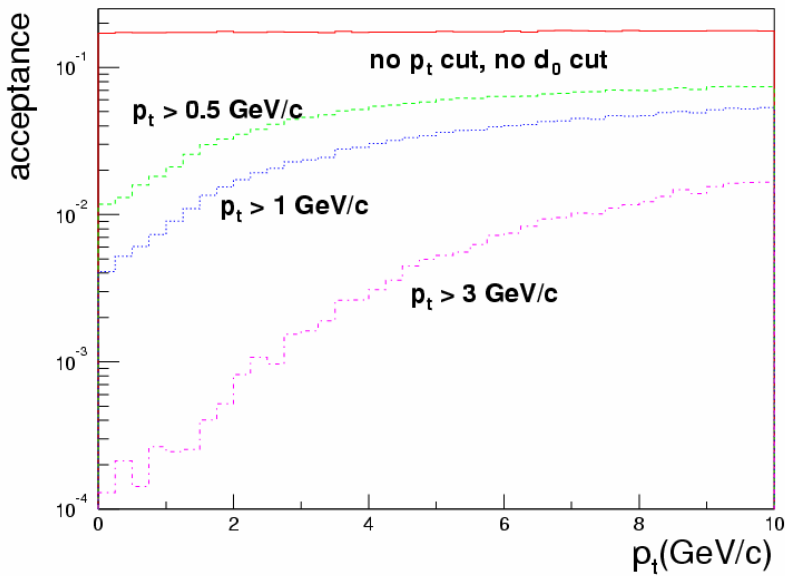


**Figure 12.14:** Transverse momentum acceptance for B mesons without cuts and for various cuts on the  $p_t$  of the decay electron. All  $p_t$  cuts contain also a cut on the  $d_0$  variable discussed in the text.

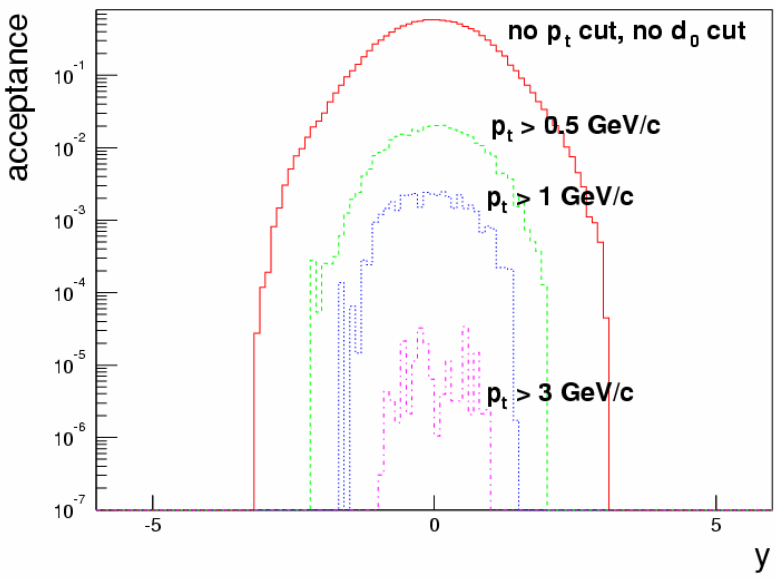


**Figure 12.15:** Rapidity acceptance for D mesons without cuts and for various cuts on the  $p_t$  of the decay electron. All  $p_t$  cuts contain also a cut on the  $d_0$  variable discussed in the text.

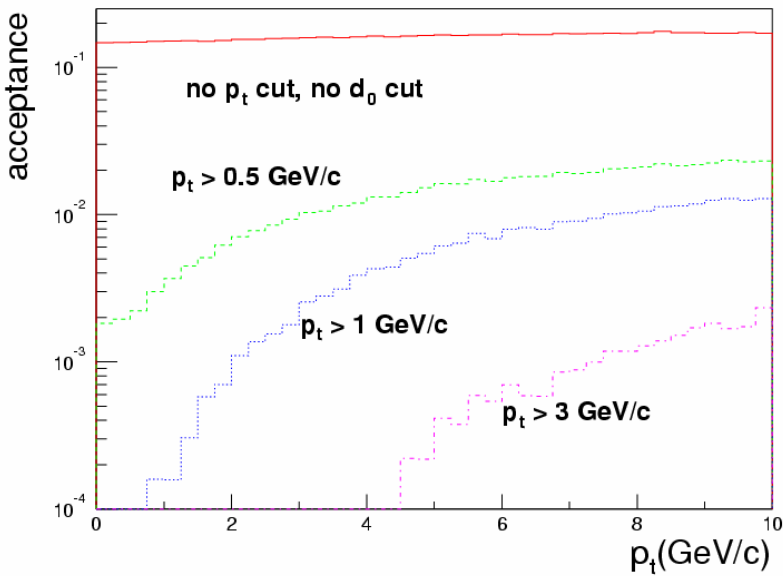


**Figure 12.16:** Transverse momentum acceptance for D mesons without cuts and for various cuts on the  $p_t$  of the decay electron. All  $p_t$  cuts contain also a cut on the  $d_0$  variable discussed in the text.

## 12.6 TRD acceptance for different geometrical configurations

The number of detector modules that can be afforded by the Collaboration on time for the start-up of the LHC is not presently known. Therefore, a study was performed to evaluate the TRD acceptance for different geometrical configurations [25]. Different considerations were taken into account in optimizing the detector acceptance, namely the number of currently affordable stacks of detector modules, different strategies for the completion of the detector and how they would affect the overall installation planning.

The financing of the construction of the full TRD detector, consisting of 540 detector modules arranged in 90 stacks, which would cover the pseudo-rapidity range  $-0.9 \leq \eta \leq 0.9$  and the full azimuth is so far not assured. The present commitments until the start-up of the LHC are sufficient to build only about half of the total number of the TRD modules. Participation of other groups that would make possible the construction of the full TRD on time for the start-up is sought but currently not guaranteed. Additional funding for the completion of the full TRD detector is expected from the funding agencies of the TRD groups; in this case the detector will be completed later than the start-up date. Therefore, at present, it cannot be ruled out that a partial TRD will be finally all that might be affordable by the Collaboration.

Those considerations lead to three possible scenarios; (a) completion of the full detector for start-up, (b) partial construction and installation of the TRD for start-up with its completion after 2 or 3 years and (c) undesirable but not excluded currently, a partial TRD only.

As discussed in Chapter 16, the TRD stacks will be assembled in supermodules which will then be inserted in the space frame. In the case that only a part of the full TRD detector would be constructed at start-up and its completion would follow at a later stage, one would have to optimise the installation procedure even at the expense of the physics performance for the first year of running. It is difficult to imagine that the supermodules would be only partially filled and installed in the space frame at a first stage, to be taken out and completed in a later stage; this would also imply redoing all the services, alignment and calibrations.

The acceptance for the detection of the semi-leptonic decays of D and B mesons is proportional to the solid angle covered by a given TRD layout. For  $\Upsilon$  and  $J/\psi$  this is not the case since electron pairs have to be detected in coincidence, introducing geometrical correlations. The low  $p_t$  primary particles decay emitting the  $e^+e^-$  pair back to back in the laboratory frame and therefore the coverage at the opposite sides of the interaction point gives the largest yields of detected  $\Upsilon$ . As the  $p_t$  of the primary particle increases, the decay kinematics focuses the electron-positron pair closer and closer and therefore a large coverage at the same side of the interaction point is optimal.

The acceptance of  $\Upsilon$ ,  $J/\psi$ , B and D mesons were calculated for three partial TRD configurations and compared to that for the full TRD detector.

The configuration called ‘WING’ has 10 fully filled supermodules distributed as a symmetric two-arm spectrometer with a total of 50 stacks. From the installation point of view this would be the preferred configuration for a partial TRD at a first stage which would be completed one or two years after start-up.

On the other hand, if at a certain point it becomes clear that there will not be enough funds to complete the full TRD detector, one would have to optimize the phase space coverage and distributing the available modules into complete supermodules might not be the best strategy.

The two other configurations ‘SHORT’ and ‘SHORTASYM’ consist of a compact TRD with no holes in azimuth, however, with only 3 out of 5 stacks of each supermodule being installed. Both of them have 54 stacks. The configuration ‘SHORT’, being centered in  $z$  around the interaction point, provides a symmetric coverage in rapidity. The ‘SHORTASYM’ is displaced having the two empty stacks on the same side of the supermodule. In this way the ‘SHORTASYM’ provides larger coverage of rapidity; however it implies an asymmetric weight distribution on the space frame. Those two configurations represent the type of solution one might choose in case it would be clear that the TRD could not be fully financed.

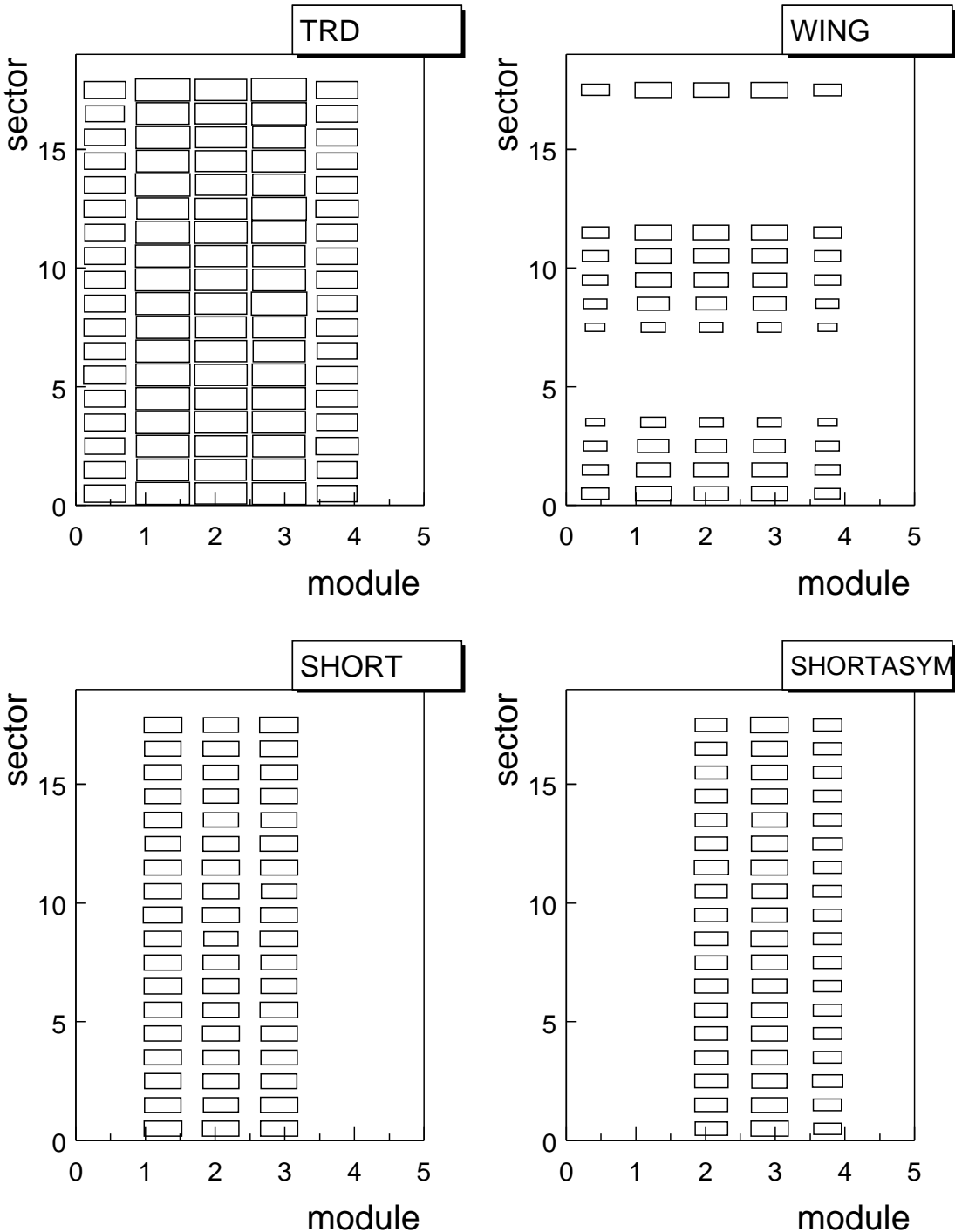


**Figure 12.17:** The inner layer of the TRD for the different geometries considered; the horizontal axis gives the segmentation in  $z$  and the vertical in  $\varphi$ . Each module is represented by a rectangle. The area of each rectangle is proportional to the acceptance of the corresponding module for  $e^+e^-$  from  $\gamma$  decays. From the top left to bottom right the geometries are: ‘TRD’, ‘WING’, ‘SHORT’ and ‘SHORTASYM’.

Figure 12.17 shows in a graphical way the  $\gamma$  acceptance for the different geometrical configurations. Figure 12.18 shows the  $B$  acceptance for the same configurations. Top row left shows the full TRD geometry (labelled “TRD”) and right the ‘WING’ configuration. The bottom row left shows the ‘SHORT’

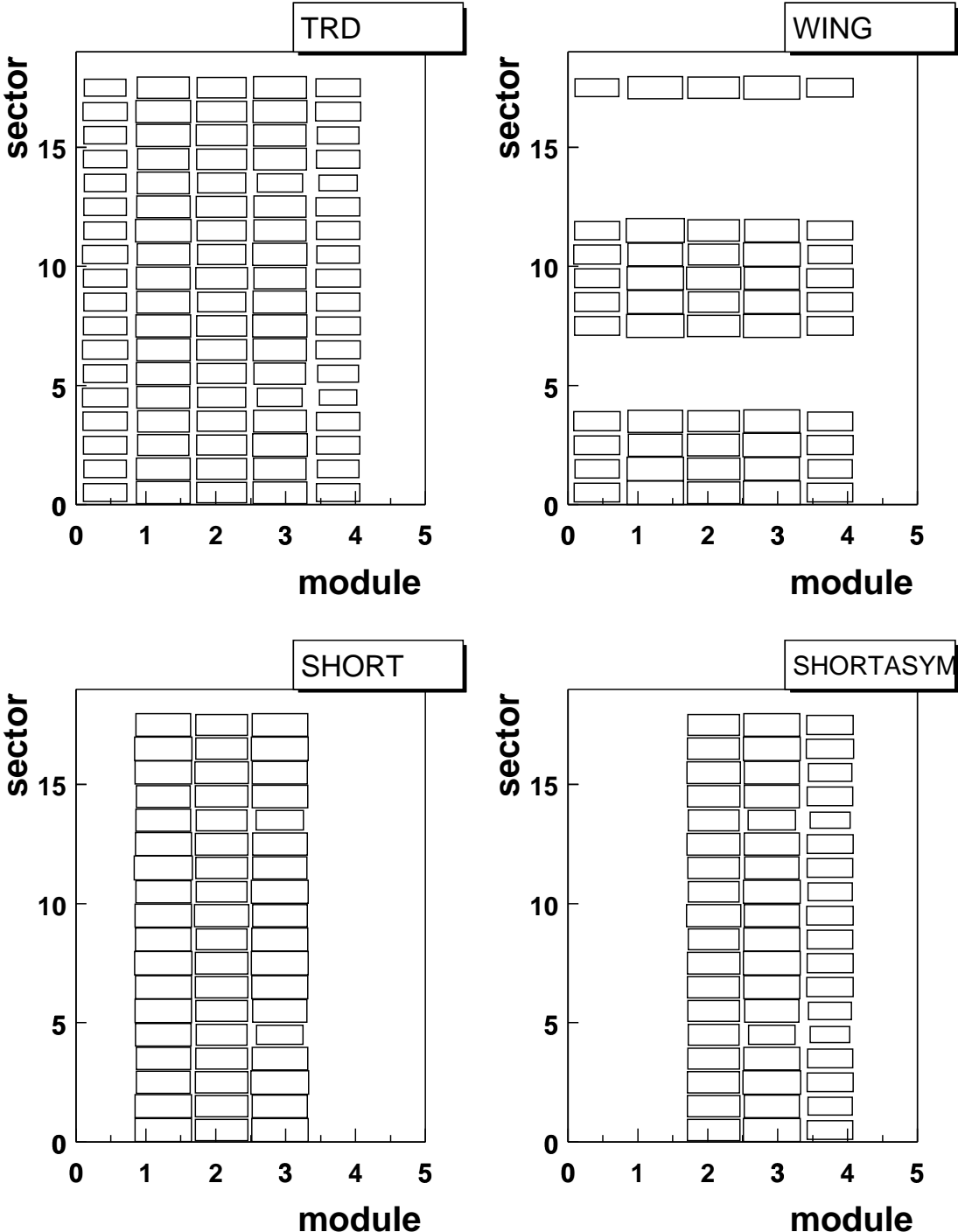


**Figure 12.18:** Same as Fig. 12.17 for electrons from B decays.

and right the ‘SHORTASYM’ configuration. Since the distribution of chambers is identical for all layers only the innermost layer for each configuration is shown with each rectangle representing a module; the horizontal axis gives the segmentation in  $z$  and the vertical that in  $\phi$ , hence each row corresponds to a sector and represents a supermodule. Clearly visible are the holes in the TRD layout for each one of the studied configurations. The area of each module is proportional to the number of electrons from  $\Upsilon$  or B decays, respectively, that the module accepts.

The acceptances for the three studied partial configurations, relative to the full TRD, are summarized in Table 12.4.

**Table 12.4:** Fractional acceptance in % of the different TRD configurations relative to the full TRD for the detection of decay electrons from  $\Upsilon$ ,  $J/\psi$ , B and D mesons.

primary particle	'WING'	'SHORT'	'SHORTASYM'
$\Upsilon$	17.4	42.8	46.1
$J/\psi$	34.5	47.9	43.3
B	55.9	64.3	59.9
D	55.7	63.7	59.7

## 12.7 Background

There are several sources of background that have to be considered while reconstructing  $\Upsilon$  and  $J/\psi$  from their  $e^+e^-$  decay detected in the TRD.

- One of them is real  $e^+e^-$  pairs originating from Dalitz decays of  $\pi^0$ ,  $\eta$ ,  $\rho$ ,  $\omega$ ,  $\phi$  or semi-leptonic decays of B and D mesons. Their contribution as evaluated in the TRD TP [2] is shown in Fig 12.19. At large  $p_t$  this background is dominated by  $e^+e^-$  originating from semi-leptonic decays of B and D mesons as well as from Dalitz decays of  $\pi^0$ .
- Another source of background from real electron or positrons, is due to  $\gamma$  conversions, bremsstrahlung and secondary interactions.
- A third source of background is due to charged pions misidentified as electrons by the TRD detector.

The last two sources of background were evaluated using 100 ‘parametrized HIJING’ events as input to the simulation with all the central barrel detectors enabled. Figure 12.20 shows the  $p_t$  spectra of charged pions, electrons from conversions, bremsstrahlung and secondary interactions as well as  $e^+e^-$  from Dalitz decays of  $\pi^0$  that reach the TRD detector. The  $e^+e^-$  from conversions and bremsstrahlung in the material before the TRD are an order of magnitude larger than those from  $\pi^0$  Dalitz decays.

What fraction of the charged pion spectrum will contribute to the background depends on the electron identification and pion rejection capabilities that the final detector will achieve. As was shown in Chapter 11 the fraction of pions misidentified as electrons depends on the required purity of the electron sample and on the multiplicity of the event. Also the global tracking will accept only a fraction of electrons and ‘electron like’ particles, namely those having a good  $\chi^2$  for being primary particles and having a good likelihood of being electrons according to the  $dE/dx$  in the ITS, TPC and TRD and according to the transition radiation in the TRD.

## 12.8 Summary

The main conclusions from the studies presented here are:

1. Acceptances for  $\Upsilon$  and high  $p_t$   $J/\psi$  measurements need the full TRD.
2. The mass resolution for  $\Upsilon$  measurements is of the order of 1% if the magnetic field of the L3 magnet is  $B = 0.4$  T or larger.
3. The main background sources in the electron channel are misidentified pions and conversions.

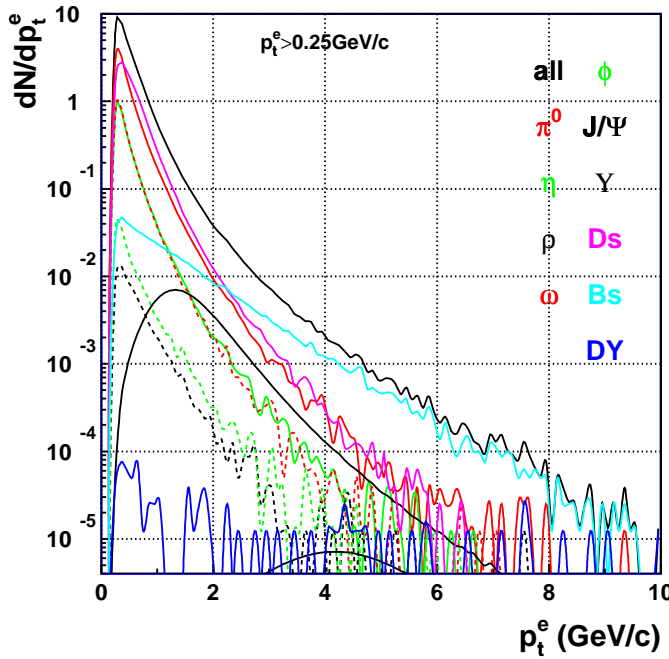


**Figure 12.19:** Transverse momentum spectrum of single electrons in the TRD acceptance from decays of primary particles.

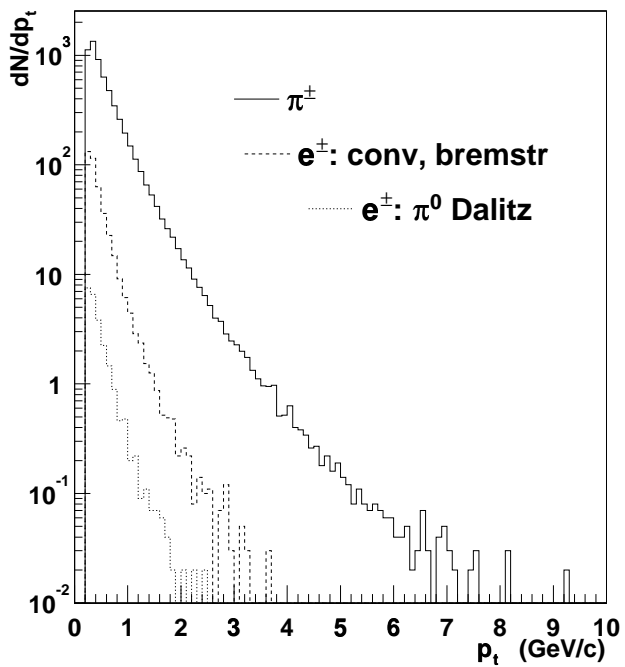


**Figure 12.20:** Transverse momentum spectrum of charged pions (solid line),  $e^+e^-$  from conversions, bremsstrahlung and secondary interactions (dashed line) and  $e^+e^-$  from  $\pi^0$  Dalitz decays (dotted line) in the TRD detector.

4. The measurement of D and B mesons via their semi-leptonic decays can be performed with high efficiency for  $p_t$  cuts of the order of  $1 \text{ GeV}/c$  and higher.

## 13 Detector control

---

The ALICE Detector Control System (DCS) is designed for monitoring and control of correct operational conditions of the ALICE sub-detectors. As this task also involves safety aspects, the hardware links used are independent of the DAQ. The ALICE DCS project is presented in Ref. [1]. The ALICE DCS system is described in Ref [2] and will be described in detail in a future document. Its functionalities include (see also Ref. [3]):

- starting or shutting off a detector, or components of a detector, in a controlled way;
- monitoring of characteristics (analog and/or status values) which are necessary for detector operation and/or the physics data analysis;
- reporting of alarm conditions and initiation of the appropriate response;
- logging and archiving of characteristics, alarms and operator interactions;
- retrieving archived data for trend displays or detector analysis;

In addition, interactions are required with a number of external systems like the area safety system, gas system, cooling and ventilation system, electricity mains supply, LHC, and magnets. However, certain of these systems will only provide informative links to the DCS:

- during normal physics data-taking the DCS will control starting and operation of all the ALICE sub-detectors. For this purpose standard operator commands will be available. Malfunctioning will be signalled to the detector-dedicated control station via centralized alarms.
- during installation and/or maintenance periods it will be necessary to run different detectors, or partitions of them, separately but simultaneously. In this case interference among detectors or between them and external services must be screened.

To satisfy the above requirements the DCS architecture will have two essential features –scalability and modularity– and will be based on distributed intelligence. The detector control system will be designed and organized in layers, corresponding to different levels of visibility and access rights. The higher levels will have a more global view, and will only be allowed to make a limited set of macroscopic actions. On the other end, lower layers will have access to more detailed information and control. At the highest level of the experiment a Supervisory Control layer will provide the communications among the main ALICE subsystems such as the Data Acquisition Control (DAQC), the Trigger Control (TRC) and the DCS. The DCS will be accessed through the Supervisory Control layer. No peer-to-peer connection between DCS and DAQ is envisaged. The Supervisory Control will have the following features:

- provide a global view of the whole experiment to the operator.
- allow the control of the experiment through commands to the DCS, the DAQC and the TRC. It will be capable of generating the sequence of operations in order to bring the experiment to a given working condition. However, detailed actions will be the responsibility of the subsystems.
- collect and dispatch all the communications between the subsystems.
- monitor the operation of the subsystems, generate alarms, and provide the interlock logic where necessary.

- allow the dynamic splitting of the detector into independent partitions and the possibility of concurrent data-taking from the partitions.

Hardware protection of TRD components will be implemented wherever possible. This is the case, for example, for the ramp-down of sense wire high voltages in the presence of sustained over-currents.

## 13.1 Hardware

Within ALICE we intend to develop a DCS system which is as standardized and identical across detector boundaries as technically feasible. Consequently, similar to the general ALICE DCS, the hardware structure of the TRD DCS will be structured in three layers.

- **Field layer.** This is the layer of field instrumentation such as sensor heads, actuators, etc. The field instrumentation has to comply with the requirements of the detector hardware. The interfaces to the control equipment will follow well-established electrical standards like 0–10 V for voltage interfaces or 4–20 mA for current-loop interfaces. The signals to be monitored for the TRD detector are listed in Table 13.1.

Each front end Multi Chip Module (MCM) which acquires and processes signals from 18 pads also implements measurements of chip temperature, power voltages and currents and power on/off control of the readout-related section of MCM.

Sensors of gas temperature, LV connector and cable temperature, LV regulator current and voltage and humidity will be read out by a dedicated DCS ADC located on the MCM.

For monitoring of the detector status outside the running period we foresee operation of the MCM in standby mode, where only the part essential for DCS (multiplexed ADC, duplex synchronous daisy-chained serial link and DCS control) will be powered (See architecture of the DCS communication in Fig. 13.1).

Independent power distribution will be used only for key components of the system such as controllers, sensors and actuators of the cooling and gas system and hubs distributing the information between them and workstations on control and supervisory layers.

In the process controllers the CAN interface will be implemented as backup option.

- **Control layer.** This corresponds to multipurpose-control computer equipment of the Programmable Logic Controller (PLC) type, in compliance with the relevant recommendation [4]. However, wherever convenient in the case of a large number of field-instrumentation channels to be controlled, VME-based controllers may be used. This hardware layer also includes self-contained intelligent instruments like high- and low-voltage power supplies.

For the part of the DCS system located on the detector we currently investigate Ethernet as a detector control field bus. Ethernet is rather rugged and AC coupled. In tree configuration and using twisted pair distributions it permits 100 Mbit/s throughput over long distances. Failure on one of the branch nodes does not disturb the rest of the network communication. This solution is two orders of magnitude faster than the top speed of CAN Bus over short distances. For the Ethernet solution to be viable, it has to be ensured that the implementation of all links under any operational condition is provided by fully standard, well supported industrial solutions.

The currently very rapid development of single-board CPUs and programmable gate arrays (FPGA) running Linux permits the use of miniature controllers which allow implementation of the Ethernet interface and any other controls functionality together with the CPU. The only additional external components required are an Ethernet transceiver (small SMT chip), one flash ROM, and a single chip DRAM. Typical configurations include 8 MB flash ROM and 64 MB DRAM.

Concerning the development of controllers we plan three phases:

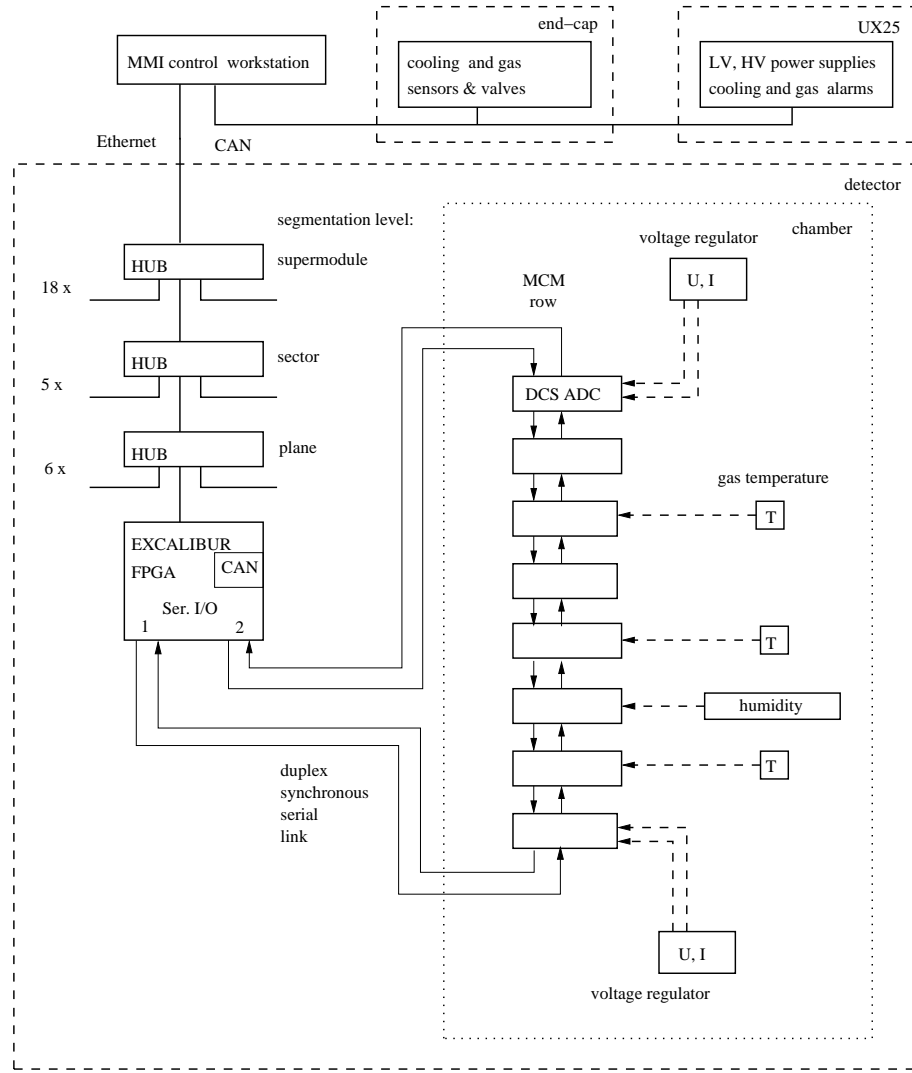


**Figure 13.1:** Architecture of the DCS communication.

- a miniature single-board computer based on MC68EZ328 DragonBall microcontroller is currently used for evaluation tests . It will be used also for tests of compatibility of Ethernet and the ALICE environment (operation in 0.5 T magnetic field) this year. This board supports only the 10 Mbit Ethernet.
- in the second phase, a controller based on the ALTERA 20K200 FPGA chip will be developed. This controller will implement a synthesized UC ( NIOS processor with a 40 MIPS 16-bit CPU) together with Ethernet and an optional CAN interface.
- finally, at the beginning of next year, the Altera Excalibur chip (also from ALTERA 20k FPGA family but with a hard processor core ARM or MIPS both able to run beyond 200 MHz) will be available also with Ethernet on the FPGA as IP core with no need of external chips. Both FPGA Ethernet implementations run 100 Mbit/s. In the long run ALTERA will probably not be the only supplier of such devices. Other possibilities might include Xilinx, appropriate market surveys are underway.
- **Supervisory layer.** The equipment in this layer consists of general-purpose workstations which will be linked to the control layer through TCP/IP. The workstations will provide the Man-Machine Interface (MMI) to the DCS and will behave as server stations for detector monitoring and data

logging, or as client stations for detector control. At the level of general supervisory control, the workstations will be dedicated to the management of configuration data for all the detectors and equipment, partitioning, alarms, logging and archiving, and data communication.

## 13.2 Communication

The data transmission links can be classified in layers equivalent to the hardware architecture. At the field-instrumentation level, point-to-point links for voltage or current signals will be the general case.

Most analog sensors placed on the detector will be read by the DCS ADC located on the MCM. Voltage for the MCM is regulated on-board and output voltage and load current of the regulator will also be read by the DCS ADC on the MCM .

Devices and sensors placed on the detector end-cap and in UX25 will be read out using one of the recommended field buses.

For communication between the DCS controller and the MCM we foresee a fast duplex synchronous serial link running at  $\approx 100$  Mbit/s. This link will be used for downloading the MCM CPU software, setup, DCS control, and preamplifier pulser test. A serial link will be connected on both sides of the MCM chain to the controller, so that a failure of one MCM will not cut the communication to the rest of chain.

This configuration does not change the hardware architecture since the bus system will be seen as an extension of the controller station.

## 13.3 Software

The controller-level software, which will reside in the control computers that are directly linked to the process, will be configured individually for each sub-detector.

For controllers based on the proposed FPGA, Linux (UCLinux) kernels are available which do not implement a man-machine-interface (MMI) but otherwise are complete Linux systems allowing, for example, to NFS mount external discs, run http , secure shell or telnet.

Software development becomes very simple, the front-end mounts the host's disk, the software is cross compiled into the mounted /bin partition and the program under test is started via remote shell.

For development and maintenance of the detectors each group will also configure a personalized MMI. This software will be based on the same product(s) as for the ALICE DCS system and will therefore allow integration into the overall system during operation of the experiment and will grant separate access and control of each subsystem during other periods.

It is planned that the driver software for the controller stations to interface the field instrumentation to the ALICE DCS architecture will be based on the OPC [5] standard. This means that hardware and applications from different manufacturers can be easily connected. OPC is currently being evaluated in the context of the CERN JCOP project. It is based on the Microsoft technology DCOM (Distributed Component Object Model) and provides a standardized access method and unified interface between the control layer and a SCADA (Supervisory Control And Data Acquisition) system on the supervisory layer. The OPC interface standard is defined and developed by the OPC Foundation which includes the major companies in the automation sector (Siemens, Fisher-Rosemount, National Instruments, Rockwell Software, et al.). A wide range of OPC servers and applications are already available and additional companies have announced their adherence to this standard.

## 13.4 Safety and quality management

### 13.4.1 Mechanical

All mechanical components will be designed and built according to the quality assurance standard ISO 9001 or an equivalent national standard.

Although the TRD detector will be operated at a pressure of 1 mbar above atmospheric pressure, the detectors are designed for a maximum over-pressure of 2 mbar.

### 13.4.2 Gas

In addition to adherence to mechanical tolerances, the fabrication, finishing, and choice of materials must ensure an adequate gas purity in order to run the detector with the desired performance and within operational cost. Since the TRD detectors are filled with a Xe,CO<sub>2</sub> mixture, excessive leaks lead to intolerable gas flows and the need for the injection of fresh gas. Avoiding such leaks is especially important in view of the cost of Xe gas. It is therefore foreseen that detailed leak tests will be performed at the detector construction sites.

The gases used in the TRD are non-flammable. As far as the detectors are concerned, redundant and stand-alone safety mechanisms have been implemented in order to protect the TRD from under- or over-pressures.

## 13.5 Radiation protection

The two main mechanisms that may induce radioactivity in the TRD are low-energy neutron activation and inelastic hadronic interactions at high energy. The maximum neutron fluences over a period of ten years at the mean radius of the TRD are below  $1.0 \times 10^{11}/\text{cm}^2$ , respectively. Scaling from the equivalent dose rates induced by the high-luminosity pp interaction regions [7] to those of the ALICE experimental conditions (approximately a factor of 100 lower), we do not expect any radiation hazards to be caused by the accumulation of radionuclides in the TRD.

## 13.6 Electrical system protection

### 13.6.1 High voltage for readout chambers

The readout chambers require an operating voltage of less than 1700 V. In total, 540 supply lines are needed. In addition, there are 540 supply lines for the HV to the field cage of each chamber. Here the operating voltage will be less than 3000 V. The installation is based on standard coaxial high-voltage cables rated for at least 3 kV, together with standard high-voltage connectors.

Standard, remotely-controlled power supplies with voltage and current monitoring will be used. If an over-current is detected, the corresponding voltage will be ramped down at a preset rate. Operation of the HV system will be interlocked in case of a cooling water leak. No parts of the readout chambers under high voltage are accessible once the chambers have been installed.

### 13.6.2 Low voltage

The front-end electronics of the TRD is a typical low-voltage high-current system ( $\approx 20$  kA in total), which may run the risk of fire in case of uncontrolled currents. To avoid any danger to the TRD and its readout system, the following strategy has been adopted.

The power supplies themselves are ground-free. The ground reference is obtained only at the detector side. This avoids any accidental parasitic currents in the conducting paths (not adapted to such large currents) flowing back to the power supply if one of the ground lines is broken.

Powering of the system will be monitored by the DCS. Each MCM provides a measurement of all the incoming voltages and currents. If there is a voltage drop or over-current, the system can be powered down on a time-scale of milliseconds. By monitoring also the temperature of each MCM, the DCS can react to temperature excursions, and shut off the relevant section of the system.

Furthermore, the design of the MCM and their connections to the ground of the readout chamber is such that the copper cross-section is sufficiently large to accommodate high current densities (see Section 9.1.2). This could be required if the ground return line is accidentally connected to the general ground, which would lead to a parasitic current through the TRD support structure.

**Table 13.1:** Main parameters of the Detector Control System for the TRD.

Systems/sub-systems	Location	Controlled parameters	Number	Link type	Parameters	Control
FEE cooling	end-cap	inlet and outlet liquid-coolant temperature	216	analog	temperature	Read/Write
	end-cap	inlet and outlet liquid-coolant pressure	36	analog	pressure	R
	end-cap	liquid-coolant valve control	18	binary	voltage	R/W
	detector	gas temperature	4860	analog	temperature	R
	UX25	temperature threshold for cooling alarm	2	analog	voltage	R/W
	UX25	pressure threshold for cooling alarm	2	analog	voltage	R/W
	detector	humidity sensor for water leak alarm	1620	analog	humidity	R
	PX24	safety switch	1	binary	voltage	on/off
FEE control	detector	FEE temperature	64224	bus	temperature	R
	detector	FEE voltage regulation	64224	bus	current	R/W
	detector	interface (status, exceptions, pedestals, events)	64224	bus	complex	R/W
	detector	MCM on/standby	64224	bus	bit pattern	on/standby
FEE low voltage	UX25	FEE power supply	108	serial	current	R/W
	UX25	FEE power supply temperature	108	analog	temperature	R
	UX25	FEE power supply status/enable word	108	serial	bit pattern	R/W
	detector	FEE voltage regulation	16056	bus	current/voltage	R/W
	end-cap	connector and cable temperature	648	analog	temperature	R
	PX24	safety switch	1	binary	voltage	on/off

**Table 13.2:** Main parameters of the Detector Control System for the TRD, continued.

Systems/sub-systems	Location	Controlled parameters	Number	Link type	Parameters	Control
Drift HV	UX25	HV supply on/off	540	serial	voltage	R/W
	UX25	HV settings and readings	540	serial	complex	R/W
	UX25	safety switch	1	binary	voltage	on/off
Readout chambers	PX24	HV supply on/off	540	serial	voltage	R/W
	PX24	HV settings and readings	540	serial	complex	R/W
	PX24	safety switch	1	serial	voltage	on/off
Gas system	PX24	primary inlet and outlet gas temperature	2	analog	temperature	R
	PX24	primary inlet and outlet pressure	4	analog	pressure	R
	PX24	primary inlet and outlet gas flow regulation	2	analog	flow	R
	PX24	safety switch	5	serial	complex	R
	PX24	purity control	1	serial	voltage	on/off
	PX24	detector primary inlet and outlet gas temperature	2	serial	complex	bit pattern
	detector	primary inlet and outlet pressure	28	analog	temperature	R
	detector	primary inlet and outlet gas flow	28	analog	pressure	R

# 14 Tests with prototypes

---

In this chapter we describe the most relevant results of the tests with detector prototypes, carried out during the past three years. Section 14.1 contains a brief description of the prototypes and of the data acquisition system. In Section 14.2 we present the results of tests with radioactive sources ( $^{55}\text{Fe}$ ) and in Section 14.3 the results of tests in beam will be shown. In Section 14.4 we summarize the on-going activities and the plans for future test measurements.

## 14.1 Prototype description

Most of the results were obtained using a prototype Drift Chamber (DC) with dimensions identical to those anticipated for the final detector (see Chapter 4), except concerning the area, which is only  $0.5 \times 0.6 \text{ m}^2$ . Chevron pad planes [1] with a pad area of  $4.5 \text{ cm}^2$  are used for the readout. A sketch of the chevron geometry is presented in Fig. 14.1. The width of the pads is  $w=10 \text{ mm}$ , the step (matching the anode wire pitch) is  $s=5 \text{ mm}$ , and the overlap factor  $f_x=1.05$ . Nine chevron units (shaded area) are connected together to form a pad of  $4.5 \text{ cm}$  length. For mechanical stability, the pad plane thickness is  $3.5 \text{ mm}$ . The average capacitance of a pad is about  $22 \text{ pF}$ . Both the anode (W-Au,  $25 \mu\text{m}$  diameter) and cathode wires (Cu-Be,  $75 \mu\text{m}$  diameter) have a pitch of  $5 \text{ mm}$  and we use a staggered geometry. The drift region is  $30 \text{ mm}$  in length and the anode-cathode gap ( $h$ ) is  $3 \text{ mm}$ . The entrance window of  $25 \mu\text{m}$  aluminized kapton simultaneously serves as gas barrier and as drift electrode.

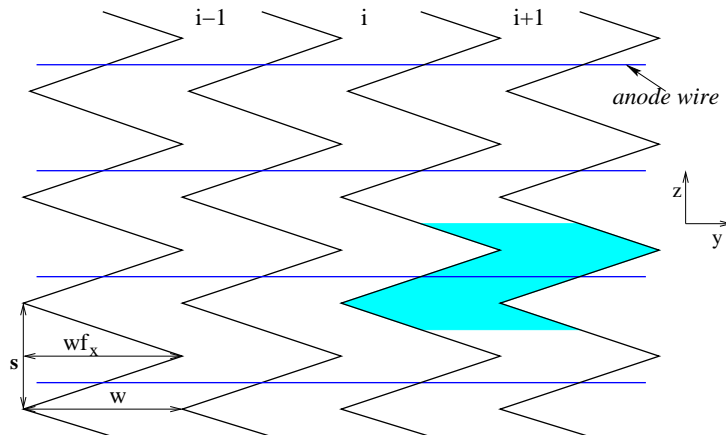


**Figure 14.1:** Sketch of the chevron pad plane layout.

Current- and charge-sensitive preamplifiers/shapers (PASA) were specially designed and built with discrete components. They are described in Section 5.3.3. For the results presented in the following, the charge-sensitive PASA was used. It has a gain of  $2 \text{ mV/fC}$  and a noise of about 1800 electrons r.m.s.. The FWHM of the output pulse is about 100 ns. For the readout of the DC we use an 8-bit non-linear Flash ADC (FADC) system with 100 MHz sampling frequency, 0.6 V voltage swing and adjustable baseline. The FADC sampling was rebinned in the off-line analysis in order to be closer to the final detector specifications. The data acquisition (DAQ) is the GSI-standard, MBS [2], based on the VME event builder RIO2 [3]. Usually we limited the readout of the DC to 8 pads, to minimize the data transfer on the VSB bus connecting the FADC to the event builder.

## 14.2 Source tests with $^{55}\text{Fe}$

The prototypes have been tested with Ar- and Xe-based gas mixtures, using an  $^{55}\text{Fe}$  X-ray source of 5.9 keV. These measurements were aimed at determining the operation point of the detector (in terms of gas gain), checking its energy resolution and for determination of the pad response function (PRF).

### 14.2.1 Signals and spectra

In Fig. 14.2 a collection of signals is shown, as obtained with the  $^{55}\text{Fe}$  source for four gas mixtures: Ar,CH<sub>4</sub> (10%) , Xe,CH<sub>4</sub> (10%) , Xe,CO<sub>2</sub> (15%) and Xe,CO<sub>2</sub> (20%) . These signals are from the pad on which the collimated source was centered. The shape of the signals is a convolution of the detector signal (determined mainly by the slow ion motion) and the PASA response. The longer tails in case of Xe-based mixtures is the result of the slower ion motion. Note that the mobility of the Xe ions is almost 3 times lower than that of Ar ions [4]. From the signals illustrated in Fig. 14.2 we produce the energy spectra of the  $^{55}\text{Fe}$  source with two methods: i) integrating the pulses over a gate of 1  $\mu\text{s}$ , starting at 0.2  $\mu\text{s}$ ; ii) taking the maximum pulse height. In both cases we performed a sum over pads to obtain the total deposited charge, as shared by the adjacent pads.

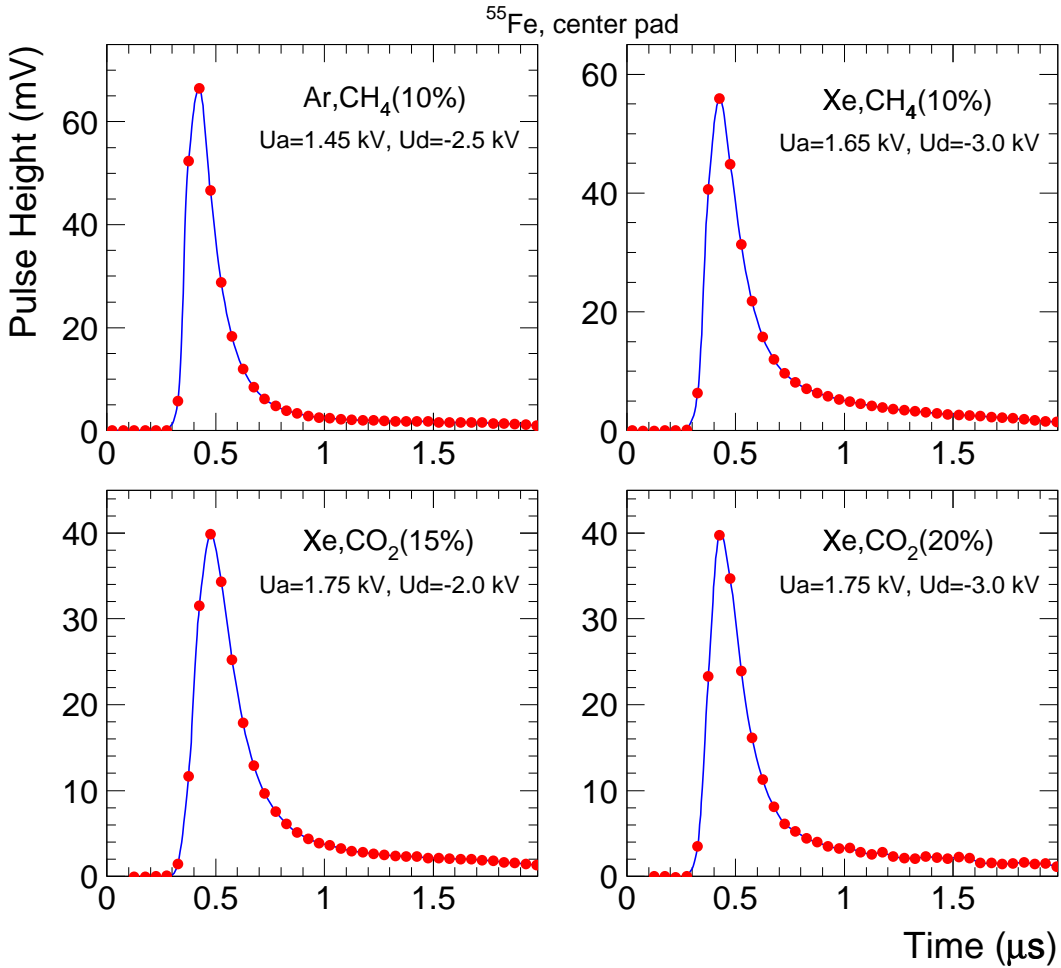


**Figure 14.2:** Average signals on the center pad from the  $^{55}\text{Fe}$  source for four gas mixtures.

In Fig. 14.3 we present the spectrum of  $^{55}\text{Fe}$  for the Ar,CH<sub>4</sub> (10%) gas mixture for the voltages U<sub>a</sub>=1.45 kV and U<sub>d</sub>=-2.5 kV, using the integrated charge Q (left panel) and the maximum pulse height PH (right panel). Besides the main peak corresponding to the full energy deposit of 5.9 keV, the escape

peak corresponding to the partial energy deposit of 2.9 keV is clearly visible. The curves are the results of gaussian fits to the main peak. Resolutions below 10% are achieved with both methods.

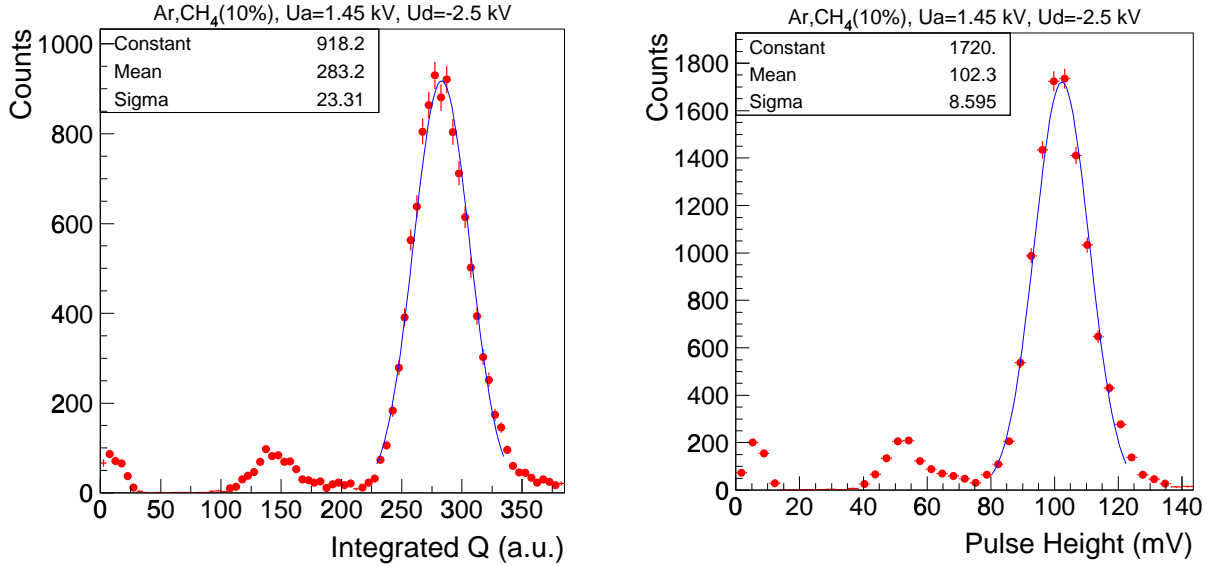


**Figure 14.3:** The spectra of  $^{55}\text{Fe}$  measured with  $\text{Ar},\text{CH}_4(10\%)$ . Left panel: integrated charge value, right panel: maximum pulse height. The curves are the results of gaussian fits of the main peak.

In Fig. 14.4 we present the spectra of  $^{55}\text{Fe}$  for the case of the  $\text{Xe},\text{CH}_4(10\%)$  mixture. In this case too, resolutions below 10% at the main peak are obtained. For roughly equal values of  $Q$  for the two mixtures (Fig. 14.3 and 14.4), the corresponding PH spectra are clearly smaller in case of  $\text{Xe},\text{CH}_4(10\%)$  mixture. As noted above in connection to the signals presented in Fig. 14.2, this is the result of a different contribution of the tails from positive ions.

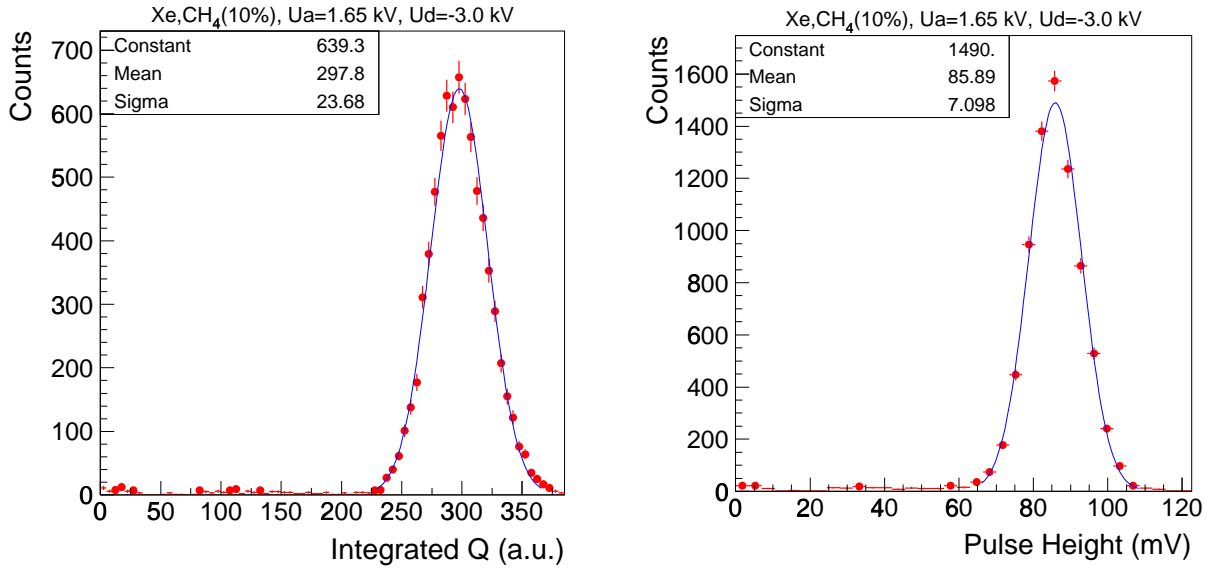


**Figure 14.4:** As Fig. 14.3, but for  $\text{Xe},\text{CH}_4(10\%)$  gas mixture. Note the higher voltages ( $U_d=-3\text{ kV}$ ,  $U_a=1.65\text{ kV}$ ) used to achieve integrated charge values comparable to the  $\text{Ar},\text{CH}_4(10\%)$  case (see Fig. 14.3).

In Fig. 14.5 we present the energy spectra of  $^{55}\text{Fe}$  for the  $\text{Xe},\text{CO}_2(20\%)$  gas mixture, for different anode voltages. Note that the resolution is in all cases below 10%. For high values of the gas gain the  $\text{Xe}$  escape peak of about 1.2 keV becomes visible.

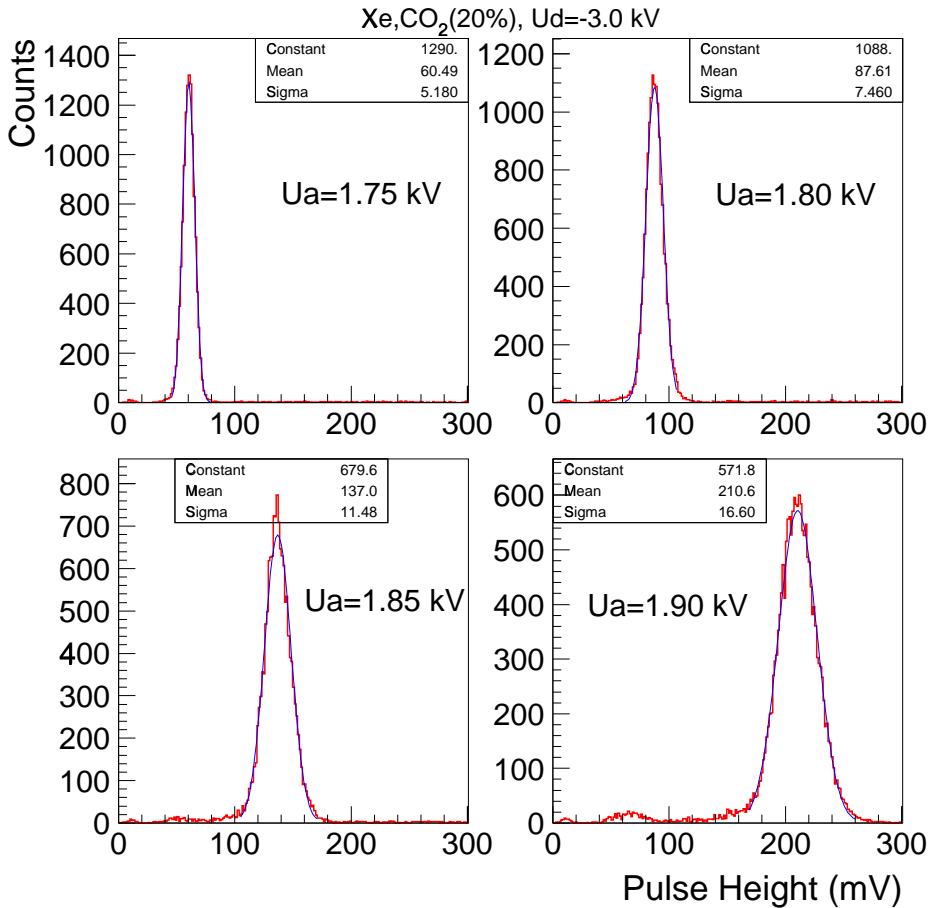


**Figure 14.5:**  $^{55}\text{Fe}$  spectra measured with  $\text{Xe},\text{CO}_2$  (20%) for four different anode voltages.

### 14.2.2 Gas gain

In Fig. 14.6 we present the average energy deposit corresponding to the full energy of 5.9 keV of the  $^{55}\text{Fe}$  source as a function of the anode voltage. Four different gas mixtures (both Ar- and Xe-based) are compared, both in terms of the average pulse height and of the average integrated charge.

The gas gain for each anode voltage was determined in a separate measurement by measuring the anode current and the activity, using a non-collimated  $^{55}\text{Fe}$  source (to get high activity for good precision of the current measurement). A pulse height of 100 mV corresponds to a gas gain of about  $10^4$  in case of the Ar mixture. For the Xe mixtures, due to a larger primary number of electrons ( $\approx 270$ , compared to  $\approx 220$ ), the gas gain is correspondingly lower at the same pulse height. The drift voltages were not kept constant and this influences the gas gain (see Section 14.4). Despite this effect, one can see that different anode voltages are needed in order to achieve the same gain, depending on the gas mixture. In case of  $\text{CO}_2$  quencher, the higher voltage necessary for  $\text{Xe},\text{CO}_2$  (20%) compared to  $\text{Xe},\text{CO}_2$  (15%) is almost compensated by the larger drift voltage, which contributes to the gain (see below, section 14.4).

### 14.2.3 Pad response function

The PRF is a measure of the degree of sharing of the image charge on the cathode plane by adjacent pads. The PRF, measured using the  $^{55}\text{Fe}$  source, is presented in Fig. 14.7. Shown is the ratio of the charge (integrated over a gate of  $1 \mu\text{s}$ ) on the central pad ( $Q_{cen}$ ) to the sum of charges on the center pad and two neighbouring ones on each side ( $Q_{tot}$ ) as function of the position of the hit. This position,  $y$ , is expressed relative to the pad width,  $w$ , which is 10 mm in our case. It has been calculated using a formula derived

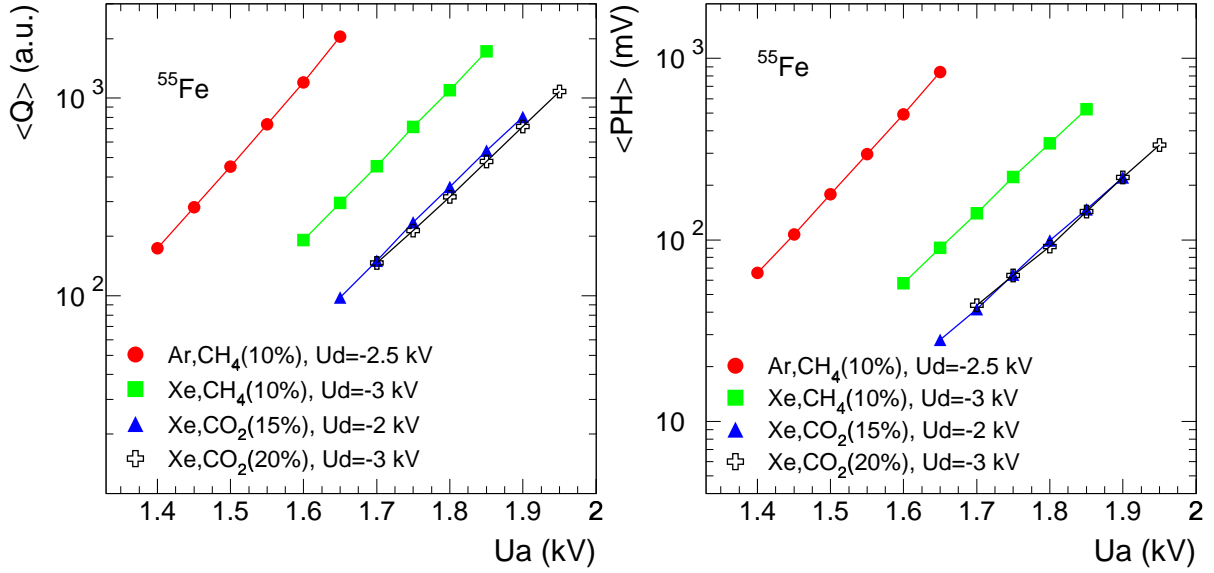


**Figure 14.6:** Gain curves for four gas mixtures. Average integrated charge (left panel) and average pulse height (right panel) of the main peak of  $^{55}\text{Fe}$  as function of the anode voltage. An average pulse height of 100 mV corresponds to a gas gain of  $\approx 10^4$  in case of Ar,CH<sub>4</sub> (10%) .

assuming a gaussian PRF [5,6]:

$$y = \frac{w}{2} \frac{\ln(Q_{i+1}/Q_{i-1})}{\ln(Q_i^2/Q_{i+1}Q_{i-1})}, \quad (14.1)$$

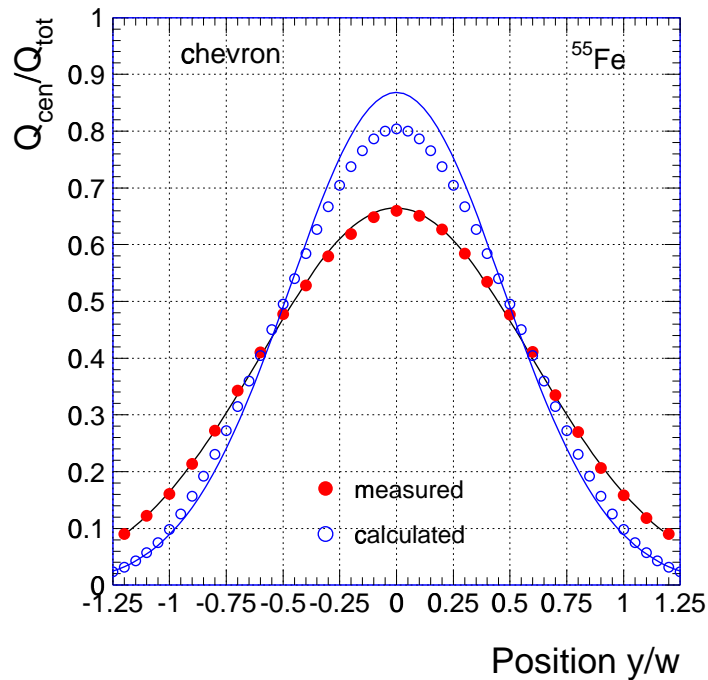


**Figure 14.7:** Pad response function: measured with  $^{55}\text{Fe}$  source, for Ar,CH<sub>4</sub> (10%) (dots) and calculated (circles). The continuous lines are results of gaussian fits.

where  $Q_i$  is the integrated signal for pad  $i$  (which is the pad with the largest signal). The full dots denote the measured values, while the circles are for calculated values using the Mathieson recipe [7]. It is evident that the measured PRF does not agree with the calculated one, which is clearly narrower. This broadening is the effect of capacitive cross-talk between adjacent PASA channels which is discussed below. The continuous lines are results of gaussian fits. While the measured PRF is perfectly approximated by a gaussian (with  $\sigma=0.6 \times w$ ), the calculated one is not. The gaussian shape of the measured PRF could be an artifact of the method, but a different method, namely moving the collimated source across the pad and recording the above ratio as a function of position, gives identical results. Note that in the derivation of the Mathieson formula a symmetric amplification gap is assumed. The transparency of the cathode grid may destroy this assumption. From our most recent studies using different cathode wire pitches (see Section 14.4) we can rule out that the density of the cathode grid has a major influence on the measured PRF.

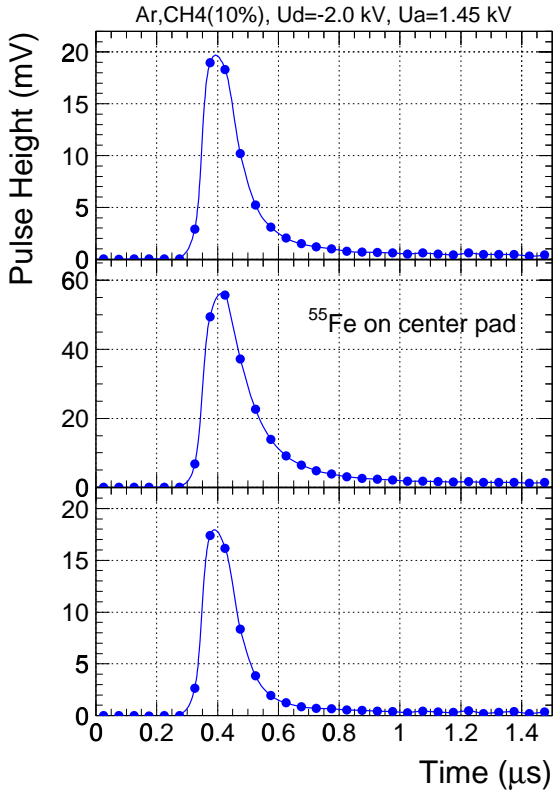


**Figure 14.8:** Signals produced by the  $^{55}\text{Fe}$  source on three adjacent pads.

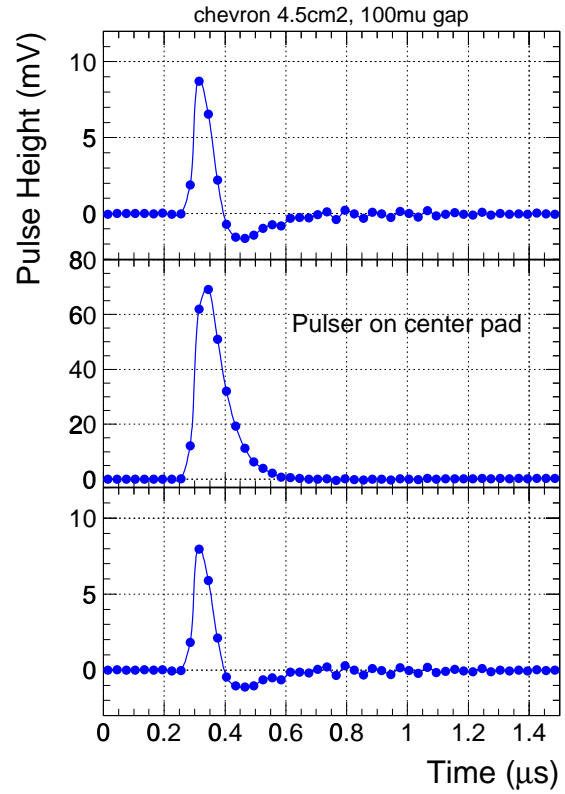


**Figure 14.9:** Signals on three adjacent pads from a pulser signal on the center pad.

To understand the reason of the discrepancy between the measured and calculated PRF, we looked in detail into the effect of the preamplifier cross-talk. We have noticed early on that the tail of  $^{55}\text{Fe}$  pulses in the neighbouring pads has a time decay smaller compared to the center pad. Fig. 14.8 shows an example of the average pulses (the average is done over many events) on three pads, when a collimated  $^{55}\text{Fe}$  source was centered on the middle pad. The different time behaviour is the result of the cross-talk between two neighbouring channels of the PASA, due to the pad to pad capacitance. This is demonstrated in Fig. 14.9, where we present average signals on three pads when a step signal (28 mV on 1 pF, 5 ns rise time) from a pulse generator was fed to the center pad, directly on the detector. In this case the neighbouring channels should ideally see no signal, since there is no charge sharing. Instead, a bipolar cross-talk is seen. On this spurious signal the true  $^{55}\text{Fe}$  signal from pad sharing would add, creating

the shapes presented in Fig. 14.8. One observes about 12% cross-talk in the pulse height in each of the adjacent channels. This cross-talk figure would explain the difference of the measured PRF compared to the calculated one. However, when integrating over 1  $\mu\text{s}$  (as it was done for the  $^{55}\text{Fe}$  signals when deriving the PRF), the cross-talk is reduced to 4%. Note that without load the channel to channel cross-talk is below 0.5%. In a second step we investigated the cross-talk as function of rise time of the input pulse (apart of 5 ns, we used 20 and 50 ns) and of the shaping time of the PASA and found only little dependence. The cross-talk is mainly determined by the input impedance of the PASA, which was in the present case about 1  $\text{k}\Omega$ . Naturally, the cross-talk increases as a function of the capacitive coupling between neighbouring channels. We established that a channel to channel capacitance of 8 pF is reproducing the cross-talk measured on the detector (Fig. 14.9), in agreement with our measurements and calculations of the pad to pad capacitance.

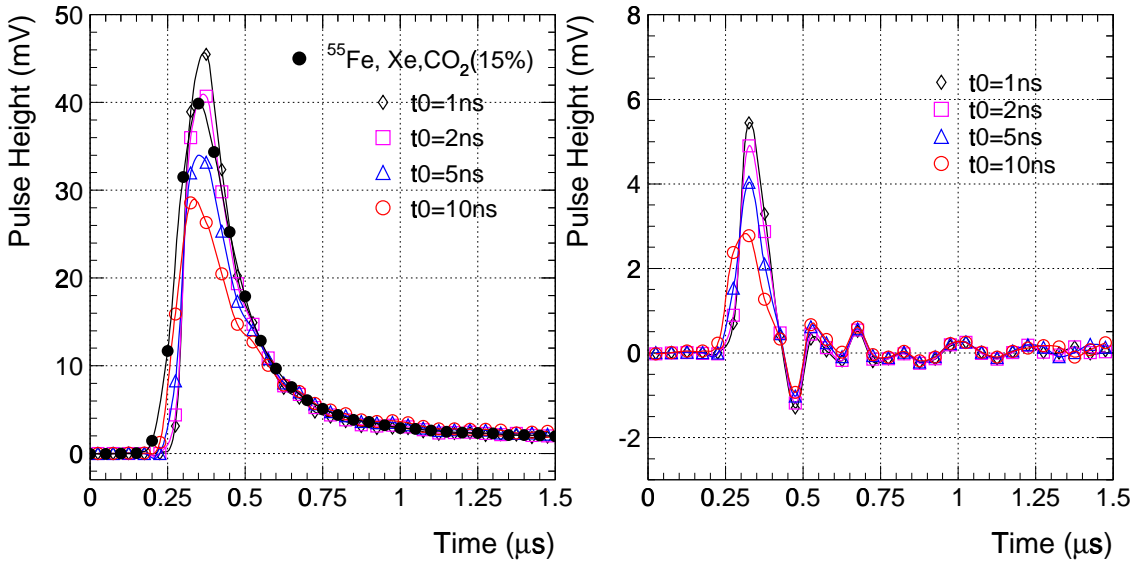


**Figure 14.10:** Pulser signals on the main pad and on a neighbouring one for different shapes of the input pulse. Note the different scales for the y axis.

The signal from the detector may be quite different from a simple step pulse. To check this particular detail, we injected pulses that simulate the time evolution of the signals from the real detector. These pulses have a fast rise time, followed by a slow logarithmic rise. The measured signals for the main pad (left panel) and neighbouring pad (right panel, note the different scale on the y axis) are presented in Fig. 14.10. The different open symbols correspond to different time constants of the fast component, while the dots are for a measured  $^{55}\text{Fe}$  signal. The values of the pulse height cross-talk are very similar to those seen with the simple step pulse (Fig. 14.9). However, one can notice that the shape of the cross-talk signal is quite different in the present case. Although the time dependence of the signal on the neighbouring pad (right panel in Fig. 14.10) is different compared to the one of the main pad (left panel), no undershoot is seen for this more realistic input pulse. When integrating over 1  $\mu\text{s}$ , the cross-talk is about 4%, identical to the case of the step input pulse. In order to improve our understanding of the discrepancies between the observed and the calculated PRF, the problem of the cross-talk is being investigated further. However, the present results are obtained with a preamplifier/shaper which is different than the final one (see Chapter 5). This integrated version is particularly optimized for a low input impedance and measurements on the detector will follow soon.

## 14.3 Beam tests

The measurements have been carried out at beam momenta between 0.7 and 2 GeV/c [8]. The electron content of the beam varies as function of momentum and is of the order of 2-3% for 1 GeV/c. We used mixed electron-pion beams provided by the secondary pion beam facility at GSI Darmstadt [9].

### 14.3.1 Setup

The setup used for the beam tests is sketched in Fig. 14.11 (see also Color Fig. 8). It comprises the following detectors:

- a one-layer TRD, composed of a radiator (R) and a readout chamber (drift chamber, DC).
- three scintillator counters ( $S_0$ ,  $S_1$ ,  $S_2$ ), used for beam definition. Their dimensions are  $5 \times 10 \text{ cm}^2$ .
- a gas-filled threshold Cherenkov detector (Ch), 2 meters in length, read out via a mirror by two photomultipliers, for electron identification.
- a Pb-glass calorimeter (Pb), with dimensions  $6 \times 10 \text{ cm}^2$  and a depth of 25 cm (equivalent to  $10 X_0$ ) for electron validation.
- a multiwire proportional chamber (MWPC) [10] with a  $20 \times 20 \text{ cm}^2$  active area, used for monitoring the beam profile.
- two silicon strip detectors ( $Si_1$ ,  $Si_2$ ) with active area of  $32 \times 32 \text{ mm}^2$ . Each has strips of  $50 \mu\text{m}$  pitch in both  $x$  and  $y$  direction, representing a total of 1280 channels per detector. As these signals are read out in a zero-suppression mode, they do not contribute significantly to the data volume. They are used off-line for tracking for the position reconstruction using the DC (see Section 14.3.7).

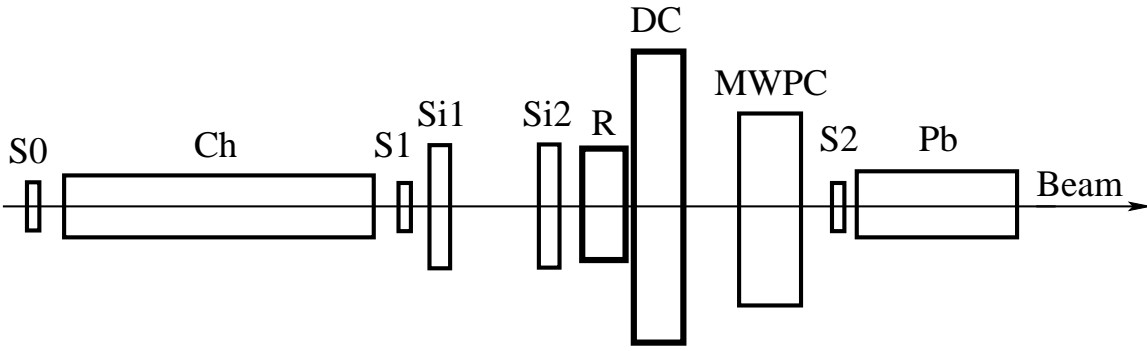


**Figure 14.11:** Sketch of the setup used for the beam tests (not to scale). The different components are explained in the text.

The beam trigger was defined by the scintillator counters  $S_1$  and  $S_2$ , to which the Cherenkov signal was added as the electron trigger. Both electron and pion events are acquired simultaneously by using appropriate pion scaledown factors. Off-line the events were selected using the correlation between the signals delivered by the Cherenkov and the Pb-glass detectors, shown in Fig. 14.12 for the momentum of 1 GeV/c. As seen, by requiring threshold signals in both detectors (the lines in Fig. 14.12) one can isolate clean samples of pions and electrons. For this momentum we used a pion scaledown factor of 8. Measured with the MWPC, the horizontal size of the beam was about 4.5 cm FWHM.

The gases used for the DC were Xe-based mixtures. We used both  $\text{CH}_4$  (10%) and  $\text{CO}_2$  (15% and 20%) quenchers. We selected the anode voltages such that the gas gain of the chamber was in the range of 5000 to 8000 for most of the measurements, except when we intentionally varied it for some particular

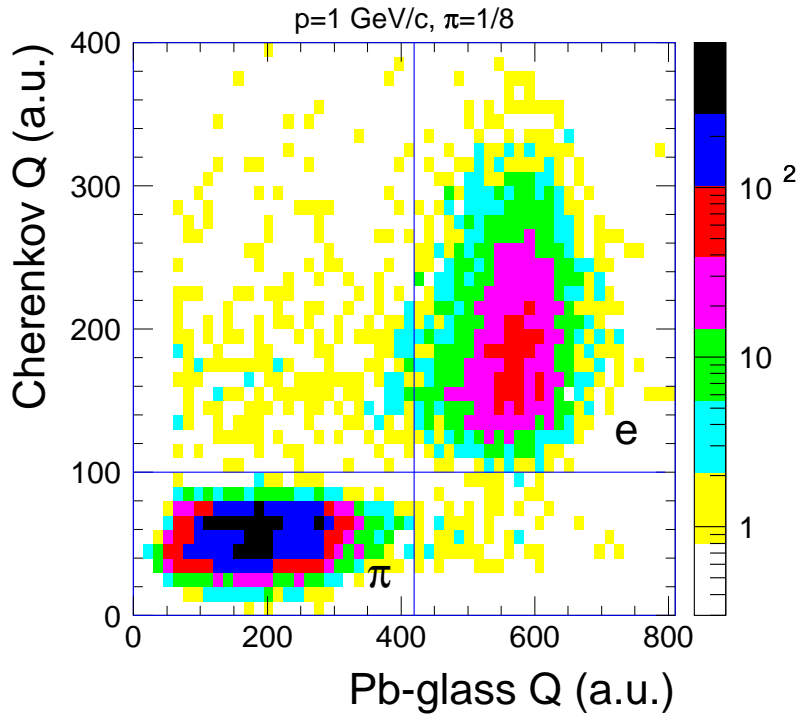


**Figure 14.12:** The correlation of the signals from the Cherenkov detector and the Pb-glass calorimeter. The thresholds used to identify negative pions and electrons are indicated.

studies (see below). The oxygen content in the gas was continuously monitored and kept below 10 ppm using a flow of 2-3 liters/hour.

### 14.3.2 General properties of the detector

Distributions of average pulse height,  $\langle PH \rangle$ , as a function of drift time for different drift voltages are shown in Fig. 14.13 for pions of 1 GeV/c momentum. Three Xe-based gas mixtures are compared: 15% CO<sub>2</sub>, anode voltage U<sub>a</sub>=1.75 kV (upper left panel), 20% CO<sub>2</sub>, U<sub>a</sub>=1.80 kV (upper right panel) and 10% CH<sub>4</sub>, U<sub>a</sub>=1.75 kV (lower panel). Note that in the case of Xe,CO<sub>2</sub> (20%) the incidence was perpendicular to the anode wires, while in the other two cases it was at about 17° with respect to the normal to the anode wires.

The time zero has been arbitrarily shifted by about 0.4  $\mu$ s to have a measurement of the baseline. Note that the average pulse height in the drift region exhibits a slight increase as a function of drift time. This is the result of build-up of detector currents from ion tails, convoluted in addition with the response of the preamplifier. The peak at the beginning of these distributions originates from the primary clusters in the amplification region, where the ionization from both sides of the anode wires contributes to the same time channel. These characteristics have been reproduced by simulations of detector signals using GARFIELD [12]. The drift voltages have been tuned to cover a similar range of drift velocities around 1.5 cm/ $\mu$ s. The voltages are different for the mixtures investigated (especially between the two quencher gases, CO<sub>2</sub> and CH<sub>4</sub>), as expected. Notice also that the behaviour with the field strength is different (see below).

Analysis of the distributions presented in Fig. 14.13 allows a rough estimate of the drift velocities for the different mixtures. This accuracy is limited by the accuracy in assigning the beginning of the drift region out of the tail of the signals in the amplification region. The results (open symbols) are plotted in Fig. 14.14 as function of the drift field for three Xe-based gas mixtures, along with calculations using GARFIELD/MAGBOLTZ [12, 13] (full symbols). While for the CO<sub>2</sub> mixtures our drift fields of the

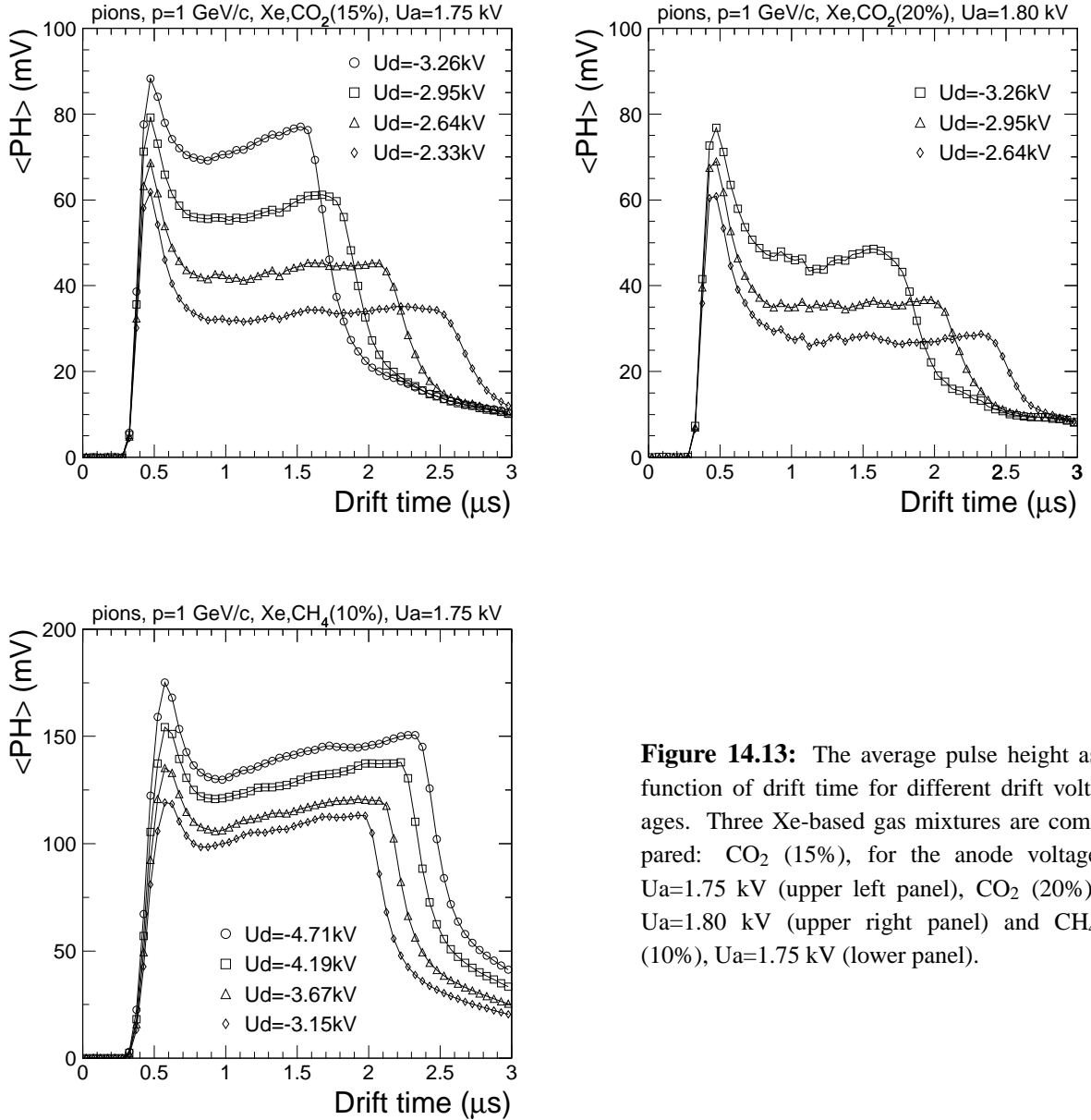


**Figure 14.13:** The average pulse height as function of drift time for different drift voltages. Three Xe-based gas mixtures are compared: CO<sub>2</sub> (15%), for the anode voltage U<sub>a</sub>=1.75 kV (upper left panel), CO<sub>2</sub> (20%), U<sub>a</sub>=1.80 kV (upper right panel) and CH<sub>4</sub> (10%), U<sub>a</sub>=1.75 kV (lower panel).

order of 1 kV/cm correspond to the rising part of the distribution, in case of the CH<sub>4</sub> quencher we are already in the slowly decreasing region after the first maximum. Within the limitations of the method, one can say that the calculations reproduce the drift velocities in case of CO<sub>2</sub> mixtures, but there seems to be a disagreement for the CH<sub>4</sub> case. For this particular case, we include in the comparison the measured data of Christophorou et al. [14], to which our values are compatible. Note that a more recent set of measurements [15] are significantly different. We mention that the water content, which influences the drift velocity quite strongly, was about 150 ppm in case of CO<sub>2</sub> mixtures, but was not measured in case of Xe,CH<sub>4</sub> (10%).

One can notice in the distributions presented in Fig. 14.13 that the relative magnitude of the peak to the plateau is varying as a function of the drift field. This is due to the compression of the same signal in progressively shorter time intervals. In detail, this behaviour seems to be mixture dependent. A detailed look at these facts is presented in Fig. 14.15. Here we show the drift field dependences of the measured

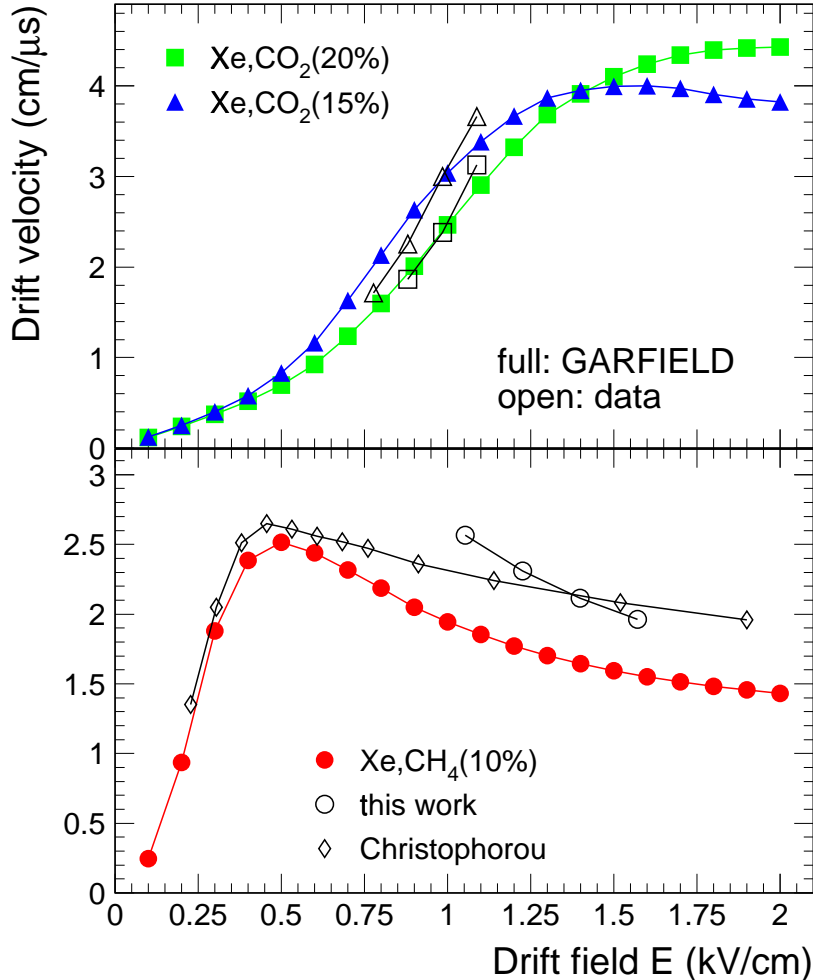


**Figure 14.14:** The dependence of the drift velocity on the drift field for three Xe-based gas mixtures. The data extracted from Fig. 14.13 (open symbols) are compared to calculations using GARFIELD/MAGBOLTZ [12, 13] (full symbols). For the Xe,CH<sub>4</sub> (10%) case we include in the comparison the measured data of Christophorou et al. [14].

charges in the drift region,  $Q_d$  and in the amplification region,  $Q_a$ . These quantities are integrals of the pulse height over the timespan of the plateau and peak, respectively. The sum of them (upper panel, note the logarithmic scale) is increasing as a function of drift field, a result of increasing gas gain (see Section 14.4). The ratio  $Q_d/Q_a$  is presented in the lower panel. Its dependence on the drift field, different for CO<sub>2</sub> and CH<sub>4</sub> quencher, is the effect of the different drift velocity variation, as seen in Fig. 14.14. The decreasing of this ratio for higher drift velocities may already point to a space charge effect (see below), which is more pronounced in case of an electron arrival more compressed in time.

Figure 14.16 shows the dependence of  $Q_d+Q_a$  and  $Q_d/Q_a$  as a function of the anode voltage. The integrated charge (upper panel, notice the logarithmic scale) is exhibiting the gas gain dependence on the anode voltage (see Section 14.2.2). The ratio  $Q_d/Q_a$ , shown in the lower panel, gives an indication of the gas gain saturation (lower gain for the late electrons due to the screening of the anode potential by the ions from previous clusters) as function of gas gain. For no gain saturation this ratio is flat. The small decrease points to a small gain saturation. However, this conclusion is somewhat ambiguous because of the uncertainty in delineating the amplification region, which may extend into the drift region as function of increasing anode voltage. We note though, that the distributions of the average pulse heights from

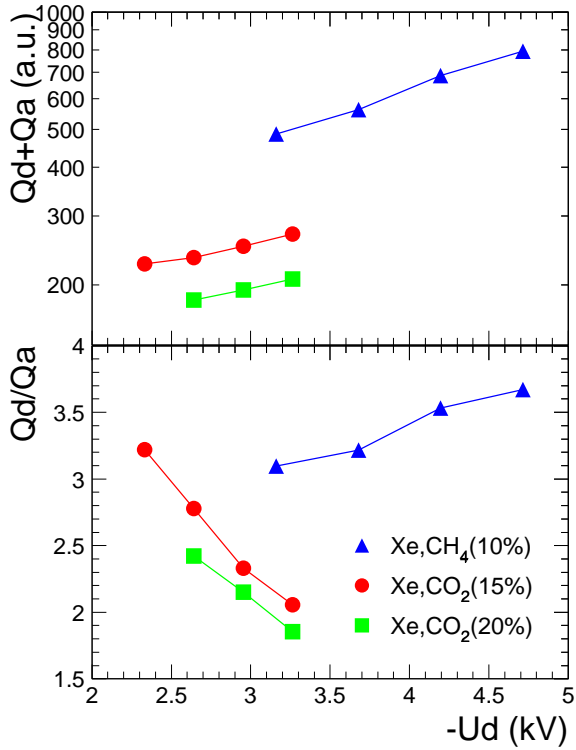


**Figure 14.15:** Summary of drift field dependences of the charges measured in the drift ( $Q_d$ ) and amplification ( $Q_a$ ) region.

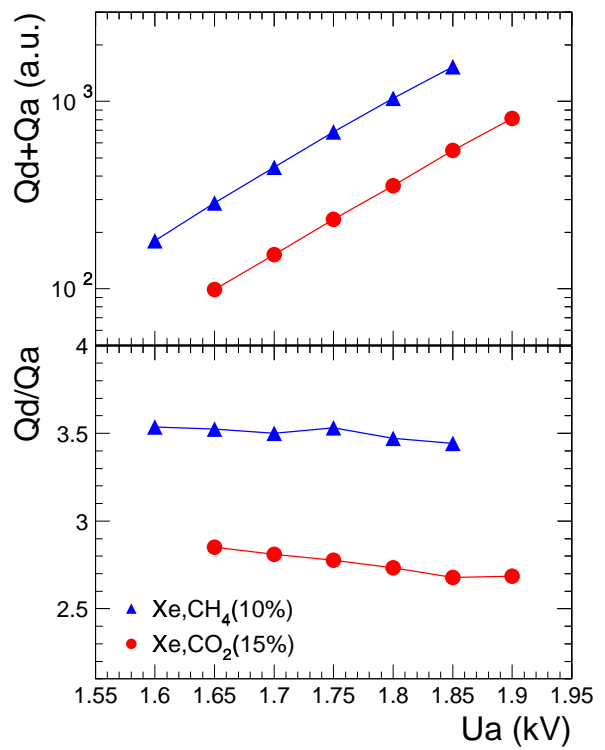


**Figure 14.16:** Summary of anode field dependences of the charges measured in the drift ( $Q_d$ ) and amplification ( $Q_a$ ) region.

which the ratio  $Q_d/Q_a$  was derived are very similar for all the anode voltages under consideration, thus pointing to a genuine gain saturation effect. The effect is rather small because the incident angle in this case was  $17^\circ$  with respect to the normal to the anode wires.

In Fig. 14.17 we present an example of the evolution of the average pulse heights as a function of drift time with respect to the incident angle along the anode wires. These distributions were recorded for a moderate gas gain of about 6000. However, decreasing the angle towards normal incidence, the signal gets progressively attenuated as function of drift time. This is a clear signature of the gas gain saturation, which is a local effect. When spreading the primary electrons along the anode wire, the effect becomes less and less important. Simulations confirm this interpretation (see Chapter 4). Note that the signal in the amplification region (the peak) is independent of the angle (there is no relative normalization of the data for different angles), since there are no precursor avalanches that can screen it.

In Fig. 14.18 we present the summary of the above effects. The ratio  $Q_d/Q_a$  is plotted as a function of the incident angle along the anode wires for three values of gas gain, separated by factors of 2.35. The variation of the ratio with the angle is very pronounced for small angles, while a saturation is reached at larger angles due to the locality of the screening, as mentioned above. The ratio has a stronger variation for larger gains, as expected. As we will show in Section 14.3.6 the gas gain saturation is affecting the pion rejection performance of the detector. Due to these effects, we envisage to operate the chambers at the lowest possible gas gain (around 5000).

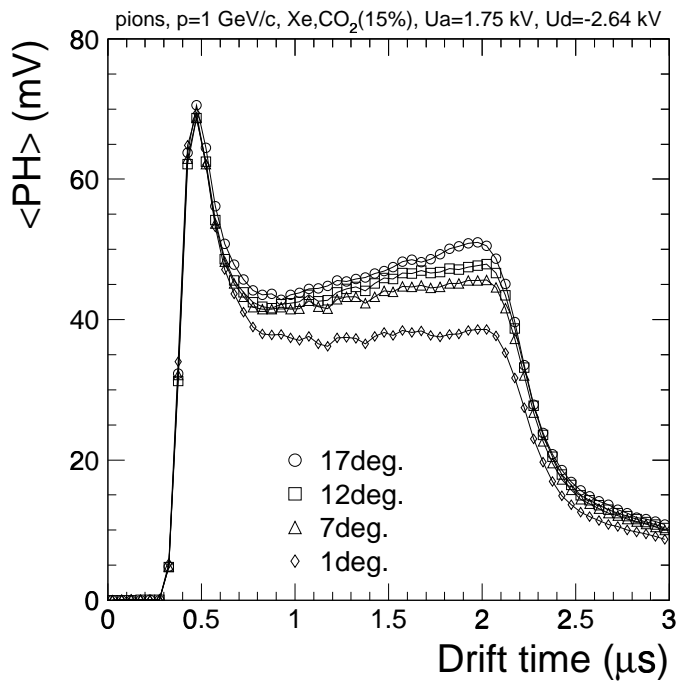


**Figure 14.17:** Average pulse heights as function of drift time for different incident angles along the anode wires.

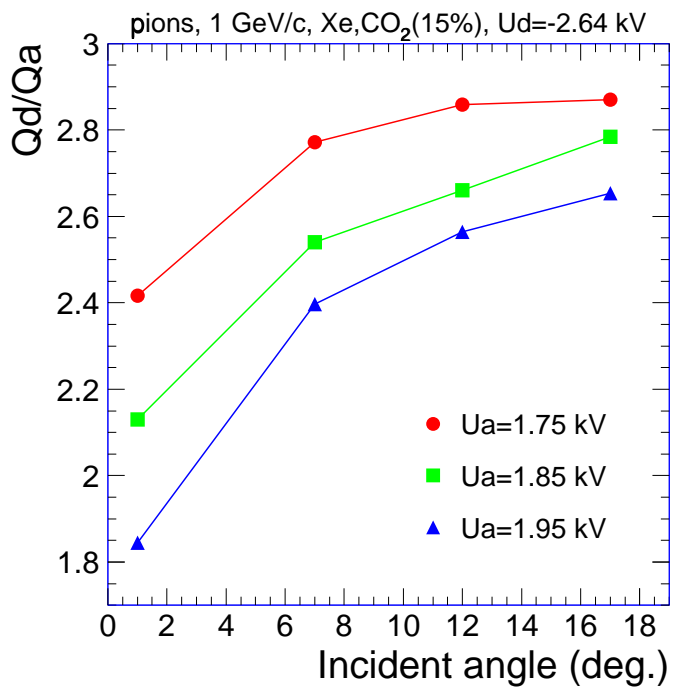


**Figure 14.18:** Ratios of charges recorded in the drift and amplification regions as function of incident angle along the anode wires for three values of the gas gain.

### 14.3.3 Pion and electron distributions

In this section we present typical distributions for pions and electrons for a momentum of 1.0 GeV/c and a fibre radiator. Unless specified, the incident angle is  $17^\circ$  with respect to the normal to the anode wires.

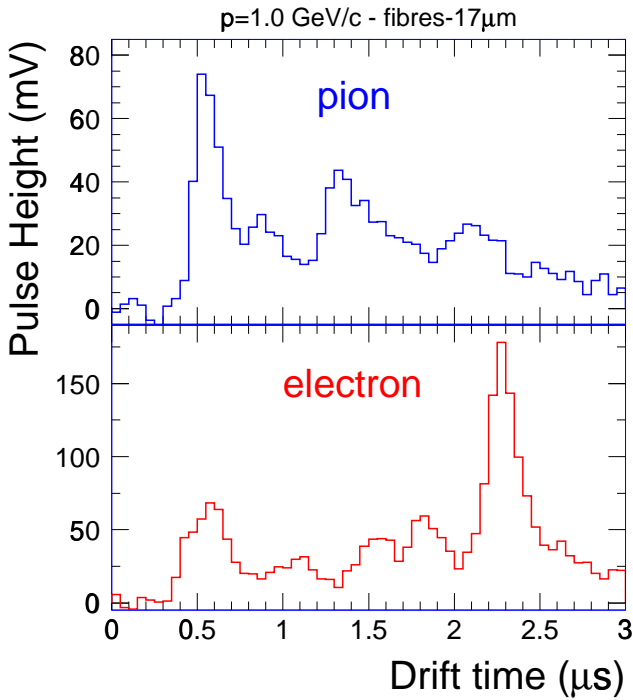


**Figure 14.19:** Typical signals as a function of drift time for a pion and an electron for the momentum of 1.0 GeV/c. Note the different scales on the vertical axes.

In Fig. 14.19 we show an example of the signal distribution as a function of drift time for a pion and an electron. Here and in what follows we are using a time bin of 50 ns, a value smaller than that of the final configuration of the TRD in ALICE. We checked that by increasing the time bin from 50 ns to 100 ns the performance of the detector with respect to the pion rejection does not change. Note the different magnitude of the two signals and, for the electron, the big cluster at late drift time, possibly corresponding to a TR photon absorbed early near the entrance of the DC. Detailed simulations [11] showed that the electron identification is significantly improved by using, along with the pulse height, the drift time information (see below).

We show in Fig. 14.20 the drift time distribution of the average pulse height summed over the adjacent pads,  $\langle PH \rangle$ , for pions and electrons in case of a fibre radiator with  $17\text{ }\mu\text{m}$  fibre diameter (thickness  $X=0.3\text{ g/cm}^2$ ). For electrons (square symbols) there is a significant increase in the average pulse height at later drift times, due to preferential absorption of TR near the entrance of the DC. The dashed line in Fig. 14.20 is the expected pulse height distribution for electrons without TR; it has been obtained by scaling the pion distribution with a factor of 1.45, measured in a separate experiment without radiator. Pulse height distributions as a function of drift time have been reported by other experiments [16, 17, 19, 20]. A decrease of the pulse height as a function of drift time was observed in all those cases and it was attributed to electron attachment [20]. We stress that it is for the first time that the expected signal is directly seen in such a detector.

The distributions of the integrated energy deposit are shown in Fig. 14.21 for pions and electrons for a momentum of 1 GeV/c, in case of a  $17\text{ }\mu\text{m}$  fibres radiator. The pure Landau distribution exhibited by pions is spread towards higher values in the case of electrons due to the contribution of the TR.

The distributions of the position of the largest cluster found in the drift region are shown in Fig. 14.22. The detector depth is expressed here in time bin (50 ns) number, where the counting starts at  $0.75\text{ }\mu\text{s}$  (see Fig. 14.20) and increases towards the entrance window for a total of 32 time bins. The trends seen in Fig. 14.20 are present in these distributions as well. For the case of electrons the probability to find the largest cluster is strongly increasing towards the entrance of the detector (higher time bin number) due

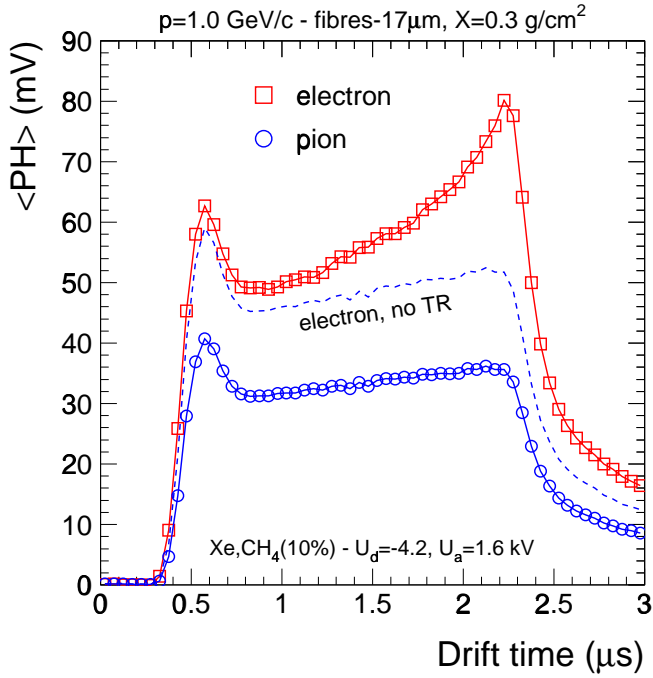


**Figure 14.20:** Average pulse height as a function of the drift time for pions and electrons for a radiator of  $17 \mu\text{m}$  diameter fibres at the momentum of  $1 \text{ GeV}/c$ . The dashed line represents the energy deposit by pure ionization in case of electrons (see text).

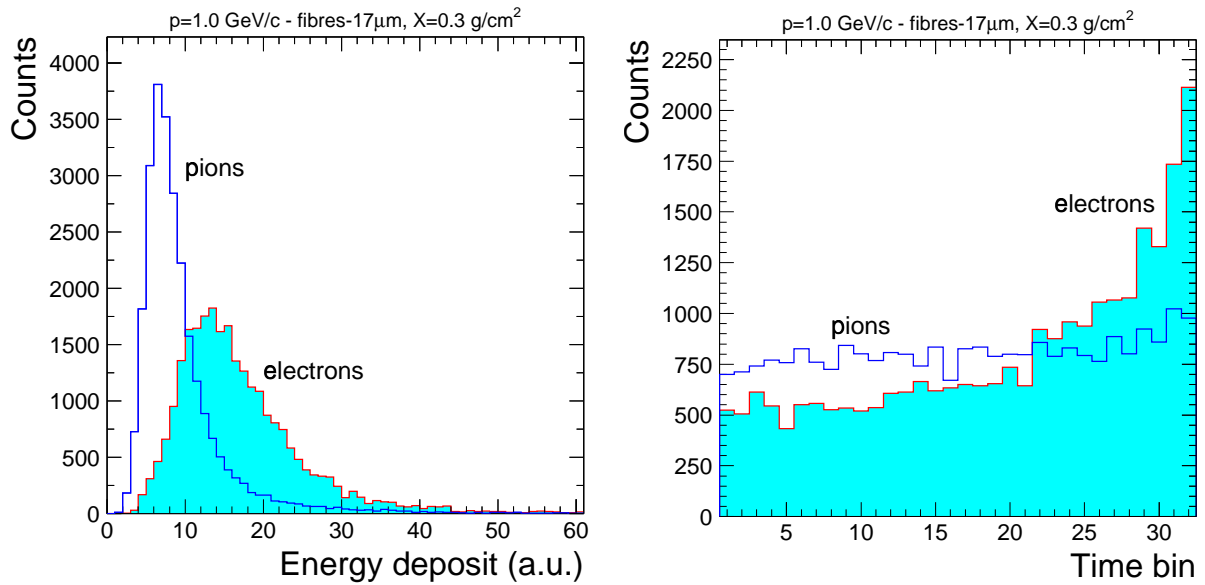


**Figure 14.21:** Integrated energy deposit for pions and electrons for a momentum of  $1.0 \text{ GeV}/c$ . A radiator with  $17 \mu\text{m}$  fibre has been used.

**Figure 14.22:** The distributions of position of the largest cluster found in the drift region for pions and electrons.

mainly to the contribution of TR, while for pions there is only a slight increase which is due to the ion and preamplifier tail build-up explained above. The distributions presented in Fig. 14.21 and Fig. 14.22 are normalized to the same number of events.

### 14.3.4 Radiator comparison

Various radiators were tested: regular foils of polypropylene (PP), mats of irregular PP fibres with various fibre diameters (between 15 and 33  $\mu\text{m}$ ) and foams of different material type: PP, polyethylene (PE) and Rohacell (RC). These radiators spanned a large range in densities and structural properties, as one can see in Table 14.1. The quantity  $d$  quoted here is the linear dimension of the structural unit, which for the foils means foil/gap thicknesses, for the fibres the diameter and for the foams the typical pore size. The variation in total thicknesses is also large, from 3 to 10 cm.

**Table 14.1:** The properties of various radiators.

Name	Material	$\rho$ (g/cm <sup>3</sup> )	$d$ ( $\mu\text{m}$ )
foils120	PP	120 foils	20/500
foils220	PP	220 foils	25/250
fibres17	PP	0.074	17
fibres20	PP	0.05	15-20
RG30	PP	0.03	1300
RG60	PP	0.06	700
WF110	RC	0.11	700
HF110	RC	0.11	$\approx 75$
HF71	RC	0.07	$\approx 75$
IG51	RC	0.05	$\approx 75$
HF31	RC	0.03	$\approx 75$
EF700	PE	0.12	800
S-HF110	RC/PP	0.086	sandwich
S-HF71	RC/PP	0.073	sandwich

To study the relative performance of the various radiators presented in Table 14.1 we have classified them according to the equivalent thickness into two classes, with roughly  $X=0.3 \text{ g/cm}^2$  and  $X=0.6 \text{ g/cm}^2$  (the radiation length for some of these materials is provided in Chapter 3). The measurements are summarized in Fig. 14.23 in terms of the ratio between the average pulse height of electrons and pions,  $\langle PH \rangle_e / \langle PH \rangle_\pi$ , as function of detector depth. The detector depth is divided here into 5 zones, where zone 0 is the amplification region and each of the others is a quarter of the chamber's drift region (drift time between 0.75 and 2.35  $\mu\text{s}$  in Fig. 14.20). The numbering goes from the cathode wire plane towards the entrance of the DC. In this representation, a better relative performance of the radiator amounts to a higher ratio between electron and pion pulse height, while the increase towards the entrance of the detector gives information about the characteristics of the spectrum of the TR. The case of no TR would produce a flat distribution at about 1.45 for the momentum of 1 GeV/c. These measurements were performed using the Xe,CH<sub>4</sub> (10%) gas mixture.

The most important conclusion from Fig. 14.23 is that the fibre radiators exhibit performances comparable to that of radiators with foils, being only slightly worse. Taking into account that the foil radiators are significantly lighter than the other radiators in both cases (with  $X=0.22 \text{ g/cm}^2$  and  $X=0.5 \text{ g/cm}^2$ , respectively), our conclusion is in agreement with previous studies [17]. The fibres with lower density, fibres20, produce slightly more TR compared to the more dense ones, fibres17. In a separate study we have found that the fibre diameter influences the TR yield only marginally. Radiators composed of fibres with 17 and 33  $\mu\text{m}$  diameter show similar TR performance for the same density and thickness. We note that in a previous measurement it was found that the momentum dependence of the pion rejection is influenced by the fibre diameter [23].

The performance of the foams is comparable to the fibres only in the case of the light PP foam, RG30.

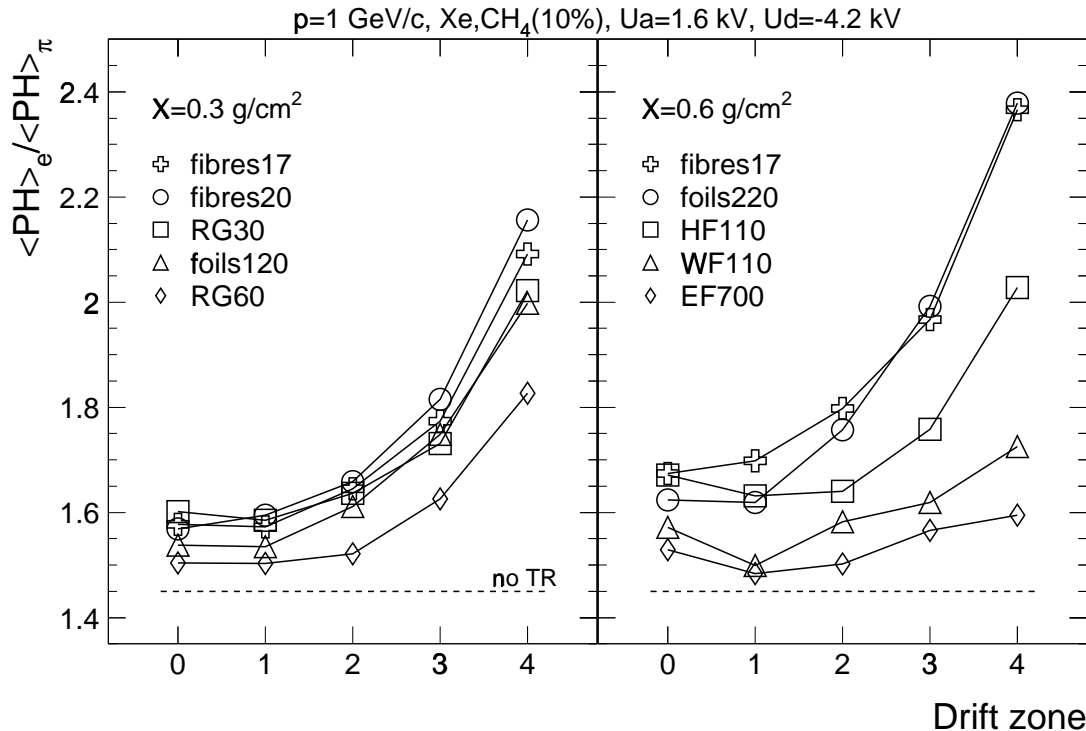


**Figure 14.23:** Average relative electron/pion pulse height as function of the drift zone for various radiators (see Table 14.1) of two thicknesses for the momentum of 1 GeV/c. These measurements were performed using the Xe,CH<sub>4</sub> (10%) gas mixture. See text for details.

However, in this case the 10 cm thick radiator is a serious disadvantage (at least for the ALICE TRD). The more packed version of the same material, RG60, produces significantly less TR (furthermore, it is thicker,  $X=0.36\text{ g/cm}^2$ ). We found that the Rohacell foams HF110 and WF110 exhibit very different features. Contrary to the expectations, it is the version with less structure (invisible pores), HF110, that gives higher TR yield. The other Rohacell foam, WF110, as well as the Ethafoam, EF700, are basically excluded as radiator candidates. Judging by their apparent structure, these foams would have been expected to deliver reasonably good TR performance. Their low TR yield may be the consequence of a higher absorption due to their chemical compositions. In particular, especially concerning their TR spectra, Ethafoams were established early on as promising candidates for radiators [18]. Note that it was found that even PE foil radiators exhibit poor TR performance [17], presumably due to a low TR yield. In general, similar results concerning the relative comparison of different radiator materials have been obtained in other experiments [17, 21, 22].

After the first step of selecting the best candidates for a radiator, we have extended our study towards finding a more realistic radiator that would satisfy both the TR performance and the mechanical stability requirements (see Chapter 3). We have investigated sandwich radiators composed of 17  $\mu\text{m}$  fibres and Rohacell foams. The results are presented in Fig. 14.24, where we compare the ratio of electron to pion pulse heights as function of drift zone for sandwich radiators (S-X) and for pure Rohacell foams and pure 17  $\mu\text{m}$  fibre radiators. A measurement without radiator is included. This comparison is done for a fixed geometrical thickness of 4.8 cm. The pure fibre radiator has a thickness of only 4 cm, to allow direct comparison to our previous measurements. The sandwiches contain 3.2 cm of fibres between 2 sheets of Rohacell foams of 0.8 cm each. The detection gas was Xe,CO<sub>2</sub> (15%). It is evident that all cases

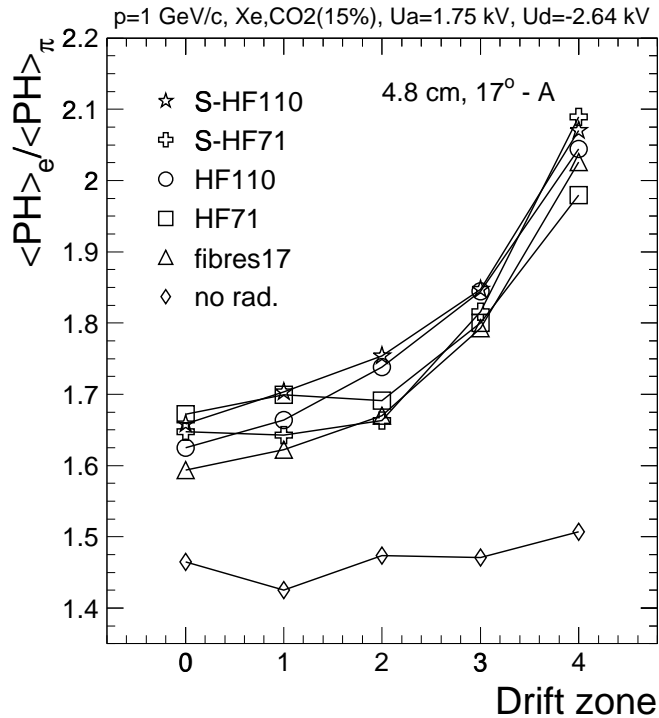


**Figure 14.24:** Average relative electron/pion pulse height as a function of the drift zone. Pure Rohacell foams and 17  $\mu\text{m}$  fibres radiators are compared to sandwich radiators (S-X) built from both materials. The detection gas was in this case Xe,CO<sub>2</sub> (15%) mixture. A measurement without radiator is included.

under study yield very similar TR performance, essentially because of their different densities within the constraint of the same thicknesses (with the exception of pure fibres radiator, as mentioned).

### 14.3.5 Pion rejection performance

The distributions presented in Fig. 14.21 and Fig. 14.22 have been used as probability distributions in simulations aimed at determining the pion rejection factor for the proposed configuration of the ALICE TRD. To extract the pion rejection factor we have studied three different methods: i) truncated mean of integrated energy deposit, TMQ; ii) likelihood on integrated energy deposit (see Fig. 14.21), L-Q [23]; iii) two-dimensional likelihood on energy deposit and position of the largest cluster found in the drift region of the DC (see Fig. 14.22), L-QX [19].

For a certain energy deposit  $E_i$  in layer  $i$ ,  $P(E_i|e)$  is the probability that it was produced by an electron and  $P(E_i|\pi)$  is the probability that it was produced by a pion. The likelihood (to be an electron),  $L$ , is given by:

$$L = \frac{P_e}{P_e + P_\pi} , \quad (14.2)$$

where

$$P_e = \prod_{i=1}^N P(E_i|e) \quad ; \quad P_\pi = \prod_{i=1}^N P(E_i|\pi) . \quad (14.3)$$

We assume that the six layers have identical performance as represented by the measured distributions of Fig. 14.21 and Fig. 14.22 and that there is no correlation between the layers. Both the truncated mean (the truncation is done by excluding the highest value of the integral energy deposit among the layers) and the likelihood distributions (Eq. 14.2) were constructed over the six layers for the same number of simulated pion and electron events. Cuts on electron efficiency were imposed on these distributions and

the pion efficiency was derived within these cuts. We note that another method, “cluster counting” [25] is widely used, in particular for “fine grained” TRDs like those used in ATLAS [26] and in HERA-B [27]. As it was shown in [17, 19] and as our own simulations have demonstrated [11], the likelihood on integrated charge gives better pion rejection than the cluster counting method.

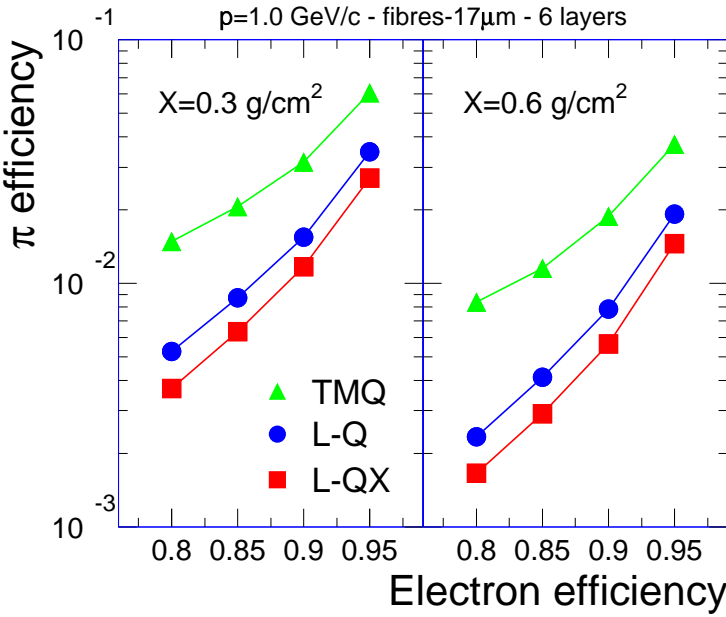


**Figure 14.25:** Pion efficiency as a function of electron efficiency determined with truncated mean on energy deposit (TMQ), likelihood on total energy deposit (L-Q), two-dimensional likelihood on charge deposit and DC depth (L-QX).

The radiator used for these studies is composed of pure fibres with  $17\text{ }\mu\text{m}$  diameter and the detection gas is  $\text{Xe},\text{CH}_4$  (10%). In Fig. 14.25 we present the pion efficiency (the inverse of the rejection factor) as function of electron efficiency (90% electron efficiency is the commonly used value) for the beam momentum of 1 GeV/c. The three methods introduced above are compared. The truncated mean method, although it delivers sizeably worse identification, has the advantage of being very easy to use, being advantageous especially for an on-line identification. The bidimensional likelihood delivers the best rejection factor and will be studied further in order to optimize the final detector design. As emphasized earlier [19], the use of FADCs to process the signals in a TRD can improve the pion rejection power by up to a factor of 2. In general, the three methods employed here give results in good agreement with earlier studies [17, 19].

By doubling the equivalent thickness of the radiator from  $X=0.3\text{ g/cm}^2$  (left panel of Fig. 14.25) to  $X=0.6\text{ g/cm}^2$  (right panel) one gains a factor of about 2 in pion rejection power. However, as discussed before, it remains to be seen how the additional material will influence the performance of the TRD itself and whether it can be tolerated by other ALICE subdetectors.

The pion efficiency at 90% electron efficiency as a function of momentum is shown in Fig. 14.26. The steep decrease of pion efficiency at momenta around 1 GeV/c is due to the onset of TR production [23, 24]. Towards our highest momentum value, 2 GeV/c, the pion efficiency reaches saturation, determined by the TR yield saturation and by the relativistic rise of the pion. Due to these effects the pion rejection is expected to get slightly worse for momenta above 3 GeV/c [16, 17, 23, 28].

As one can see in Fig. 14.26, at momenta around 2 GeV/c the pion rejection factor of 300 to 500 achieved during these tests is above the required value for the ALICE TRD. However, one has to bear in mind that a significant degradation of TRD performance has been registered when going from prototype tests to real detectors [30]. This is the effect of detector loads in a multiparticle environment, as demonstrated for our case using simulations (see Section 11.5). On the other hand, impressive pion rejection

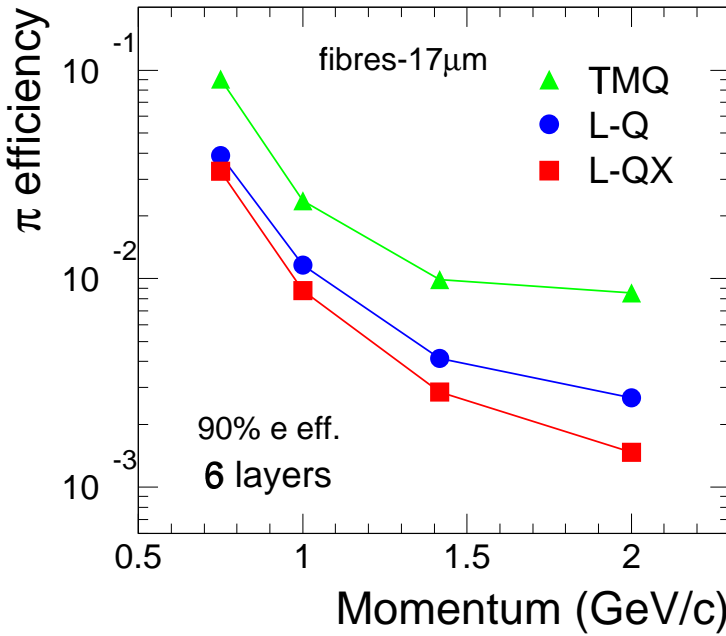


**Figure 14.26:** Pion efficiency as a function of momentum for a radiator with  $17 \mu\text{m}$  fibres. The three methods used are discussed in the text.

factors of 1000 and above have been achieved in full size TRDs by NOMAD [24] and HERMES [29].

#### 14.3.6 TR performance as a function of incident angle

As shown above (Section 14.3.2), the detector performance depends on the incident angle with respect to the anode wires. Because of the higher energy deposit in case of the electrons (electrons are at the Fermi plateau in the energy loss), they will suffer from stronger gas gain saturation than the pions and this will expectedly affect the pion rejection performance. The radiator used for these studies is the S-HF71 sandwich and the detection gas was  $\text{Xe},\text{CO}_2$  (15%). In Fig. 14.27 we show the electron-pion performance as function of the incident angle. The ratios of pulse heights as a function of the detector depth are shown in the left panel. One can see the expected degradation of these ratios as the incident angle approaches normal incidence. This translates into a degradation of the pion rejection performance, as shown in the right panel. The L-Q method was used to obtain these pion efficiencies extrapolated for 6 layers. The sandwich radiator S-HF71 has been used, for the momentum of 1 GeV/c. The gas gain of the chamber was about 7000.

A higher gas gain obviously contributes to a stronger degradation of the pion rejection performance as seen in Fig. 14.28, where we present the dependence of the pion efficiency at 90% electron efficiency as function of incident angle. Three values of the gas gain are compared, increasing from about 7000 by a factor of 2.35 for each 100 V of the anode voltage. The momentum is 1 GeV/c and the radiator is the sandwich S-HF71. While at the lowest gas gain the degradation in pion rejection is about 30% from  $17^\circ$  to normal incidence, for the higher gains the situation is considerably worse. Almost a factor of four worse pion rejection is observed for the highest gain at normal incidence. One can notice that for incident angles above roughly  $10^\circ$  there is basically no difference in pion rejection for different gains. As discussed above (Section 14.3.2), the gas avalanche is a local process and this explains also the observed dependence of the pion efficiency as a function of angle for different gains (see also related Fig. 14.18).

The degradation of the pion rejection performance as a function of incident angle for high values of the gas gain is an important argument for operating the detectors at the lowest possible gain.

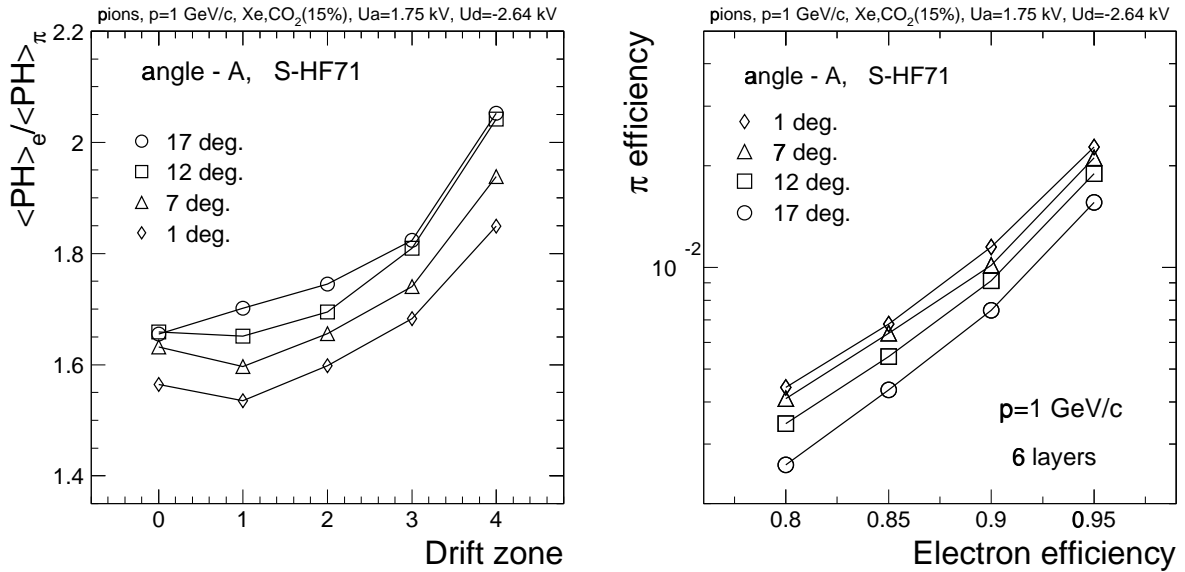


**Figure 14.27:** Pion rejection performance as a function of incident angle along the anode wires. Left panel: average pulse height ratios; right panel: pion efficiency as a function of electron efficiency. The momentum is 1 GeV/c and the radiator is a sandwich of HF71 foam and 17  $\mu\text{m}$  fibres.

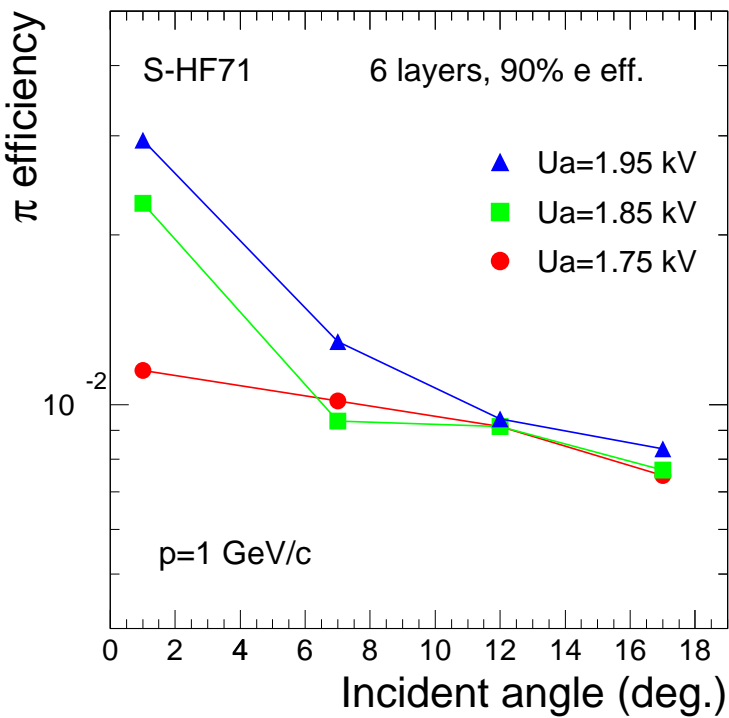


**Figure 14.28:** Pion rejection performance as a function of incident angle along the anode wires. Three values of the gas gain are compared, increasing by a factor of 2.35 for each 100 V of the anode voltage. The gas mixture is Xe,CO<sub>2</sub> (15%),  $U_d=-2.64 \text{ kV}$ . The momentum is 1 GeV/c and the radiator is the S-HF71.

### 14.3.7 Position reconstruction performance

In this section we present results on the position reconstruction performance using a single drift chamber. We study the dependence of the performance on the signal-to-noise ratio for the data without any corrections. Then we justify and apply corrections for the time evolution of the signal and conclude with a study on the influence of a tail cancellation technique, proving its suitability for our data processing chain.

Unless specified, for this study we use 14 time bins of 100 ns each, spanning the full drift region of the DC. Note that there is an uncertainty in assigning the beginning of the drift region (see Fig. 14.13). While this influences the value of the reconstructed angle of incidence, the resolution is changed only marginally. In Fig. 14.29 we present an example of the angle fit. The pulse height distributions over eight pads are presented in the left panel. The fit of the displacement (with respect to the center pad) for each time bin is shown on the right panel. The incident angle was  $17^\circ$  along the anode wires (across pads). It corresponds to a 9.2 mm deflection over the 30 mm drift length.

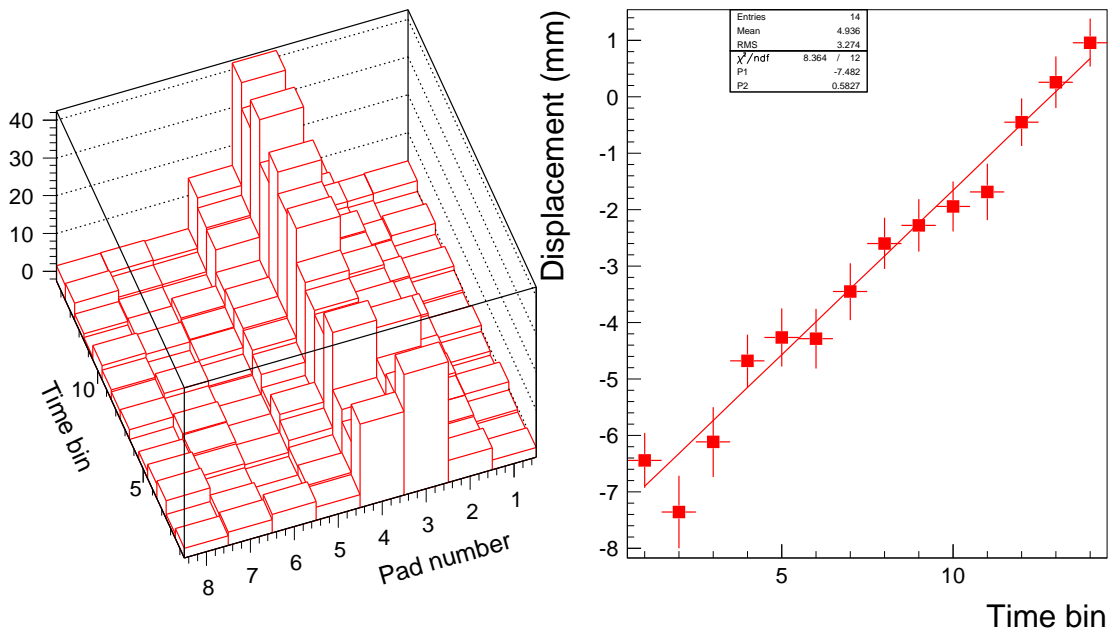


**Figure 14.29:** Left panel: the pulse height in the drift region versus time bin number on eight pads. Right panel: the displacement from the center pad as a function of time bin number.

In Fig. 14.30 is shown a summary of results as function of signal-to-noise ratio, S/N. The signal is the average pulse height per time bin (for the drift region only) on the center pad, for pions. To vary S/N we increased the gas gain of the detector by varying the anode voltage. The beam incidence was  $17^\circ$  with respect to the normal on the detector, along the anode wires. The upper row presents the average number of pads,  $\langle N_{\text{pad}} \rangle$ , with a signal above threshold (cluster width) for each time bin (the threshold was 2 times the noise value) and the average number of points used for the angle fit,  $\langle N_{\text{fit}} \rangle$ . We compare three methods for the position reconstruction:

1. the center of gravity using 5 pads, labeled COG5. The displacement from the center of the pad with the maximum signal (pad  $i$ ) is:

$$x = \frac{-2 \cdot P_{i-2} - P_{i-1} + P_{i+1} + 2 \cdot P_{i+2}}{P_{i-2} + P_{i-1} + P_i + P_{i+1} + P_{i+2}}, \quad (14.4)$$

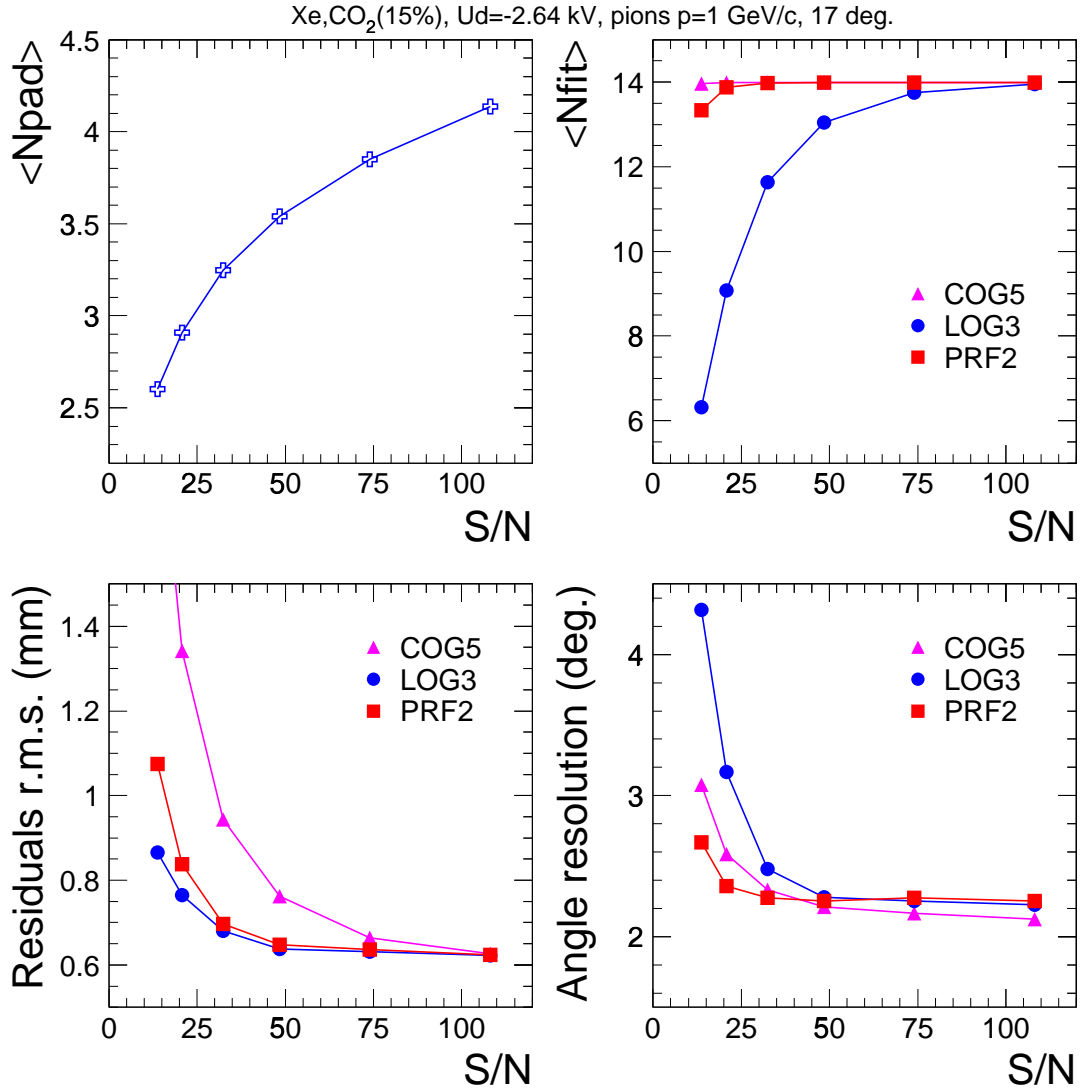


**Figure 14.30:** The position performance as function of signal-to-noise ratio, S/N. Clockwise from top left: average number of pads with signal over threshold for each time bin,  $\langle N_{pad} \rangle$ ; average number of points used for the angle fit,  $\langle N_{fit} \rangle$ ; angular resolution; r.m.s. of the residuals. The methods used for the position calculation are described in the text.

where  $P_i$  is the signal (pulse height for a given time bin) for pad  $i$ . The threshold is required only for the central pad.

2. using (for each time bin) formula 14.1, derived under the assumption of a gaussian PRF [5, 6], labeled LOG3. For this method we require that three pads have signals above threshold.
3. an analytical formula using the measured pad response function (see Section 14.2.3), labeled PRF2 [4]. At least two pads are required to be above threshold in this case. In case three pads are above threshold, a weighted mean of two measurements is used [4], so that the displacement for a given

time bin is:

$$x = \frac{1}{w_1 + w_2} \left[ w_1 \left( \frac{\sigma_P^2}{w} \ln \frac{P_i}{P_{i-1}} - \frac{w}{2} \right) + w_2 \left( \frac{\sigma_P^2}{w} \ln \frac{P_{i+1}}{P_i} + \frac{w}{2} \right) \right], \quad (14.5)$$

where  $\sigma_P=0.6\cdot w$  is the known (gaussian) width of the PRF,  $w=10$  mm is the pad width and  $w_1, w_2$  are weights:  $w_1 = P_{i-1}^2$ ,  $w_2 = P_{i+1}^2$  [4]. In case the signal in one of the neighbouring pads is below threshold, this pad is not included in the position calculation. Note that from the beam data using Xe,CO<sub>2</sub> (15%) , we found the PRF to be identical to that measured with Ar,CH<sub>4</sub>(10%).

As a consequence of their specific conditions, the three methods have different average number of fit points, as seen in Fig. 14.30 upper right panel.

The lower row in Fig. 14.30 presents the position reconstruction performance: the r.m.s. of the residuals (distance from fit point to the fit value) and the angle resolution ( $\sigma$  of gaussian fit). Here again the three methods show specific behaviour. As expected, as a consequence of different sensitivities to noise for the three methods used, the LOG3 method gives the best resolution at low S/N, while the COG5 method is the worst case. Both the LOG3 and the PRF2 method reach a saturation for S/N>50, while the COG5 method converges to the same resolution only at very high values of S/N. This saturation of resolution as function of S/N indicate the presence of additional sources of errors besides the noise contribution (see below).

Concerning the angular resolution, the three methods differ substantially only at low values of S/N. The poor resolution in case of LOG3 method is a result of the small number of fit points (see upper right panel of Fig. 14.30), while the PRF2 method is a compromise between noise sensitivity and number of fit points. Surprisingly, despite the scatter of the fit points for the COG5 method, leading to sizeably higher values of r.m.s. of residuals, the resolution in angle is only slightly worse than for the PRF2 method at low S/N and even slightly better at large values of S/N.

One can notice from Fig. 14.30 that the angular resolution saturates at lower values of S/N compared to the points resolution (r.m.s. of residuals, which we shall denote as  $\sigma_y$ ). This hints to a systematic contribution to the error of the angle that is investigated below. The angle resolution,  $\sigma_\alpha$ , can be written as function of  $\sigma_y$ :

$$\sigma_\alpha \simeq \sqrt{\frac{12}{N_{fit}}} \cdot \frac{\sigma_y}{D} \quad (14.6)$$

where  $N_{fit}$  is the number of (independent) fit points and  $D$  is the detector depth. For  $N_{fit}=15$  over the drift region  $D=30$  mm, one expects at the limit of high S/N values a limiting resolution of about 1° . The measured values of about 2° are sizeably worse.

The angle determination is sensitive to the Landau fluctuations of the energy deposit along the track. They are biasing the values of the displacement as a function of drift time (and hence the angle) via the asymmetric time response function (TRF) of the detector, due to the ion tail, and of the PASA, due to pole/zero cancellation (see Fig. 14.2, Section 14.2.1). In Fig. 14.31 we give an example of the correlation of the reconstructed angle with the shape of the individual signal. The left panel shows two (extreme) cases, in which the signal is predominantly at the beginning or at the end of the drift time (expressed as time bin number). The arrows mark the drift time position of the average signal,  $t_{\langle Q \rangle}$ , for each case. The right panel shows, for both cases, the displacement distributions, along with the fits. There is a considerable difference between the two cases: in case of larger clusters at the beginning of the drift (dots) the reconstructed angle is much smaller compared to the case with large clusters later in time (squares). Here and in the following, unless specified, the studies are performed for a moderate value of S/N≈32.

In Fig. 14.32 we present the correlation of the reconstructed angle with the drift time position of the average signal,  $t_{\langle Q \rangle}$  for samples of events in case of pions and electrons. The scale on  $z$  is logarithmic. The incidence was 17° with respect to the normal to the anode wires. Pions and electrons show a similar

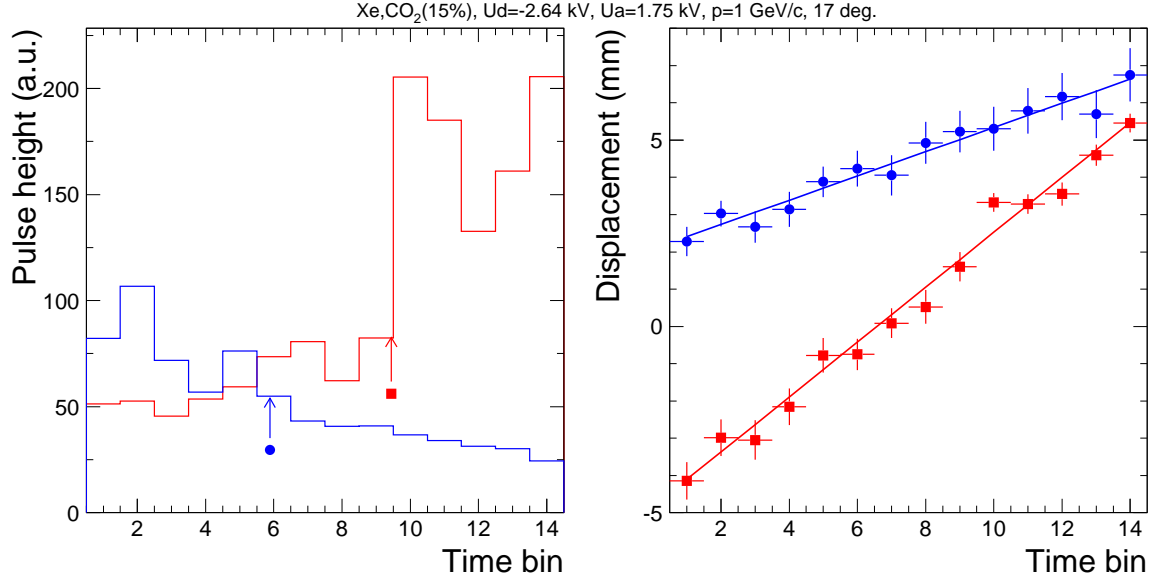


**Figure 14.31:** Left panel: two examples of the pulse height in the drift region summed up over all pads. Right panel: the displacement from the center pad as a function of time bin number and the result of the fit for the two events of the left panel.

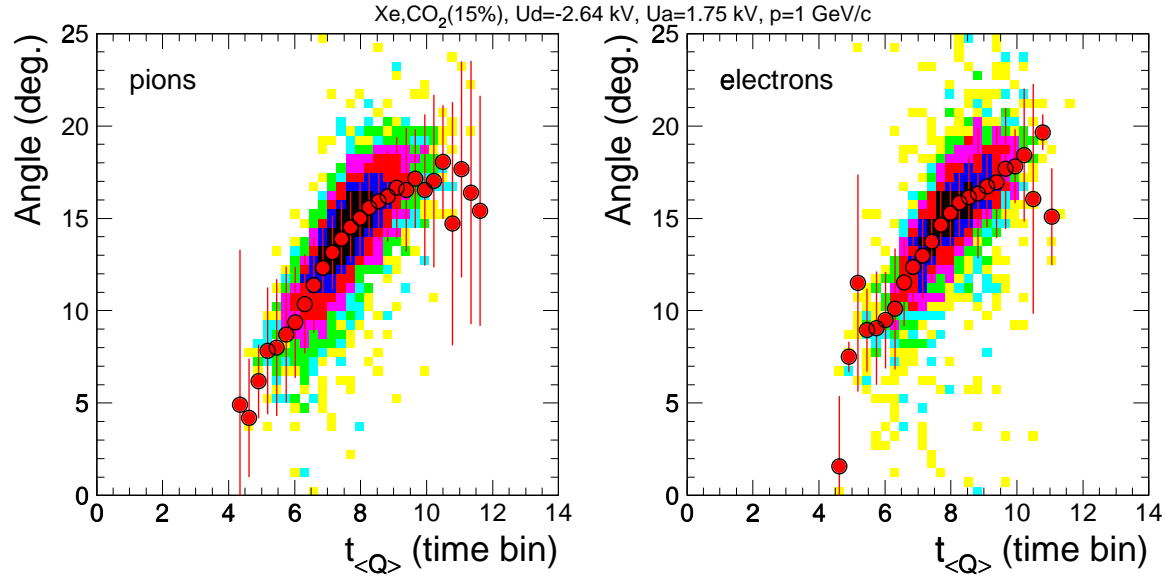


**Figure 14.32:** The distribution of reconstructed angle vs. the position of the mean charge deposit in the drift time,  $t_{\langle Q \rangle}$ . The average values are overlayed as dots. The PRF2 method was used for the position reconstruction.

correlation, namely a systematically smaller angle in case of events with large clusters early in time, as illustrated in Fig. 14.31. For higher values of  $t_{\langle Q \rangle}$  the reconstructed angle approaches a saturation. The dots in Fig. 14.32 denote the average values of the respective distributions (the errors are the r.m.s.). These values have been used to establish a correction for the angle, taking as reference the largest mea-

sured value (which is actually the true incident angle of  $17^\circ$ ). The correction of the angle is done for each track individually, as function of  $t_{(Q)}$ . The correction is the same for electrons and pions.

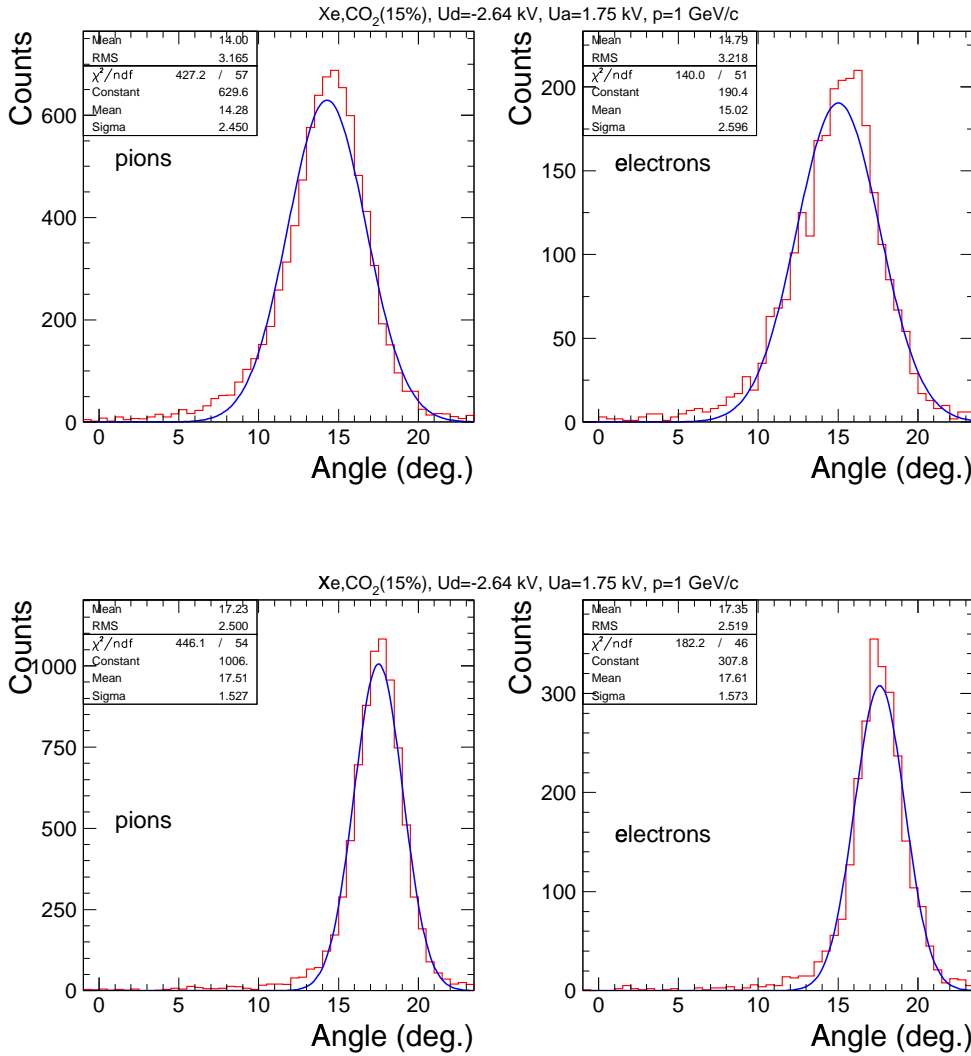


**Figure 14.33:** Angle reconstruction performance for pions and electrons, before (upper row) and after (lower row) the correction for the mean charge deposit. The PRF2 method was used for the position reconstruction and the incident angle was  $17^\circ$ .

Figure 14.33 presents the distributions of the reconstructed angles for both pions and electrons, before (upper row) and after (lower row) the correction for the mean charge deposit. The thicker curves are the result of gaussian fits. A clear improvement of the angular resolution, by about  $1^\circ$ , is seen as a result of the correction. Obviously, the centroid of the angle distribution is also affected by the correction.

A summary of the effect of the above correction as a function of the incident angle is presented in Fig. 14.34 for both pions and electrons. The correction was determined separately for each angle. Notice that not only the resolution is worse prior to the correction, but also the reconstructed angle is smaller than the real angle by several degrees. The correction restores the original angle and improves the resolution, as seen already in Fig. 14.33. The correction is less significant for smaller incident angles, with no effect at normal incidence (in fact, at normal incidence there is no correlation of angle vs.  $t_{(Q)}$ ).

We turn now to a more detailed study of the position and angular resolution as a function of the

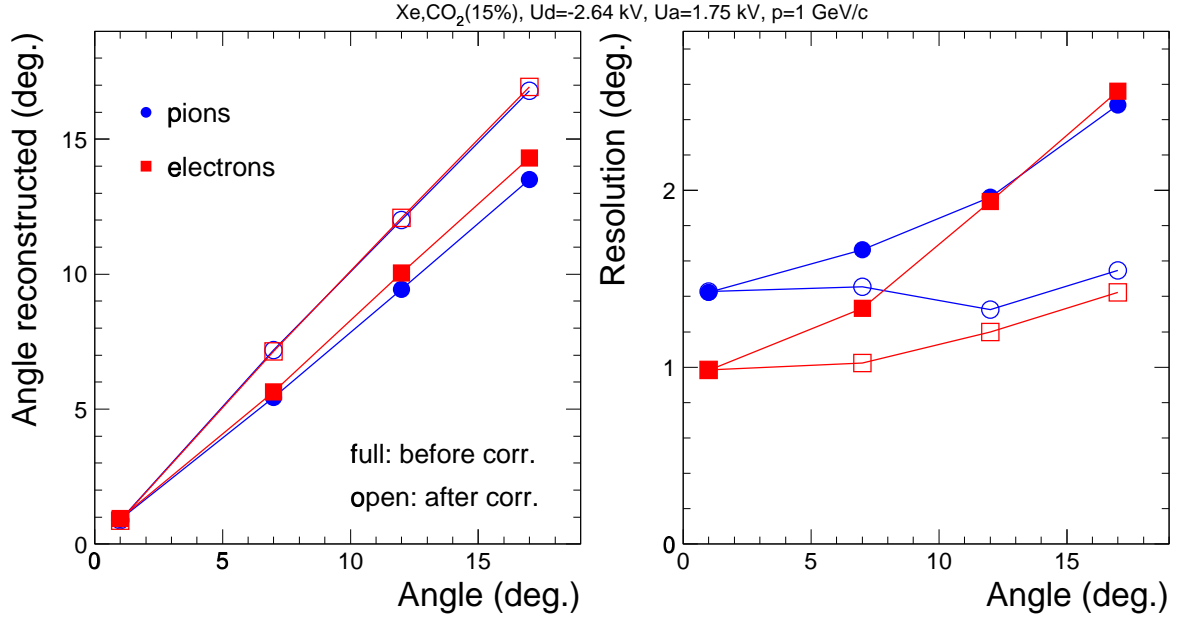


**Figure 14.34:** Angle reconstruction performance for pions and electrons, as a function of the incident angle, before (full symbols) and after (open symbols) the correction. The PRF2 method was used for the position reconstruction.

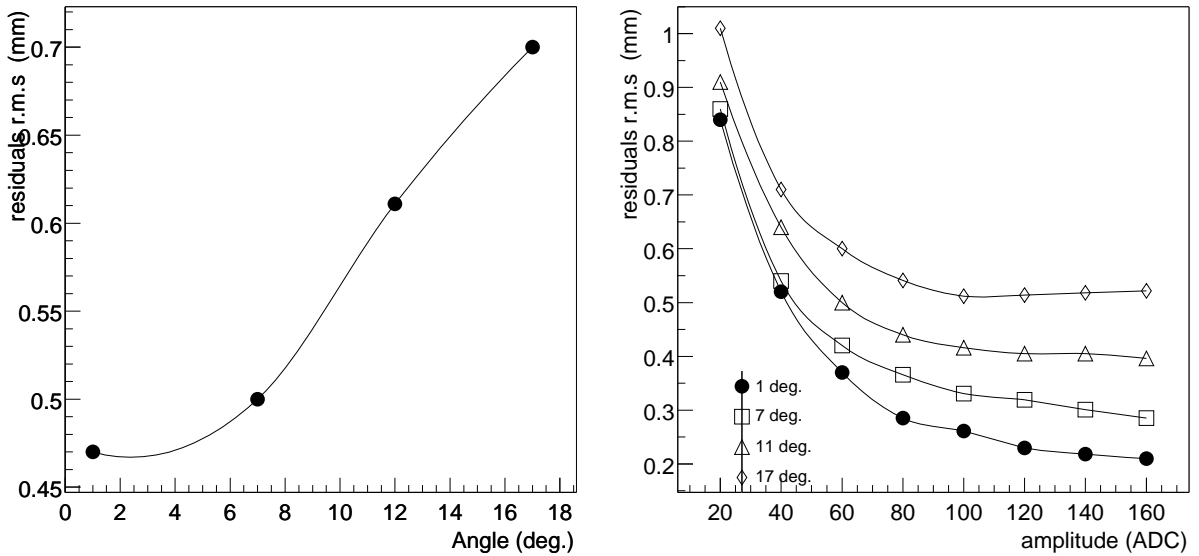


**Figure 14.35:** Left panel: r.m.s. of residuals as a function of incident angle. Right panel: r.m.s. of residuals as a function of signal magnitude for different incident angles.

incident angle. In Fig. 14.35 we show a summary of the position resolution (r.m.s. of the residuals) as function of the incident angle. The left panel shows the resolution as a function of incident angle, while the right panel presents a differential view of the resolution, namely its variation as a function of the amplitude (the sum of the signal over the pad cluster in each time bin) for the four incident angles. The noise level is about 1.2 ADC channels. In the limit of large signals, resolutions down to 200  $\mu\text{m}$

are achieved for normal incidence. Also in this representation, the resolution exhibits a saturation as a function of the signal magnitude, however, the saturation is reached for higher values of S/N and for lower values of the resolution as compared to the integral values presented in Fig. 14.30. Notice also the different amplitude dependence in the approach to saturation as a function of the incident angle. Here and for the following results a look-up table method (LUT) based on the known PRF was used for the position reconstruction. It gives results comparable to the PRF2 method presented above and has the advantage that it is easy to use for position calculations at the trigger level (see Chapter 6).

Despite the fact that the correction of the angles due to Landau fluctuations is quite effective, a more natural approach is the so-called “tail cancellation”, namely subtracting the known signal tail as a function of time. It can be done either at the level of the analog electronics, as it was originally proposed, using a pole/zero network [31] or at the level of the digitized signal by employing a digital filter [32]. In either case, the operations are the equivalent of de-convoluting the signal with the following transfer function [31]:

$$f(s) = \frac{s + 1/\tau}{s + k/\tau} \quad (14.7)$$

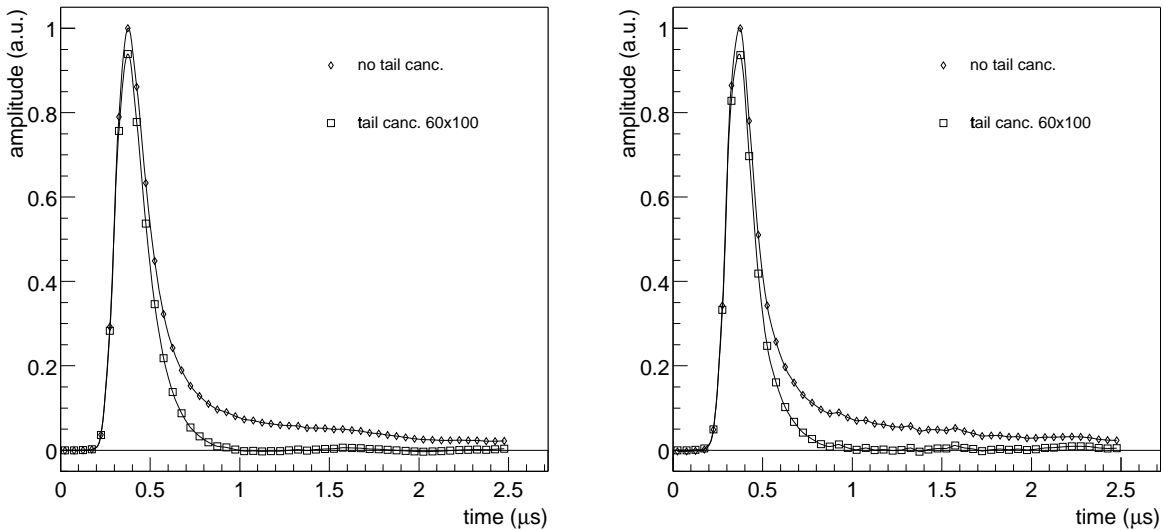


**Figure 14.36:** Average signals for  $^{55}\text{Fe}$  source on center (left panel) and neighbouring pad (right panel), before (diamond symbols) and after the tail cancellation (squares).

We applied such a deconvolution for the measured data in the off-line data analysis. Fig. 14.36 shows average signals from the  $^{55}\text{Fe}$  source on the center pad (left panel) and on a neighbouring pad (right panel) before and after the deconvolution with the function 14.7. One can see that the long tail is cancelled quite accurately for the chosen set of parameters ( $k \times \tau$ , where  $\tau$  is expressed in time bins of 10 ns each). The values  $\tau=1.0 \mu\text{s}$ ,  $k=1.67$  were found to provide the optimum angular resolution and are used in the following studies.

In Fig. 14.37 we present an example of the average pulse height as function of drift time for pions, before (left panel) and after (right panel) the tail cancellation. Two effects of the cancellation are seen: i) the originally slightly rising plateau (left panel) is made perfectly flat (right panel); ii) the average signal in the drift region is reduced by about 37%, as can be seen from the fits of the plateau regions (thick straight lines); this implies the necessity to work at higher gas gain in order to compensate for the signal loss.

In Fig. 14.38 we compare the angular resolution for the original data (upper left panel), after the  $t_{(Q)}$  correction (upper right panel) and after the tail cancellation algorithm (lower panel). For this investigation

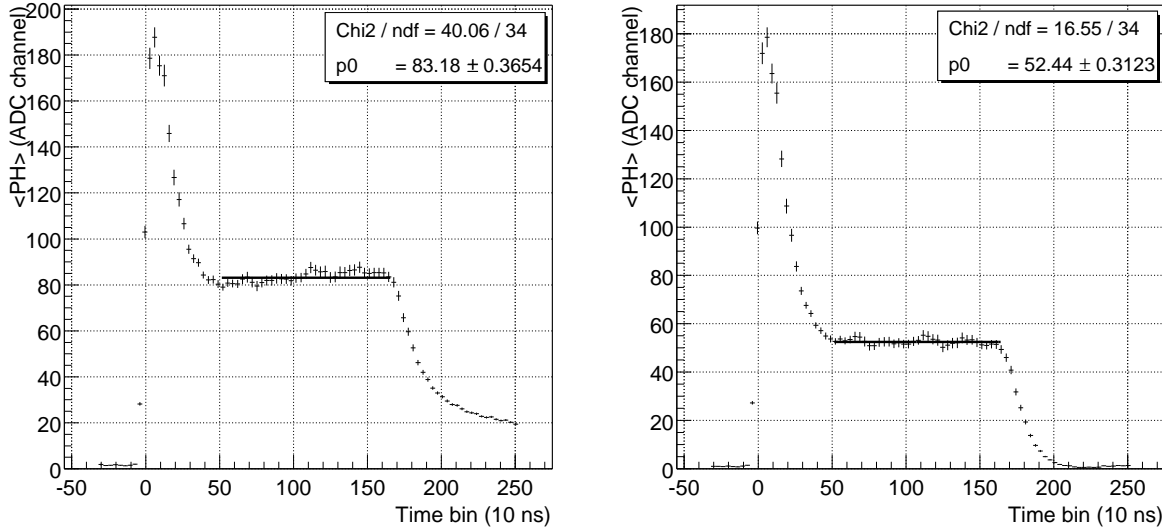


**Figure 14.37:** Average pulse height as function of drift time for pions, before (left panel) and after (right panel) the tail cancellation.

the amplification region was included in the angle fit, amounting to additional 3 time bins of 100 ns each. Despite the fact that the drift velocity is not constant in the amplification region, clean clusters contribute there to a better angle resolution for the uncorrected data, compared to the case when only the drift region was used (see previous Fig. 14.35 and below). Different methods of data analysis are compared in Fig. 14.38: i) 17 points (time samples of 100 ns each) are used for the fit (this is closest to the configuration of the final detector); ii) 33 samples of 50 ns are fitted; iii) 160 samples of 10 ns (our highest sampling resolution) each are used; iv) 160 samples are used, but the fit points are weighted by their individual pulse heights. For the last two cases in addition a cut on the cluster width (in the pad direction) is used, to minimize the contribution of  $\delta$ -rays. The different ways of analysis show little differences in case of both uncorrected and  $t_{\langle Q \rangle}$ -corrected cases, but in case of the tail cancellation analysis, as expected, a finer time sampling clearly leads to a better angle resolution. Overall, the tail cancellation leads to angular resolutions below 1° for all the incident angles, sizeably better compared to the  $t_{\langle Q \rangle}$  correction. Note that at the lowest incident angle the tail cancellation amounts to a small degradation of the angle resolution, mainly as a result of the degradation of the S/N ratio.

In Fig. 14.39 we summarize the S/N dependence of the position (left panel) and angle (right panel) resolution for 17° incidence, using various corrections. The uncorrected data (crosses) are compared to the values after the  $t_{\langle Q \rangle}$  correction (dots) and after the tail cancellation (squares) for 14 fit points in the drift region. Obviously, the  $t_{\langle Q \rangle}$  correction does not affect the point resolution (the dots are overlapping the crosses), but acts only on the angular resolution. Conversely, the tail cancellation is affecting the point resolution as well and this translates into a better angular resolution. The triangles indicate the tail cancellation method for the case of including the amplification region into the fit. For this last case the S/N value is improved for a given gas gain. However, for the same value of S/N, the point resolution suffers a degradation, presumably as a result of non-constant drift velocity in the amplification region. This is reflected in the angular resolution, where the improvement is less than expected from the scaling to the number of fit points (a factor of 1.16 improvement compared to the ratio 17/14=1.21). One can notice that the approach towards saturation for increasing S/N is different for the various cases presented, essentially the corrected values having a more accentuated dependence of S/N, as expected after essentially removing the systematic (dominant) contributions.

Finally, in Fig. 14.40 we show the distribution of the time of the first electron arrival,  $t_{first}$ , as a function of the position across the anode wires,  $y$ , measured with the Si-strip detectors. The 5 mm

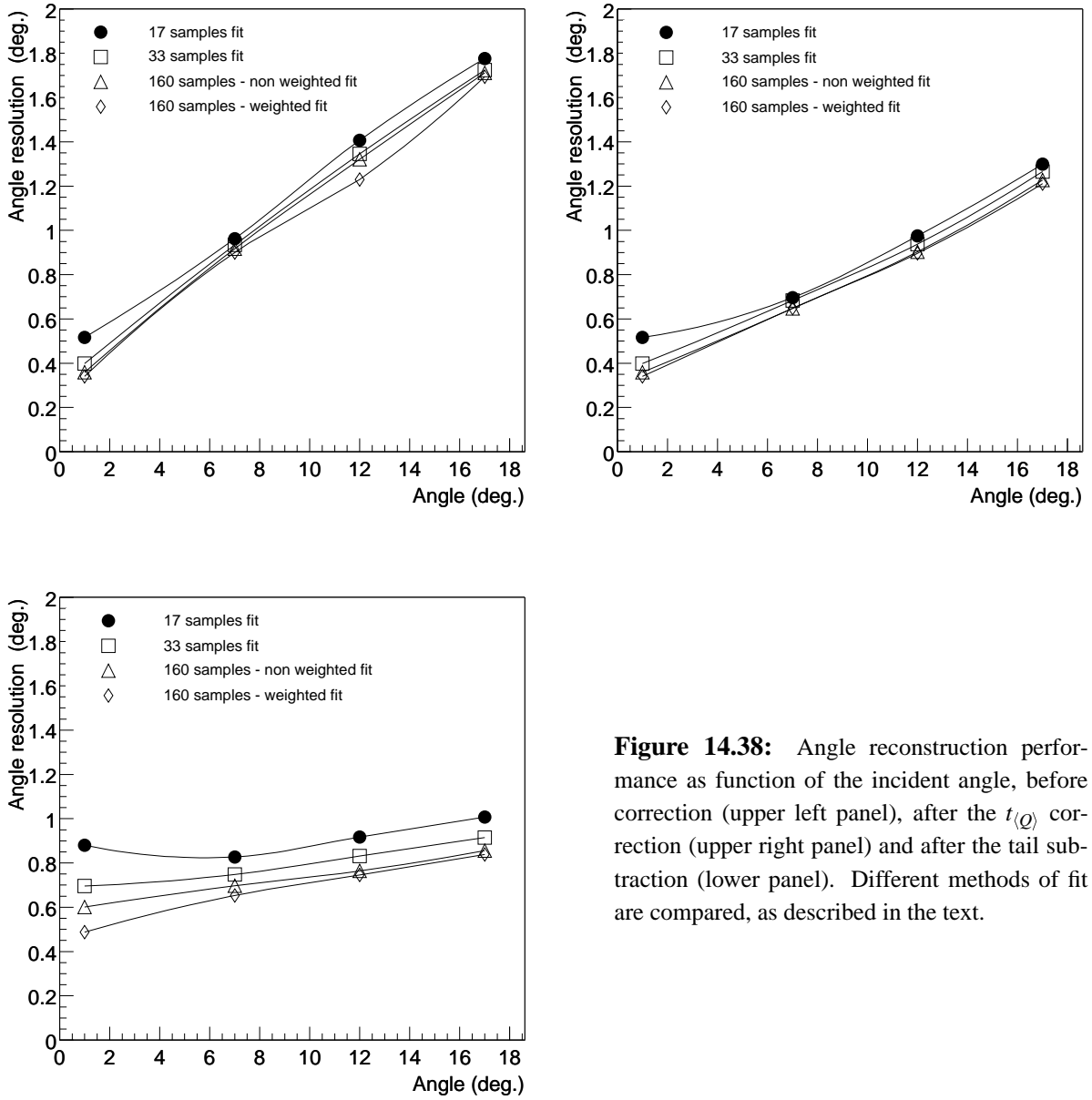


**Figure 14.38:** Angle reconstruction performance as function of the incident angle, before correction (upper left panel), after the  $t_{\langle Q \rangle}$  correction (upper right panel) and after the tail subtraction (lower panel). Different methods of fit are compared, as described in the text.

periodicity reflects the wire pitch. The variation of the arrival time within one drift cell is the result of the isochrony variation due to the field configuration. When exploited in a pad geometry staggered across the anode wires (in the real detector  $z$  direction, along the beam), the information on  $t_{first}$  can provide a position accuracy much better than the wire pitch. This feature can be an important constraint for the TPC tracking and may also be used for its absolute drift calibration.

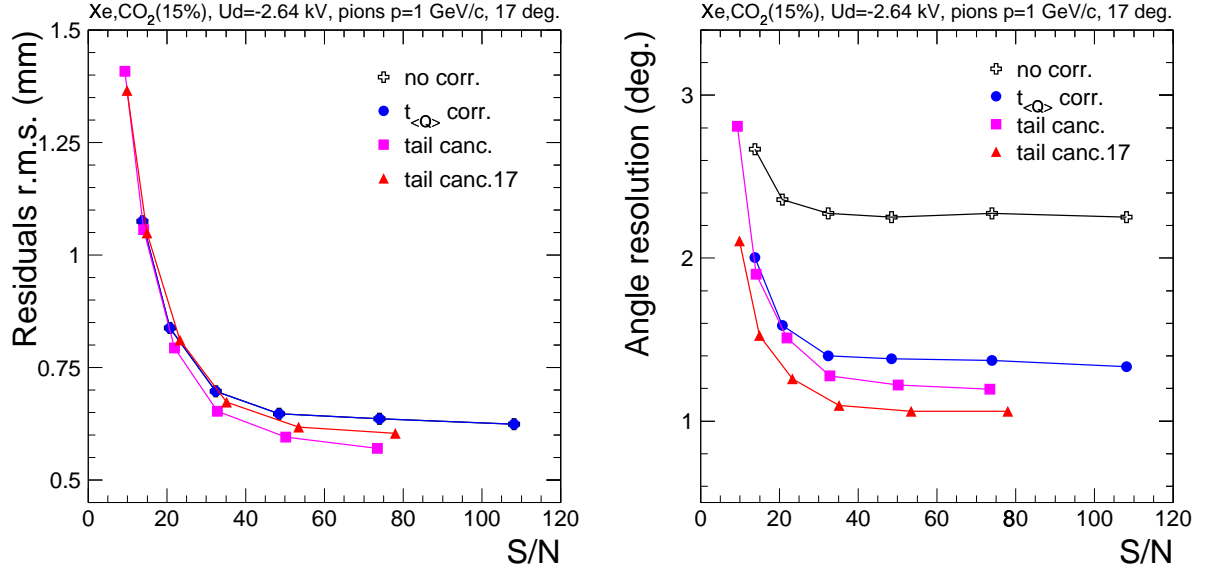


**Figure 14.39:** Position (left panel) and angular (right panel) resolution as a function of S/N for data without correction (crosses), after the  $t_{\langle Q \rangle}$  correction (dots) and after the tail cancellation (squares) for 14 fit points in the drift region. The triangles denote the tail cancellation method, but including the amplification region into the fit.

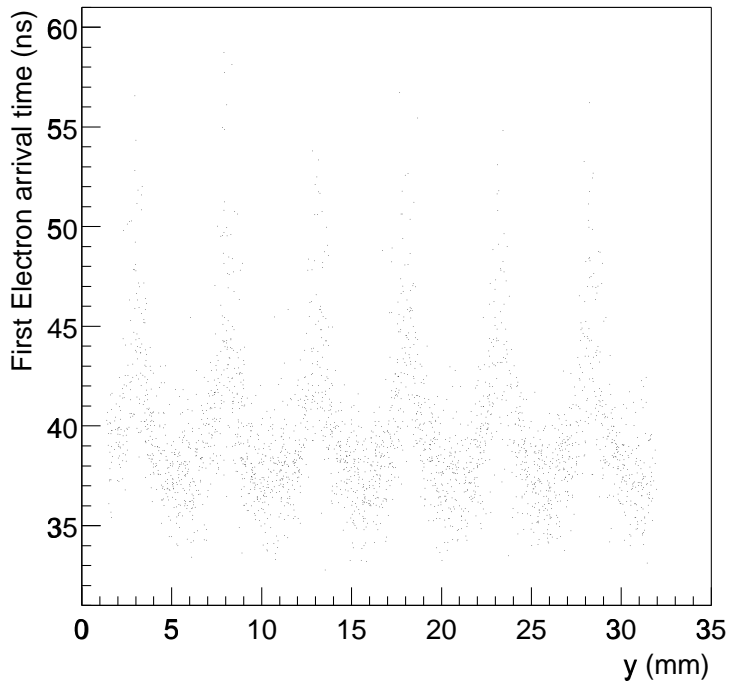


**Figure 14.40:** The distribution of the time of the first electron arrival as a function of the coordinate across the wires, measured by the Si-strip detectors.

## 14.4 Work in progress

New prototypes were recently built with pads both of chevron type ( $w=10\text{ mm}$ ,  $l=60\text{ mm}$ ) and rectangular ( $w=7.5\text{ mm}$ ,  $l=80\text{ mm}$ ). To have a similar pad response function, the anode-cathode gap ( $h$ ) is  $2.5\text{ mm}$  in case of chevron pads and  $3.5\text{ mm}$  for the rectangles. The anode wire diameter is  $20\text{ }\mu\text{m}$ . To facilitate a fast exchange of different pad planes on the same detector body, these new prototypes have smaller dimensions:  $25\times31\text{ cm}^2$ . Two wire configurations for the cathode plane were realized, with  $5\text{ mm}$  and  $2.5\text{ mm}$  wire pitch. In both cases we used a staggered geometry (see Chapter 4). Photographs of both the chevron (left panel) and rectangle (right panel) pad planes are shown in Fig. 14.41. These prototypes were tested with an  $^{55}\text{Fe}$  source and in beam at GSI in August 2001. We present here the detailed measurements with the  $^{55}\text{Fe}$  source and some results from the beam measurements.

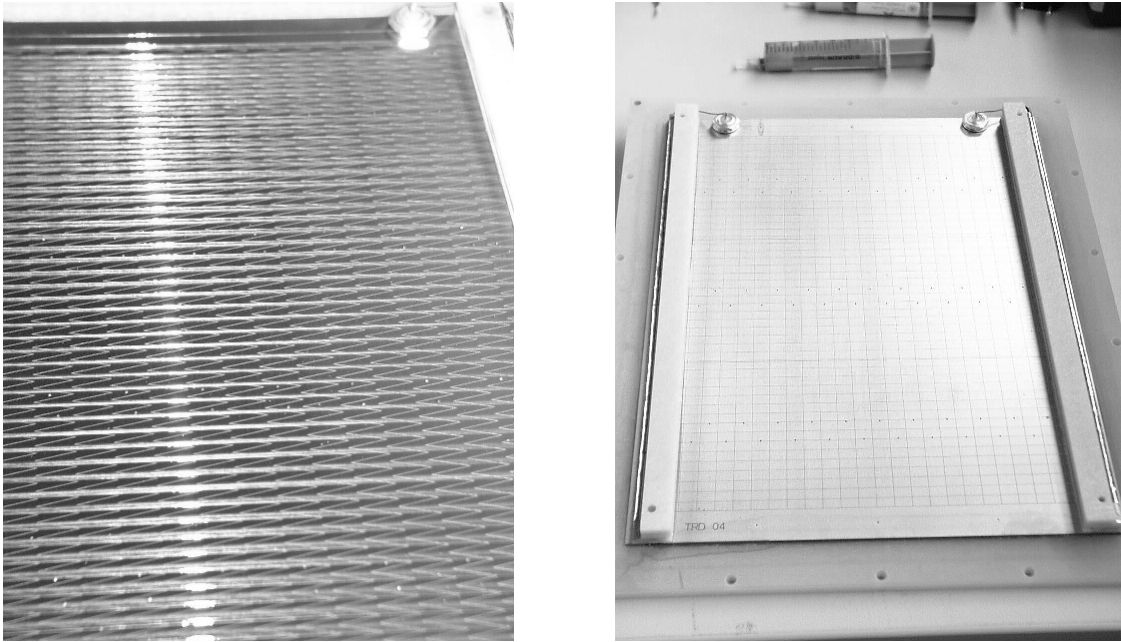


**Figure 14.41:** Photographs of the pad planes with chevron type (left panel) and rectangular (right panel) pads.

In Fig. 14.42 we present the gain curves: the average pulse height for the main peak of the  $^{55}\text{Fe}$  source as function of the anode voltage. Roughly  $100\text{ V}$  higher anode voltage is necessary in order to achieve the same gas gain for the  $h=3.5\text{ mm}$  configuration (rectangles), compared to the  $h=2.5\text{ mm}$  case (dots). This is slightly less than the difference predicted by GARFIELD [12] calculations (Section 4.6, Fig. 4.17).

Note that comparable values of the pulse height are obtained for lower voltages compared to the first prototype (see Fig. 14.6 in Section 14.2.2). The interpolation of the case  $h=3.0\text{ mm}$  of the first prototype leads us to conclude that roughly  $150\text{ V}$  less are needed for the same gas gain when changing the anode wire diameter from  $25$  to  $20\text{ }\mu\text{m}$ . In case of the denser cathode wire grid, with wire pitch of  $2.5\text{ mm}$  (open symbols in Fig. 14.42), the gas gain is slightly higher for the same anode voltage, as a result of a better confined amplification region.

In Fig. 14.43 we present the dependence of the  $^{55}\text{Fe}$  pulse height on the drift voltage. As a result of the drift field penetrating the cathode wire grid, the gas gain is increasing as function of the drift voltage. It is evident that the magnitude of this effect is different for the two cathode wire configurations. At fixed anode voltage, in case of  $5\text{ mm}$  cathode pitch (full symbols) the gas gain increases by almost  $60\%$  for an increase of  $1.5\text{ kV}$  in drift voltage. For  $2.5\text{ mm}$  pitch (open symbols) the increase is only  $26\%$ . The two cases of anode-cathode gap show similar dependence of the gas gain as a function of the drift voltage. Apparently, the difference on gain between the two configurations (at fixed drift voltage) is higher for the  $2.5\text{ mm}$  cathode wire pitch, as seen also in Fig. 14.42.

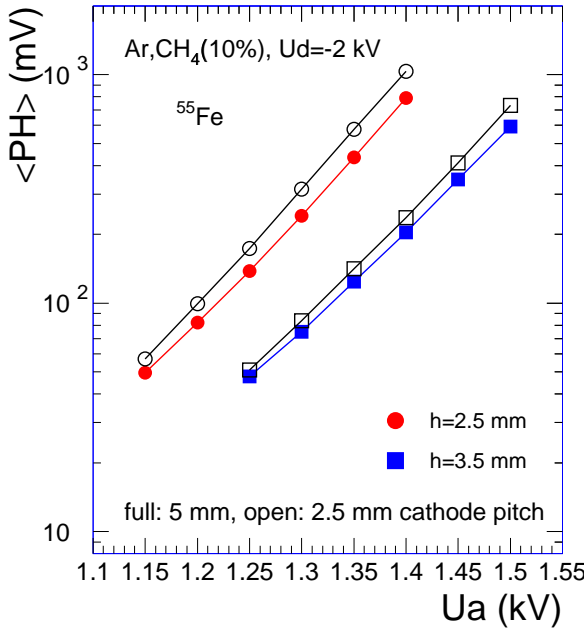


**Figure 14.42:** Pulse height of  $^{55}\text{Fe}$  as a function of the anode voltage for two cases of anode-cathode gap, for cathode wire pitch of 5 mm (full symbols) and 2.5 mm (open symbols).

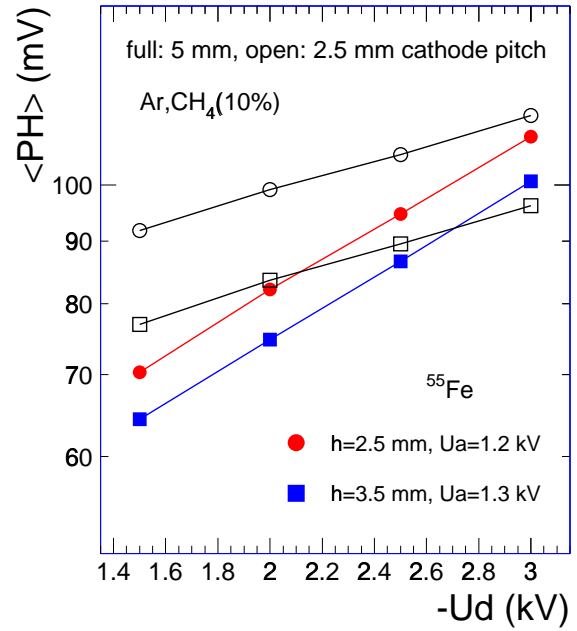


**Figure 14.43:** Pulse height of  $^{55}\text{Fe}$  as a function of the drift voltage for cathode wire pitch of 5 mm (full symbols) and 2.5 mm (open symbols) for two cases of anode-cathode gap.

In Fig. 14.44 are shown the PRFs for the chevron (left panel) and the rectangle (right panel) pad planes. We compare the 5 mm and 2.5 mm cathode wire pitch and conclude that the cathode grid density influences only marginally the PRFs. As seen already in Section 14.2.3 (Fig. 14.7), the calculated values do not agree with the measured ones. This disagreement is similar for chevron and rectangle pad planes and is being investigated further.

During the beam measurements in August 2001 we have performed the following:

- a relative comparison of the position reconstruction performance of the chevron and rectangular pads.
- a study of sandwich radiators reinforced with carbon or glass fibre.
- a study of the drift chambers performance as a function of the oxygen content in the detection gas.
- we placed the detectors in a magnetic field of up to 0.3 T, with the aim to measure Lorentz angles and to compare the position resolution with and without magnetic field.

While the bulk of the data evaluation is in progress, we present here the results on the study of the chamber performance under oxygen contamination. In Fig. 14.45 we show the average pulse height distributions as a function of drift time (left panel) and the pion efficiency as a function of electron efficiency for different values of the oxygen content in the range of a few hundred ppm. From the measurements of the pulse height distributions as a function of drift time we deduced an attachment coefficient  $C_{att}=400 \text{ atm}^{-2} \mu\text{s}^{-1}$  (see Chapter 4). As seen in the right panel of Fig. 14.45, the pion rejection performance is slightly degrading for increasing oxygen contamination. This is one argument to keep the oxygen at the lowest possible value.

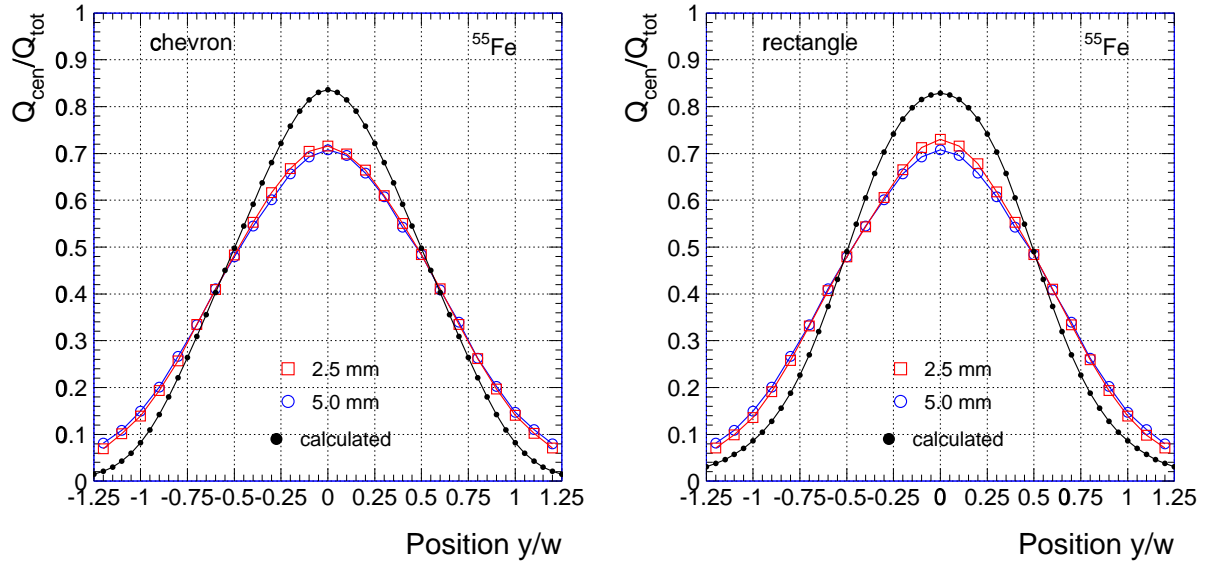


**Figure 14.44:** Pad response functions for chevron (left panel) and rectangle (right panel) pad planes. The 5 mm (circles) and 2.5 mm (rectangles) cathode pitch are compared.

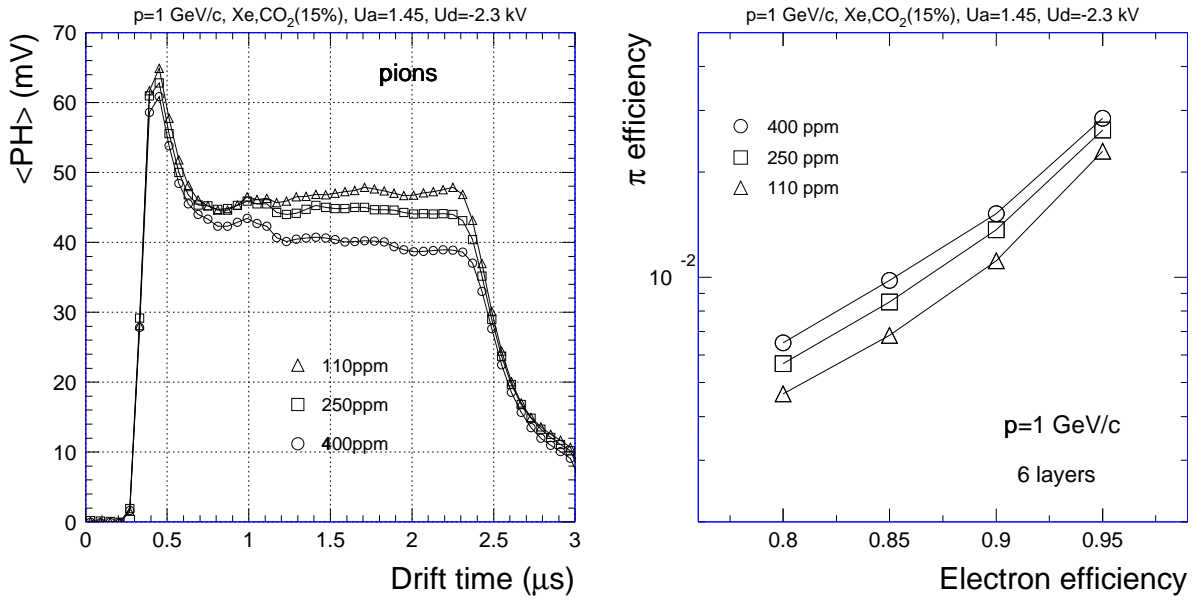


**Figure 14.45:** Drift chamber performance as a function of oxygen content. Left panel: average pulse height distributions as a function of drift time. Right panel: pion efficiency as a function of electron efficiency.

Apart from the analysis of newly measured data, ongoing work include on-detector implementation of the integrated electronics and preparations for beam tests at CERN, where in particular the TR performance for momenta above 2 GeV/c will be measured. These measurements are scheduled for October-November 2001.

# 15 Mass production

---

As described in this Technical Design Report a total of 18 supermodules containing altogether 540 individual detectors need to be constructed, tested, and finally installed in the ALICE central barrel not including spares. This task cannot be handled by a single institution. Therefore, it is currently foreseen to involve a number of major construction sites in the assembly of the individual detectors or major parts thereof.

## 15.1 General concepts

The anticipated design of the readout chambers lead to entities that, once assembled, cannot easily be taken apart again. This fact makes a high level of quality assurance at each individual step during construction an essential requirement. Since it is currently foreseen to have five major construction sites (Bucharest, Dubna, Heidelberg, Darmstadt, and Münster), it is also necessary to standardize and merge all data gathered during construction in a common database. To guarantee equal standards in the production the equipment of the individual construction sites will be standardized. This will include equipment of the clean rooms for assembly, winding machines, test gas systems, and data acquisition systems both for optical alignment equipment as well as electronic testing of the final detectors.

Another important aspect in this distributed production scheme is a centrally coordinated distribution of raw materials. It is anticipated that all individual components will be acquired through the same vendors and will be qualified in the same fashion. Also, final stacking, alignment, and testing of complete supermodules will be done in a central place

## 15.2 Equipment of production sites

It is anticipated that each production site is equipped with:

- a clean room
- large flat tables
- a winding machine
- a video setup for optical alignment and measurements
- a test gas system
- a pulsed X-ray source
- a data acquisition system
- access to a common database
- appropriate space for storage of raw materials and finished detectors

## 15.3 Database

A common database following the internal guidelines of ALICE for detector databases will be used for data storage. The database will archive part numbers for the construction of individual detector elements as well as all data gathered during the individual production, quality assurance and calibration

steps. When the TRD comes online, this database will permits retrieval of all data relevant for setup and calibration during running and later during offline analysis. The exact specifications for this database are currently being worked out within the ALICE collaboration.

# 16 Implementation, infrastructure, and safety

---

## 16.1 ALICE experimental area

The ALICE detector will be installed at Point 2 of the LHC accelerator. The Point 2 experimental area was designed for the L3 experiment. The main access shaft, 23 m in diameter, provides a  $15 \times 7 \text{ m}^2$  installation passage and space for counting rooms. The counting rooms are separated from the experimental area by a concrete shielding plug (see Fig. 16.1). The experimental cavern is 21.4 m in diameter and will be re-equipped with a  $2 \times 20 \text{ t}$  crane having a clearance of about 3 m above the L3 magnet. The L3 magnet provides an 11.6 m long and 11.2 m diameter solenoidal field of up to 0.5 T. The end-caps have a door-like construction. The door frames will support large beams traversing the L3 magnet, from which the ALICE central detectors will be supported.

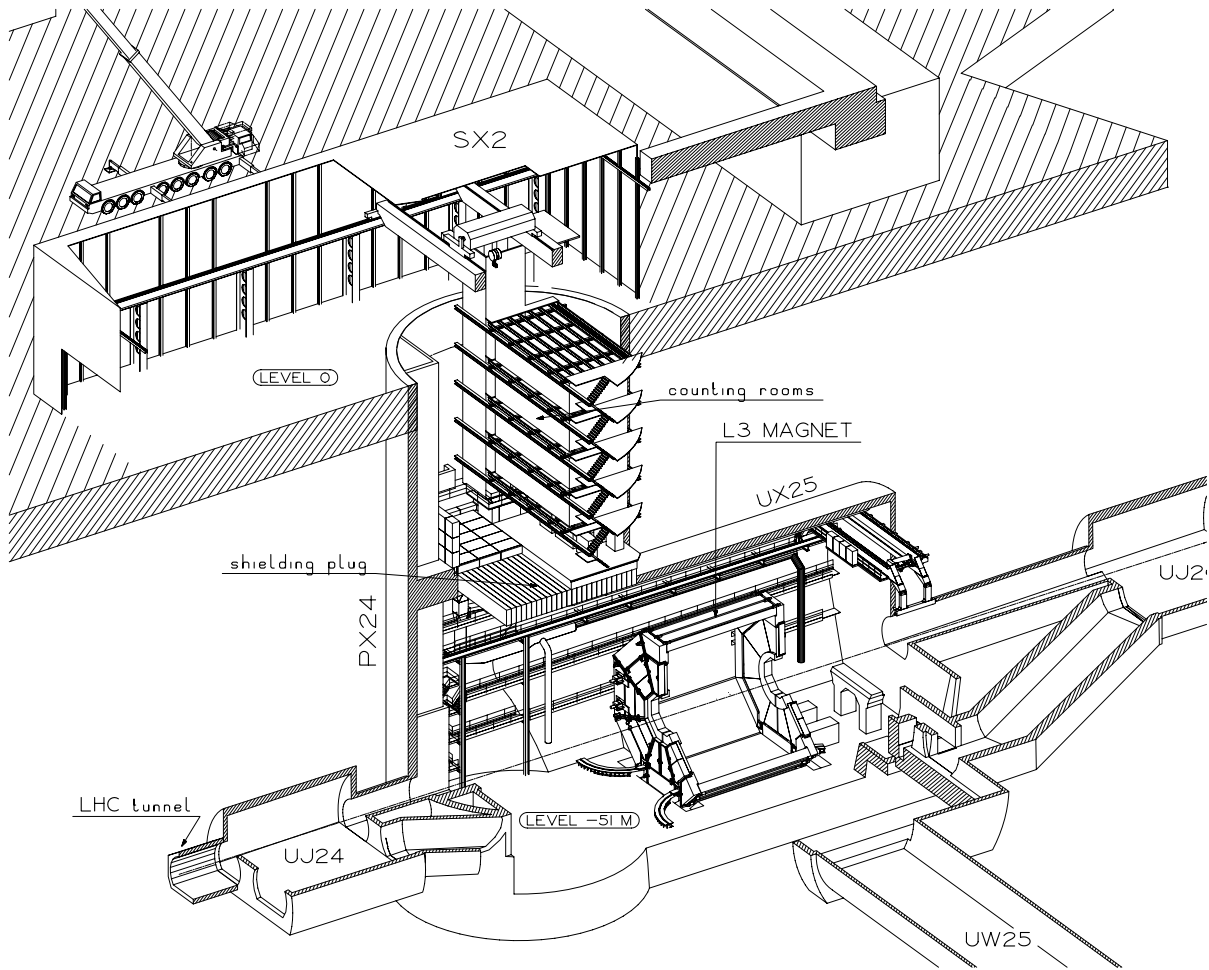


**Figure 16.1:** General layout of the basic underground structures at Point 2, showing the L3 magnet and the counting rooms.

## 16.2 Implementation of the TRD detector

### 16.2.1 General integration considerations

The TRD detector is supported by a cylindrical space frame construction, which also serves as a support for all the central detector units. The space frame is placed on large support beams straddling the coil section of the L3 magnet. This allows for the complete assembly of the central detector units to take place outside the L3 magnet. Each of the 18 TRD supermodules will be individually supported by two rails attached to the inner rings of the space frame (see Fig. 16.2). The services for the TRD will be supported by separate support frames, which will also serve as access platforms. The service support frame on the muon-arm side will be installed as a fixed structure, however, the service support frame on the access shaft side, will be installed on the same rails as the space frame and have the same diameter and modularity (it will be referred to as the ‘baby’ space frame). The main purpose of the ‘baby’ space frame is to carry the weight of all services of the central detectors, but also serve as a convenient installation frame for the TRD modules.

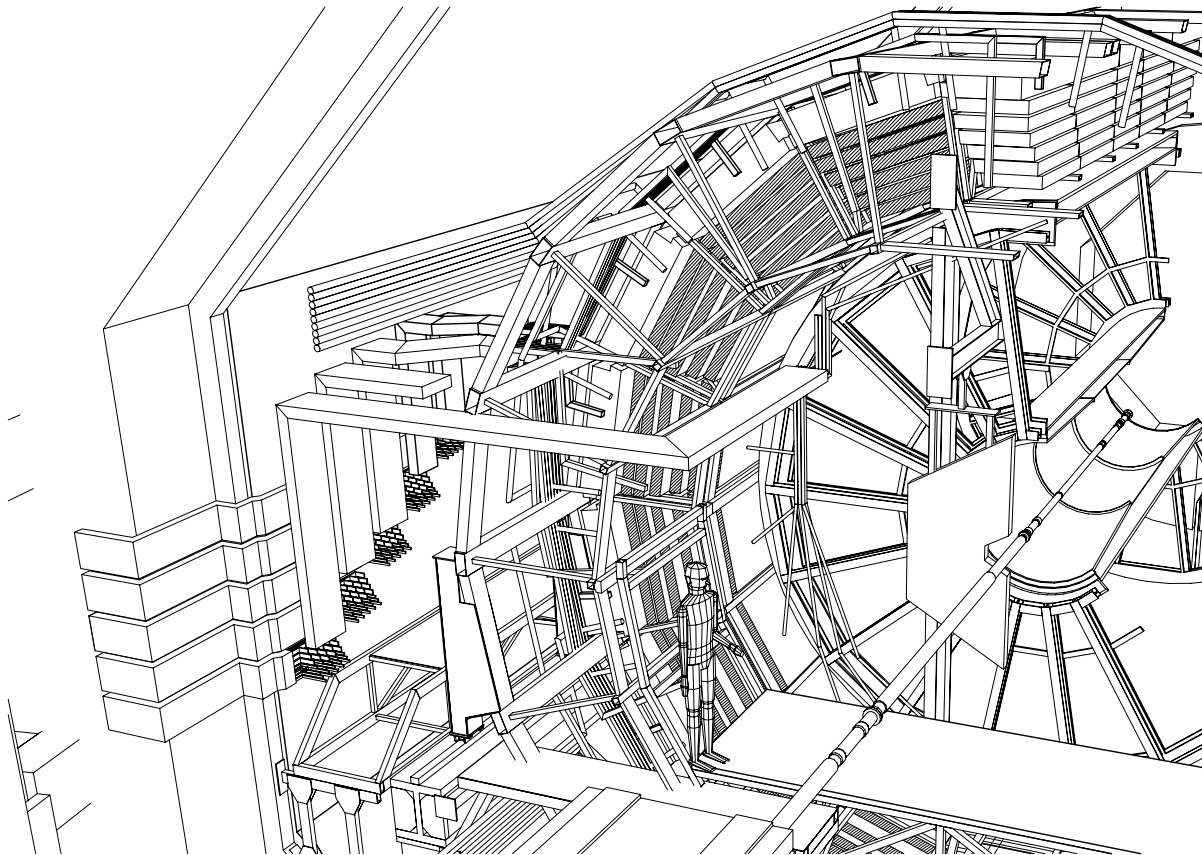


**Figure 16.2:** General view of the TRD detector and the space frame inside the L3 magnet. The ‘baby’ space frame is also partly visible.

### 16.2.2 The space frame

The space frame is divided into 18 sectors of  $20^\circ$  (following the agreed sectorization of the central detectors). All material has been concentrated at the sector boundaries and two concentrically placed support rings as indicated in Fig. 16.3.

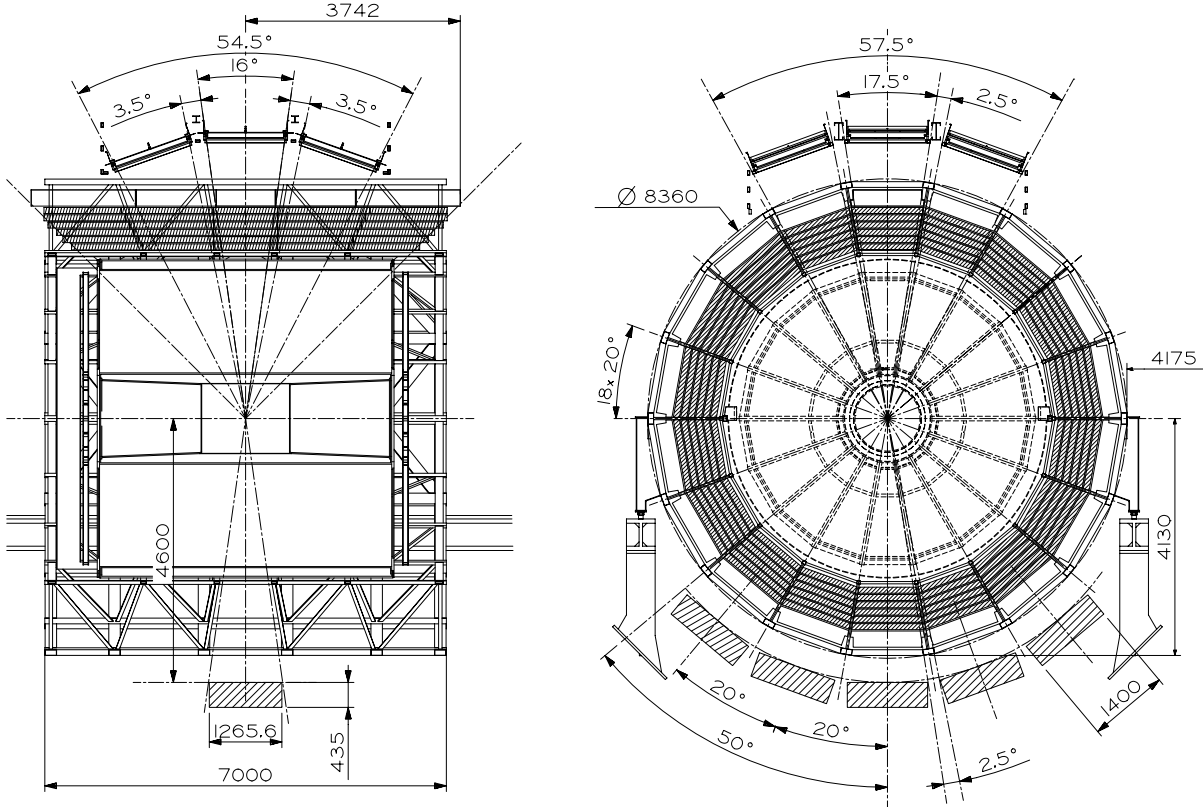


**Figure 16.3:** General layout of the space frame showing the geometrical arrangement of the central detectors.

The frame is supported on two support beams. There are two support points on each beam, which assures the same vertical displacement of the frame and the beams at all support points. The horizontal displacement of the frame is blocked on one side and free to move on the other side. The support beams are 12.1 m long and supported at their extremities by the L3 door structure. The combined space frame and support beam structure has been calculated for a total load of 75 t (Ref. [1]). The calculations were based on reducing the deformation of any two points on the space frame to a few mm and to limit the overall vertical displacement to less than 5mm. These calculations show that the movements of the TRD support rails can be limited to the displacements quoted in Chapter 2.

### 16.2.3 Pre-assembly phase

The present surface zone at Point 2 includes sufficient assembly hall space to meet the ALICE requirements and no new hall construction will be necessary for the detector assembly. The overall ALICE planning foresees a pre-assembly phase for the complete TRD detector to take place in the SXL2 assembly hall prior to the installation in the underground area, as indicated in Fig. 16.4. The detector will be fully assembled together with the space frame structure. This will allow an early preparation of the various detector services and permit the installation and access scenarios to be analyzed and corrected before lowering the TRD into the experimental cavern. All handling of the TRD outside the space frame will be made using a transport jig, which must also be able to orient the modules, such as to align the modules with the corresponding azimuthal position.

### 16.2.4 Installation in the underground cavern

It is conceivable that the complete space frame, with the TRD detector installed, is lowered down as one unit into the experimental area, however, the present installation scenario foresees a separate installation

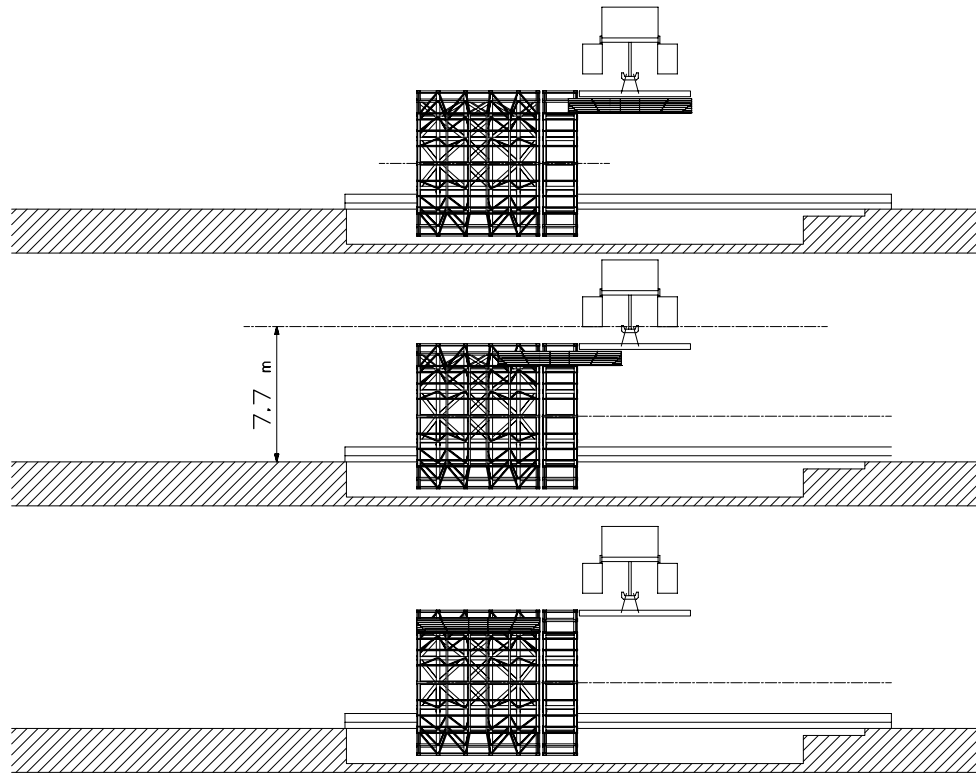


**Figure 16.4:** Pre-assembly of the TRD modules in the SXL assembly hall at Point 2. The figure shows the installation of a supermodule, using the transport jig and the baby space frame.

of the supermodules inside the experimental area (see Fig. 16.5). The space frame and the baby space frame will first be lowered down into the experimental area and placed on temporary support beams outside the L3 magnet. In this position the TRD modules can be relatively conveniently inserted into the space frame and some preparation of services can be made. The space frame is thereafter moved into the final position inside the L3 magnet. Alternatively, the TRD modules can also be inserted directly into the space frame in the final position inside the L3 magnet, however, this would be more restrictive and time consuming. This possibility is important for maintenance a possible staged installation.

## 16.3 Access, maintenance and services

### 16.3.1 Access for maintenance and repair

Access for maintenance to the various parts of the TRD detector is relatively straightforward. All services are concentrated to the side of the baby space frame and are easily accessible from platforms placed at several levels.

### 16.3.2 Services

The TRD services have been described in a previous chapter (Chapter 9). All services will have to pass through the narrow chicane shaped clearance (100 mm) between the magnet doors and the door frames (as shown in Fig. 16.2). In order to install the services the door will have to be opened, which prohibits any further service installations on the absorber side, once the Muon spectrometer is installed. The baby space frame will serve as a support for the services and allow a convenient distribution of cables, gas tubes and cooling tubes to the different sectors (see Fig. 16.6). It is estimated that the total weight of the services for the TRD detector is about 20 t.

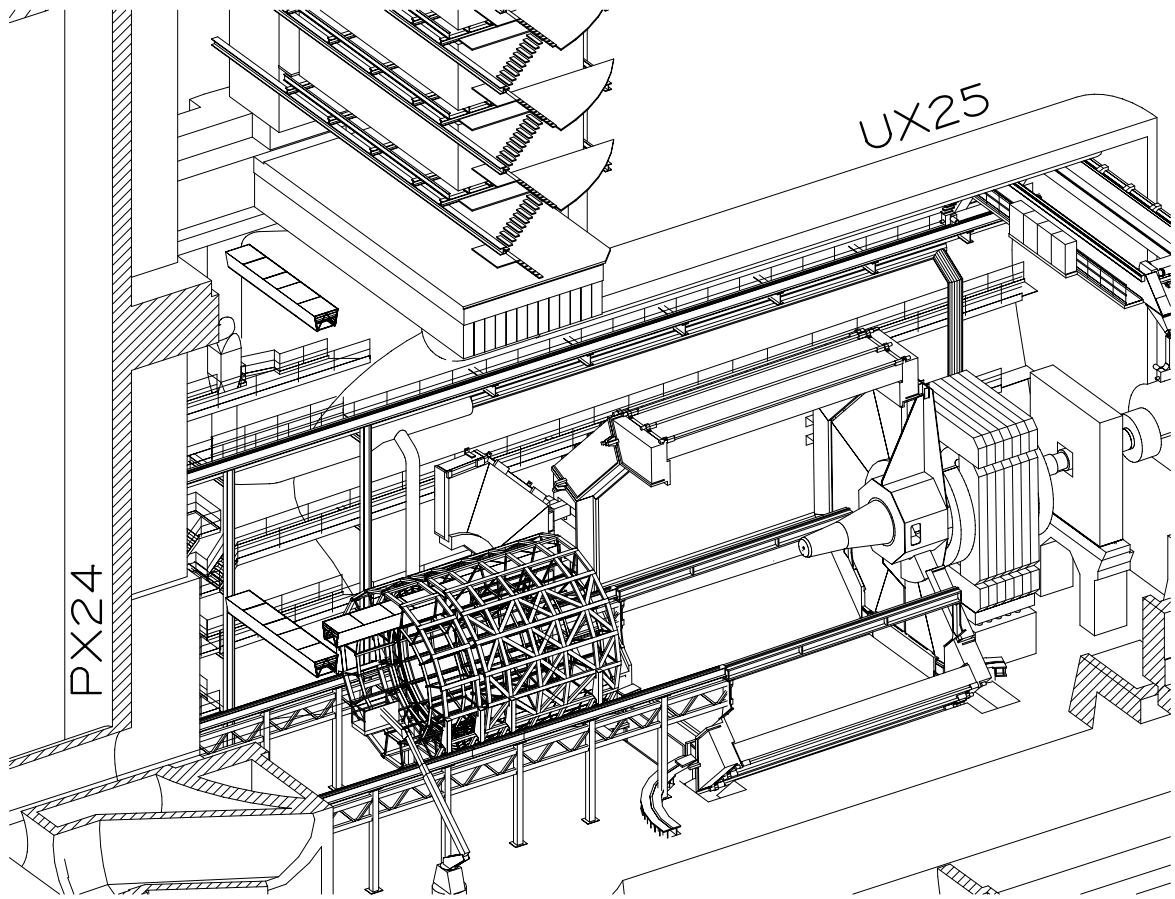


**Figure 16.5:** Installation of the TRD modules into the space frame inside the ALICE experimental area.

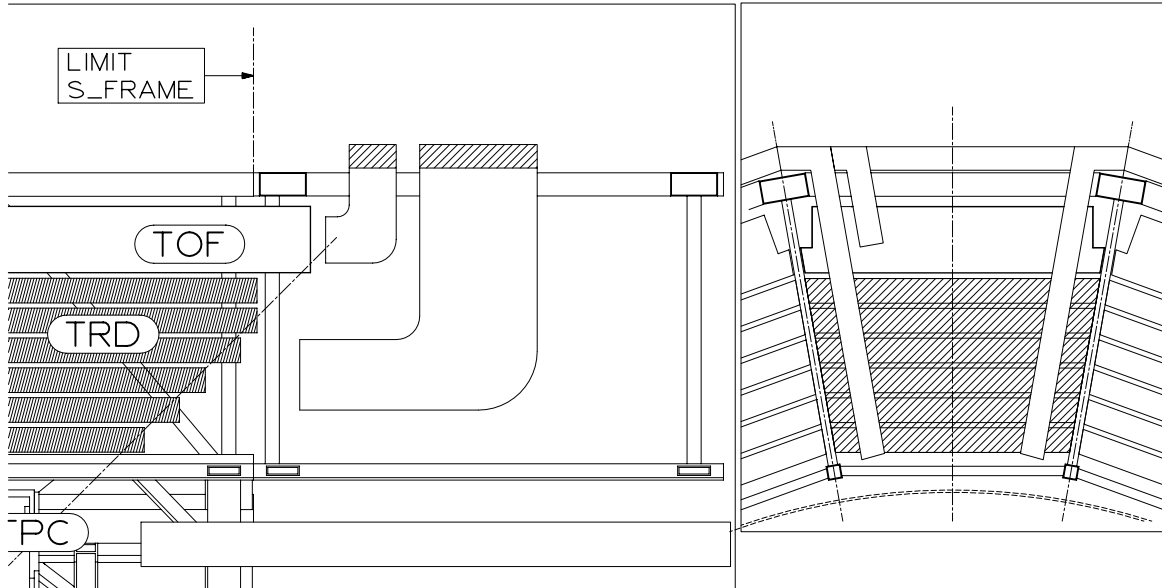


**Figure 16.6:** Conceptual routing of services. The services are attached to the outside of the support frame and distributed to the 18 supermodules.

The gas supply will come from the existing surface building, and the distribution units will be located on the shielding plug in PX24. In order to keep the losses and cost of cable installation as low as possible the racks for the power supplies will be installed as close as possible to the L3 magnet. They will be located at both sides of the L3 magnet at floor level. In the event of a removing a TRD module all services will have to be disconnected. This is facilitated by installing ‘patch-panels’ on the baby space frame.

## 16.4 Safety aspects

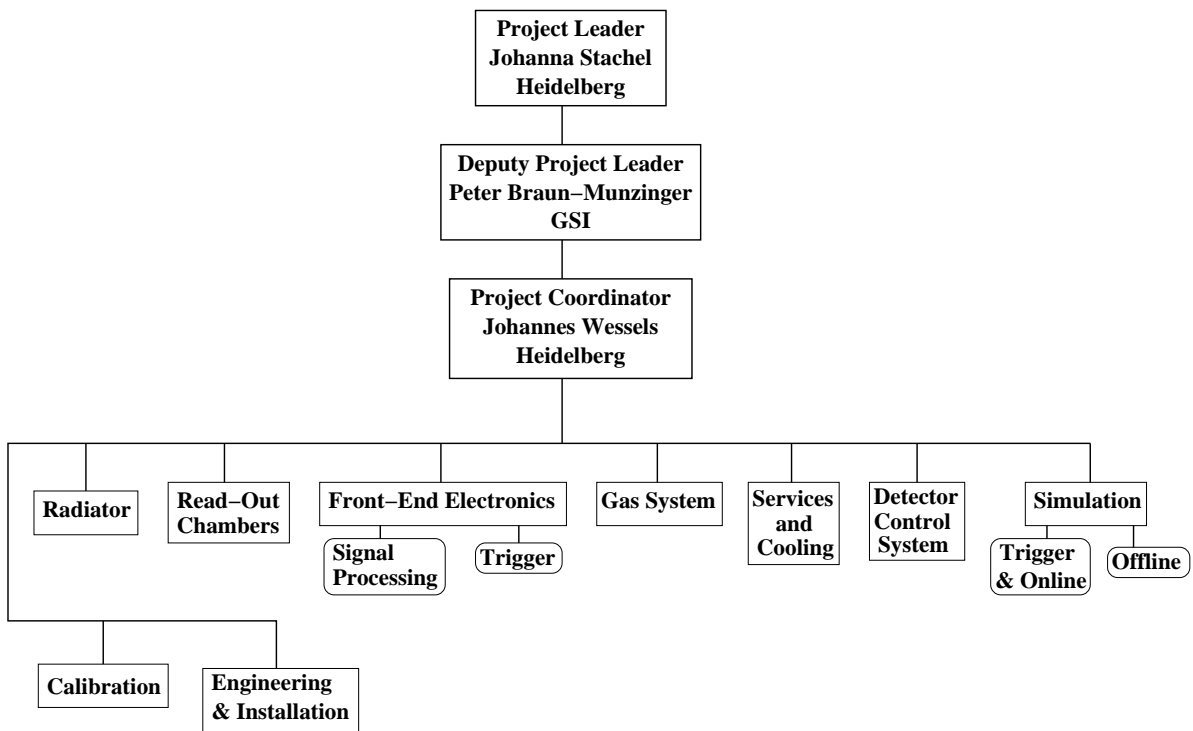
The TRD detector has been the subject of a recent Initial Safety Discussion (Ref. [2]). The outcome of this ISD was that the concept of the TRD detector did not include any major safety risks. The TRD detector uses non-flammable gas mixtures and the absence of toxic, corrosive, or flammable components makes the TRD an intrinsically safe detector. Apart from the initial construction period the handling of the TRD will always rely on the mechanical stability of the space frame, which will reduce the probability of any mechanical failure. The closed volume inside the dipole magnet and the part of the Muon spectrometer that penetrates into the L3 magnet will be separately monitored for both flammable gas and oxygen deficiency. The access to the inside of the L3 magnet will be restricted and regarded as a confined space. All construction materials and electronics printed circuit boards will conform to the CERN safety Instruction TIS IS41 and IS 23 concerning the use of plastic and other non-metallic materials at CERN with respect to fire safety and radiation resistance.

# 17 Responsibilities, cost, and schedule

---

## TRD organization

The ALICE TRD organization comprises a project leader, a deputy project leader, a project coordinator and nine sections: Radiator, Read-Out Chambers, Front-End Electronics, Gas System, Services and Cooling, Detector Control System (Slow Control), Simulation, Calibration, and Engineering & Installation. The section Front-End Electronics contains two groups, (i) the processing, storage and read-out of the detector signals, and (ii) the hardware and software preparing the level 1 trigger decision. Similarly, the Simulation section contains two groups, (i) simulations of the online tracking and trigger performance, and (ii) development and application of the offline software.



## TRD task force

The following persons have contributed to the work presented in this Technical Design Report.

A. Andronic, V. Angelov, A. Anjam, H. Appelhäuser, C. Blume, P. Braun-Munzinger, D. Bucher, O. Busch, A. Castillo-Ramirez, V. Catanescu, M. Ciobanu, S. Chernenko, V. Chepurnov, J. de Cuveland, H. Daues, A. Devismes, M. Dorn, M. Eichhorn, L. Efimov, O. Fateev, Ch. Finck, P. Foka, C. Garabatos, M. Gersabeck, P. Glässel, R. Glasow, M. Gutfleisch, J. Hehner, N. Heine, N. Herrmann, A. Ierusalimov, M. Ivanov, M. Keller, S. Keßen, F. Lesser, V. Lindenstruth, T. Lister, S. Martens, T. Mahmoud, A. Marin, M. Marquardt, D. Miskowiec, W. Niebur, Yu. Panebratsev, T. Peitzmann, V. Petracek, A. Petrov, M. Petrovici, A. Radu, C. Reichling, A. Reischl, K. Reygers, M.J. Richter, I. Rusanov, A. Sandoval, H. Sann, R. Santo, R. Schicker, R. Schneider, M. Schulz, W. Seipp, S. Sedykh, S. Shimanski, R.S. Simon, L. Smykov, H.K. Soltveit, H.J. Specht, J. Stachel, H. Stelzer, H. Tilsner, W. Verhoeven, B. Vulpescu, A. Walte, I. Weimann, S. Wende, J.P. Wessels, B. Windelband, O. Winkelmann, C. Xu, V. Yurevich, Yu. Zanevsky, O. Zaudtke, R. Ziegler, A. Zubarev.

## TRD TDR editorial committee

The TRD TDR editorial committee was composed of the following persons:

A. Andronic (editor), H. Appelshäuser, C. Blume, P. Braun-Munzinger, D. Bucher, P. Foka, C. Garabatos, N. Herrmann, V. Lindenstruth, A. Marin, V. Petracek, A. Sandoval, R. Simon, J. Stachel, J.P. Wessels

## Participating institutions

The following institutions will participate in the construction of the TRD detector.

- Bucharest, Romania, National Institute for Physics and Nuclear Engineering.
- Darmstadt, Germany, Gesellschaft für Schwerionenforschung
- Dubna, Russia, Joint Institute for Nuclear Research.
- Heidelberg, Germany, Kirchhoff Institut für Physik, Ruprecht-Karls-Universität.
- Heidelberg, Germany, Physikalisches Institut, Ruprecht-Karls-Universität.
- Kaiserslautern, Germany, Fachbereich Elektrotechnik und Informationstechnik, Universität Kaiserslautern.
- Münster, Germany, Institut für Kernphysik, Westfälische Wilhelms-Universität.

## Responsibilities

Table 17.1 presents the sharing of responsibilities for the construction of the TRD detector.

**Table 17.1:** Sharing of responsibilities for the construction and installation of the TRD detector.

Item	Institution
Radiator	Münster
Readout chambers	Bucharest, Dubna, GSI, HD (PI), Münster
FEE and trigger	Bucharest, HD (KIP), HD (PI), Kaiserslautern, Münster
Gas System	GSI
DCS	HD (PI)
HV, LV, cooling	GSI
Overall mechanics	HD (PI)

**Table 17.2:** Global cost of the TRD in kCHF.

Item	Cost (kCHF)
Radiator	423
Readout chambers	3 057
Services (HV/LV, cooling)	1 919
Front end electronics, trigger	7 825
Gas system	525
General	1 220
Total	14 969

## Cost estimate and resources

Wherever possible budgetary industrial quotes were used in the cost estimate of the TRD. This was done especially for special components such as: very large printed circuit boards, chip productions, special foams, and carbon fiber materials. In the budget for the readout chambers the numbers rely on actual costs from previous projects and projects under construction (CERES/NA45, ALICE/TPC). In the

cost for the electronics realistic estimates for chip yields and yields for multi-chip modules have been considered. The total cost quoted in Table 17.2 reflects the amount needed to build 100% of the detector.

The resources of the participating institutions cover at present 8.28 MCHF of the costs of the construction, installation and commissioning of the TRD. Additional funds are sought actively.

## **Construction program**

The design, construction, test, and installation schedule of the TRD components is summarized in Fig. 17.1. While it is hoped that additional funds can be found in the near future, the time-line for the construction of the TRD assumes production of roughly 50% of the detectors. Assumptions with regard to the design and prototyping phase of the various sub-projects are based on the current progress in these fields.

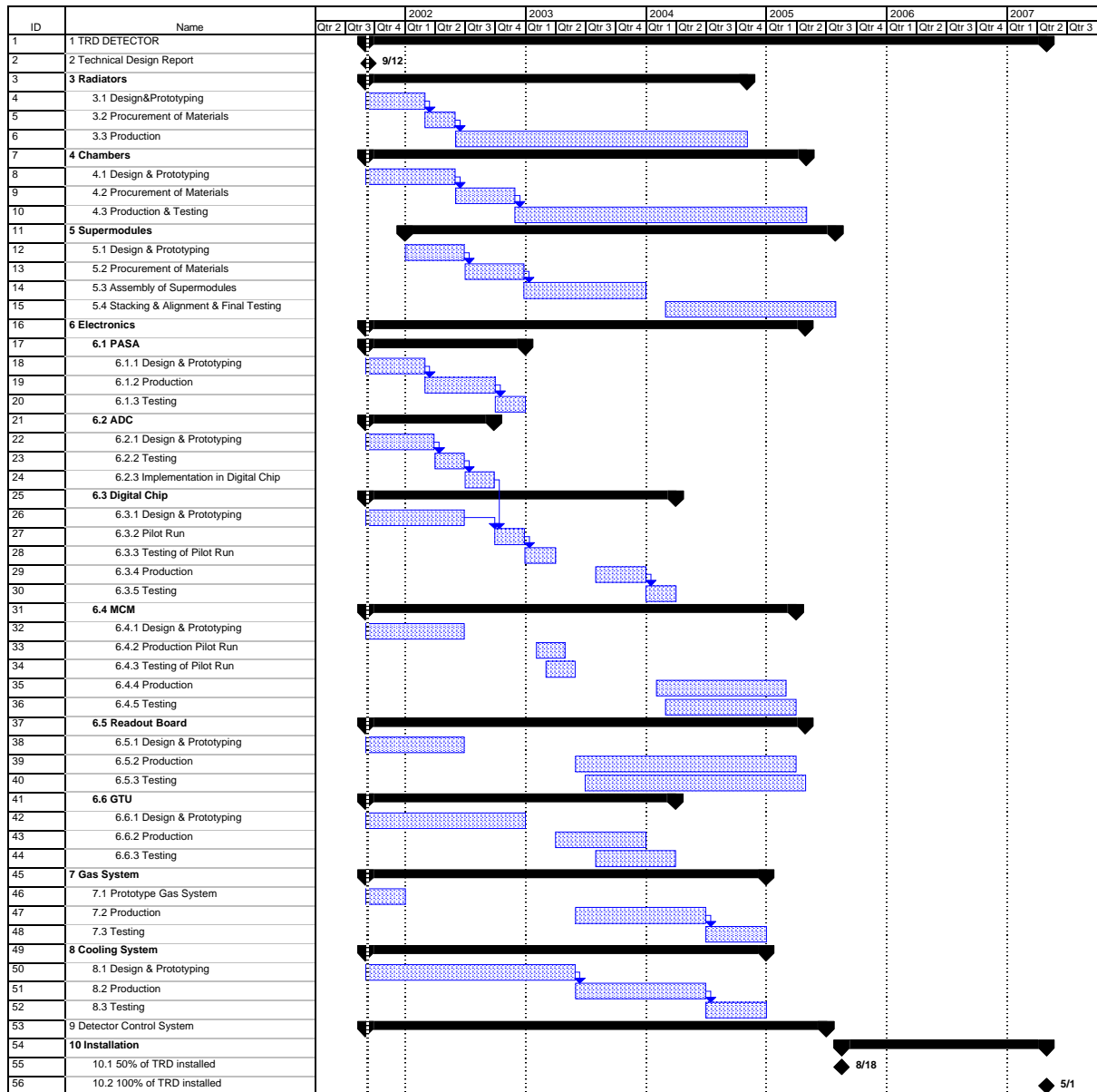


**Figure 17.1:** Chart of the time-line for the construction of the TRD.



# References

---

## Chapter 1

- [1] ALICE Collaboration, Technical Proposal, CERN/LHCC/95–71.
- [2] K.J. Eskola, K. Kajantie, P.V. Ruuskanen, Multiplicities for LHC Nuclear Collisions Using HERA Structure Functions, Phys. Lett. **B332** (1994) 191.
- [3] E.Shuryak, Two-stage equilibration in high energy heavy ion collisions, Phys. Rev. Lett. **68** (1992) 3270.
- [4] ALICE Collaboration, Technical Proposal, Addendum 1, CERN/LHCC/96–32.
- [5] ALICE Collaboration, A Transition Radiation Detector, Technical Proposal, Addendum 2, CERN/LHCC/99-13.
- [6] K. Adcox et al., PHENIX Collaboration, Phys.Rev.Lett. **86** (2001) 3500; B. Back et al., PHOBOS collaboration, nucl-ex/0105011.
- [7] A. Capella, C. Merino, J. Tran Thanh Van, Phys.Lett. **B265** (1991) 415 and Nucl.Phys. **A544** (1992) 581; K. Werner, Phys.Rept. **232** (1993) 87; A. Capella, A. Kaidalov, J. Tran Thanh Van, Heavy Ion Phys. **9** (1999) 169, hep-ph/9903244; N.S. Amelin, N. Armesto, C. Pajares, D. Sousa, hep-ph/0103060; K.J. Eskola, K. Kajantie, K. Tuominen, hep-ph/0106330.
- [8] D. Kharzeev and E. Levin, nucl-th/0108006.
- [9] P. Vande Vyvre, Physics Requirements for the ALICE DAQ system, ALICE-INT-2000-30.
- [10] P. Giubellino, S.Kiselev, W. Klempert, A. Morsch, G. Paic, J.P. Revol, K. Safarik, Day One Proton-Proton Physics with the ALICE Central Detector, ALICE-INT-2000-28.

## Chapter 2

- [1] J. Bielski, ALICE space frame design, February 2001, Annex to ALICE Internal Note 97–32 (1997) and new calculations in July 2001.

## Chapter 3

- [1] V.L. Ginzburg and I.M. Frank, Zh. Eskp. Teor. Fiz. **16** (1946) 15.
- [2] R. D. Appuhn et al., Nucl. Instr. Meth. **A263** (1988) 309.
- [3] G.E. Graham et al., Nucl. Instr. Meth. **A367** (1995) 224.
- [4] B. Dolgoshein, Nucl. Instr. Meth. **A326** (1993) 434.
- [5] produced by Röhm GmbH, D-64275 Darmstadt, Germany.
- [6] produced by Freudenberg Vliesstoffe KG, D-69465 Weinheim, Germany.

## Chapter 4

- [1] ALICE Collaboration, Technical Proposal, Addendum 2, CERN/LHCC/99-13.
- [2] R. Veenhof, Nucl. Instr. Meth. **A419** (1998) 726, <http://consult.cern.ch/writeup/garfield/>
- [3] S. Biaggi, Nucl. Instr. Meth. **A421** (1999) 234.
- [4] S. Afanasiev et al. (NA49 Collaboration), Nucl. Instr. Meth. **A430** (1999) 210.
- [5] G. Agakichiev et al. (CERES Collaboration), Nucl. Phys. **A661** (1999) 673c.
- [6] S. Wenig et al., GSI Annual Report (1994) 264.

- [7] W. Blum and L. Rolandi, Particle Detection with Drift Chambers, Springer Verlag, Berlin, Heidelberg, New York, 1993, ISBN 3-540-56425-X.
- [8] B. Yu et al., IEEE Trans. Nucl. Sci. **38** (1991) 454.
- [9] E. Mathieson, Nucl. Instr. Meth. **A270** (1988) 602.

## Chapter 5

- [1] IEEE Std 1596.3-1996. IEEE Standard for Low-Voltage Differential Signals (LVDS) for Scalable Coherent Interface (SCI).
- [2] A. Hastings, The Art of Analog Layout, Prentice Hall, 2001.
- [3] B. Bevensee, F. M. Newcomer, R. Van Berg, and H. H. Williams, IEEE Trans. Nucl. Sci. **43** (1996) 1725.
- [4] P. R. Gray, R. G. Meyer, Analysis and Design of Analog Integrated Circuits, Wiley, New York, 1993.
- [5] D. Johns, K. Martin, Analog Integrated Circuit Design, Wiley, New York, 1997.

## Chapter 6

- [1] F. Karsch, H. Satz, Z. Phys. **C51** (1991) 209.
- [2] P. Braun-Munzinger, J. Stachel, Phys. Lett. **B490** (2000) 196 [nucl-th/0007059].
- [3] ALICE Collaboration, Addendum 2 to ALICE Technical Proposal, CERN/LHCC/99-13.
- [4] H. Satz, Nucl. Phys. Proc. Suppl. **94** (2001) 204 [hep-ph/0009099].
- [5] P. Braun-Munzinger, J. Stachel, Nucl. Phys. **A690** (2001) 119 [nucl-th/0012064].
- [6] I. Koren, Computer Arithmetic Algorithms, Brookside Court Publisher, Amherst Massachusetts, 1998.
- [7] R.A. Boie, A.T. Hrisoho and P. Rehak, Nucl. Instr. Meth. **A192** (1982) 365.
- [8] B. Mota, L. Musa, R. Esteve and A. Jimenez de Parga, Digital implementation of a tail cancellation filter for the time projection chamber of the ALICE experiment, Prepared for 6th Workshop on Electronic for LHC Experiments, Cracow, Poland, 11-15 Sep 2000.
- [9] J.F. Gunion, R. Vogt, Nucl. Phys. **B492** (1997) 301.
- [10] A. Morsch, ALICE Luminosity and Beam Requirements, ALICE-INT-2001-10.
- [11] R.Gavai et al., Int. J. Mod. Phys. **A10** (1995) 3043.
- [12] G. Baur et al., CMS Collaboration, CMS Note 2000/60.
- [13] P.P. Yepes, CMS Collaboration, [nucl-ex/0104026].
- [14] D.M. Alde et al., E772 Collaboration, Phys. Rev. Lett. **66** (1991) 133.
- [15] V. Lindenstruth, D. Röhrlrich, ALICE High-Level Trigger Conceptual Design Report, internal ALICE note (2001)

## Chapter 7

- [1] ALICE Internal Note 2001-19 v.1, TPC data compression, May 2001.
- [2] TPC data compression, to be published.
- [3] ALICE Internal Note 98-21, ALICE Detector Data Link (ALICE DDL) Hardware Guide for the Front-end Designers (HG), 19 May 1998.
- [4] IEEE Std 1596.3-1996. IEEE Standard for Low-Voltage Differential Signals (LVDS) for Scalable Coherent Interface (SCI).
- [5] W. Buchanan, Handbook of Data Communication and Networks, Kluwer Academic Publishers, Boston, 1999.

## Chapter 8

- [1] See <http://nomadinfo.cern.ch/Public/detect/trd/trd.html>.
- [2] L'Air Liquide, Notice d'utilisation de l'épurateur Xe+CO<sub>2</sub>, DTA/CGP1/RLD/SG/87.0027, 1987.
- [3] M. Billault, Centre de Physique des Particules de Marseille, private communication.

## Chapter 9

- [1] C. Rivetta, CERN 2000-010; CERN/LHCC/2000-041 (25 Oct 2000).
- [2] P. Bonneau and M. Bosteels, CERN/LHCC 1999-33.
- [3] ALICE TPC TDR, CERN/LHCC 2000-001.

## Chapter 11

- [1] <http://AliSoft.cern.ch/offline/>
- [2] <http://root.cern.ch/>
- [3] GEANT 3.21 Package, CERN Program Library W5013.
- [4] V.C. Ermilova et al. Nucl. Instr. Meth. **145** (1977) 555.
- [5] TPC Technical Design Report, CERN/LHCC 2000-001.
- [6] G.F. Knoll, Radiation Detection and Measurements, Wiley, New York, 1979.
- [7] W. Blum and L. Rolandi, Particle Detection with Drift Chambers, Springer Verlag, Berlin, Heidelberg, New York, 1993, ISBN 3-540-56425-X.
- [8] F. Sauli, CERN Report 77-09 (1977).
- [9] J. Fischer et al., Nucl. Instr. Meth. **127** (1975) 525.
- [10] A.H. Walenta et al., Nucl. Instr. Meth. **161** (1979) 45.
- [11] W.-D. Herold et al., Nucl. Instr. Meth. **217** (1983) 277.
- [12] W.W.M. Allison and J.H. Cobb, Ann. Rev. Nucl. Part. Sc. **30** (1980) 253.
- [13] J. Apostolakis et al., Nucl. Instr. Meth. **A453** (2000) 597.
- [14] M.L. Cherry et al., Phys. Rev. **D 10** (3594) 1974.
- [15] X. Artru et al., Phys. Rev. **D 12** (1289) 1975.
- [16] L. Durand, Phys. Rev. **D 11** (89) 1975.
- [17] C.W. Fabjan and W. Struczinski, Phys. Lett. **B57** (1975) 483.
- [18] R.D. Appuhn et al., Nucl. Instr. Meth. **A263** (1988) 309.
- [19] <http://physics.nist.gov/PhysRefData/>
- [20] R. Veenhof, Nucl. Instr. Meth. **A419** (1998) 726, <http://consult.cern.ch/writeup/garfield/>.
- [21] E. Mathieson et al. Nucl. Instr. Meth. **A270** (1988) 602.
- [22] Particle Data Group, Eur. J. Phys. **C3** (1) 1998.

## Chapter 12

- [1] ALICE Collaboration, Technical Proposal, CERN/LHCC/95-71.
- [2] ALICE Collaboration, A Transition Radiation Detector, Technical Proposal, Addendum 2, CERN/LHCC/99-13.
- [3] P. Braun-Munzinger, Nucl. Phys. **A661** (1999) 261.
- [4] ALICE Internal Note 32-1995.
- [5] D. Kharzeev and E. Levin, BNL-NT-01/18, nucl-th/0108006.
- [6] B.B. Back et. al., PHOBOS Collaboration, nucl-ex/01089009.
- [7] K.J. Eskola et. al., hep-ph/0104010.
- [8] F. Abe et al., Phys. Rev. Lett. **61** (1988) 1819.

- [9] X.N. Wang and M. Gyulassy, Phys. Rev. **D44** (1991) 3501.
- [10] G. David, PHENIX Collaboration, nucl-ex/0105014.
- [11] G.Baur et al., CMS Collaboration, CMS Note 2000/60.
- [12] N. Carrer, ALICE-AW-2001-14; Estimate of heavy-flavor production rates for ALICE simulations.
- [13] T. Sjostrand, Comput. Phys. Commun. **39** (1986) 347.
- [14] A.D. Martin et al., Eur. J. Phys. **C4** (1998) 463.
- [15] H.L. Lai et al., Eur. J. Phys. **C12** (2000) 375.
- [16] M. Gluck, E. Reya, A. Vogt, Eur. J. Phys. **C5** (1998) 461.
- [17] K.J. Eskola et al., Eur. J. Phys. **C9** (1999) 61.
- [18] AliRoot <http://AliSoft.cern.ch/offline/>, Root <http://root.cern.ch/>.
- [19] GEANT 3.21 Package, CERN Program Library W5013.
- [20] J. Apostolakis et al., Nucl. Instr. Meth. **A453** (2000) 597. .
- [21] A. Fasso et al., Proc. IV Int. Conf. on Calorimeters and their Applications, World Scientific, Singapore, 1994, p. 493.
- [22] A. Morsch, <http://AliSoft.cern.ch/offline/simulation.html..>
- [23] ALICE Internal Note 28–2001.
- [24] A. Wroblewski and L. Leistam, proceedings of the Fourth International Congress on Thermal Stresses, June 8-11 2001, Osaka Japan, pp. 433-436.
- [25] ALICE Internal Note 36–2001; TRD acceptance for different geometrical configurations.
- [26] ALICE Collaboration, Inner Tracking System, Technical Design Report, CERN/LHCC/99-12.
- [27] ALICE Collaboration, Time Projection Chamber, Technical Design Report, CERN/LHCC/2000-001.

## Chapter 13

- [1] L. Jirden, ALICE Detector Control System (DCS) Project, Internal Note ALICE-INT-2001-24
- [2] O. Villalobos et al., Internal Note ALICE 98-23. New updated version in preparation.
- [3] ALICE/LHCb Teams, Internal Note ALICE/98-03.
- [4] D. Blanc et al., CERN-EP-071 (EOS) May 1998.
- [5] The OPC foundation. See for instance:  
<http://www.opceurope.org> and <http://www.opcfoundation.org/opc-public-tech.htm>
- [6] The OLE/COM and DCOMM technologies. See for instance:  
<http://www.microsoft.com/activex/default.asp>
- [7] CMS The tracker project, Technical design report, CERN/LHCC 98-6, CMS TDR 5, 15 April 1998.

## Chapter 14

- [1] B. Yu et al., IEEE Trans. Nucl. Sci. **38** (1991) 454.
- [2] H.G. Essel and N. Kurz, IEEE Trans. Nucl. Sci. **47** (2000) 337.
- [3] RIO2 8062, Creative Electronic Systems S.A., <http://www.ces.ch>.
- [4] W. Blum and L. Rolandi, Particle Detection with Drift Chambers, Springer-Verlag, 1994.
- [5] D.L. Fancher and A.C. Schaffer, IEEE Trans. Nucl. Sci. **26** (1979) 150.
- [6] S.R. Amendolia et al., Nucl. Instr. Meth. **217** (1983) 317.
- [7] J.S. Gordon and E. Mathieson, Nucl. Instr. Meth. **227** (1984) 267; E. Mathieson and J.S. Gordon, Nucl. Instr. Meth. **227** (1984) 277; E. Mathieson, Nucl. Instr. Meth. **A270** (1988) 602.
- [8] A. Andronic et al., IEEE Trans. Nucl. Sci. **48** (2001) 1259; nucl-ex/0102017.
- [9] R.S. Simon, Prog. Part. Nucl. Phys. **42** (1999) 247.

- [10] H. Stelzer, Nucl. Instr. Meth. **A310** (1991) 103.
- [11] TRD Proposal, CERN/LHCC 99-13, <http://www.gsi.de/~alice>.
- [12] R. Veenhof, Nucl. Instr. Meth. **A419** (1998) 726, <http://consult.cern.ch/writeup/garfield/>
- [13] S. Biaggi, Nucl. Instr. Meth. **A421** (1999) 234.
- [14] L.G. Christophorou et al., Nucl. Instr. Meth. **171** (1980) 491.
- [15] U. Becker et al., Nucl. Instr. Meth. **A421** (1999) 54.
- [16] Y. Watase et al., Nucl. Instr. Meth. **A248** (1986) 379.
- [17] R.D. Appuhn et al., Nucl. Instr. Meth. **A263** (1988) 309.
- [18] C.W. Fabjan, Nucl. Instr. Meth. **146** (1977) 343.
- [19] M. Holder and H. Suhr, Nucl. Instr. Meth. **A263** (1988) 319.
- [20] J.-F. Detoeuf et al., Nucl. Instr. Meth. **A265** (1988) 157.
- [21] E. O'Brien et al., IEEE Trans. Nucl. Sci. **40** (1993) 153.
- [22] W. Brückner et al., Nucl. Instr. Meth. **A378** (1996) 451.
- [23] A. Büngener et al., Nucl. Instr. Meth. **214** (1983) 261.
- [24] G. Bassompierre et al., Nucl. Instr. Meth. **A411** (1998) 63.
- [25] C.W. Fabjan et al., Nucl. Instr. Meth. **185** (1981) 119.
- [26] T. Akesson et al., Nucl. Instr. Meth. **A372** (1996) 70.
- [27] V. Egorytchev et al., Nucl. Instr. Meth. **A453** (2000) 346.
- [28] H.J. Butt et al., Nucl. Instr. Meth. **A252** (1986) 483.
- [29] K. Ackerstaff et al., Nucl. Instr. Meth. **A417** (1998) 230.
- [30] B. Dolgoshein, Nucl. Instr. Meth. **A326** (1993) 434.
- [31] R.A. Boie et al., Nucl. Instr. Meth. **192** (1982) 365.
- [32] ALICE TPC Technical Design Report, ALICE TDR 7, CERN/LHCC 2001-001 (Jan. 2000).

## Chapter 16

- [1] The mechanical properties of the ALICE space frame supporting structure, J. Bielski, ALICE Internal Note / 97-32, November 1997. Updated with an annex in February 2001 and new calculations in July 2001.
- [2] Initial Safety Discussion for the ALICE TPC Detector, TIS/GS/WW-cn(2001-12), August 2001



# Glossary

---

## Detector nomenclature

Module (M)	one unit of TRD (readout chamber plus radiator)
Layer (L)	$5 \times M$ in longitudinal direction
Stack (S)	$6 \times M$ in radial direction
Supermodule (SM)	$5 \times S$ in longitudinal direction $6 \times L$ in radial direction
Plane (P)	one layer in full azimuth, P= $18 \times 5 \times M$

## Acronyms

### A

ADC	Analog to Digital Converter
ALTO	ALICE TPC Readout (digital chip)
ALU	Arithmetic Lookup Unit

### B

BGA	Ball Grid Array
-----	-----------------

### C

CAN	Controller Area Network
CMOS	Complementary Metal-Oxide-Semiconductor
COG	Center Of Gravity
CPU	Central Processing Unit
CTP	Central Trigger Processor

### D

DAC	Digital to Analog Converter
DAQ	Data Aquisition
DAQC	Data Acquisition Control
DC	Drift Chamber (also used for Direct Current)
DCOM	Distributed Component Object Model
DCS	Detector Control System
DRAM	Dynamic Random Access Memory

### E

ENC	Equivalent Noise Charge
EOS	Electrical Over-Stress
ESD	Electrostatic Discharge

**F**

FADC	Flash Analog to Digital Converter
FEE	Front End Electronics
FIFO	First In First Out
FF	Flip-Flop
FPC	Flat Printed Circuit
FPGA	Field Programmable Gate Array
FWHM	Full Width Half Maximum

**G**

GND	Ground
GRF	Global Register File
GTU	Global Tracking Unit

**H**

HBM	Human Body Model
HLT	High Level Trigger
HTTP	Hyper Text Transfer Protocol
HMPID	High Momentum Particle Identification Detector
HV	High Voltage

**I**

I2C	Inter-IC
IP	Internet Protocol
ITS	Inner Tracking System

**J**

JCOP	Joint Control Project
JTAG	Joint Test Action Group

**L**

L0	Level-0 (trigger)
L1	Level-1 (trigger)
L1A	Level-1 Accept
L1R	Level-1 Reject
L2	Level-2 (trigger)
L2A	Level-2 Accept
L2R	Level-2 Reject
LHC	Large Hadron Collider
LN <sub>2</sub>	Liquid Nitrogen
LSB	Least Significant Bit
LTU	Local Tracking Unit
LUT	Look-Up Table
LV	Low Voltage
LVDS	Low Voltage Differential Signal

**M**

MBS	Multi Branch System (DAQ)
MCM	Multi Chip Module
MIMD	Multiple Instruction Multiple Data
MIP	Minimum Ionizing Particle
MIPS	Mega Instructions Per Second
MM	Machine Model
MMI	Man-Machine Interface
MSB	Most Significant Bit
MWPC	Multi-Wire Proportional Chamber

**N**

NMOS	Negative Channel Metal-Oxide-Semiconductor
------	--

**O**

OE	Output Enable
OLE	Object Linking and Embedding
OPC	OLE for Process Control

**P**

PASA	Preamplifier/shaper
PCI	Peripheral Component Interconnect
PHOS	Photon Spectrometer
PID	Particle Identification
PLC	Programable Logic Controller
PLL	Phase Locked Loop
PMOS	Positive Channel Metal-Oxide-Semiconductor
PRF	Pad Response Function
pRF	private Register File

**Q**

QGP	Quark-Gluon Plasma
-----	--------------------

**R**

RAM	Random Access Memory
RMS	Root Mean Square
ROM	Read-Only Memory

**S**

SCADA	Supervisory Control And Data Acquisition
SIMM	Single Inline Memory Module
SMT	Surface-Mount Technology
SRAM	Static RAM
S/N	Signal-to-Noise ratio

**T**

TMU	Track-Matching Unit
TOF	Time-Of-Flight (Detector)
TP	Tracklet Processor
TPC	Time Projection Chamber
TPP	Tracklet Preprocessor
TR	Transition Radiation
TRC	Trigger Control
TRD	Transition Radiation Detector
TRF	Time Response Function
TTC	Timing, Trigger and Control

**V**

VDD	Power Supply for Digital part of FEE
VDDA	Power Supply for Analog part of FEE

**W**

WE	Write Enable
----	--------------